

**UNIVERSIDADE FEDERAL DO RIO GRANDE DO SUL  
PROGRAMA DE PÓS GRADUAÇÃO EM FÍSICA  
DEPARTAMENTO DE ASTRONOMIA**

**O gás ionizado em galáxias ativas no *survey* MaNGA**

The ionized gas in active galaxies in the MaNGA survey

Janaína Corrêa do Nascimento

Tese de Doutorado realizada sob orientação da Prof. Dra. Thaisa Storchi Bergmann e coorientação do Prof. Dr Rogério Riffel apresentada ao Programa de Pós- Graduação em Física da Universidade Federal do Rio Grande do Sul, como requisito parcial para a obtenção do grau de Doutora em Ciências.

Porto Alegre, RS, Brasil  
Outubro de 2019

\* Trabalho financiado pelo CNPq

# Resumo

Apresentamos mapas para as distribuições de fluxo nas linhas de emissão, excitação, densidade superficial de massa de gás ionizado e taxa de formação estelar para 150 Núcleos Ativos de Galáxias (AGN) observados com o SDSS-IV MaNGA, comparando-os com os obtidos para uma amostra controle de galáxias não ativas. Descobrimos que, para os AGNs *early-type*, o gás ionizado é mais concentrado na região nuclear quando comparado com as galáxias de controle, enquanto que para as galáxias *late-type* a distribuição de gás é semelhante à das galáxias de controle, sendo distribuída mais uniformemente por todo a galáxia. A massa total de gás ionizado varia de  $\approx 10^4 M_{\odot}$  a  $\approx 10^9 M_{\odot}$ . A principal diferença entre os AGNs e os controles está na densidade superficial central de massa de gás ionizado – dentro de  $0,2R_e$  (raio efetivo) – que é maior para os AGNs do que para os controles, com uma diferença maior observada para as *early-types* do que para as *late-types*. Essa diferença entre os AGNs e os controles é maior para os AGNs de maior luminosidade e torna-se mais baixa à medida que a luminosidade dos AGNs diminui. Calculamos os perfis espaciais médios da densidade superficial de massa de gás ionizado e mostramos que eles decrescem mais rapidamente com o raio para os AGNs do que para os controles dentro de  $0,4R_e$  no caso dos AGNs de maior luminosidade ( $L(\text{[OIII]}\lambda 5007) \geq 3.8 \times 10^{40} \text{ erg s}^{-1}$ ) sendo semelhantes aos dos controles além deste raio e para AGNs de menor luminosidade. Calculamos a taxa de formação estelar SFR nas regiões HII do corpo das galáxias hospedeiras de AGN e controles, encontrando uma diferença somente para as galáxias *early-type*, para as quais as que têm AGN apresentam um pequeno excesso no valor da SFR em relação às galáxias de controle. Estudamos também a relação entre o raio  $R_{NLR}$  (onde NLR é a sigla para representar a *Narrow Line Region*) da região ionizada pelo AGN e a luminosidade L[OIII] do AGN e encontramos uma correlação positiva. Esta correlação indica que a região de gás ionizado pelo AGN cresce com a luminosidade do mesmo, de forma semelhante à encontrada previamente para a *Broad Line Region* e por outros autores para a NLR. Finalmente, obtivemos a metalicidade do gás para as regiões HII no corpo da galáxia que, extrapolada para a região central, mostra um bom acordo com a metalicidade derivada para o gás da NLR a partir de calibrações em termos de razões de linhas de emissão obtidas a partir de modelos de fotoionização.

# Abstract

We present maps for the ionized gas flux distributions, excitation, surface mass density and star formation rates for 150 Active Galactic Nuclei (AGN) observed with SDSS-IV MaNGA, and compare them with those of a control sample of non-active galaxies. We find that, for the early-type AGN, the ionized gas is more concentrated in the nuclear region, when compared with the controls, while for the late-type galaxies the gas distribution is similar to that in the controls, being spread throughout the galaxies. The total ionized gas mass ranges from  $\approx 10^4 M_\odot$  to  $\approx 10^9 M_\odot$ . The main difference between the AGN and controls is on the central ionized gas surface mass density – within  $0.2R_e$  (effective radius) – that is larger for the AGN than for the controls, with a larger difference observed for the early-type than for the late-type galaxies. This difference between the AGN and controls is highest for the highest luminosity AGN and becomes lower as the AGN luminosity decreases. We have calculated average profiles of the gas surface mass density and show that they are steeper in the AGN when compared to controls within the inner  $0.4R_e$  for the highest luminosity AGN ( $L(\text{[OIII]}\lambda 5007) \geq 3.8 \times 10^{40} \text{ erg s}^{-1}$ ), being similar to those of the controls beyond this radius and for lower luminosity AGN. We have obtained the star-formation rate SFR for the HII regions along the body of the AGN host galaxies and controls, finding a difference only for the early-type galaxies, for which the AGN hosts present a small excess in the integrated SFR as compared to the control galaxies. We have also investigated the relation between the radius of the region ionized by the AGN  $R_{NLR}$  (where NLR stands for Narrow-Line Region) and the AGN luminosity  $L[\text{OIII}]$ , finding a positive correlation. This correlation indicates that the radius of the region ionized by the AGN increases with its luminosity, similarly to previously found for the Broad-Line Region and for the NLR itself in previous studies. Finally, we have derived the gas metallicity for the HII regions over the body of the galaxy that, when extrapolated to the central region, shows good agreement with the gas metallicity of the NLR obtained from calibrations in terms of emission-line ratios derived from photoionization models.

# Conteúdo

<b>Conteúdo</b>	<b>III</b>
<b>1 Introdução</b>	<b>2</b>
1.1 Galáxias ativas . . . . .	2
1.2 Paradigma do Buraco Negro Supermassivo . . . . .	4
1.3 Principais componentes de um AGN . . . . .	5
1.4 A coevolução entre o SMBH e a galáxia hospedeira . . . . .	7
1.5 Excitação do gás . . . . .	10
1.5.1 Diagramas diagnóstico . . . . .	10
1.5.2 A extensão R da região ionizada pelo AGN . . . . .	11
1.5.3 A massa de gás ionizado e a taxa de formação estelar . . . . .	13
1.5.4 A abundância química do gás . . . . .	15
1.6 O projeto MaNGA . . . . .	17
1.7 Resultado anteriores com O MaNGA (e outros <i>surveys</i> ) . . . . .	19
1.7.1 O AGNIFS no MaNGA . . . . .	20
1.8 Objetivos . . . . .	23
<b>2 Amostra</b>	<b>26</b>
2.1 Seleção da amostra de galáxias hospedeiras de AGN e da amostra de controle . . . . .	26
<b>3 Resultados</b>	<b>36</b>
3.1 A relação R vs. L[OIII] . . . . .	36
3.2 A taxa de formação estelar SFR . . . . .	37
3.3 Densidades de massa superficial de gás ionizado . . . . .	40
3.4 Massa total de gás ionizado . . . . .	42
<b>4 Conclusões</b>	<b>64</b>

**CONTEÚDO**

---

**1****Apêndice A** **68****Referências Bibliográficas** **148**

# Capítulo 1

## Introdução

### 1.1 Galáxias ativas

Durante as últimas décadas, observações com telescópios cada vez mais sofisticados e sensíveis, bem como trabalhos teóricos, levaram os estudos sobre núcleos ativos de galáxias (AGN, do inglês *Active Galactic Nuclei*) para um lugar de destaque na pesquisa em astronomia extragalática. Após passado mais de um século das primeiras observações que os registraram, ficou claro que eles estão entre as fontes de energia mais poderosas do Universo, emitindo radiação em todas as faixas de energia e cobrindo uma grande faixa de luminosidade.

A fonte dessa energia foi fortemente debatida por um longo tempo, a idéia predominante sendo do acréscimo de massa a um buraco negro supermassivo (SMBH, do inglês *Supermassive Black Hole*), por exemplo em (Salpeter, 1964, Lynden-Bell, 1969, Rees, 1984). Um conjunto de evidências levaram a um consenso sobre este cenário. A evidência da existência de SMBHs nas regiões internas das galáxias no Universo local foi estabelecida através do trabalho conjunto de muitos estudos usando a modelagem dinâmica da cinemática de estrelas, gás – através de suas linhas de emissão – e masers moleculares (Sargent et al., 1978, Dressler & Richstone, 1988, Harms et al., 1994, Miyoshi et al., 1995). Os AGNs surgem quando o SMBH está sendo “alimentado” pela captura de matéria, que forma um “disco de acreção” antes de cair no buraco negro, por conservação de momentum angular.

Atualmente os AGNs englobam uma ampla taxonomia que inclui Seyfert-1s, Seyfert-2s, AGNs com jatos de partículas aceleradas por campos magnéticos, sem jatos, QSOs, BL Lac, Blazars etc., conforme discutem Padovani et al. (2017). Hoje em dia sabe-se que os AGNs sem jatos compreendem cerca de 90% da população de AGNs. Uma grande parte destas categorias de AGNs pode ser explicada pelo

chamado “Modelo Unificado” (Antonucci, 1993, Urry & Padovani, 1995).

Os representantes mais luminosos dos AGNs são os quasares (*Quasi Stellar radio sources*), o seu espectro mostra linhas de emissão fortes que podem ser extremamente largas, com uma largura relativa de  $\Delta\lambda / \lambda \approx 0,03$ . A largura da linha é causada por velocidades muito altas do gás que emite essas linhas, que podem chegar a  $\Delta v \approx 10000 \text{ km s}^{-1}$ . A fonte central dos quasares é muito mais brilhante que o restante da galáxia, fazendo com que essas fontes apareçam quase como puntuais em imagens (o núcleo brilhante ofusca o resto da galáxia). Sua luminosidade corresponde a magnitudes absolutas de  $M_r \sim -24$ , e são encontrados tipicamente em alto *redshift*. Em Bañados et al. (2018) é apresentada a descoberta de um quasar a  $z \sim 6$ , com uma emissão de rádio que é uma ordem de magnitude mais brilhante do que qualquer outra fonte de rádio conhecida nesses redshifts.

Muitas propriedades dos quasares se assemelham às das galáxias Seyfert tipo 1, que são aquelas que apresentam linhas de emissão permitidas muito mais largas do que as proibidas. Nas galáxias Seyfert 2 as linhas permitidas e as linhas proibidas têm largura semelhante (Weedman, 1970, Khachikian & Weedman, 1971). As Seyfert 1 também têm um núcleo muito luminoso e linhas de emissão permitidas muito largas, e, por esse motivo, os quasares são frequentemente interpretados como membros extremos dessa classe em termos de luminosidade, alguns deles emitindo mais de mil vezes a luminosidade da nossa galáxia.

Outros processos, além das altas luminosidades nucleares, também são observados em decorrência da atividade nuclear, como por exemplo, processos de “retroalimentação” do SMBH (*feedback*). Estes processos incluem a emissão de radiação que ioniza grandes regiões de gás circundando o núcleo e também de ejeções de matéria, seja na forma de jatos de partículas relativísticas, originados na borda interna do disco de acreção ou na forma de ventos originados de partes mais externas do disco de acreção.

Há vários processos que podem desencadear a acreção de matéria ao SMBH. Um deles é a fusão entre galáxias, o que tem sido mostrado por meio de simulações cosmológicas, que além de desencadear a formação estelar, também geram influxo de gás que, ao chegar ao núcleo da galáxia começa a alimentar (*feed*) o SMBH, acionando a atividade nuclear, e originando emissão de radiação e os *outflows* a partir do disco de acreção.

Por muito tempo, esses núcleos ativos, que residem no centro das galáxias, foram amplamente considerados objetos raros. Entretanto, a teoria de evolução de galáxias e observações atuais permitem concluir que SMBHs crescem no núcleo das

galáxias através de eventos de acreção de massa, durante os quais eles são visíveis como AGNs. Com evidências observacionais cada vez mais robustas sobre a evolução de galáxias e AGNs, atualmente acredita-se que os SMBHs residem no núcleo da maioria das galáxias massivas (principalmente nas que têm uma componente bojo), e consequentemente todas essas galáxias sofrem atividade nuclear – ou seja, tornam-se AGNs, possivelmente mais do que uma vez durante sua “vida”. Porém, a atividade nuclear somente pode ser observada quando há um reservatório de gás disponível para “alimentar” (*feed*) o SMBH. Trabalhos teóricos agora sugerem que a atividade nuclear tenha influenciado a evolução da galáxia hospedeira bem como o ambiente em larga escala em que reside. No entanto, a quantificação dos efeitos físicos/influência do AGN na evolução das galáxias continua a ser uma área aberta de pesquisa, com muitas questões importantes ainda não respondidas.

## 1.2 Paradigma do Buraco Negro Supermassivo

Com raio menor que um parsec, a parte central dos AGNs (ver descrição dos componentes abaixo) no centro das galáxias são regiões não resolvidas espacialmente, cuja distribuição espectral de energia (*Spectral Energy Distribution* – SED) não pode ser considerada originária da radiação de estrelas. Os AGNs de baixa luminosidade como os LINER’s (*Low-ionization emission-line region*, Heckman, 1980), apresentam luminosidades bolométricas no intervalo  $L_{Bol} \sim 10^{42-43}$  erg s $^{-1}$ , enquanto que Quasares possuem  $L_{Bol} \sim 10^{46-48}$  erg s $^{-1}$ . Luminosidades intermediárias entre as dos núcleos LINER’s e de Quasares são observadas nas galáxias Seyferts, que têm luminosidades típicas de  $L_{Bol} \sim 10^{43-46}$  erg s $^{-1}$ .

A enorme quantidade de energia liberada do disco de acreção é muito maior do que a liberada em reações de fusão nuclear, como no caso das estrelas. Como citado anteriormente, um mecanismo mais poderoso e eficiente – o acréscimo da matéria a um buraco negro, é a explicação mais plausível. A luminosidade liberada durante um processo de acreção  $L$ , pode ser quantificada pela equação abaixo, onde  $\dot{m}$  é a taxa de acreção de massa ao SMBH e  $\eta$  é a eficiência de conversão de energia gravitacional em radiação.

Podemos expressar este resultado em termos da taxa de conversão da energia de repouso do corpo de massa  $m$  em radiação, com uma eficiência  $\eta$ :

$$L = \eta \dot{m} c^2 \quad (1.1)$$

A eficiência resultante desse processo ( $\eta \sim 0.1$ ) é muito maior do que a obtida nos processos de fusão nuclear em estrelas ( $\eta_{star} \sim 0.007$ ).

A máxima  $L$  possível é atingida quando a pressão de radiação (para “fora”) gerada pelos processos de acreção no buraco negro é igual à pressão gravitacional da matéria circundante (para “dentro”)(Peterson, 1997); essa luminosidade é chamada de *Luminosidade de Eddington*:

$$L = \frac{4\pi G c m_p M_\bullet}{\sigma_T} \quad (1.2)$$

onde  $m_p$  é a massa do próton,  $\sigma_T$  é a sessão de choque de espalhamento de Thompson e  $M_\bullet$  é a massa do SMBH.

### 1.3 Principais componentes de um AGN

O modelo padrão de um AGN tem como elemento principal um SMBH circundado por um disco de acreção. Outra estruturas presentes são ilustradas na figura 1.1 de forma esquemática.

- Disco de acreção: Tem papel fundamental no processo de acreção de matéria ao SMBH central, uma vez que, através dele, a energia potencial gravitacional é convertida em energia térmica, cinética e luminosa.
- Região de linhas largas-BRL: Umas das características notáveis do espectro dos AGNs tipo 1 é a presença de linhas largas, isto é, linhas de emissão permitidas do Hidrogênio e Hélio com valores de largura a meia altura ou FWHM (*Full Width Half Maximum*) tipicamente na faixa de  $2000 \text{ km s}^{-1} \lesssim \text{FWHM}_{broad} \lesssim 5000 \text{ km s}^{-1}$ . Esta característica é resultado do alargamento *Doppler* das linhas emitidas pelo gás da BLR, que se move no campo gravitacional do SMBH e é ionizado pelos fótons emitidos pelo disco de acreção. O raio da BRL é de  $\approx 0.01 - 0.1 \text{ pc}$ , e pode ser determinado através da técnica de *mapas de reverberação* (Peterson & Wandel, 2000, Peterson et al., 2004), no qual se mede o atraso entre as variações do fluxo das linhas largas de emissão e as variações do fluxo do contínuo, já que qualquer mudança na emissão contínua leva um tempo finito para alcançar as nuvens da BLR.
- Meio obscurecedor: De acordo com o modelo unificado, as partes centrais dos AGNs acima descritas (disco de acreção e BLR), são **circundadas** por uma região opticamente espessa na forma e um toróide de gás molecular e

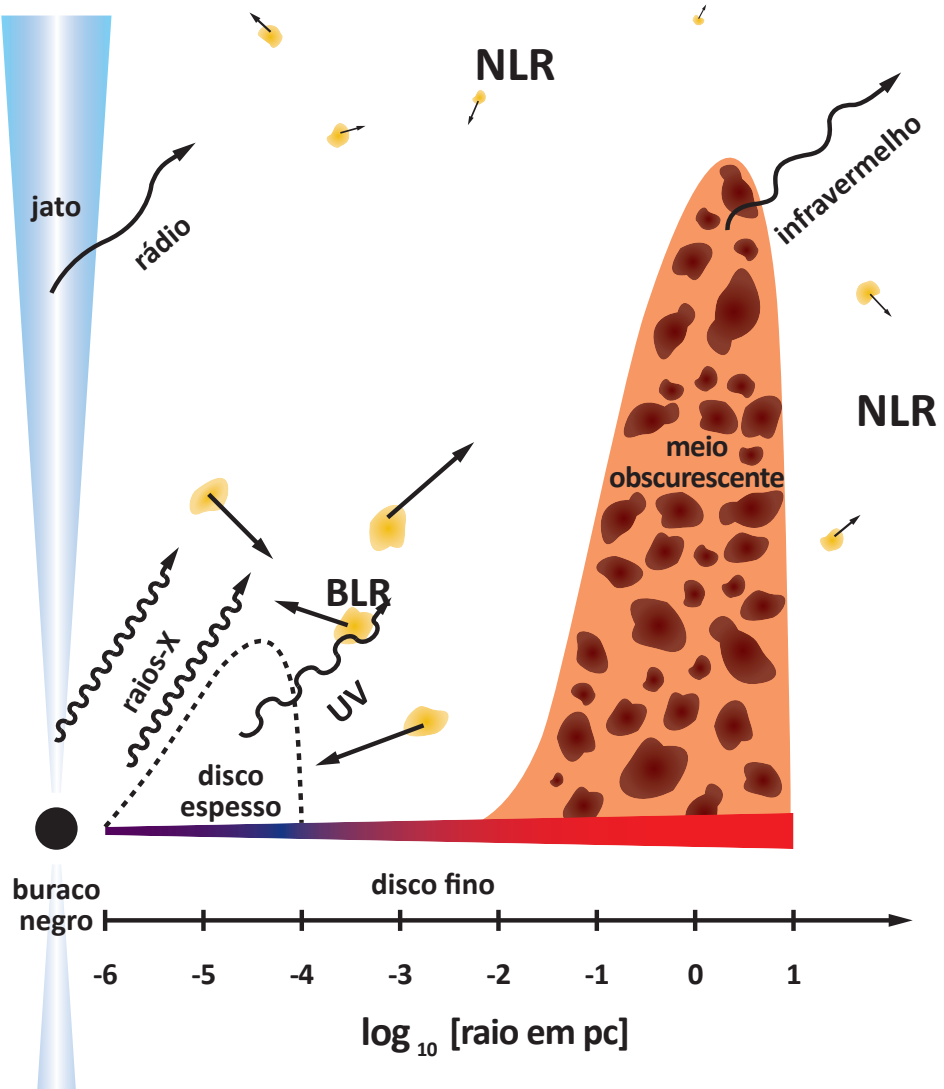


Figura 1.1: Esquema representativo das principais estruturas presentes nos AGNs: SMBH, disco de acreção de matéria (fino e/ou espesso), região de linhas largas (BLR—*Broad Line Region*), meio obscurecedor na forma de um toróide composto por nuvens de poeira, região de linhas estreitas (NLR—*Narrow Line Region*) e jatos de partículas relativísticas. (Adaptado de Frank et al. (2002).)

poeira. Embora cenários antigos ilustrem o toro como uma estrutura contínua, modelos mais recentes e realistas consideram o toróide não como uma estrutura contínua, mas composta de um grande número de nuvens orbitando o SMBH (Nenkova et al., 2002). Essa região tem tamanho de  $\approx 1$  pc. Esse meio obscurecedor, segundo o modelo unificado, dependendo da orientação do AGN em relação a linha de visada pode obscurecer a BLR, e por isso, linhas de emissão largas estão ausentes nos AGNs do tipo 2; ao passo que essas linhas

são visíveis em AGNs do tipo 1 porque não há obscurecimento ao longo da linha de visada. Baseado no esquema estrutural dos AGNs descrito acima, o Modelo Unificado argumenta que diferentes classes de AGNs são intrinsecamente as mesmas, mas parecem diferentes meramente devido ao efeito de orientação.

- A região de linhas estreitas-NLR: Ao contrário da BLR, esta região é resolvida devido a sua grande extensão espacial, pois está localizada a distâncias que variam de dezenas a centenas de parsecs do SMBH central, sendo formada por nuvens de gás a mais baixas velocidades do que as da BLR ( $200 \lesssim \text{FWHM}_{\text{narrow}} \lesssim 900 \text{ km s}^{-1}$ ), uma vez que elas estão além do raio de influência do SMBH e sua cinemática é dominada pelo potencial gravitacional da galáxia ou por *outflows* com origem no disco de acreção. Devido a uma possível mistura de radiação ionizante de estrelas e do AGN, a NLR é a chave para desvendar o impacto do feedback estelar e do AGN sobre as suas galáxias hospedeiras. Devido às baixas densidades da NLR, entre  $10^{2-4} \text{ cm}^{-3}$ , muitas linhas proibidas são observadas. O tamanho da NLR pode variar de centenas de parsecs a poucos kiloparsecs ( $\approx 100 \text{ pc} - 4 \text{ kpc}$ ) (Bennert et al., 2006, Peterson et al., 2013).

Além das estruturas acima, podem ainda ocorrer jatos de partículas relativísticas colimadas por campos magnéticos, originados na região interna do disco de acreção.

## 1.4 A coevolução entre o SMBH e a galáxia hospedeira

Durante a evolução das galáxias no Universo há dois tipos de episódios marcantes que não só são fundamentais para moldar as próprias galáxias mas também possibilitam a observação dos fenômenos físicos envolvidos. Isto ocorre devido à alta emissão de energia associada aos mesmos: a atividade Starburst – devida à formação estelar intensa, e a atividade nuclear num AGN – provocada pela alimentação do SMBH.

A atividade Starburst em galáxias é caracterizada pela alta taxa de formação estelar em um curto intervalo de tempo ( $\sim 10^6$  anos), que ocorre intercalada com períodos de “quietude”, onde não há formação de estrelas (Schneider, 2015, Bordalo et al., 2009). Isto acontece em regiões HII, onde a radiação ultravioleta de estrelas recém-formadas em associações de estrelas massivas jovens tipo O e B ioniza o gás circundante. Uma característica marcante desses objetos é o excesso de emissão

ultravioleta e no infravermelho (Schneider, 2015). O espectro óptico desse gás é marcado por linhas de emissão nebulares intensas (Bordalo et al., 2009), que permitem obter informações sobre a cinemática do gás, tais como campo de velocidade e dispersão de velocidades; bem como a metalicidade do gás e abundância química. A taxa de formação estelar observada em galáxias *Starburst* é maior que a observada em galáxias normais (Schneider, 2015). Ainda não são bem compreendidos os mecanismos que provocam o surto de formação estelar, mas observações e modelos mostram que a colisão entre galáxias e instabilidades relacionadas a formação de uma barra na galáxia podem dar origem a esses surtos.

A atividade nuclear, como já foi descrito acima, é caracterizada pela “ativação” do SMBH, que parece estar presente na grande maioria das galáxias que contém na sua região central um bojo estelar massivo (Ferrarese & Ford, 2005). A coevolução dos SMBHs e suas galáxias hospedeiras (Di Matteo et al., 2008, Kormendy & Ho, 2013) se dá através de episódios de migração de gás para as regiões mais internas, que, ao alimentar o buraco negro, dão início à atividade nuclear (Storchi-Bergmann & Schnorr-Müller, 2019). A atividade nuclear por sua vez produz efeitos de *feedback*, resultantes da emissão de energia, ventos e jatos que se originam no disco de acreção formado pela matéria que orbita em torno do SMBH antes de cair dentro dele.

*Outflows* de gás observados em AGNs são mecanismos promissores de feedback (Zubovas & King, 2012, Faucher-Giguère & Quataert, 2012). Estes outflows foram observadas nos últimos anos em gás ionizado (Rupke & Veilleux, 2011, Cano-Díaz et al., 2012, Harrison et al., 2014, Brusa et al., 2015, Carniani et al., 2015, Bischetti et al., 2017) e gás molecular (Feruglio et al., 2017, Brusa et al., 2018). No entanto, as suas características e o impacto de tais outflows ainda não são bem compreendidos. Portanto, a importância e os detalhes do feedback de AGNs em suas galáxias hospedeiras e no seu entorno continua sendo uma questão em aberto.

Um exemplo de *feedback* do AGN – observado em grande escala – é encontrado no centro de aglomerado de galáxias, do tipo *cool-core clusters*. É sabido há muito tempo que a escala de tempo de resfriamento do gás quente nestes aglomerados se torna menor do que o tempo de Hubble no centro, e fluxos de resfriamento são esperados. No entanto, apenas 10% da taxa de resfriamento esperada é observada, e isso agora é entendido como sendo devido aos jatos rádio do AGN central reaquecendo o gás. As regiões mais densas em torno das cavidades formadas pela pressão dos jatos no meio circungaláctico resfriam em filamentos, que caem nas galáxias centrais de aglomerados após perder seu suporte de pressão (Salomé et al., 2006, 2008). Estes estudos foram feitos via observações em raios-X, uma ferramenta importante para

mapear gas muito quente, e estudar – não só o efeito de AGNs em aglomerados de galáxias, mas também localizar AGNs, já que o raio-X de mais alta energia atravessa nuvens espessas de poeira, que bloqueiam a radiação de outras bandas espectrais.

Uma outra ferramenta importante para o estudo da alimentação e retroalimentação de SMBH em AGNs detectados no ótico e infravermelho é a espectroscopia de campo integral, que têm permitido estudos mais completos sobre *outflows*, tendo em vista que através desta técnica é possível obter informações espacialmente resolvidas sobre a morfologia do *outflow* na NLR e Extended NLR (ENLR) e das distâncias envolvidas, por exemplo.

Em trabalhos desenvolvidos pelo grupo AGNIFS (AGN Integral Field Spectroscopy), incluindo Riffel et al. (2008, 2011), Schnorr Müller et al. (2011), Simões Lopes et al. (2007), Storchi-Bergmann et al. (2009, 2010) usando espectroscopia de campo integral com os telescópios Gemini, tanto no óptico como no infravermelho próximo, foram obtidos resultados que mostram *inflows* de gás ao longo de espirais nucleares e discos compactos dentro de regiões de dimensões de dezenas a centenas de parsec em galáxias hospedeiras de AGNs próximos. Estes autores sugerem que estes inflows são as fontes de combustível para o AGN. As taxas de *inflow* – maiores do que a taxa de acreção do AGN, indicam que o excesso de gás deve ser consumido na formação de novas estrelas no bojo. Em muitos casos, encontraram-se anéis circumnucleares (com raios da ordem de centenas de parsec) com formação estelar recente (idades de 10 a 500 milhões de anos) que podem ser interpretados como uma assinatura da coevolução da galáxia hospedeira e seu AGN.

Outras observações de espectroscopia de campo integral de galáxias a baixo e alto redshift, mostram evidências da presença de outflows no gás ionizado em galáxias hospedeiras de AGN. Estas observações incluem trabalhos do grupo AGNIFS (Storchi-Bergmann et al., 2010, Barbosa et al., 2014, Schnorr-Müller et al., 2014, Riffel et al., 2015), além de outros (Cano-Díaz et al., 2012, Rupke & Veilleux, 2013, Harrison et al., 2014, Liu et al., 2013, McElroy et al., 2015, Husemann et al., 2016, Kakkad et al., 2016, Wylezalek et al., 2016, Wylezalek & Zakamska, 2016, Carniani et al., 2015, Cresci et al., 2015). Muitas dessas observações encontraram uma evidência direta da supressão de formação de estrelas (*feedback* negativo), onde o *outflow* é proeminente (Cano-Díaz et al., 2012, Cresci et al., 2015, Carniani et al., 2016), mas alguns encontraram um aumento na formação de estrelas (*feedback* positivo), provavelmente devido a choques no meio interestelar (Cresci et al., 2015). Assim, os AGNs são possivelmente capazes de extinguir ou provocar a formação de novas estrelas. De acordo com Rosario et al. (2018) não parece existir uma correlação

entre a luminosidade do AGN e o reservatório de gás necessário para alimentar o AGN e possivelmente formar novas estrelas, embora seu estudo tenha se restringido a AGNs de baixa luminosidade.

De modo geral pode ser concluído que o feedback do AGN pode afetar a evolução da galáxia, uma vez que, ao compreender tanto a emissão de energia como a ejeção de matéria da região nuclear da galáxia, acaba regulando o seu crescimento. Ao expelir gás da região central, evita a formação de novas estrelas a partir deste gás. Modelos de evolução de galáxias que não consideram estes efeitos de feedback resultam na formação de galáxias mais massivas do que as existentes na natureza.

## 1.5 Excitação do gás

### 1.5.1 Diagramas diagnóstico

A luminosidade e a intensidade relativa das linhas de emissão permitem a obtenção de propriedades do AGN, como sua potência e a natureza da fonte ionizante, sua geometria, as condições físicas (como densidade e temperatura) e a composição química do gás, bem como sobre a quantidade de poeira das regiões emissoras. Mesmo quando essas propriedades não podem ser determinadas sem ambiguidade, as intensidades relativas das linhas de emissão permitem atribuir classes a diferentes regiões de gás observadas nas galáxias, como: regiões de gás ionizado por estrelas quentes que resultam da formação estelar (FS), ou regiões ionizadas por AGNs, e ainda dividí-las em categorias mais específicas de acordo com seu grau de ionização: de alta ionização (Seyfert) e região emissora nuclear de baixa ionização (LINER).

Ao avaliar o efeito do AGN na sua galáxia hospedeira, é importante distinguir regiões que foram ionizadas pelo AGN central de outras fontes de ionização. Para isso podemos usar os chamados diagramas de diagnóstico, ferramentas importantes para mapear a natureza do gás emissor nas galáxias, distinguindo regiões ionizadas pelo AGN de regiões ionizadas por estrelas quentes, por exemplo. Os diagramas diagnósticos mais utilizados são os chamados BPT (Baldwin, Phillips & Terlevich (1981), atualizados mais tarde por Veilleux & Osterbrock (1987). Dentre eles o mais frequentemente empregado é o que usa as razões de linhas  $[\text{OIII}] \lambda 5007 / \text{H}\beta$  vs.  $[\text{NII}]\lambda 6584 / \text{H}\alpha$  para separar regiões de gás emissor com diferentes fontes ionizantes. Kauffmann et al. (2003) e Kewley et al. (2006) usaram esses diagramas para melhorar empiricamente a definição da fronteira que separa as regiões ionizadas

pelo AGN das regiões ionizadas por estrelas jovens, introduzindo também a chamada região de transição entre elas. Os objetos com razões de linhas nessas regiões são também chamados AGN-Starburst ou “composite”, e a explicação mais frequente para emissão destas regiões é a inclusão na mesma abertura tanto de regiões de formação estelar como de regiões ionizadas pelo AGN.

Além de AGN e estrelas jovens de regiões de formação estelar (Regiões HII), estrelas quentes evoluídas (pós-AGB - Assymptotic Giant Branch) podem ionizar o gás local e produzir um espectro similar ao de um LINER, como foi mostrado por Cid Fernandes et al. (2011) e referências ali citadas. Para identificar essas regiões, Cid Fernandes et al. (2011) propôs o diagrama WHAN, uma relação entre a largura equivalente de  $W(H\alpha)$  e a razão  $[NII] \lambda 6584 / H\alpha$ . Cid Fernandes et al. (2011) concluíram que quando  $W(H\alpha)$  é menor que 3 Å, a fonte de ionização do gás pode ser estrelas pós-AGB, e não necessariamente um AGN ou um “Starburst”. Galáxias com emissão nuclear com  $W(H\alpha) \leq 3$  Å, são consideradas “retired”, no sentido de que a origem da emissão do gás não é devida nem à atividade nuclear nem à ionização por estrelas jovens de regiões HII. Como as razões  $[NII]/H\alpha$  dessas galáxias “retired” são semelhantes às dos LINERs, esses objetos foram apelidados de “LIERs”. Por isso, usamos o diagrama WHAN juntamente com o diagrama BPT, para assim podermos identificar tais regiões.

Por outro lado, notamos algumas discrepâncias entre a classificação inferida do WHAN e do BPT. Por exemplo, usando o BPT, algumas regiões que apareciam como “composites” ou mesmo regiões de formação estelar, apareciam no WHAN como regiões Seyfert ou LINER. A razão disso se deve ao fato de que, enquanto no WHAN a divisão entre regiões Starburst e AGN se dá para um valor constante de  $\log([NII]/H\alpha) = -0.4$ , correspondente a uma linha vertical reta, no BPT esta divisão é curva, além de haver entre as regiões starburst e AGN a região de transição, que não é definida no WHAN. No BPT a razão  $\log([NII]/H\alpha)$  desta divisão pode alcançar valores de 0.1 para LINERs e até -0.1 para Seyferts, bem maior do que o valor fixado de -0.4 no diagrama WHAN. Para conciliar o WHAN com o BPT, utilizamos primeiramente o BPT para classificar a região, e somente usamos o WHAN para descartar as regiões LIER.

### 1.5.2 A extensão R da região ionizada pelo AGN

A “Narrow Line Region” NLR é uma componente importante dos AGNs pelo fato de ser espacialmente resolvida, sendo onde se observam também os *outflows* discutidos acima. As observações destas regiões por vários autores, inclusive do nosso grupo

AGNIFS revela que o seu raio é da ordem de centenas de parsecs a alguns kiloparsecs. Imagens de banda estreita revelam que a região ionizada pelo AGN pode se estender a raios bem maiores, atingindo dezenas de kpc em algumas galáxias (Keel et al., 2012, Liu et al., 2013, Obied et al., 2016, Storchi-Bergmann et al., 2018). Essas nebulosas mais estendidas são chamadas de “*Extended Narrow Line Regions*” (ENLRs) (Storchi-Bergmann et al., 2018).

A ENRL foi assim denominada em trabalhos realizados há 30 anos atrás, que abordaram o estudo da região emissora muito estendida encontrada em rádio-galáxias luminosas (Unger et al., 1987). A origem destas regiões foi atribuída à interação entre o jato rádio e o gás ambiente (Fu, H. & Stockton, 2009). Estudos mais recentes, como os citados no parágrafo anterior, têm mostrado que não somente rádio galáxias apresentam ENLRs, mas galáxias Seyfert também mostram ENLRs similares (Bennert et al., 2002, Schmitt et al., 2003a,b).

Muitos modelos foram propostos para explicar a origem e emissão da (E)NLR. Os modelos de fotoionização padrão assumem um conjunto de nuvens de densidade constante ionizado por uma fonte de ionização com espectro em lei de potência ou lei de potência quebrada (Osterbrock & Ferland, 2006). Excitação do gás por choques é adicionada para algumas ENLRs associadas a jatos. No entanto, os modelos padrão de ionização apresentam problemas para reproduzir alguns casos. Por exemplo, as linhas coronais fortes observadas em algumas galáxias Seyfert não são reproduzidas nesses modelos, (Dopita et al., 2002, Groves et al., 2004a,b), e a relação entre o tamanho de ENLR e a luminosidade do AGN tem, em alguns casos, um declive que difere do valor previsto de 0,5 (Schmitt et al., 2003b, Netzer et al., 2004).

Modelos mais recentes de ENLR substituem as nuvens de densidade constante por nuvens de mais de uma densidade, considerando a presença de múltiplas componentes, incluindo contribuição de poeira (Dopita et al., 2002, Groves et al., 2004a,b, Dempsey & Zakamska, 2018), que produzem diferentes inclinações na relação tamanho-luminosidade. São necessários mais vínculos observacionais para distinguir os diferentes modelos.

A diferença entre as declividades observadas e previstas pelos modelos (para a relação R vs., L[OIII]) pode ser atribuída às diferentes definições do tamanho da ENLR, diferentes indicadores da luminosidade do AGN ou diferentes limites de detecção da emissão do gás. O advento da espectroscopia com unidades de campo integral (IFU), especialmente as que produzem grandes volumes de dados como o SDSS-IV/MaNGA (Bundy et al., 2015), oferecem uma nova oportunidade para medir a relação tamanho-luminosidade de ENLRs com uma amostra muito maior e

uniforme. Os espectros espacialmente resolvidos também nos permitem identificar a ENLR utilizando diagramas diagnóstico, que é uma maneira eficaz de isolar a ENLR para AGNs de baixa luminosidade. Com a grande amostra disponível, podemos obter vínculos mais robustos para a relação tamanho-luminosidade das ENLRs em uma ampla faixa de luminosidade dos AGN.

Sendo possível mapear a excitação do gás na maior parte da galáxia via diagramas diagnóstico, é possível também medir a extensão R da região ionizada pelo AGN – a região de linhas estreitas NLR ou ENLR. É então possível investigar a relação entre R e L ([OIII]) que tem sido abordada ao longo dos anos por vários autores (Schmitt et al., 2003a, Bennert et al., 2002, Greene et al., 2011, Liu et al., 2014, Fischer et al., 2018, Storchi-Bergmann et al., 2018), utilizando amostras pequenas, às vezes combinando dados não homogêneos e encontrando declives variados para a relação R vs. L[OIII]. Com a nossa amostra observada com o MaNGA, contribuímos para esta investigação em particular para o estudo da relação para AGNs de baixa luminosidade com uma amostra homogênea e maior do que em estudos anteriores.

### 1.5.3 A massa de gás ionizado e a taxa de formação estelar

O acionamento do AGN depende da disponibilidade de gás para alimentar o SMBH no centro. Alguns estudos argumentam que as galáxias hospedeiras de AGN têm mais gás nos poucos kpc internos do que as galáxias não ativas, o que parece ser o caso, pelo menos, das galáxias “early-type” próximas (Simões Lopes et al., 2007, Martini et al., 2003). Por sua vez Hicks et al. (2013) encontraram densidades superficiais de massa de gás molecular dentro dos  $\approx 50$  pc internos de galáxias Seyfert próximas mais altas do que em uma amostra de controle.

Outros estudos apontam que a taxa de formação estelar (SFR) parece ser aumentada na região nuclear ( $\sim$  dentro do kpc central) de AGNs (Diamond-Stanic & Rieke, 2012, Esquej et al., 2014, Mushotzky et al., 2014) quando comparados com galáxias de controle, em estudos feitos no infravermelho, através da observação das bandas espectrais do Hidrocarboneto Aromático Policíclico (PAH) em  $11,25\,\mu\text{m}$  ou fluxos do contínuo em  $70\,\mu\text{m}$  e  $160\,\mu\text{m}$  como indicadores de formação estelar, presumivelmente não afetados pela presença de um AGN.

A SFR é um dos parâmetros físicos mais fundamentais para mapear e datar a formação e evolução das galáxias. Ao longo dos anos, uma variedade de indicadores tem sido calibrados para estimar a SFR. Nas regiões de formação estelar, o gás ionizado absorve a luz ultravioleta (UV) proveniente de estrelas jovens e massivas, ionizando o gás ao seu redor que, ao se recombinar, emite linhas espectrais brilhantes

no óptico. A linha de recombinação nebulosa  $\text{H}\alpha\lambda6563$  é considerada como o indicador da SFR mais confiável. Proporcional à radiação ionizante de estrelas jovens ( $\leq 20$  Myr) e massivas ( $> 10 M_{\odot}$ ), a linha  $\text{H}\alpha$  é uma das mais brilhantes emitidas por nebulosas gasosas e amplamente acessível via observações, fornecendo uma sonda direta da SFR instantânea, independente da história anterior de formação estelar (Kennicutt, 1998).

Para as galáxias hospedeiras de AGNs, tem se concluído que o crescimento dos SMBHs está intimamente relacionado à evolução das galáxias, através da relação entre a massa do SMBH e a massa da componente estelar do bojo. Isto é demonstrado pela correlação entre a massa do SMBH e a massa do bojo estelar nuclear – cujo indicador é a dispersão de velocidade estelar, a relação  $M-\sigma_*$  do Universo local (Ferrarese & Merritt, 2000, Gebhardt et al., 2000). Bojos de galáxias ativas próximas parecem estar ainda crescendo, e por isto tem sido chamado de pseudo-bojos (Kormendy & Ho, 2013), sugerindo uma relação entre a taxa de acreção do buraco negro e a taxa de formação estelar (Marconi et al., 2004, Silverman et al., 2008, Mullaney et al., 2012).

Entender a interação entre o acréscimo de massa ao SMBH e a formação de estrelas na região central das galáxias é essencial para o entendimento da evolução das galáxias. A maioria dos modelos de formação e evolução de galáxias, incluindo Modelos Semi-Analíticos (SAMs) e simulações hidrodinâmicas, sugerem que a formação de estrelas e o crescimento dos buracos negros estejam ligados através da migração ao centro das galáxias de gás frio/molecular, que alimentam tanto a formação estelar como o SMBH no centro da galáxia. Estes processos podem ser desencadeados através de fusões entre galáxias (por exemplo, (Di Matteo et al., 2005, Somerville et al., 2008, Hirschmann et al., 2014)). Esses modelos geralmente resultam num feedback forte do AGN, através da emissão de radiação e *outflows* que regulam o crescimento dos próprios buracos negros bem como do bojo das galáxias ao aquecer e expulsar o gás circundante cessando a formação estelar (Croton et al., 2006, Fabian, 2012).

Para entender o papel do feedback dos AGNs, Zubovas & Bourne (2017) utilizaram modelos que sugerem que existe uma luminosidade crítica do AGN a partir da qual o feedback é poderoso o suficiente para suspender a fragmentação de nuvens de gás (que presumivelmente formarão novas estrelas). Como discutido acima, o AGN e a formação estelar podem ser “iniciados”, ou “acendidos” num episódio de migração de gás para a região central de galáxias. Mas ainda não há consenso sobre se o início da atividade nuclear (AGN) ocorre ao mesmo tempo que a fase starburst

(de intensa formação estelar) (Kawakatu & Wada, 2008), ou se a atividade AGN segue a atividade starburst (Cid Fernandes et al., 2005, Davies et al., 2009) ou se não há associação entre os dois processos (Sarzi et al., 2007, Hicks et al., 2013).

É portanto importante determinar a SFR em galáxias hospedeiras de AGNs, para investigar se ela se correlaciona com a taxa de acreção ao SMBH e/ou se há supressão da formação estelar devido ao feedback do AGN. Entretanto, no óptico, os indicadores da SFR – em particular a luminosidade na linha de emissão de H $\alpha$  – só é válida para regiões gasosas ionizadas por estrelas quentes.

Para calcular a SFR a partir de H $\alpha$  no caso de AGNs, devemos nos restringir a regiões dominadas por ionização por estrelas quentes. É então necessário primeiramente usar um diagnóstico - como os diagramas BPT - para encontrar as regiões ionizadas por estrelas quentes jovens, onde podemos calcular a SFR. Assim, não seremos capazes de calcular a SFR na região ionizada pelo AGN a partir de espectros ópticos. Na região ionizada pelo AGN nós calculamos alternativamente a massa de gás ionizado. E para complementar esta informação, obtivemos-la para todas as galáxias, mapeando sua distribuição sobre o corpo de todas as galáxias.

#### 1.5.4 A abundância química do gás

As linhas de emissão dos espectros ópticos são também ferramentas poderosas para a derivação das propriedades físicas do gás, como sua temperatura e densidade bem como a abundância química dos elementos pesados (usualmente chamados de metais) em regiões de formação estelar. No entanto, o número de linhas detectadas com razão sinal/ruído suficiente para o cálculos destas propriedades nem sempre permitem uma derivação precisa dos seus valores. Isto é particularmente verdadeiro para a derivação da metalicidade (Pérez-Montero & Contini, 2009). O método clássico chamado de método direto para medir a abundância de metais em nebulosas gasosas depende da capacidade de medir a temperatura eletrônica T<sub>e</sub>, porque as intensidades das linhas metálicas dependem exponencialmente do valor desta temperatura. T<sub>e</sub> é obtido a partir das razões entre linhas aurorais (fracas) e nebulares (fortes) como [OIII] $\lambda 4363/\lambda 5007$ .

No entanto, para galáxias ou regiões nebulares dentro delas com emissão fraca e/ou em galáxias distantes, bem como em nebulosas ricas em metais, T<sub>e</sub> não pode ser determinada pois as linhas aurorais são muito fracas ou mesmo não detectadas e a metalicidade só pode ser obtida usando calibrações. Estas calibrações são baseadas em relações entre a metalicidade e razões que envolvem linhas de emissão colisional fortes (intensas). Este método é também chamado de método de linha forte, pois

com ele é possível obter, por exemplo, a abundância de oxigênio a partir não só da intensidade de linhas deste elemento mas também da intensidade de linhas de emissão de outros elementos como nitrogênio e enxofre.

Há muitos estudos que têm explorado diferentes calibradores de metalicidade nebulosa baseados em linhas fortes, como, por exemplo, os de Perez-Montero & Diaz (2005), Kewley & Ellison (2008). A calibração pode ser empírica – isto é, utilizando medições diretas da abundância de oxigênio no Universo local, ou teórica – i.e. utilizando modelos de fotoionização cobrindo diferentes propriedades físicas e metalicidades do gás. Infelizmente, a precisão das calibrações e a faixa de metalicidade coberta por elas dependem fortemente da qualidade das observações e representatividade das amostras observacionais usadas e/ou dos modelos utilizados.

Essas calibrações podem, também, depender da relação de abundância relativa entre elementos metálicos. Este é o caso, por exemplo, do parâmetro S<sub>23</sub> (Díaz & Pérez-Montero, 2000), baseado em linhas de emissão de enxofre, que foi definido para calcular a abundância de oxigênio. Este também é o caso de alguns outros calibradores baseados em linhas de emissão do [NII] $\lambda 6584\text{\AA}$ , como o parâmetro N2 (entre outros Storchi-Bergmann et al. (1998) Storchi-Bergmann et al., 1994) ou o parâmetro O3N2 Pettini & Pagel (2004), que são usados para derivar a abundância total de oxigênio. Além dos trabalhos acima, vários outros têm utilizado calibrações em termos de linhas intensas (Pilyugin, 2000, 2001, Kewley & Dopita, 2002, Dors & Copetti, 2005, Maiolino et al., 2008, Berg et al., 2011, Pilyugin & Grebel, 2016, Vale Asari et al., 2016, Dors et al., 2017).

O “método T<sub>e</sub>”, que utiliza a intensidade das linhas e o valor da temperatura eletrônica, foi desenvolvido para nebulosas ionizadas por estrelas jovens e quentes. De fato, Pilyugin et al. (2003) mostrou que o método é robusto pois há uma boa concordância (pelo menos para a vizinhança solar) entre as determinações de oxigênio baseadas no método T<sub>e</sub> e aquelas derivadas através das observações da linha interestelar fraca O I $\lambda 1356$  em direção às estrelas, também (Moos et al., 2002, Deharveng et al., 2000, Rolleston et al., 2000).

Porém, Dors et al. (2015) mostraram que o método T<sub>e</sub> não funciona para regiões de gás ionizadas por AGNs, embora outros autores também tenham previamente concluído isto pelo fato de que o método assume ionização por estrelas quentes (Storchi-Bergmann et al., 1998). Em Dors et al. (2015) os autores estimaram abundâncias de oxigênio (geralmente usadas como traçador de metalicidade) nas regiões de linhas estreitas (NLRs) de AGNs a partir do método T<sub>e</sub> – o chamado método da linhas fortes. Eles então compararam estas abundâncias com as extrapo-

ladas para a região central das galáxias a partir de gradientes radiais de metalicidade determinados a partir dos valores obtidos para regiões de formação estelar ao longo do corpo da galáxia. Foi concluído que o método  $T_e$  subestima as abundâncias de oxigênio esperadas para a região da NLR em até  $0,8\ dex$  e que este fato deve ser devido à natureza diferente da fonte ionizante, com mais fótons de alta energia produzidos nas partes internas do AGN (disco de acreção), que também consiste numa fonte adicional de aquecimento do gás.

Ao longo de décadas, várias relações entre linhas de emissão fortes e a abundância de oxigênio (como representativa da metalicidade) foram propostas para regiões de formação estelar como mostrado em (López-Sánchez & Esteban, 2010). Mas no caso dos AGNs, suas metalicidades têm sido estimadas por muitos autores, como por exemplo em Warner et al. (2002), Ferland et al. (1996), Richardson et al. (2014), Dhanda Batra & Baldwin (2014), Dors et al. (2015), Feltre, Charlot & Gutkin (2016) e outros, com base em modelos de fotoionização. Mas, em termos de calibrações, parece que as únicas disponíveis na literatura são as propostas por Storchi-Bergmann et al. (1998) e Dors et al. (2015). Estes autores utilizaram resultados de modelos de fotoionização para obter calibrações em termos de razões entre linhas de emissão fortes, facilmente observáveis nas regiões óptica e ultravioleta do espectro.

## 1.6 O projeto MaNGA

O projeto MaNGA (*Mapping Nearby Galaxies at Apache Point Observatory*, Bundy et al. (2015) é um dos três componentes da quarta geração do SDSS *Sloan Digital Sky Survey – IV*, que visa obter um estudo detalhado da estrutura espacial, propriedades cinemáticas e populações estelares de uma amostra de cerca de 10.000 galáxias próximas. As galáxias da amostra têm massa estelar  $M_\star > 10^9 M_\odot$  e redshifts entre  $0,01 < z < 0,15$ . O mapeamento, que está sendo realizado entre 2014 e 2020, consiste em espectroscopia de campo integral com unidades IFU de diferentes tamanhos, compostas por grupos de 19 a 127 fibras por unidade, o que resulta em diâmetros entre  $12.5''$  e  $32''$ , respectivamente. Além disso, é usado um feixe com apenas 7 fibras para a calibração em fluxo. As fibras são conectadas ao espectrógrafo BOSS (Baryon Oscillation Spectroscopic Survey), usado no SDSS-III, que possui dois braços, vermelho e azul, cobrindo um intervalo de  $3.600\text{Å}$  a  $10.300\text{Å}$ , e atinge resolução espectral média de  $R \sim 2000$ . A cobertura espacial é dada em termos do raio efetivo,  $R_e$ , para permitir o estudo de gradientes e mapas em função

deste  $R_e$ . O MaNGA atinge cobertura espacial de  $1.5R_e$  a  $2.5 R_e$ , com resolução espacial de  $2.5''$  (FWHM), sendo que  $2/3$  da amostra atinge  $1.5R_e$  e  $1/3$  da amostra  $2.5R_e$ , formando duas subamostras.

O projeto MaNGA é um survey inédito tendo em vista principalmente o grande número de galáxias quando comparado com outros *surveys* que utilizam IFU. O grande número de galáxias da amostra permite a análise estatística do comportamento das propriedades físicas das galáxias em função do ambiente, massa, tipo morfológico e do halo de matéria escura. Além disso, permite investigar de que maneira o ambiente local e o halo de matéria escura influenciam o processo de formação e evolução das galáxias. Também estão sendo observadas subamostras de objetos raros, como galáxias em fusão e post-starburst, por exemplo.

A partir dos dados do MaNGA está sendo possível obter mapas bidimensionais da cinemática do gás e das estrelas, curvas de rotação, metacilidade, SFR (Star Formation Rate), SFH (Star Formation History), estado de ionização do gás do meio interestelar, classificação BPT (através dos diagramas diagnóstico propostos por Baldwin, Phillips & Terlevich (1981), abundância química, etc. A partir destes dados o MaNGA pretende responder à questões relacionadas ao ciclo de vida das galáxias, dentre as três principais: 1) A natureza do atual crescimento das galáxias via interações de fusão e gradual incremento de gás (*gas accretion*); 2) Os processos responsáveis por cessar (*quench*) a formação estelar em galáxias; e 3) O histórico de formação de subcomponentes da galáxia, incluindo disco, bojo e halo de matéria escura.

Além do projeto principal, existe um projeto auxiliar proposto por Greene et al. (2014), no qual o propósito é aumentar a amostra de AGNs do MaNGA. Devido a baixa densidade numérica de AGNs luminosos no Universo local, amostras robustas de galáxias com SMBHs não podem ser construídas a partir da amostra de referência MaNGA. Portanto, a proposta é usar uma variedade de métodos de seleção complementares para completar a amostra de AGNs do MaNGA com fontes mais luminosas, para  $z \sim 0.1$ . A seleção de AGNs se baseará na emissão de raios X, cores no infravermelho médio, propriedades de linha de emissão e luminosidade de fontes rádio. Tendo em mãos uma amostra mais robusta de AGNs, está sendo possível estudar as propriedades do hospedeiro e a cinemática do gás.

## 1.7 Resultado anteriores com O MaNGA (e outros surveys)

Aqui descrevemos alguns resultados de surveys usando observações de espectroscopia de campo integral de galáxias com AGN.

Em Harrison et al. (2014) observações feitas com GMOS-IFU (*Gemini Multi Object Spectrograph-Integral Field Unit*) para resolver espacialmente a cinemática do gás ionizado em uma amostra de 16 AGNs luminosos de tipo 2 ( $L[\text{OIII}] > 10^{41} \text{ erg s}^{-1}$ ), mostram que *outflows* estão presente na maior parte dos casos, e que se estendem a escalas de kiloparsecs. O estudo também mostra que os *outflows* não estão restritos às galáxias com intensa formação estelar ou àquelas que têm somente AGNs. No entanto, parece haver uma maior incidência de velocidades extremas de *outflows* nos AGNs hospedados em galáxias infravermelhas ultraluminosas. Tanto a formação estelar intensa quanto a atividade do AGN parecem ser energeticamente viáveis para impulsionar os *outflows*, porém não obteve-se evidências definitivas que favoreçam um processo sobre o outro nesta amostra.

No trabalho de Davies et al. (2014) foi analisada a contribuição relativa para a ionização do gás de estrelas jovens e AGNs em função da distância ao núcleo em quatro galáxias hospedeiras de AGNs, usando dados de IFU no óptico com o survey CALIFA. Os resultados obtidos mostram a contribuição decrescente do AGN e crescente das estrelas jovens à medida que o raio aumenta. Eles mostram como se observa e pode-se diagnosticar a mistura dos dois processos de ionização: formação estelar e radiação do AGN e mostra a necessidade de corrigir o cálculo de taxa de formação estelar usando H $\alpha$  ou [OII] da contribuição do AGN.

Através de observações com o instrumento protótipo do MaNGA (P-MaNGA) Belfiore et al. (2015) explorou uma amostra de 14 galáxias com o objetivo de investigar propriedades espacialmente resolvidas da excitação e da abundância química do gás, através da distribuição das intensidades das linhas de emissão nebulosa. O uso de EW(H $\alpha$ ) para diferenciar a fotoionização do AGN e a ionização provocada por estrelas evoluídas de acordo com Cid Fernandes et al. (2010), mostra que na amostra investigada a ionização é dominada por estrelas evoluídas. Esta descoberta está de acordo com as galáxias crescendo “de dentro para fora”, com regiões nucleares de galáxias massivas já tendo processado a maior parte de seu combustível e apresentando populações estelares mais antigas, maior metalicidade e pouca ou nenhuma formação estelar em andamento.

No artigo de Wylezalek et al. (2018), foram investigados dados MaNGA de 2727 galáxias na tentativa de identificar assinaturas de AGNs. Foram identificados 303 candidatos. Os autores concluíram que a combinação de diagramas diagnóstico espacialmente resolvidos, combinados com os valores de brilho superficial de H $\alpha$  e largura equivalente de H $\alpha$  permitem a distinção entre excitação por AGNs e galáxias de alta metalicidade com espectros do tipo LINER. Galáxias de baixa massa com altas taxas de formação estelar específica são particularmente difíceis de diagnosticar e rotineiramente mostram razões de linhas fora do intervalo padrão de formação estelar nos diagramas diagnóstico. Foram encontradas 173 galáxias que não teriam sido selecionadas como candidatas a AGN com base em medidas espectrais nucleares, mas que exibem assinaturas de fotoionização sugestivas de atividade AGN nas partes mais externas, ressaltando o poder de levantamentos espectrais com IFUs. Um censo completo desses novos candidatos a AGN é necessário para entender sua natureza.

Sanchez et al. (2017) apresentou a caracterização das principais propriedades de uma amostra de 98 galáxias hospedeiras de AGN, tanto do tipo 2 quanto do tipo 1, em comparação com 2700 galáxias não ativas observadas pelo MaNGA. Os principais resultados encontrados são: AGNs parecem ocorrer principalmente em galáxias *early-type* ou *early-type* espirais; as galáxias hospedeiras de AGN estão localizadas na região intermediária / transição entre galáxias que estão formando estrelas e não formadoras de estrelas (ou seja, no chamado *green valley* do diagrama cor-magnitude). Levando em consideração a distribuição em termos de metalicidade estelar e abundância do gás e uma estimativa aproximada de seu conteúdo de gás molecular, conclui-se que essas galáxias estão em processo de cessação da formação estelar, em uma transição real entre os dois grupos de galáxias no Universo: as galáxias azuis com formação estelar e as galáxias vermelhas quiescentes. A análise das distribuições radiais da taxa de formação estelar, taxa de formação estelar específica e densidade de gás molecular mostram que a extinção da formação estelar (ou *quenching*) ocorre de dentro para fora, envolvendo tanto uma diminuição da eficiência de formação estelar como um déficit de gás molecular.

### 1.7.1 O AGNIFS no MaNGA

O nosso grupo AGNIFS juntou-se à colaboração SDSS-IV através do laboratório LIneA (Laboratório Interinstitucional de e-Astronomia), com o objetivo de investigar a relação entre os AGNs observados com o MaNGA e suas galáxias hospedeiras.

A seguir é apresentada uma breve descrição dos trabalhos já finalizados pelo grupo, divididos por áreas de estudo: Paper I - estabelecimento da amostra de

controle; Paper II - estudo da população estelar; Paper III - estudo das propriedades do gás ionizado - massas e excitação (presente trabalho) e Paper IV - cinemática do gás e estrelas.

O Paper I foi liderado por Rembold et al. (2017), onde o objetivo foi caracterizar amplamente as propriedades de uma amostra inicial de 62 AGNs e selecionar uma amostra de controle de galáxias inativas com propriedades iguais às das galáxias hospedeiras dos AGNs em termos da magnitude absoluta, massa da galáxia, redshift, tipo da galáxia e inclinação. Alguns exemplos são mostrados na Figura 2.1. Além disso foram investigadas as semelhanças e diferenças entre as populações estelares dentro dos 3" centrais das duas amostras usando a síntese espectral de populações estelares usando os dados do *survey* SDSS-III. De forma sucinta podemos dizer que os resultados obtidos mostram que os AGNs com  $L([OIII]) \leq 3.8 \times 10^{40}$  erg s<sup>-1</sup> apresentam população estelar semelhante às das galáxias controle. Já os AGNs com  $L([OIII]) \geq 3.8 \times 10^{40}$  erg s<sup>-1</sup> mostraram uma maior contribuição de estrelas jovens e uma contribuição menor de estrelas mais velhas. Além disso, com o aumento de  $L([OIII])$ , os AGNs exibem uma contribuição decrescente de população estelar mais velha ( $> 4$  Gyr) em relação às galáxias controle, e uma contribuição crescente dos componentes mais jovens com idades  $\leq 40$  Myr. Foi também observada uma correlação entre a diferença de idade média (AGN - controle) com  $L([OIII])$ : a população estelar das galáxias hospedeiras dos AGN mais luminosos é mais jovem do que nos objetos de controle, enquanto que para os AGNs de baixa luminosidade sua população estelar parece ser mais velha do que na amostra de controle. Estes resultados sustentam a conexão entre o crescimento do bojo da galáxia através da formação de novas estrelas, e o crescimento do SMBH via acreção de matéria na fase AGN.

O Paper II foi liderado por Mallmann et al. (2018) e consiste no estudo detalhado da composição da população estelar espacialmente resolvida das mesmas 62 galáxias com núcleo ativo em comparação com a amostra de controle. Os resultados obtidos mostram que a fração de populações estelares jovens em AGNs de alta luminosidade é maior nas regiões internas ( $R \leq 0.5 R_e$ ) quando comparadas com a amostra de controle; já os AGNs de baixa luminosidade, apresentam frações muito semelhantes de estrelas jovens para os AGNs e para a amostra de controle para toda a faixa estudada ( $1 R_e$  - raio efetivo). A região interna das galáxias em ambas amostras apresentam uma população estelar antiga dominante, cuja fração diminui para fora. Resumidamente, os resultados sugerem que os AGNs mais luminosos parecem ter sido desencadeados por um suprimento recente de gás que também desencadeou

recente formação de estrelas ( $t \leq 40$  Myrs) na região central. A Figura 1.2 mostra perfis radiais médios da contribuição percentual combinada das populações mais jovens ao contínuo em 5500 Å dos AGNs em comparação com suas galáxias de controle, separados em bins de luminosidade do AGN.

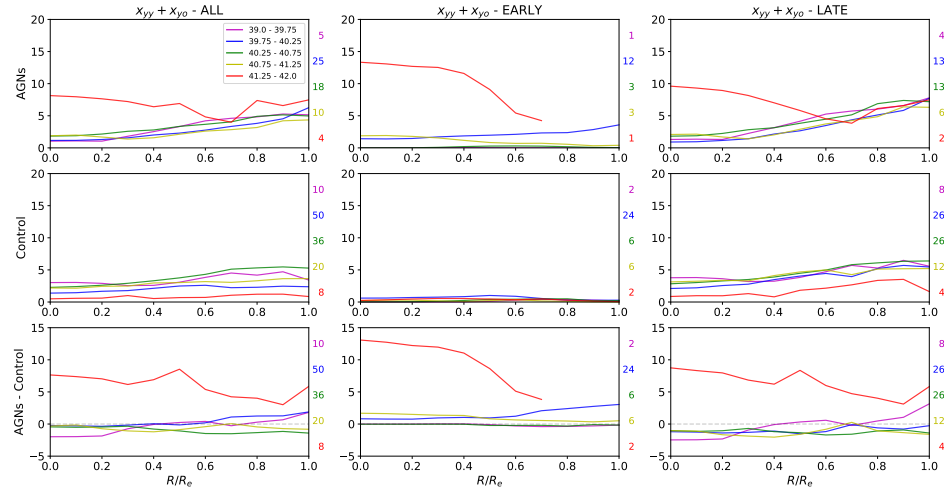


Figura 1.2: Perfis radiais médios (separados em L[OIII]) da contribuição percentual ao contínuo em 5500 Å das componentes de população estelar  $x_{yy}$  (*young-young*) e  $x_{yo}$  (*young-old*) combinadas. As diferentes cores correspondem a diferentes luminosidades dos AGNs. Os números coloridos à direita de cada linha são o número de galáxias usado para calcular o perfil médio correspondente. A primeira coluna corresponde a todos os AGNs e controles enquanto que na segunda e terceira colunas estes estão separados em *early-type* e *late-type*. As linhas de painéis, de cima para baixo, mostram os perfis médios para os AGNs, as galáxias de controle (do respectivo grupo AGN) e as diferenças. Figura extraída de Mallmann et al. (2018, em prep.).

O Paper IV foi lideado por Ilha et al. (2019) e investiga os efeitos do AGN na cinemática do gás da galáxia hospedeira. Para isto, foi feita uma comparação dos campos de velocidade dos gás e das estrelas para as duas amostras (AGN e controle). O principal resultado foi encontrar uma diferença entre a dispersão de velocidades do gás e das estrelas dividida pela das estrelas ( $\sigma_{frac}$ ), maior para as galáxias ativas do que não ativas na região central, indicando que, em pequenas escalas, o feedback do AGN tem um efeito muito importante na cinemática do gás das suas galáxias hospedeiras. A figura 1.3, extraída deste paper, mostra que há uma correlação entre a luminosidade L[OIII] quando se colocam junto os dados também das galáxias ativas e não ativas de controle. Os autores encontraram também que

não há diferença significativa na orientação do eixo principal cinemático estelar e gasoso entre as galáxias ativas e inativas, indicando que a cinemática do gás em larga escala é dominada por movimentos devido ao potencial gravitacional das galáxias e não está relacionada ao AGN.

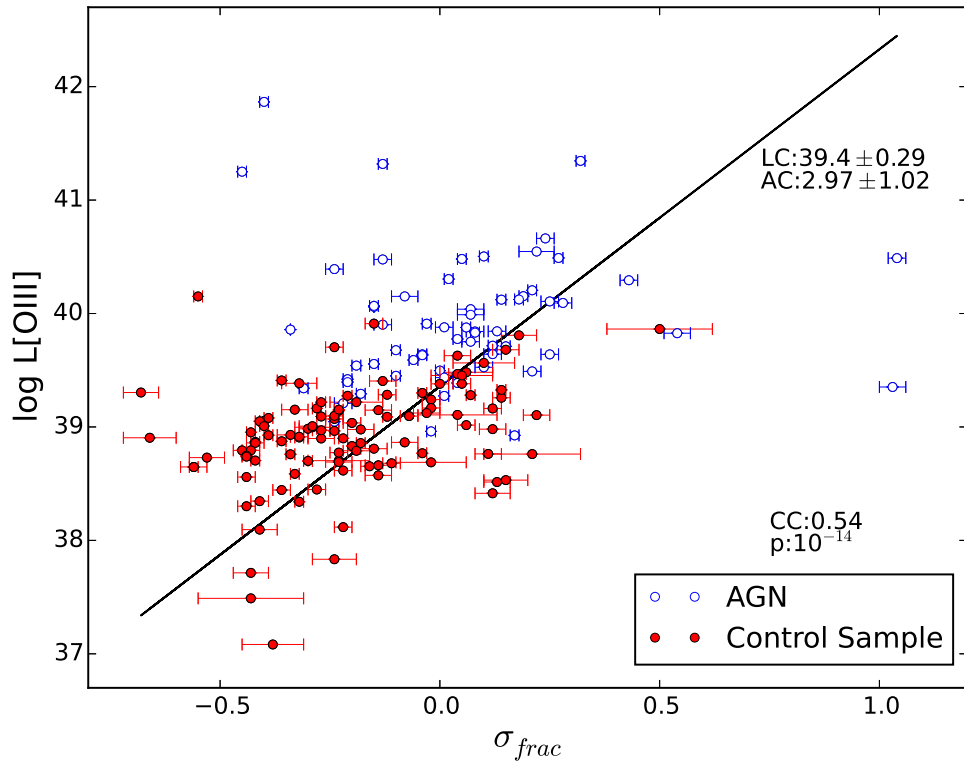


Figura 1.3: Relação entre o logaritmo da luminosidade de [OIII] $\lambda 5007\text{\AA}$  e o  $\sigma_{frac}$  (ver definição no texto) para os AGNs (círculos azuis) e para as galáxias inativas (círculos vermelhos). Através do teste Spearman confirma-se que estas propriedades estão correlacionadas. A linha preta é o resultado de um ajuste linear dos dados. Figura extraída de Ilha et al. (2019)

## 1.8 Objetivos

O objetivo global dos nossos trabalhos (AGNIFS no MaNGA) é investigar a relação entre o AGN e a galáxia hospedeira, contribuindo para o entendimento de como se dá sua coevolução através de observações resolvidas das suas propriedades com o *survey* MaNGA. Entre os processos mais importantes para esta coevolução estão a alimentação e a retroalimentação do Buraco Negro Supermassivo, que ocor-

rem nos AGNs. Estudamos estes processos neste trabalho através do mapeamento das propriedades do gás ionizado, em particular as suas massas, sua distribuição, bem como sua excitação e metalicidade, investigando também como estas propriedades se relacionam com o tipo de galáxia hospedeira (early e late-type) e com a luminosidade do AGN. Para investigar a relação com a galáxia hospedeira, obtivemos também a taxa de formação estelar nas regiões ionizadas por estrelas quentes. E para verificar se estas propriedades se correlacionam com a presença do AGN, fazemos o mesmo mapeamento na amostra de controle, selecionada em Rembold et al. (2017), e atualizada nesta tese para incorporar novos AGNs e suas amostras de controles até a última “*data release*” DR18.

Os objetivos específicos deste trabalho são:

- Mapear a distribuição de gás ionizado nos AGNs em comparação com a amostra de controle;
- Mapear a excitação do gás ionizado nos AGNs em comparação com a amostra de controle;
- Determinar a extensão da região ionizada pelo AGN (NLR ou ENLR);
- Calcular as massas de gás e mapear sua densidade superficial em comparação com a amostra de controle;
- Calcular as taxas de formação estelar na galáxia hospedeira em comparação com a amostra de controle;
- Calcular a metalicidade do gás na região ionizada pelo AGN e nas regiões de formação estelar circundantes e comparar com as de amostra de controle;
- Verificar a dependência da metalicidade do gás da NLR no tipo de galáxia hospedeira (early e late-type);
- Investigar como as propriedades obtidas para os AGNs e as regiões ionizadas por eles se relacionam com o tipo de galáxia hospedeira (early e late-type);
- Investigar como as propriedades obtidas para os AGNs e as regiões ionizadas pelo AGN se relacionam com sua luminosidade.

Este trabalho segue a seguinte ordenação: no Capítulo 2, apresentamos a amostra, no Capítulo 3, apresentamos os resultados principais da tese publicados no Paper III e complementados pelos novos dados da DR18, no Capítulo 4 discutimos os

resultados do novo paper sobre a metalicidade do gás e por fim no Capítulo 5 apresentamos as nossas conclusões.

# Capítulo 2

## Amostra

Com o fim de investigar a relação entre as propriedades dos AGNs e sua galaxia hospedeira foram usados os cubos de dados do MaNGA. Até a presente data, cubos de dados de 6457 galáxias estão disponíveis no 8º *MaNGA Product Launch* (MPL-8), obtidos entre 2014 e 2018, que foram processados usando o *MaNGA Data Reduction Pipeline* (versão 2.5.3) (Law et al., 2016) para MPL-8. Parte da amostra de dados utilizada neste trabalho é descrita em Rembold et al. (2017), onde é feita uma caracterização completa das amostras de AGNs e controle, e a sua seleção é descrita. Os demais dados adicionados, que fazem parte da MPL-8 foram obtidos usando os mesmos critérios da seleção anterior. Estes novos AGNs estão apresentados nas Tabelas A1 e A2 retirados de Machado et al. (2019,em prep.)

Ainda em Rembold et al. (2017) é apresentado um estudo sobre a população estelar dos 3” centrais, usando o espectro integrado do SDSS-III (Gunn et al., 2006, Eisenstein et al., 2011, Smee et al., 2013).

### 2.1 Seleção da amostra de galáxias hospedeiras de AGN e da amostra de controle

O conjunto de cubos de dados estudados contém 150 galáxias de núcleo ativo, selecionados usando diagramas diagnóstico que utilizam razões entre linhas de emissão do espectro óptico. Estas razões permitiram a seleção de alvos cujo padrão de linhas de emissão no espectro integrado do SDSS-III indicava ionização por um núcleo ativo, conforme foi indicado pelos diagramas de diagnóstico BPT (Baldwin, Phillips & Terlevich , 1981) e WHAN (Cid Fernandes et al., 2011). O critério aplicado para identificar as galáxias hospedeiras de AGNs foi que, no diagrama diagnóstico, as

razões de linha no diagrama BPT, bem como a largura equivalente da linha H $\alpha$  no diagrama WHAN deveriam indicar, dentro das incertezas, ionização do tipo Seyfert ou LINER. Esse critério elimina os potenciais LIERs (que não são ionizados por AGNs mas por estrelas velhas) e também objetos de transição entre AGN e formação estelar. Apenas 62 galáxias preencheram estes critérios, compreendendo 45 AGNs de baixa luminosidade ( $L[OIII] < 3,8 \times 10^{40}$  erg s $^{-1}$ ) e 17 com luminosidades superiores a esse valor. Foi utilizado esse limite – postulado por Kauffmann et al. (2003) para caracterizar estes 17 AGNs como “*Strong AGN*” e os demais com luminosidade abaixo deste, como “*Weak AGN*”. As imagens negativas do SDSS-III ugriz (Fukugita et al., 1996) das galáxias hospedeiras dos quatro AGNs mais luminosos são mostradas na Figura 2.1.

Para a seleção das galáxias de controle, foram consideradas todas as galáxias do MPL-8 que apresentaram linhas de emissão não detectáveis, cuja fonte ionizante não era um AGN. Assim considerou-se uma galáxia como um potencial candidato para a amostra de controle se ela cumprisse qualquer uma das seguintes quatro condições:

- Está localizada, dentro das incertezas, na região de formação estelar do diagrama BPT;
- Está localizada, dentro das incertezas, na região de transição ou na região LINER do BPT, mas o diagrama WHAN descarta ionização por um AGN com base no valor de EWH $\alpha$ ;
- Apresenta uma incerteza muito grande em log[OIII]/H $\beta$ , não permitindo uma classificação segura no diagrama BPT, mas o diagrama WHAN descarta a ionização por um AGN com base no valor de EWH $\alpha$ ;
- A galáxia não apresenta linhas de emissão.

Estas condições garantem que as galáxias com linhas de emissão proeminentes na amostra de controle sejam dominadas por ionização devido à formação de estrelas e não por um núcleo ativo. As galáxias que atenderam a qualquer uma dessas condições foram consideradas inativas.

De forma simplificada podemos dizer que, as galáxias inativas candidatas a controle foram pareadas com os AGNs correspondentes, em *redshift*  $z$  e massa estelar  $M_{\star}$ . Além disso, passaram também por uma inspeção visual para que se pudesse obter galáxias com morfologias e razões axiais similares com as da galáxia hospedeira. A prioridade na análise morfológica foi dada às estruturas mais próximas do

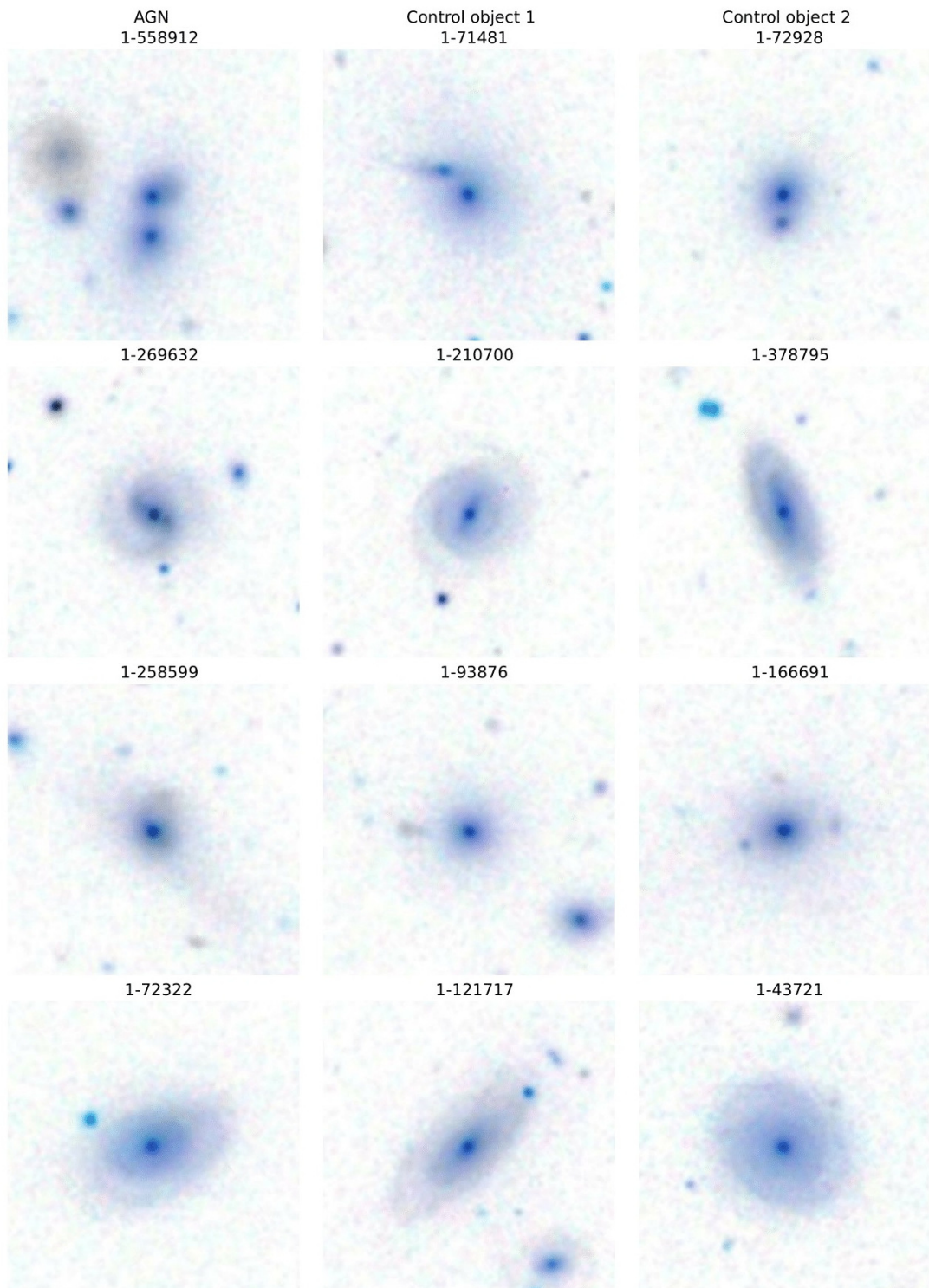


Figura 2.1: Imagens *ugriz* do SDSS-III, das galáxias hospedeiras dos quatro AGNs mais luminosos da amostra (painéis da coluna esquerda) e suas respectivas galáxias controle (colunas do centro e da direita). A identificação de cada galáxia é dada pelo seu número de identificação no survey mangaID. Cada imagem tem 51 arcsec de lado; o norte está para cima e o leste para a esquerda. (Adaptado de Rembold et al. (2017)).

núcleo; isto é, atribuiu-se maior peso à presença de barras e anéis do que à morfologia dos braços nas regiões externas da galáxia. Com o intuito de produzir a melhor comparação estatística entre as propriedades do AGN e seus controles, apenas as duas galáxias que melhor correspondiam à morfologia da galáxia hospedeira, foram escolhidas para cada AGN na amostra.

Para avaliar quantitativamente a variedade morfológica do AGN e da amostra de controle, foram obtidos o índice de concentração C e o índice de assimetria A das galáxias da amostra usando o código publicamente disponível PyCA (Menanteau et al., 2006).

Este cálculo foi feito usando as imagens na banda-r para maximizar a relação sinal/ruído da galáxia. Também foram obtidas para todas as galáxias da amostra as classificações morfológicas de GZ1 (Lintott et al., 2011). A partir das probabilidades associadas à classificação GZ1, as galáxias foram separadas em quatro grandes classes: elípticas (E), espirais (S), em fusão (M) e intermediárias elípticas/espirais (E/S); esta última classe corresponde a galáxias cujas probabilidades de serem elípticas e espirais GZ1 são rigorosamente iguais e excedem 50% quando combinadas.

Na amostra de Rembold et al. (2017), alguns dos objetos da amostra de controle foram selecionados para um ou mais AGN simultaneamente. Para melhor caracterizar a amostra, ainda em Rembold et al. (2017) foi feita síntese da população estelar do espectro integrado do SDSS-III, com o objetivo de identificar as populações presentes na amostra de AGN e na amostra de controle, e fez-se um estudo comparativo entre ambas.

Tabela 2.1: MPL-8 *exclusive* AGN sample parameters. The objects released at MPL-5 had their parameters cataloged at Rembold et al. (2017). (1) galaxy identification in the MaNGA survey; (2)-(3) RA/DEC (2000) in degrees; (4) spectroscopic redshift from SDSS-III; (5) integrated absolute  $r$ -band magnitude from SDSS-III; (6) stellar mass in units of  $M_{\odot}$ ; (7) elliptical/spiral classification from Galaxy Zoo I; (8) [O III] $\lambda 5007$  luminosity in units of  $10^{40} \text{erg s}^{-1}$  Machado et al. (2019,em prep.)

mangaID (1)	RA (2)	DEC (3)	$z$ (4)	$M_r$ (5)	$\log M^*/M_{\odot}$ (6)	GZ1 <sub>c</sub> (7)	$L(\text{[O III]})$ (8)
1-150947	183.263962	51.648602	0.0849	-20.23	10.96	M	$51.03 \pm 1.41$
1-71987	119.486328	39.993370	0.0658	-20.31	10.85	E	$24.66 \pm 0.29$
1-458092	203.190094	26.580387	0.0470	-18.08	9.64	E	$23.89 \pm 0.49$
1-605069	122.972969	57.951878	0.0278	-18.61	10.70	E	$19.59 \pm 0.27$
1-295542	246.255997	24.263163	0.0503	-19.34	10.73	E	$18.43 \pm 0.20$
1-318148	241.944656	25.537500	0.0407	-18.37	10.02	E	$17.44 \pm 0.19$
1-296733	241.717346	27.927526	0.0460	-19.70	10.65	-	$16.63 \pm 0.27$
1-163966	120.087456	26.613560	0.0267	-20.13	10.90	S	$15.27 \pm 0.13$
1-635348	313.902130	-0.636590	0.0535	-20.74	11.06	E	$14.99 \pm 0.21$
1-229862	120.996666	23.755680	0.0294	-19.53	10.49	E	$12.19 \pm 0.08$
1-196637	206.669998	52.476833	0.0292	-19.08	10.62	E	$11.74 \pm 0.09$
1-24660	262.399231	54.494442	0.0819	-20.54	11.49	S	$11.49 \pm 0.46$
1-317962	240.779495	24.523991	0.0467	-19.24	10.55	-	$11.43 \pm 0.20$
1-31788	9.399217	0.280681	0.0349	-20.49	11.25	-	$10.84 \pm 0.12$
1-323794	245.346649	32.349022	0.0347	-19.73	10.59	S	$10.83 \pm 0.16$
1-413061	130.187042	22.294455	0.1091	-21.63	11.59	S	$10.23 \pm 0.50$
1-46056	126.015343	51.904324	0.0315	-18.01	10.14	E	$9.57 \pm 0.15$
1-175889	184.652023	51.414715	0.0472	-20.63	11.31	S	$9.57 \pm 0.15$
1-382452	118.162300	18.321600	0.0449	-19.80	10.77	E	$9.02 \pm 0.13$
1-153627	121.779922	36.233479	0.0323	-20.11	10.99	S	$8.91 \pm 0.08$
1-258373	182.286713	44.003197	0.0375	-20.78	11.14	S	$8.76 \pm 0.17$
1-122304	121.920799	39.004238	0.0233	-19.49	10.29	E	$8.69 \pm 0.10$
31-115	119.917160	15.386813	0.0155	-18.39	*****	S	$8.55 \pm 0.06$
1-298938	127.105942	26.397352	0.0809	-20.59	11.43	S	$8.10 \pm 0.37$
1-603039	29.052231	14.906663	0.0269	-18.93	10.53	S	$7.66 \pm 0.09$
1-270129	248.140854	26.380728	0.0586	-20.59	11.21	S	$7.46 \pm 0.25$
1-174631	173.537552	49.254547	0.0371	-18.05	10.00	S	$7.37 \pm 0.12$
1-229731	119.972862	23.390062	0.0291	-20.19	11.24	S	$7.19 \pm 0.10$
1-403982	187.419128	36.199409	0.0717	-20.05	10.90	M	$6.89 \pm 0.16$
1-176644	255.523315	31.797436	0.0650	-19.94	10.88	S	$6.85 \pm 0.15$
1-605353	129.312103	4.695890	0.0470	-20.25	10.91	S	$6.63 \pm 0.09$
1-251458	212.376053	41.110920	0.0771	-21.46	11.48	S	$6.28 \pm 0.34$
1-268479	240.475067	31.892050	0.0450	-18.22	10.35	S	$6.20 \pm 0.10$
1-547402	258.495850	33.607109	0.0387	-17.75	10.46	-	$6.02 \pm 0.19$
1-537120	207.608215	23.456924	0.0557	-19.45	10.68	S	$5.66 \pm 0.12$
1-55037	145.163864	2.489887	0.1445	-19.97	11.10	E	$5.16 \pm 0.71$
1-43868	118.774513	40.041302	0.0688	-20.28	11.12	S	$5.14 \pm 0.13$
1-397613	186.251175	40.157330	0.0736	-20.61	11.87	-	$4.89 \pm 0.48$
1-457424	197.770111	26.972677	0.0594	-19.39	11.01	S	$4.84 \pm 0.19$
1-299561	130.320068	27.659315	0.0951	-20.45	11.43	E	$4.24 \pm 0.39$
1-314409	223.867447	32.840015	0.0602	-18.42	10.49	-	$4.16 \pm 0.22$
1-60653	150.529343	3.057688	0.0234	-19.26	10.81	-	$4.13 \pm 0.04$
1-209707	241.029068	44.549763	0.0430	-18.32	10.22	E	$3.92 \pm 0.09$
1-617323	177.440353	50.527004	0.0264	-19.16	10.56	S	$3.82 \pm 0.05$
1-37440	45.954613	-1.103748	0.0136	-19.21	11.24	S	$3.37 \pm 0.02$
1-295041	247.828110	24.712290	0.0582	-20.18	10.86	E	$3.37 \pm 0.14$
1-264729	240.044479	27.605145	0.0330	-18.10	10.59	S	$3.33 \pm 0.10$
1-78719	151.006760	4.051177	0.0441	-18.87	10.24	E	$2.99 \pm 0.10$
1-23670	263.050812	59.941525	0.0279	-19.63	11.00	E	$2.97 \pm 0.06$
1-352063	124.546165	52.452419	0.1386	-21.22	11.58	E	$2.97 \pm 0.56$
1-604912	120.082359	26.701445	0.0278	-19.35	11.22	-	$2.93 \pm 0.07$
1-298778	127.107796	25.014637	0.0287	-19.32	10.77	S	$2.91 \pm 0.04$
1-196597	208.289124	51.812504	0.0676	-19.86	11.35	S	$2.58 \pm 0.21$
1-625513	200.222839	32.190769	0.0230	-18.67	10.20	S	$2.15 \pm 0.04$
1-210020	241.301605	45.453297	0.0435	-18.29	10.27	S	$2.04 \pm 0.14$

Tabela 2.1

mangaID (1)	RA (2)	DEC (3)	$z$ (4)	$M_r$ (5)	$\log M^*/M_\odot$ (6)	GZ1 <sub>c</sub> (7)	L([O III]) (8)
1-633942	246.050766	30.162258	0.0482	-20.43	11.21	S	$2.01 \pm 0.07$
1-37385	46.294197	-1.075454	0.0450	-20.00	10.92	S	$1.96 \pm 0.07$
1-626658	203.830200	26.424761	0.0254	-19.17	10.49	S	$1.81 \pm 0.03$
1-163789	118.071083	25.669090	0.0454	-19.10	*****	-	$1.80 \pm 0.06$
1-46057	126.002457	51.540470	0.0812	-20.63	11.05	E	$1.78 \pm 0.25$
1-546819	257.001343	36.344421	0.0362	-19.87	11.14	-	$1.76 \pm 0.08$
1-605215	126.084358	20.533237	0.0199	-18.17	10.32	S	$1.61 \pm 0.02$
1-114252	322.933350	11.381229	0.0476	-18.85	10.74	E	$1.50 \pm 0.07$
1-603941	45.960236	-0.204459	0.0276	-19.82	10.55	S	$1.49 \pm 0.04$
1-210186	241.150986	43.879803	0.0598	-20.03	11.08	S	$1.48 \pm 0.11$
1-380097	124.064056	57.530540	0.0272	-18.78	10.46	S	$1.48 \pm 0.03$
1-177972	259.356384	29.185535	0.0286	-17.93	10.00	E	$1.47 \pm 0.03$
1-296537	245.478149	26.600502	0.0642	-20.00	11.09	-	$1.34 \pm 0.14$
1-263219	230.483093	33.515083	0.0616	-19.64	11.15	E	$1.32 \pm 0.11$
1-281125	182.253723	42.475266	0.0236	-16.94	9.32	E	$1.30 \pm 0.02$
1-295721	245.807465	26.479288	0.0645	-20.58	11.21	E	$1.28 \pm 0.14$
1-295671	245.012238	26.054241	0.1321	-20.70	11.10	-	$1.26 \pm 0.39$
1-149561	171.657227	51.573059	0.0264	-18.28	10.08	S	$1.24 \pm 0.03$
1-232143	140.944122	35.483402	0.0266	-18.87	9.98	S	$1.14 \pm 0.03$
1-209772	239.974945	44.709000	0.0417	-19.83	11.19	E	$1.14 \pm 0.06$
1-299013	128.494568	26.106792	0.0587	-19.99	10.78	S	$1.07 \pm 0.07$
1-382355	117.239517	17.577110	0.0287	-19.20	10.73	E	$0.99 \pm 0.04$
1-376346	241.152710	23.663198	0.0310	-18.93	10.75	E	$0.98 \pm 0.04$
1-277257	165.910126	45.179966	0.0205	-18.81	10.46	S	$0.95 \pm 0.02$
1-401864	185.944061	36.152798	0.0333	-19.84	10.90	S	$0.95 \pm 0.05$
1-265134	241.431732	27.204987	0.0306	-18.89	10.79	-	$0.85 \pm 0.05$
1-382697	119.207581	17.380337	0.0364	-19.25	10.61	E	$0.85 \pm 0.06$
1-201969	120.825859	31.776365	0.0364	-19.54	10.76	S	$0.82 \pm 0.03$
1-145679	118.423225	26.492683	0.0374	-20.02	10.87	S	$0.82 \pm 0.04$
1-174945	176.288589	49.718784	0.0322	-20.17	11.32	E	$0.78 \pm 0.06$
1-153901	123.857376	37.340519	0.0397	-18.44	10.10	-	$0.75 \pm 0.05$
1-77016	135.622437	3.384990	0.0271	-19.28	10.88	E	$0.74 \pm 0.04$
1-179679	317.314880	0.523471	0.0507	-20.78	11.15	E	$0.73 \pm 0.10$
1-121973	121.272995	37.625591	0.0328	-18.97	10.44	E	$0.70 \pm 0.03$
1-229879	121.037064	24.558607	0.0438	-18.66	10.68	E	$0.70 \pm 0.07$
1-632610	231.100784	30.277443	0.0312	-19.13	11.20	S	$0.67 \pm 0.05$
1-405760	196.102692	36.479977	0.0232	-18.35	10.31	S	$0.62 \pm 0.05$
1-189584	179.117249	55.125233	0.0037	-17.71	9.70	-	$0.56 \pm 0.00$
1-298298	120.538361	21.252752	0.0304	-18.67	10.33	S	$0.56 \pm 0.02$
1-272639	247.361282	29.541122	0.0530	-20.24	11.36	S	$0.52 \pm 0.06$
1-384124	126.216408	20.991213	0.0229	-17.83	10.23	S	$0.48 \pm 0.02$
1-201392	117.860481	28.234207	0.0227	-18.36	10.20	S	$0.46 \pm 0.02$
1-150899	184.871429	51.775913	0.0572	-19.72	10.84	S	$0.43 \pm 0.07$
1-604022	49.487793	-0.169089	0.0228	-19.88	10.97	S	$0.40 \pm 0.03$
1-248618	243.155045	39.419041	0.0322	-19.08	10.54	E	$0.38 \pm 0.03$
1-523167	205.213150	24.473293	0.0270	-19.93	11.03	S	$0.38 \pm 0.03$
1-261224	213.230209	39.312641	0.0251	-17.95	10.19	S	$0.38 \pm 0.03$
1-389509	147.539001	33.569332	0.0270	-19.16	10.60	-	$0.33 \pm 0.03$
1-420924	204.554367	32.822872	0.0245	-19.57	10.55	S	$0.32 \pm 0.01$
1-37633	47.142967	0.550920	0.0309	-18.68	10.70	E	$0.30 \pm 0.03$
1-325918	256.196747	24.583965	0.0425	-17.72	10.49	S	$0.29 \pm 0.06$
1-298498	122.938751	23.473812	0.0157	-16.29	9.03	E	$0.27 \pm 0.01$
1-298693	124.698280	24.537426	0.0249	-18.78	10.37	S	$0.23 \pm 0.02$
1-519412	203.777222	22.661844	0.0317	-17.91	10.08	E	$0.22 \pm 0.02$
1-297172	241.941223	29.336777	0.0241	-18.03	10.03	S	$0.20 \pm 0.01$
1-379811	123.717453	55.610264	0.0404	-17.55	9.96	-	$0.15 \pm 0.03$

Tabela 2.2: MPL-8 *exclusive* control sample parameters. The objects released at MPL-5 had their parameters cataloged at ?). (1) identification in the MaNGA survey of the AGN host related to the control galaxy. (2)-(9) same as (1)-(8) of Table 2.1 Machado et al. (2019,em prep.)

AGN mangaID (1)	mangaID (2)	RA (3)	DEC (4)	z (5)	$M_r$ (6)	$\log M^*/M_{\odot}$ (7)	GZ1 <sub>c</sub> (8)	L([O III]) (9)
1-150947	1-338555	114.374146	41.737232	0.0870	-20.00	11.48	M	$1.26 \pm 0.25$
	1-248214	240.347046	43.085068	0.0600	-19.80	10.97	-	$0.69 \pm 0.11$
1-71987	1-399581	204.287720	35.247829	0.0596	-19.68	11.09	E	$0.70 \pm 0.08$
	1-201449	118.470055	29.196974	0.0632	-20.01	10.88	E	$0.17 \pm 0.07$
1-458092	1-38319	51.609447	-0.311683	0.0377	-17.24	9.76	E	$0.02 \pm 0.04$
	1-323888	245.686615	32.659184	0.0410	-18.64	9.54	E	$12.28 \pm 0.29$
1-605069	1-115437	334.218323	13.425960	0.0256	-18.28	10.17	-	$0.02 \pm 0.02$
	1-135129	247.280273	40.591011	0.0328	-19.60	10.84	E	$0.01 \pm 0.04$
1-295542	1-94228	248.018265	47.764774	0.0494	-19.19	10.58	E	$0.44 \pm 0.06$
	1-92774	243.407730	49.069405	0.0552	-19.28	10.75	E	$0.11 \pm 0.08$
1-318148	1-209113	235.579727	48.465721	0.0379	-17.58	9.80	E	$0.02 \pm 0.02$
	1-256457	166.781357	42.825489	0.0369	-17.29	9.75	E	$0.05 \pm 0.01$
1-296733	1-547596	260.479370	29.846418	0.0468	-19.23	10.55	-	$0.41 \pm 0.05$
	1-38348	51.155499	-0.444021	0.0368	-19.91	10.95	S	$0.56 \pm 0.06$
1-163966	1-155926	141.539307	49.310215	0.0269	-19.61	10.76	S	$0.08 \pm 0.01$
	1-625070	198.784225	30.403770	0.0232	-18.76	10.61	-	$0.65 \pm 0.05$
1-635348	1-298950	127.374084	26.549948	0.0567	-20.59	11.27	E	$0.30 \pm 0.09$
	1-213825	129.594009	4.355987	0.0475	-20.16	11.02	E	$0.32 \pm 0.07$
1-229862	1-178782	310.450012	-0.468316	0.0269	-18.36	10.56	E	$0.13 \pm 0.01$
	1-153103	119.738312	32.612251	0.0283	-19.82	10.93	E	$0.15 \pm 0.02$
1-196637	1-389238	148.073685	33.063740	0.0270	-19.49	10.84	E	$0.25 \pm 0.03$
	1-458301	204.891373	25.556107	0.0264	-18.54	10.38	E	$0.11 \pm 0.02$
1-24660	1-217637	116.183792	22.160177	0.0851	-20.96	11.41	S	$0.80 \pm 0.24$
	1-175200	178.462463	51.031166	0.0785	-20.59	11.07	S	$0.40 \pm 0.15$
1-317962	1-217358	147.035645	44.797245	0.0427	-18.20	10.20	E	$0.04 \pm 0.03$
	1-218077	120.251175	24.639851	0.0469	-18.78	10.24	E	$0.22 \pm 0.04$
1-31788	1-379708	121.054840	55.397655	0.0324	-19.78	11.21	S	$0.33 \pm 0.03$
	1-317822	242.810043	24.225016	0.0325	-19.62	10.81	S	$1.24 \pm 0.06$
1-323794	1-379708	121.054840	55.397655	0.0324	-19.78	11.21	S	$0.33 \pm 0.03$
	1-316945	236.006317	28.277027	0.0332	-19.95	10.95	S	$0.95 \pm 0.05$
1-413061	1-72914	127.580803	45.075878	0.0970	-20.88	11.31	S	$0.35 \pm 0.19$
	1-146247	120.723969	28.457113	0.0772	-21.25	11.48	S	$0.22 \pm 0.09$
1-46056	1-279544	172.365723	47.696297	0.0331	-18.08	10.10	E	$0.16 \pm 0.02$
	1-178103	257.910370	31.173557	0.0302	-18.21	10.16	E	$0.12 \pm 0.02$
1-175889	1-269638	247.688416	26.095259	0.0477	-20.29	11.20	S	$0.27 \pm 0.05$
	1-459018	119.505577	14.702627	0.0473	-20.64	11.34	S	$0.63 \pm 0.08$
1-382452	1-256009	167.103851	43.012966	0.0494	-20.02	11.41	E	$1.05 \pm 0.08$
	1-166613	144.515976	42.974327	0.0468	-20.35	11.06	E	$0.29 \pm 0.08$
1-153627	1-43783	117.898453	42.880112	0.0320	-20.02	10.89	S	$0.18 \pm 0.03$
	1-120935	114.775040	29.160080	0.0389	-20.63	11.16	S	$0.22 \pm 0.04$
1-258373	1-284485	196.232391	47.503643	0.0393	-20.35	11.05	S	$0.18 \pm 0.03$
	1-266039	213.416824	43.866589	0.0350	-20.45	10.94	S	$0.13 \pm 0.02$
1-122304	1-455924	192.932434	27.962835	0.0231	-18.65	10.41	E	$0.12 \pm 0.01$
	1-199454	235.176651	43.751255	0.0196	-18.41	10.20	E	$0.05 \pm 0.01$
1-298938	1-217637	116.183792	22.160177	0.0851	-20.96	11.41	S	$0.80 \pm 0.24$
	1-248056	238.746338	42.105366	0.0705	-20.56	10.97	S	$0.66 \pm 0.12$
1-603039	1-155463	137.562439	46.293282	0.0267	-18.65	10.28	S	$0.22 \pm 0.02$
	1-135625	248.507462	41.347958	0.0284	-19.06	10.56	S	$0.55 \pm 0.04$
1-270129	1-259537	194.925018	43.753204	0.0578	-20.72	11.22	S	$0.79 \pm 0.12$
	1-164053	119.039497	26.875776	0.0616	-20.95	11.10	S	$0.84 \pm 0.13$
1-174631	1-322679	235.709442	38.223858	0.0405	-18.16	9.99	-	$0.12 \pm 0.03$
	1-295343	246.480728	25.411606	0.0393	-18.31	9.88	E	$0.20 \pm 0.03$
1-229731	1-153028	118.319862	32.543751	0.0280	-19.49	10.90	S	$0.15 \pm 0.03$
	1-379741	121.664742	55.147083	0.0329	-19.67	10.98	S	$0.25 \pm 0.03$
1-403982	1-167083	148.897781	45.554783	0.0725	-19.69	11.21	M	$0.67 \pm 0.18$
	1-634328	254.309799	34.024044	0.0845	-19.94	11.22	M	$1.34 \pm 0.20$
1-176644	1-401783	200.532242	30.144417	0.0611	-20.10	11.01	S	$0.46 \pm 0.10$
	1-201875	119.500206	30.795589	0.0766	-20.60	11.21	S	$0.29 \pm 0.11$
1-605353	1-317809	241.003906	25.955408	0.0486	-20.75	11.42	S	$1.43 \pm 0.13$
	1-459018	119.505577	14.702627	0.0473	-20.64	11.34	S	$0.63 \pm 0.08$

Tabela 2.2

AGN mangaID (1)	mangaID (2)	RA (3)	DEC (4)	z (5)	$M_r$ (6)	$\log M^*/M_\odot$ (7)	GZ1c (8)	L([O III]) (9)
1-251458	1-321276	218.364853	46.468266	0.0725	-21.04	11.32	S	$0.27 \pm 0.09$
	1-146247	120.723969	28.457113	0.0772	-21.25	11.48	S	$0.22 \pm 0.09$
1-268479	1-459018	119.505577	14.702627	0.0473	-20.64	11.34	S	$0.63 \pm 0.08$
	1-71525	118.344826	36.274372	0.0457	-20.17	10.97	S	$0.26 \pm 0.06$
1-547402	1-247769	235.899033	43.842239	0.0370	-17.46	10.40	S	$0.11 \pm 0.03$
	1-351563	117.863930	48.595043	0.0420	-17.96	10.22	S	$0.46 \pm 0.09$
1-537120	1-207914	222.394577	52.967297	0.0577	-19.69	10.63	E	$0.44 \pm 0.08$
	1-399581	204.287720	35.247829	0.0596	-19.68	11.09	E	$0.70 \pm 0.08$
1-55037	1-322336	230.357635	43.454380	0.1350	-20.89	11.82	E	$1.81 \pm 0.68$
	1-218427	124.342300	27.796207	0.1496	-21.30	11.47	E	$0.25 \pm 0.61$
1-43868	1-91339	237.653854	53.390640	0.0651	-20.00	10.98	S	$0.44 \pm 0.10$
	1-315099	228.632706	31.030952	0.0711	-20.78	11.26	E	$0.81 \pm 0.16$
1-397613	1-603793	42.811310	-0.329249	0.0669	-19.88	11.28	S	$6.54 \pm 0.55$
	1-627000	205.321152	26.272047	0.0639	-20.12	11.24	-	$0.90 \pm 0.14$
1-457424	1-214751	136.212570	5.115862	0.0678	-19.81	11.32	S	$0.35 \pm 0.15$
	1-229660	118.475914	22.465721	0.0447	-18.56	10.70	S	$0.89 \pm 0.10$
1-299561	1-109419	51.228935	0.605940	0.1032	-21.26	11.70	-	$0.12 \pm 0.19$
	1-42703	27.529861	13.110405	0.0863	-20.35	11.24	E	$0.60 \pm 0.22$
1-314409	1-260534	206.334427	41.388924	0.0595	-20.47	11.15	S	$0.85 \pm 0.10$
	1-339028	116.097931	44.527737	0.0497	-20.01	11.24	S	$0.44 \pm 0.04$
1-60653	1-122284	122.084496	39.023632	0.0225	-18.50	10.43	E	$0.38 \pm 0.03$
	1-277103	163.734802	41.498428	0.0246	-18.85	10.44	S	$0.11 \pm 0.02$
1-209707	1-419555	182.871414	36.788422	0.0437	-18.36	10.24	E	$0.15 \pm 0.03$
	1-198238	226.436111	46.788612	0.0382	-17.58	9.96	E	$0.16 \pm 0.03$
1-617323	1-149147	171.102646	51.234928	0.0272	-19.99	10.82	S	$0.32 \pm 0.03$
	1-216958	136.200272	40.591717	0.0270	-18.95	10.41	S	$0.22 \pm 0.01$
1-295041	1-351622	119.520950	49.417927	0.0586	-19.99	10.97	S	$0.40 \pm 0.10$
	1-458504	206.036118	26.348915	0.0651	-20.41	11.12	S	$0.35 \pm 0.10$
1-264729	1-633994	247.419922	40.686970	0.0305	-18.27	11.04	S	$0.22 \pm 0.05$
	1-93835	248.055710	44.403236	0.0310	-18.72	10.58	S	$0.23 \pm 0.03$
1-78719	1-286261	209.444366	45.040859	0.0427	-18.60	10.02	-	$0.27 \pm 0.04$
	1-218019	120.696320	24.771385	0.0413	-18.57	10.27	E	$0.45 \pm 0.05$
1-23670	1-43541	116.847771	39.195915	0.0256	-17.94	10.10	E	$0.05 \pm 0.01$
	1-93793	249.074463	44.135708	0.0313	-19.93	11.24	S	$0.51 \pm 0.08$
1-352063	1-378770	119.119957	50.287872	0.1336	-21.50	11.66	E	$3.76 \pm 0.62$
	1-201464	118.307030	28.828293	0.1428	-20.79	11.59	E	$1.68 \pm 0.54$
1-604912	1-278057	166.767365	45.822124	0.0252	-19.29	11.01	S	$0.43 \pm 0.04$
	1-379741	121.664742	55.147083	0.0329	-19.67	10.98	S	$0.25 \pm 0.03$
1-298778	1-177250	256.664032	34.542995	0.0302	-18.93	10.65	E/S	$0.20 \pm 0.03$
	1-155926	141.539307	49.310215	0.0269	-19.61	10.76	S	$0.08 \pm 0.01$
1-196597	1-36925	41.840462	-0.462501	0.0752	-20.18	11.16	S	$0.56 \pm 0.15$
	1-255916	164.115005	43.496521	0.0509	-19.04	11.21	S	$0.26 \pm 0.09$
1-625513	1-201356	116.993591	28.324781	0.0235	-18.24	10.13	S	$0.14 \pm 0.02$
	1-25740	263.892517	59.889927	0.0284	-19.24	10.83	S	$0.29 \pm 0.04$
1-210020	1-375129	232.433380	27.111996	0.0453	-18.61	10.51	S	$0.61 \pm 0.09$
	1-229888	121.365593	24.795309	0.0464	-18.53	10.60	S	$0.91 \pm 0.09$
1-633942	1-150370	177.844543	53.444172	0.0518	-20.98	11.29	S	$0.55 \pm 0.08$
	1-201913	119.799034	31.807886	0.0592	-20.67	11.20	S	$0.43 \pm 0.08$
1-37385	1-338220	113.056976	39.560085	0.0488	-20.07	10.99	S	$0.32 \pm 0.05$
	1-45179	123.571182	46.010307	0.0499	-20.16	11.01	S	$0.28 \pm 0.06$
1-626658	1-631640	223.610977	53.217445	0.0269	-19.34	10.73	S	$0.08 \pm 0.02$
	1-24161	259.682190	58.135117	0.0291	-19.73	10.99	S	$0.14 \pm 0.03$
1-163789	1-45179	123.571182	46.010307	0.0499	-20.16	11.01	S	$0.28 \pm 0.06$
	1-489642	171.578049	21.096226	0.0428	-20.44	11.13	S	$0.34 \pm 0.06$
1-46057	1-54008	139.740814	1.148929	0.0878	-20.42	11.19	E	$0.29 \pm 0.16$
	1-316675	237.024704	27.962372	0.0783	-20.28	11.17	E	$0.18 \pm 0.11$
1-546819	1-439760	234.196091	25.416805	0.0341	-20.03	11.29	E	$0.02 \pm 0.02$
	1-604153	55.808205	-1.018715	0.0367	-20.07	11.09	E	$0.25 \pm 0.04$
1-605215	1-605482	131.982544	25.831669	0.0188	-18.86	10.58	S	$0.18 \pm 0.02$
	1-491047	172.143173	21.010717	0.0208	-19.23	10.57	-	$0.17 \pm 0.02$
1-114252	1-187419	171.954208	53.739437	0.0492	-18.87	10.44	E	$0.14 \pm 0.04$
	1-197280	215.752075	51.709568	0.0443	-18.75	10.33	E	$0.10 \pm 0.03$
1-603941	1-626684	203.910034	25.875259	0.0256	-19.13	10.65	S	$0.08 \pm 0.02$
	1-37213	42.416527	-0.069862	0.0282	-19.93	10.71	S	$0.20 \pm 0.04$

Tabela 2.2

AGN mangaID (1)	mangaID (2)	RA (3)	DEC (4)	z (5)	$M_r$ (6)	$\log M^*/M_\odot$ (7)	GZ1 <sub>c</sub> (8)	L([O III]) (9)
1-210186	1-262322	224.024506	34.481831	0.0657	-20.28	10.97	E	$0.32 \pm 0.10$
	1-351622	119.520950	49.417927	0.0586	-19.99	10.97	S	$0.40 \pm 0.10$
1-380097	1-25740	263.892517	59.889927	0.0284	-19.24	10.83	S	$0.29 \pm 0.04$
	1-625070	198.784225	30.403770	0.0232	-18.76	10.61	-	$0.65 \pm 0.05$
1-177972	1-149496	172.621918	50.765255	0.0261	-17.87	10.15	E	$0.18 \pm 0.02$
	1-385108	129.495453	25.048773	0.0280	-18.02	10.15	-	$0.10 \pm 0.02$
1-296537	1-319961	205.178177	51.888725	0.0615	-19.94	11.03	S	$0.65 \pm 0.13$
	1-91010	235.803574	57.411175	0.0739	-20.11	11.17	E	$0.63 \pm 0.14$
1-263219	1-491063	172.481781	21.517881	0.0494	-19.18	10.63	E	$0.19 \pm 0.07$
	1-316030	230.652557	29.895750	0.0753	-20.16	11.14	E	$0.81 \pm 0.21$
1-281125	1-404052	188.084030	36.513367	0.0227	-17.47	9.75	E	$0.34 \pm 0.01$
	1-323766	246.175964	32.064373	0.0216	-17.62	9.79	E	$0.14 \pm 0.01$
1-295721	1-627086	205.606705	26.212439	0.0658	-20.53	11.24	E	$0.17 \pm 0.12$
	1-254546	155.274689	44.377712	0.0586	-20.33	11.40	-	$0.59 \pm 0.10$
1-295671	1-384945	129.147400	23.119572	0.1252	-21.18	11.52	-	$3.45 \pm 0.60$
	1-25771	260.555542	54.318096	0.1115	-19.57	10.88	-	$1.01 \pm 0.24$
1-149561	1-37813	46.521252	-0.534056	0.0248	-17.69	9.88	E/S	$0.01 \pm 0.01$
	1-456341	194.506500	27.489666	0.0254	-18.93	10.39	S	$0.01 \pm 0.01$
1-232143	1-173966	167.556808	48.951408	0.0243	-18.56	9.88	-	$0.16 \pm 0.02$
	1-627397	206.769058	24.996494	0.0291	-19.48	10.34	S	$0.16 \pm 0.02$
1-209772	1-37754	47.320751	-0.906658	0.0393	-19.96	10.94	E	$0.54 \pm 0.06$
	1-38293	51.680000	-0.769450	0.0388	-20.08	10.96	E	$0.20 \pm 0.04$
1-299013	1-201391	117.811562	28.153616	0.0524	-19.61	10.83	S	$0.46 \pm 0.07$
	1-149471	173.037842	50.765541	0.0486	-19.15	10.50	-	$0.27 \pm 0.05$
1-382355	1-627945	208.388306	24.875233	0.0304	-19.55	11.17	E	$0.05 \pm 0.02$
	1-604841	117.310547	28.611589	0.0275	-18.98	10.63	E	$0.02 \pm 0.02$
1-376346	1-627945	208.388306	24.875233	0.0304	-19.55	11.17	E	$0.05 \pm 0.02$
	1-51886	58.485626	-7.072957	0.0332	-19.97	11.28	E	$0.11 \pm 0.04$
1-277257	1-605482	131.982544	25.831669	0.0188	-18.86	10.58	S	$0.18 \pm 0.02$
	1-491047	172.143173	21.010717	0.0208	-19.23	10.57	-	$0.17 \pm 0.02$
1-401864	1-174947	176.358749	49.879044	0.0333	-19.09	10.64	S	$0.24 \pm 0.03$
	1-246470	223.320786	52.044247	0.0369	-19.95	10.87	S	$0.16 \pm 0.04$
1-265134	1-633776	243.142075	25.500761	0.0326	-19.23	10.83	S	$0.17 \pm 0.03$
	1-135157	247.041306	40.695595	0.0324	-19.10	10.70	E	$0.02 \pm 0.04$
1-382697	1-458127	203.550644	27.003183	0.0355	-18.96	10.74	S	$0.31 \pm 0.04$
	1-44526	118.713310	43.182655	0.0331	-19.26	10.65	E	$0.06 \pm 0.02$
1-201969	1-199368	233.283417	44.535683	0.0367	-20.15	10.87	S	$0.26 \pm 0.03$
	1-278113	167.133606	47.336300	0.0358	-19.76	10.99	S	$0.22 \pm 0.04$
1-145679	1-247977	239.491852	41.792603	0.0350	-19.82	10.74	S	$0.20 \pm 0.04$
	1-201756	120.814369	30.796497	0.0403	-20.81	11.15	-	$0.30 \pm 0.04$
1-174945	1-137845	139.308823	44.489189	0.0320	-20.07	11.05	E	$0.07 \pm 0.02$
	1-135372	250.116730	39.320141	0.0301	-20.29	11.08	E	$0.12 \pm 0.27$
1-153901	1-257627	178.474884	43.818771	0.0427	-18.12	10.41	S	$0.21 \pm 0.04$
	1-383017	121.720436	19.859211	0.0392	-17.86	9.99	S	$0.03 \pm 0.02$
1-77016	1-246542	225.804214	49.851166	0.0281	-19.13	10.60	E	$0.17 \pm 0.03$
	1-210731	247.318756	39.401039	0.0281	-18.95	10.74	S	$0.03 \pm 0.02$
1-179679	1-188844	176.507980	55.419613	0.0526	-20.52	11.05	E	$0.32 \pm 0.07$
	1-285729	203.896530	40.111118	0.0542	-20.69	11.25	E	$0.49 \pm 0.08$
1-121973	1-23890	260.386475	56.988865	0.0301	-18.59	10.43	E	$0.03 \pm 0.02$
	1-488526	167.509247	21.982172	0.0316	-19.45	10.70	-	$0.20 \pm 0.03$
1-229879	1-382352	117.186905	17.966072	0.0462	-18.85	10.39	E	$0.20 \pm 0.05$
	1-46757	128.164383	53.233246	0.0431	-18.56	10.27	E	$0.11 \pm 0.03$
1-632610	1-95982	254.828979	38.866302	0.0336	-19.41	11.17	S	$0.33 \pm 0.04$
	1-94717	250.734619	43.996899	0.0311	-19.04	11.07	S	$0.38 \pm 0.05$
1-405760	1-457236	196.651642	27.872952	0.0209	-18.30	10.18	S	$0.57 \pm 0.03$
	1-384095	126.590126	20.270557	0.0253	-18.54	10.22	S	$0.68 \pm 0.04$
1-298298	1-633990	247.304108	41.150887	0.0296	-19.06	10.46	-	$0.15 \pm 0.02$
	1-316872	235.152634	28.512455	0.0328	-19.44	11.01	S	$0.26 \pm 0.04$
1-272639	1-269638	247.688416	26.095259	0.0477	-20.29	11.20	S	$0.27 \pm 0.05$
	1-71525	118.344826	36.274372	0.0457	-20.17	10.97	S	$0.26 \pm 0.06$
1-384124	1-457813	201.906998	26.965712	0.0236	-18.35	10.31	E	$0.02 \pm 0.02$
	1-38543	54.032406	-0.596429	0.0234	-18.57	10.41	E	$0.19 \pm 0.02$

Tabela 2.2

AGN mangaID (1)	mangaID (2)	RA (3)	DEC (4)	z (5)	$M_r$ (6)	$\log M^*/M_\odot$ (7)	GZ1 <sub>c</sub> (8)	L([O III]) (9)
1-201392	1-210604	243.880661	41.407021	0.0263	-18.59	10.65	E	0.09 ± 0.02
	1-211055	247.336441	39.820419	0.0261	-18.70	10.58	E	0.09 ± 0.02
1-150899	1-73042	126.143761	45.479832	0.0539	-19.74	10.77	S	0.13 ± 0.05
	1-201391	117.811562	28.153616	0.0524	-19.61	10.83	S	0.46 ± 0.07
1-604022	1-137908	139.559158	45.651695	0.0269	-20.01	10.86	S	0.08 ± 0.01
	1-146028	118.592606	27.008795	0.0266	-19.78	10.71	S	0.12 ± 0.02
1-248618	1-50971	48.267513	-8.398560	0.0299	-19.29	10.76	E	0.12 ± 0.02
	1-23890	260.386475	56.988865	0.0301	-18.59	10.43	E	0.03 ± 0.02
1-523167	1-113540	317.903198	11.496931	0.0294	-19.29	10.58	S	0.64 ± 0.03
	1-318334	243.084869	23.002010	0.0323	-19.84	10.92	S	0.19 ± 0.03
1-261224	1-44483	119.834816	42.057072	0.0245	-18.17	10.21	S	0.11 ± 0.01
	1-458011	201.948044	25.449587	0.0250	-17.95	10.10	S	0.03 ± 0.01
1-389509	1-146046	118.323959	27.460728	0.0268	-19.11	10.65	E	0.13 ± 0.02
	1-277103	163.734802	41.498428	0.0246	-18.85	10.44	S	0.11 ± 0.02
1-420924	1-218280	124.003319	27.075884	0.0255	-19.57	10.81	S	0.14 ± 0.02
	1-137908	139.559158	45.651695	0.0269	-20.01	10.86	S	0.08 ± 0.01
1-37633	1-318434	243.032089	23.718149	0.0319	-18.88	10.86	-	0.26 ± 0.03
	1-135193	246.959641	40.937443	0.0309	-18.73	10.60	E	0.01 ± 0.03
1-325918	1-383017	121.720436	19.859211	0.0392	-17.86	9.99	S	0.03 ± 0.02
	1-269212	242.487350	30.106516	0.0482	-18.12	10.92	-	0.45 ± 0.10
1-298498	1-42253	27.565296	13.140800	0.0161	-15.18	9.22	E	0.02 ± 0.01
	1-153224	119.391342	33.121433	0.0169	-16.59	9.33	E	0.15 ± 0.01
1-298693	1-603795	42.896332	-0.733768	0.0232	-19.26	10.61	S	0.15 ± 0.02
	1-146046	118.323959	27.460728	0.0268	-19.11	10.65	E	0.13 ± 0.02
1-519412	1-210748	247.142441	39.418610	0.0309	-18.04	10.27	-	0.02 ± 0.02
	1-395547	203.240433	27.717840	0.0291	-18.48	10.43	E	0.05 ± 0.03
1-297172	1-456656	195.522995	27.297272	0.0243	-17.25	9.71	S	0.01 ± 0.01
	1-395508	203.965042	27.866846	0.0262	-18.37	10.35	S	0.04 ± 0.02
1-379811	1-245908	217.542267	53.982250	0.0430	-18.03	10.29	E	0.03 ± 0.03
	1-44044	119.583427	41.568043	0.0413	-18.40	10.13	E	0.08 ± 0.02

# Capítulo 3

## Resultados

Os resultados obtidos neste trabalho estão descritos no artigo publicado na revista científica Monthly Notices of the Royal Astronomical Society: “**The first 62 AGN observed with SDSS-IV MaNGA - IV: gas excitation and star-formation rate distributions**”, MNRAS, 486, 5075.

E os resultados sobre a metalicidade estão no artigo em preparação do Nascimento et al. (2020,em prep.) intitulado **The gas metallicities in nearby MaNGA AGN**, que será submetido também à revista Monthly Notices of the Royal Astronomical Society.

Anexamos o Paper III ao final deste capítulo, enquanto que o novo paper sobre a metalicidade anexamos ao final da tese juntamente com os outros trabalhos publicados durante a tese nos quais fui colaboradora.

Aqui neste capítulo apresentamos somente os novos resultados correspondentes ao estudo feito no Paper III, mas que compreendem, além dos 62 trios (AGN mais dois controles cada) dos Papers I, II, III e IV (MPL-5), mais 88 novos trios (MPL-8).

### 3.1 A relação R vs. L[OIII]

Com o aumento da amostra, uma nova relação entre a extensão R da região ionizada pelo AGN a sua luminosidade L[OIII] foi obtida. Na Fig. 3.1 temos as duas subamostras dos AGNs identificados como MPL-5 (azul), MPL-7 (magenta), MPL-8(laranja), em vermelho temos o ajuste considerando todas subamostras juntas. Apesar da grande dispersão podemos confirmar que em média, a extensão da região ionizada pelo AGN aumenta com a luminosidade L[OIII], confirmando a tendência de que a região ionizada pelo AGN fica maior quando a luminosidade do AGN aumenta como mostrado em do Nascimento et al. (2019). Os valores encontrados para

$R$  considerando a amostra total variam no intervalo de 1.03 kpc a 27 kpc, com incertezas estimadas de cerca de 15%. Devido à incerteza relativamente grande nas medidas, preferimos não corrigir os dados pela inclinação da galáxia.

Uma regressão linear de mínimos quadrados aplicada aos conjunto completo de dados dá a seguinte relação:

$$\log(R) = (0.15 \pm 0.04) \log L[\text{OIII}] - (5.62 \pm 1.72) \quad (3.1)$$

com o coeficiente de correlação  $r = 0.3$ .

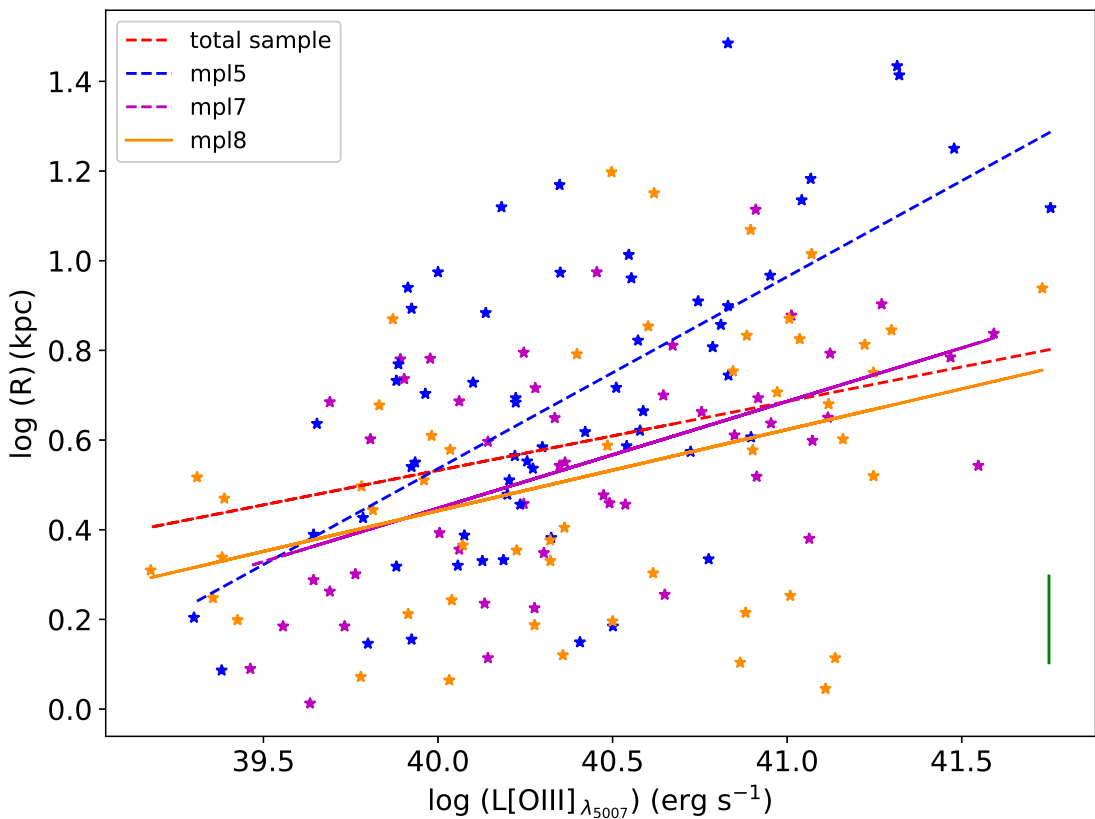


Figura 3.1: Relação entre a extensão da região ionizada  $R$  pelo AGN e  $L[\text{OIII}]$ , mostrando também a regressão linear para os dados. A barra verde indica a incerteza típica de  $R$  em torno de 10%

## 3.2 A taxa de formação estelar SFR

Nas figuras seguintes são mostrados os histogramas de SFR, obtidos a partir da amostra total de AGNs obtida até agora pelo MaNGA. Os valores totais de SFR foram obtidos somando os valores de SFRs de todos os *spaxels* ao longo de toda a

galáxia, onde a formação estelar está presente, incluindo tanto as regiões de excitação HII como as regiões de transição.

A Fig. 3.2 mostra os histogramas da SFR total para o AGN (em vermelho), quando comparados com os da galáxias controles (em azul), separados em três painéis: no painel esquerdo mostramos os histogramas para toda a amostra, no centro apenas para as galáxias *early-type* e no painel direito para as galáxias *late-type*.

As distribuições para os AGNs e controles nos três casos parecem ser semelhantes. Para confirmar se as distribuições são de fato indistinguíveis, usamos o teste Anderson-Darling (A-D) de 2 amostras. A probabilidade  $p$  que as duas distribuições possam ser derivadas de uma mesma população de origem é dada nos painéis correspondentes. Lembramos que o valor  $p$  de referência é 0,05, o que significa que, para valores menores, existe mais de 95% de chance de que as duas distribuições sejam derivadas de populações distintas. De acordo com o teste A-D para a amostra total e late-type, a probabilidade das distribuições serem estatisticamente iguais são,  $\approx 20\%$  e  $\approx 30\%$  respectivamente, enquanto que para as early-type este valor está exatamente no limite do valor de referência.

Na Fig. 3.3 apresentamos histogramas semelhantes aos da figura anterior para o SFR total, porém agora separados em diferentes *bins* de luminosidade do AGN ( $\log_{10} L[\text{OIII}]$ , em unidades de  $\text{erg s}^{-1}$ ). Os painéis mostram os AGNs mais luminosos (41,25 - 42,0) para a esquerda e com luminosidade decrescente para a direita até as menos luminosas (39,0 - 39,75). Novamente as distribuições para AGN e controles são similares de acordo com o teste A-D, com probabilidade de as distribuições serem estatisticamente iguais entre 20% e 90% para os diferentes *bins* de luminosidades.

Como parte também dessa análise estatística, construímos histogramas em que apresentamos a distribuição das diferenças entre o SFR do AGN e cada uma de suas galáxias controle, ou seja, pareando os AGNs com seus controles (300 combinações). O resultado é mostrado na Fig. 3.4 na forma de histogramas dos valores de:  $(\text{SFR}_{AGN} - \text{SFR}_{ctr}) / \text{SFR}_{AGN}$ . A divisão por  $\text{SFR}_{AGN}$  é necessária para trazer as diferenças para uma escala similar.

Nestes novos histogramas, ao considerar toda a amostra,  $\approx 49\%$  das combinações AGN-controle mostram diferenças fracionais positivas (SFR no AGN maior que no controle), com uma diferença média positiva de 0,05 e mediana de 0,37. Ao considerar apenas a subamostra das galáxias *early-type*, esse percentual aumenta para  $\approx 67\%$ , com média de 0,54 e mediana de 0,90, enquanto para as *late-type* esse percentual diminui para 41%. Estes resultados mostram que, enquanto para as

galáxias *early-type*, a maioria dos AGNs tem mais formação estelar do que seus controles, para as galáxias *late-type*, em  $\approx 59\%$  dos casos, há mais formação estelar nos controles e nos outros  $41\%$  há mais formação estelar nos AGNs.

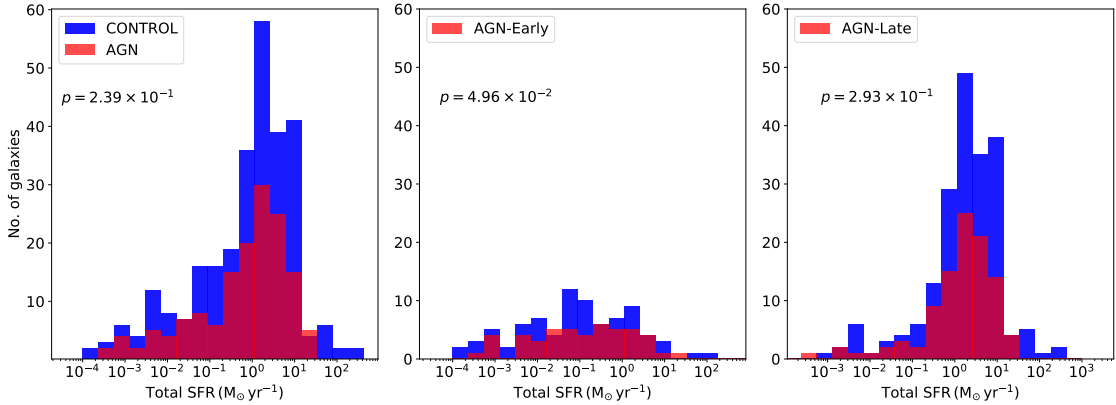


Figura 3.2: Histogramas comparando a SFR total entre AGNs e controles. Painel esquerdo: amostra total; painel central: AGN *early-type*; painel direito: AGN *late-type*. O valor  $p$  em cada painel fornece a probabilidade das duas distribuições serem extraídas da mesma população.

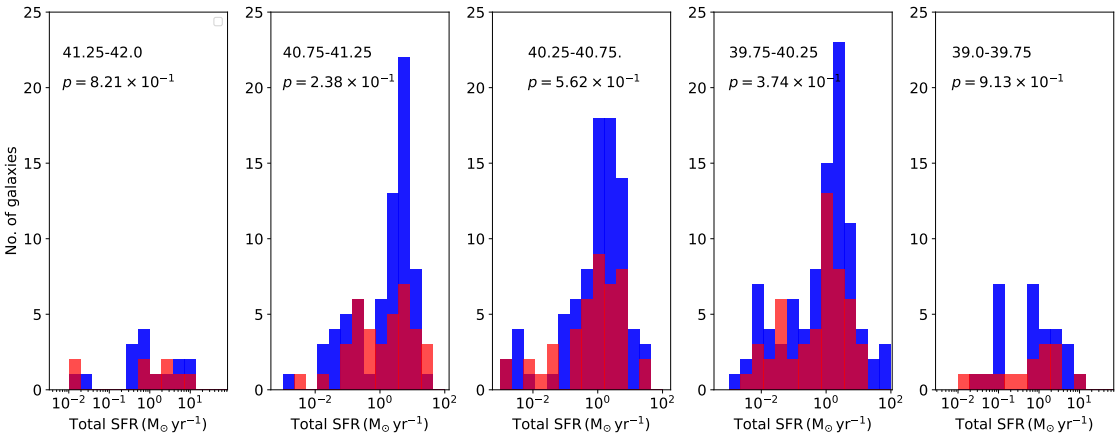


Figura 3.3: Histogramas comparando a SFR total entre AGNs e controle, separadas de acordo com o log da luminosidade  $L[\text{OIII}]$  dos AGNs. O valor de  $L[\text{OIII}]$  diminui da esquerda para a direita. Os valores de  $\log(L[\text{OIII}])$  são identificados no topo de cada painel com  $L[\text{OIII}]$  em unidades de  $\text{erg s}^{-1}$ . O valor  $p$  em cada painel fornece a probabilidade de que as duas distribuições sejam extraídas da mesma população.

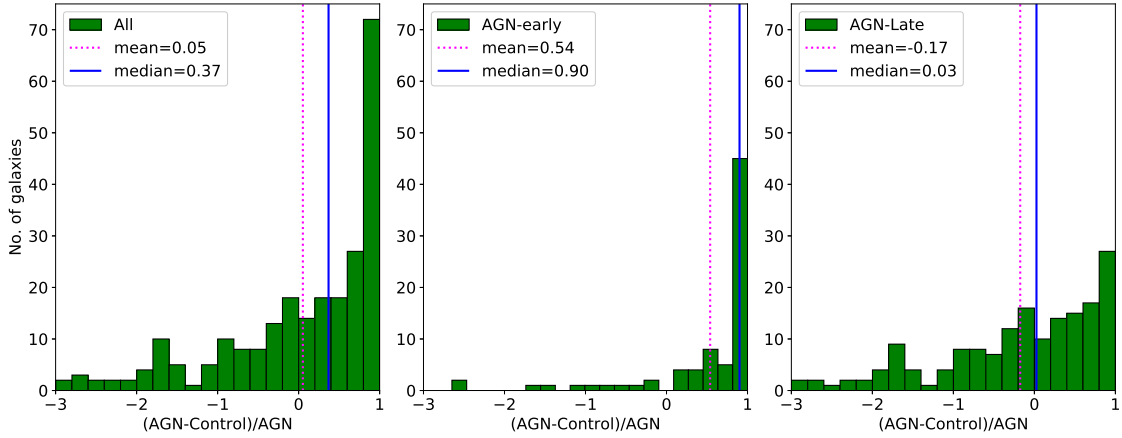


Figura 3.4: Histogramas para a diferença fracional em SFR entre o AGN e cada uma de suas duas galáxias de controle:  $(\text{SFR}_{AGN} - \text{SFR}_{ctr}) / \text{SFR}_{AGN}$ . Painel esquerdo: amostra total; painel central: AGN *early-type*; painel direito: AGN *late-type*.

### 3.3 Densidades de massa superficial de gás ionizado

Calculamos a densidade superficial média central da massa de gás ionizado  $\Sigma_{nuc}$  como a densidade de massa de gás superficial dentro de uma área circular de raio  $0.2 R_e$  ao redor do núcleo. Esses valores variam de  $5.45 \times 10^3$  a  $3.36 \times 10^6 M_\odot \text{ kpc}^{-2}$  para o AGN e para os controles de  $30$  a  $6.01 \times 10^9 M_\odot \text{ kpc}^{-2}$ .

Os histogramas desses valores são mostrados nas Fig. 3.5 e Fig. 3.6, a distribuição de valores para toda a amostra nos painéis da esquerda e separadamente para as subamostras AGN *early-type* e AGN *late-type* no centro e na direita.

De acordo com o teste A-D, as probabilidades  $p$  que o AGN e a amostra de controle são tiradas da mesma população são menores que  $10^{-5}$  para a amostra total e *early-type* e  $p = 2.71 - 1.28 \times 10^{-5}$  e para a amostra *late-type* menor que  $10^{-3}$ , com  $p = 6.06 \times 10^{-3}$ . Os valores médios de  $\Sigma_{nuc}$  são  $3,22 \times 10^5 M_\odot \text{ kpc}^{-2}$  para todos os AGN e  $3.05 \times 10^7 M_\odot \text{ kpc}^{-2}$ , considerando todos os controles.

Na Fig. 3.6, em que os AGN são separados em *bins* de luminosidade, embora o número de objetos em cada *bin* seja pequeno, as distribuições são estatisticamente diferentes - com os valores de  $p \leq 0.02$  para todas as painéis, exceto a de menor luminosidade.

Os resultados dos histogramas da Fig. 3.7 mostram as diferenças fracionais entre os AGNs e controles  $(\Sigma_{nuc,AGN} - \Sigma_{nuc,ctr}) / \Sigma_{nuc,AGN}$  como no caso anterior, temos que 58 % da amostra mostram diferenças fracionais positivas, indicando que  $\Sigma_{nuc}$  é

mais alto no AGN do que nos controles da maior parte da amostra. Ao considerar apenas a subamostra , esse percentual aumenta para  $\approx 70\%$ , enquanto para a subamostra do *late-type* esse percentual é 51 %. As diferenças fracionais médias de  $\Sigma_{nuc}$  entre o AGN e os controles são: 0,70 para a amostra total, 0,90 para o grupo *early-type* e 0,54 para *late-type*.

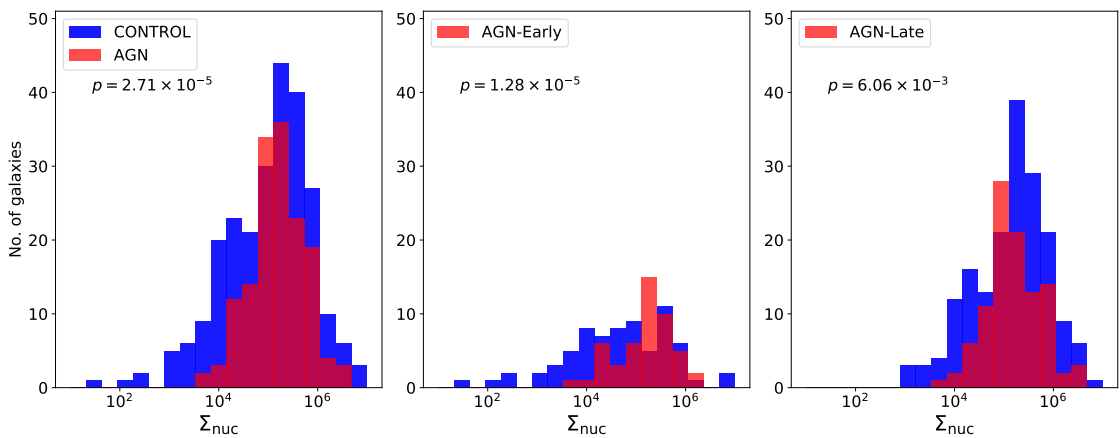


Figura 3.5: Histogramas do  $\Sigma_{nuc}$  (em unidades de  $M_{\odot} \text{ kpc}^{-2}$ ) dentro de  $0.2 R_e$  (raio efetivo); esquerda: amostra total; centro: amostra AGN *early-type*; direita: amostra AGN *late-type*.

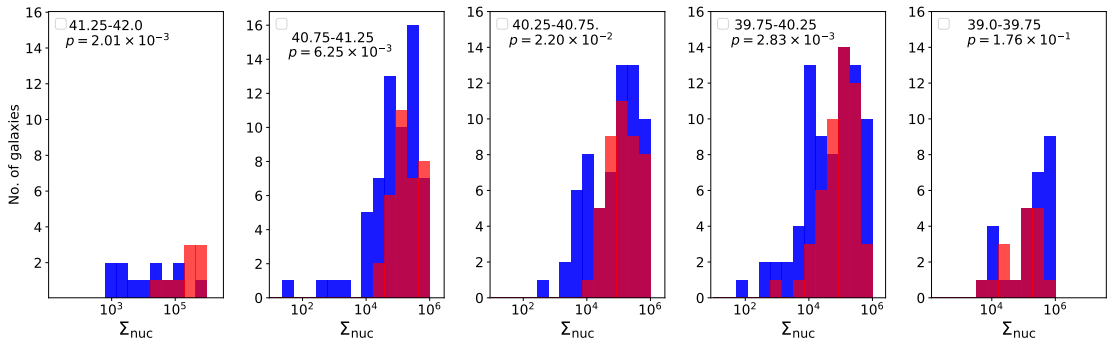


Figura 3.6: Histogramas do  $\Sigma_{nuc}$  separados em *bins* de luminosidade do AGN - mostrados no topo de cada painel como  $\log_{10}(L[\text{OIII}])$ , em unidades de  $10^{40} \text{ erg s}^{-1}$ , juntamente com o valor de  $p$  do teste A-D, desde o AGN mais luminoso (esquerda) até o menos luminoso (direita). Cores como na Fig. 3.5

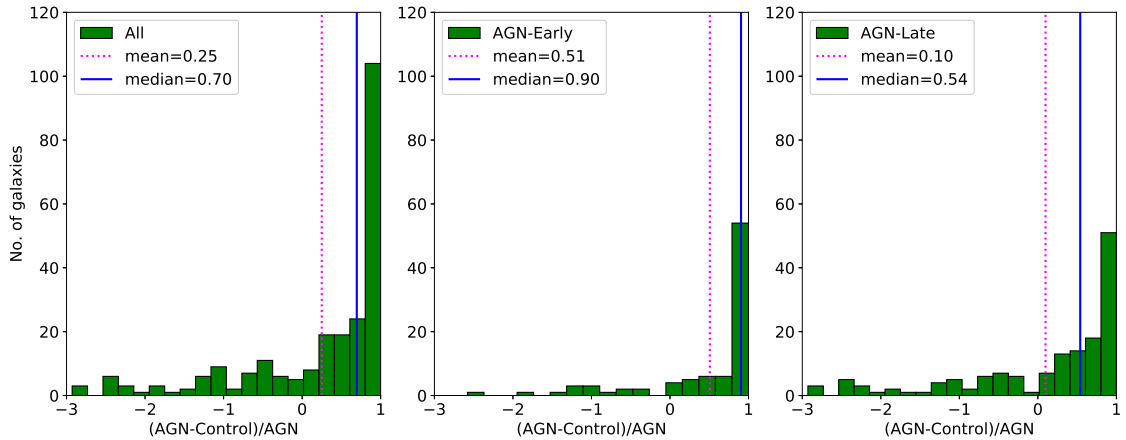


Figura 3.7: Histogramas das diferenças fracionais  $(\Sigma_{nuc,AGN} - \Sigma_{nuc,ctr})/\Sigma_{nuc,AGN}$ ; esquerda: amostra total; centro: amostra AGN *early-type*; direita: amostra AGN *late-type*

### 3.4 Massa total de gás ionizado

O intervalo de valores de massa total de gás ionizado obtidos para os AGNs é semelhantes ao intervalo de valores medidos para os controles, e isso pode ser visto nos histogramas da Fig. 3.8. Mas a distribuição de valores é diferente para as amostras de AGN e controle como indicado pelo teste A-D, que dá uma probabilidade maior que 95% que as distribuições para o primeiro e segundo caso, a amostra total de AGNs comparada com a amostra de controles, e no outro temos somente os AGNs do tipo *early-type* e seus controles) sejam diferentes entre si. Já para o AGNs *late-type* a probabilidade que as duas distribuições AGN-controles sejam de mesma origem é maior, cerca de 30% .

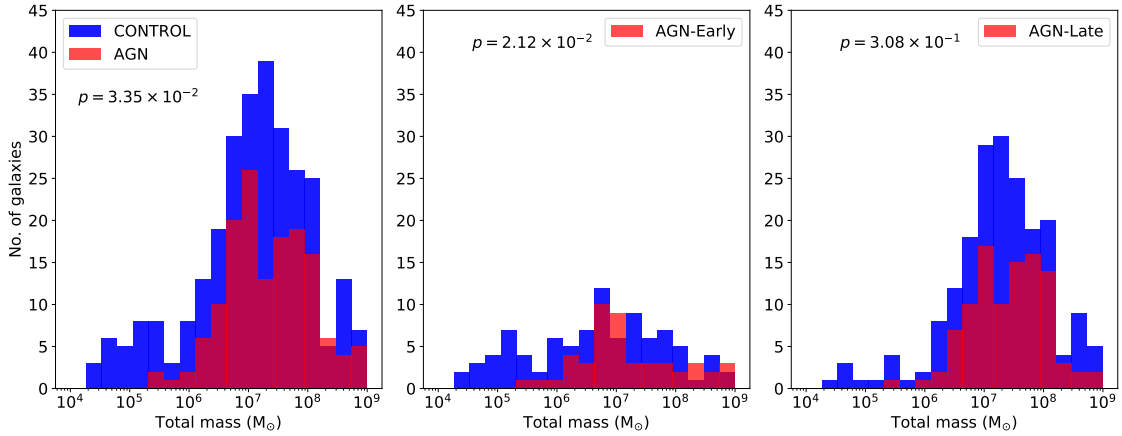


Figura 3.8: Histogramas da massa total de gás ionizado; esquerda: amostra total; centro: amostra AGN *early-type*; direita: amostra AGN *late-type*

Calculando as diferenças fracionais da massa total de gás ionizado entre cada par AGN e controle ( $M_{AGN} - M_{ctr}$ )/ $M_{AGN}$  (300 combinações) obtemos os resultados mostrados nos histogramas da Fig. 3.9 para diferenças fracionais entre -3 e 1. Os casos de valores menores que -3, foram excluídos do plot, mesmo considerando estes casos,  $\approx 56\%$  da amostra total apresenta valores positivos, com  $\approx 66\%$  para os AGNs *early-type* e  $\approx 49\%$  para os AGNs *late-type*. Os valores medianos são: 0,59 para a amostra total, 0,78 para os *early-type* e 0,49 para os *late-type*. Assim, embora as faixas de massas de gás ionizado do AGN apresentem grande sobreposição com aquelas das galáxias de controle, quando pareadas de acordo com as propriedades da galáxia hospedeira, a maioria dos AGN mostra um excesso de massa de gás ionizado (valores maiores que 0 nos histogramas da Fig. 3.9) em relação aos seus pares de controle, com exceção do caso dos AGNs *late-type*.

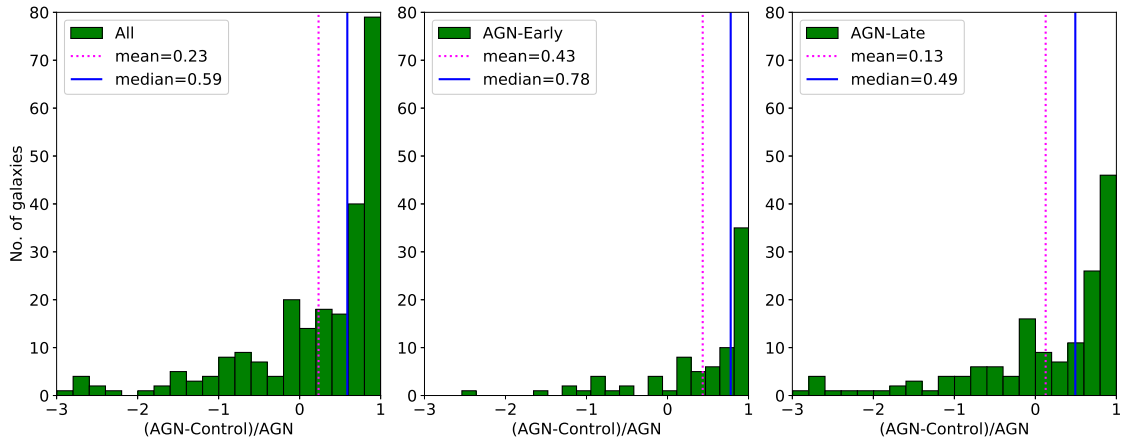


Figura 3.9: Histogramas das diferenças fracionais  $(M_{AGN} - M_{ctr})/M_{AGN}$ ; esquerda: amostra total; centro: amostra AGN *early-type*; direita: amostra AGN *late-type*



# The first 62 AGN observed with SDSS-IV MaNGA – IV. Gas excitation and star formation rate distributions

Janaína C. do Nascimento,<sup>1,2\*</sup> Thaisa Storchi-Bergmann,<sup>1,2</sup> Nícolas D. Mallmann<sup>1,2</sup>, Rogério Riffel<sup>1,2</sup>, Gabriele S. Ilha<sup>1,2,3</sup>, Rogemar A. Riffel<sup>1,2,3</sup>, Sandro B. Rembold,<sup>2,3</sup> Jáderson Schimoia,<sup>2,4</sup> Luiz Nicolaci da Costa,<sup>2,5</sup> Marcio A. G. Maia<sup>2,5</sup> and Alice D. Machado<sup>2,3</sup>

<sup>1</sup>Departamento de Astronomia, IF, Universidade Federal do Rio Grande do Sul, CP 15051, 91501-970 Porto Alegre, RS, Brazil

<sup>2</sup>Laboratório Interinstitucional de e-Astronomia - LIneA, Rua General José Cristino 77, Rio de Janeiro, RJ - 20921-400, Brazil

<sup>3</sup>Departamento de Física, CCNE, Universidade Federal de Santa Maria, 97105-900 Santa Maria, RS, Brazil

<sup>4</sup>Departamento de Física, Universidade Federal de Santa Catarina, CP 88040-900, Florianópolis, SC, Brazil

<sup>5</sup>Observatório Nacional, Rua General José Cristino, 77, Rio de Janeiro, RJ 20921-400, Brazil

Accepted 2019 April 12. Received 2019 April 1; in original form 2018 July 19

## ABSTRACT

We present maps of the ionized gas flux distributions, excitation, star formation rate (SFR), surface mass density  $\Sigma_{H+}$ , and obtain total values of SFR and ionized gas masses  $M$  for 62 active galactic nuclei (AGN) observed with SDSS-IV MaNGA and compare them with those of a control sample of 112 non-active galaxies. The most luminous AGN – with  $L([\text{O III}]\lambda 5007) \gtrsim 3.8 \times 10^{40} \text{ erg s}^{-1}$ , and those hosted by earlier type galaxies are dominated by Seyfert excitation within 0.2 effective radius  $R_e$  from the nucleus, surrounded by LINER excitation or transition regions, while the less luminous and hosted by later-type galaxies show equally frequent LINER and Seyfert excitation within 0.2  $R_e$ . The extent  $R$  of the region ionized by the AGN follows the relation  $R \propto L([\text{O III}])^{0.5}$  – as in the case of the broad-line region. The SFR distribution over the region ionized by hot stars is similar for AGN and controls, while the integrated SFR – in the range  $10^{-3}$ – $10 \text{ M}_\odot \text{ yr}^{-1}$  is also similar for the late-type subsample, but higher in the AGN for 75 per cent of the early-type subsample. We thus conclude that there is no signature of AGN quenching star formation in the body of the galaxy in our sample. We also find that 66 per cent of the AGN have higher ionized gas masses  $M$  than the controls – in the range  $10^5$ – $3 \times 10^7 \text{ M}_\odot$  – while 75 per cent of the AGN have higher  $\Sigma_{H+}$  within 0.2  $R_e$  than the control galaxies.

**Key words:** galaxies: active.

## 1 INTRODUCTION

Active galactic nuclei (AGN), that are triggered when supermassive black holes (SMBH) accrete gas at the centre of galaxies (Storchi-Bergmann & Schnorr-Müller 2019), play a major role in their evolution. This occurs as a result of radiative and mechanical feedback from the AGN: the generation of large regions of hot, photoionized gas by the AGN, as well as associated outflows, may affect the evolution of the galaxy over time by quenching their star formation (Harrison et al. 2014; Brusa et al. 2016; Carniani et al. 2016). This quenching, as the galaxy evolves, ends up setting limits to the total mass of the host galaxy (Somerville et al. 2008).

The investigation of the effect of AGN on its host galaxy has been facilitated in recent years via the use of Integral Field Spectroscopy.

One project that does just that, for  $\sim 10\,000$  nearby galaxies, is the MaNGA (Mapping Nearby Galaxies at the Apache Point Observatory) survey, described in Bundy et al. (2015), which is part of the fourth-generation Sloan Digital Sky Survey (SDSS-IV; Law et al. 2016; Yan et al. 2016; Blanton et al. 2017). The Integral Field Units design and performance are characterized in Drory et al. (2015). During the survey’s operation time – from 2014 to 2020 – a total of 300 active galaxies – the MaNGA AGN – are expected to be observed.

Our group AGNIFS (AGN Integral Field Spectroscopy) has joined the SDSS-IV collaboration via the LIneA laboratory (Laboratório Interinstitucional de e-Astronomia) with the goal of investigating the relation between MaNGA AGN and their host galaxies comparing the properties of the host galaxies with those of a control sample of non-active galaxies. This is the fourth paper of a series in which we aim at comparing the resolved stellar and gas properties of the AGN observed with MaNGA with those of the control sample.

\* E-mail: [janaaina.nascimento@ufrgs.br](mailto:janaaina.nascimento@ufrgs.br)

In Paper I (Rembold et al. 2017) we have reported the selection of the first 62 AGN observed with MaNGA, released in its fifth Product Launch (MPL-5) of the MaNGA data reduction pipeline (Law et al. 2016) as well as that of a control sample of 112 non-active galaxies, and compared the nuclear stellar population of the two samples. The cubes have been processed using the version 2.0.1 of the MaNGA Data Reduction Pipeline (Law et al. 2016). In Paper II (Mallmann et al. 2018) we have studied the spatial distribution of the stellar population properties including the resolved star formation history, while in Paper III (Ilha et al. 2019) we have compared the gas and stellar kinematics.

In this paper, our goal is to map the gas excitation, the extent of the region ionized by the AGN (the narrow-line region – NLR), quantify and map the star formation rate (hereafter SFR) as well as to obtain the total ionized gas masses of the AGN host galaxies. In order to verify which properties are related to the AGN, we have compared them with those of a sample of control galaxies, investigating also if and how these properties depend on the host galaxy type and AGN luminosity.

In evaluating the effect of the AGN on its host galaxy, it is important to distinguish regions that have been ionized by the central AGN from other ionization sources. We have used for this the BPT diagnostic diagrams (Baldwin, Phillips & Terlevich 1981; Veilleux & Osterbrock 1987), in particular  $[\text{O III}]\lambda 5007/\text{H}\beta$  versus  $[\text{N II}]\lambda 6584/\text{H}\alpha$ . Kauffmann et al. (2003) and Kewley et al. (2006) used this diagrams to empirically improve the definition of the boundary separating AGN from star-forming galaxies, introducing the so-called transition region, with objects of these regions also called composite AGN-Starburst, most frequently due to the inclusion in the same observation aperture of both an AGN and nearby star-forming regions.

Besides AGN and young stars, hot evolved stars can ionize the local gas and produce a spectrum similar to that of a LINER, as has been shown by Cid Fernandes et al. (2010) and references therein. In order to identify these regions, Cid Fernandes et al. (2010) proposed the WHAN diagram, a relation between the equivalent width of  $\text{H}\alpha$   $W(\text{H}\alpha)$  versus the  $[\text{N II}]\lambda 6584/\text{H}\alpha$  line ratio. When  $W(\text{H}\alpha)$  is lower than  $3\text{\AA}$ , the source of gas ionization can be post-AGB stars, and not necessarily an AGN or a starburst. Galaxies with  $W(\text{H}\alpha) \leq 3\text{\AA}$  are thus considered ‘retired’, in the sense that the origin of the gas emission is due neither to nuclear nor to starburst activity. As the  $[\text{N II}]/\text{H}\alpha$  ratio of these galaxies are similar to those of LINERs, these objects have been dubbed ‘LIERS’. We have thus used the WHAN diagram to locate these regions.

By being able to map the gas excitation over most of the galaxy, we have measured the extent  $R$  of the region excited by the AGN – NLR. We investigate the relation between  $R$  and  $L([\text{O III}])$  that has been addressed over the years by a number of authors (Bennert et al. 2002; Schmitt et al. 2003a; Greene et al. 2011; Hainline et al. 2013; Liu et al. 2013; Storchi-Bergmann et al. 2018), using small samples, sometimes combining in-homogeneous data and finding varying slopes for the relation. With our MaNGA sample we contribute to this investigation in the low-luminosity end with a homogeneous and larger sample than in previous studies.

The triggering of the AGN depends on the availability of gas to feed the SMBH at the centre. Some studies argue that AGN host galaxies have more gas in the inner few kpc than non-active galaxies, from which the nuclear activity is triggered, what seems indeed to be the case at least for early-type galaxies (Martini et al. 2003; Simões Lopes et al. 2007), while Hicks et al. (2013) found higher molecular gas surface mass densities within the inner  $\approx 50$  pc of nearby Seyfert galaxies than in a matched control sample. Other studies point out

that the SFR seems to be enhanced in the nuclear region ( $\sim$ inner kpc) of AGN (Diamond-Stanic & Rieke 2012; Esquej et al. 2014; Mushotzky et al. 2014), but these studies have been done in the infrared, using the PAH (Polycyclic Aromatic Hydrocarbon) feature at  $11.25\text{\mu m}$  or continuum fluxes at  $70$  and  $160\text{\mu m}$  as indicators of star formation, presumably not affected by the presence of an AGN. In the optical spectra, there is no such feature, and we must first use a diagnostic – e.g. the BPT diagram – to find the regions ionized by star formation where we can then calculate the SFR. We will thus not be able to calculate the SFR at the nucleus of the AGN but we have calculated and mapped the SFR in the regions of the galaxies ionized by hot stars. In the AGN nuclear region we have calculated the mass of ionized gas instead. For completeness, we have also mapped the distribution of ionized gas over the body of all the galaxies.

This paper is organized as follows. We present a brief description of the sample chosen for this work in Section 2. We then describe the measurements from the MaNGA data and present the corresponding maps in Section 3. These results are discussed in Section 4 and the conclusions presented in Section 5.

## 2 SAMPLE AND DATA

The sample studied in this paper comprises the first 62 AGN observed with MaNGA and 112 control galaxies listed in Table 1, and has been described in Paper I (Rembold et al. 2017). In summary, in order to investigate the relation between the AGN and their host galaxy properties, we have identified in the fourteenth data release (DR14; Abolfathi et al. 2018) all galaxies observed by MaNGA whose emission-line ratios in the SDSS-III (Gunn et al. 2006) single nuclear spectrum were dominated by ionization by an active nucleus, as indicated in the BPT (Baldwin et al. 1981) diagnostic diagram. We have also used the WHAN (Cid Fernandes et al. 2010) diagnostic diagram in the selection of the AGN, in order to avoid ‘LIERS’, as discussed in the Introduction. For each AGN, Rembold et al. (2017) have chosen two control non-active galaxies matching the AGN host stellar mass, morphology, distance, and inclination.

The data thus comprise the MaNGA data cubes of the 62 AGN and 112 control sample galaxies of Paper I and listed in Table 1, resampled to square pixels of  $0''.5 \times 0''.5$ .

In our sample of 62 AGN, there are 20 early-type hosts, 38 late-type hosts, with 2 in interaction, according to the classification in the Galaxy Zoo GZ1 (Lintott et al. 2011). There are two galaxies that are undefined, corresponding to galaxies whose probabilities of being elliptical and spiral in GZ1 are rigorously the same. These galaxies were excluded from the part of the analysis in which we separate early- and late-type galaxies.

Regarding the AGN luminosity, our sample comprises 17 luminous AGN – as we have called in Paper I – and 45 low-luminosity AGN, with the division between the two set at  $L([\text{O III}])\lambda 5007 = 3.8 \times 10^{40} \text{ erg s}^{-1}$ .

## 3 MEASUREMENTS AND MAPS

In this section, we describe the measurements we have obtained from the data and present their corresponding maps.

The emission-line fluxes were obtained by fitting the line profiles with Gaussian curves using the Gas AND Absorption Line Fitting (GANDALF; Sarzi et al. 2006) routine, written in IDL (Interactive Data Language). This routine was adapted for the analysis of the MaNGA data cubes and details about the measurements can be

**Table 1.** I – Parameters of the AGN hosts (columns 1–5) and control galaxies (columns 6–10): (1) galaxy identification in the MaNGA survey; (2)  $\log_{10}(L[\text{O III}])$  for L in units of  $10^{40}$  erg s $^{-1}$ ; (3)  $\log_{10}$  of the extent of AGN excitation region in kpc; (4) total ionized gas mass in units of  $\log_{10}(M_\odot)$ ; (5) mean nuclear (within  $0.2 R_e$ ) ionized gas surface mass density in units of  $(M_\odot \text{ kpc}^{-2})$ ; (6) total SFR in logarithm units of  $M_\odot \text{ yr}^{-1}$ ; (6)–(10): same properties for the control sample.

AGN ID (1)	L[O III] (2)	R (3)	Gas mass (4)	$\Sigma_{\text{nuc}}$ (5)	SFR (6)	CS ID (7)	L[O III] (8)	Gas mass (9)	$\Sigma_{\text{nuc}}$ (10)	SFR (11)
1-558912	$56.82 \pm 1.25$	1.12	6.75	3.99	-0.42	1-71481 1-72928	$0.10 \pm 0.20$ $0.09 \pm 0.23$	6.10 5.80	3.38 3.56	-0.93 -1.54
1-269632	$30.08 \pm 1.69$	1.25	6.88	4.68	-0.23	1-210700 1-378795	$1.55 \pm 0.44$ $0.72 \pm 0.31$	6.75 6.94	3.65 3.66	-0.51 0.14
1-258599	$20.95 \pm 0.67$	1.41	7.39	5.32	-0.41	1-93876 1-166691	$0.46 \pm 0.36$ $0.09 \pm 0.49$	5.94 5.69	3.07 3.31	-1.59 -1.67
1-72322	$20.66 \pm 0.43$	1.43	6.92	4.07	-0.28	1-121717 1-43721	$1.40 \pm 0.57$ $1.91 \pm 0.52$	7.09 5.95	3.81 3.12	0.67 -1.06
1-121532	$11.68 \pm 0.96$	1.18	6.68	4.59	0.30	1-218427 1-177493	$0.72 \pm 0.62$ $2.29 \pm 0.28$	5.49 6.08	1.63 3.63	-2.13 -1.22
1-209980	$11.01 \pm 0.17$	1.14	6.23	4.77	-0.69	1-295095 1-92626	$0.15 \pm 0.03$ $0.76 \pm 0.07$	5.99 5.98	2.92 3.17	-0.54 -0.53
1-44379	$8.94 \pm 0.14$	0.98	7.10	4.25	-0.03	1-211082 1-135371	$0.19 \pm 0.04$ $0.25 \pm 0.07$	6.05 6.59	3.27 4.31	-0.35 -0.26
1-149211	$7.88 \pm 0.14$	0.61	6.50	4.46	-0.93	1-377321 1-491233	$4.53 \pm 0.13$ $0.25 \pm 0.03$	6.72 6.78	5.31 6.33	-0.32 -0.28
1-173958	$6.79 \pm 0.30$	0.74	7.32	4.24	0.83	1-247456 1-24246	$0.57 \pm 0.16$ $0.11 \pm 0.06$	6.87 6.20	4.47 2.85	0.23 -0.23
1-338922	$6.77 \pm 0.90$	1.49	7.84	5.08	0.89	1-286804 1-109493	$2.23 \pm 0.43$ $0.15 \pm 0.18$	7.34 5.62	3.67 2.62	0.25 -1.64
1-279147	$6.77 \pm 0.20$	0.90	5.72	4.19	-0.76	1-283246 1-351538	$0.23 \pm 0.06$ $0.46 \pm 0.13$	5.00 6.36	2.36 4.14	-1.31 -0.23
1-460812	$6.46 \pm 0.31$	0.86	6.33	4.98	-1.12	1-270160 1-258455	$0.70 \pm 0.39$ $0.49 \pm 0.14$	5.71 5.33	3.45 2.79	-1.85 -2.14
1-92866	$6.12 \pm 0.30$	0.81	6.12	4.14	-1.71	1-94514 1-210614	- $0.40 \pm 0.14$	4.79 5.10	3.23 2.84	-4.04 -1.92
1-94784	$5.96 \pm 0.12$	0.33	6.34	4.57	-0.49	1-211063 1-135502	$0.20 \pm 0.04$ $0.50 \pm 0.05$	6.45 5.70	3.64 3.37	-0.29 -0.90
1-44303	$5.56 \pm 0.12$	0.91	6.57	3.99	-0.21	1-339028 1-379087	$0.44 \pm 0.08$ $0.72 \pm 0.13$	5.44 6.76	3.35 4.72	-1.31 0.12
1-339094	$5.29 \pm 0.09$	0.57	5.99	4.57	2.53	1-274646 1-24099	$0.35 \pm 0.04$ $0.06 \pm 0.03$	5.01 4.80	3.76 3.10	-3.28 -2.99
1-137883	$3.87 \pm 0.12$	0.66	6.42	4.86	-1.54	1-178838 1-36878	$0.10 \pm 0.02$ $0.28 \pm 0.04$	5.44 6.68	1.92 5.48	-1.29 -0.15
1-48116	$3.79 \pm 0.08$	0.62	6.49	4.90	-0.26	1-386452 1-24416	$0.32 \pm 0.04$ $0.22 \pm 0.03$	6.31 5.58	5.40 3.43	-0.50 -1.01
1-256446	$3.74 \pm 0.15$	0.82	5.83	3.97	-1.25	1-322671 1-256465	- $0.59 \pm 0.11$	4.28 5.68	1.63 4.27	-3.38 -1.40
1-95585	$3.58 \pm 0.16$	0.96	7.03	3.74	0.23	1-166947 1-210593	$0.13 \pm 0.08$ $0.43 \pm 0.14$	5.68 6.01	3.08 2.87	-0.88 -0.56
1-135641	$3.52 \pm 0.09$	1.01	6.75	4.93	-0.09	1-635503 1-235398	$0.15 \pm 0.06$ $0.16 \pm 0.05$	7.35 6.39	5.41 5.26	0.37 -0.34
1-259142	$3.47 \pm 0.20$	0.59	6.63	4.28	-0.35	1-55572 1-489649	$0.12 \pm 0.04$ $0.30 \pm 0.08$	6.49 5.61	3.14 3.35	-0.40 -1.34
1-109056	$3.24 \pm 0.08$	0.72	6.35	4.64	-0.37	1-73005 1-43009	$0.20 \pm 0.06$ $0.12 \pm 0.04$	6.37 6.53	3.27 4.20	-0.33 -0.26
1-24148	$3.17 \pm 0.05$	0.18	5.16	4.32	-2.81	1-285031 1-236099	$0.26 \pm 0.04$ $0.07 \pm 0.01$	6.61 5.24	5.67 4.53	-0.61 -2.19
1-166919	$2.64 \pm 0.25$	0.62	6.78	3.81	-0.01	12-129446 1-90849	$0.28 \pm 0.09$ $0.28 \pm 0.05$	6.99 6.49	4.43 3.71	0.21 -0.10
1-248389	$2.55 \pm 0.09$	0.15	4.99	3.79	-2.96	1-94554 1-245774	$0.22 \pm 0.04$ $0.29 \pm 0.07$	5.09 6.67	3.75 4.14	-3.08 -0.13

**Table 1** – *continued*

AGN ID (1)	L[O III] (2)	R (3)	Gas mass (4)	$\Sigma_{\text{nuc}}$ (5)	SFR (6)	CS ID (7)	L[O III] (8)	Gas mass (9)	$\Sigma_{\text{nuc}}$ (10)	SFR (11)
1-321739	$2.24 \pm 0.10$	0.97	6.93	4.69	0.06	1-247417 1-633994	$0.16 \pm 0.04$ $0.36 \pm 0.09$	7.27 5.90	4.94 3.14	0.18 –0.68
1-234618	$2.23 \pm 0.23$	1.17	7.09	4.60	–0.10	1-282144 1-339125	$0.10 \pm 0.02$ $0.45 \pm 0.23$	7.83 5.62	4.46 2.90	0.17 –1.32
1-229010	$2.11 \pm 0.09$	0.38	6.31	3.51	–0.46	1-210962 1-613211	$0.35 \pm 0.06$ $0.16 \pm 0.06$	5.60 5.90	3.11 3.64	–1.16 –3.15
1-211311	$1.99 \pm 0.06$	0.58	5.68	3.76	–0.95	1-25688 1-94422	$0.10 \pm 0.02$ $0.24 \pm 0.03$	5.66 5.88	4.03 3.82	–0.70 –0.96
1-373161	$1.87 \pm 0.11$	0.54	5.90	3.98	–2.34	1-259650 1-289865	$0.67 \pm 0.20$ $0.11 \pm 0.09$	5.53 7.17	3.72 3.11	–1.81 –2.47
1-210646	$1.80 \pm 0.10$	0.55	7.09	3.48	0.22	1-114306 1-487130	$0.33 \pm 0.16$ $0.27 \pm 0.10$	6.92 4.32	4.09 4.72	0.22 0.15
1-351790	$1.72 \pm 0.03$	0.46	5.40	4.01	–inf	1-23731 1-167334	$0.02 \pm 0.01$ $0.47 \pm 0.05$	4.76 6.87	3.76 1.63	–3.87 –2.72
1-163831	$1.67 \pm 0.13$	0.68	6.82	3.60	0.12	1-247456 1-210593	$0.57 \pm 0.16$ $0.43 \pm 0.14$	6.01 6.81	4.47 2.87	–0.03 –0.56
1-22301	$1.67 \pm 0.23$	0.69	7.05	4.16	0.31	1-251871 1-72914	$0.24 \pm 0.18$ $0.13 \pm 0.07$	8.23 6.45	3.11 3.35	0.26 0.46
1-248420	$1.66 \pm 0.06$	0.56	6.92	3.96	–0.11	1-211063 1-211074	$0.20 \pm 0.04$ $0.20 \pm 0.04$	6.15 4.53	3.64 3.26	–0.25 –0.46
1-23979	$1.60 \pm 0.05$	0.51	5.34	4.62	–2.37	1-320681 1-519738	$0.09 \pm 0.07$ $0.11 \pm 0.04$	5.25 6.46	3.25 2.60	–inf –4.21
1-542318	$1.58 \pm 0.07$	0.48	5.64	3.94	–1.62	1-285052 1-377125	$0.11 \pm 0.03$ $0.57 \pm 0.14$	5.30 5.60	3.37 1.63	–0.49 –0.54
1-95092	$1.54 \pm 0.07$	0.33	6.49	4.65	–0.12	1-210962 1-251279	$0.35 \pm 0.06$ $0.37 \pm 0.06$	6.35 5.43	3.11 4.31	–1.14 –0.32
1-279676	$1.52 \pm 0.14$	1.12	6.07	3.35	–0.55	1-44789 1-378401	$0.32 \pm 0.09$ $0.57 \pm 0.14$	5.39 6.20	2.95 2.86	–1.72 –2.16
1-201561	$1.37 \pm 0.15$	0.88	6.34	4.55	–0.69	1-24246 1-285052	$0.11 \pm 0.06$ $0.11 \pm 0.03$	6.46 5.87	2.85 3.37	–0.54 –0.50
1-198182	$1.34 \pm 0.11$	0.33	5.74	4.30	–2.44	1-256185 1-48053	$0.25 \pm 0.04$ –	5.12 5.68	3.32 3.70	–1.60 –1.82
1-96075	$1.26 \pm 0.13$	0.73	7.10	3.66	0.39	1-166947 1-52259	$0.13 \pm 0.08$ $0.30 \pm 0.09$	5.70 6.87	3.08 4.36	–0.78 0.22
1-519742	$1.19 \pm 0.03$	0.39	5.68	4.14	–1.00	1-37079 1-276679	$0.02 \pm 0.01$ $0.05 \pm 0.01$	4.97 6.17	3.15 4.58	–1.55 –0.61
1-491229	$1.14 \pm 0.11$	0.32	5.69	4.35	–2.38	1-94554 1-604048	$0.22 \pm 0.04$ $0.39 \pm 0.08$	5.09 6.80	3.75 4.32	–3.21 –0.03
1-604761	$1.00 \pm 0.13$	0.97	6.86	3.49	–0.11	1-210173 1-71525	$0.52 \pm 0.13$ $0.19 \pm 0.06$	7.12 6.84	3.01 3.27	0.0 0.07
1-25725	$0.92 \pm 0.05$	0.70	5.91	4.69	–1.01	1-211079 1-322074	$0.03 \pm 0.04$ –	4.48 4.43	3.58 2.95	–inf –2.64
1-94604	$0.86 \pm 0.07$	0.55	6.20	4.07	–0.49	1-295095 1-134239	$0.15 \pm 0.03$ $0.23 \pm 0.06$	5.99 6.53	2.92 3.89	–0.30 –0.29
1-37036	$0.84 \pm 0.06$	0.16	5.36	4.07	–2.16	1-210785 1-25680	– $0.34 \pm 0.04$	4.37 5.65	1.97 4.42	–4.06 –2.08
1-167688	$0.84 \pm 0.02$	0.54	5.54	5.42	–3.59	1-235587 1-37062	$0.08 \pm 0.02$ $0.27 \pm 0.03$	4.97 6.45	3.36 5.53	–2.04 –0.60
1-279666	$0.84 \pm 0.07$	0.89	5.57	3.92	–1.54	1-392976 1-47499	$0.10 \pm 0.03$ $0.15 \pm 0.06$	5.16 4.63	3.59 2.51	–2.17 –2.67
1-339163	$0.82 \pm 0.07$	0.94	6.74	4.02	–0.26	1-136125 1-626830	$0.08 \pm 0.02$ $0.15 \pm 0.04$	6.42 5.93	2.78 3.67	–0.41 –0.80
1-258774	$0.77 \pm 0.10$	0.77	5.75	4.98	–1.85	1-379660 1-48208	$0.37 \pm 0.07$ $0.12 \pm 0.04$	5.45 5.06	3.88 2.88	–2.02 –2.41
1-198153	$0.76 \pm 0.08$	0.32	6.42	4.24	–0.50	1-211063 1-135810	$0.20 \pm 0.04$ $0.08 \pm 0.02$	6.45 6.47	3.64 2.95	–0.31 –0.34

**Table 1** – *continued*

AGN ID (1)	L[O III] (2)	R (3)	Gas mass (4)	$\Sigma_{\text{nuc}}$ (5)	SFR (6)	CS ID (7)	L[O III] (8)	Gas mass (9)	$\Sigma_{\text{nuc}}$ (10)	SFR (11)
1-91016	$0.76 \pm 0.09$	0.73	6.50	4.44	-0.52	1-338828 1-386695	$0.43 \pm 0.05$ $0.81 \pm 0.09$	6.62 6.81	5.15 5.37	-0.01 -0.03
1-279073	$0.63 \pm 0.06$	0.15	5.62	4.21	-2.10	1-211100 1-210784	– $0.15 \pm 0.05$	6.70 4.42	2.36 3.62	-4.88 -3.86
1-135044	$0.61 \pm 0.04$	0.43	6.32	4.49	-0.29	1-218280 1-211063	$0.12 \pm 0.03$ $0.20 \pm 0.04$	6.40 6.45	3.78 3.64	-0.10 -0.22
1-148068	$0.45 \pm 0.15$	0.64	6.72	2.87	-0.18	1-166947 1-55572	$0.13 \pm 0.08$ $0.12 \pm 0.04$	5.68 6.49	3.08 3.14	-1.13 -0.30
1-277552	$0.44 \pm 0.05$	0.39	7.46	3.78	0.20	1-264513 1-136125	$0.33 \pm 0.05$ $0.08 \pm 0.02$	7.54 6.42	5.17 2.78	0.61 -0.31
1-217050	$0.43 \pm 0.03$	–	5.64	4.64	-2.43	1-135372 1-274663	$0.01 \pm 0.23$ $0.08 \pm 0.02$	5.04 5.34	3.16 4.29	-2.71 -3.64
1-25554	$0.24 \pm 0.03$	0.09	6.11	4.75	-0.61	1-135625 1-216958	$0.56 \pm 0.04$ $0.23 \pm 0.02$	6.55 6.12	5.15 4.89	-0.10 -0.50
1-135285	$0.20 \pm 0.04$	0.20	6.41	4.23	-0.25	1-633990 1-25688	$0.25 \pm 0.03$ $0.10 \pm 0.02$	5.82 5.90	4.68 4.03	-0.83 -0.77

found in Ilha et al. (2019). The choice of this routine was due to the fact that it fits both the stellar population spectra and the profiles of the emission lines, after the subtraction of the stellar population contribution.

Results are presented in Figs 3–6 for four representative trios of AGN hosts and their respective control galaxies. These trios were selected to sample, respectively, an early-type AGN, a late-type AGN, a luminous AGN, and a low-luminosity AGN. The maps for the remaining objects are shown in Figs A1–A58 (see online) of the Appendix.

### 3.1 Line fluxes

Line fluxes were obtained from the integrated line profiles, from which the luminosities were calculated. Uncertainties in the fluxes range from less than 1 per cent to a few per cent in the central region up to  $\approx 10$  per cent at the borders of the FoV. Resulting luminosity maps are shown for the [O III]  $\lambda 5007\text{\AA}$  emission line in units of  $10^{38} \text{ ergs s}^{-1}$  per spaxel for each active galaxy and its two controls in the fourth row of the left set of panels of Figs 3–6, for the four representative trios and in the Appendix for the remaining galaxies.

An average one-dimensional profile was also built and is shown in the corresponding right-hand panel of the figures above. These profiles were obtained following the method described in Mallmann et al. (2018): averages of 30 radial profiles equally spaced in the azimuthal direction of the galaxy, limited to angular distances from the major axis of  $\theta_{\text{max}} = \tan^{-1}(b/a)$  deg, where  $a$  is the galaxy semimajor axis and  $b$  is the semiminor axis, extracted from the MaNGA’s *drpall* table. This choice was made because profiles closest to the minor axis, when corrected for projection, introduced too much noise in the average profiles, probably as a result of obscuration effects when the galaxies have high inclinations.

### 3.2 Gas excitation

In order to map the excitation of the gas, emission-line ratio maps were obtained and used to build the diagnostic diagram (Baldwin et al. 1981) [O III]  $\lambda 5007/\text{H}\beta$  versus [N II]  $\lambda 6583/\text{H}\alpha$  (hereafter

called BPT diagram) as well as the WHAN diagram (Cid Fernandes et al. 2010) for each galaxy.

From the above diagrams, excitation maps were obtained, according to the following procedure: we first built the BPT diagram and corresponding excitation map, ‘painting’ the regions of the galaxy with different colours corresponding to the different excitation regions: green for Seyfert excitation, magenta for LINER excitation, blue for starburst excitation, and grey for composite (or transition region).

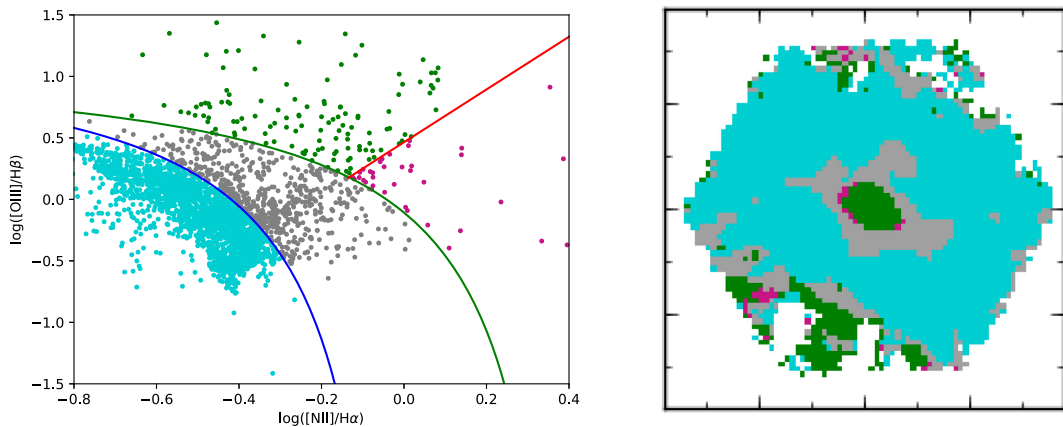
After building the BPT excitation map, we built the WHAN diagram in order to check if the regions with AGN excitation (Seyfert and LINER) were ‘LIERs’, in which case we painted the corresponding regions orange.

Fig. 1 shows an example of BPT diagram in which each point is a spaxel of the data cube of the control galaxy ‘plateifu 8613–12702’ in the left-hand panel and the corresponding excitation map is shown in the right-hand panel. The red line – marking the separation between Seyfert and LINER excitation and the blue line – marking the separation between the starburst and transition region, were obtained from Kauffmann et al. (2003). The green line – marking the separation between the transition region and AGN was obtained from Kewley et al. (2001).

Fig. 2 shows the WHAN diagram (Cid Fernandes et al. 2010) on the left-hand panel, and the corresponding excitation map on the right-hand panel. The blue line separates starburst and AGN and the red line separates Seyferts and LINERs as in the BPT diagram, but the green line here separates the LINERs (above the line) from the LIERs (below the line).

Uncertainties in the line ratios range from a few per cent in the central regions, up to 10–30 per cent at the borders of the FOV.

We note that the excitation maps obtained using the BPT diagram shows some differences when compared to the one obtained using the WHAN diagram: many regions classified as composite and even starburst in the BPT diagrams appear as Seyfert or LINER in the WHAN diagram. The reason for this can be understood through a comparison between Figs 1 and 2: while the division line between starburst and AGN in the WHAN diagram corresponds to  $\log([\text{N II}]/\text{H}\alpha) = -0.4$ , in the BPT diagram this division is curved and has the transition region between the starburst and AGN, while



**Figure 1.** BPT diagram (left) for the control galaxy plateifu 8613-12702 where each point represents each spaxel, different colours identifying each type of excitation and the corresponding excitation maps to the right, where the tick markers are separated by 5 arcsec. The blue lines separate the starburst excitation and composite (or transition region), the green line separates the composite and AGN excitation, while the red line separates Seyfert (top) and LINER (bottom) excitation. Typical uncertainties in logarithmic in the range 0.02–0.1.

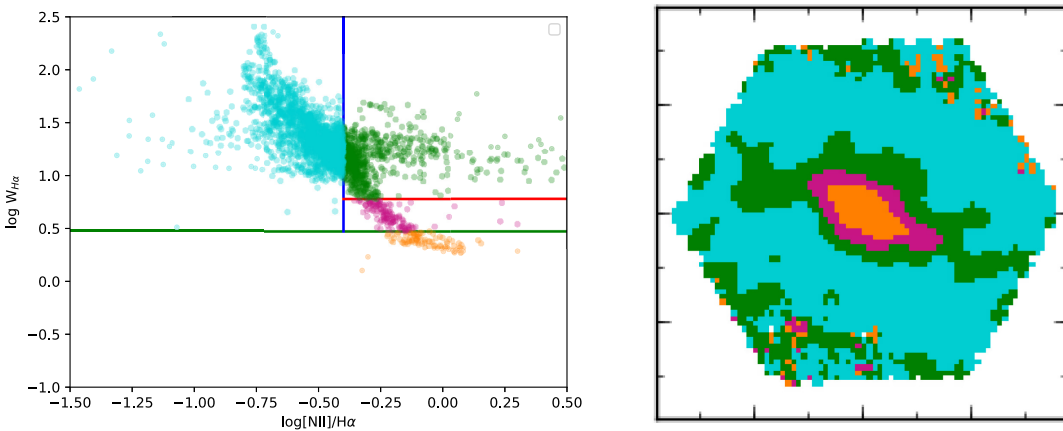


**Figure 2.** WHAN diagram (left) and excitation map (right) of the control galaxy identified as plateifu 8613-12702. In the excitation map the tick marks are separated by 5 arcsec. Blue lines separate starburst excitation to the left, while the red line separates Seyfert (top) and LINER (bottom) excitation. The green line shows the limit below which the excitation corresponds to a LINER. The dashed vertical line shows an alternative (proposed by us) division between starburst and AGN excitation that gives an excitation classification in better agreement with that of the BPT diagram. Typical uncertainties in logarithm are in the range 0.02–0.1.

this transition region is not defined in the WHAN diagram. In the BPT diagram, the  $\log([\mathrm{N}\,\mathrm{II}]/)$  ratios can reach a value of 0.1 for LINERs and up to  $-0.1$  for Seyferts, higher than the fixed value of  $-0.4$  of the WHAN diagram.

Considering the above, we have adopted the excitation classification of the BPT diagram and only changed it to LINER in the cases where the excitation in the BPT diagram is Seyfert or LINER but is LINER in the WHAN diagram, keeping the transition region and starburst classifications of the BPT diagram.

We note that in order to improve the consistency of the two excitation maps for our sample, the division line in the WHAN diagram should correspond to somewhat a larger value than proposed in Cid Fernandes et al. (2010) of  $\log([\mathrm{N}\,\mathrm{II}]/\mathrm{H}\,\alpha) \approx -0.25$ . We have drawn a vertical blue dashed line in Fig. 1 at this value in the WHAN diagram in Fig. 1.

We have used the procedure above to map the different type of excitation over the body of the galaxy and build the excitation maps

shown in the second line of Figs 3–6 and Figs A1–A58 (see online) of the Appendix.

### 3.3 Star formation rate

The excitation maps of both the AGN and controls show many locations in which the excitation is typical of starbursts or H II regions, in which the line emission is due to ionization of the gas by young stars, and the SFR can be obtained from the  $\mathrm{H}\,\alpha$  luminosity  $L(\mathrm{H}\,\alpha)$ . We decided to include in the calculation of the SFR also the transition regions, which, although have some contribution from AGN excitation, do include a large contribution of a starburst component. As there may be some additional ‘hidden’ star formation contribution in the region dominated by AGN excitation, the assumption that all  $\mathrm{H}\,\alpha$  emission is due to starbursts in the transition region may compensate for this ‘hidden’ star formation contribution.

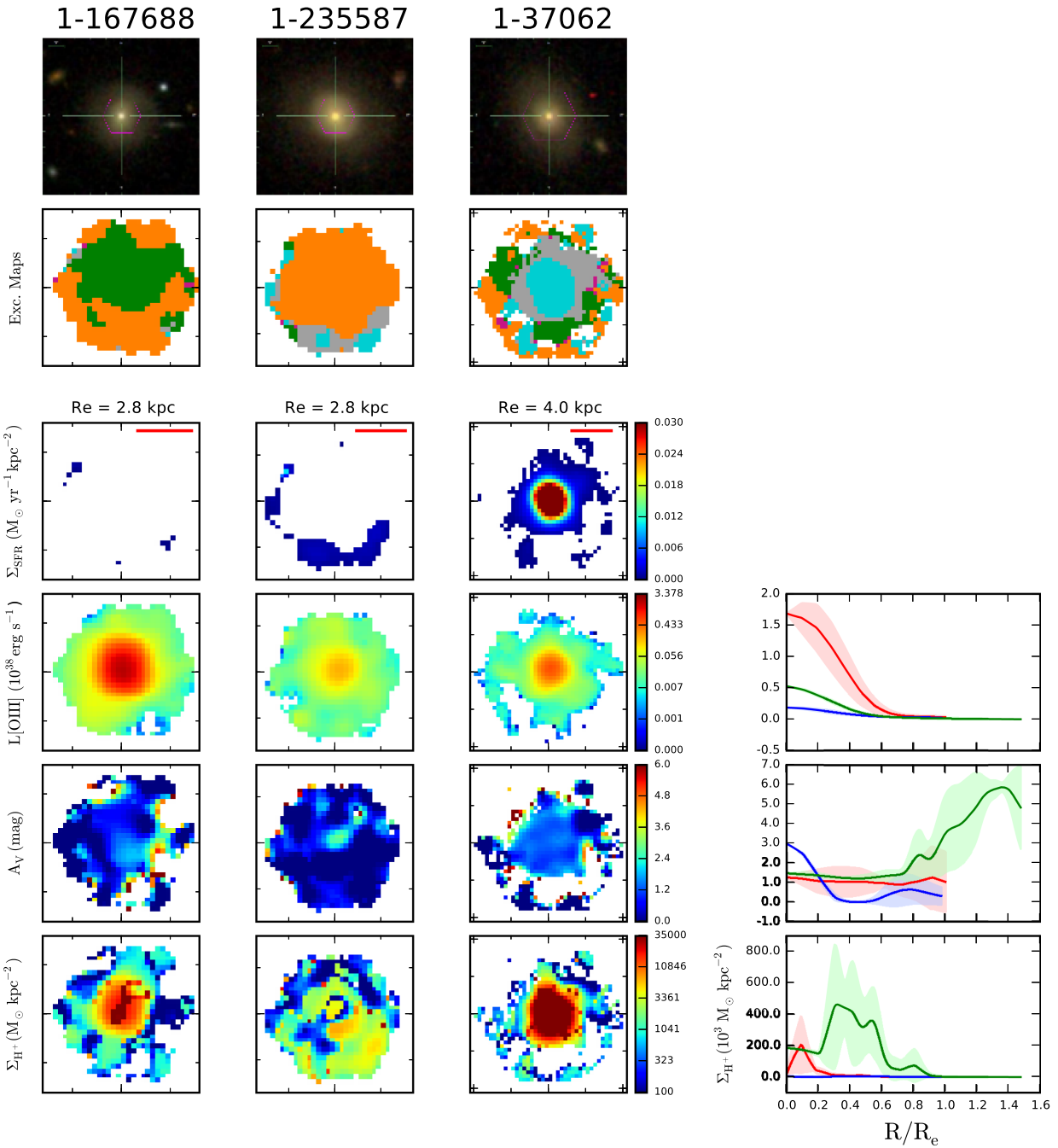


**Figure 3.** Surface distribution of the properties measured for a typical early-type AGN and its two controls, showing the AGN on the left and the two control galaxies at the centre and right. Top row: SDSS-IV images with the MaNGA footprint overplotted in pink; second row: excitation maps where green corresponds to Seyfert, magenta to LINER, blue to starburst, grey to transition region, and orange to LIER excitation; third row:  $\Sigma_{\text{SFR}}$  maps; fourth row:  $L[\text{O III}]$  in units ( $10^{38} \text{ erg s}^{-1} \text{ spaxel}^{-1}$ ); fifth row: extinction maps; bottom row:  $\Sigma_{\text{H}^+}$  maps. Bottom right: azimuthally averaged properties of the bottom three left-hand panels, where the AGN is shown in red, the first control in blue and second control in green. The tick marks are separated by 5 arcsec, and the scale at the galaxy is given by the red horizontal line shown in the  $\Sigma_{\text{SFR}}$  map panels. This line corresponds to the galaxy effective radius  $R_e$  with extent in kpc given above the panel.

We have used the following expression to obtain the SFR, from Kennicutt (1998):

$$\text{SFR} = 7.9 \times 10^{-42} \times L(\text{H}\alpha). \quad (1)$$

In order to calculate the  $\text{H}\alpha$  luminosity, we have corrected the  $\text{H}\alpha$  flux,  $F(\text{H}\alpha)$ , for reddening, using the extinction law of Cardelli,

Clayton & Mathis (1989):

$$L(\text{H}\alpha) = 4\pi d^2 F(\text{H}\alpha) 10^{C(\text{H}\alpha)}, \quad (2)$$

where  $d$  is the galaxy distance obtained from the redshift values listed in Paper I,  $F(\text{H}\alpha)$  is the  $\text{H}\alpha$  flux and  $C(\text{H}\alpha)$  is the interstellar extinction coefficient at the  $\text{H}\alpha$  wavelength calculated as described in the next subsection.

We have obtained both the integrated SFR, shown in the last column of Table 1 as well as the SFR surface density  $\Sigma_{\text{SFR}}$  dividing the SFR at each spaxel by the corresponding area ( $0'.5 \times 0'.5$ ) in  $\text{kpc}^2$ , obtaining its value in units of  $M_{\odot} \text{ yr}^{-1} \text{ kpc}^{-2}$ .

The  $\Sigma_{\text{SFR}}$  maps for the AGN and their control galaxies are shown in the third row of Figs 3–6 and Figs A1–A58 (see online) of the Appendix.

### 3.4 Extinction

The gas extinction was calculated from the observed  $H\alpha/H\beta$  line ratio adopting case B recombination (Osterbrock & Ferland 2006) and the Cardelli et al. (1989) reddening law:

$$A_V = 7.23 \times \log \left[ \frac{F(H\alpha)}{F(H\beta)} \times \frac{1}{2.87} \right], \quad (3)$$

where  $F(H\alpha)$  and  $F(H\beta)$  are the observed fluxes.

The extinction maps for the AGN and their control galaxies are shown in the fifth row of the panels of Figs 3–6 and Figs A1–A58 (see online) of the Appendix.

### 3.5 Ionized gas masses

As we cannot calculate the SFR at the regions that are not ionized by hot stars, we have calculated the mass of ionized gas, that can be obtained at all locations with  $H\alpha$  or  $H\beta$  emission using (Osterbrock & Ferland 2006):

$$M = V f n_e m_p, \quad (4)$$

where  $V$  is the volume of the emitting region,  $f$  is the filling factor,  $n_e$  is the electron density, and  $m_p$  the proton mass.

Based on Osterbrock & Ferland (2006), assuming case B recombination, we obtain:

$$V f = 8.1 \times 10^{59} \frac{L_{41}(H\beta)}{n_3^2} \text{ cm}^{-3}, \quad (5)$$

where  $L_{41}(H\beta)$  is the  $H\beta$  luminosity in units of  $10^{41} \text{ erg s}^{-1}$  and  $n_3$  is the electron density in units of  $10^3 \text{ cm}^{-3}$ .

The emitting gas mass can be calculated by combining equations (4) and (5) (Peterson 1997) where we replaced  $L(H\beta)$  for  $L(H\alpha)/2.87$ :

$$M \approx 2.4 \times 10^5 \frac{L_{41}(H\alpha)}{n_3} M_{\odot}. \quad (6)$$

In order to obtain the gas density  $n$ , we have used the ratio between the doublet lines  $[\text{S II}] \lambda 6717$  and  $[\text{S II}] \lambda 6731 \text{ \AA}$ , as the corresponding two levels have different collision forces and radiative transition probabilities. The flux observed in each component of the doublet depends on the relative population at each energy level, which is sensitive to the electron density (Osterbrock & Ferland 2006). The calculation was done using the task *temden* of the package *stsdas.nebular* of *iraf* and the adopted gas temperature was 10 000 K. In many locations the line ratio was above the limit  $[\text{S II}] \lambda 6717 / [\text{S II}] \lambda 6731 \text{ \AA} = 1.45$ , which corresponds to densities of  $\approx 100 \text{ cm}^{-3}$  or lower. In these cases, we have adopted the value of  $100 \text{ cm}^{-3}$ . Due to low-signal-to-noise ratio, some measurements of the  $[\text{S II}]$  lines were not possible, and, in order to be able to calculate the gas masses at these locations, we decided to adopt also a density value of  $100 \text{ cm}^{-3}$ . This is justified by the fact that these regions were surrounded by line ratios indicating this density or lower.

Considering that the mass of the gas is inversely proportional to  $n$ , the resulting ionized gas masses are actually lower limits. In order to evaluate the effect of the density on the estimated gas masses, we have repeated the calculations for gas densities of 10 and  $1 \text{ cm}^{-3}$ . The result is an increase in the gas masses in the range 10–40 per cent, depending on the galaxy. This small increase is due to the fact that most of the gas emission comes from the regions with the highest line fluxes, for which the density value could be obtained.

As for the  $\Sigma_{\text{SFR}}$ , we have also obtained the ionized gas surface mass density  $\Sigma_{H^+}$  by dividing the mass at each pixel by its area. The corresponding maps are shown in the bottom row of Figs 3–6 and Figs A1–A58 (see online) of the Appendix.

## 4 DISCUSSION

In this section, we discuss the properties mapped in the previous section in Figs 3–6, respectively, for an early-type host, a late-type host, a high-luminosity, and a low-luminosity AGN host. Figs A1–A58 (see online) of the Appendix show the maps for the remaining galaxies.

We present and discuss also here the extents of the regions ionized by the AGN and their relation with  $L[\text{O III}]$ , as well as histograms of the total SFRs, ionized gas masses, and nuclear surface mass densities, comparing the results obtained for the AGN with those of the control sample.

### 4.1 Excitation

#### 4.1.1 Early- and late-type AGN hosts

In the excitation maps of the 20 early-type AGN hosts, 9 (45 per cent) present Seyfert type excitation in their nuclear region (which we define as the region within  $0.2 R_e$ ) and up to distances ranging from  $\approx 3$  to 25 kpc. Beyond this region, the excitation varies, including types H II, transition, LIER, or LINER.

The control galaxies, in their majority, present LIER excitation at the nucleus and surroundings, while H II excitation, as seen in the control 2 of Fig. 3 is less frequently seen in early-type hosts.

Four galaxies (20 per cent of the early-type hosts) have nuclear LINER excitation, that can also be observed beyond the nucleus, reaching  $\approx 1.5$ –3.5 kpc, and extranuclear LIER excitation. The controls in turn have mostly LIER cores. Another six galaxies exhibit both LINER and Seyfert type excitation in the nucleus (within  $R_e$ ), indicating that the line ratios are borderline between the Seyfert and LINER regions of the BPT diagram. Their controls usually have LIER excitation in the nucleus.

Regarding the group of 38 late-type AGN, as the one in Fig. 4: 16 (42 per cent) show LINER excitation from the nucleus until distances in the range 1.6–27 kpc; 13 (34 per cent) present Seyfert excitation extending to 2.4–18 kpc; the remaining 9 (24 per cent) show LINER/Seyfert nuclear excitation. The controls all show similar maps, with LIER, H II, or transition excitation in the nucleus.

#### 4.1.2 High- and low-luminosity AGN hosts

Regarding the 17 most luminous AGN, 12 (70 per cent) have Seyfert excitation at the nucleus and throughout most of the galaxy, up to distances from the nucleus in the range 4–26 kpc. Three (20 per cent) galaxies show LINER excitation at the nucleus usually surrounded by Seyfert excitation, and extended to distances in the range 5.5–27 kpc, and two (12 per cent) present Seyfert excitation

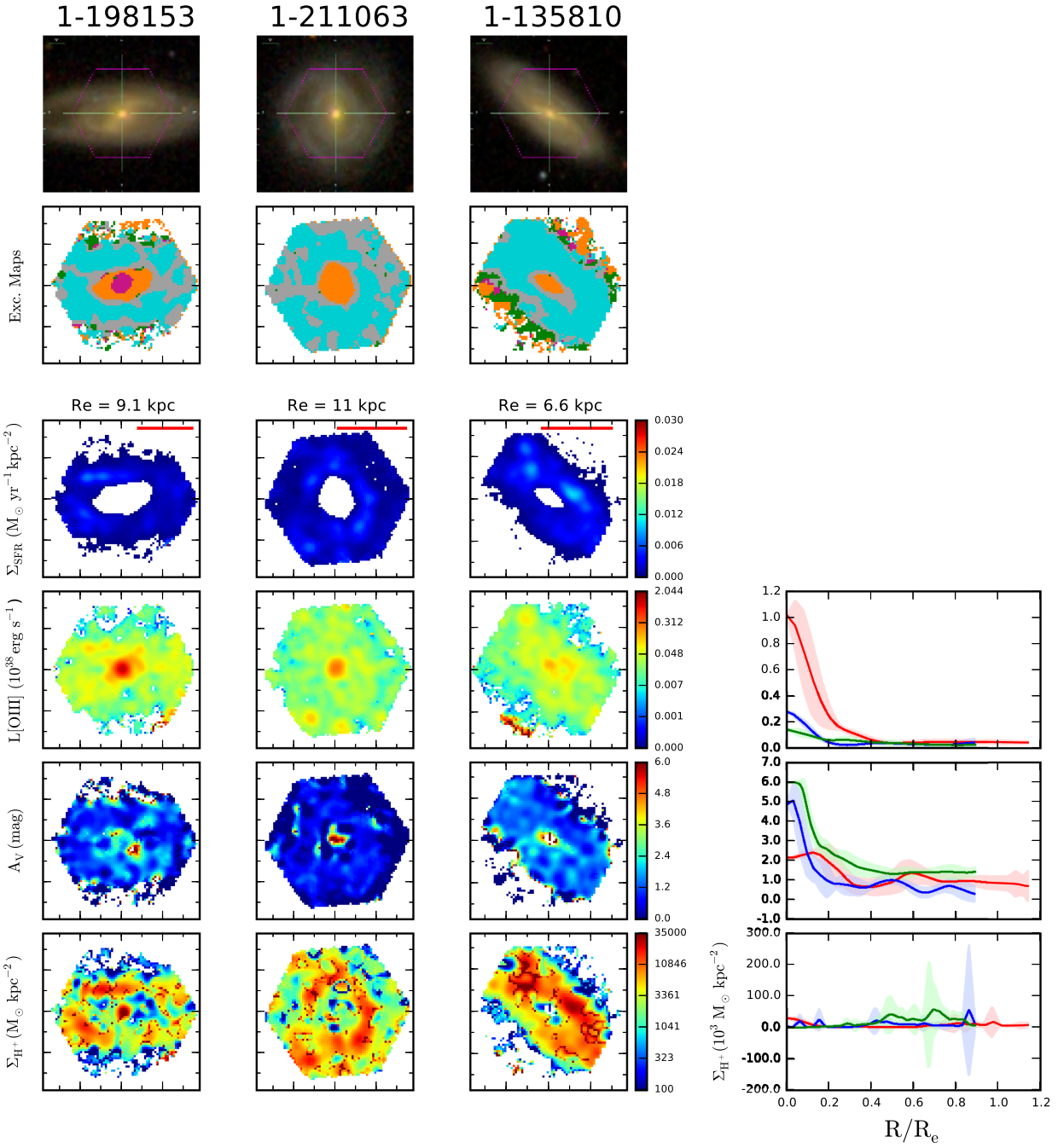


**Figure 4.** Same as Fig. 3 for a typical late-type AGN.

at the nucleus surrounded by LINER excitation. The nuclear excitation of the control galaxies include type H II, transition, and LIER.

The 45 low-luminosity AGN show varied types of nuclear excitation:  $\approx 30$  per cent have mixed LINER/Seyfert excitation,  $\approx 40$  per cent have LINER excitation at the nucleus and up to 1.4–9.4 kpc, while the other  $\approx 30$  per cent have Seyfert excitation at the nucleus and up to 2.4–15 kpc. At the nucleus, the controls show LIER or starburst excitation, while, outside the nucleus, AGN and controls present similar maps, dominated by star-forming discs in the late types and LIER excitation in the

early types, what can be attributed to the low level of activity of the AGN.

Finally, there are five controls that present Seyfert or LINER excitation at the nucleus and one case of one AGN (1-217050) which presents LIER excitation. This result indicates disagreement between the line ratios measured in the SDSS-III spectra (that we have used to select the sample) and in the nuclear MaNGA spectrum, which could be due to aperture size differences between SDSS-III and IFU MaNGA and/or measurement uncertainties and/or intrinsic variation of the AGN.

In the case of the control galaxy 1-286804, which are actually two galaxies in interaction, one galaxy nucleus present Seyfert and

the other LINER excitation, what was also not seen in the SDSS-III spectrum.

#### 4.1.3 Extranuclear AGN excitation

We have measured the extent  $R$  of the region ionized by the AGN in the excitation map – that can be identified with the NLR of the AGN – in order to verify if it increases with the AGN luminosity, as expected (Schmitt et al. 2003a,b). These values are listed in column 2 of Table 1, and range from 1.2 kpc to 27 kpc, with estimated measurement uncertainties of about 15 per cent. Due to the relatively large uncertainty, we preferred not to correct the data for the galaxy inclination.

We have plotted the  $R$  values against  $L[\text{O III}]$  in Fig. 7, showing that, on average, the extent of the region ionized by the AGN do increase with the AGN luminosity. A linear least-squares regression applied to the data gives the following relation:

$$\log(R) = (0.43 \pm 0.07) \log L[\text{O III}] - (16.58 \pm 2.78) \quad (7)$$

with a correlation coefficient of  $r = 0.62$ .

It is interesting to compare the above relation with a similar one obtained between the extent of the NLR and  $L[\text{O III}]$  by Bennert et al. (2002) and more recently by Storchi-Bergmann et al. (2018). We note that the regression coefficients above agree with those of the latter authors within the uncertainties. There is a vertical shift to larger values in our relation compared to that of Storchi-Bergmann et al. (2018), which we attribute to the poorer resolution of the MaNGA data, that can barely resolve 1 kpc in the closest galaxies of our sample, while Storchi-Bergmann et al. (2018) can resolve down to  $\approx 100$  pc.

The above relation supports the proportionality  $R \propto L^{0.5}$ , known to be valid for the broad-line region (BLR; Kaspi et al. 2005; Peterson 2014). Given the expression for the ionization parameter  $U \propto (L_{\text{AGN}}/(4\pi R^2 n_e c))$ , where  $c$  is the light speed and  $n_e$  is the gas density,  $R$  is  $\propto L^{0.5}$  if the product  $U n_e$  is a constant.

In many galaxies, both AGN and controls, there are some external spaxels, detached from the inner AGN excitation region, that show Seyfert or LINER excitation, according to the BPT diagram. This finding in the MaNGA data has been already pointed out by previous authors such as Wylezalek et al. (2018). One possible interpretation is that this gas has been previously ionized by an AGN, but which has presently ‘turned off’, thus characterizing a ‘relic AGN’.

We have nevertheless noticed, that in many cases these spaxels are surrounded by LIER excitation. When we consider that our adopted ‘division’ between AGN and LIERs is a sharp limit of the equivalent width  $W(\text{H}\alpha) = 3 \text{ \AA}$ , typical uncertainties of 10–30 per cent in such small  $W(\text{H}\alpha)$  values will move the spaxel from AGN to LIER excitation and vice versa. We thus do not favour the ‘relic AGN’ hypothesis in these cases, and attribute to possible uncertainties in  $W(\text{H}\alpha)$  values.

We have also noted that in many cases the extranuclear spaxels with AGN excitation correspond to high-latitude locations in a galaxy seen close to edge-on, suggesting an origin in a warm ionized medium (WIM; e.g. Storchi-Bergmann et al. 1996), that shows  $[\text{N II}]/\text{H}\alpha$  ratios similar to those of AGN (Brinchmann, Kunth & Durret 2008), such as the case of Fig. A2 in the appendix.

There are a few cases that may be indeed ‘relic AGN’, and should be further investigated for having more extended detached regions with AGN excitation. The following objects are candidates for being

relic AGN: MaNGA ID 1-121717, 1-43721, 1-178838, 1-37062, 1-377125, 1-386695, and 1-25688.

#### 4.2 Star formation rate (SFR)

The SFR surface density  $\Sigma_{\text{SFR}}$  maps are presented in the third row of Figs 3–6 for the four selected AGN and in the Appendix for the other galaxies.

In the case of the early-type AGN of Fig. 3, there is almost no star formation, while the first control galaxy presents some star formation at its border with low  $\Sigma_{\text{SFR}}$  (below  $0.006 M_{\odot} \text{ yr}^{-1} \text{ kpc}^{-2}$ ) and the second shows a high  $\Sigma_{\text{SFR}}$  (above  $0.03 M_{\odot} \text{ yr}^{-1} \text{ kpc}^{-2}$ ) in the nuclear region. The other early-type AGN hosts exhibit either more extranuclear star formation than the controls (11 cases) or similar values (8 cases), with only 3 cases with lower SFR in the AGN than in the controls. The  $\Sigma_{\text{SFR}}$  values are usually low, as above. A minority of control galaxies present higher values of  $\Sigma_{\text{SFR}}$  than the AGN, and when this happens, the  $\Sigma_{\text{SFR}}$  is highest in the central region of the galaxies.

In the case of the late-type AGN, as illustrated in Fig. 4, the  $\Sigma_{\text{SFR}}$  maps of AGN and controls are similar to each other, with typical values that do not vary much and are in the range  $\approx 0.003\text{--}0.01 M_{\odot} \text{ yr}^{-1} \text{ kpc}^{-2}$ . There is a large extranuclear region with star formation, with the  $\Sigma_{\text{SFR}}$  values being usually larger in the inner radii and decreasing outwards, although in some cases there are enhancements associated with spiral arms. Some control galaxies show star formation in the nuclear region, in which case  $\Sigma_{\text{SFR}}$  peaks at the nucleus. In these cases, the  $\Sigma_{\text{SFR}}$  values are  $\approx 30$  times larger than that in the AGN.

In the high-luminosity AGN of Fig. 5, there is star formation both in the AGN and controls only in the disc of the galaxies (thus beyond the nuclear region). The  $\Sigma_{\text{SFR}}$  values do not vary much; only in this AGN we notice an increase in the values towards the centre but this could be due also to the increase in the  $\text{H}\alpha$  flux due to the AGN proximity, as most of the region is a transition one (AGN combined with star formation, that we included in the calculation of the SFR). The remaining trios in this group show similar behaviour, with  $\Sigma_{\text{SFR}}$  maps for the AGN similar to those of the controls, in which star formation is only observed outside the nucleus. There are a few cases with almost no star formation, and a few others in which the controls show high  $\Sigma_{\text{SFR}}$  values in the centre.

In Fig. 6, for a low-luminosity AGN, we observe that the AGN has star formation only in the galaxy disc – with an enhancement in  $\Sigma_{\text{SFR}}$  in what appears to be a star-forming ring. Both controls present similar  $\Sigma_{\text{SFR}}$  values at the galaxy discs but larger values mostly at the nucleus, but also in an elongated structure beyond the nucleus that seems to be a bar. The values at the nucleus are at least 30 times higher than the typical values in the disc.

For the other low-luminosity AGN, only in 8 ( $\approx 20$  per cent) of the 45 trios the situation is similar to that of Fig. 6, in which one or the two controls present higher  $\Sigma_{\text{SFR}}$  values in the centre and decrease outwards, whereas in the AGN the star formation is only observed at the disc, with similar values to those quoted above. In most ( $\approx 80$  per cent) of the cases, the  $\Sigma_{\text{SFR}}$  maps are similar between the AGN and controls, in the sense that in the controls, also the star formation is larger in the outer part of the galaxies than in their centres, while in the central part, instead of an AGN, there is a LIER.

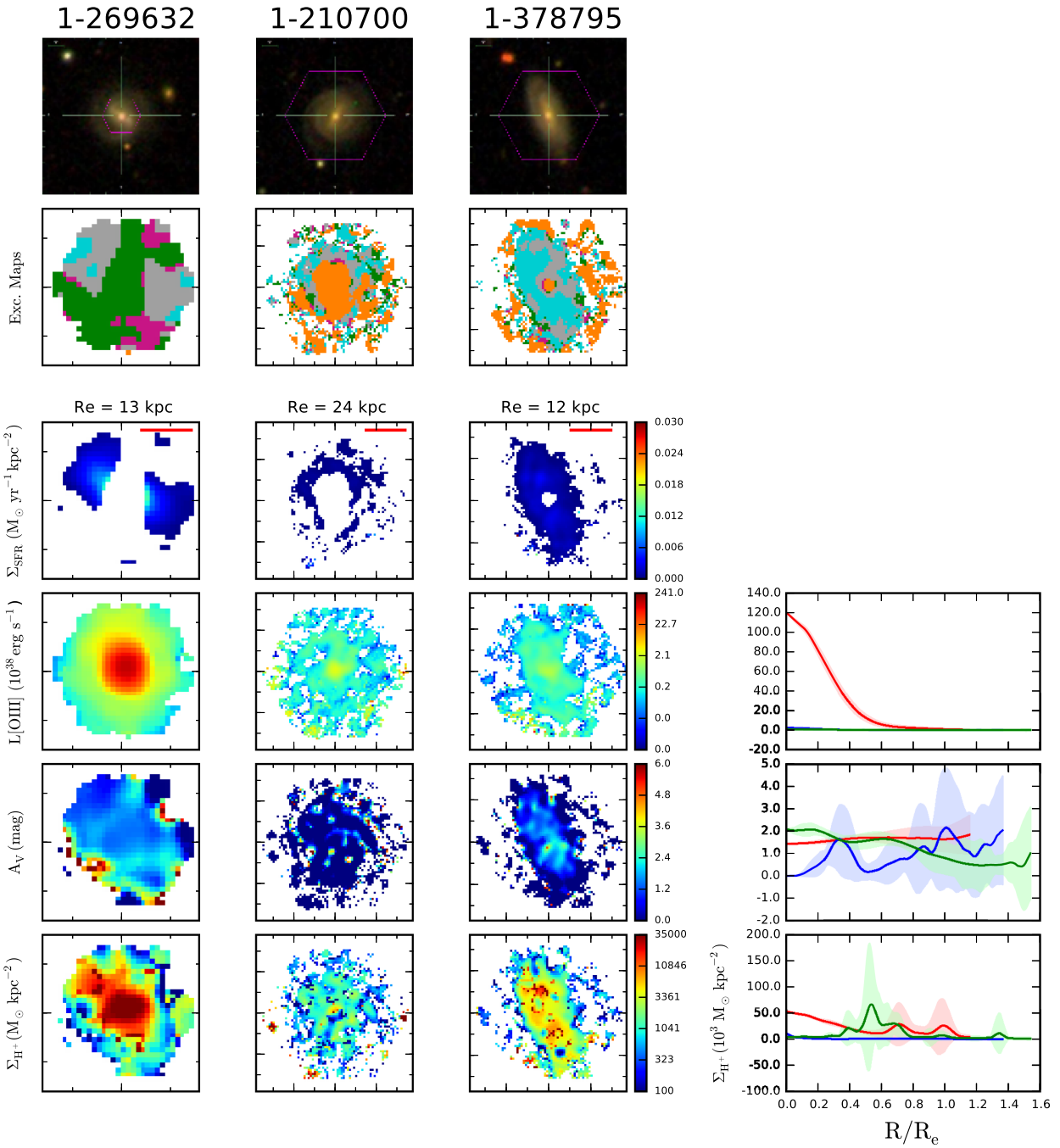


**Figure 5.** Same as Fig. 3 for a high-luminosity AGN.

#### 4.2.1 SFR histograms

We have built histograms for the total SFR as listed – in  $\log_{10}$  units of  $M_\odot \text{ yr}^{-1}$  – in the last column of Table 1. The total SFR values were obtained by adding the SFRs from all regions over the whole galaxy, where star formation is present, including the H II excitation regions and the transition regions.

Fig. 8 shows the histograms of the total SFR for the AGN (in red), as compared to those of the control galaxies (in blue), separated in three panels: in the left-hand panel we show the histograms for the whole sample, in the centre panel only for the early-type galaxies, and in the right-hand panel for the late-type galaxies. The distributions for the AGN and controls in the three cases are

very similar, what is confirmed by a two-sample Anderson–Darling (A–D) test. The probability  $p$  that the two distributions are drawn from the same parent population is given in the corresponding panels (the reference  $p$  is 0.05, meaning that for smaller values, there is more than 95 per cent chance that the two distributions are distinct). According the A–D test for the above three cases, the probability that the distributions are statistically equal are,  $\approx 30$  per cent,  $\approx 13$  per cent, and  $\approx 43$  per cent for the total, early-type, and late-type samples, respectively.

In Fig. 9 we present similar histograms for the total SFR now separated in different bins of AGN luminosity ( $\log_{10} L[\text{OIII}]$ , in units of  $\text{erg s}^{-1}$ ), from the most luminous (41.25–42.0) to the

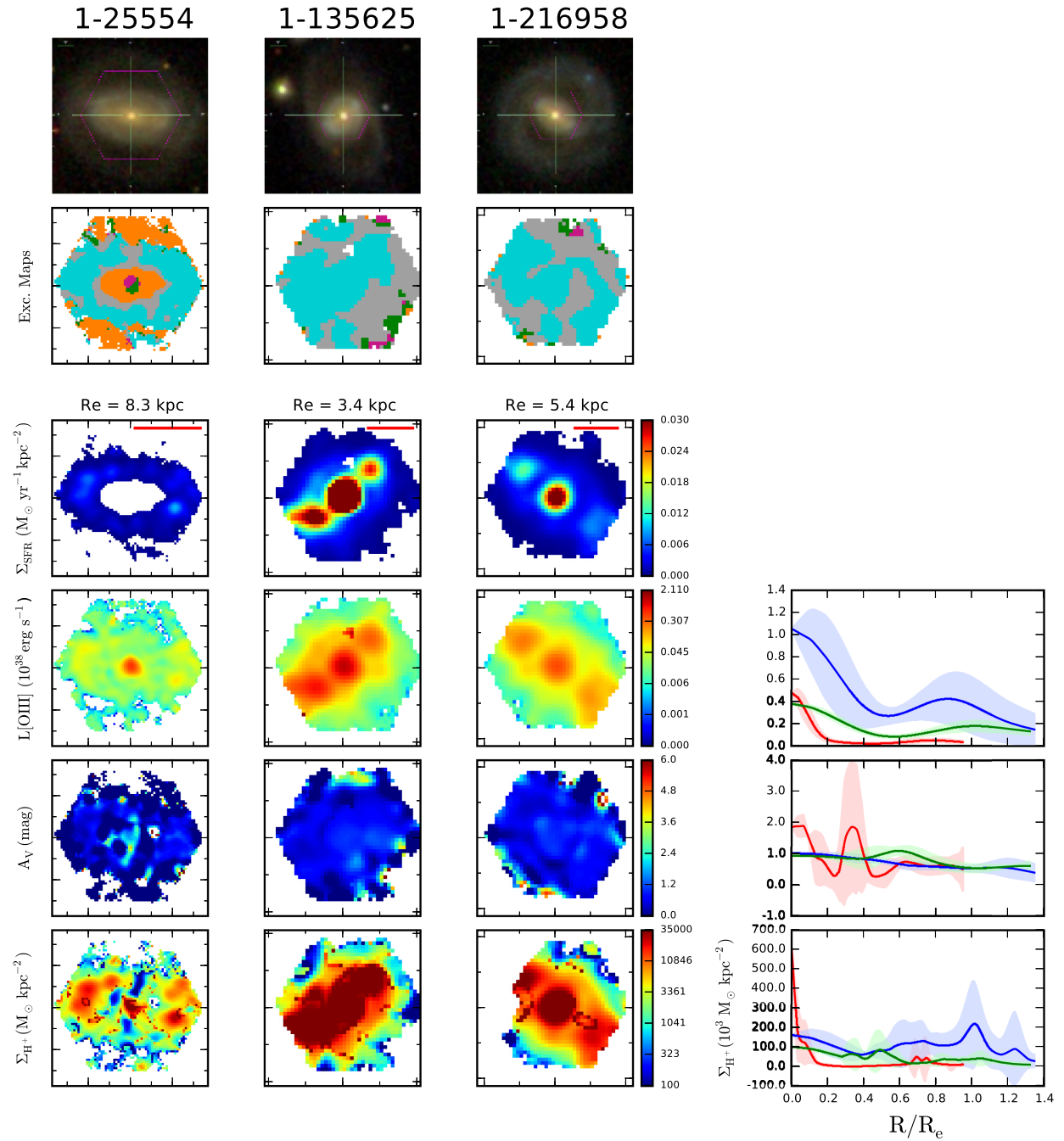


**Figure 6.** Same as Fig. 3 for a low-luminosity AGN.

left to the less luminous (39.0–39.75) to the right. Again the distributions for AGN and controls are similar, with a probability that the distributions are statistically the same between 9 per cent and 92 per cent for the different luminosity bins, according to the A–D test.

It can thus be concluded, from the above two histograms, that the total SFR, over the whole galaxies is similar for AGN and control galaxies.

As we have carefully built the control sample to match the AGN host galaxy properties, we now compare the SFR of each AGN to those of its two control galaxies. Although the range of

SFR of the two samples are similar, there may be a systematic difference between a galaxy in an AGN phase and one that is not (the corresponding control galaxies).

We have thus built another histogram in which we present the distribution of differences between the SFR of the AGN and each of its control galaxies. In order to take into account the fact that the range of SFR values is very large, we have divided the difference in SFR by the AGN SFR. The histogram of these fractional differences is shown in Fig. 10, for each pair AGN-control (112 combinations):  $(SFR_{AGN} - SFR_{ctr})/SFR_{AGN}$ . The division by  $SFR_{AGN}$  is necessary in order to bring the differences to a similar scale.

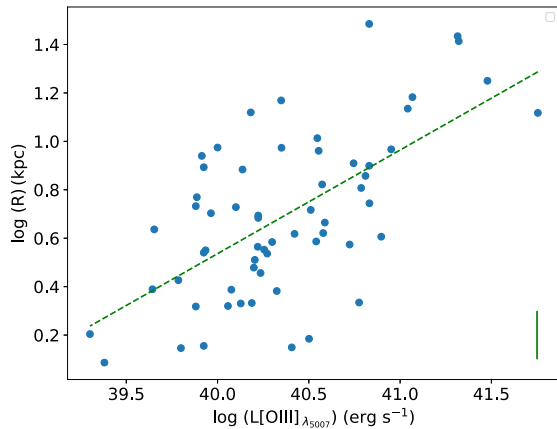


**Figure 7.** Relation between the extent of the region ionized by the AGN  $R$  and  $L[\text{O III}]$ , showing also a linear regression to the data (see text). The bar in the bottom corner shows a typical uncertainty in  $R$  of about 10 per cent.

In these new histograms, when considering the whole sample,  $\approx 61$  per cent of the combinations AGN-control show positive fractional differences (SFR in the AGN larger than in the control), with a positive mean fractional difference of 0.2 and median of 0.47. When considering only the early-type subsample, this percentage increases to  $\approx 76$  per cent, mean of 0.69 and median of 0.93, while for the late-types this percentage decreases to  $\approx 51$  per cent. These results mean that, while for the early-type galaxies, most AGN have more star formation than its controls, for the late-type galaxies, in  $\approx 50$  per cent of the cases there is more star formation in AGN and in the other 50 per cent there is more star formation in the controls.

#### 4.3 L[O III] maps

The fourth row of panels (from top to bottom) of Figs 3–5 shows that, for these three AGN hosts – early and late types and high-luminosity AGN –  $L[\text{O III}]$  at the nucleus is higher than those of the control galaxies, as expected. But in the case of the low-luminosity AGN of Fig. 6  $L[\text{O III}]$  is lower in the AGN than in its controls. This can be due to the fact that  $L[\text{O III}]$  in the control galaxies, due to star formation, can be higher than that of a low-luminosity AGN. This happens not only at the nucleus but also outside the nucleus, as seen also in Fig. 6.

When inspecting Figs A1–A58 (see online) of the Appendix we note that the example of Fig. 6 is more the exception than the rule, and most active galaxies do present the nuclear region more luminous in  $L[\text{O III}]$  than their controls. There are only three more cases in which at least one control galaxy has the central region with higher  $L[\text{O III}]$  than the AGN, but the profiles and the maps show that there is not a large difference between the AGN and its controls.

#### 4.4 Extinction

The fifth row of Figs 3–5 show that the extinction maps and corresponding one-dimensional profiles present a very diverse behaviour. For some AGN hosts and control galaxies, the extinction is larger at large radial distances; for others, the largest extinction values are found close to the centre of the galaxy. There are also many cases of irregular extinction maps. We have not detected any significant difference between the extinction maps of the AGN and

the control galaxies. As the estimate of extinction requires a valid flux measurement of both  $H\alpha$  and  $H\beta$ , and in many cases we could not measure the  $H\beta$  flux due to the low-signal-to-noise ratio of this line, the resulting extinction maps often present ‘holes’, what may have masked possible differences between AGN and control galaxies.

#### 4.5 Ionized gas surface mass densities $\Sigma_{H^+}$

The bottom panels of Figs 3–6 show the  $\Sigma_{H^+}$  maps and average one-dimensional profiles.

For the 20 early-type galaxies, including Fig. 3, both the AGN and the non-active galaxies present ionized gas over the whole galaxy in 90 per cent of them, with the AGN – as observed in the one-dimensional profiles – showing higher  $\Sigma_{H^+}$  than the controls at the centre – reaching several  $10^3 M_\odot \text{ kpc}^2$  within  $0.2 R_e$  (the nuclear region) and decreasing outwards, while the control galaxies frequently have higher  $\Sigma_{H^+}$  values than the AGN beyond  $0.2 R_e$ . In two (10 per cent) cases the  $\Sigma_{H^+}$  is lower in the nuclear region of AGN than in the control galaxies.

The 38 late-type galaxies, as illustrated in Fig. 4, show that the ionized gas is spread all over the galaxies for both AGN and controls, mostly due to star formation in the galaxy discs. According to the one-dimensional profiles, about half of the AGN have higher  $\Sigma_{H^+}$  than the control galaxies within  $0.2 R_e$  (the nuclear region). In the other half, the difference between AGN and controls is of the order of the typical azimuthal variation of the  $\Sigma_{H^+}$  within each galaxy (shaded areas in the one-dimensional profiles). In general, the one-dimensional profiles do not show a large radial variation in  $\Sigma_{H^+}$  values for both AGN and controls.

In the  $\Sigma_{H^+}$  maps of the high-luminosity AGN of Fig. 5, we observe much higher  $\Sigma_{H^+}$  values for the AGN than in the controls within  $0.2 R_e$ , while outside  $0.4 R_e$  the values are similar for the AGN and controls. Considering all high-luminosity AGN, approximately 64 per cent (11) (including the example of Fig. 5), present higher values for the AGN than in the controls within  $0.2 R_e$ , while outside  $0.4 R_e$ , the values are similar for the AGN and controls. For the remaining 36 per cent (6 cases), in half the AGN show  $\Sigma_{H^+}$  values smaller than their controls in the nucleus, and in the other half the AGN and controls have similar  $\Sigma_{H^+}$  values. Some controls show an increase in the  $\Sigma_{H^+}$  values outwards.

For the 45 low-luminosity AGN, including the example of Fig. 6, approximately 45 percent exhibit – for both the AGN and control galaxies – the ionized gas spread all over the galaxy. The one-dimensional profiles show that, while the AGN shows a higher  $\Sigma_{H^+}$  inside  $0.2 R_e$ , the controls have higher values than the AGN beyond the nuclear region. For approximately 22 per cent of the low-luminosity AGN, the nuclei of the AGN and controls present similar  $\Sigma_{H^+}$  values, whereas for 33 per cent the AGN have lower  $\Sigma_{H^+}$  values than their controls. For regions beyond  $0.2 R_e$ , the profiles are mostly similar for the AGN and controls.

#### 4.6 Central ionized gas surface mass densities $\Sigma_{\text{nuc}}$

We have calculated the mean central surface mass density  $\Sigma_{\text{nuc}}$  as the ionized gas surface mass density within a circular area of radius  $0.2 R_e$  around the nucleus. This value is listed in columns 4 and 8 of Table 1, respectively, for the AGN and controls. These values range from  $7.35 \times 10^2$  to  $2.61 \times 10^5$  for the AGN and  $0.43 \times 10^2$  to  $2.14 \times 10^6$  for the controls.

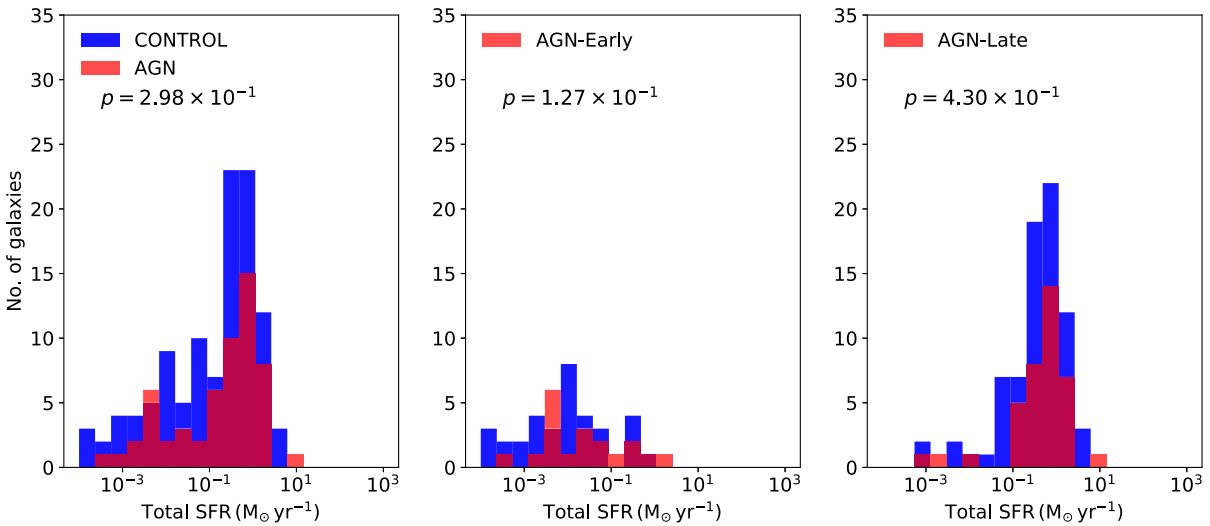


**Figure 8.** Histograms comparing the total SFR for the AGN and control galaxies. Left-hand panel: whole sample; central panel: early-type hosts; right-hand panel: late-type hosts. The  $p$  value in each panel gives the probability that the two distributions are drawn from the same parent population.

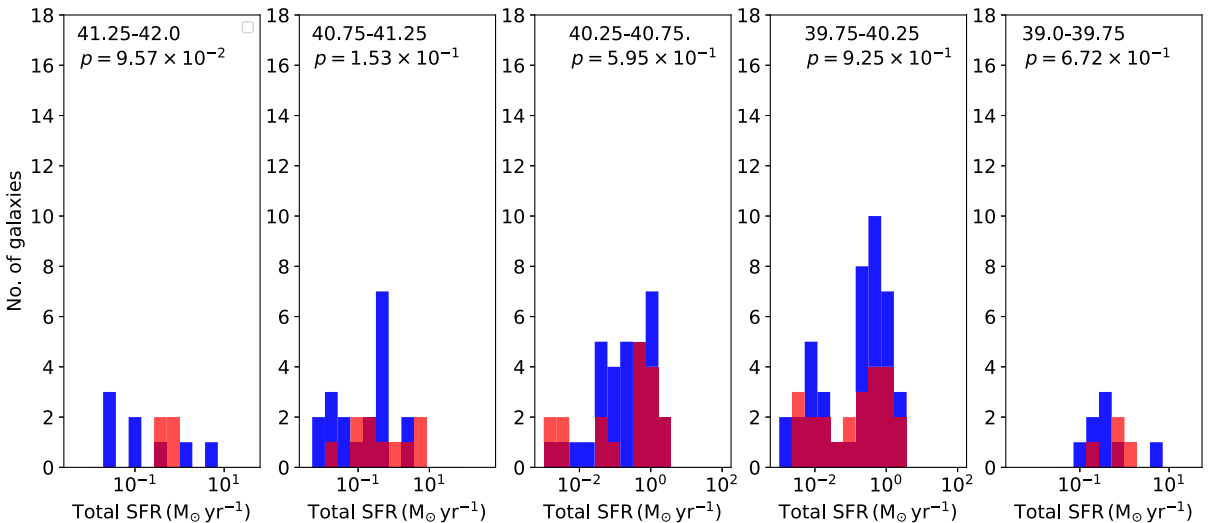


**Figure 9.** Histograms comparing the total SFR of AGN and control galaxies separated according to the AGN [O III] luminosity  $\log(L[\text{O III}])$ . From left to right: decreasing  $L[\text{O III}]$ , with values identified in the top of each panel in logarithm units of  $\text{erg s}^{-1}$ . The  $p$  value in each panel gives the probability that the two distributions are drawn from the same parent population.

We show histograms of these values in Figs 11 and 12. In Fig. 11, we show the distribution of  $\Sigma_{\text{nuc}}$  values for the whole sample in the left-hand panels, and separately for the early- and late-type subsamples in the central and right-hand panels.

According to the A–D test, the probabilities  $p$  that the AGN and control sample are drawn from the same population are smaller than  $10^{-5}$  for the total and early-type sample and  $p = 4.09 \times 10^{-4}$  for the late-type sample. The median values of  $\Sigma_{\text{nuc}}$  are  $1.74 \times 10^4 \text{ M}_\odot \text{kpc}^{-2}$  for all the AGN and  $2.72 \times 10^3 \text{ M}_\odot \text{kpc}^{-2}$ , for all the controls.

In Fig. 12, in which the AGN are separated in luminosity bins, even though the number of objects in each bin is small, the distributions are statistically different – with the values of  $p \leq 0.05$  for all bins except the lowest luminosity one.

We further explore the differences between the AGN and control galaxies via histograms of the fractional differences of  $\Sigma_{\text{nuc}}$  for each pair AGN-control (112 combinations), as previously done for the SFR:  $(\Sigma_{\text{nuc,AGN}} - \Sigma_{\text{nuc,ctr}})/\Sigma_{\text{nuc,AGN}}$ . The histograms for these values are shown in Fig. 13 for the total sample on the left and for the early- and late-type subsamples in the central and right-hand panels. There were only a few cases for which the values are more negative than  $-1$ , which we have opted to exclude from the graph for visualization purposes. But even when taking them into account, we have that  $\approx 74$  per cent of the sample show positive fractional differences, indicating that  $\Sigma_{\text{nuc}}$  is higher in the AGN than in the controls for most of the sample. When considering only the early-type subsample, this percentage increases to  $\approx 93$  per cent, while for the late-type subsample this percentage is  $\approx 63$  per cent. The median fractional differences of  $\Sigma_{\text{nuc}}$  between the AGN and controls are:

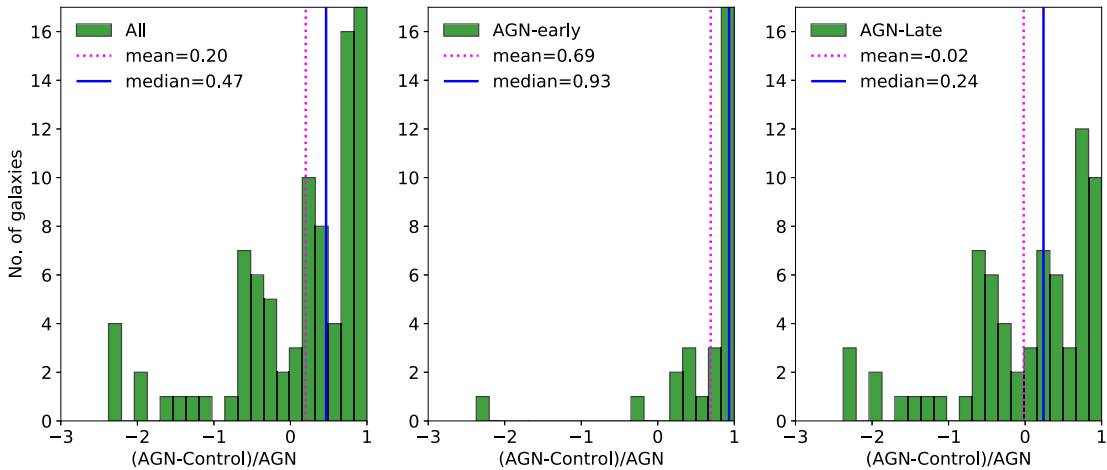


**Figure 10.** Histograms for the fractional difference in SFR between the AGN and each of its two control galaxies:  $(\text{SFR}_{\text{AGN}} - \text{SFR}_{\text{ctr}})/\text{SFR}_{\text{AGN}}$ . Left-hand panel: total sample; central panel: early-type hosts; right-hand panel: late-type hosts.

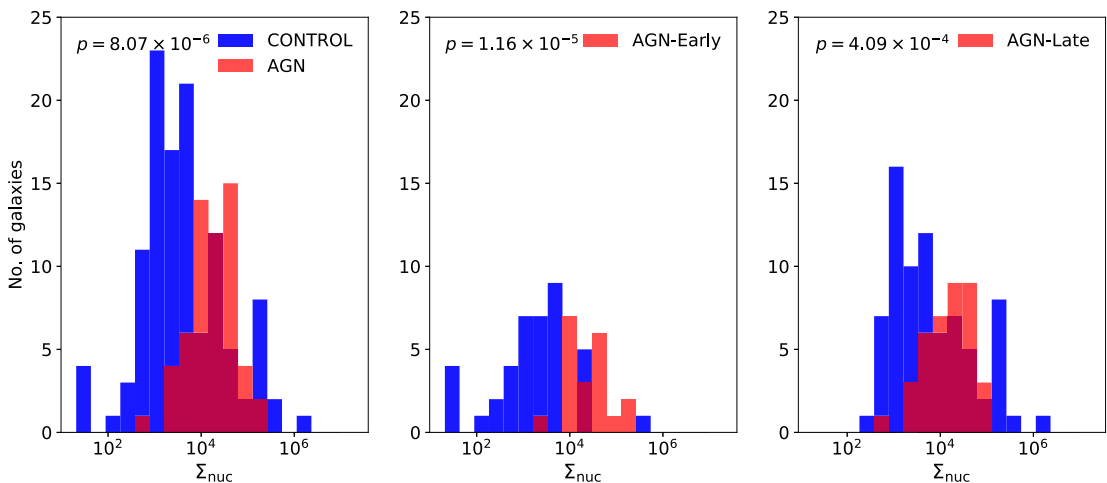


**Figure 11.** Histograms of central surface mass densities  $\Sigma_{\text{nuc}}$  (in units of  $M_{\odot} \text{ kpc}^{-2}$ ) within the inner  $0.2 R_{\text{e}}$  (effective radius); left: total sample; centre: early-type sample; right: late-type sample.

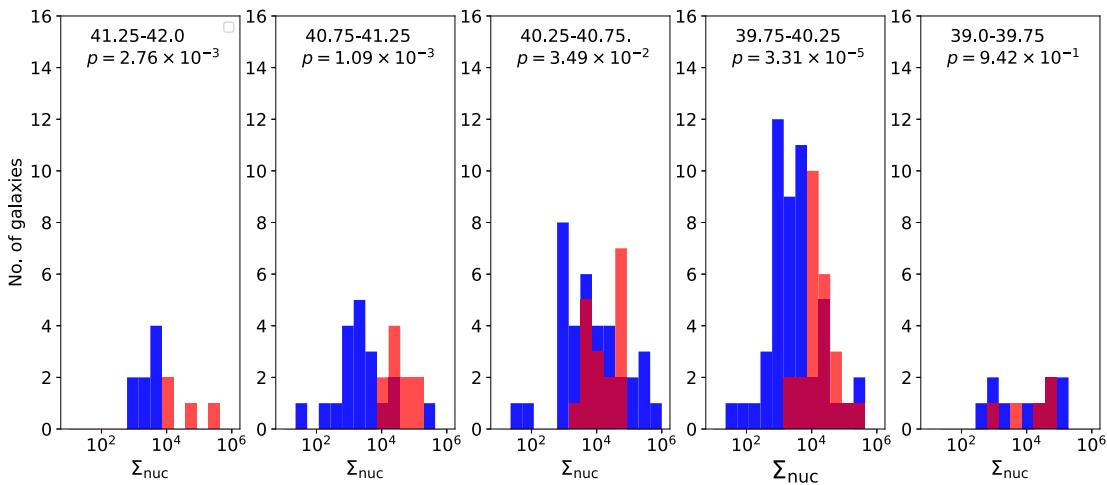


**Figure 12.** Histograms of  $\Sigma_{\text{nuc}}$  separated in AGN luminosity bins – shown in the top of each panel as  $\log_{10}(L[\text{O III}])$ , in units of  $10^{40} \text{ erg s}^{-1}$ , together with the A–D test  $p$  value, from the most luminous (left) to the less luminous AGN (right). Colours as in Fig. 11.

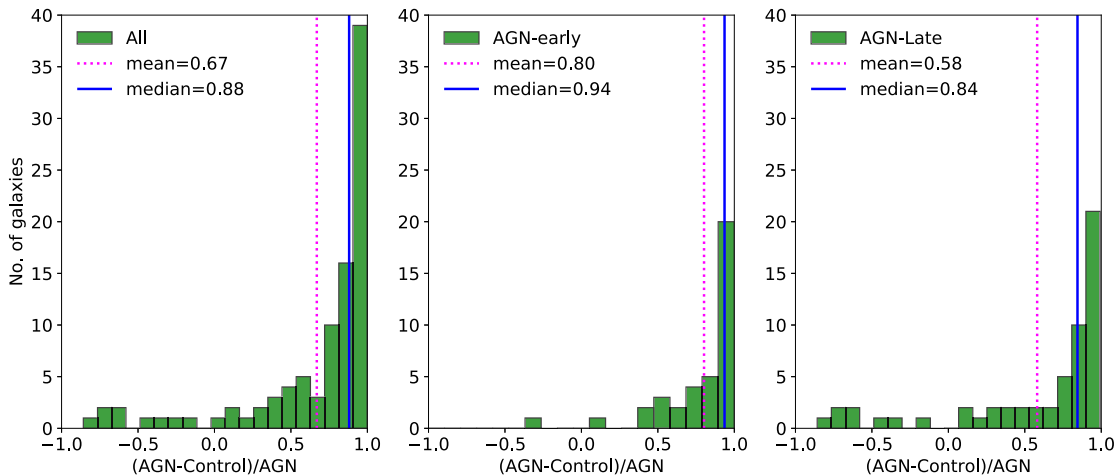


**Figure 13.** Histograms of the fractional differences  $(\Sigma_{\text{nuc},\text{AGN}} - \Sigma_{\text{nuc},\text{ctr}})/\Sigma_{\text{nuc},\text{AGN}}$ ; left: total sample; centre: early-type sample; right: late-type sample.

0.88 for the total sample, 0.94 for the early-types, and 0.84 for the late-types.

In summary,  $\Sigma_{\text{nuc}}$  is in most cases higher in AGN than in the control galaxies, with the largest fractional differences being observed for the early-type galaxies.

#### 4.7 Total ionized gas mass

The total mass of ionized gas was obtained by integrating the whole H $\alpha$  emission from the galaxy. The corresponding values are shown in columns 3 and 7 of Table 1, respectively, for the AGN and their controls.

The range of values for the total ionized gas mass are:

- (1) For the total sample:  $9.9 \times 10^4$ – $2.9 \times 10^7 M_\odot$  for the AGN, compared to  $1.9 \times 10^4$ – $1.7 \times 10^8 M_\odot$  for the controls;
- (2) For the early-type sub-sample:  $2.2 \times 10^5$ – $2.5 \times 10^7 M_\odot$  for the AGN and  $1.9 \times 10^4$ – $6.3 \times 10^6 M_\odot$  for the controls;
- (3) For the late-type sub-sample:  $9.9 \times 10^4$ – $2.9 \times 10^7 M_\odot$  for the AGN and  $9.3 \times 10^4$ – $1.7 \times 10^8 M_\odot$  for the controls.

The ionized gas mass values obtained for our AGN sample are consistent with those obtained in previous studies of similar AGN hosts, such as Harrison et al. (2014), where the total mass for a sample of 16 AGN, inside the inner 6–16 kpc was found in the range  $(2\text{--}40) \times 10^7 M_\odot$  under the assumption that  $n_e = 100 \text{ cm}^{-3}$  (and lower for  $n_e = 500$ ). In Couto et al. (2013) and Couto, Storchi-Bergmann & Schnorr-Müller (2017) the total ionized gas mass obtained for a sample of radio galaxies ranges between  $3.1 \times 10^5$  and  $4.1 \times 10^8 M_\odot$ , also consistent with the range of values that we obtained in this work.

The ranges of total ionized gas masses obtained for the AGN are similar to the ranges obtained for the controls, and this can be seen in the histograms in Fig. 14. But the distribution of values is different for the AGN and control samples, as indicated by the A-D test that gives a probability larger than 95 per cent that the distributions are not drawn from the same parent population.

Calculating again the fractional differences of total ionized gas masses between each pair of AGN and control ( $M_{\text{AGN}} - M_{\text{ctr}})/M_{\text{AGN}}$  (112 combinations), we obtain the results shown in the histograms of Fig. 15 for fractional differences between –1 and 1. Again, as

in the case of  $\Sigma_{\text{nuc}}$ , there are a few cases of values lower than –1, which we have excluded from the plot. But, even when considering these cases, ≈66 per cent of the total sample shows positive values, with ≈85 per cent for the early-type hosts and ≈57 per cent for the late-type hosts. The median values are: 0.70 for the total sample, 0.81 for the early-types, and 0.43 for the late-types. Thus, even though the ranges of ionized gas masses of the AGN present large overlap with those of the control galaxies, when paired according to the host galaxy properties, most AGN show an excess of ionized gas mass (values larger than 0 in the histograms of Fig. 15) relative to their control pairs.

In terms of AGN luminosity, the ranges of obtained total ionized gas masses are: (1) for the high-luminosity AGN,  $5.2 \times 10^5$ – $6.9 \times 10^7 M_\odot$ , which is skewed to larger values than the corresponding range for the controls of  $6.2 \times 10^4$ – $2.2 \times 10^7$ , while for the lower luminosity AGN the range is  $9.9 \times 10^4$ – $2.9 \times 10^7 M_\odot$  and  $1.9 \times 10^4$ – $1.7 \times 10^8 M_\odot$  for the controls, thus showing complete overlap in the values.

#### 4.8 Average gradients of $\Sigma_{H^+}$

We have used the azimuthally averaged profiles of  $\Sigma_{H^+}$  of each galaxy to calculate the average profile of groups of AGN separated according to their luminosity, as well as of their control galaxies, following the methodology described in Mallmann et al. (2018). In Fig. 16 we show these for each of the following AGN luminosity bins of  $\log(L[\text{O III}])$ , with  $L[\text{O III}]$  in  $\text{erg s}^{-1}$ : 41.25–42.0 (shown in red), 40.75–41.25 (light green), 40.25–40.75 (dark green), 39.75–40.25 (blue), 39.0–39.75 (purple).

In this figure, the left column of panels shows the average profiles for the total sample, the central column shows the results for the early-type sub-sample and in the right column, for the late-type sub-sample. The first line of panels show the AGN profiles, the middle shows the corresponding control galaxies, and the bottom shows the difference between AGN and controls.

Considering the whole sample, there is a tendency for the higher luminosity AGN to show larger values of gas surface mass density than the control galaxies from the nucleus up to about  $0.4 R_e$ ; beyond this radius there is no difference, what can be understood as due to the fact that the presence of a luminous AGN requires more gas than in non-AGN, combined with the presence of a nuclear source

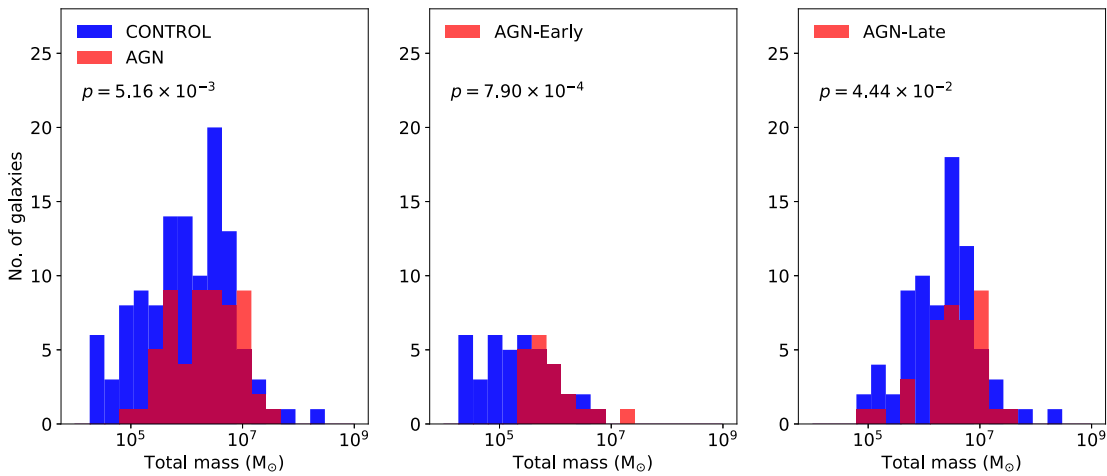


**Figure 14.** Histograms of the total mass of ionized gas; left: total sample; central: early-type sample; right: late-type sample.

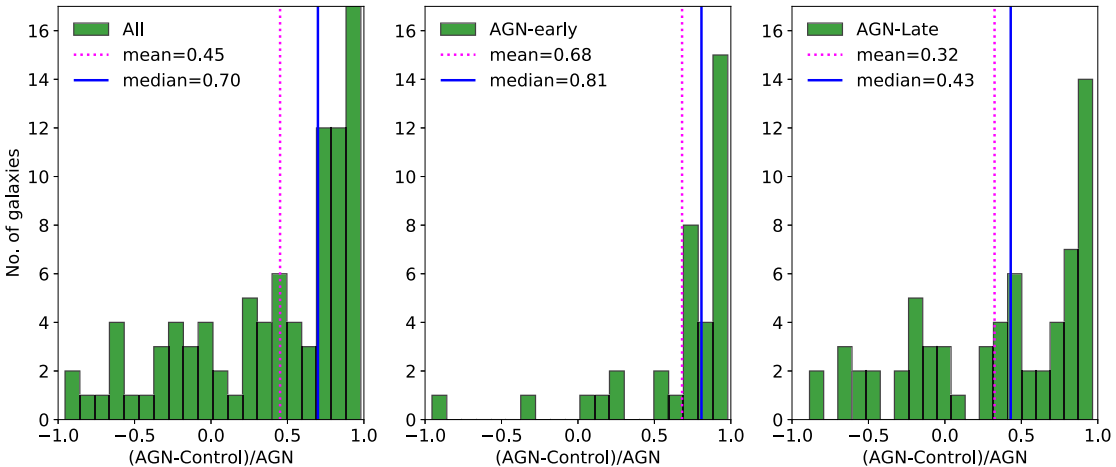


**Figure 15.** Histograms of the fractional differences  $(M_{\text{AGN}} - M_{\text{ctr}})/M_{\text{AGN}}$ ; left: total sample; centre: early-type sample; right: late-type sample.

of radiation, what is restricted to the inner regions of the galaxy. As the AGN luminosity decreases, the difference becomes smaller, and in the case of the lowest luminosity bin, the control galaxies have even more ionized gas than the AGN.

The central and right-hand panels of Fig. 16 show that the tendency discussed above seems to hold both for the early- and late-type galaxies, even though in our sample we do not have an early-type AGN in the highest luminosity bin.

## 5 SUMMARY AND CONCLUSIONS

We have mapped the gas excitation, SFR, and ionized gas mass distributions of 62 AGN host galaxies as compared with a control sample of 112 galaxies using MaNGA-SDSS-IV data cubes. The sample comprises 20 early-type, 38 late-type galaxies, and 4 galaxies in interaction with a companion. In terms of the AGN luminosity, 17 have  $L([\text{O III}])\lambda 5007 > 3.8 \times 10^{40} \text{ erg s}^{-1}$ , that we have called high luminosity, and 45 have lower luminosity than this (called low-luminosity AGN). The results of our measurements and analysis are summarized below.

(i) Nuclear excitation: We have mapped the gas excitation using the BPT and WHAN diagrams. Defining the nuclear region as having a radius  $\leq 0.2 R_e$  (effective radius), 2/3 of the high-luminosity AGN have nuclear Seyfert (Sy) excitation, and the rest have either LINER or mixed Sy/LINER excitation. Of the 45 low-luminosity AGN, 30 per cent have Sy, 40 per cent LINER, and 30 per cent mixed nuclear excitation. Regarding the controls, using only the BPT diagram, many nuclear regions result classified as AGN – especially in the early-type hosts, but the WHAN diagram reveals that most of these cases are LIERs (excited by evolved hot stars). In the late-type galaxies, besides LIERs there are also a number of controls with starburst nuclei.

(ii) Extranuclear excitation: We have measured the extent  $R$  of the NLR defined as the region surrounding the nucleus with AGN excitation, obtaining values ranging from 1.5 to 27 kpc, and found the relation  $R \propto (L(\text{O III}))^{0.5}$ , similar to that valid for the BLR and recently obtained also for the NLR of luminous AGN by Storchi-Bergmann et al. (2018) and previously by Bennert et al. (2002).

Both in AGN and controls there are some extranuclear regions (detached from the nucleus) that are classified as AGN according

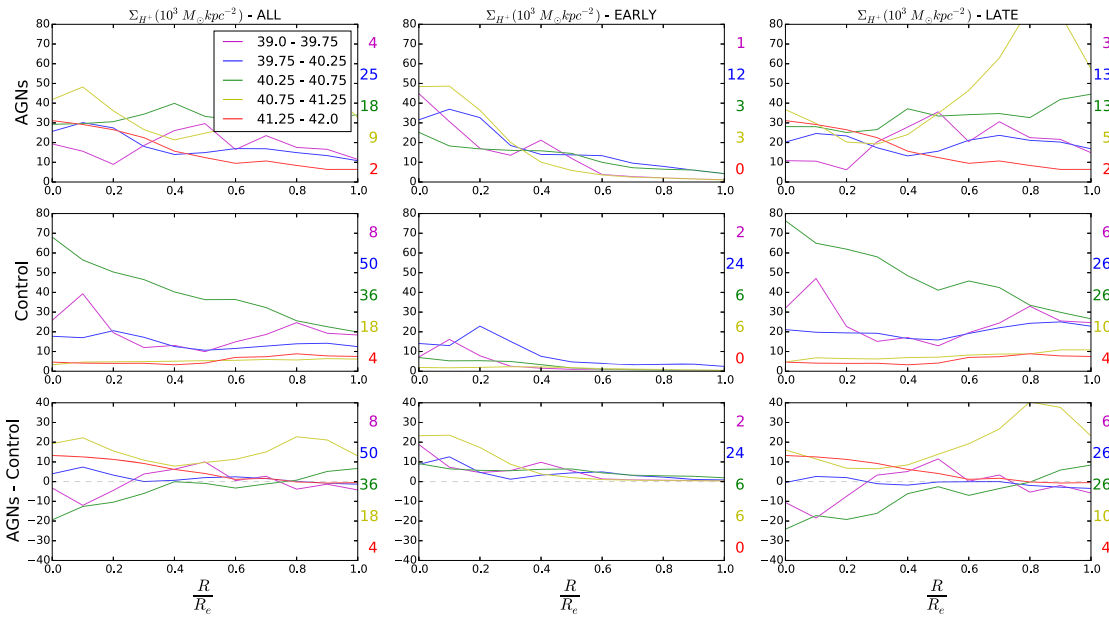


**Figure 16.** Average profiles of the ionized gas surface mass densities (in units of  $10^3 M_\odot \text{ kpc}^{-2}$ ) of groups of AGN separated according to the AGN luminosity (according to the insert in the top left-hand panel). Top panels, from left to right: total AGN sample, early-type AGN, late-type AGN; middle panels: control sample corresponding to each top panel; bottom panels: difference between each AGN and control sample group.

to the BPT diagram; using also the WHAN diagram, most of these regions become LIERs, although the emission of some of them could be signatures of warm ionized gas (seen mostly in highly inclined galaxies) and some could also be signatures of ‘relic AGN’.

(iii) Star formation rate: The SFR surface density  $\Sigma_{\text{SFR}}$  was obtained in the region of the galaxies dominated by star formation, mostly in the galaxy discs. The  $\Sigma_{\text{SFR}}$  maps are similar for the AGN and controls. Some control galaxies show star formation also in the nuclear region, reaching the highest values there in the case of late-type galaxies.

The total SFR of both the AGN and control galaxies range from  $10^{-3}$  to  $10 M_\odot \text{ yr}^{-1}$ , with a difference between AGN and controls seen only for the early-type galaxies: 75 per cent of the early-type AGN have higher SFR than their controls. This result suggests that the gas that is feeding the AGN also triggers star formation in the outer parts of the galaxy, and that the AGN is not quenching star formation there. As we do not see differences in SFR between AGN and controls for the late-type galaxies, we do not see signature of quenching in the discs of late-type galaxies as well.

(iv) Surface mass densities of ionized gas  $\Sigma_{H^+}$ : Within  $0.2 R_e$ ,  $\Sigma_{H^+} = \Sigma_{\text{nuc}}$  is larger for the AGN than for the control galaxies in 75 percent of the sample, with median values of  $1.74 \times 10^4 M_\odot \text{ kpc}^{-2}$  for the AGN and  $2.72 \times 10^3 M_\odot \text{ kpc}^{-2}$  for the controls. The control galaxies of the early types usually have higher  $\Sigma_{H^+}$  values in the outer regions than in their nuclei. In the case of late-type hosts, the regions of highest  $\Sigma_{H^+}$  are more extended (throughout the galaxy discs) than in the early-types, with similar values in the galaxy discs for the AGN and controls, while in the nucleus, it is higher in the AGN for half of the sample and lower in the other half.

(v) Gradients of  $\Sigma_{H^+}$ : Average gradients constructed from the above  $\Sigma_{H^+}$  maps are usually steeper for the AGN than for the controls from the centre to about  $0.4 R_e$ , with the difference decreasing as the AGN luminosity decreases.

(vi) Total ionized gas masses: We have obtained lower limits for the integrated ionized gas masses, with the total values estimated to be 10 per cent–40 per cent higher, depending on the galaxy. The lower limits range from  $9.9 \times 10^4$  to  $2.9 \times 10^7 M_\odot$  for the AGN, compared to the range of  $1.9 \times 10^4$  to  $1.7 \times 10^8 M_\odot$  for the controls. When pairing each AGN with its controls, for the early-type hosts, 85 per cent of the AGN have more ionized gas than the controls, while this percentage decreases to 57 per cent for the late-type hosts.

In summary, the main differences between AGN and controls is observed for early-type galaxies, that have: (1) higher SFR than the controls in 75 per cent of the cases; (2) larger ionized gas masses than the controls in 85 per cent of the cases. This suggests a connection between the star formation and nuclear activity in the early-type galaxies: the same gas that feeds the AGN is also triggering star formation in its vicinity and these results also do not support that AGN feedback is quenching star formation for the luminosities probed by this nearby sample.

Another important result is the increase of the extent of the region excited by the AGN with its luminosity, reaching the galaxy limits for the highest luminosities probed here, of  $\log(L[\text{O III}]) = 41.8$ , and suggesting that this radiation will escape the galaxy for higher luminosities.

## ACKNOWLEDGEMENTS

JCN thanks to CNPq for financial support. TSB, RAR, RR, and SR acknowledge the support of the Brazilian funding agencies FAPERGS and CNPq. We would like to thank the support of the Instituto Nacional de Ciéncia e Tecnologia (INCT) e-Universe project (CNPq grant 465376/2014-2).

Funding for the Sloan Digital Sky Survey IV has been provided by the Alfred P. Sloan Foundation, the U.S. Department of Energy Office of Science, and the Participating Institutions. SDSS

acknowledges support and resources from the Center for High-Performance Computing at the University of Utah. The SDSS web site is [www.sdss.org](http://www.sdss.org).

SDSS is managed by the Astrophysical Research Consortium for the Participating Institutions of the SDSS Collaboration including the Brazilian Participation Group, the Carnegie Institution for Science, Carnegie Mellon University, the Chilean Participation Group, the French Participation Group, Harvard-Smithsonian Center for Astrophysics, Instituto de Astrofísica de Canarias, The Johns Hopkins University, Kavli Institute for the Physics and Mathematics of the Universe (IPMU) / University of Tokyo, Lawrence Berkeley National Laboratory, Leibniz Institut für Astrophysik Potsdam (AIP), Max-Planck-Institut für Astronomie (MPIA Heidelberg), Max-Planck-Institut für Astrophysik (MPA Garching), Max-Planck-Institut für Extraterrestrische Physik (MPE), National Astronomical Observatories of China, New Mexico State University, New York University, University of Notre Dame, Observatório Nacional / MCTI, The Ohio State University, Pennsylvania State University, Shanghai Astronomical Observatory, United Kingdom Participation Group, Universidad Nacional Autónoma de México, University of Arizona, University of Colorado Boulder, University of Oxford, University of Portsmouth, University of Utah, University of Virginia, University of Washington, University of Wisconsin, Vanderbilt University, and Yale University.

## REFERENCES

- Abolfathi B. et al., 2018, *ApJS*, 235, 42  
 Baldwin J. A., Phillips M. M., Terlevich R., 1981, *PASP*, 93, 5  
 Bennert N., Falcke H., Schulz H., Wilson A. S., Wills B. J., 2002, *ApJ*, 574, L105  
 Blanton M. R. et al., 2017, *AJ*, 154, 28  
 Brinchmann J., Kunth D., Durret F., 2008, *A&A*, 485, 657  
 Brusa M. et al., 2016, *A&A*, 588, A58  
 Bundy K. et al., 2015, *ApJ*, 798, 7  
 Cardelli J. A., Clayton G. C., Mathis J. S., 1989, *ApJ*, 345, 245.  
 Carniani S. et al., 2016, *A&A*, 591, A28  
 Cid Fernandes R., Stasińska G., Schlickmann M. S., Mateus A., Vale Asari N., Schoenell W., Sodré L., 2010, *MNRAS*, 403, 1036  
 Couto G. S., Storchi-Bergmann T., Axon D. J., Robinson A., Kharb P., Riffel R. A., 2013, *MNRAS*, 435, 2982  
 Couto G. S., Storchi-Bergmann T., Schnorr-Müller A., 2017, *MNRAS*, 469, 1573  
 Diamond-Stanic A. M., Rieke G. H., 2012, *ApJ*, 746, 168  
 Drory N. et al., 2015, *AJ*, 149, 77  
 Esquej P. et al., 2014, *ApJ*, 780, 86  
 Greene J. E., Zakamska N. L., Ho L. C., Barth A. J., 2011, *ApJ*, 732, 9  
 Gunn J. E. et al., 2006, *AJ*, 131, 2332  
 Hainline K. N., Hickox R., Greene J., Myers A. D., Zakamska N. L., 2013, *ApJ*, 774, 145  
 Harrison C. M., Alexander D. M., Mullaney J. R., Swinbank A. M., 2014, *MNRAS*, 441, 3306  
 Hicks E. K. S., Davies R. I., Maciejewski W., Emsellem E., Malkan M. A., Dumas G., Müller-Sánchez F., Rivers A., 2013, *ApJ*, 768, 107  
 Ilha G. S. et al., 2019, *MNRAS*, 484, 252  
 Kaspi S., Maoz D., Netzer H., Peterson B. M., Vestergaard M., Jannuzzi T., 2005, *ApJ*, 629, 61  
 Kauffmann G. et al., 2003, *MNRAS*, 346, 1055  
 Kennicutt R. C., 1998, *ARA&A*, 36, 189  
 Kewley L. J., Dopita M. A., Sutherland R. S., Heisler C. A., Trevena J., 2001, *ApJ*, 556, 121  
 Kewley L. J., Groves B., Kauffmann G., Heckman T., 2006, *MNRAS*, 372, 961  
 Law D. R. et al., 2016, *AJ*, 152, 83  
 Lintott C. et al., 2011, *MNRAS*, 410, 166  
 Liu G., Zakamska N. L., Greene J. E., Nesvadba N. P. H., Liu X., 2013, *MNRAS*, 436, 2576  
 Mallmann N. D. et al., 2018, *MNRAS*, 478, 5491  
 Martini P., Regan M. W., Mulchaey J. S., Pogge R. W., 2003, *ApJ*, 589, 774  
 Mushotzky R. F., Taro Shimizu T., Meléndez M., Koss M., 2014, *ApJ*, L34  
 Osterbrock D. E., Ferland G. J., 1989, *Astrophysics of Gaseous Nebulae and Active Galactic Nuclei*, 2nd edn. University Science Books, California  
 Peterson B. M., 1997, *An Introduction to Active Galactic Nuclei*. Cambridge Univ. Press, Cambridge  
 Peterson B. M., 2014, *Space Sci. Rev.*, 183, 253  
 Rembold S. B. et al. 2017, *MNRAS*, 472, 4382  
 Sarzi M. et al., 2006, *MNRAS*, 366, 1151  
 Schmitt H. R., Donley J. L., Antonucci R. R. J., Hutchings J. B., Kinney A. L., 2003a, *ApJS*, 148, 327  
 Schmitt H. R., Donley J. L., Antonucci R. R. J., Hutchings J. B., Kinney A. L., Pringle J. E., 2003b, *ApJ*, 597, 768  
 Simões Lopes R. D., Storchi-Bergmann T., de Fátima Saraiva M., Martini P., 2007, *ApJ*, 655, 718  
 Somerville R. S., Hopkins P. F., Cox T. J., Robertson B. E., Hernquist L., 2008, *MNRAS*, 391, 481  
 Storchi-Bergmann T., Rodriguez-Ardila A., Schmitt H. R., Wilson A. S., Baldwin J. A., 1996, *ApJ*, 472, 83  
 Storchi-Bergmann T. et al., 2018, *ApJ*, 868, 14  
 Storchi-Bergmann T., Schnorr-Müller A., 2019, *Nat. Astron.*, 3, 48  
 Veilleux S., Osterbrock D. E., 1987, *ApJS*, 63, 295  
 Wylezalek D., Zakamska N. L., Greene J. E., Riffel R. A., Drory N., Andrews B. H., Merloni A., Thomas D., 2018, *MNRAS*, 474, 1499  
 Yan R. et al., 2016, *AJ*, 151, 8

## SUPPORTING INFORMATION

Supplementary data are available at *MNRAS* online.

### appendix.pdf

Please note: Oxford University Press is not responsible for the content or functionality of any supporting materials supplied by the authors. Any queries (other than missing material) should be directed to the corresponding author for the article.

## APPENDIX A: AGN – CONTROL GALAXIES IMAGES

We present all the comparisons between AGN and its control galaxies in Figs A1–A58 (available in supplementary material).

This paper has been typeset from a TeX/LaTeX file prepared by the author.

# Capítulo 4

## Conclusões

Este trabalho é parte de um esforço do grupo AGNIFS para entender o papel dos SMBHs na evolução das galáxias através do estudo das propriedades de uma amostra de galáxias hospedeiras de AGNs – nos quais o SMBH está ativamente capturando matéria – em comparação com as de uma amostra de controle. Neste trabalho concentramos o estudo nas seguintes propriedades do gás ionizado: excitação, massa, extensão da região ionizada pelo AGN, taxa de formação estelar SFR e metalicidade.

Estudamos as propriedades acima para uma amostra de 150 AGNs e cerca 300 galáxias de controle. Foram mapeadas as luminosidades na linha de emissão  $[OIII]\lambda 5007$ , a extinção, densidade superficial de massa, a densidade superficial da SFR. Além disso, foi feito também o mapeamento da excitação do gás através de razões entre linhas de emissão para os AGNs e controles, determinando-se também a extensão da região ionizada pelo AGN. Foram também comparadas a massa total, a densidade superficial de massa de gás ionizado, e a SFR total entre as amostras, e investigada a relação entre a luminosidade do AGN e extensão NLR. Finalmente, mapeamos também a metalicidade do gás na região central e corpo da galáxia.

As principais conclusões são:

- Excitação Nuclear: Mapeamos a excitação de gás usando os diagramas BPT e WHAN. Definindo a região nuclear como tendo raio  $\leq 0.2 R_e$  (raio efectivo), 2/3 dos *high-luminosity AGN* tem excitação nuclear Seyfert (Sy), e o restante tem LINER ou Sy juntamente com LINER. Dos 45 *low-luminosity AGN*, 30% possuem núcleo Sy, 40% LINER e 30% de excitação nuclear mista. Em relação aos controles, usando apenas o diagrama BPT, muitas regiões nucleares são classificadas como AGN - especialmente nos hospedeiros *early-type*,

mas o diagrama WHAN revela que a maioria desses casos são LIERs (excitados por estrelas quentes evoluídas). Nas galáxias *late-type*, além dos LIERs, há também um número de controles com núcleos com excitação de regiões HII.

- Excitação extra-nuclear :

Medimos a extensão  $R$  da região excitada pelo AGN (NLR ou ENLR) obtendo valores variando de 1,5 a 27 kpc. No Paper III encontramos a relação  $R \propto (L(OIII))^{0.5}$ , semelhante ao válido para a BLR e recentemente obtido também para a ENLR de AGN luminosos por Storchi-Bergmann et al. (2018) e anteriormente por Bennert et al. (2002). Ao ampliarmos a amostra de 62 para 150 AGNs, obtivemos uma pendente e correlação mais fracas, o que aparentemente é devido ao uma maior variedade na natureza dos AGNs observados (por exemplo, galáxias tipo Seyfert 1 que têm o eixo de ionização ao longo da linha de visada e tendem a ter NLR e ENLR menos estendidas dentro do Modelo Unificado).

Tanto nas galáxias hospedeiras de AGN quanto nos controles existem algumas regiões extra-nucleares (mas separadas do núcleo) que são classificadas como AGN de acordo com o diagrama BPT. Usando também o diagrama WHAN, a maioria dessas regiões torna-se LIERs, embora a emissão de algumas delas possa ser uma assinatura de gás ionizado morno (visto principalmente em galáxias altamente inclinadas) em algumas também podem ser assinaturas de “*relic AGN*”.

- Taxa de Formação Estelar:

A densidade superficial da SFR –  $\Sigma_{SFR}$  foi obtida na região, dentro das galáxias, dominadas pela formação estelar, o que ocorre principalmente nos discos das galáxias. Encontramos que os mapas de  $\Sigma_{SFR}$  são em geral semelhantes para o AGN e seus controles. Algumas galáxias de controle mostram a formação estelar também na região nuclear, alcançando ali os maiores valores, como é o caso de várias galáxias *late-type*.

A SFR total das galáxias AGN e controle variam de  $10^{-3}$  a  $10 M_{\odot} \text{ yr}^{-1}$ , com diferença entre AGN e controles vistos somente em galáxias *early-type*: 75% dos AGNs *early-type* têm maior SFR que seus controles. Este resultado sugere que o gás que alimenta o AGN também desencadeia a formação de estrelas nas partes externas da galáxia e que o AGN não cessa esta formação de estrelas. Como não vemos diferenças na SFR entre AGN e controles para as galáxias

*late-type*, também não vemos assinatura de extinção da formação estelar nos discos destas galáxias também.

Com a adição de novos objetos da MPL-8, as distribuições de SFR total separado tanto por tipo da morfologia da galáxia, quanto pela luminosidade do AGN mantiveram concordância com o observado em do Nascimento et al. (2019). Com relação as distribuições fracionais, apesar de ter havido uma pequena queda na proporção de valores positivos em ambos os casos *early-type* e *late-type* em comparação com valores obtidos anteriormente, esse resultados também concordam com os anteriores, mostrando que em geral os AGNs *early-type* apresentam mais formação estelar quando comparado com seus respectivos controles, enquanto que para os AGNs *late-type*, os controles em geral apresentam mais formação estelar que os mesmos.

- Densidade superficial da massa de gás ionizado  $\Sigma_{H^+}$ : Dentro de  $0.2 R_e$ ,  $\Sigma_{H^+}$  – que chamamos de  $\Sigma_{nuc}$ , é maior para o AGN do que para as galáxias de controle em 75% da amostra, com valores médios de  $1,74 \times 10^4 M_\odot \text{ kpc}^{-2}$  para o AGN e  $2.72 \times 10^3 M_\odot \text{ kpc}^{-2}$  para os controles. As galáxias de controle dos AGN *early-type* geralmente têm valores maiores de  $\Sigma_{H^+}$  nas regiões externas que em seus núcleos. No caso das hospedeiras *late-type*, as regiões de maior  $\Sigma_{H^+}$  são mais estendidas do que nas *early-type*, estendendo-se por grande parte dos discos das galáxias, com valores semelhantes para AGNs e controles.

Quando aumentamos a amostra de AGNs de 62 para 150, obtivemos o mesmo resultado para o  $\Sigma_{nuc}$ : é maior para os AGNs do que para os controles na maioria da amostra, com o teste A-D revelando que as amostras de AGNs e controles tem pouca probabilidade de serem iguais. Para as distribuições de  $\Sigma_{nuc}$  sparadas em *bins* de luminosidade do AGN, encontramos uma pequena mudança com relação ao resultado obtido no Paper III. No Paper III via-se claramente a diferença diminuindo entre AGNs e controles à medida que a luminosidade L(O[III]) do AGN diminui. Com a amostra maior, o efeito é somente observado quando comparamos os dois extremos de luminosidade: para os AGNs mais luminosos o  $\Sigma_{nuc}$  é bem maior do que nos controles, mas para os de baixa luminosidade  $\Sigma_{nuc}$  se assemelha ao dos controles.

- Gradientes de  $\Sigma_{H^+}$ :

Os gradientes radiais médios dos  $\Sigma_{H^+}$  são geralmente mais acentuados para os AGNs do que para os controles desde o centro ate cerca de  $0.4 R_e$ , com a diferença diminuindo à medida que a luminosidade do AGN diminui.

- Massa total de gás ionizado:

Obtivemos limites inferiores para as massas de gás ionizado integradas, com valores totais estimados em 10% - 40% maiores, dependendo da galáxia. No Paper III estes valores variam de  $9.9 \times 10^4 M_{\odot}$  a  $2.9 \times 10^7 M_{\odot}$  para o AGN, comparado ao intervalo de  $1.9 \times 10^4 M_{\odot}$  a  $1.7 \times 10^8 M_{\odot}$  para os controles. Ao parear cada AGN com seus controles, para os AGNs *early-type*, 85% da AGN tem mais gás ionizado do que os controles, enquanto essa porcentagem diminui para 57% para AGNs *late-type*.

No Paper III obtivemos as seguintes médias para a massas totais de gás ionizado: (1) para os AGNs mais luminosos ( $L(\text{[OIII]}\lambda 5007\text{\AA}) \geq 3.8 \times 10^{40} \text{ erg s}^{-1}$ ):  $1.61 \pm 3.55 \times 10^7 M_{\odot}$  comparada a  $3.12 \pm 4.93 \times 10^6 M_{\odot}$  para as galáxias de controle; (2) para os demais AGNs a média é de  $6.29 \pm 20.7 \times 10^6 M_{\odot}$  comparada a  $7.11 \pm 33.3 \times 10^6 M_{\odot}$  para os controles; (3) Para os AGNs *early-type* a média é  $2.18 \pm 4.63 \times 10^6 M_{\odot}$ , e para os controles  $1.12 \pm 2.19 \times 10^6 M_{\odot}$ ; (4) para os AGNs *late-type* é  $9.26 \pm 2.31 \times 10^6 M_{\odot}$  e  $8.87 \pm 3.61 \times 10^6 M_{\odot}$  para os controles.

Com o acréscimo dos novos dados, ampliou-se a faixa de valores de massa total de gás ionizado, tanto para AGNs quanto para controles, variando de  $10^4$  a  $10^9 M_{\odot}$ . No entanto, a forma das distribuições nos histogramas de massa se mantém. E ao parear cada galáxia com seus controles ainda se confirma que os AGN *early-type* apresentam maior massa total de gás ionizado que seus controles.

- Metalicidade do gás  $12 + \log(O/H)$ :

Foi obtida a metalicidade do gás das regiões HII no corpo da galáxia, e se estudou a presença de gradientes, que permitiram estimar o valor da metalicidade para a região central dos AGNs. Verificou-se que tal valor está de acordo com calibrações específicas para a NLR. Um claro gradiente foi observado no valor de N/O, que cresce em direção ao centro.

# Apêndice A: Artigos em colaboração

## 1. The gas metallicities in nearby MaNGA AGN

Janaína C. do Nascimento, Thaisa Storchi-Bergmann, Nícolas D. Mallmann Rogério Riffel. Em preparação.

## 2. THE FIRST 62 AGN OBSERVED WITH SDSS-IV MaNGA-I: THEIR CHARACTERIZATION AND DEFINITION OF A CONTROL SAMPLE

Sandro B. Rembold, Jaderson Schimoia, Thaisa Storchi-Bergmann, Rogério Riffel, Rogemar Riffel, Nícolas D. Mallmann, Janaína C. do Nascimento, Thales N. Moreira, Gabriele S. Ilha, Alice D. Machado, Rafael Cirolini, Luiz N. da Costa, Marcio A. G. Maia, Basílio X. Santiago, Donald P. Schneider, Dominika Wylezalek, Dmitry Bizyaev, Kaike Pan & Francisco Müller-Sánchez, MNRAS, 2017, v.472, p.4382-4403.

## 3. THE FIRST 62 AGN OBSERVED WITH SDSS-IV MANGA -II: RESOLVED STELLAR POPULATIONS

Nícolas D. Mallmann, Rogério Riffel, Thaisa Storchi-Bergmann, Sandro Barboza Rembold, Rogemar A. Riffel, Jaderson Schimoia, Luiz Nicolaci da Costa, Vladimir Ávila-Reese, Sebastian F. Sanchez, Alice D. Machado, Rafael Cirolini, Gabriele S. Ilha and Janaína C. do Nascimento, MNRAS, 478, 5491

## 4. THE FIRST 62 AGN OBSERVED WITH SDSS-IV MaNGA - III: STELLAR AND GAS KINEMATICS

Ilha, Gabriele S.; Riffel, Rogemar A.; Schimoia, Jaderson S.; Storchi-Bergmann, Thaisa; Rembold, Sandro B.; Riffel, Rogério; Wylezalek, Dominika; Shi, Yong; da Costa, Luiz N.; Machado, Alice D.; Law, David R.; Bizyaev, Dmitry; Mallmann, Nicolas D.; Nascimento, Janaina; Maia, Marcio A. G.; Cirolini, Rafael, MNRAS, 484, 252.

**5. THE FOURTEENTH DATA RELEASE OF THE SLOAN DIGITAL SKY SURVEY: FIRST SPECTROSCOPIC DATA FROM THE EXTENDED BARYON OSCILLATION SPECTROSCOPIC SURVEY AND FROM THE SECOND PHASE OF THE APACHE POINT OBSERVATORY GALACTIC EVOLUTION EXPERIMENT**

Bela Abolfathi, D. S. Aguado, Gabriela Aguilar, Carlos Allende Prieto, Andres Almeida, Tonima Tasnim Ananna, Friedrich Anders, Scott F. Anderson, Brett H. Andrews, Borja Anguiano, Alfonso Aragón-Salamanca, María Argudo-Fernández, Eric Armengaud, Metin Ata, Eric Aubourg, Vladimir Avila-Reese, Carles Badenes, Stephen Bailey, Kathleen A. Barger, Jorge Barrera-Ballesteros, Curtis Bartosz, Dominic Bates, Falk Baumgarten, Julian Bautista, Rachael Beaton, Timothy C. Beers , Francesco Belfiore , Chad F. Bender , Mariangela Bernardi , Matthew A. Bershadsky, Florian Beutler, Jonathan C. Bird, Dmitry Bizyaev, Guillermo A. Blanc, Michael R. Blanton, Michael Blomqvist, Adam S. Bolton, Médéric Boquien, Jura Borissova, Jo Bovy, Christian Andres Bradna Diaz, William Nielsen Brandt, Jonathan Brinkmann, Joel R. Brownstein, Kevin Bundy, Adam J. Burgasser, Etienne Burtin, Nicolás G. Busca, Caleb I. Cañas, Mariana Cano-Díaz, Michele Cappellari, Ricardo Carrera , Andrew R. Casey, Yanping Chen, Brian Cherinka, Cristina Chiappini, Peter Doohyun Choi, Drew Chojnowski, Chia-Hsun Chuang, Haeun Chung, Nicolas Clerc, Roger E. Cohen, Johan Comparat, Janaina Correa do Nascimento, Luiz da Costa et. al. [último draft em novembro de 2017]

# The gas metallicities in nearby MaNGA AGN

Janaína C. do Nascimento<sup>1,3</sup>★, Thaisa Storchi-Bergmann<sup>1,3</sup>, Nícolas D. Mallmann<sup>1,3</sup>, Rogério Riffel<sup>1,3</sup>, Gabriele S. Ilha<sup>2,3</sup>,

<sup>1</sup>Departamento de Astronomia, IF, Universidade Federal do Rio Grande do Sul, CP 15051, 91501-970, Porto Alegre, RS, Brazil

<sup>2</sup>Departamento de Física, CCNE, Universidade Federal de Santa Maria, 97105-900, Santa Maria, RS, Brazil

<sup>3</sup>Laboratório Interinstitucional de e-Astronomia - LIneA, Rua General José Cristino 77, Rio de Janeiro, RJ - 20921-400, Brazil

Accepted XXX. Received YYY; in original form ZZZ

## ABSTRACT

We obtain the gas metallicites  $12 + \log(O/H)$  in HII regions along the body of 150 AGN hosts as compared to 300 control galaxies observed with MaNGA on the basis of calibrations using strong emmision-line ratios. Radial gradients are obtained with N/O ratios increasing towards the center. The derived metallicities are then extrapolated to the center via the observed radial gradients in order to estimate the expected values for the NLR (Narrow-Line Region) of the AGN hosts. These metallities are them compared to those obtained via specific calibrations for the NLR obtained using photoioization models.

**Key words:** Active Galactic Nuclei – Gas metallicities – MaNGA survey

## 1 INTRODUCTION

Our AGNIFS (AGN Integral Field Spectroscopy) group has been studying the AGN host galaxies observed with MaNGA in order to investigate the properties of the stellar population as well as of the emitting gas. The present sample comprises 150 AGN. In order to investigate which properties are linked to the nuclear activity, we have defined also a control sample of  $\approx 300$  galaxies matched to the AGN according to the properties of the host galaxies, as described in Rembold et al. (2017), (hereafter Paper I). The AGNIFS collaboration has already published Papers I-IV, with 3 others in preparation.

In Paper III (do Nascimento, et al. 2019), we have mapped the gas excitation, delimiting regions of different excitation over the body of the galaxies. In the present paper we obtain the chemical abundance of the gas and its gradient over the body of the galaxy in order to investigate any possible trends with the strength of the nuclear activity, excitation, activity type and galaxy host. As gas abundance determinations depend on the gas excitation, we aim also at testing different calculation methods by comparing the chemical abundances in contiguous regions of the galaxy disk which show different excitation, e.g. in the border between narrow-line region (NLR) and HII emitting regions. As we do not expect a discontinuity in the gas metallicity at such borders, this study will also provide tests for the different methods to determine the gas metallicities.

## 2 SAMPLE

The sample studied here is the one introduced by Paper I (corresponding to the MaNGA Product Launch MPL-5), complemented with further AGN observed with MaNGA in the subsequent product launches, up to MPL-8. The total sample now comprises 150 AGN and  $\approx 300$  control galaxies. The new AGN (that are not in Papers I-IV), as well as their control galaxies, were selected using the same criteria of Paper I. These new AGNs are listed in Table A1 e A2 of Machado et al. (2019, in prep.), together with their controls.

## 3 CHEMICAL ABUNDANCES

Chemical abundances for the gas can be determined from emission-line ratios once enough lines are available to allow the determination of the temperature and density of the gas. Unfortunately we do not have many lines, in particular the auroral line [OIII] $\lambda 4363\text{\AA}$  or other similar lines that are usually faint and can only be observed with high signal-to-noise ratio spectra. We thus cannot directly derive the temperature of the gas.

We had thus to rely on calibrations in terms of the strongest emission lines in order to estimate the gas abundances. These calibrations are described in the following sections.

★ E-mail:

### 3.1 HII regions calibrations

We have used the metallicity calibrations from Pérez-Montero & Contini (2009) to calculate the chemical abundances for star-forming regions (HII regions) along the body of the galaxy.

Pérez-Montero & Contini (2009) studied the relationship between the abundances of nitrogen and oxygen (N/O ratio) as a function of metallicity for a sample of emission line objects for which the metallicity could be obtained directly. By comparing the N/O ratios with those of O/H the authors realized that there was a large dispersion in O/H values due to the different N/O values that was present in all metallicity regimes.

? then investigated the effects of the N / O ratio on two empirical calibrators, the first of them, called N2, defined below in Equation (1):

$$N2 = \log \frac{I([NII]\lambda 6584)}{I(H\alpha)} \quad (1)$$

that has been widely used in the literature to derive oxygen abundance, e.g. (Storchi-Bergmann et al. 1994).

A relation was then derived between the oxygen abundance  $12 + \log(O/H)$  and the N2 parameter, as given by Eq. 2 :

$$12 + \log(O/H) = 0.79 \times N2 + 9.07 \quad (2)$$

However, according to the authors, the resulting relation does not provide a smaller dispersion compared to previous calibrations from Denicoló, Terlevich & Terlevich (2002); Pettini & Pagel (2004).

The authors in Pérez-Montero & Contini (2009) also claim that additionally, a substantial part of the observed dispersion is due to N/O ratio variations, a consequence of using nitrogen emission lines to derive oxygen abundances.

With the same sample studied and divided into bins of  $\log(N/O)$  and compared with photoionization model sequences with the same N/O ratio values, a strong correlation was observed between the metallicity derived from the N2 parameter and the N/O ratio, such that the metallicity predicted by N2 is overestimated in those objects with a high N/O ratio and vice versa.

After quantifying this dependence between N2 and N/O, the following expression 3 for the relation between N2 and oxygen abundance is:

$$12 + \log(O/H) = 0.79N2 - 0.56 \log(N/O) + 8.41 \quad (3)$$

Another calibration based on [NII] is the N2S2 parameter, it has been proposed to derive metallicities by Viironen et al. (2007).

$$N2S2 = \log \frac{I([NII]\lambda 6584)}{I([SII]\lambda\lambda 6717, 6731)} \quad (4)$$

The correlation between this parameter and the N / O ratio is linear, and the least-squares linear bisector fit this parameter as a function of the N / O ratio gives the eq. 5

$$\log(N/O) = 1.26N2S2 - 0.86 \quad (5)$$

### 3.2 AGN calibrations

For the NLR or Extended NLR (ENLR) excited by the AGN (Seyfert and LINER excitation) we have used one of the two calibrations proposed by Storchi-Bergmann et al. (1998) that used the photoionization code CLOUDY (Ferland 1996). The decision it was basically because of the available data. The relation is:

$$(O/H)_{SB98} = 8.4 + (0.212x) - (0.0212x^2) - (0.02y) \\ + (0.007xy) - (0.002x^2y) + (6.52 \times 10^{-4}y^2) \\ + (2.27 \times 10^{-4}xy^2) + (8.87 \times 10^{-5}x^2y^2) \quad (6)$$

where  $x = [NII]\lambda\lambda 6548, 6584 / H\alpha$  and  $y = [OIII]\lambda\lambda 6548, 6584 / H\beta$ .

We also used from Storchi-Bergmann et al. (1998) the following relation for N/O

$$\log(N/O) = 0.96[12 + \log(O/H)] - 9.29 \quad (7)$$

This calibration is valid for  $8.4 \leq 12 + \log(O/H) \leq 9.4$ . In order to take into account the dependence of these relations on the gas density  $n_e$ , we have applied a correction proposed by (Storchi-Bergmann et al. 1998):

$$(O/H)_{final} = (O/H) - \log(n_e/300) \quad (8)$$

We have thus estimated the (O/H) abundance using the expressions above. We have first used this calibration only for the regions with Seyfert, LINER and LIER excitation, and then have used them to estimate (O/H) also for the transition regions.

### 3.3 Results and Discussion

In this section, we show results of the metallicity distributions obtained according to the calibrations discussed above. Equation 2 and Equation 3 was used to obtain the metallicities of the star-forming regions, the fisrts equation was applied in the galaxies from the firs row of the figs.1 - 4 and the second equation in the last one, while equation 8 was used for the regions ionized by the AGN in both situation. The transition regions was calculated as AGN when we applied the equation 2 and when the equation 3 was used we calculated the transition region as star-forming.

Figures 1 - 4 show typical results separated according to for 4 types of AGN: early-type hosts, late-type hosts, strong AGN and weak AGN.

For the first case we have a typical early-type hosts presented in the fig. 1 the AGN map shows that the center of the galaxy is identified as Seyfert excitation, apart from that we have only small pieces identified as the HII or LIER region, the control galaxies have similar maps with each other, with the center identified as HII and in addition small pieces. of LIER regions. According to AGN radial maps and profiles and controls do not show large fluctuations in abundance values within approximately 0.4Re, but show that the controls have larger values than those observed in AGN. The controls have a fluctuation due to discrepancy between the HII region and the transition region, showing that the largest abundance values are within the HII region, which decay in the transition region.

The following N/O maps also show similarity to each other: According to radial profiles, the do Nascimento J. C., et al., 2019, MNRAS, 486, 5075re is an overlap between AGN and control N / O values. On one of the controls, a spike appears, but it should not be taken into account, it may have been because of some bad pixel. The latest maps also prove to be similar to each other, quasi-linear profiles showing minimal variations in abundance values in the three cases, with a slight increase in abundance beyond the center of the galaxies.

In this second figure 2 we can see that the galaxy that hosts the AGN has the center identified by the magenta contour indicating that it is a LINER region, the blue contour indicates star-forming region, the non-contoured parts indicate transition regions, which for this case were calculated as AGN (Seyfert, LINER, LIER and transition). Regarding the abundances, we see that the center has larger values that decline sharply as it moves away from the nucleus, and then increases again when it reaches the HII regions. We can see this transition clearly through the radial profiles. For the control galaxies, as the maps show the entire galaxies have HII regions, only one of the controls has a transition region around the nucleus, so what we have is that in control 1 due to the transition region there is a drop In the value of the abundances as also shown by the profile (blue), for controls 2 the values are practically constant, as can also be seen through the profile (green) that shows almost linear throughout the galaxy.

On the maps of the second row, we have the log (N/O) values, we can see that in general these values are higher for the AGN, whereas in the controls, the values decay when you move away from the center of the galaxy. We can see that the variations are very small in the case of AGN, and for the controls the variation is greater.

In the last maps, referring to the last row of the figure, we see that for AGN there is a greater variation of abundance values when compared to the first map of the first row, we also observed that not a sharp increase again in these values. For the controls the values of the abundances are smaller when compared to those of the first row, there is a slight oscillation to larger values as it moves away from the center.

In the figure 3 we have a strong AGN, the maps of the first line show that: the host galaxy of the AGN has the nucleus identified as a Seyfert region, surrounded by a transition region, and shortly thereafter we have a ring identified as HII region and more externally. transition region again. Observing this, we have that the nucleus presents smaller values of abundance when compared to the outer part, we see this clearly in the radial profile, showing that when it reaches the HII region these values increase and then decay. the controls present the nucleus and beyond it regions of star formation, as in the previous case fig 2 the density values present small variations that we can only identify through the radial profiles of the galaxies.

N/O maps for AGN and controls are similar to each other. They have the highest values in the center of the galaxy, which decrease as it move away from the center of the galaxy. The three radial profiles show that they decay smoothly with the distance

The last line maps behave similarly also to figure 2. For AGN, we have a greater abundance in the center of the galaxy that decays with the distance from the nucleus

and becomes smoother when it reaches a transition region again, in profile, we can see this behavior more clearly. While controls show that in the HII region the abundances are smaller than the outer region, which is a transition region, with the profiles, we see the same behavior in the two control galaxies.

For weak AGN, we have the nucleus identified as Seyfert and transition, but the rest of the galaxy's body is identified as HII regions, which makes it look like control galaxies in terms of abundances. In the profiles we see that from approximately 0.4 Re, the three radial profiles overlap, presenting approximately the same abundance values. The galaxies differ in the nucleus and, for AGN, the abundances are smaller than in the controls.

The N/O maps for AGN and controls also resemble each other, with larger values in the center that shrink as they move away from it. In the profiles that clearly observe this behavior, the only difference is that, for AGN, the profile presents a larger variation of N/O.

The last maps in the figure 4 show AGN a slight fluctuation in abundance values according to the map and profile. Controls have different behaviors, while control 1 shows a slight fluctuation, as shown in the profile, controls 2 show a greater variation in abundance values, the latter being higher in the center and decreasing sharply from it.

## 4 CONCLUSIONS

### ACKNOWLEDGEMENTS

The Acknowledgements section is not numbered. Here you can thank helpful colleagues, acknowledge funding agencies, telescopes and facilities used etc. Try to keep it short.

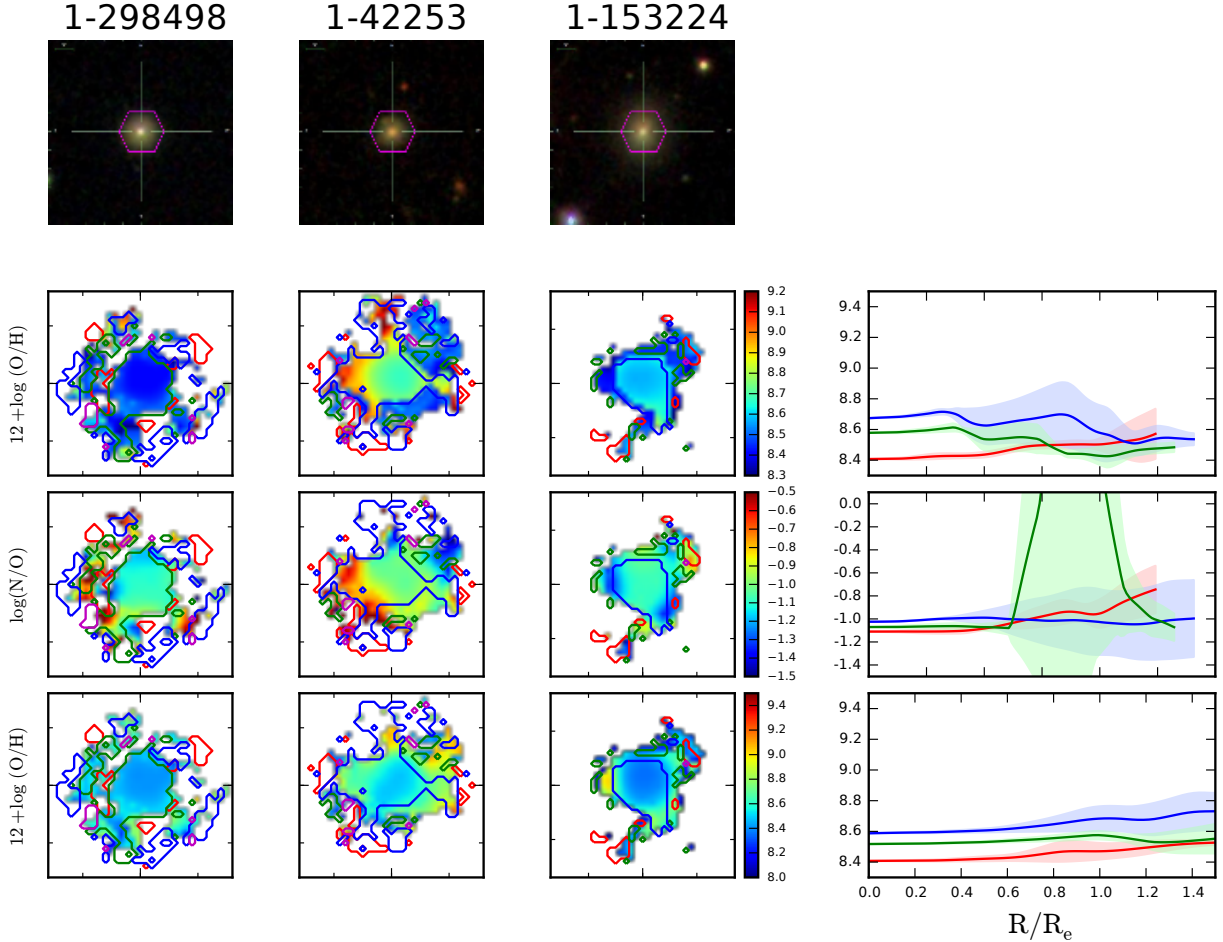
### REFERENCES

- Denicoló G., Terlevich R., Terlevich E., 2002, MNRAS, 330, 69.
- do Nascimento J. C., et al., 2019, MNRAS, 486, 5075
- Ferland G. J., 1996, hbic.book
- Ilha, G. S., et al., 2018, MNRAS, 484, 252
- Machado, Alice D., et al.
- Mallmann, N. et al., 2018, MNRAS, 478, 5491.
- Pérez-Montero E., Contini T., 2009, MNRAS, 398, 949
- Pettini M., Pagel B. E. J., 2004, MNRAS, 348, L59
- Rembold, S. B., Shimoia, J. S., Storchi-Bergmann, T., et al. 2017, MNRAS, 472, 4382
- Storchi-Bergmann T., Schmitt H. R., Calzetti D., Kinney A. L., 1998, AJ, 115, 909
- Storchi-Bergmann, T., Calzetti, D., & Kinney, A. L. 1994, ApJ, 429, 572
- Viironen K., Delgado-Ingla G., Mampaso A., Magrini L., Corradi R. L.M., 2007, MNRAS, 381, 1719

### APPENDIX A: SOME EXTRA MATERIAL

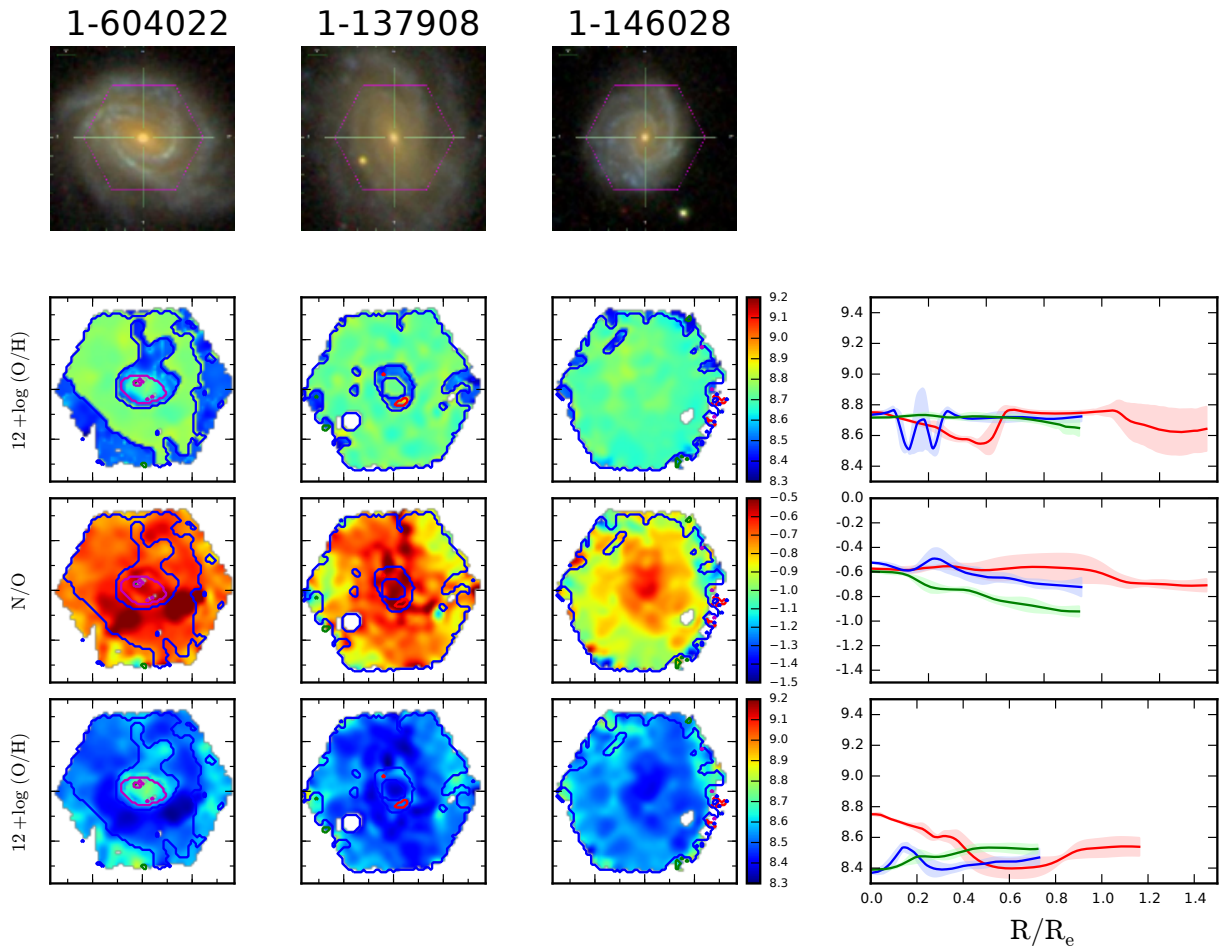
If you want to present additional material which would interrupt the flow of the main paper, it can be placed in an Appendix which appears after the list of references.

This paper has been typeset from a Te<sub>X</sub>/L<sub>A</sub>T<sub>E</sub>X file prepared by the author.

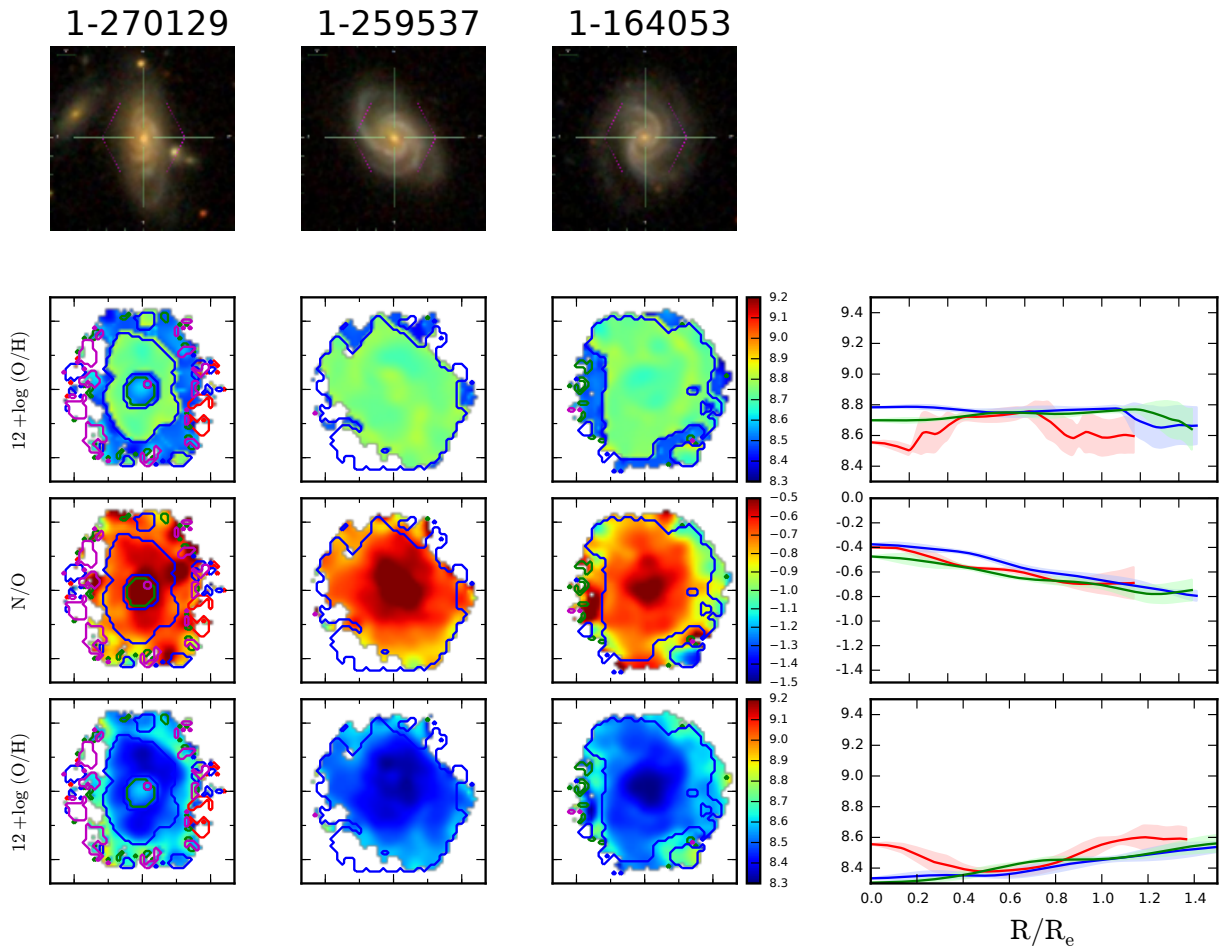


**Figure 1.** Surface distributions of the metallicites  $12 + \log(O/H)$  and (N/O) ratios measured for a typical early-type AGN and its two controls, showing the AGN on the left and the two control galaxies at the center and right. For the first three columns: Top row: SDSS-IV images with the MaNGA footprint over-plotted in pink; second row: metallicites  $12 + \log(O/H)$  determined with eq. 2 for star-forming regions and eq. 8 for AGN ; third row: (N/O) values determined by eq. 5-HII regions and eq. 7 AGN; fourth row: Star-forming and AGN metallicites  $12 + \log(O/H)$  determined by eq. 3 and 8 respectively. The contours limit separate the different excitatio regions: green and magenta for the AGN excitation, blue for star-forming regions and red for LIER regions. Panels to the right: azimuthally averaged metallicities corresponding to the bottom three left panels, where the AGN is shown in red, the first control in blue and second control in green. The tick marks are separated by  $5''$

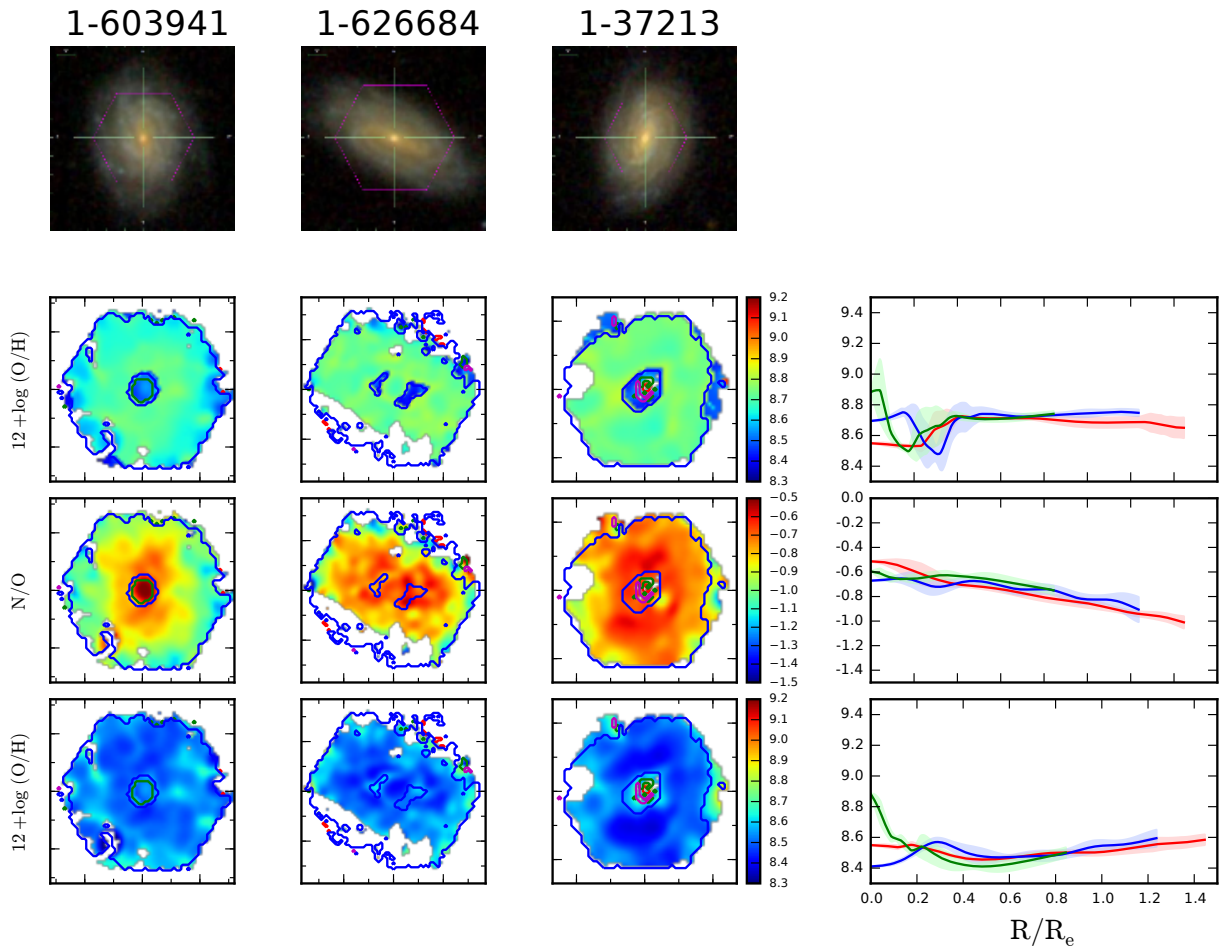
do Nascimento J. C., et al., 2019, MNRAS, 486, 5075



**Figure 2.** Same as Fig. 1 for a late-type AGN and its controls.



**Figure 3.** Same as Fig. 1 for a strong AGN and its controls.

**Figure 4.** Same as Fig. 1 for a weak AGN and its controls.



# The first 62 AGNs observed with SDSS-IV MaNGA – I. Their characterization and definition of a control sample

Sandro B. Rembold,<sup>1,2\*</sup> Jáderson S. Shimoia,<sup>2,3\*</sup> Thaisa Storchi-Bergmann,<sup>2,3\*</sup> Rogério Riffel,<sup>2,3</sup> Rogemar A. Riffel,<sup>1,2</sup> Nícolas D. Mallmann,<sup>2,3</sup> Janaína C. do Nascimento,<sup>2,3</sup> Thales N. Moreira,<sup>1,2</sup> Gabriele S. Ilha,<sup>1,2</sup> Alice D. Machado,<sup>1,2</sup> Rafael Cirolini,<sup>1,2</sup> Luiz N. da Costa,<sup>2,4</sup> Marcio A. G. Maia,<sup>2,4</sup> Basílio X. Santiago,<sup>2,3</sup> Donald P. Schneider,<sup>5,6</sup> Dominika Wylezalek,<sup>7</sup> Dmitry Bizyaev,<sup>8,9</sup> Kaike Pan<sup>8</sup> and Francisco Müller-Sánchez<sup>10</sup>

<sup>1</sup>Departamento de Física, CCNE, Universidade Federal de Santa Maria, 97105-900, Santa Maria, RS, Brazil

<sup>2</sup>Laboratório Interinstitucional de e-Astronomia - LIneA, Rua Gal. José Cristino 77, Rio de Janeiro, RJ - 20921-400, Brazil

<sup>3</sup>Departamento de Física, IF, Universidade Federal do Rio Grande do Sul, CP 15051, 91501-970, Porto Alegre, RS, Brazil

<sup>4</sup>Observatório Nacional - MCT, Rua General José Cristino 77, Rio de Janeiro, RJ - 20921-400, Brazil

<sup>5</sup>Institute for Gravitation and the Cosmos, The Pennsylvania State University, University Park, PA 16802, USA

<sup>6</sup>Department of Astronomy and Astrophysics, The Pennsylvania State University, University Park, PA 16802, USA

<sup>7</sup>Center for Astrophysical Sciences, Department of Physics and Astronomy, Johns Hopkins University, 3400 North Charles Street, Baltimore, MD 21218, USA

<sup>8</sup>Apache Point Observatory, PO Box 59, Sunspot, NM 88349, USA

<sup>9</sup>Sternberg Astronomical Institute, Moscow State University, 119992 Moscow, Russia

<sup>10</sup>Center for Astrophysics and Space Astronomy, Department of Astrophysical and Planetary Sciences, University of Colorado, 389 UCB, Boulder, CO 80309-0389, USA

Accepted 2017 August 30. Received 2017 August 28; in original form 2016 July 6

## ABSTRACT

We report the characterization of the first 62 Mapping Nearby Galaxies at the Apache Point Observatory active galactic nuclei (AGNs) hosts and the definition of a control sample of non-active galaxies. This control sample was selected in order to match the AGN hosts in terms of stellar mass, redshift, visual morphology and inclination. The stellar masses are in the range  $9.4 < \log(M/M_\odot) < 11.5$ , and most objects have redshifts  $\leq 0.08$ . The AGN sample is mostly comprised low-luminosity AGN, with only 17 ‘strong AGN’ with  $L([\text{O III}]\lambda 5007 \text{ Å}) \geq 3.8 \times 10^{40} \text{ erg s}^{-1}$ . The inner 1–3 kpc of the control sample galaxies are dominated by the oldest ( $\geq 4$  Gyr) component, with a small contribution of intermediate age and young stars ( $< 940$  Myr). Examining the relationship between the stellar population properties and  $L([\text{O III}])$ , we find that with increasing  $L([\text{O III}])$ , the AGN exhibit a decreasing contribution from the oldest stellar population relative to control galaxies and an increasing contribution from the younger components ( $\sim 40$  Myr). We also find a correlation of the mean age differences (AGN–control) with  $L([\text{O III}])$ , in the sense that more luminous AGNs are younger than the control objects, while the low-luminosity AGNs are older. These results support a connection between the growth of the galaxy bulge via formation of new stars and the growth of the Supermassive Black Hole via accretion in the AGN phase.

**Key words:** galaxies: active – galaxies: stellar content.

## 1 INTRODUCTION

The MaNGA (Mapping Nearby Galaxies at the Apache Point Observatory) survey, a core program of the fourth-generation Sloan Digital Sky Survey (SDSS-IV), operating between 2014 and 2020, will deliver optical integral field spectroscopic observations of  $\sim 10\,000$

galaxies. It has been conceived in order to produce homogeneous spectroscopic information of these galaxies out to a radial position of at least  $1.5r_e$  (effective radius). An overview of the main science objectives and survey design is presented in Bundy et al. (2015). The integral field unit design and performance are described in Drory et al. (2015). Details about the observing strategy in order to ensure spectrophotometric accuracy are given in Law et al. (2015). The spectrophotometric calibration technique is described in Yan et al. (2016).

\* E-mail: [sandro.rembold@ufrgs.br](mailto:sandro.rembold@ufrgs.br) (SBR); [silva.shimoia@ufrgs.br](mailto:silva.shimoia@ufrgs.br) (JS); [thaisa@ufrgs.br](mailto:thaisa@ufrgs.br) (TS-B)

Among the 10 000 galaxies, there are expected to be  $\sim 300$  galaxies hosting active galactic nuclei (AGNs). One of the primary goals of the MaNGA survey is to explore the relation between the AGN and their host galaxies. This investigation will be accomplished via the mapping of the ionized and neutral gas kinematics, searching in particular for outflows and investigating the corresponding feedback effects on the host galaxy (Zakamska & Greene 2014). The empirical relationship between the mass of the central Supermassive Black Hole (SMBH) in AGNs and the stellar velocity dispersion of the spheroidal component of galaxies (the  $M_{\bullet} - \sigma$  relationship) suggests that the growth of a galaxy (due to star formation) and its central SMBH (due to gas accretion) may be coupled (e.g. Ferrarese & Merritt 2000; Gebhardt et al. 2000), although some non-causal explanations have been also recently proposed (e.g. Peng 2007; Jahnke & Macciò 2011). The observed  $M_{\bullet} - \sigma$  relationship has been explained as being originated by the AGN feeding and feedback processes that couple the growth of the SMBHs and their host galaxies (Ferrarese & Ford 2005; Somerville et al. 2008; Kormendy & Ho 2013). Indeed, cosmological simulations suggest that AGN plays a fundamental role in the evolution of its host galaxy (Di Matteo, Springel & Hernquist 2005; Springel, Di Matteo & Hernquist 2005; Bower et al. 2006), as while the SMBH evolves together with the galaxy, it is fed by surrounding material and periodically produces gas ejections that retard the growth of the galaxy by preventing the accretion of extragalactic gas in these active phases (e.g. Nemmen et al. 2007; Fabian et al. 2012; Terrazas et al. 2016).

AGN feeding and feedback effects are related to the stellar population of the host galaxy. Previous studies have suggested that the feeding, leading to the growth of the central SMBH, appears to be related to recent episodes of star formation in the circumnuclear region (e.g. Heckman et al. 1997; Storchi-Bergmann et al. 2001; Davies et al. 2007; Hickox et al. 2014; Diamond-Stanic & Rieke 2012; Esquej et al. 2014). These studies found an excess of young to intermediate age stars in the inner few hundred parsecs of AGN hosts when compared to non-active galaxies and support the existence of an AGN-Starburst connection (Perry & Dyson 1985; Terlevich & Melnick 1985; Norman & Scoville 1988). This connection can be understood, as both star formation and nuclear activity may be fed by gas inflows towards the centre or, alternatively the central AGN may be triggered due to mass-loss from evolving stars (e.g. Wild, Heckman & Charlot 2010). The AGN feedback, both via radiative and kinetic power, may, in turn, also affect the stellar populations of the host galaxy in the vicinity of the AGN by quenching star formation (e.g. Fabian et al. 2012; Dubois et al. 2013; Ishibashi & Fabian 2017; Pontzen et al. 2017; Xie, Yuan & Ho 2017).

This study is the first of a series of papers in which we will use the MaNGA data cubes to obtain the properties of AGN and a matched sample of inactive galaxies. We have so far used the 2778 galaxy data cubes released in the 5th MaNGA Product Launch (MPL-5), obtained between 2014 and 2016. The cubes have been processed using the version 2.0.1 of the MaNGA Data Reduction Pipeline Law et al. (2016). This set of data cubes contains 62 AGN hosts, selected using optical emission-line diagnostics as described in Section 2.1, comprising 45 low-luminosity ( $L_{[O\text{ III}]} < 3.8 \times 10^{40} \text{ erg s}^{-1}$ ) AGNs and 17 higher luminosity ones from both the baseline MaNGA sample and the Ancillary AGN sample.<sup>1</sup>

<sup>1</sup> As the baseline MaNGA sample contains limited dynamic range in AGN luminosity, reaching only  $L_{[O\text{ III}]} \approx 10^{40} \text{ erg s}^{-1}$  ( $L_{\text{bol}} \approx 10^{43} \text{ erg s}^{-1}$ ), it is not well suited to explore the relationship between the AGN power and both the outflows and stellar populations of the host galaxy. In order to address

Our goal with this first paper is to broadly characterize the properties of this initial AGN sample and select a control sample of inactive galaxies matched to the AGN hosts in absolute magnitude, galaxy mass, redshift, galaxy type and inclination. The definition of a control sample is essential in order to investigate the effects of AGN feeding and feedback on the host galaxy properties, and in order to do this, it is necessary to make sure that eventual differences are not related to properties such as Hubble type or galaxy mass. We have found so far 62 AGNs and 109 control sample galaxies, but the criteria introduced in this paper will be used to increase our sample to at least 300 AGNs (estimated to be observed) and corresponding control sample galaxies by the conclusion of the MaNGA survey.

Besides presenting and characterizing the AGN and control samples, we investigate the similarities and differences between the stellar populations of the two samples. This study was performed in two steps: In this paper, we compare the stellar population of the AGN hosts and control galaxies using stellar population synthesis of the nuclear spectra over the inner 3 arcsec from the SDSS-III survey (Gunn et al. 2006; Eisenstein et al. 2011; Smee et al. 2013). In a forthcoming paper (Mallmann et al., in preparation), we will use the MaNGA data cubes to compare the resolved stellar population properties up to  $1.5r_e$ .

This paper is organized as follows. In Section 2, we present and describe the AGN and control samples; in Section 3, we compare the properties of the two samples; in Section 4, we describe the stellar population synthesis method; in Section 5, we discuss the results and in Section 6 we present our conclusions. We have assumed a cosmology with  $H_0 = 70 \text{ km s}^{-1} \text{ Mpc}^{-1}$ ,  $\Omega_m = 0.3$  and  $\Omega_V = 0.7$ .

## 2 SAMPLE SELECTION AND CHARACTERIZATION

### 2.1 Galaxies hosting an active nucleus

AGN produce a spectral energy distribution consistently harder than massive main-sequence stars. A common tool for identifying the origin of the ionizing photons in optical emission-line galaxies (active nuclei, starbursts or transition objects) is the BPT diagram (Baldwin, Phillips & Terlevich 1981), which is based on line ratios between high- and low-ionization potential species. But one weakness of the BPT diagram is its inability to discriminate between a genuine low-ionization AGN and emission-line galaxies, whose ionizing photons are produced in the atmospheres of evolved low-mass stars (the so-called post-AGB stars). In order to circumvent this limitation, Cid Fernandes et al. (2010) have introduced a new diagnostic diagram that makes use of the equivalent width of  $\text{H}\alpha$  ( $\text{EW}_{\text{H}\alpha}$ ) – the so-called WHAN diagram. These authors have shown that galaxies that have  $\text{EW}_{\text{H}\alpha}$  smaller than 3 Å are not ionized by AGNs but instead are ionized by post-AGB stars, and have been dubbed ‘LIERS’.

In order to identify hosts of ‘true’ AGN in the MaNGA MPL-5 sample, we have made use of the BPT and the WHAN diagrams simultaneously. We have cross-matched all galaxy data cubes observed in MPL-5 with the SDSS-III spectroscopic data from DR12 (Alam et al. 2015). We have obtained line fluxes and equivalent widths of  $\text{H}\beta$ ,  $\text{H}\alpha$ ,  $[\text{O III}] \lambda 5007$  and  $[\text{N II}] \lambda 6584$ , measured in the

this issue, an auxiliary program to cover a wider range of AGN luminosities was proposed by a group led by PI Jenny Greene. This successful proposal will lead to the observation of an additional  $\approx 150$  AGN with luminosities up to  $L_{\text{bol}} \approx 10^{45} \text{ erg s}^{-1}$ .

**Table 1.** Parameters of AGN in MaNGA-MPL5. (1) galaxy identification in the MaNGA survey; (2) MaNGA plate-IFU identification of the observation; (3)–(4): RA/Dec. (2000) in degrees; (5) spectroscopic redshift from SDSS-III; (6): integrated absolute  $r$ -band magnitude from SDSS-III; (7): stellar mass in units of  $M_{\odot}$ ; errors associated with the stellar masses of galaxies in our sample are typically under 0.03 dex (Conroy, Gunn & White 2009); (8) elliptical/spiral/merging classification from Galaxy Zoo I; (9)–(10):  $r$ -band concentration and asymmetry derived with PYCA; and (11) [O III] luminosity in units of  $10^{40}$  erg s $^{-1}$ .

mangaID (1)	RA (2)	Dec. (3)	$z$ (4)	$M_r$ (5)	$\log M^*/M_{\odot}$ (6)	GZ1 $_c$ (7)	$C$ (8)	$A$ (9)	$L(\text{[O III]})$ (10)
1-558912	166.129 410	42.624 554	0.1261	−20.46	11.25	—	0.37	0.12	56.82 ± 1.25
1-269632	247.560 974	26.206 474	0.1315	−21.78	11.62	S	0.47	0.05	30.08 ± 1.69
1-258599	186.181 000	44.410 770	0.1256	−21.24	11.68	E	0.50	0.11	20.95 ± 0.67
1-72322	121.014 198	40.802 612	0.1262	−21.81	12.05	S	0.34	0.08	20.66 ± 0.43
1-121532	118.091 110	34.326 569	0.1400	−20.51	11.34	E	0.33	0.05	11.68 ± 0.96
1-209980	240.470 871	45.351 940	0.0420	−19.70	10.79	S	0.57	0.04	11.01 ± 0.17
1-44379	120.700 706	45.034 554	0.0389	−19.89	10.97	S	0.24	0.06	8.94 ± 0.14
1-149211	168.947 800	50.401 634	0.0473	−18.27	10.16	S	0.29	0.03	7.88 ± 0.14
1-173958	167.306 015	49.519 432	0.0724	−20.53	11.31	S	0.33	0.06	6.79 ± 0.30
1-338922	114.775 749	44.402 767	0.1345	−20.27	11.13	M	0.44	0.03	6.77 ± 0.90
1-279147	168.957 733	46.319 565	0.0533	−19.51	10.66	S	0.45	0.03	6.77 ± 0.20
1-460812	127.170 799	17.581 400	0.0665	−19.81	11.44	—	0.38	0.05	6.46 ± 0.31
1-92866	243.581 818	50.465 611	0.0603	−20.56	11.69	E	0.49	0.05	6.12 ± 0.30
1-94784	249.318 420	44.418 228	0.0314	−20.06	10.85	S	0.42	0.03	5.96 ± 0.12
1-44303	119.182 152	44.856 709	0.0499	−19.72	10.62	S	0.29	0.10	5.56 ± 0.12
1-339094	117.472 420	45.248 482	0.0313	−19.02	10.52	E	0.36	0.03	5.29 ± 0.09
1-137883	137.874 756	45.468 319	0.0268	−18.06	10.77	E/S	0.41	0.01	3.87 ± 0.12
1-48116	132.653 992	57.359 669	0.0261	−19.18	10.60	S	0.31	0.06	3.79 ± 0.08
1-256446	166.509 872	43.173 473	0.0584	−19.40	11.14	E	0.49	0.05	3.74 ± 0.15
1-95585	255.029 877	37.839 500	0.0633	−20.88	11.24	S	0.27	0.08	3.58 ± 0.16
1-135641	249.557 312	40.146 820	0.0304	−19.03	11.19	S	0.28	0.08	3.52 ± 0.09
1-259142	193.703 995	44.155 567	0.0543	−20.75	11.29	S	0.39	0.06	3.47 ± 0.20
1-109056	39.446 587	0.405 085	0.0473	−19.27	10.57	—	0.32	0.05	3.24 ± 0.08
1-24148	258.827 423	57.658 772	0.0282	−18.51	10.56	S	0.31	0.04	3.17 ± 0.05
1-166919	146.709 106	43.423 843	0.0722	−20.85	11.28	S	0.37	0.06	2.64 ± 0.25
1-248389	240.658 051	41.293 427	0.0348	−19.36	10.57	S	0.49	0.12	2.55 ± 0.09
1-321739	226.431 656	44.404 903	0.0283	−18.91	11.12	S	0.40	0.14	2.24 ± 0.10
1-234618	202.128 433	47.714 039	0.0608	−19.64	11.37	S	0.31	0.09	2.23 ± 0.23
1-229010	57.243 038	−1.144 831	0.0407	−20.51	11.46	—	0.41	0.03	2.11 ± 0.09
1-211311	248.426 392	39.185 120	0.0298	−19.04	10.44	E/S	0.43	0.02	1.99 ± 0.06
1-373161	222.810 074	30.692 245	0.0547	−21.30	11.60	E	0.43	0.00	1.87 ± 0.11
1-210646	245.157 181	41.466 873	0.0606	−20.38	10.98	S	0.18	0.05	1.80 ± 0.10
1-351790	121.147 926	50.708 557	0.0227	−18.09	9.92	E	0.39	0.02	1.72 ± 0.03
1-163831	118.627 846	25.815 987	0.0631	−20.84	11.26	S	0.27	0.05	1.67 ± 0.13
1-22301	253.405 563	63.031 269	0.1052	−21.19	11.18	S	0.29	0.08	1.67 ± 0.23
1-248420	241.823 395	41.403 603	0.0346	−19.71	10.90	S	0.21	0.07	1.66 ± 0.06
1-23979	258.158 752	57.322 422	0.0266	−18.27	10.42	E	0.44	0.06	1.60 ± 0.05
1-542318	245.248 306	49.001 778	0.0582	−19.75	10.91	E	0.34	0.01	1.58 ± 0.07
1-95092	250.846 420	39.806 461	0.0302	−19.95	11.20	E	0.47	0.04	1.54 ± 0.07
1-279676	173.981 888	48.021 458	0.0587	−19.40	10.81	—	0.32	0.02	1.52 ± 0.14
1-201561	118.053 215	28.772 579	0.0637	−19.73	10.88	S	0.30	0.07	1.37 ± 0.15
1-198182	224.749 649	48.409 855	0.0359	−20.22	11.09	E	0.49	0.01	1.34 ± 0.11
1-96075	253.946 381	39.310 535	0.0631	−21.12	11.35	S	0.29	0.07	1.26 ± 0.13
1-519742	206.612 457	22.076 742	0.0276	−17.62	9.64	S	0.23	0.04	1.19 ± 0.03
1-491229	172.607 544	22.216 530	0.0393	−20.25	11.12	E	0.51	0.02	1.14 ± 0.11
1-604761	113.472 275	37.025 906	0.0618	−20.92	11.34	S	0.26	0.12	1.00 ± 0.13
1-25725	262.996 735	59.971 638	0.0291	−18.30	10.55	E	0.44	0.04	0.92 ± 0.05
1-94604	251.335 938	42.757 790	0.0493	−19.44	10.52	S	0.37	0.01	0.86 ± 0.07
1-37036	41.699 909	0.421 577	0.0283	−19.02	10.66	E	0.40	0.09	0.84 ± 0.06
1-167688	155.885 559	46.057 755	0.0258	−17.86	9.75	E	0.52	0.04	0.84 ± 0.02
1-279666	173.911 240	47.515 518	0.0455	−18.83	10.42	E	0.31	0.02	0.84 ± 0.07
1-339163	116.280 205	46.072 422	0.0312	−20.02	10.97	S	0.30	0.10	0.82 ± 0.07
1-258774	186.400 864	45.083 858	0.0384	−19.60	10.77	—	0.55	0.03	0.77 ± 0.10
1-198153	224.289 078	48.633 968	0.0354	−19.83	11.00	S	0.27	0.07	0.76 ± 0.08
1-91016	234.810 974	56.670 856	0.0463	−18.60	10.56	S	0.27	0.06	0.76 ± 0.09
1-279073	170.588 150	46.430 504	0.0323	−19.53	10.79	E	0.51	0.01	0.63 ± 0.06
1-135044	247.907 990	41.493 645	0.0303	−19.76	10.65	S	0.31	0.05	0.61 ± 0.04

**Table 1** – *continued*

mangaID (1)	RA (2)	Dec. (3)	$z$ (4)	$M_r$ (5)	$\log M^*/M_\odot$ (6)	GZ1 <sub>c</sub> (7)	$C$ (8)	$A$ (9)	$L([O\text{ III}])$ (10)
1-148068	156.805 679	48.244 793	0.0610	– 20.72	11.41	S	0.22	0.04	0.45 ± 0.15
1-277552	167.034 561	45.984 623	0.0362	– 19.72	10.83	S	0.21	0.15	0.44 ± 0.05
1-217050	136.719 986	41.408 253	0.0274	– 19.66	10.93	E	0.47	0.02	0.43 ± 0.03
1-25554	262.486 053	58.397 408	0.0268	– 19.27	10.52	S	0.36	0.04	0.24 ± 0.03
1-135285	247.216 949	42.812 012	0.0316	– 19.66	10.78	–	0.32	0.05	0.20 ± 0.04

SDSS-III integrated nuclear spectrum, from Thomas et al. (2013). The criterion we have applied to identify galaxies hosting AGN was that it must be located, within the uncertainties, simultaneously in the Seyfert or LINER region of both the BPT and the WHAN diagrams. This criterion eliminates from the sample potential LIERs, and also transition objects. Only 62 galaxies have fulfilled this criterion.

Figs 2 (a) and (b) present the BPT and WHAN diagrams for all MPL-5 emission-line galaxies and indicate the location of galaxies, we have considered as AGN hosts following the criteria above. Table 1 lists relevant parameters of the AGN host galaxies. Besides identifications and coordinates, redshifts, absolute  $r$  magnitudes and stellar masses, we also list the galaxy classification in Galaxy Zoo (GZ1, Lintott et al. 2011), the  $r$ -band concentration index  $C$  and asymmetry parameter  $A$  (described below) and the  $[O\text{ III}] \lambda 5007$  luminosity derived from SDSS-III data (Thomas et al. 2013).

In order to assess quantitatively the morphological variety of the AGN and control samples, we have derived the concentration index  $C$  and asymmetry index  $A$  of the sample galaxies using the publicly available code PYCA (Menanteau et al. 2005). This calculation was made using the  $r$ -band images in order to maximize the galaxy signal-to-noise ratio. We have also obtained for all galaxies of the sample the morphological classifications from GZ1 (Lintott et al. 2011). From the GZ1 classification probabilities, we have separated the galaxies in four large classes: ellipticals (E), spirals (S), merging (M) and intermediate elliptical/spiral (E/S); this last class corresponds to galaxies whose GZ1 elliptical and spiral probabilities are rigorously the same and exceed 50 per cent when combined.

Most of the 62 AGN in our sample have luminosities  $L([O\text{ III}]) < 3.8 \times 10^{40}$  erg s $^{-1}$ , with only 17 having larger luminosities. We use this threshold – postulated by Kauffmann et al. (2003) – to characterize these 17 AGNs as ‘strong AGN’. SDSS-III  $ugriz$  negative images (Fukugita et al. 1996) of the four most luminous of these strong AGNs are shown in Fig. 1; the remainder are available online.

Inspection of the SDSS-III spectra showed that most of the strong AGN in our sample present coronal lines: at least one of the lines  $[\text{NeV}] \lambda 3425$  Å,  $[\text{FeV}\text{ II}] \lambda 3760$  Å or  $[\text{FeX}] \lambda 6374$  Å are detectable above  $3\sigma$ . A small number of objects among the most  $[O\text{ III}]$ -luminous ‘weak AGN’ also present some of these lines. Coronal lines are thought to be produced by photoionization from the AGN (Mazzalay, Rodríguez-Ardila & Komossa 2010; Rodríguez-Ardila et al. 2011) and to be associated with outflows (Müller-Sánchez et al. 2011). Being insensitive to star formation as opposed to the  $[O\text{ III}] \lambda 5007$  Å, the presence of coronal lines reinforces the AGN nature of the 17 most  $[O\text{ III}]$ -luminous objects in our sample, and suggests a transition between high- and low-ionization AGN at  $L([O\text{ III}]) = 3.8 \times 10^{40}$  erg s $^{-1}$ , in concordance with Kauffmann et al. (2003).

We note that our AGN selection is based on single-fibre SDSS-III observations, which limits us to sources with AGN-photoionization signatures within 3 arcsec of the galactic centre. Wylezalek et al. (in preparation) has recently developed an AGN

selection algorithm taking full advantage of the spatial dimension of AGN ionization signatures provided through the MaNGA data. Wylezalek et al. (in preparation) show that about a third to a half of the MaNGA-selected AGN candidates would not have been selected based on the SDSS-III single-fibre observations since AGN ionization signatures are only prevalent beyond the 3 arcsec coverage of the single-fibre spectra. Reasons for this can be manyfold (off-nuclear AGN, star formation signatures dominate in the centre due to a nuclear starburst, recently turned-off AGN) and are currently under investigation by Wylezalek et al. (in preparation).

In this paper, we focus on the classical AGN with nuclear photoionization signatures. In a forthcoming paper, we will also investigate the nature of the stellar populations in the ‘unusual’ off-nuclear MaNGA-selected AGN candidates.

## 2.2 Control sample

We have extracted from MPL-5 a control sample of galaxies with properties matched to those of the AGN hosts, except that their nuclei are quiescent. The control sample was built as follows:

(i) First, we selected from MPL-5 all galaxies, presenting or not detectable emission lines, whose ionizing source is not an AGN (as discussed in Section 2.1). We therefore consider a galaxy as a potential control sample candidate if it fulfills any one of these four conditions: (a) it is located, within the uncertainties, in the star-forming region of the BPT diagram; (b) it is located, within the uncertainties, in the transition or LINER region of the BPT, but the WHAN diagram discards ionization from an AGN based on the value of  $\text{EWH}\alpha$ ; (c) it presents a very large uncertainty in  $\log [O\text{ III}]/H\beta$ , not allowing for a secure classification in the BPT diagram, but the WHAN diagram discards ionization from an AGN based on the value of  $\text{EWH}\alpha$ ; (d) the galaxy does not present emission lines. These conditions make sure that galaxies with prominent emission lines are dominated by star formation, not by an active nucleus; the remaining objects are galaxies whose emission lines can be completely accounted for by hot evolved low-mass stars. Galaxies which fulfill any one of these conditions are considered inactive.

(ii) We have then selected two control galaxies for each AGN, matching them according to the redshift  $z$  and total stellar mass  $M_*$ . A preliminary list of control sample candidates was drawn for each galaxy in the AGN sample by exploring the full ( $z, M_*$ ) parameter space for all inactive galaxies in MPL-5. Galaxies for which both  $z$  and  $M_*$  did not differ by more than 30 per cent from those of the AGN sample values were visually inspected, allowing for a large number of control objects to be selected while keeping low the dispersion of values in the parameter space. The number of control sample candidates selected at this point for each galaxy was typically  $\approx 50$  (with a larger/smaller number of candidates for galaxies at low/high redshift).

**Table 2.** Control sample parameters. (1) identification of the AGN host associated with the control galaxy; (2)–(12) same as (1)–(11) of Table 1. Twelve control sample objects have been paired to more than one AGN hosts and appear more than once in the table.

AGN mangaID (1)	mangaID (2)	RA (3)	Dec. (4)	$z$ (5)	$M_r$ (6)	$\log M^*/M_\odot$ (7)	GZ1 <sub>c</sub> (8)	C (9)	A (10)	$L([\text{O III}])$ (11)
1-558912	1-71481	117.456 001	34.883 911	0.1312	−20.95	11.70	E	0.47	0.02	0.10 ± 0.20
	1-72928	127.256 485	45.016 773	0.1270	−20.62	11.52	E	0.40	0.21	0.09 ± 0.23
1-269632	1-210700	248.140 564	39.131 020	0.1303	−20.96	11.67	S	0.36	0.03	1.55 ± 0.44
	1-378795	118.925 613	50.172 771	0.0967	−20.77	11.35	S	0.32	0.03	0.72 ± 0.31
1-258599	1-93876	246.942 947	44.177 521	0.1394	−20.75	11.50	E	0.44	0.01	0.46 ± 0.36
	1-166691	146.047 348	42.900 040	0.1052	−20.50	11.36	E	0.51	0.04	0.09 ± 0.49
1-72322	1-121717	118.803 429	35.596 798	0.1098	−21.11	11.61	S	0.39	0.12	1.40 ± 0.57
	1-43721	116.967 567	43.383 499	0.1114	−21.41	11.86	S	0.32	0.01	1.91 ± 0.52
1-121532	1-218427	124.342 316	27.796 206	0.1496	−21.30	11.47	E	0.47	0.04	0.72 ± 0.62
	1-177493	257.085 754	31.746 916	0.1081	−20.90	11.30	E	0.38	0.06	2.29 ± 0.28
1-209980	1-295095	248.348 663	24.776 577	0.0410	−18.40	10.14	E	0.35	0.05	0.15 ± 0.03
	1-92626	241.799 545	48.572 563	0.0434	−20.04	11.04	S	0.36	0.03	0.76 ± 0.07
1-44379	1-211082	247.620 041	39.626 045	0.0304	−19.72	11.07	E	0.31	0.06	0.19 ± 0.04
	1-135371	250.156 235	39.221 634	0.0352	−19.20	10.76	S	0.28	0.11	0.25 ± 0.07
1-149211	1-377321	110.556 152	42.183 643	0.0444	−19.02	9.89	S	0.31	0.03	4.53 ± 0.13
	1-491233	172.563 995	22.992 010	0.0332	−18.39	10.59	S	0.29	0.06	0.25 ± 0.03
1-173958	1-247456	232.823 196	45.416 538	0.0705	−20.05	10.83	—	0.40	0.02	0.57 ± 0.16
	1-24246	264.840 790	56.567 070	0.0818	−19.91	10.57	S	0.75	0.36	0.11 ± 0.06
1-338922	1-286804	211.904 861	44.482 269	0.1429	−20.03	10.50	M	0.44	0.32	2.23 ± 0.43
	1-109493	56.425 140	−0.378 460	0.1093	−20.46	11.26	—	0.49	−0.01	0.15 ± 0.18
1-279147	1-283246	191.078 873	46.407 131	0.0496	−19.17	10.55	S	0.47	0.04	0.23 ± 0.06
	1-351538	119.145 126	47.563 850	0.0692	−19.67	11.00	S	0.35	0.08	0.46 ± 0.13
1-460812	1-270160	248.274 612	26.211 815	0.0660	−20.37	11.46	S	0.50	0.02	0.70 ± 0.39
	1-258455	183.612 198	45.195 454	0.0653	−20.02	11.03	E	0.40	0.03	0.49 ± 0.14
1-92866	1-94514	248.241 180	42.524 670	0.0614	−20.60	11.17	E	0.51	0.00	—
	1-210614	244.501 755	41.392 189	0.0612	−20.64	11.48	E	0.49	0.01	0.40 ± 0.14
1-94784	1-211063	247.058 411	40.313 835	0.0331	−19.87	10.79	S	0.33	0.09	0.20 ± 0.04
	1-135502	247.764 175	39.838 505	0.0305	−19.51	11.13	S	0.40	0.09	0.50 ± 0.05
1-44303	1-339028	116.097 923	44.527 740	0.0497	−20.01	11.24	S	0.36	0.06	0.44 ± 0.08
	1-379087	119.910 118	51.792 362	0.0534	−19.60	11.02	S	0.38	0.10	0.72 ± 0.13
1-339094	1-274646	158.017 029	43.859 268	0.0284	−18.70	10.36	E	0.53	0.02	0.35 ± 0.04
	1-24099	258.027 618	57.504 009	0.0282	−18.67	10.34	E	0.44	0.01	0.06 ± 0.03
1-137883	1-178838	312.023 621	0.068 841	0.0247	−17.54	10.46	—	0.51	0.19	0.10 ± 0.02
	1-36878	42.542 126	−0.867 116	0.0232	−18.88	10.77	E	0.45	0.07	0.28 ± 0.04
1-48116	1-386452	136.228 333	28.384 314	0.0269	−19.54	10.57	S	0.49	0.09	0.32 ± 0.04
	1-24416	263.033 173	56.878 746	0.0281	−19.16	10.66	S	0.37	0.03	0.22 ± 0.03
1-256446	1-322671	235.797 028	39.238 773	0.0637	−19.77	10.82	E	0.49	0.04	—
	1-256465	166.752 243	43.089 901	0.0575	−19.70	10.79	E	0.50	0.01	0.59 ± 0.11
1-95585	1-166947	147.335 007	43.442 989	0.0720	−20.79	10.81	S	0.29	0.02	0.13 ± 0.08
	1-210593	244.419 754	41.899 155	0.0605	−19.76	10.90	S	0.36	0.06	0.43 ± 0.14
1-135641	1-635503	318.990 448	9.543 076	0.0293	−19.37	10.91	S	0.22	0.10	0.15 ± 0.06
	1-235398	213.149 185	47.253 059	0.0281	−18.91	10.99	S	0.28	0.10	0.16 ± 0.05
1-259142	1-55572	133.121 307	56.112 690	0.0454	−20.11	11.03	S	0.40	0.06	0.12 ± 0.04
	1-489649	171.954 834	21.386 103	0.0406	−19.94	10.95	S	0.40	0.03	0.30 ± 0.08
1-109056	1-73005	125.402 306	45.585 476	0.0514	−19.47	10.65	S	0.31	0.05	0.20 ± 0.06
	1-43009	113.553 879	39.076 836	0.0510	−19.41	10.43	S	0.26	0.03	0.12 ± 0.04
1-24148	1-285031	198.701 370	47.351 547	0.0303	−18.47	10.72	S	0.34	0.05	0.26 ± 0.04
	1-236099	225.236 221	41.566 265	0.0205	−17.36	9.91	S	0.33	0.04	0.07 ± 0.01
1-166919	12-129446	203.943 542	26.101 791	0.0670	−20.57	11.32	S	0.34	0.03	0.28 ± 0.09
	1-90849	237.582 748	56.131 981	0.0661	−20.39	11.16	E	0.30	0.04	0.28 ± 0.05
1-248389	1-94554	248.914 688	42.461 296	0.0318	−18.96	10.57	S	0.55	0.07	0.22 ± 0.04
	1-245774	214.863 297	54.100 300	0.0426	−20.22	10.83	S	0.40	0.08	0.29 ± 0.07
1-321739	1-247417	233.319 382	45.698 528	0.0294	−19.25	10.76	S	0.28	0.09	0.16 ± 0.04
	1-633994	247.419 952	40.686 954	0.0305	−18.27	11.04	S	0.39	0.11	0.36 ± 0.09
1-234618	1-282144	184.592 514	46.155 350	0.0492	−18.92	10.31	S	0.21	0.08	0.10 ± 0.02
	1-339125	117.739 944	45.989 529	0.0534	−18.97	11.17	S	0.35	0.05	0.45 ± 0.23
1-229010	1-210962	246.358719	39.870 697	0.0290	−20.49	11.09	S	0.47	0.07	0.35 ± 0.06
	1-613211	167.861847	22.970 764	0.0323	−19.87	11.32	E	0.48	0.04	0.16 ± 0.06

**Table 2** – *continued*

AGN mangaID (1)	mangaID (2)	RA (3)	Dec. (4)	$z$ (5)	$M_r$ (6)	$\log M^*/M_\odot$ (7)	GZ1 <sub>c</sub> (8)	C (9)	A (10)	$L([\text{O III}])$ (11)
1-211311	1-25688	261.284 851	58.764 687	0.0292	–18.79	10.32	S	0.29	0.06	0.10 ± 0.02
	1-94422	250.453 201	41.818 737	0.0316	–19.15	10.55	S	0.37	0.05	0.24 ± 0.03
1-373161	1-259650	196.611 053	45.289 001	0.0509	–21.07	11.68	E	0.44	0.06	0.67 ± 0.20
	1-289865	322.048 584	0.299 885	0.0525	–20.90	11.35	–	0.49	0.02	0.11 ± 0.09
1-210646	1-114306	323.742 737	11.296 529	0.0637	–20.58	10.83	S	0.26	0.05	0.33 ± 0.16
	1-487130	164.447 296	21.233 431	0.0587	–20.47	10.86	S	0.26	0.11	0.27 ± 0.10
1-351790	1-23731	260.746 704	60.559 292	0.0205	–18.20	10.19	E	0.40	0.02	0.02 ± 0.01
	1-167334	151.894 836	46.093 983	0.0243	–18.89	10.60	E	0.43	0.04	0.47 ± 0.05
1-163831	1-247456	232.823 196	45.416 538	0.0705	–20.05	10.83	–	0.40	0.02	0.57 ± 0.16
	1-210593	244.419 754	41.899 155	0.0605	–19.76	10.90	S	0.36	0.06	0.43 ± 0.14
1-22301	1-251871	214.506 760	41.827 644	0.1027	–21.17	11.68	S	0.26	0.05	0.24 ± 0.18
	1-72914	127.580 818	45.075 867	0.0970	–20.88	11.31	S	0.23	0.08	0.13 ± 0.07
1-248420	1-211063	247.058 411	40.313 835	0.0331	–19.87	10.79	S	0.33	0.09	0.20 ± 0.04
	1-211074	247.462 692	39.766 510	0.0318	–19.71	10.79	S	0.30	0.18	0.20 ± 0.04
1-23979	1-320681	213.813 095	47.873 344	0.0279	–18.76	10.77	E	0.48	0.01	0.09 ± 0.07
	1-519738	206.514 709	22.118 843	0.0277	–19.49	10.73	E	0.45	0.03	0.11 ± 0.04
1-542318	1-285052	199.061 493	47.599 365	0.0573	–19.77	10.85	S	0.32	0.04	0.11 ± 0.03
	1-377125	112.221 359	41.307 812	0.0585	–19.67	10.84	S	0.41	0.02	0.57 ± 0.14
1-95092	1-210962	246.358 719	39.870 697	0.0290	–20.49	11.09	S	0.47	0.07	0.35 ± 0.06
	1-251279	209.251 984	43.362 034	0.0329	–20.11	10.97	E	0.47	0.04	0.37 ± 0.06
1-279676	1-44789	120.890 366	47.892 406	0.0586	–19.33	10.92	–	0.31	0.13	0.32 ± 0.09
	1-378401	117.904 335	48.000 526	0.0612	–19.65	11.02	E	0.41	0.02	0.57 ± 0.14
1-201561	1-24246	264.840 790	56.567 070	0.0818	–19.91	10.57	S	0.75	0.36	0.11 ± 0.06
	1-285052	199.061 493	47.599 365	0.0573	–19.77	10.85	S	0.32	0.04	0.11 ± 0.03
1-198182	1-256185	165.568 695	44.271 709	0.0370	–20.00	11.03	E	0.50	0.06	0.25 ± 0.04
	1-48053	132.595 016	55.378 742	0.0308	–20.24	11.49	E	0.50	0.01	–
1-96075	1-166947	147.335 007	43.442 989	0.0720	–20.79	10.81	S	0.29	0.02	0.13 ± 0.08
	1-52259	59.411 037	–6.274 680	0.0678	–20.69	11.12	S	0.23	0.07	0.30 ± 0.09
1-519742	1-37079	42.092 335	0.986 465	0.0274	–17.25	9.55	E	0.27	0.02	0.02 ± 0.01
	1-276679	161.272 629	44.054 291	0.0253	–18.27	10.10	S	0.24	0.03	0.05 ± 0.01
1-491229	1-94554	248.914 688	42.461 296	0.0318	–18.96	10.57	S	0.55	0.07	0.22 ± 0.04
	1-604048	50.536 137	–0.836 265	0.0365	–20.37	10.91	S	0.42	0.09	0.39 ± 0.08
1-604761	1-210173	241.341 766	42.488 312	0.0778	–20.71	11.10	S	0.33	0.07	0.52 ± 0.13
	1-71525	118.344 856	36.274 380	0.0457	–20.17	10.97	S	0.27	0.10	0.19 ± 0.06
1-25725	1-211079	247.438 034	39.810 539	0.0304	–18.97	10.54	E	0.54	0.01	0.03 ± 0.04
	1-322074	228.700 729	43.665 970	0.0274	–18.15	10.10	E	0.45	0.02	–
1-94604	1-295095	248.348 663	24.776 577	0.0410	–18.40	10.14	E	0.35	0.05	0.15 ± 0.03
	1-134239	241.416 443	46.846 561	0.0571	–19.83	10.70	S	0.36	0.04	0.23 ± 0.06
1-37036	1-210785	246.765 076	39.527 386	0.0338	–20.22	10.97	E	0.47	0.01	–
	1-25680	261.968 872	60.097 275	0.0278	–19.41	10.84	E	0.52	0.02	0.34 ± 0.04
1-167688	1-235587	214.854 660	45.864 250	0.0267	–18.88	10.48	E	0.44	0.01	0.08 ± 0.02
	1-37062	41.846 367	0.058757	0.0248	–18.30	10.40	E	0.49	0.03	0.27 ± 0.03
1-279666	1-392976	156.428 894	37.497 524	0.0432	–17.91	10.09	E	0.37	0.02	0.10 ± 0.03
	1-47499	132.037 582	54.309 921	0.0461	–18.53	10.51	E	0.27	0.04	0.15 ± 0.06
1-339163	1-136125	254.044 144	34.836 521	0.0316	–19.33	10.50	S	0.25	0.09	0.08 ± 0.02
	1-626830	204.683 838	26.328 539	0.0282	–19.23	10.67	S	0.28	0.07	0.15 ± 0.04
1-258774	1-379660	119.973 717	55.374 817	0.0357	–19.44	10.74	E	0.47	0.03	0.37 ± 0.07
	1-48208	134.008 118	57.390 965	0.0406	–19.57	10.85	S	0.50	0.01	0.12 ± 0.04
1-198153	1-211063	247.058 411	40.313 835	0.0331	–19.87	10.79	S	0.33	0.09	0.20 ± 0.04
	1-135810	250.123 138	39.235 115	0.0297	–19.38	10.59	S	0.24	0.09	0.08 ± 0.02
1-91016	1-338828	115.641 609	44.215 858	0.0418	–18.10	10.42	S	0.28	0.03	0.43 ± 0.05
	1-386695	137.983 505	27.899 269	0.0474	–19.33	10.48	S	0.27	0.09	0.81 ± 0.09
1-279073	1-211100	247.830 322	39.744 129	0.0309	–19.15	10.62	E	0.56	0.02	–
	1-210784	247.097 122	39.570 305	0.0292	–19.61	10.86	E	0.48	0.00	0.15 ± 0.05
1-135044	1-218280	124.003 311	27.075 895	0.0255	–19.57	10.81	S	0.27	0.08	0.12 ± 0.03
	1-211063	247.058 411	40.313 835	0.0331	–19.87	10.79	S	0.33	0.09	0.20 ± 0.04
1-148068	1-166947	147.335 007	43.442 989	0.0720	–20.79	10.81	S	0.29	0.02	0.13 ± 0.08
	1-55572	133.121 307	56.112 690	0.0454	–20.11	11.03	S	0.40	0.06	0.12 ± 0.04

**Table 2** – *continued*

AGN mangaID (1)	mangaID (2)	RA (3)	Dec. (4)	$z$ (5)	$M_r$ (6)	$\log M^*/M_\odot$ (7)	GZ1 <sub>c</sub> (8)	$C$ (9)	$A$ (10)	$L(\text{[O III]})$ (11)
1-277552	1-264513	236.941 513	28.641 697	0.0333	−20.92	11.28	S	0.25	0.18	0.33 ± 0.05
	1-136125	254.044 144	34.836 521	0.0316	−19.33	10.50	S	0.25	0.09	0.08 ± 0.02
1-217050	1-135372	250.116 714	39.320 118	0.0301	−20.29	11.08	E	0.49	0.02	0.01 ± 0.23
	1-274663	157.660 522	44.012 722	0.0280	−19.88	11.00	E	0.50	0.01	0.08 ± 0.02
1-25554	1-135625	248.507 462	41.347 946	0.0284	−19.06	10.56	S	0.43	0.05	0.56 ± 0.04
	1-216958	136.200 287	40.591 721	0.0270	−18.95	10.41	S	0.51	0.03	0.23 ± 0.02
1-135285	1-633990	247.304 123	41.150 871	0.0296	−19.06	10.46	S	0.34	0.03	0.25 ± 0.03
	1-25688	261.284 851	58.764 687	0.0292	−18.79	10.32	S	0.29	0.06	0.10 ± 0.02

(iii) The images of the control candidates for each galaxy in the AGN sample were then visually inspected to select control galaxies with similar morphologies and axial ratios to those of the AGN host galaxies. For late-type galaxies, we have tried to reproduce both the structure and development of the arms and the relative bulge size, as well as the line-of-sight orientation and the presence of dust lanes. The priority in the morphological analysis was given to structures closer to the nucleus; i.e. we have assigned more weight to the presence of bars and rings than to the morphology of the arms in the outer galaxy regions. During this step the number of potentially good candidates, i.e. galaxies that are morphologically comparable to the respective AGN host, decreased in many cases to only two galaxies. In order to produce the best statistical comparison with the AGN sample properties, keeping an homogeneous representation of all AGN hosts in the control sample, only the two galaxies that best matched the morphology of the AGN host, according to the above criteria, were chosen for each AGN in the sample.

We have thus produced 124 pairs of AGN and control partners. Twelve of the control sample objects were selected as ‘control partners’ of two or more AGN hosts simultaneously; therefore, our control sample comprises 109 non-active galaxies, reproducing the distribution of redshift and stellar mass of the AGN sample. Figs 2(c) and (d) present the BPT and WHAN diagrams for the control sample, superimposed on the distribution of the full MPL-5 sample. Six control sample galaxies did not present any emission lines, and thus do not appear in the figures. We can see a bimodal distribution with a clear separation between star-forming galaxies and LIERS. Comparing with the diagrams shown in Figs 2(a) and (b), we can see that AGN and non-AGN have markedly distinct distributions.

### 3 STELLAR POPULATIONS

In order to characterize the stellar population of the inner  $3 \times 3 \text{ arcsec}^2$  of the galaxies, we performed stellar population synthesis using the STARLIGHT code, developed by Cid Fernandes et al. (2005). This code combines, in different proportions,  $N_*$  single stellar populations (SSPs) in order to reproduce a galaxy observed spectrum – excluding emission lines –,  $O_\lambda$ , with a model spectrum,  $M_\lambda$ . Each combination is found by solving the equation

$$M_\lambda = M_{\lambda_0} \left[ \sum_{j=1}^{N_*} x_j b_{j,\lambda} r_\lambda \right] \otimes G(v_*, \sigma_*), \quad (1)$$

where  $b_{j,\lambda}$  is the reddened spectrum of the  $j$ -th SSP normalized at  $\lambda_0$ ;  $r_\lambda = 10^{-0.4(A_\lambda - A_{\lambda_0})}$  is the reddening term;  $M_{\lambda_0}$  is the synthetic flux at the normalization wavelength;  $x$  is the population vector. The symbol  $\otimes$  denotes the convolution operator and  $G(v_*, \sigma_*)$  is the Gaussian distribution used to model the line-of-sight stellar mo-

tions; it is centred at velocity  $v_*$  with dispersion  $\sigma_*$ . The reddening law, we have used is that presented by Cardelli, Clayton & Mathis (1989). The adopted normalization wavelength was  $\lambda_0 = 5700 \text{ \AA}$ . This wavelength, usually selected to avoid emission and absorption features, is similar to those adopted on other spectral synthesis studies, allowing a comparison of our results with previous ones.

The best-fitting model is determined by minimizing (through a simulated annealing plus Metropolis scheme) the equation

$$\chi^2 = \sum_{\lambda} [(O_\lambda - M_\lambda) w_\lambda]^2, \quad (2)$$

where emission lines and spurious features are masked by assigning  $w_\lambda = 0$  to these regions.

The spectral basis comprise the ‘standard’ 45 elements set, which is a sample of the Evolutionary Population Synthesis models presented by Bruzual & Charlot (2003). It covers 15 ages: 0.001, 0.0031, 0.005, 0.01, 0.025, 0.04, 0.10, 0.28, 0.64, 0.94, 1.43, 2.5, 5.0, 11.0 and 13.0 Gyr, and three different metallicities: 0.004, 0.02, 0.05  $Z_\odot$ .

Since, we are fitting the spectra of AGN, the signature of the central engine cannot be ignored. This component was represented by a featureless continuum (FC) of power-law form that follows the expression  $F_\lambda \propto \lambda^{-0.5}$  (see Koski 1978; Riffel et al. 2009, for example).

### 3.1 Results for the stellar population

Running the STARLIGHT code allows the measurement of the relative contribution of each SSP vector, characterized by age and metallicity, to the total stellar light at  $5700 \text{ \AA}$  ( $x_j$ ) and its corresponding contribution to the total stellar mass ( $\mu_j$ ), that are the main quantities required to characterize the star formation history of the centre of these galaxies. The individual contribution of each SSP allows the derivation of the contribution of the main age and metallicity components to the total flux at  $5700 \text{ \AA}$ , although there are other parameters that globally represent the age and metallicity of the stars: the mean light-weighted and mass-weighted ages ( $\langle t_L \rangle$  and  $\langle t_M \rangle$ ) and the light-weighted and mass-weighted metallicities ( $\langle Z_L \rangle$  and  $\langle Z_M \rangle$ , Cid Fernandes et al. 2005). The mean age, weighted by light and mass are, respectively, given by

$$\langle t_L \rangle = \sum_{j=1}^{N_*} x_j \log t_j \quad \langle t_M \rangle = \sum_{j=1}^{N_*} \mu_j \log t_j, \quad (3)$$

and the mean metallicities, weighted by light and mass, are expressed by

$$\langle Z_L \rangle = \sum_{j=1}^{N_*} x_j Z_j \quad \langle Z_M \rangle = \sum_{j=1}^{N_*} \mu_j Z_j, \quad (4)$$

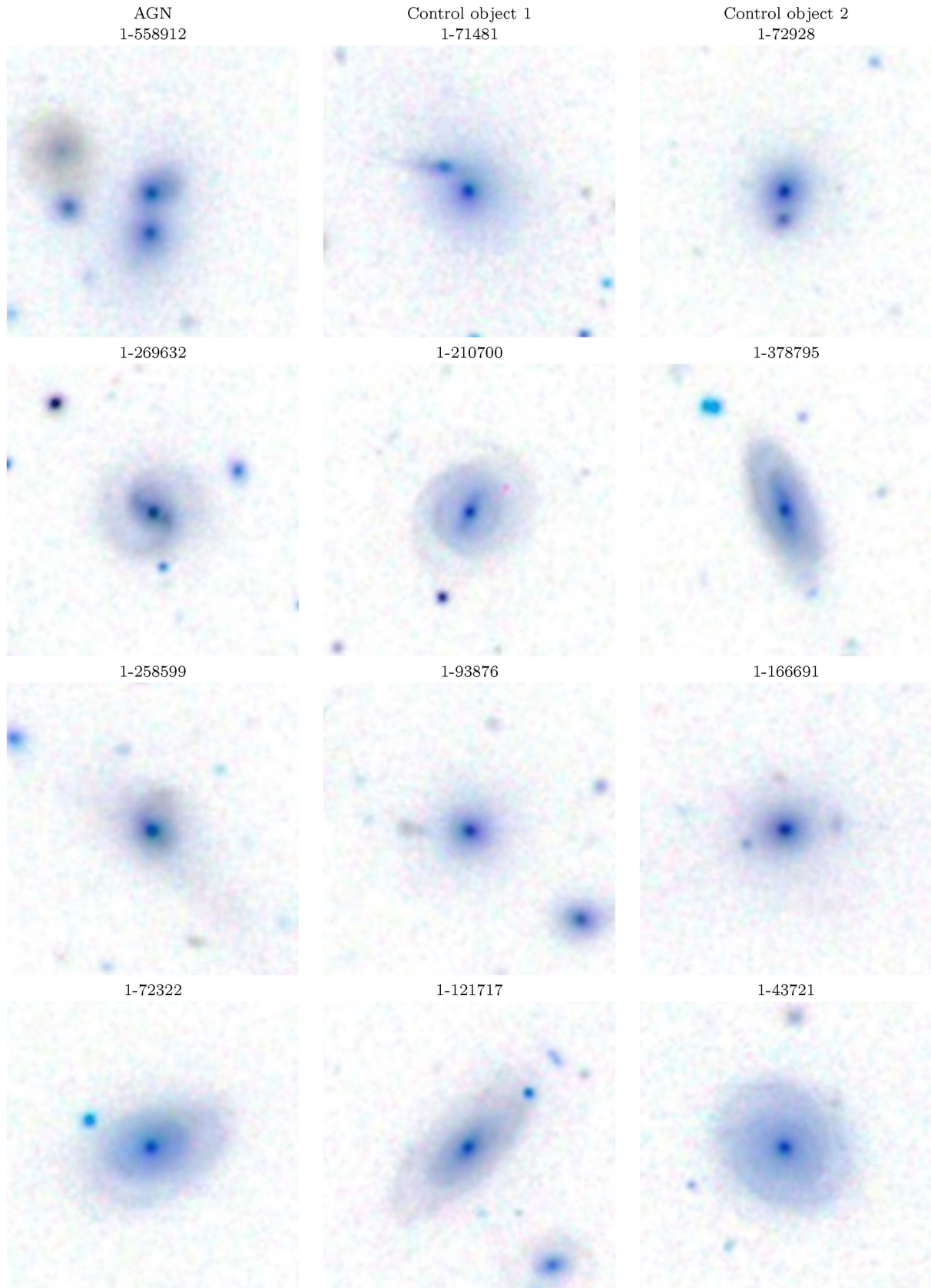


**Figure 1.** SDSS-III  $ugriz$  negative images of the four strongest AGN from our sample (left-hand columns) and their control sample equivalents (centre and right-hand columns). The mangaID of each host is indicated above its respective panel. Each chart is 51 arcsec on a side; north is up, east to the left.

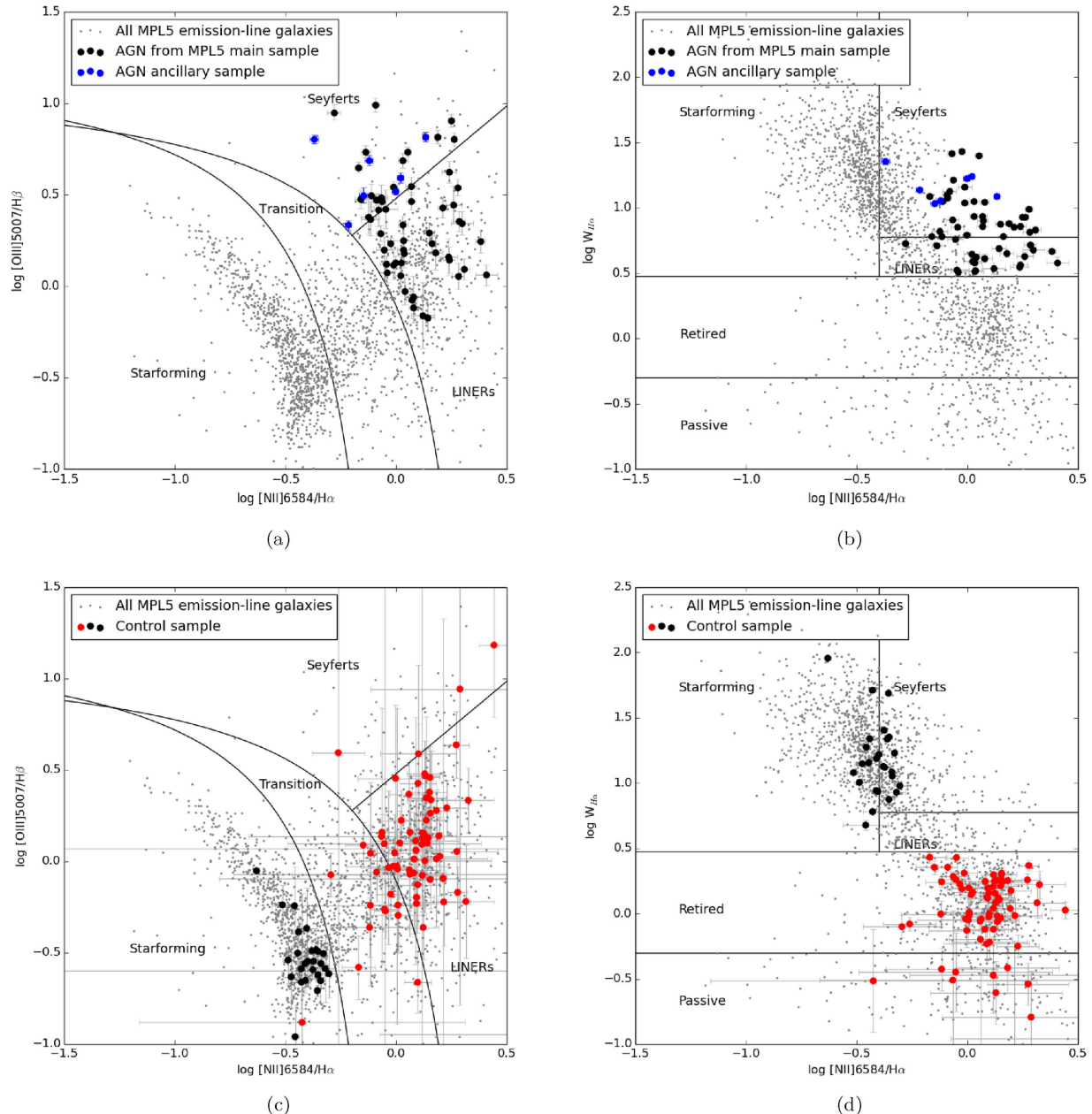


**Figure 2.** BPT and WHAM diagrams for our sample of confirmed AGN (top panels) and control sample (bottom panels), using the fluxes from Thomas et al. (2013). We only include objects where the emission lines are detected at the  $3\sigma$  level. The continuous lines separating Seyferts, transition objects, LINERs and star-forming galaxies are from Kauffmann et al. (2003), Kewley et al. (2001) and Cid Fernandes et al. (2010). Grey dots indicate the position of all emission-line galaxies in MPL-5. In the top panels, we indicate as black (blue) circles the confirmed AGN drawn from the MaNGA MPL-5 main sample (AGN Ancillary Sample). In the bottom diagrams, star-forming (retired/passive) control sample objects are represented by black (red) circles. Six objects from the control sample do not present detectable emission lines and are not shown in the diagrams.

respectively.

A strong contribution of one single SSP age tends to be spread over different SSP components of similar ages (Cid Fernandes et al. 2001); thus, one must be careful interpreting a single SSP component. In order to obtain a more robust and reliable description of the SFH, the SSPs are usually grouped in age bins (e.g. Dametto et al. 2014), which we have chosen as follows: *young-young*:  $x_{yy}$  ( $t \leq 10 \times 10^6$  yr), *young-old*:  $x_{yo}$  ( $25 \leq t \leq 40 \times 10^6$  yr), *intermediate-young*:  $x_{iy}$  ( $0.100 \leq t \leq 0.287 \times 10^9$  yr), *intermediate-*

*intermediate*:  $x_{ii}$  ( $0.640 \leq t \leq 0.905 \times 10^9$  yr), *intermediate-old*:  $x_{io}$  ( $1.0 \leq t \leq 2.5 \times 10^9$  yr) and *old*:  $x_o$  ( $4.0 \leq t \leq 13.1 \times 10^9$  yr).

Fig. 3 presents an example of the results of the stellar population synthesis for the strong AGN mangaID 1-269632. The upper panels show the observed and synthetic spectrum as well as the corresponding residuals; the bottom panels display the resulting light (percent contribution of each age bin above to the light at 5700 Å) and mass contributions of single and binned SSPs vectors. Also shown are the mean ages and metallicities. The inner  $\sim 3.7$  kpc of

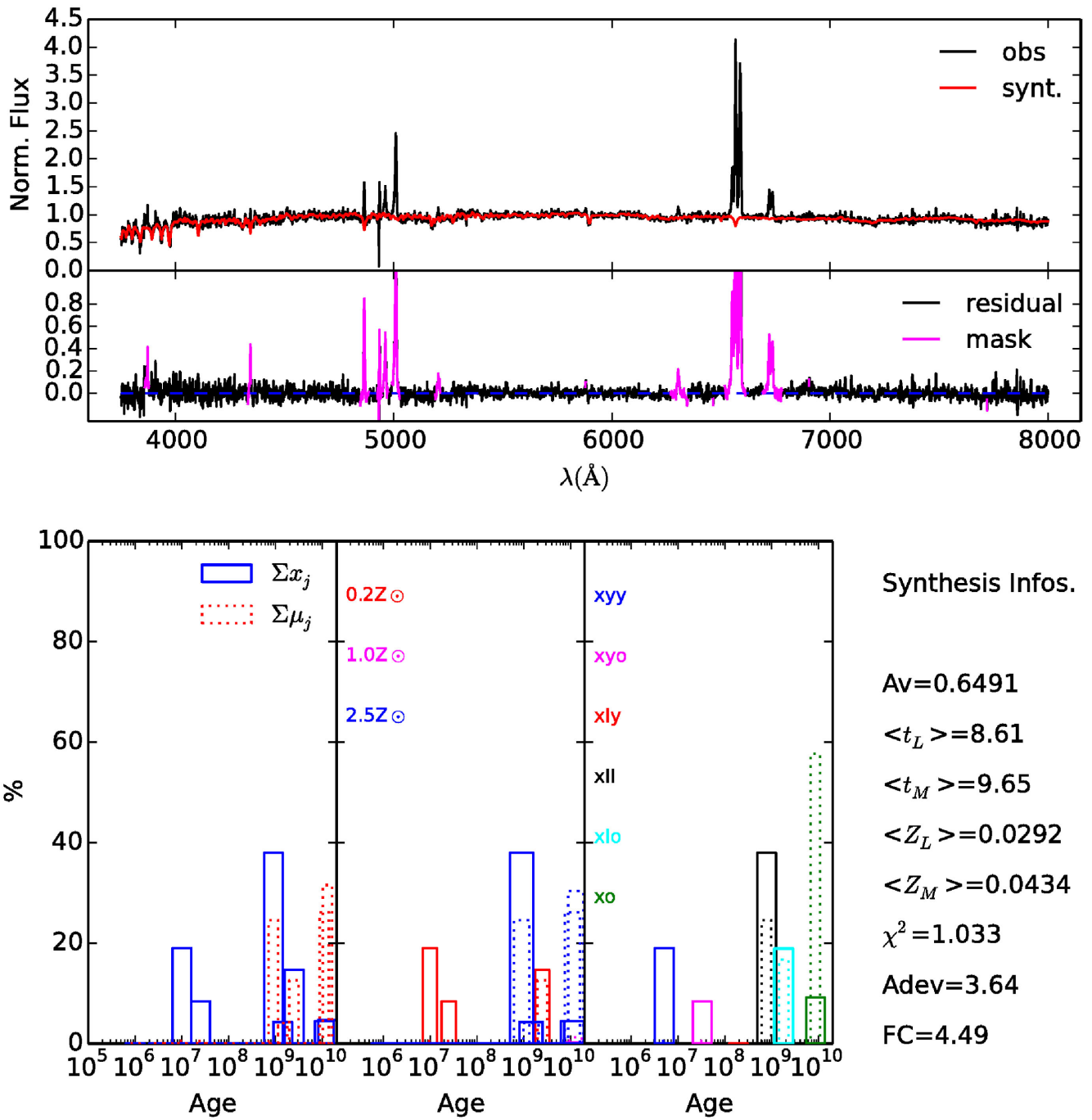


**Figure 3.** Results from the stellar population synthesis for the strong AGN mangaid 1-269632. Upper two panels: top panel – observed (black) and synthetic (red) spectrum; bottom panel – residuals (observed spectrum - synthetic), with the masked regions highlighted in magenta. Bottom three panels: histograms where solid lines represent the light-weighted contribution of the SSPs and the dashed lines represent the mass-weighted contribution. The left histogram shows the individual contribution of each SSP, sorting the SSP vectors by age and summing the metallicities; the middle histogram displays the same as the left histogram but separating the contribution of each SSP in metallicity, with different colours indicating different metallicities; the right histogram presents the mass contributions of the SSPs divided in six age bins (see the text), and summing the metallicities. To the right and bottom are presented the derived average ages and metallicities (both mass- and light-weighted), the extinction  $A_V$ , the contribution of the FC in percent units, the chi-squared value of the fit and the average of the absolute percent difference between observed and synthesized spectra, Adev, that parameterizes the quality of the fit.

this galaxy is dominated by the contribution of intermediate age stars ( $x_{ii} \approx 38$  per cent and  $x_{io} = 19$  per cent) with old stars contributing  $x_o \approx 9$  per cent and young stars  $x_{yy} \approx 19$  per cent, which implies that at least one episode of star formation has occurred in the last 10 Myr. Tables with the synthesis results for all galaxies,

both for the AGN and control samples, showing the contribution of the six age bins listed above (both in percent flux at 5700 Å and in mass) are presented in the Appendix.

Fig. 6 summarizes the results from the synthesis in histograms of the percent contribution of each age bin to the continuum at 5700 Å.

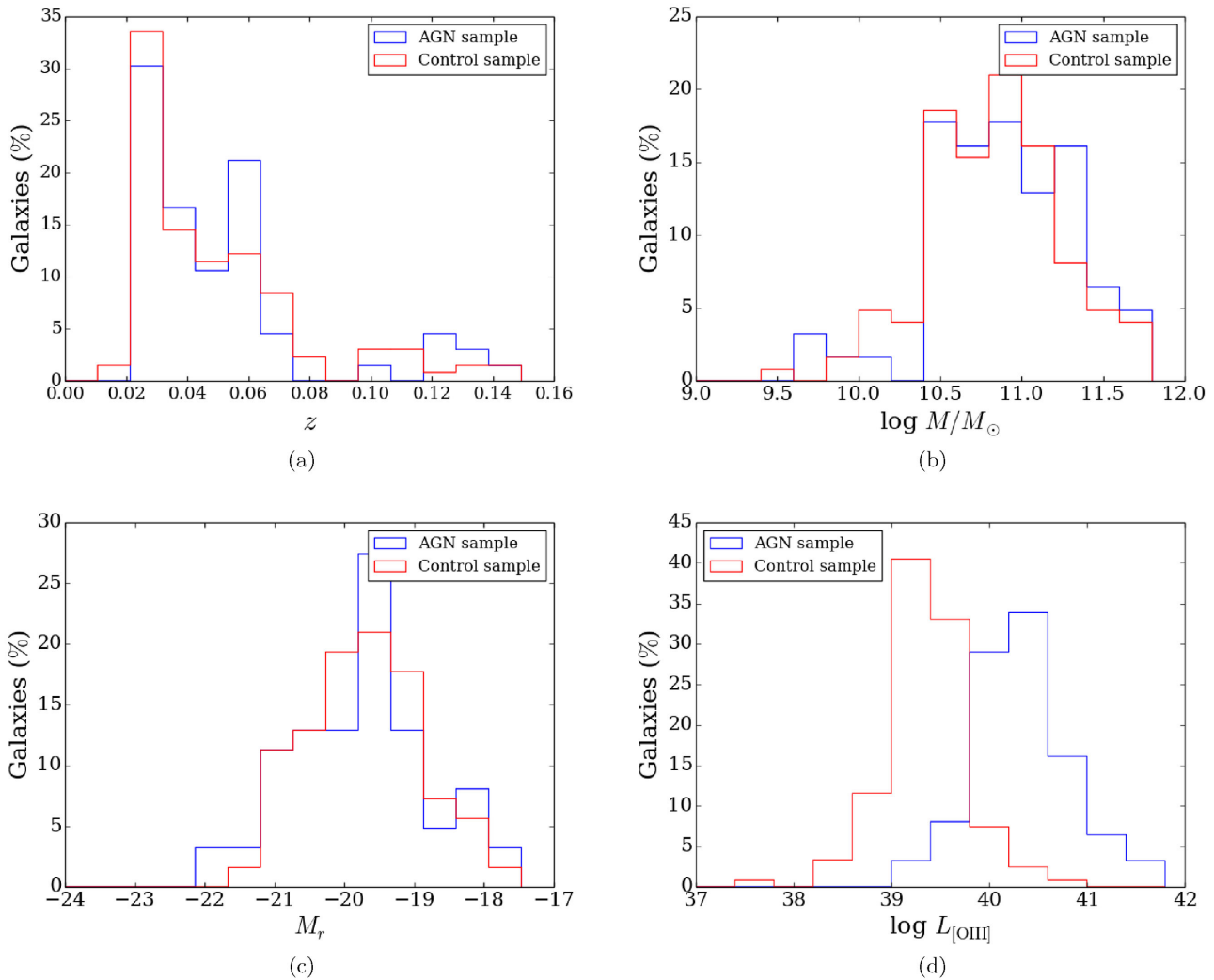


**Figure 4.** Distributions of redshift (a), stellar mass (b), absolute  $r$ -band magnitude (c) and  $\text{[O III]}$  luminosity (d) of the AGN host sample (blue) and the control sample (red). The AGN and the control sample present markedly different distributions of  $L(\text{[O III]})$ , but have the other parameters similar between the two samples.

The results for the AGN sample are shown in blue for the ‘weak AGN’ ( $L(\text{[O III]}) < 3.8 \times 10^{40} \text{ erg s}^{-1}$ ), in green for the strong AGN and red for the control sample. In these histograms, we have chosen to present the results in bins of 10 per cent for the three oldest age ranges and in bins of 3 per cent for the three youngest ages ranges. We have adopted these smaller bins for the youngest ages to better sample the age distributions, as these ages never contribute more than 30 per cent to the total flux at 5700 Å, allowing us to restrict the  $x$ -axis to a maximum contribution of 30 per cent.

## 4 DISCUSSION

### 4.1 Comparison between the AGN hosts and control sample

After selecting the control sample objects according to the criteria described in Section 2.2, we now check if the resulting distribution of stellar masses and redshifts are indeed compatible with that of the AGN hosts. In Fig. 4, we show the distributions of stellar mass,  $r$ -band absolute magnitude and redshifts of the AGN sample and the control sample. The distributions of stellar mass and  $r$ -band absolute magnitude of the two samples are very similar. The probability

that these distributions for the AGN and non-AGN galaxies are not drawn from the same distribution is less than 5 per cent as indicated by an Anderson–Darling test (A-D test). Regarding the redshift distribution, the two samples are also similar; the statistical significance of the A-D test is lower (16 per cent), but this is not critical to our analysis. The only significant difference observed in Fig. 4 is for the distribution of the  $\text{[O III]}$  luminosity  $L(\text{[O III]})$ , as expected: while the centroid of the distribution for the AGN sample is  $\log L(\text{[O III]}) \approx 40.5$ , for the control sample the centroid is  $\log L(\text{[O III]}) \approx 39.3$ .

We have also made a quantitative assessment of how well the control sample morphological distribution matches that of the AGN hosts. The GZ1 classification reveals that the AGN sample contains 34 (55 per cent) spiral and 18 (29 per cent) elliptical galaxies. The remaining 10 objects (16 per cent) comprise 6 E/S galaxies, 1 merger and 3 unclassified objects. The morphological distribution of the control sample is the same within the uncertainties: 60 per cent spiral and 34 per cent elliptical galaxies. Fig. 5 displays the concentration and asymmetry distributions of the AGN and the control sample galaxies. The dashed line is the optimal separation between the GZ1 major classes (ellipticals and spirals) in the diagram. The

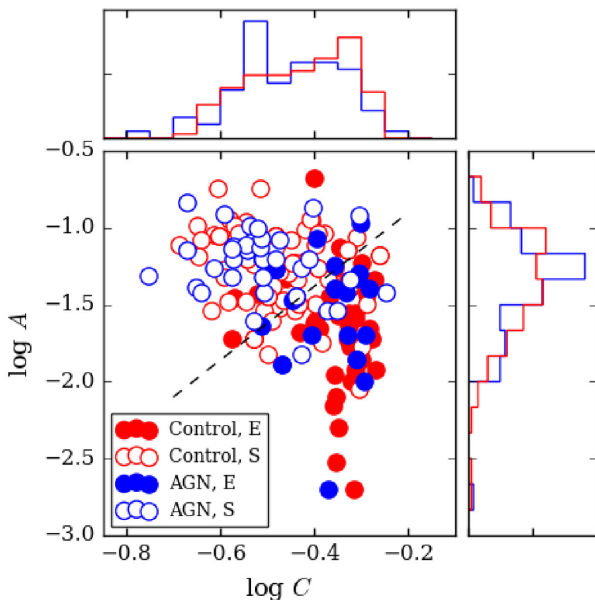


**Figure 5.** Concentration  $C$  and asymmetry  $A$  indices values for AGN and the control sample galaxies. The Galaxy Zoo I morphological classification as ellipticals or spirals is represented by filled and open circles, respectively. Blue (red) circles represent AGN (control sample). The dashed line roughly separates the spiral and elliptical-dominated regions in the diagram. The distributions of  $A$  and  $C$  are similar, but the AGN present a small tendency to be more concentrated near the dashed line.

code PYCA does not calculate uncertainties in  $C$  and  $A$ , but the good separation between elliptical and spiral galaxies in the  $C$ - $A$  plane, with elliptical galaxies occupying the locus of low asymmetry and high concentration, suggests that the estimates of these parameters are robust. The distributions of AGN hosts and non-active galaxies in the  $C$ - $A$  plane are similar, although a small systematic effect is discernible in the sense of a wider distribution of the control sample galaxies in the  $C$ - $A$  diagram relative to the AGN. This behaviour is produced by the fact that AGN galaxies appear to be less common in the extremes of low concentration/low asymmetry indices. This result suggests that the AGN sample is morphologically less diverse than the control sample, preferring to populate the intermediate region between ellipticals and spirals. This trend is, however, secondary, as the A-D test results in a  $p$ -value larger than 0.2 for the null hypothesis that the  $C$  and  $A$  distributions for AGN and control sample are drawn from the same distribution.

The combined SDSS-III  $ugriz$  images of the four strongest AGN from our sample and their ‘control partners’ are shown in Fig. 1. Those for the rest of the sample are available online. Both figures reveal an apparent very good match in the morphology and axial ratios between the AGN and control sample.

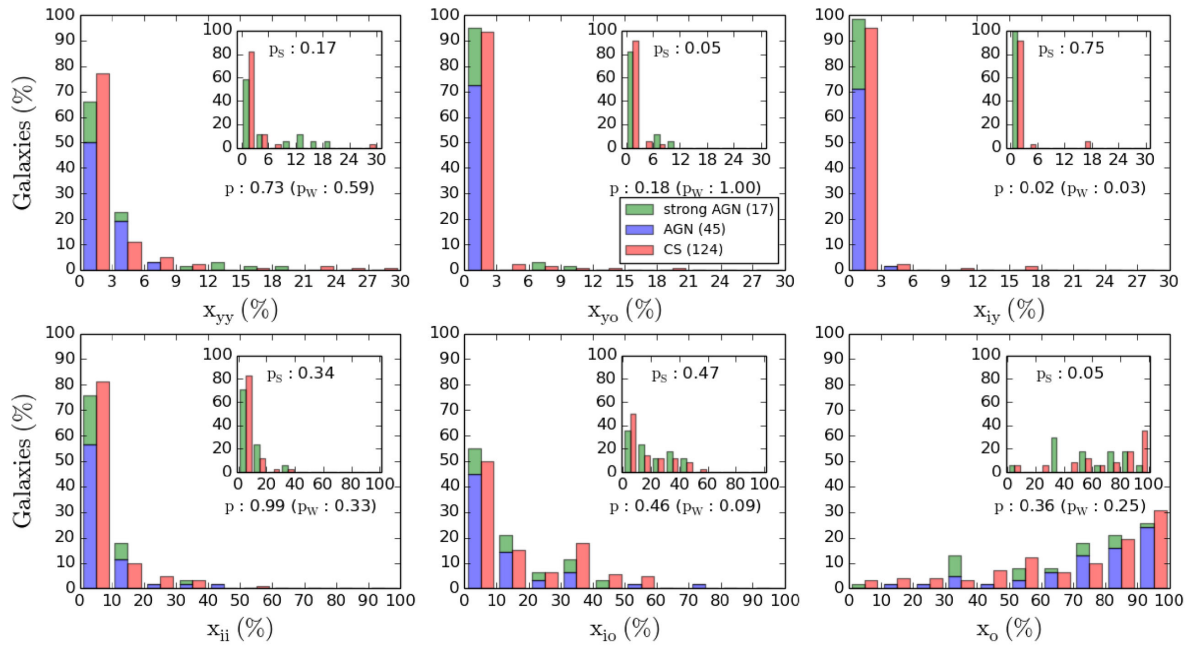
#### 4.2 Stellar population properties

Fig. 6 shows that there is no clear difference between the stellar population of all AGNs – considering both the weak and strong AGNs together – and the control sample. But, when comparing only strong AGN with their control sample, the distributions differ at the  $2\sigma$  level for  $x_{yo}$  and  $x_o$ . Though the differences between the distributions are not obvious in these plots due to the histogram binning, they can be seen with smaller bin widths and are confirmed by the results of the A-D tests. The numbers in

the top right-hand corners of each panel in Fig. 6 give the probability that the two distributions are derived from the same sample. The small values for  $x_{yo}$  and  $x_o$  indicate that the contribution of these populations to the light at 5700 Å differ between the strong AGN and the control sample, in the sense that the strong AGN show a smaller contribution from the old stellar population and a larger contribution from the young-old component than the control sample.

The above results suggest that, when comparing weak and strong AGNs, the contribution of old stellar populations decreases, while that of the younger stellar populations increases in the latter. This trend agrees with the previous results by Kauffmann et al. (2003), who compared the stellar population properties of AGN-host galaxies and normal galaxies for a sample of  $\sim 22\,600$  galaxies with SDSS-I spectra (York et al. 2000). These authors studied the mean stellar age and stellar formation history of these AGN by measuring the indices  $D_n(4000) \times W(H\delta)$  (Balogh et al. 1999). They found that weak AGNs have mostly old stellar populations that are similar to those of early-type galaxies (non-AGN), while the strong AGNs have much younger stellar ages and typically strong H $\delta$  absorption-line equivalent width, indicating that they have experienced a burst of star formation in the past 1–2 Gyr. Our sample of strong AGN is comprised so far by 17 hosts, but our results are robust, as supported by the A-D tests, and will be increased as more of these objects are observed with MaNGA.

The results of the synthesis for the FC continuum, presented in Fig. 7, show a clear difference between the AGN and control sample: while the control sample tend to show very small contribution of FC in most cases, for the AGN, and in particular for the strong AGN, the FC contribution tends to be larger, as expected. In any case, this contribution is usually smaller than 10 per cent, and in only a few cases it reaches  $\sim 20$  per cent. But we also point out that a common problem of stellar population syntheses of the spectra of active galaxies is that a reddened young starburst ( $t \leq 5$  M yr) is very difficult to distinguish from that of an AGN continuum, as discussed in previous studies (Cid Fernandes & Terlevich 1995; Storchi-Bergmann et al. 2000; Cid Fernandes et al. 2004; Riffel et al. 2009). This is particularly true when the FC contribution is smaller than  $\approx 20$  per cent, as is the case here. We thus conclude that, although some degeneracy may be occurring, the fact that we are finding more FC contribution for the AGN than for the control sample supports that we are being able to separate this contribution in many cases. In order to estimate the impact of this degeneracy on the derived population fractions, we have performed a series of simulations. We have combined a set of SSPs from our base with contributions similar to those we have found of our sample, and added a moderate FC contribution of 10 per cent. We have then perturbed the individual flux values using the same error distribution as the sample spectra, and run STARLIGHT with the same configuration as before, both allowing or not allowing for an FC in the fit. We have found that, when the FC is present but the synthesis does not allow for an FC in the fit, the contributions of young and intermediate stellar populations are overestimated by  $\sim 5$  per cent, on average. However, when the FC is allowed, the contribution of young stellar populations is only slightly overestimated ( $\sim 2$  per cent). This agrees with the recent results of Cardoso, Gomes & Papaderos (2017) that have shown that, for a broad range in star formation histories, the effect of an FC in the derived mean stellar ages is typically lower than 0.1 dex even for FC contributions as large as 40 per cent. Therefore, in the cases that there may be some degeneracy, the effect should be small, with no significant influence on the results of the synthesis discussed above.



**Figure 6.** Histograms of the distribution of galaxies according to the fractional contribution of each age bin to the total light at rest frame 5700 Å. Weak AGNs are represented in blue, strong AGNs in green and control sample in red. For the age bins  $x_{ii}$ ,  $x_{io}$  and  $x_o$ , we show, in an insert, histograms comparing only the strong AGN (green) with its respective control sample (red). For each histogram, the  $p$ -value of the A-D test is given. We also present, below the insert in each plot, the  $p$ -value of the comparison between the weak AGN and the control sample.  $p_w$  refers to the weak AGN,  $p_s$  refer to the strong AGN and  $p$  to the combined sample of strong and weak AGNs.

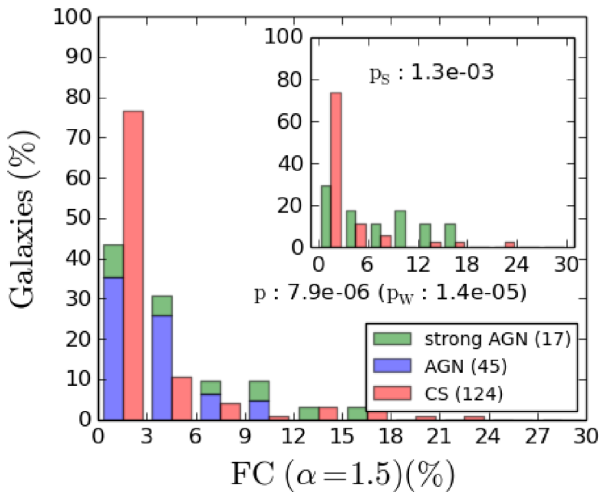


**Figure 7.** Distribution of galaxies according to the fractional contribution of the FC to the total light at rest frame 5700 Å. Weak AGNs are represented in blue, strong AGN in green and control sample in red. In the insert, we show the histogram comparing only the strong AGN (green) with its respective control sample (red). The  $p$ -values of the A-D test of the comparison between the AGN sample and the control sample are also shown.  $p_w$  refers to the weak AGN,  $p_s$  refer to the strong AGN and  $p$  to the combined sample of strong and weak AGNs.

The distribution of the global parameters, mean ages,  $\langle t_L \rangle$  and  $\langle t_M \rangle$ , and mean metallicities,  $\langle Z_L \rangle$  and  $\langle Z_M \rangle$ , are presented in Fig. 8. This figure shows that the distribution of mean ages (weighted in light) differ at the  $2\sigma$  level between the weak AGN and the control sample, while no such difference is observed for the strong AGN. On the other hand, if one calculates the median age for all weak

and all strong AGN, one finds no difference relative to the controls for the weak AGN ( $\langle t_L \rangle = 9.90 \pm 0.25$ ) but a difference of 0.2 dex (younger) for the strong AGN ( $\langle t_L \rangle = 9.70 \pm 0.25$ , with the controls presenting the same value as observed for the weak AGN).

Regarding the metallicity, Fig. 8 reveals a small difference between the weak AGN and their control sample, with a probability of only about 1 per cent that the distributions are similar in the case of normalization in light ( $Z_L$ ), while no such difference is observed for the strong AGN. Although the difference in metallicity between the AGN hosts and control galaxies may be due to a different origin for the stars, there is also the possibility that we are observing the effect of degeneracy between age and metallicity in optical spectra (Worley et al. 1994). This degeneracy arises because the lower metallicity leads to bluer stellar atmospheres, what is also the signature of young stars. As this effect is small, we defer its analysis to a future study, when we have a larger sample of AGN hosts.

#### 4.2.1 The effect of the AGN luminosity

Although we have explored the effect of the AGN luminosity above by separating the analysis of the stellar population in only two populations – strong and weak AGNs – we now investigate in more detail this effect by looking for possible correlations of the stellar population properties with  $L[\text{O III}]$ . We also take advantage of our careful selection of the control sample to explore the differences between the properties of each AGN host and its two controls, investigating how these differences may be associated with the AGN luminosity.

For this exercise, we calculated the differential fractional contributions (AGN - control): the differences  $\Delta x$  (in each age bin  $x$ ) of the fractional contributions to the light at 5700 Å between each AGN and its two control partners, and verified how, and if, it depends on the AGN [O III] luminosity. The results are shown in Fig. 9,

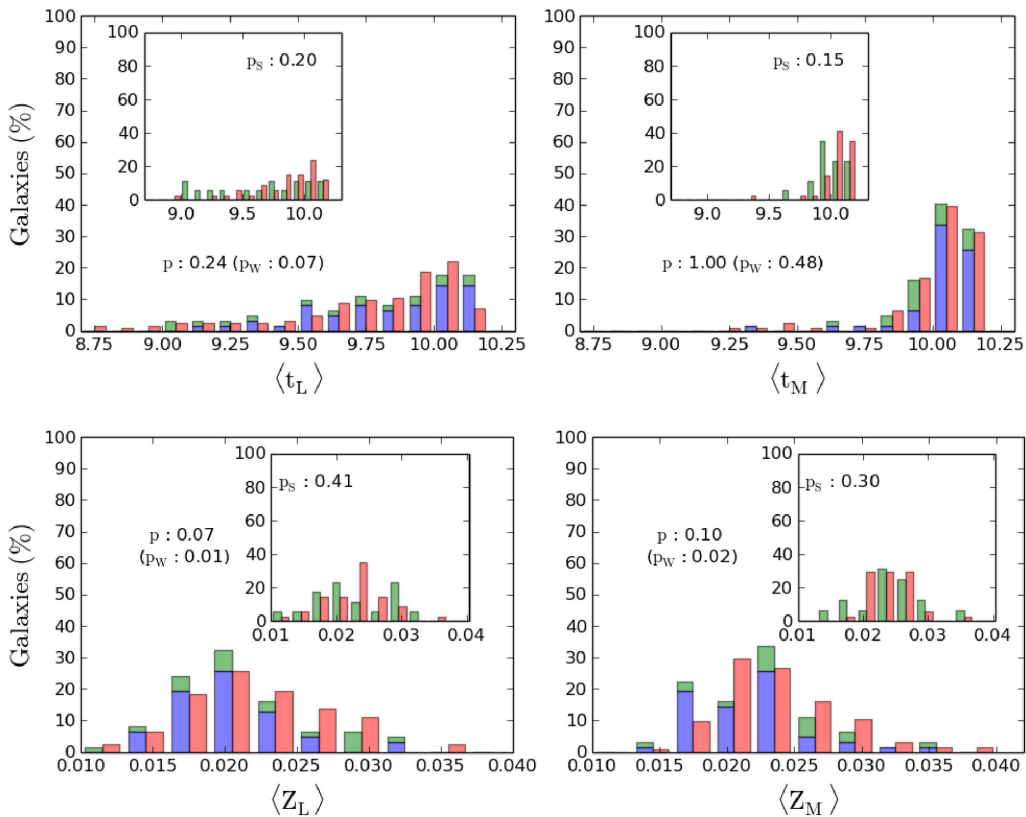


**Figure 8.** Histograms showing the distributions of the mean ages (top panel) and metallicities (bottom panel), for the AGN (blue for weak and green for strong) and control sample (red). In the insert of each panel, we plot the histograms comparing the strong AGN (green) with its respective control sample (red). For each histogram, the  $p$ -value of the A-D test is given.  $p_w$  refers to the weak AGN,  $p_s$  refer to the strong AGN and  $p$  to the combined sample of strong and weak AGNs.

where the limit between strong and weak AGN is shown as a vertical dashed line. We have performed a linear regression between  $\Delta x$  and  $L[\text{O III}]$  for each age bin and the best fit is shown as a continuous line in the different panels of the figure.

There is an obvious correlation between  $\Delta x$  and  $L[\text{O III}]$  for some age bins. This is the case for  $x_{yo}$ : a Spearman test gives a correlation coefficient of 0.53 with a  $p$ -value of 0.0039. For the oldest age bin,  $x_o$ , there is an anticorrelation between  $\Delta x$  and  $L[\text{O III}]$ , with a Spearman correlation coefficient of  $-0.30$  and a statistical significance higher than  $3\sigma$ . Another result from this figure is that an AGN host can have a higher or lower contribution of a given age bin, depending on the AGN luminosity. In the bin  $x_o$ , for example, the contribution is higher in lower-luminosity AGN than in their ‘control partners’, while the opposite is true for luminous AGN, which present a smaller contribution of this age bin than their respective control galaxies. A similar behaviour can be seen in the bin  $x_{yo}$ : the relative contribution of this age bin for low-luminosity AGN is smaller, but for high-luminosity AGN is higher.

We have also explored how the differences  $\Delta\langle t \rangle$  in the (light-weighted and mass-weighted) logarithmic mean stellar age between AGN and control sample (which we will refer to as ‘differential age’) depends on the AGN luminosity. The result is shown in Fig. 10. It is evident that  $\Delta\langle t \rangle$  and  $L[\text{O III}]$  show an inverse correlation, especially for the light-weighted mean ages. The resulting Spearman correlation coefficient is  $-0.27$ , with a statistical significance higher than  $2\sigma$ . The overall results agree with those obtained in Fig. 9 and indicate that luminous AGN are younger, on average, than inactive galaxies with similar properties. Low-luminosity

AGN, in contrast, present older stellar populations than the control sample. Note, also, that the separation between these two AGN categories is very close to the threshold  $L[\text{O III}] = 3.8 \times 10^{40} \text{ erg s}^{-1}$  (the vertical dashed line), which marks the separation between our weak and strong AGN samples. These results agree with those from Kauffmann et al. (2003), which showed that, at fixed stellar mass density, luminous AGNs present younger stellar populations than inactive galaxies, while low-luminosity AGNs are older, on average.

In order to translate the above results in numbers, we show in Table 3 the mean ages of the AGN and their control galaxies separated in bins of AGN luminosity. Although some bins still have a few galaxies (that we hope to increase as the survey progresses), and the dispersion in the mean age values is large, Table 3 shows a steady decrease of the mean age of the host galaxy as the AGN luminosity increases, besides showing also the trend discussed regarding the difference in age between the AGN hosts and controls.

#### 4.3 Results from MaNGA data

As pointed out in the Introduction, we are applying the same methodology described above to study the resolved stellar population in the MaNGA data (Mallmann et al., in preparation, hereafter Paper II). The SDSS-III spectra correspond to a region of radius 1.5 arcsec around the nucleus – corresponding to a range of radii from  $\approx 1$  to 3 kpc at the distance of the galaxies. This is similar to the area covered by the central pixel of the MaNGA array. Thus we have checked, for a subsample of representative galaxies, whether

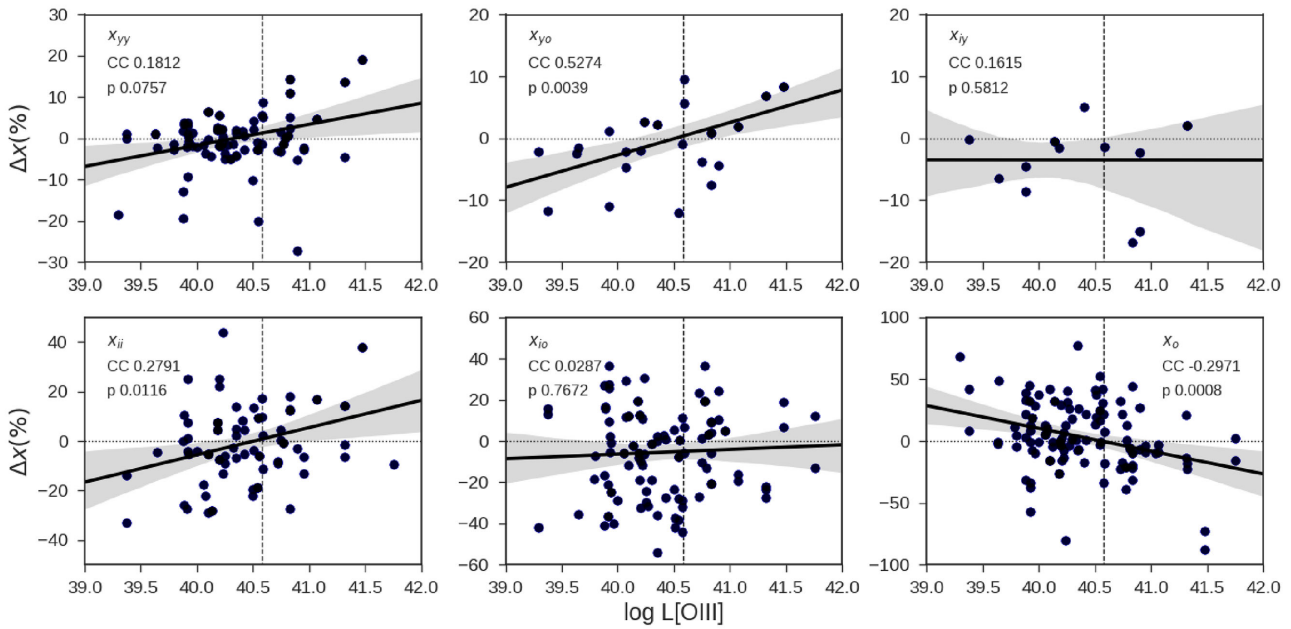


**Figure 9.** Differences  $\Delta x$  in the fractional contribution of each age bin to the total light at rest frame 5700 Å between AGNs and control galaxies, as a function of the AGN [OIII] luminosity. Each circle correspond to a pair AGN/control object. We have excluded pairs for which the fractional contributions are both zero. The best-fitting linear regression and its uncertainties are shown with a thick line and a shaded area, respectively. The Spearman correlation coefficient and the p-value of the test are given in each pannel. The [OIII] luminosity that separates strong and weak AGN is shown as a vertical dashed line. The locus  $\Delta x = 0$  is shown by a dotted line.

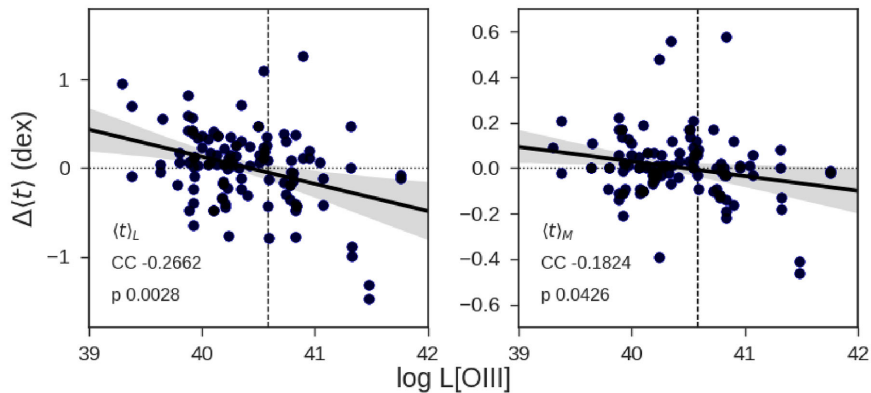


**Figure 10.** Light-weighted (left-hand panel) and mass-weighted (right-hand panel) differences  $\Delta(t)$  in the mean stellar age between AGNs and control galaxies, as a function of the AGN [OIII] luminosity. The symbols are the same as in Fig. 9.

**Table 3.** Average of global parameters  $\langle t_L \rangle$  and  $\langle t_M \rangle$ , for the AGN and their control galaxies separated by luminosity.

$\log_{10} L[\text{OIII}]$ ( $\text{erg s}^{-1}$ )	N (AGN)	Sample	$\langle t \rangle_L$ $\log_{10}$ (yr)	$\Delta \langle t \rangle_L$ dex/yr)	$\langle t \rangle_M$ $\log_{10}$ (yr)	$\Delta \langle t \rangle_M$ dex/yr)
39.0–39.75	5	AGN	$9.89 \pm 0.16$	0.24	$10.07 \pm 0.03$	0.05
		control	$9.65 \pm 0.42$		$10.02 \pm 0.10$	
39.75–40.25	25	AGN	$9.81 \pm 0.30$	0.05	$10.00 \pm 0.17$	0.0
		control	$9.76 \pm 0.36$		$10.00 \pm 0.19$	
40.25–40.75	18	AGN	$9.81 \pm 0.27$	0.10	$10.05 \pm 0.06$	0.04
		control	$9.71 \pm 0.32$		$10.01 \pm 0.12$	
40.75–41.25	10	AGN	$9.66 \pm 0.35$	-0.08	$9.99 \pm 0.11$	-0.01
		control	$9.74 \pm 0.43$		$10.00 \pm 0.18$	
41.25 – 42.0	4	AGN	$9.43 \pm 0.64$	-0.55	$9.94 \pm 0.64$	-0.14
		control	$9.98 \pm 0.15$		$10.08 \pm 0.03$	

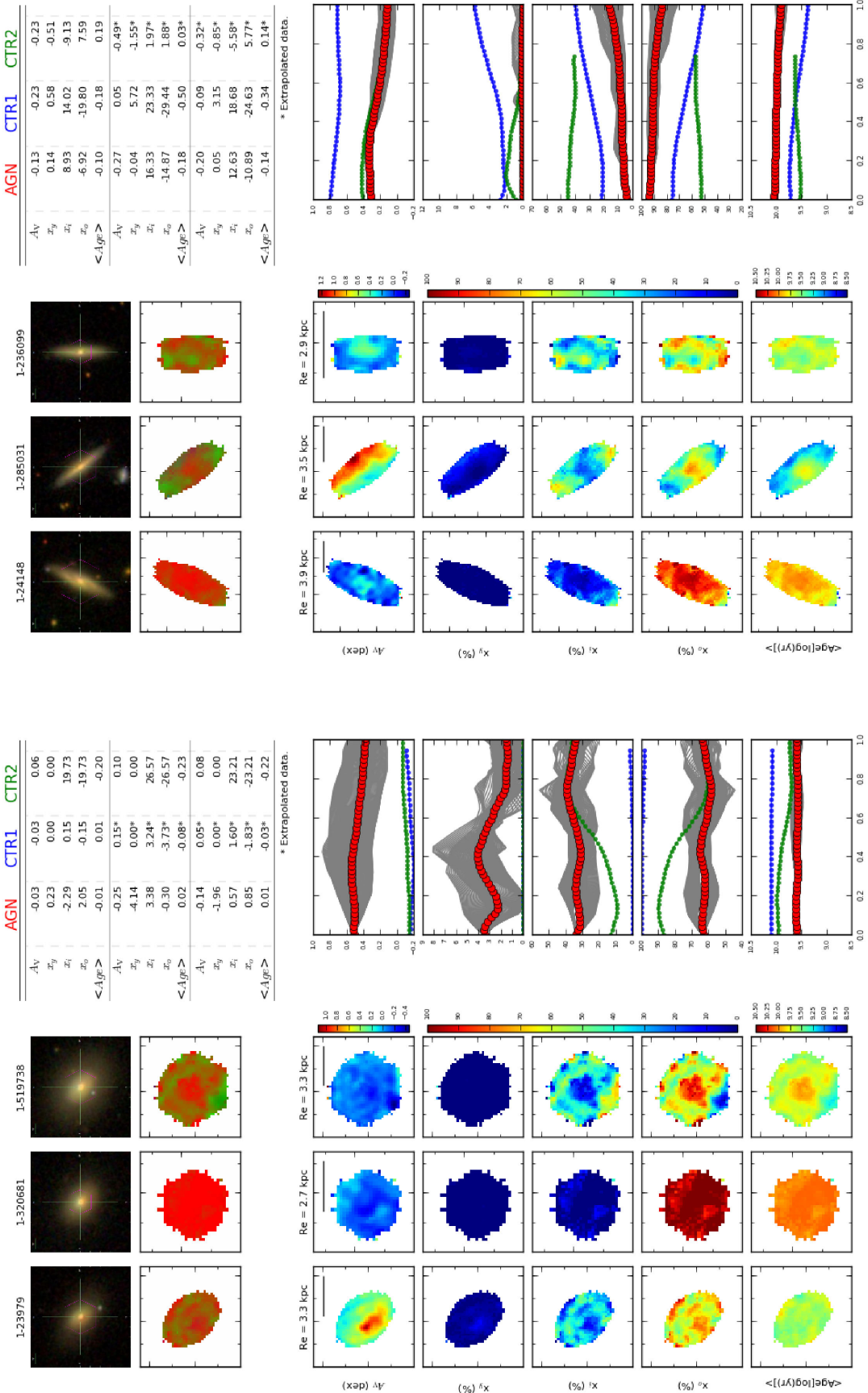


**Figure 11.** Comparison between the spatially resolved stellar population of an AGN (first column) and its two control galaxies (second and third columns). Top left-hand panel: two rows of panels, SDSS image of the galaxies (top) and RGB maps (bottom) showing the relative percent contribution of the young ( $<40$  Myr, blue), intermediate age (50 Myr–2 Gyr, green) and old ( $>2$  Gyr, red) stellar population. Top right-hand panel: table summarizing the average gradient values for the different properties calculated at three effective radius ranges (0.0–0.5, 0.5–1.0 and 0.0–1.0  $R_e$ ) using the mean profiles shown. Bottom panel: five rows of panels, from the top to bottom: visual extinction  $A_v$ , percent contribution of the young ( $x_y$ ), intermediate age ( $x_i$ ) and old ( $x_o$ ), and average age ( $<A_{Age}>$ ). Fourth column: mean profiles of the properties shown in the left figures, as a function of effective radius. Active galaxy in red, control galaxies in blue and green. Grey lines show the profiles of the active galaxy for each sector of  $35^\circ$  (see further explanations in the text). For display purposes, we used tick marks separated by 5 arcsec. The solid horizontal line in the  $A_v$  maps represent 5 kpc.

our synthesis result for the inner pixel was consistent with that obtained from the SDSS-III spectra. We concluded that the results were the same within the uncertainties, as expected.

The resolved synthesis (beyond the inner  $\sim 1.5$  arcsec) will be discussed in Paper II, and preliminary results are shown in Fig. 11 for two sets of AGN and control sample galaxies: the first set corresponds to an early-type host and the second to a late-type host. The area covered by the central fibre of the MaNGA array, at the mean distance of these galaxies, is around 1.5 kpc. In these figures, we have further collapsed the ages in three bins: young ( $x_y, t < 10$  Myr), intermediate age ( $x_i, 51$  Myr  $\leq t \leq 2$  Gyr) and old ( $x_o, t > 2$  Gyr). In the case of the early-type galaxy, it can be seen that the AGN host has (1) a stronger reddening over the whole galaxy than the two control galaxies, suggesting the presence of more gas in the AGN host galaxy; (2) a larger contribution of the young component; (3) a larger contribution of the intermediate age component in the inner region and then it becomes similar to that of the second control galaxy (green) outwards; (4) a smaller contribution of the old component everywhere in the galaxy, being approximately the same as that of the second control galaxy in the outer part of the galaxy; and (5) an average age that is smaller than those of the two controls in the inner region and similar to that of the second control in the outer parts of the galaxy.

In the case of the late-type galaxy, the AGN host has (1) a similar reddening to that of the second control galaxy, being smaller than that of the first control galaxy; (2) a lower contribution of the young component than the first control everywhere, a lower contribution than the second control in the inner parts but similar outwards; (3) a smaller contribution of the intermediate-age component to that of the controls everywhere; and (4) a larger contribution of the old component everywhere and a (5) a larger mean age everywhere.

In summary, we have find a difference in the resolved stellar population properties between the AGN and control galaxies for the early-type AGN host and found no difference in the late-type AGN host. We note that the difference between the stellar population of the early-type AGN host and those of the control galaxies is not restricted to the nucleus, but is observed out to about 0.6 effective radii. In Paper II, we will present the results for the whole sample, as well as a statistical analysis to investigate the difference between the AGN and control sample in terms of their resolved stellar population properties.

## 5 CONCLUSIONS

We have characterized the first 62 AGN host galaxies observed in the MaNGA survey, defining and also characterizing a control sample of 2 galaxies for each AGN, matched according to global properties of the host galaxy such as stellar mass, distance, inclination and galaxy type. We compare the stellar population properties of the two samples within the inner  $\sim 1.5$  arcsec radius around the nucleus (1–3 kpc at their typical distances) using stellar population synthesis of their SDSS-III spectra and the central spectrum of the MaNGA array, which are identical within the uncertainties. This study will be followed by the study of the resolved stellar population (Paper II) and gas properties (Paper III) over the whole region of the galaxy covered by the MaNGA observations.

The main results of this paper are as follows:

(i) The stellar mass, redshift,  $r$ -band absolute magnitude, concentration and asymmetry distributions of the AGN hosts are well matched by those of the control sample. The galaxy morphologies are similar, with  $\approx 65$  per cent spiral and  $\approx 33$  per cent spheroidal

galaxies. The luminosity  $L(\text{[O III]})$ , however, is markedly lower ( $\sim 1.4$  dex) for the control sample galaxies, as expected.

(ii) Only 17 AGNs of our sample have AGN luminosities larger than  $L(\text{[O III]}) > 3.8 \times 10^{40}$  erg s $^{-1}$  (which we call strong AGN). Of these, three show signs of disturbed morphology, a much higher proportion than among the remaining, weak AGN.

(iii) The stellar population of the 45 weak AGNs ( $L(\text{[O III]}) < 3.8 \times 10^{40}$  erg s $^{-1}$ ) is dominated (down to 60 per cent contribution to the light at 5700 Å) by old stars (with ages  $4.0 \leq t \leq 13.1 \times 10^9$  yr) with a smaller contribution (up to 40 per cent) of intermediate age stars ( $0.64 \leq t \leq 2.5 \times 10^9$  yr) and almost no contribution of younger stars; similar results are observed for the control sample;

(iv) The strong AGN, on the other hand, show, on average, a larger contribution (of up to  $\approx 20$  per cent) of younger ( $\leq 5 \times 10^7$  yr) stars and a decreased contribution of the old stars relative to both the weak AGN and control sample;

(v) A correlation between the stellar population properties and the AGN luminosity, extending also to lower  $L(\text{[O III]})$  values, is found when pairing each AGN with its controls, via differential properties AGN-control, evidencing the importance in a careful selection of a control sample;

(vi) Via this pairing, we find a correlation between the differential contribution (AGN-control) of the stellar population age component  $x_{yo}$  ( $25\text{--}48 \times 10^6$  yr) and the AGN luminosity  $L(\text{[O III]})$ , and an inverse correlation between the differential contribution of the old age component  $x_o$  ( $4\text{--}13 \times 10^9$  yr) and  $L(\text{[O III]})$ ;

(vii) The pairing also reveals a trend in the mean differential age (AGN-control) and the AGN luminosity, in the sense that more luminous AGNs are younger than the control sample. There is also a trend for weak AGNs to be older than the control sample, while those with intermediate luminosity show similar ages to those of the control galaxies.

In summary, our results point to a difference between the stellar population of the AGN hosts and control sample that is correlated with the AGN luminosity: The most luminous the AGN, the younger is its stellar population in the inner kiloparsecs. This result supports the evolutionary scenario (Storchi-Bergmann *et al.* 2001; Davies *et al.* 2007) in which episodes of nuclear activity are preceded by episodes of star formation in the galaxy as both star formation and the nuclear activity feed on gas accretion towards the central regions of the galaxy.

In forthcoming papers, we will expand the present investigation to include more AGN as they become observed with MaNGA, studying also the spatially resolved properties of the stellar population (Paper II), the gas excitation (Paper III) and kinematics, as well as the environment of our AGN sample as compared with those of the control sample using the spatially resolved spectroscopic data from MaNGA.

## ACKNOWLEDGEMENTS

We would like to thank the support of the Instituto Nacional de Ciéncia e Tecnologia (INCT) e-Universe project (CNPq grant 465376/2014-2). RAR acknowledges support from FAPERGS (project no. 2366-2551/14-0) and CNPq (project no. 470090/2013-8 and 302683/2013-5). RR thanks to FAPERGS (16/2551-0000251-7) and CNPq for financial support.

Funding for the Sloan Digital Sky Survey IV has been provided by the Alfred P. Sloan Foundation and the Participating Institutions. SDSS-IV acknowledges support and resources from the

Center for High-Performance Computing at the University of Utah. The SDSS web site is [www.sdss.org](http://www.sdss.org). SDSS-IV is managed by the Astrophysical Research Consortium for the Participating Institutions of the SDSS Collaboration including the Brazilian Participation Group, the Carnegie Institution for Science, Carnegie Mellon University, the Chilean Participation Group, Harvard-Smithsonian Center for Astrophysics, Instituto de Astrofísica de Canarias, The Johns Hopkins University, Kavli Institute for the Physics and Mathematics of the Universe (IPMU) / University of Tokyo, Lawrence Berkeley National Laboratory, Leibniz Institut für Astrofysik Potsdam (AIP), Max-Planck-Institut für Astrophysik (MPA Garching), Max-Planck-Institut für Extraterrestrische Physik (MPE), Max-Planck-Institut für Astronomie (MPIA Heidelberg), National Astronomical Observatory of China, New Mexico State University, New York University, The Ohio State University, Pennsylvania State University, Shanghai Astronomical Observatory, United Kingdom Participation Group, Universidad Nacional Autónoma de México, University of Arizona, University of Colorado Boulder, University of Portsmouth, University of Utah, University of Washington, University of Wisconsin, Vanderbilt University and Yale University.

## REFERENCES

- Alam S. et al., 2015, *ApJS*, 219, 12  
 Baldwin J. A., Phillips M. M., Terlevich R., 1981, *PASP*, 93, 5  
 Balogh M. L., Morris S. L., Yee H. K. C., Carlberg R. G., Ellingson E., 1999, *ApJ*, 527, 54  
 Bower R. G., Benson A. J., Malbon R., Helly J. C., Frenk C. S., Baugh C. M., Cole S., Lacey C. G., 2006, *MNRAS*, 370, 645  
 Bruzual G., Charlot S., 2003, *MNRAS*, 344, 1000  
 Bundy K. et al., 2015, *ApJ*, 798, 7  
 Cardelli J. A., Clayton G. C., Mathis J. S., 1989, *IAUS*, 135, 5  
 Cardoso L. S. M., Gomes J. M., Papaderos P., 2017, *A&A*, 604, A99  
 Cid Fernandes R., Sodré L., Schmitt H. R., Leão J. R. S., 2001, *MNRAS*, 325, 60  
 Cid Fernandes R., Gu Q., Melnick J., Terlevich E., Terlevich R., Kunth D., Rodrigues Lacerda R., Joguet B., 2004, *MNRAS*, 355, 273  
 Cid Fernandes R., Mateus A., Sodré L., Stasińska G., Gomes J. M., 2005, *MNRAS*, 358, 363  
 Cid Fernandes R., Stasińska G., Schlickmann M. S., Mateus A., Vale Asari N., Schoenell W., Sodré L., 2010, *MNRAS*, 403, 103  
 Cid Fernandes R. J. Terlevich R., 1995, *MNRAS*, 272, 423  
 Conroy C., Gunn J. E., White M., 2009, *ApJ*, 699, 486  
 Dametto N. Z., Riffel R., Pastoriza M. G., Rodríguez-Ardila A., Hernandez-Jimenez J. A., Carvalho E. A., 2014, *MNRAS*, 443, 1754  
 Davies R., Müller Sánchez F., Genzel R., Tacconi L. J., Hicks E. K. S., Friedrich S., Sternberg A., 2007, *ApJ*, 671, 1388  
 Di Matteo T., Springel V., Hernquist L., 2005, *Nature*, 433, 604  
 Diamond-Stanic A. M., Rieke G. H., 2012, *ApJ*, 746, 168  
 Drory N. et al., 2015, *AJ*, 149, 77  
 Dubois Y., Gavazzi R., Peirani S., Silk J., 2013, *MNRAS*, 433, 3297  
 Eisenstein D. J. et al., 2011, *AJ*, 142, 72  
 Esquej P. et al., 2014, *ApJ*, 780, 86  
 Fabian A., 2012, *ARA&A*, 50, 455  
 Ferrarese L., Ford H. C., 2005, *Space Sci. Rev.*, 116, 523  
 Ferrarese L., Merritt D., 2000, *ApJ*, 547, 140  
 Fukugita M., Ichikawa T., Gunn J. E., Doi M., Shimasaku K., Schneider D. P., 1996, *AJ*, 111, 1748  
 Gebhardt K. et al., 2000, *ApJ*, 539, 13  
 Gunn J. E. et al., 2006, *AJ*, 131, 2332  
 Heckman T. M., González-Delgado R., Leitherer C., Meurer G. R., Krolik J., Wilson A. S., Koratkar A., Kinney A., 1997, *ApJ*, 482, 114  
 Hickox R. C., Mullaney J. R., Alexander D. M., Chen C.-T. J., Civano F. M., Goulding A. D., Hainline K. N., 2014, *ApJ*, 782, 9  
 Ishibashi W., Fabian A. C., 2014, *MNRAS*, 441, 1474  
 Jahnke K., Macciò A. V., 2011, *ApJ*, 734, 92  
 Kauffmann G., Heckman T. M., Tremonti C. et al., 2003, *MNRAS*, 346, 1055  
 Kewley L. J., Dopita M. A., Sutherland R. S., Heisler C. A., Trevena J., 2001, *ApJ*, 556, 121  
 Kormendy J., Ho L. C., 2013, *ARA&A*, 51, 511  
 Koski A. T., 1978, *ApJ*, 223, 56  
 Law D. R. et al., 2015, *AJ*, 150, 19  
 Law D. R. et al., 2016, *AJ*, 152, 83  
 Lintott C. et al., 2011, *MNRAS*, 410, 166  
 Mazzalay X., Rodríguez-Ardila A., Komossa S., 2010, *MNRAS*, 405, 1315  
 Menanteau F., Ford H. C., Motta V., Benítez N., Martel A. R., Blakeslee J. P., Infante L., 2005, *AJ*, 131, 208  
 Müller-Sánchez F., Prieto M. A., Hicks E. K. S., Vives-Arias H., Davies R. I., Malkan M., Tacconi L. J., Genzel R., 2011, *ApJ*, 739, 69  
 Nemmen R., Bower R., Babul A., Storchi-Bergmann T., 2007, *MNRAS*, 377, 1652  
 Norman C., Scoville N., 1988, *ApJ*, 332, 124  
 Peng C. Y., 2007, *ApJ*, 671, 1098  
 Perry J. J., Dyson J. E., 1985, *MNRAS*, 213, 665  
 Pontzen A., Tremmel M., Roth N., Peiris H. V., Saintonge A., Volonteri M., Quinn T., Governato F., 2017, *MNRAS*, 465, 547  
 Riffel R., Pastoriza M. G., Rodríguez-Ardila A., Bonatto C., 2009, *MNRAS*, 400, 273  
 Rodríguez-Ardila A., Prieto M. A., Portilla J. G., Tejeiro J. M., 2011, *ApJ*, 743, 100  
 Smee S. A. et al., 2013, *AJ*, 126, 32  
 Somerville R. S., Hopkins P. F., Cox T. J., Robertson B. E., Hernquist L., 2008, *MNRAS*, 391, 481  
 Springel V., Di Matteo T., Hernquist L., 2005, *ApJ*, 620, 79  
 Storchi-Bergmann T., Raimann D., Bica E. L. D., Fraquelli H. A., 2000, *ApJ*, 544, 747  
 Storchi-Bergmann T., González Delgado R. M., Schmitt H. R., Cid Fernandes R., Heckman T., 2001, *ApJ*, 559, 147  
 Terlevich R., Melnick J., 1985, *MNRAS*, 213, 841  
 Terrazas B. A., Bell E. F., Henriques B. M. B., White S. D. M., Cattaneo A., Woo J., 2016, *ApJ*, 830, L12  
 Thomas D. et al., 2013, *MNRAS*, 431, 1383  
 Wild V., Heckman T., Charlot S., 2010, *MNRAS*, 405, 933  
 Worthey G., 1994, *ApJS*, 95, 107  
 Xie F., Yuan F., Ho L. C., 2017, *ApJ*, 844, 42  
 Yan R. et al., 2016, *AJ*, 151, 8  
 York D. G. et al., 2000, *AJ*, 120, 1579  
 Zakamska N., Greene J., 2014, *MNRAS*, 442, 784

## SUPPORTING INFORMATION

Supplementary data are available at [MNRA](http://mnras.oxfordjournals.org)s online.

### **appendix.pdf**

Please note: Oxford University Press is not responsible for the content or functionality of any supporting materials supplied by the authors. Any queries (other than missing material) should be directed to the corresponding author for the article.

## APPENDIX A: DETAILED RESULTS FROM THE STELLAR POPULATION SYNTHESIS

**Table A1.** Synthesis results for AGN in MaNGA MPL5. (1) galaxy identification in the MaNGA survey; (2) flux contribution of the FC; (3)–(8): percentual of the flux corresponding to each of the six age bins defined in Section 3.1; (9)–(14): mass contribution of the same age bins; (15) visual extinction in magnitudes; (16)–(17): light and mass weighted mean stellar age; (18)–(19): light and mass weighted mean stellar metallicity; and (20): mean relative deviation between the fit and the galaxy spectrum.

mangaID (1)	FC (2)	xyy (3)	xyo (4)	xIy (5)	xII (6)	xIo (7)	xo (8)	myy (9)	myo (10)	mIy (11)	mII (12)	mIo (13)	mo (14)	$A_V$ (15)	$\langle t_L \rangle$ (16)	$\langle t_M \rangle$ (17)	$\langle Z_L \rangle$ (18)	$\langle Z_M \rangle$ (19)	Adev (20)
1-109056	3.38	4.25	0.00	0.00	13.65	0.00	76.37	0.07	0.00	0.00	2.54	0.00	97.39	0.14	9.75	10.07	0.01957	0.01864	2.90
1-121532	4.42	4.63	1.96	0.00	17.07	0.00	71.26	0.08	0.06	0.00	2.85	0.00	97.01	0.50	9.70	10.08	0.01965	0.02309	5.40
1-135044	7.63	0.00	0.00	0.00	0.00	4.03	85.79	0.00	0.00	0.00	0.00	1.22	98.78	0.14	9.92	10.02	0.01727	0.01877	2.58
1-135285	0.04	0.00	0.00	0.00	0.00	0.00	97.15	0.00	0.00	0.00	0.00	100.00	0.17	10.00	10.07	0.01475	0.01761	2.76	
1-135641	4.24	2.54	0.00	0.00	9.54	0.00	80.90	0.04	0.00	0.00	1.34	0.00	98.62	0.91	9.88	10.10	0.01857	0.02283	2.45
1-137883	0.00	10.51	9.50	0.00	2.28	40.64	34.75	0.16	0.31	0.00	0.62	14.82	84.10	1.58	9.12	9.98	0.01446	0.02749	3.28
1-148068	3.61	0.00	0.00	0.00	0.00	13.03	79.76	0.00	0.00	0.00	0.00	3.14	96.86	0.26	9.98	10.08	0.0246	0.02462	3.86
1-149211	12.13	0.00	0.00	0.00	0.00	49.60	36.05	0.00	0.00	0.00	0.00	27.91	72.09	0.18	9.55	9.83	0.03361	0.02262	3.96
1-163831	3.93	1.36	0.00	0.00	0.00	9.75	81.93	0.02	0.00	0.00	0.00	2.32	97.66	0.24	9.90	10.06	0.01905	0.02243	3.05
1-166919	4.98	1.72	0.00	0.00	4.70	13.33	72.58	0.03	0.00	0.00	0.83	2.28	96.86	0.23	9.84	10.08	0.01942	0.01996	2.39
1-167688	3.56	3.80	1.15	0.00	34.40	25.77	30.48	0.12	0.05	0.00	11.29	10.72	77.83	0.15	9.27	9.87	0.01905	0.02004	2.16
1-173958	7.42	16.37	0.85	0.00	19.93	20.47	33.50	0.28	0.02	0.00	6.16	8.44	85.11	0.62	9.05	9.96	0.02302	0.02879	3.47
1-198153	0.00	1.69	0.00	0.00	0.00	0.00	96.20	0.02	0.00	0.00	0.00	99.98	0.41	10.04	10.11	0.01435	0.01666	2.63	
1-198182	4.95	0.00	0.00	0.00	0.00	0.00	92.01	0.00	0.00	0.00	0.00	100.00	-0.06	10.11	10.11	0.02216	0.02484	1.87	
1-201561	4.08	0.00	0.00	0.00	0.00	0.00	91.27	0.00	0.00	0.00	0.00	100.00	-0.03	10.11	10.11	0.02364	0.02726	3.79	
1-209980	17.08	0.00	0.00	0.00	0.00	81.52	0.00	0.00	0.00	0.00	100.00	0.03	10.11	10.11	0.01671	0.01897	2.00		
1-210646	3.37	4.78	0.00	0.00	0.00	18.12	71.64	0.11	0.00	0.00	0.00	7.47	92.42	0.45	9.54	9.92	0.01784	0.01777	4.77
1-211311	4.34	0.00	0.00	0.00	0.00	6.11	85.90	0.00	0.00	0.00	0.00	1.67	98.33	-0.02	9.97	10.05	0.0176	0.01795	2.45
1-217050	1.26	1.12	0.00	0.00	0.00	0.00	94.71	0.01	0.00	0.00	0.00	99.99	0.00	10.07	10.11	0.02053	0.0238	1.64	
1-22301	7.65	2.15	0.00	0.00	0.00	11.75	74.97	0.02	0.00	0.00	0.00	2.40	97.58	0.18	9.89	10.08	0.01894	0.0237	2.59
1-229010	2.42	0.00	0.00	0.00	0.00	93.18	0.00	0.00	0.00	0.00	100.00	-0.10	10.06	10.09	0.01987	0.02236	1.58		
1-234618	0.00	3.91	0.00	0.00	2.10	2.29	88.13	0.06	0.00	0.00	0.42	0.61	98.92	0.78	9.78	10.04	0.01416	0.01897	5.22
1-23979	1.60	5.66	0.00	0.00	25.10	0.00	65.77	0.10	0.00	0.00	5.11	0.00	94.79	0.54	9.57	10.05	0.02522	0.02186	2.63
1-24148	8.51	0.00	0.00	0.00	0.00	5.64	83.67	0.00	0.00	0.00	0.00	1.32	98.68	0.26	10.05	10.10	0.02232	0.02433	2.28
1-248389	0.00	3.03	0.00	5.12	11.80	38.14	39.81	0.07	0.00	0.51	2.83	9.95	86.65	0.45	9.41	9.98	0.01949	0.03118	1.99
1-248420	9.48	0.00	0.00	0.00	0.00	87.58	0.00	0.00	0.00	0.00	100.00	0.18	10.09	10.09	0.01447	0.01568	3.07		
1-25554	0.00	3.36	0.00	0.00	0.00	34.06	59.68	0.06	0.00	0.00	0.00	9.95	89.99	0.32	9.68	10.03	0.01957	0.01902	2.66
1-256446	1.36	0.00	0.00	0.00	0.00	0.00	94.32	0.00	0.00	0.00	0.00	100.00	-0.04	10.11	10.11	0.01799	0.01905	2.96	
1-25725	11.87	1.28	0.00	0.00	0.00	0.00	85.18	0.00	0.00	0.00	0.00	100.00	0.17	10.06	10.11	0.03177	0.03529	3.20	
1-258599	9.11	13.62	6.83	2.11	14.44	12.09	39.36	0.20	0.22	0.29	5.15	5.75	88.39	0.62	9.01	9.92	0.02181	0.03697	3.19
1-258774	1.79	4.81	0.00	0.00	10.70	27.62	51.72	0.04	0.00	0.00	2.43	8.96	88.57	0.41	9.56	10.00	0.02701	0.0221	2.02
1-259142	3.62	0.00	0.00	0.00	0.00	92.92	0.00	0.00	0.00	0.00	100.00	-0.00	10.11	10.11	0.02069	0.02218	2.20		
1-269632	4.49	18.98	8.39	0.00	37.97	18.93	9.14	0.51	0.50	0.00	24.60	16.72	57.68	0.65	8.61	9.65	0.02923	0.04336	3.64
1-277552	0.00	5.96	0.00	0.00	10.34	0.00	79.53	0.10	0.00	0.00	1.55	0.00	98.35	0.64	9.71	10.04	0.01871	0.0161	4.72
1-279073	5.45	0.00	0.00	0.00	0.00	0.00	90.99	0.00	0.00	0.00	0.00	100.00	-0.13	10.11	10.11	0.02647	0.02996	2.19	
1-279147	5.08	5.23	0.00	0.00	18.03	37.63	31.30	0.09	0.00	0.00	6.78	20.13	73.00	0.56	9.25	9.81	0.03086	0.0274	2.75
1-279666	0.00	3.12	0.00	0.00	7.44	36.36	49.72	0.07	0.00	0.00	1.90	11.48	86.55	0.26	9.54	9.93	0.01997	0.02375	2.44
1-279676	0.00	1.99	0.00	0.00	7.49	19.39	69.58	0.03	0.00	0.00	1.48	5.64	92.84	0.32	9.75	10.04	0.02402	0.01853	3.36
1-321739	0.00	2.74	2.19	0.00	15.14	9.42	68.96	0.03	0.05	0.00	2.80	2.45	94.67	1.08	9.69	10.06	0.02029	0.02271	2.96
1-338922	0.00	14.28	0.00	0.00	32.92	51.74	0.16	0.00	0.00	0.00	17.42	82.41	0.48	9.33	9.92	0.01828	0.02573	6.43	
1-339094	7.03	0.00	0.00	0.00	7.66	23.20	59.24	0.00	0.00	0.00	1.90	8.37	89.73	0.29	9.72	9.98	0.02492	0.01955	1.86
1-339163	5.93	0.00	0.00	0.00	0.00	92.23	0.00	0.00	0.00	0.00	100.00	0.00	10.08	10.10	0.01674	0.02013	1.94		
1-351790	5.46	2.08	2.60	0.00	43.77	30.59	13.55	0.10	0.16	0.00	22.41	22.30	55.03	0.41	9.16	9.68	0.02216	0.02057	2.20
1-37036	0.00	1.59	0.00	0.00	2.20	93.97	0.02	0.00	0.00	0.00	0.27	99.71	0.22	10.03	10.11	0.01886	0.02278	2.11	
1-373161	4.82	0.00	0.00	0.00	0.00	91.52	0.00	0.00	0.00	0.00	100.00	0.16	10.11	10.11	0.02199	0.02394	2.64		
1-44303	11.93	1.62	0.00	0.00	4.50	12.94	68.16	0.03	0.00	0.00	1.04	7.58	91.34	0.35	9.82	10.02	0.01984	0.0175	3.13
1-44379	12.87	0.00	0.00	0.00	0.92	5.16	78.93	0.00	0.00	0.00	0.18	0.87	98.95	0.17	10.04	10.10	0.0124	0.01433	2.08
1-460812	1.82	1.94	0.00	0.00	0.00	3.39	89.71	0.02	0.00	0.00	0.00	0.78	99.20	0.73	9.92	10.08	0.01719	0.0231	3.26
1-48116	0.00	6.62	0.00	0.00	17.37	11.44	62.82	0.12	0.00	0.00	3.80	3.19	92.89	0.56	9.54	10.04	0.0195	0.01876	1.92
1-491229	6.52	0.00	0.00	0.00	0.00	91.23	0.00	0.00	0.00	0.00	0.00	100.00	0.00	10.11	10.11	0.02215	0.02543	2.03	
1-519742	2.59	0.00	0.00	0.00	0.00	71.52	23.59	0.00	0.00	0.00	0.00	64.99	35.01	0.26	9.32	9.37	0.033	0.02945	5.97
1-542318	2.68	0.00	0.00	0.00	0.00	12.83	82.73	0.00	0.00	0.00	0.00	4.09	95.91	0.30	9.99	10.08	0.01777	0.01604	4.66
1-558912	11.71	0.00	0.00	0.00	0.00	12.28</td													

**Table A1.** – *continued*

mangaID (1)	FC (2)	xxy (3)	xyo (4)	xIy (5)	xII (6)	xIo (7)	xo (8)	myy (9)	myo (10)	mIy (11)	mII (12)	mIo (13)	mo (14)	$A_V$ (15)	$\langle t_L \rangle$ (16)	$\langle t_M \rangle$ (17)	$\langle Z_L \rangle$ (18)	$\langle Z_M \rangle$ (19)	Adev (20)
1-604761	2.77	0.00	0.00	0.00	0.00	0.00	93.55	0.00	0.00	0.00	0.00	0.00	100.00	0.11	10.11	10.11	0.018 29	0.020 73	2.67
1-72322	16.54	0.00	0.00	0.00	0.00	0.00	80.48	0.00	0.00	0.00	0.00	0.00	100.00	0.19	10.11	10.11	0.028 89	0.030 89	3.34
1-91016	0.00	4.63	0.00	0.00	0.00	56.04	37.49	0.11	0.00	0.00	0.00	29.37	70.52	0.70	9.37	9.75	0.019 53	0.023 14	4.36
1-92866	0.00	1.29	0.00	0.00	0.00	0.00	95.45	0.02	0.00	0.00	0.00	99.98	0.32	10.02	10.10	0.019 64	0.022 29	2.97	
1-94604	9.35	0.00	0.00	0.00	0.00	13.18	74.83	0.00	0.00	0.00	0.00	7.74	92.26	−0.01	9.82	9.97	0.020 21	0.02463	3.16
1-94784	2.90	0.00	0.00	0.00	0.00	36.69	55.88	0.00	0.00	0.00	0.00	12.99	87.01	0.24	9.68	9.95	0.029 94	0.02287	2.13
1-95092	0.00	3.74	0.00	0.00	11.56	0.00	82.36	0.03	0.00	0.00	2.06	0.00	97.91	0.39	9.75	10.06	0.020 84	0.0195	2.03
1-95585	4.16	0.00	0.00	0.00	0.00	0.63	91.02	0.00	0.00	0.00	0.00	0.22	99.78	−0.02	10.11	10.11	0.022 65	0.02563	3.11
1-96075	2.81	6.57	0.00	0.00	0.00	16.27	71.05	0.06	0.00	0.00	0.00	5.30	94.63	0.38	9.63	10.01	0.016 34	0.01836	4.50

**Table A2.** Synthesis results for the control sample. The columns are the same as in Table A1.

mangaID (1)	FC (2)	xxy (3)	xyo (4)	xIy (5)	xII (6)	xIo (7)	xo (8)	myy (9)	myo (10)	mIy (11)	mII (12)	mIo (13)	mo (14)	$A_V$ (15)	$\langle t_L \rangle$ (16)	$\langle t_M \rangle$ (17)	$\langle Z_L \rangle$ (18)	$\langle Z_M \rangle$ (19)	Adev (20)
1-109493	2.97	0.00	0.00	0.00	0.00	0.00	91.99	0.00	0.00	0.00	0.00	0.00	100.00	−0.15	10.11	10.11	0.0219	0.023 06	3.52
1-114306	1.09	8.07	0.00	0.00	7.78	34.00	46.61	0.13	0.00	0.00	2.22	12.92	84.73	0.44	9.39	9.95	0.014 19	0.0174	4.47
1-121717	0.00	4.42	0.00	0.00	4.38	32.26	56.85	0.07	0.00	0.00	0.88	8.77	90.28	0.53	9.63	10.03	0.018 83	0.021 78	3.11
1-134239	0.00	0.00	0.00	0.00	14.05	82.24	0.00	0.00	0.00	0.00	3.52	96.48	0.11	9.91	10.06	0.022 97	0.021 96	3.03	
1-135371	0.00	2.66	0.00	0.00	14.05	0.00	82.30	0.02	0.00	0.00	2.41	0.00	97.57	0.65	9.84	10.09	0.021 58	0.020 76	2.76
1-135372	0.00	0.00	3.19	0.00	0.00	0.00	96.37	0.00	0.05	0.00	0.00	0.00	99.95	0.02	10.03	10.11	0.019 41	0.0215	1.69
1-135502	0.60	0.00	0.00	0.00	0.00	0.00	94.52	0.00	0.00	0.00	0.00	0.00	100.00	0.13	10.03	10.08	0.017 67	0.020 35	2.18
1-135625	12.87	2.50	12.97	0.00	33.15	18.44	17.30	0.10	0.60	0.00	15.10	11.27	72.93	0.35	8.97	9.82	0.030 15	0.038 99	1.75
1-135810	0.00	0.00	0.00	0.00	0.00	41.05	57.21	0.00	0.00	0.00	0.00	16.27	83.73	0.30	9.61	9.89	0.028 52	0.022 37	2.64
1-136125	0.00	0.00	0.00	0.00	0.00	36.16	60.24	0.00	0.00	0.00	0.00	13.23	86.77	0.29	9.66	9.93	0.027 61	0.0219	4.52
1-166691	0.59	1.18	0.00	0.00	0.00	7.98	86.24	0.01	0.00	0.00	1.53	98.46	−0.14	10.00	10.10	0.022 01	0.025 57	3.00	
1-166947	3.68	0.00	0.00	0.00	0.00	0.00	92.37	0.00	0.00	0.00	0.00	0.00	100.00	−0.10	10.11	10.11	0.021 98	0.025 28	3.27
1-167334	0.00	3.03	0.00	0.00	56.89	36.57	1.18	0.11	0.00	0.00	49.04	42.99	7.86	0.55	9.04	9.20	0.036 21	0.034 18	1.65
1-177493	3.34	0.00	0.00	0.00	0.00	19.37	74.21	0.00	0.00	0.00	0.00	5.77	94.23	0.03	9.82	10.02	0.023 38	0.021 86	2.30
1-178838	12.76	0.00	0.00	0.00	3.31	17.56	62.46	0.00	0.00	0.00	0.62	4.47	94.91	−0.12	9.91	10.07	0.022 77	0.024 85	1.94
1-210173	5.84	0.00	0.00	0.00	2.29	31.23	55.48	0.00	0.00	0.00	0.33	10.10	89.57	0.24	9.74	10.00	0.0307	0.024 89	4.72
1-210593	0.00	0.00	0.00	0.00	6.32	0.00	91.27	0.00	0.00	0.00	1.07	0.00	98.93	0.28	9.91	10.05	0.0209	0.025 03	3.43
1-210614	0.00	1.24	0.00	0.00	0.00	0.00	94.97	0.01	0.00	0.00	0.00	0.00	99.98	0.09	10.06	10.11	0.020 04	0.022 73	2.48
1-210700	0.00	0.00	0.00	0.00	0.00	0.00	96.81	0.00	0.00	0.00	0.00	0.00	100.00	0.16	10.09	10.11	0.023 69	0.02721	5.73
1-210784	0.00	2.87	0.00	0.00	1.19	4.69	88.16	0.03	0.00	0.00	0.11	0.56	99.29	0.11	9.93	10.11	0.023 79	0.028 71	2.34
1-210962	0.00	1.41	0.00	0.00	5.66	8.40	81.53	0.02	0.00	0.00	0.89	1.76	97.33	0.15	9.92	10.09	0.020 33	0.021 74	1.64
1-211063	0.00	1.39	0.00	0.00	0.00	18.78	75.78	0.02	0.00	0.00	0.00	4.88	95.10	0.28	9.87	10.07	0.022 86	0.0192	2.32
1-211074	0.00	1.86	0.00	0.00	0.00	0.00	94.99	0.02	0.00	0.00	0.00	0.00	99.97	0.13	10.03	10.11	0.016 27	0.019 25	2.31
1-211079	0.00	0.00	0.00	0.00	5.97	0.00	92.39	0.00	0.00	0.00	0.59	0.00	99.41	0.03	10.03	10.10	0.020 51	0.025 51	1.93
1-211082	0.00	2.26	0.00	0.00	7.17	0.00	88.14	0.02	0.00	0.00	0.99	0.00	98.98	0.23	9.93	10.10	0.025 93	0.026 56	2.23
1-211100	0.00	1.46	0.00	0.00	0.00	95.79	0.02	0.00	0.00	0.00	0.00	0.00	99.98	0.04	10.05	10.11	0.01701	0.020 87	1.85
12-129446	1.31	4.33	0.00	0.00	0.01	40.22	51.60	0.08	0.00	0.00	0.00	12.01	87.91	0.33	9.59	10.01	0.020 53	0.022 09	2.84
1-216958	15.73	0.00	0.00	0.00	13.14	11.64	56.77	0.00	0.00	0.00	2.41	2.68	94.91	−0.08	9.77	10.05	0.026 46	0.027 07	1.60
1-218280	2.44	0.00	0.00	0.00	0.00	94.10	0.00	0.00	0.00	0.00	0.00	0.00	100.00	−0.14	10.11	10.11	0.0209	0.022 64	3.90
1-218427	2.55	0.00	0.00	0.00	0.00	94.12	0.00	0.00	0.00	0.00	0.00	0.00	100.00	−0.11	10.11	10.11	0.021 09	0.022 95	3.88
1-235398	0.00	5.31	0.00	0.00	0.00	17.60	74.64	0.08	0.00	0.00	0.00	5.14	94.78	0.81	9.64	10.01	0.0122	0.017 17	2.83
1-235587	0.00	1.71	0.00	0.00	6.86	0.00	87.88	0.02	0.00	0.00	1.13	0.00	98.85	−0.07	9.92	10.08	0.018 78	0.018 63	2.09
1-236099	3.82	0.00	0.00	0.00	22.14	28.78	42.23	0.00	0.00	0.00	6.66	12.26	81.08	0.23	9.57	9.93	0.027 43	0.019 06	2.65
1-94514	0.00	1.21	0.00	0.00	0.00	13.14	82.88	0.02	0.00	0.00	0.00	3.02	96.96	0.00	9.93	10.08	0.023 84	0.023 02	2.23
1-23731	0.00	1.71	0.00	0.00	2.08	91.90	0.02	0.00	0.00	0.00	0.45	99.52	0.02	9.93	10.07	0.017 92	0.022 15	2.01	
1-24099	0.00	0.91	0.00	0.00	16.33	0.00	80.68	0.01	0.00	0.00	2.69	0.00	97.30	0.02	9.88	10.08	0.0235	0.021 02	1.85
1-24246	6.94	0.00	0.00	0.00	30.11	0.95	58.39	0.00	0.00	0.00	6.37	0.17	93.46	0.18	9.71	10.03	0.0303	0.02221	6.43
1-24416	0.00	1.01	0.00	0.00	0.00	96.33	0.01	0.00	0.00	0.00	0.00	0.00	99.99	0.25	9.97	10.07	0.016 25	0.019 25	1.94
1-245774	0.00	1.23	0.00	0.00	5.15	33.24	57.82	0.02	0.00	0.00	1.06	9.54	89.38	0.07	9.72	10.02	0.021 76		

**Table A2.** – *continued*

mangaID (1)	FC (2)	xyy (3)	xyo (4)	xIy (5)	xII (6)	xIo (7)	xo (8)	myy (9)	myo (10)	mIy (11)	mII (12)	mIo (13)	mo (14)	$A_V$ (15)	$\langle t_L \rangle$ (16)	$\langle t_M \rangle$ (17)	$\langle Z_L \rangle$ (18)	$\langle Z_M \rangle$ (19)	Adev (20)		
1-251279	0.00	1.13	0.00	0.00	2.77	11.06	80.72	0.02	0.00	0.00	0.47	2.54	96.97	0.20	9.90	10.07	0.018	19	0.020	16	1.97
1-251871	6.57	0.00	0.00	0.00	0.00	0.00	89.51	0.00	0.00	0.00	0.00	0.00	100.00	0.06	10.11	10.11	0.021	68	0.022	98	5.18
1-256185	2.28	0.00	0.00	0.00	0.00	0.00	93.72	0.00	0.00	0.00	0.00	0.00	100.00	−0.05	10.07	10.10	0.020	02	0.022	11	1.72
1-256465	0.00	0.00	0.00	0.00	0.00	26.71	69.99	0.00	0.00	0.00	0.00	7.31	92.69	−0.10	9.85	10.04	0.026	69	0.022	67	2.58
1-25680	0.00	1.79	0.00	0.00	0.00	0.00	94.25	0.02	0.00	0.00	0.00	0.00	99.98	−0.13	10.01	10.09	0.028	93	0.033	44	2.76
1-25688	0.00	6.03	0.00	0.00	0.00	10.33	80.42	0.08	0.00	0.00	0.00	4.89	95.03	0.33	9.66	10.01	0.017	29	0.018	77	4.50
1-258455	0.00	1.27	0.00	0.00	0.00	0.00	95.81	0.02	0.00	0.00	0.00	0.00	99.98	0.26	9.98	10.08	0.0147	0	0.018	23	2.76
1-259650	0.00	1.69	0.00	0.00	0.00	0.00	94.87	0.02	0.00	0.00	0.00	0.00	99.98	0.23	10.04	10.11	0.020	89	0.023	88	1.96
1-264513	0.00	9.38	0.00	4.55	15.78	36.93	30.91	0.15	0.00	0.57	5.19	13.71	80.37	0.35	9.15	9.93	0.019	18	0.0212	1	1.82
1-270160	0.00	1.21	0.00	0.00	0.00	0.00	94.65	0.01	0.00	0.00	0.00	0.00	99.99	0.39	10.06	10.11	0.024	02	0.027	61	3.05
1-274646	0.43	2.52	0.67	0.00	15.02	52.28	25.36	0.04	0.02	0.00	5.27	25.68	68.98	0.41	9.33	9.81	0.034	76	0.027	03	1.93
1-274663	1.97	0.00	0.00	0.00	0.00	95.14	0.00	0.00	0.00	0.00	0.00	100.00	0.07	10.11	10.11	0.017	07	0.018	98	1.61	
1-276679	15.39	4.90	0.00	0.00	22.42	42.50	13.72	0.08	0.00	0.00	14.85	38.57	46.50	0.32	9.14	9.48	0.028	79	0.033	68	5.12
1-282144	13.94	8.05	0.00	0.00	8.22	57.94	10.42	0.36	0.00	0.00	4.98	53.94	40.72	0.69	9.06	9.48	0.01918	0	0.0306	6.20	
1-283246	0.00	0.00	0.00	0.00	0.00	31.06	64.84	0.00	0.00	0.00	0.00	10.34	89.66	−0.01	9.72	9.95	0.0276	0	0.022	02	2.83
1-285031	0.00	9.10	0.00	0.00	18.70	0.00	72.37	0.12	0.00	0.00	3.13	0.00	96.75	0.88	9.57	10.07	0.013	09	0.013	18	2.50
1-285052	0.00	1.84	0.00	0.00	6.78	0.00	87.30	0.01	0.00	0.00	1.06	0.00	98.92	0.12	9.95	10.10	0.0202	0	0.019	98	3.31
1-210785	0.00	2.36	0.00	0.00	5.12	7.49	81.03	0.01	0.00	0.00	0.83	1.62	97.54	0.00	9.91	10.09	0.019	56	0.021	66	1.97
1-286804	0.00	0.00	8.24	16.66	24.32	42.92	5.58	0.00	0.79	5.34	20.46	48.78	24.63	0.33	8.95	9.34	0.028	39	0.027	56	3.96
1-289865	2.24	0.00	0.00	0.00	0.00	94.47	0.00	0.00	0.00	0.00	0.00	100.00	−0.21	10.08	10.10	0.022	69	0.026	28	1.70	
1-295095	2.49	0.00	0.00	0.00	0.00	37.87	56.60	0.00	0.00	0.00	0.00	14.38	85.62	0.07	9.69	9.95	0.0273	0	0.0198	3.53	
1-320681	0.00	0.00	0.00	0.00	0.00	10.53	85.98	0.00	0.00	0.00	0.00	1.25	98.75	−0.07	10.01	10.10	0.025	25	0.029	42	1.70
1-338828	0.00	16.73	7.73	0.00	8.65	58.85	7.16	0.43	0.44	0.00	5.37	51.09	42.67	1.00	8.78	9.58	0.024	18	0.037	73	4.30
1-339028	2.72	0.00	0.00	0.00	0.00	94.05	0.00	0.00	0.00	0.00	0.00	100.00	−0.08	10.11	10.11	0.023	26	0.026	11	2.33	
1-339125	0.00	1.99	0.00	0.00	0.00	0.57	94.78	0.01	0.00	0.00	0.00	0.07	99.92	0.41	10.02	10.11	0.017	08	0.020	65	3.18
1-351538	7.68	2.73	0.00	0.00	6.55	26.05	53.68	0.05	0.00	0.00	1.18	7.80	90.97	0.32	9.65	10.03	0.024	09	0.0241	3.94	
1-36878	0.00	8.72	0.00	2.05	13.83	45.19	27.80	0.17	0.00	0.26	4.55	19.97	75.05	0.84	9.25	9.90	0.018	82	0.023	83	2.21
1-37062	1.96	5.04	18.39	0.00	32.06	16.55	23.61	0.08	0.70	0.00	12.73	8.76	77.73	0.77	8.88	9.88	0.025	67	0.028	12	2.35
1-37079	15.94	4.62	0.00	0.00	0.00	59.29	17.37	0.13	0.00	0.00	0.00	57.50	42.37	0.06	9.25	9.46	0.024	14	0.029	46	7.75
1-377125	12.64	0.00	0.00	0.00	31.51	53.78	0.00	0.00	0.00	0.00	10.73	89.27	0.16	9.77	10.01	0.035	76	0.030	91	4.22	
1-377321	21.35	27.63	0.00	15.90	0.00	25.58	7.92	1.34	0.00	5.66	0.00	25.86	67.14	0.20	8.28	9.71	0.012	03	0.035	79	2.33
1-378401	0.00	0.00	0.00	1.58	0.00	0.00	95.58	0.00	0.00	0.08	0.00	0.00	99.92	−0.05	10.09	10.11	0.027	69	0.030	87	2.46
1-378795	1.69	0.00	0.00	0.00	0.00	12.23	81.65	0.00	0.00	0.00	0.00	3.13	96.87	0.24	9.93	10.06	0.021	49	0.02	3.81	
1-379087	15.45	5.06	3.25	0.00	4.42	21.55	47.54	0.06	0.08	0.00	1.19	7.48	91.19	0.37	9.51	10.02	0.016	31	0.023	29	2.87
1-379660	0.00	1.11	0.00	0.00	36.10	12.52	47.77	0.02	0.00	0.00	9.50	4.45	86.03	0.45	9.50	9.94	0.028	92	0.023	31	1.66
1-386452	0.00	5.48	0.00	2.46	7.83	40.57	41.26	0.11	0.00	0.23	1.97	13.57	84.12	0.30	9.45	9.98	0.0168	0	0.023	26	1.60
1-386695	19.61	24.78	0.00	9.17	0.00	30.32	15.10	0.78	0.00	2.01	0.00	17.65	79.55	0.14	8.55	9.89	0.01586	0	0.033	72	3.29
1-392976	1.90	0.00	0.00	0.00	0.00	8.78	87.13	0.00	0.00	0.00	0.00	2.95	97.05	0.08	9.93	10.04	0.016	36	0.016	99	3.38
1-322671	0.00	0.00	0.00	0.00	0.00	32.03	63.35	0.00	0.00	0.00	0.00	9.53	90.47	0.00	9.76	9.99	0.029	73	0.0227	2.53	
1-43009	9.00	0.00	0.00	0.00	0.00	37.60	52.89	0.00	0.00	0.00	0.00	14.31	85.69	0.31	9.68	9.90	0.020	34	0.022	92	4.45
1-43721	4.01	0.00	0.00	0.00	0.00	94.49	0.00	0.00	0.00	0.00	0.00	100.00	0.14	10.11	10.11	0.026	41	0.030	12	3.26	
1-44789	0.00	0.00	0.00	0.00	0.00	96.11	0.00	0.00	0.00	0.00	0.00	100.00	0.17	10.08	10.10	0.019	43	0.023	04	3.57	
1-47499	0.00	1.90	0.00	0.00	11.79	0.00	83.53	0.03	0.00	0.00	2.29	0.00	97.68	0.39	9.78	10.04	0.018	92	0.018	71	2.97
1-48208	0.00	1.62	0.00	0.00	0.00	94.83	0.02	0.00	0.00	0.00	0.00	99.98	−0.11	10.04	10.11	0.021	53	0.0236	2.06		
1-487130	0.00	10.02	0.00	0.00	8.67	51.80	27.75	0.17	0.00	0.00	2.48	25.46	71.89	0.42	9.19	9.86	0.017	24	0.026	32	3.97
1-489649	0.00	0.84	0.00	0.00	0.00	95.53	0.01	0.00	0.00	0.00	0.00	99.99	0.21	9.99	10.08	0.016	46	0.018	77	2.75	
1-491233	0.00	4.43	3.77	3.32	1.99	39.65	43.89	0.07	0.09	0.32	0.51	13.43	85.59	0.60	9.44	9.99	0.01447	0	0.021	46	2.67
1-519738	0.00	0.00	0.00	0.00	0.00	15.67	79.93	0.00	0.00	0.00	0.00	3.51	96.49	−0.09	9.97	10.08	0.023	18	0.020	71	1.74
1-52259	3.49	5.53	0.00	0.00	29.55	32.81	26.06	0.17	0.00	0.00	10.76	16.19	72.88	0.43	9.22	9.82	0.028	62	0.030	64	3.23
1-55572	0.00	1.96	0.00	1.96	0.00	0.00	93.04	0.02	0.00	0.10	0.00	0.00	99.88	−0.22	10.00	10.11	0.023	72	0.0266	1.87	
1-604048	0.00	2.13																			

**Table A2.** – *continued*

mangaID	FC	xyy	xyo	xIy	xII	xIo	xo	myy	myo	mIy	mII	mIo	mo	$A_V$	$\langle t_L \rangle$	$\langle t_M \rangle$	$\langle Z_L \rangle$	$\langle Z_M \rangle$	Adev		
(1)	(2)	(3)	(4)	(5)	(6)	(7)	(8)	(9)	(10)	(11)	(12)	(13)	(14)	(15)	(16)	(17)	(18)	(19)	(20)		
1-48053	0.00	4.42	0.00	0.00	0.00	0.00	92.42	0.03	0.00	0.00	0.00	0.00	99.97	0.00	9.96	10.11	0.026	49	0.029	32	1.76
1-635503	0.00	22.47	10.86	0.00	0.00	35.45	32.37	0.39	0.41	0.00	0.00	19.28	79.93	1.15	8.78	9.89	0.010	45	0.028	39	3.25
1-71481	3.01	0.00	0.00	0.00	0.00	2.51	91.76	0.00	0.00	0.00	0.00	0.28	99.72	–0.07	10.09	10.11	0.0274		0.02989		2.22
1-71525	0.00	2.20	0.00	0.00	0.00	0.00	94.16	0.02	0.00	0.00	0.00	0.00	99.98	0.33	9.87	10.05	0.016	12	0.021	06	2.99
1-72914	5.38	0.00	0.00	0.00	0.00	23.39	68.11	0.00	0.00	0.00	0.00	5.85	94.15	0.19	9.90	10.07	0.021	55	0.022	17	3.35
1-72928	0.00	0.00	0.00	0.00	0.00	0.00	96.34	0.00	0.00	0.00	0.00	0.00	100.00	–0.14	10.06	10.10	0.022	21	0.025	26	2.31
1-73005	0.00	0.00	0.00	0.00	17.26	39.48	41.22	0.00	0.00	4.85	14.80	80.35	0.32	9.60	9.93	0.017	82	0.018	43		2.85
1-90849	4.99	0.00	0.00	0.00	18.92	1.51	70.51	0.00	0.00	3.84	0.45	95.70	0.24	9.81	10.05	0.023	69	0.019	37		3.30
1-92626	1.70	0.65	0.00	0.00	0.00	0.00	92.91	0.01	0.00	0.00	0.00	0.00	99.99	0.03	10.04	10.10	0.022	73	0.026	75	2.69
1-93876	4.73	0.00	0.00	0.00	0.00	20.53	71.66	0.00	0.00	0.00	0.00	5.07	94.93	–0.08	9.89	10.05	0.029	99	0.027	18	3.64
1-94422	3.24	0.00	0.00	0.00	0.00	25.12	67.74	0.00	0.00	0.00	0.00	6.84	93.16	0.17	9.83	10.04	0.029	05	0.0258		2.86
1-94554	4.48	0.00	0.00	0.00	0.00	5.49	86.38	0.00	0.00	0.00	0.00	1.08	98.92	0.01	10.07	10.11	0.021	74	0.024	48	2.25

This paper has been typeset from a  $\text{\TeX}/\text{\LaTeX}$  file prepared by the author.



## The first 62 AGN observed with SDSS-IV MaNGA – II. Resolved stellar populations

Nícolas Dullius Mallmann,<sup>1,2\*</sup> Rogério Riffel,<sup>1,2</sup> Thaisa Storchi-Bergmann,<sup>1,2</sup> Sandro Barboza Rembold,<sup>2,3</sup> Rogemar A. Riffel,<sup>2,3</sup> Jaderson Schimoia,<sup>1,2,3</sup> Luiz Nicolaci da Costa,<sup>2</sup> Vladimir Ávila-Reese,<sup>4</sup> Sebastian F. Sanchez,<sup>4</sup> Alice D. Machado,<sup>2,3</sup> Rafael Cirolini,<sup>2,3</sup> Gabriele S. Ilha<sup>2,3</sup> and Janaína C. do Nascimento<sup>1,2</sup>

<sup>1</sup>Departamento de Astronomia, Universidade Federal do Rio Grande do Sul - Av. Bento Gonçalves 9500, Porto Alegre, RS, Brazil

<sup>2</sup>Laboratório Interinstitucional de e-Astronomia, Rua General José Cristino, 77 Vasco da Gama, Rio de Janeiro 20921-400, Brazil

<sup>3</sup>Departamento de Física, Centro de Ciências Naturais e Exatas, Universidade Federal de Santa Maria, 97105-900, Santa Maria, RS, Brazil

<sup>4</sup>Instituto de Astronomía, Universidad Nacional Autónoma de México, A. P. 70-264, C.P. 04510, México, D.F., Mexico

Accepted 2018 May 21. Received 2018 May 21; in original form 2018 March 21

### ABSTRACT

We present spatially resolved stellar population (SP) age maps, average radial profiles and gradients for the first 62 active galactic nuclei (AGN) observed with Sloan Digital Sky Survey (SDSS)-IV Mapping Nearby Galaxies at Apache Point Observatory (MaNGA) to study the effects of the active nuclei on the star formation history of the host galaxies. These results, derived using the STARLIGHT code, are compared with a control sample of non-active galaxies matching the properties of the AGN hosts. We find that the fraction of young SPs in high-luminosity AGN is higher in the inner ( $R \leq 0.5 R_e$ ) regions when compared with the control sample; low-luminosity AGN, on the other hand, present very similar fractions of young stars to the control sample hosts for the entire studied range ( $1 R_e$ ). The fraction of intermediate-age SP of the AGN hosts increases outwards, with a clear enhancement when compared with the control sample. The inner region of the galaxies (AGN and control galaxies) presents a dominant old SP, whose fraction decreases outwards. We also compare our results (differences between AGN and control galaxies) for the early- and late-type hosts and find no significant differences. In summary, our results suggest that the most luminous AGN seems to have been triggered by a recent supply of gas that has also triggered recent star formation ( $t \leq 40$  Myr) in the central region.

**Key words:** galaxies: active – galaxies: star formation – galaxies: stellar content.

### 1 INTRODUCTION

An important galaxy evolution stage is characterized by the active galactic nuclei (AGN), a phenomenon that occurs when the galaxy's supermassive black hole (SMBH) is accreting matter from its surroundings, i.e. the accretion disc. Subsequent feedback processes start to happen, comprising radiation emitted by the hot gas in the accretion disc or by its corona, jets of relativistic particles, and winds emanating from outer regions of the disc.

Current models and simulations of gas inflows on tens to hundreds of parsec (pc) scales around galaxy nuclei lead to episodes of circumnuclear star formation (Kormendy & Ho 2013; Heckman

& Best 2014; Zubovas & Bourne 2017). Zubovas & Bourne (2017) suggest that there is a critical AGN luminosity in which the feedback of the nuclear activity increases the fragmentation of the gas clouds. Above this luminosity threshold, the feedback is powerful enough to remove the gas efficiently and stop fragmentation; for AGN luminosities under this threshold, however, the feedback is not efficient to compress the gas to high densities and enhance fragmentation. However, there is no consensus on whether AGN fuelling occurs at the same time as the star formation (Kawakatu & Wada 2008), or follows it during a post-starburst phase (Cid Fernandes et al. 2005; Davies et al. 2007, 2009) or if it is not associated with any recent star formation (Sarzi et al. 2007; Hicks et al. 2013).

A breakthrough in understanding the relation between the AGN and the surrounding stellar population (SP) can be reached by a simple, but thorough, investigation of whether young or intermediate-

\* E-mail: [nicolas.mallmann@ufrgs.br](mailto:nicolas.mallmann@ufrgs.br)

age stars are present within few hundred pc of the AGN. If the youngest stellar types are present, AGN fuelling is coeval with star formation; if instead intermediate-age stars dominate the SP, fuelling would be driven by a post-starburst, and thus the AGN phase would follow the starburst phase; finding only old stars would imply that gas inflow to the AGN is not necessarily linked to star formation.

Over the past few years, major observational effort to understand this co-evolution between AGN and the circumnuclear SP is being made using spatially resolved SP studies in large samples of galaxies (Goddard et al. 2017; Zheng et al. 2017). These studies, however, are not focused on comparing AGN hosts with non-active galaxies. One recent effort focusing on such kind of comparison was made by Sanchez et al. (2017) who found that AGN hosts are mostly morphologically early-type or early-spirals and that for a given morphology, AGN hosts are more massive, more compact, more centrally peaked, and rather pressure than rotationally supported systems when compared to the non-active galaxies. However, these studies did not use a selected control sample of galaxies to match the fundamental properties of the AGN sample, nor considered the dependence on the AGN luminosities.

This is the second paper of a series in which we aim at studying the resolved SP as well as the gas emission properties of the AGN host galaxies observed with Mapping Nearby Galaxies at Apache Point Observatory (MaNGA) and compare them with those of a control sample of non-active galaxies. In Paper I (Rembold et al. 2017), we have presented the AGN sample so far observed with MaNGA (available through the MPL-5) and have defined a control sample matching the AGN host galaxies in terms of galaxy masses, morphology, distance and inclination. In Paper I we have also characterized the SP properties of the AGN hosts as compared with those of the control sample for the single aperture SDSS-III spectrum that covers the inner 3 arcsec diameter nuclear region, using spectral synthesis via the STARLIGHT program (Cid Fernandes et al. 2005).

Aimed at investigating the relation between the nuclear activity and the hosts' star formation history (SFH), in the present paper (Paper II), we use the MaNGA datacubes of the AGN and control sample defined in Paper I to obtain the resolved SFH and SP properties for these objects. These properties were compared between the AGN hosts and inactive galaxies in different luminosity ranges. This paper is organized as follows: brief description of the MaNGA subsample chosen for this work (Section 2); the method of SP synthesis as well as the base set of SSPs (Section 3); the results of the synthesis for the AGN and control sample (Section 4); a discussion comparing the SPs of AGN and control galaxies (Section 5) and a conclusion in Section 6.

## 2 DATA

The study of spatially resolved properties in galaxies was always undermined by the small sample size of past integral field spectroscopy surveys, not to mention the less numerous AGN. To address this problem, the MaNGA survey (Bundy et al. 2015) was developed to observe a large sample of nearby galaxies with integral field spectroscopy.

MaNGA is part of the fourth-generation Sloan Digital Sky Survey (SDSS IV) along with APOGEE-2 (Majewski et al. 2017) and eBOSS (Dawson et al. 2016). The survey aims to provide optical spectroscopy (3600–10400 Å) of ∼10 000 nearby galaxies (with  $\langle z \rangle \approx 0.03$ ). The observations are carried with fibre bundles of different sizes (19–127 fibres) covering a field of 12 to 32 arc-

sec in diameter. The selected sample is divided into ‘primary’ and ‘secondary’ targets, the former are observed up to 1.5 effective radius ( $R_e$ ) whilst the latter is observed up to 2.5  $R_e$ . For more details, see Drory et al. (2015), Law et al. (2015) and Yan et al. (2015, 2016).

The data used in the present work are a sub-sample of MaNGA data (Law et al. 2016, MPL-5’s Data Reduction Pipeline, DRP) selected in Paper I. In short, the AGN were selected from the MaNGA sample by cross-matching them with SDSS-III data products, using then the BPT diagram [OIII]/H $\beta$  versus [NII]/H $\alpha$  (Baldwin, Phillips & Terlevich 1981) to select the AGN. In addition, we have used the WHAN diagram (Cid Fernandes et al. 2010; Cid Fernandes et al. 2011) to eliminate from the AGN sample the ‘LIERS’, or ‘fake AGN’. The resulting AGN sample contains 62 objects. To study the relationship between AGN and the SPs of the host, we have chosen two control galaxies to match each of the selected AGN hosts. The matching was done according to the morphology (using concentration and asymmetry indices), axial ratios, redshifts, galaxy inclination and total stellar masses. For more details regarding the AGN and control sample selection, see Rembold et al. (2017).

## 3 STELLAR POPULATION SYNTHESIS

We have used SP synthesis technique in order to derive the SFH of the galaxies of the AGN and control samples. We first briefly describe the fitting code used. We then present a summary of the data preparation and processing pipeline we have developed to manage the fitting process.

### 3.1 Fitting code

To disentangle the contribution of each SP to the integrated spectra of each spaxel in the datacubes we employed the STARLIGHT code (Cid Fernandes et al. 2005). In summary, this code combines the spectra of a base set of  $N_*$  template spectra  $b_{j,\lambda}$  – usually, simple stellar population (SSP) covering a range of ages and metallicities – in order to reproduce the observed spectra  $O_\lambda$ . To generate the modelled spectra  $M_\lambda$ , the SSPs are normalized at an arbitrary  $\lambda_0$  wavelength, reddened by the term  $r_\lambda = 10^{-0.4(A_\lambda - A_{\lambda_0})}$ , weighted by the population vector  $x_j$  (which represents the fractional contribution of the  $j$ th SSP to the light at the normalization wavelength  $\lambda_0$ ), and convolved with a Gaussian distribution  $G(v_*, \sigma_*)$  to account for the effects of velocity shifts in the central velocity  $v_*$  and velocity dispersion  $\sigma_*$ . The model spectrum can be expressed as:

$$M_\lambda = M_{\lambda_0} \left[ \sum_{n=1}^{N_*} \mathbf{x}_j b_{j,\lambda} r_\lambda \right] \otimes G(v_*, \sigma_*) \quad (1)$$

where  $M_{\lambda_0}$  is the synthetic flux at the wavelength  $\lambda_0$ . To find the best parameters for the fit, the code searches for the minimum of  $\chi^2 = \sum_{\lambda_i}^{\lambda_f} [(O_\lambda - M_\lambda)\omega_\lambda]^2$ , where  $\omega_\lambda$  is the inverse of the error, using a simulated annealing plus Metropolis scheme. Further details on the code can be found in Cid Fernandes et al. (2005).

The base set used in the spectral synthesis is a reduced number of the SSPs calculated by Bruzual & Charlot (2003). It comprises  $N_* = 46$  elements (45 SSPs + 1 featureless continuum – FC – function of the form  $F_v \propto v^{-1.5}$  to represent the AGN emission), spanning 15 ages (0.001, 0.003, 0.005, 0.010, 0.025, 0.040, 0.101, 0.286, 0.640, 0.905, 1.43, 2.50, 5.00, 11.00 and 13.00 Gyr) and three metallicities (0.1, 1 and 2.5 Z $_\odot$ ). The addition of a power law

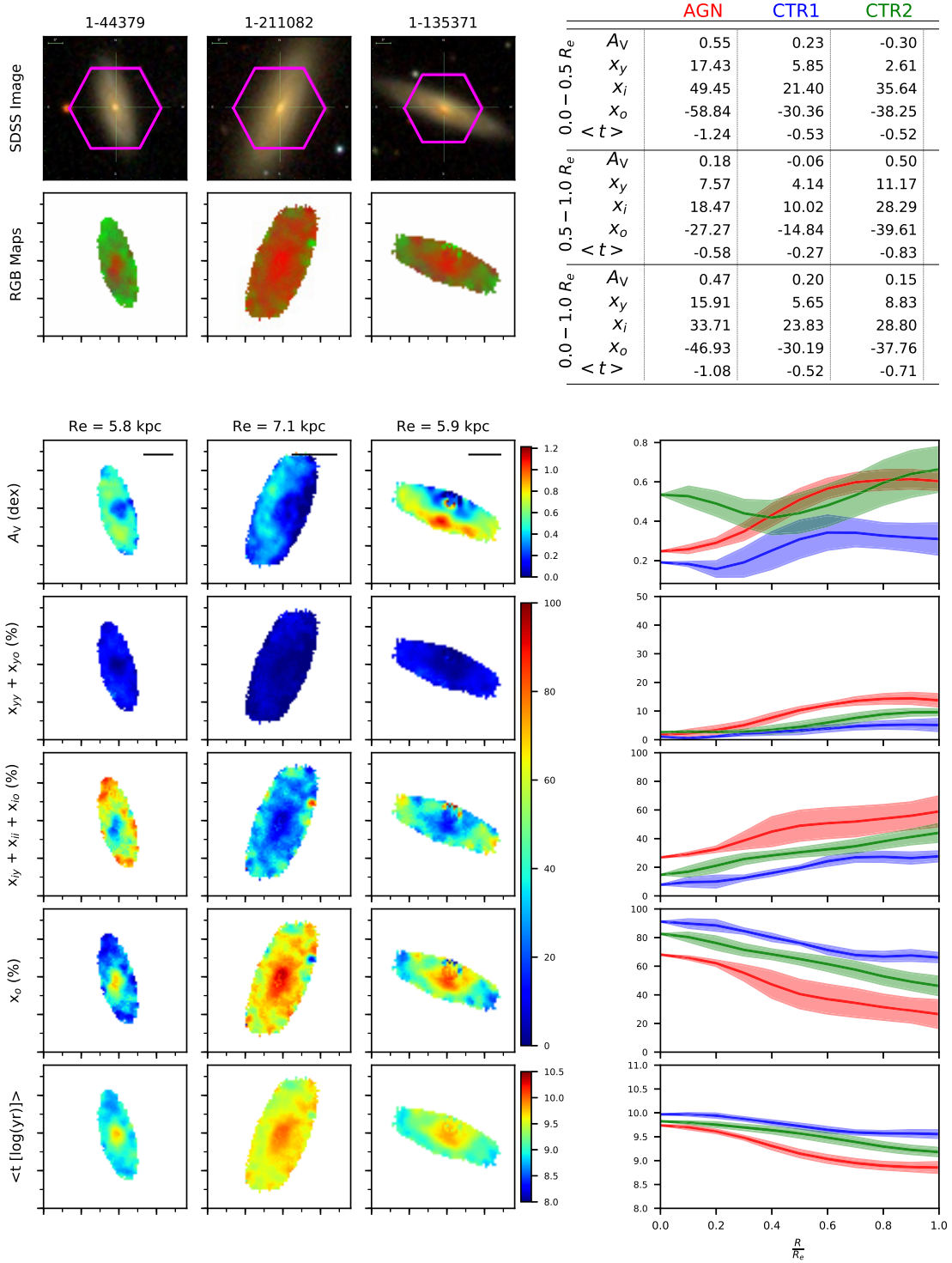


**Figure 1.** Comparison between a late-type AGN and its control galaxies. Left side panels – *Top set of panels*: SDSS image (the MaNGA field is indicated in magenta). Second row: composed RGB image using the binned population vectors [blue: young ( $\mathbf{X}_Y$ :  $t \leq 40$  Myr); green: intermediate-age ( $\mathbf{X}_I$ :  $40 \text{ Myr} < t \leq 2.5 \text{ Gyr}$ ); red: old ( $\mathbf{X}_O$ :  $t > 2.5 \text{ Gyr}$ )]. *Bottom set of panels*: From top to bottom: visual extinction ( $A_V$ ),  $\mathbf{X}_Y$ ,  $\mathbf{X}_I$ ,  $\mathbf{X}_O$  and mean age ( $\langle t \rangle$ ) maps. For display purposes we used tick marks separated by 5 arcsec. The solid horizontal line in the  $A_V$  maps represents  $1R_e$ . Right side panels – *Top*: summary table with the mean gradient values for each property in three different  $R_e$  ranges. *Bottom*: average radial profiles, up to  $1R_e$ , for AGN (red colour) and control (blue and green colours). Shaded area represents  $1\sigma$  standard deviation. For profiles smaller than  $1R_e$  the gradients were calculated using extrapolated values.

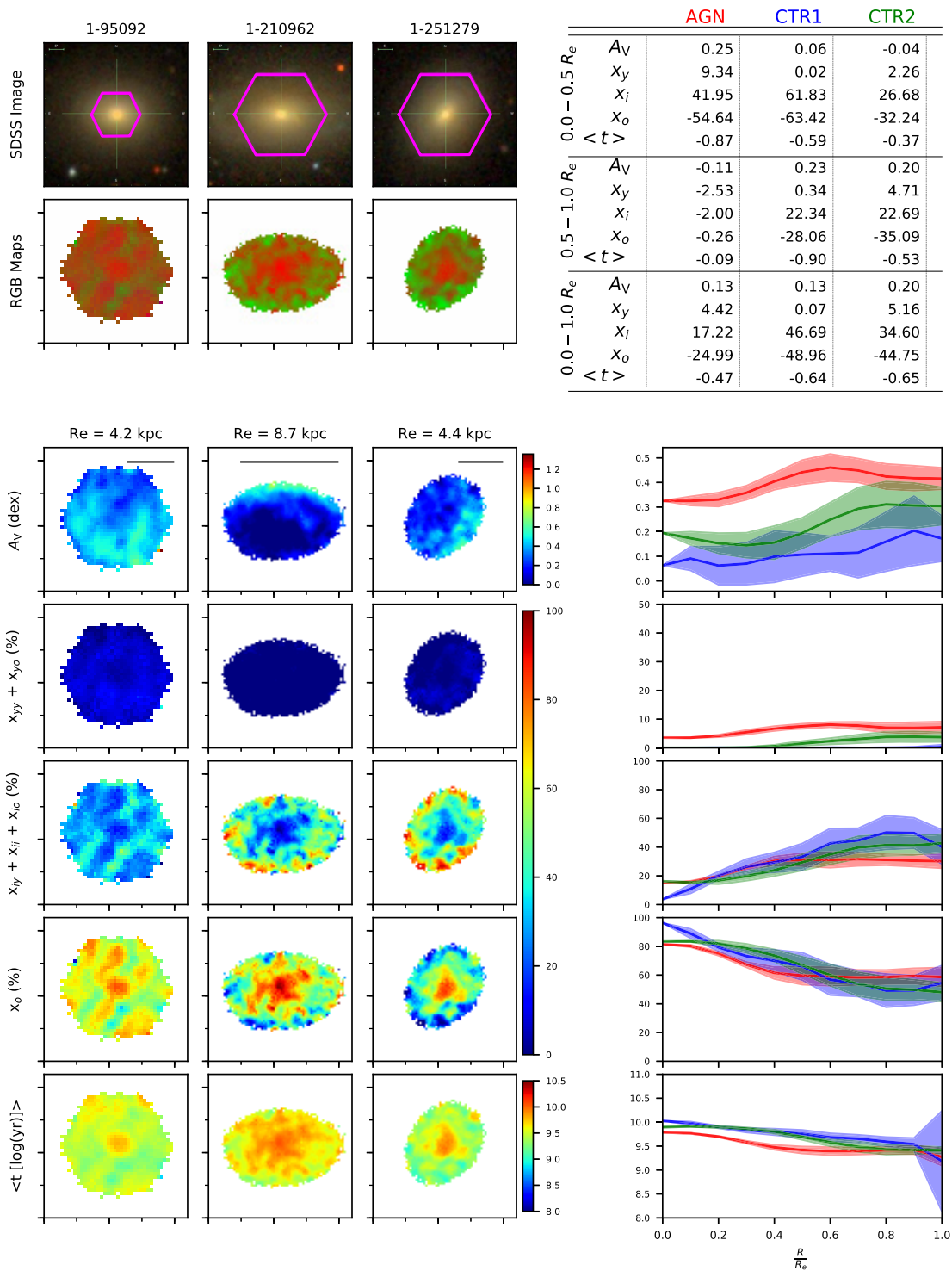


**Figure 2.** Comparison between an early-type AGN and its control galaxies (see Fig. 1 for description).

is necessary to account for the AGN continuum (Cid Fernandes et al. 2004; Riffel et al. 2009). For the foreground extinction, we used the Cardelli, Clayton & Mathis (1989, CCM) law, with  $R_V = 3.1$ . The adopted normalization wavelength was  $\lambda_0 = 5700 \text{ \AA}$  and the synthesis was performed for the spectral range from 3800 to 7000  $\text{\AA}$ .

### 3.2 Data management

In order to improve the management of the data which include STARLIGHT inputs and outputs, the compilation of the results and the analysis, we developed a software called MEGACUBE. This software is designed to work with three main modules set up by a general

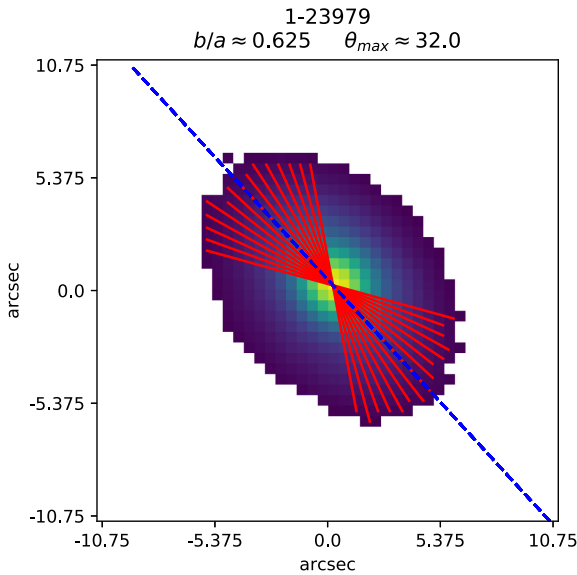


**Figure 3.** Example of radial profile cuts on the normalization flux map of a galaxy (MaNGA ID: 1-23979) with  $\approx 32$  of angle displacement from the major-axis (indicated with a blue dashed line). Red line segments are the radial profile cuts used to calculate the mean radial profile. Profiles closer to the minor axis were excluded to reduce any effects of projection (the more edge-on the galaxy is, the greater the projection distortion).

configuration file. The modular approach was chosen with adaptability in mind, e.g. if a module was programmed to work with MaNGA datacubes' extraction, we could replace it with one that extracts another survey's datacubes. The modules used in this work are (in order of execution) as follows:

*i) Data preparation:* This module is used to process and convert the MaNGA datacubes to a data format suitable for the chosen SP fitting code (STARLIGHT). The main steps are as follows:

(i) Filtering of the spectra using a two-dimensional butterworth filter to remove spurious data (e.g. spiked values) and increase the signal-to-noise ratio (SNR), without combining adjacent spaxel, thus allowing to a better exploration of the spatial resolution. A better description of this technique can be found in Riffel et al. (2016);

(ii) Galactic reddening correction of each spaxel using the Schlegel extinction maps (Schlegel, Finkbeiner & Davis 1998) and the CCM reddening law;

(iii) Redshift correction using the SDSS-III redshift provided in the *drpall* tables of the MaNGA database;

(iv) Estimation of the SNR in the wavelength range 5650–5750 Å for every spaxel;

(v) Spaxels with  $\text{SNR} < 10$  were excluded when performing the fitting. This was done in order to have a good compromise between the spatial coverage and the reliability of the fitting results (see Cid Fernandes et al. 2004, for details).

*ii) Spectral Fitting:* This module is used to invoke the fitting code and compile its results as described below:

(i) Setting up all the configuration files needed for the fits;  
(ii) Fitting each individual spaxel with STARLIGHT;

(iii) Derivation of mean ages and metallicities, as well as star formation rates, from the STARLIGHT output;

(iv) Inclusion of both standard STARLIGHT output and derived parameters to the original datacubes as additional extensions.

*iii) Analysis:* This module uses the fitting results to produce maps and radial plots (see Section 4 for a better description):

(i) RGB maps: qualitative representation of the spatially resolved SP age distribution for each galaxy, where the colours (red, green and blue) represent three main age bins (see Section 4);

(ii) Comparison figures: for each trio of galaxies (AGN and its two controls), panels showing the relevant properties (maps of SP properties derived from STARLIGHT and/or SDSS-III combined *ugriz* images);

(iii) Radial profiles and gradients: for each galaxy and property, a mean profile (as well as its mean gradient value – calculated as a function of  $R$ ,  $dX/dR$ ) is calculated to use for quantitative comparisons;

(iv) Gradients table: as a result of the analysis, we have also generated a table showing the gradients of the profiles for three different bins in terms of effective radius  $R_e$ ;

(v)  $[\text{O III}] \lambda 5007$  luminosity  $L_{[\text{O III}]}$ binned radial profiles: radial profiles of the SP properties where the profiles for the AGN (and corresponding controls) are binned in groups according to the AGN luminosity. These profiles are shown also for AGN subsamples binned according to the host galaxy type: early- and late-type.

It is worth mentioning that a similar organizer tool was developed by de Amorim et al. (2017) for the Calar Alto Legacy Integral Field Area (CALIFA) survey, which is a pioneer project of integral field spectroscopy legacy surveys.

## 4 RESULTS

The spectral synthesis gives as results a number of output parameters, but we are mostly interested in  $x_j$  – the fractional contribution of each SSP to the total light at the normalization wavelength  $\lambda_0$ , that gives the SFH of each spaxel, and from which we also obtain the mean age for each spaxel, representing the age of the SPs as a single parameter. In addition, a valuable byproduct of the fitting is the amount of extinction in the line of sight, parameterized by the visual extinction  $A_V$ . In Figs 1 and 2 we illustrate the derived data products (maps, radial profiles and gradients) for two AGN and their respective control sample galaxies; the equivalent plots for the remaining of the sample is available in the Appendix.

In order to represent the galaxies' age distribution with a single parameter at each spaxel, we calculated their light weighted mean age (Cid Fernandes et al. 2005) as follows:

$$\langle \log t_L \rangle = \frac{\sum_{j=1}^{N_*} x_j \log(t_j)}{\sum_{j=1}^{N_*} x_j}, \quad (2)$$

where  $t_j$  is the age of the template  $j$ . The distributions of mean age are shown in the bottom row of the bottom left panels of Figs 1 and 2.

As stated by Cid Fernandes et al. (2005), small differences in ages of individual SSPs are washed away in real data by noise effects. We therefore rebinned the population vectors in six SP components (SPCs):  $x_{yy}$  ( $1 \leq t \leq 10$  Myr),  $x_{yo}$  ( $10 < t \leq 40$  Myr),  $x_{iy}$  ( $40 < t \leq 286$  Myr),  $x_{ii}$  ( $286 < t \leq 905$  Myr),  $x_{io}$  ( $905 \text{ Myr} < t \leq 2.5$  Gyr) and  $x_o$  ( $2.5 < t \leq 13$  Gyr).

We have also grouped the SP vector in three major age bins, described as follows:

- (i) Young Age:  $\mathbf{X}_Y = x_{yy} + x_{yo}$
- (ii) Intermediate Age:  $\mathbf{X}_I = x_{iy} + x_{ii} + x_{io}$
- (iii) Old Age:  $\mathbf{X}_O = x_o$

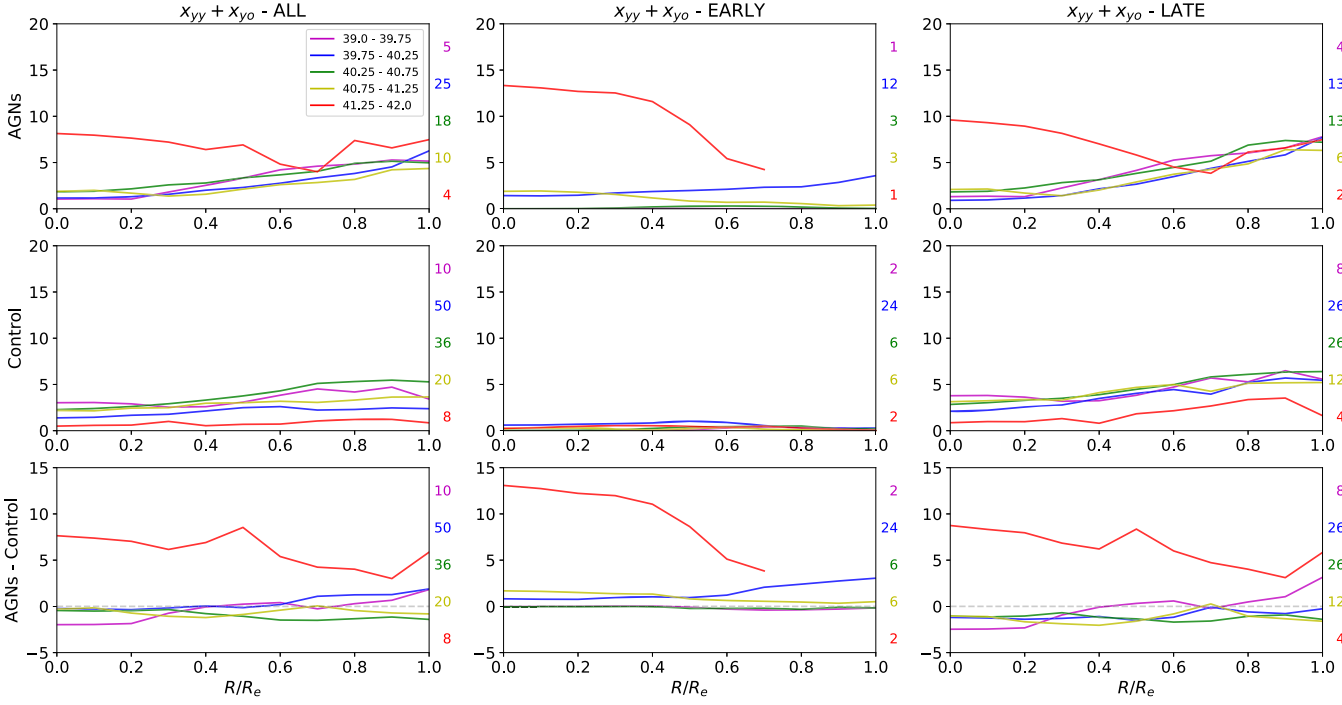


**Figure 4.**  $L_{\text{[OIII]}}$ binned mean radial profiles for the  $x_{yy}$  ( $1 \leq t \leq 10$  Myr) and  $x_{yo}$  ( $10 < t \leq 40$  Myr) components combined. Each colour pertains to the same  $L_{\text{[OIII]}}$ range for every plot. The columns represent the groups of AGN used to calculate the average profiles for the AGN, its control galaxies and their differences. The groups are, from left to right: all AGN, early-type AGN, late-type AGN. The rows, from top to bottom, show the average profiles for the AGN, the control galaxies (of the respective AGN group) and the differences. The coloured numbers to the right of every plot are the quantity of galaxies used to calculate the mean profile of the same colour.

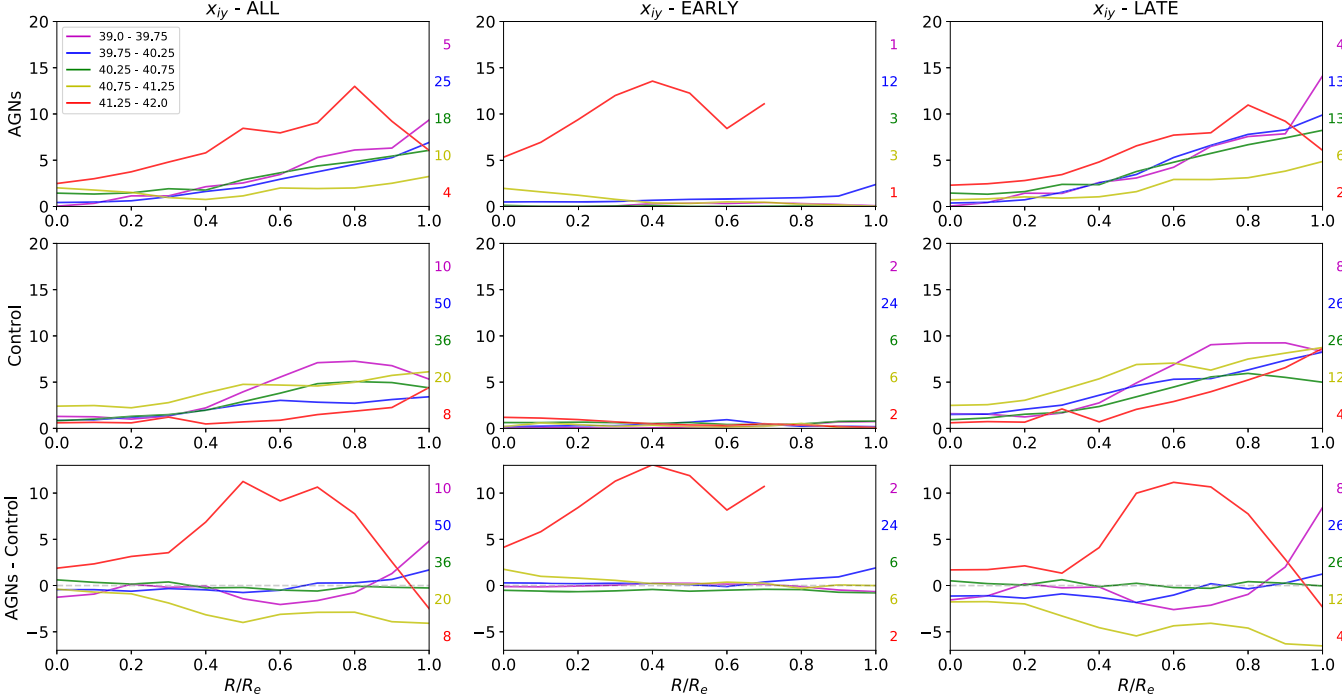


**Figure 5.**  $L_{\text{[OIII]}}$ binned mean radial profiles for the  $x_{iy}$  components ( $40 < t \leq 286$  Myr) (see fig. 4 for description).

In order to visualize the spatial distribution of the populations' relative contributions in a qualitative way, RGB images of the galaxies were created by assigning the three colours (red, green and blue) to the binned population vectors: Red represents the old  $\mathbf{X}_O$  ( $2.5 <$

$t \leq 13$  Gyr), green the intermediate-age  $\mathbf{X}_I$  ( $40 \text{ Myr} < t \leq 2.6$  Gyr) and blue the young SPs  $\mathbf{X}_Y$  ( $1 \leq t \leq 40$  Myr).

In the bottom right of Figs 1 and 2 we show mean radial profiles, up to  $1.0 R_e$ , for each galaxy and property, derived using a

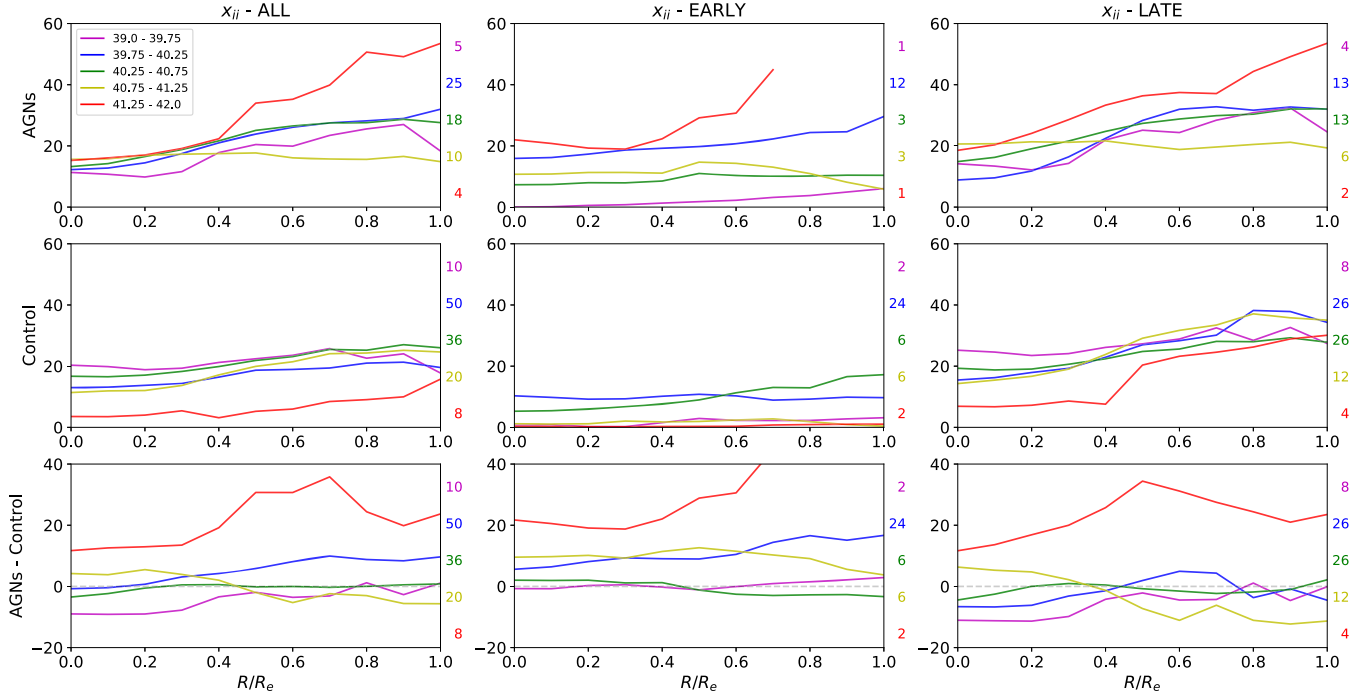


**Figure 6.**  $L_{[\text{O III}]}$  binned mean radial profiles for the  $x_{ii}$  components ( $286 < t \leq 905$  Myr) (see fig. 4 for description).

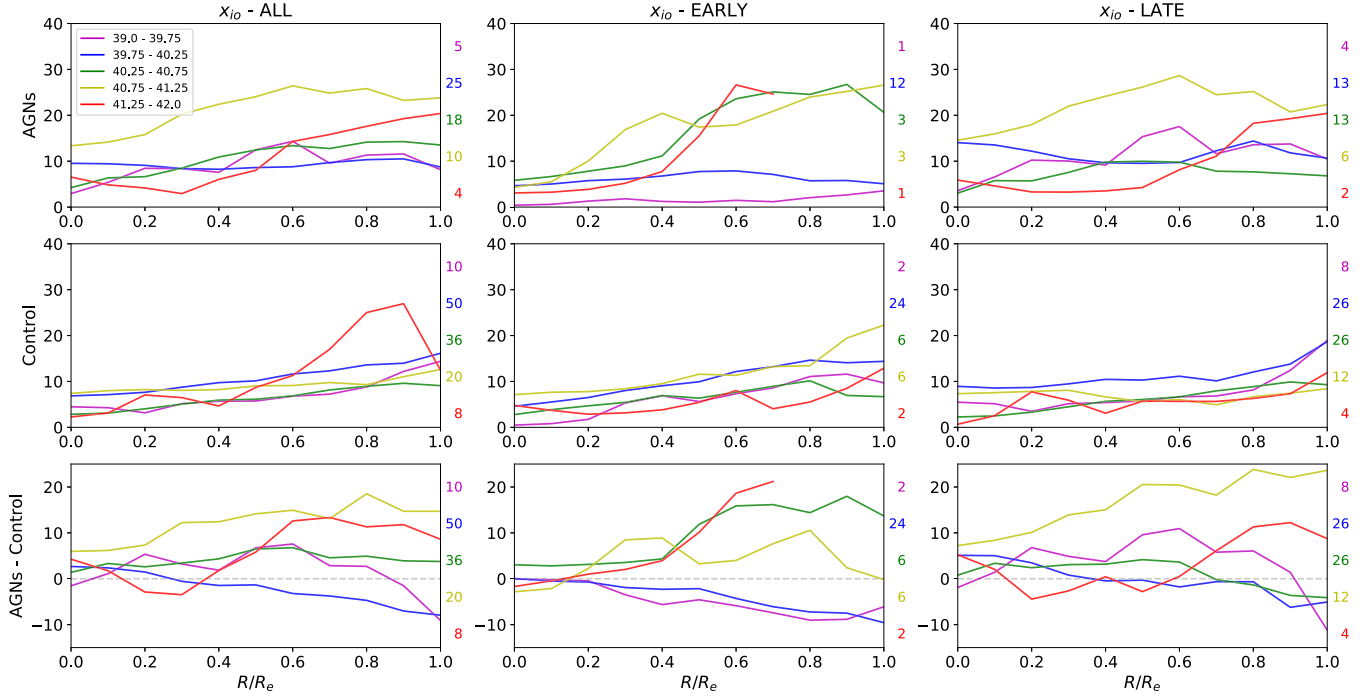


**Figure 7.**  $L_{[\text{O III}]}$  binned mean radial profiles for the  $x_{io}$  components ( $905 \text{ Myr} < t \leq 2.5 \text{ Gyr}$ ) (see Fig. 4 for description).

nearest neighbor interpolation method to generate continuous values between pixel transitions and to remove abrupt changes due to spatially discrete maps. We opted for 30 equally spaced radial profiles in the galaxy plane limited to angular distances from the major axis of  $\theta_{\max} = \tan^{-1}(b/a)$  degrees, where  $a$  and  $b$  are, respectively, the semi-major and semi-minor axis of the SDSS galaxy image, obtained from the MaNGA’s *drpall* table (calculated using Sérsic profiles), as illustrated in Fig. 3. Maximum angular displacements

from the major axis were used because the profiles closer to the minor axis, when projected, resulted too noisy, possibly due to obscuration effects when the galaxies are too inclined relative to the line of sight. Mean profiles were then calculated for each property map by averaging all these profiles.

We have also calculated the mean gradients of each property (using the mean radial profiles) for three different regions: from 0.0 to  $0.5 R_e$ , 0.5 to  $1.0 R_e$  and 0.0 to  $1.0 R_e$ . Since we are comparing rela-

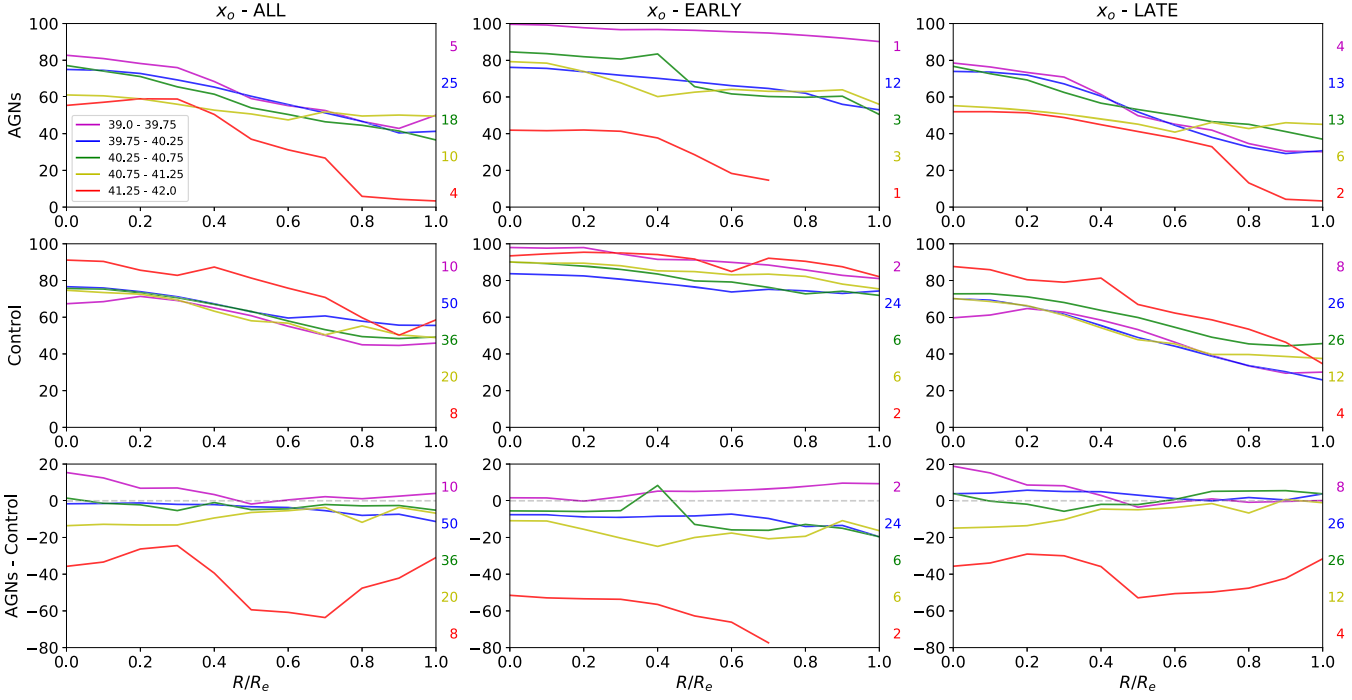


**Figure 8.**  $L_{[\text{O III}]}$  binned mean radial profiles for the  $x_o$  components ( $2.5 < t \leq 13$  Gyr) (see Fig. 4 for description).

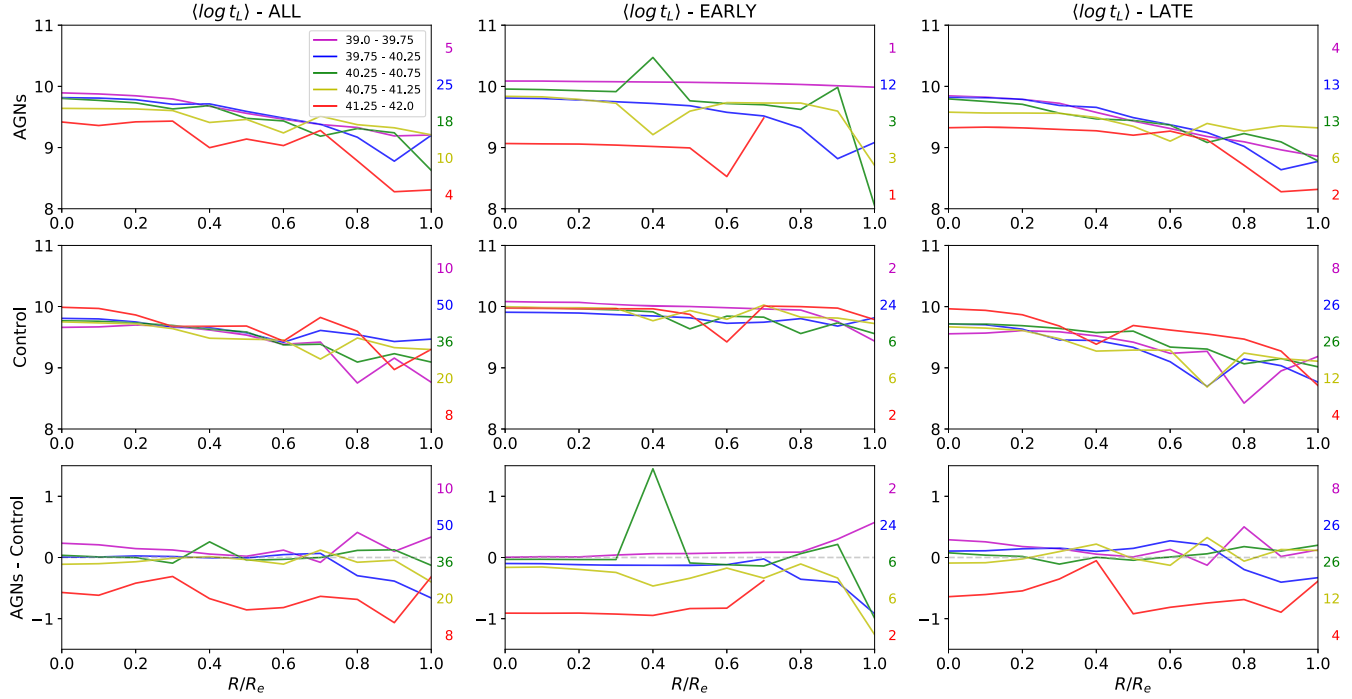


**Figure 9.**  $L_{[\text{O III}]}$  binned mean radial profiles for the mean age ( $\langle \log t \rangle$ ) (see Fig. 4 for description).

tively low luminosity active galaxies with a matched control sample of non-active galaxies, the major differences should be detected in their nuclear regions. Thus, the division we used was decided based on qualitative observation of the average radial profiles, which revealed, in most galaxies, a trend of slope changes close to  $0.5 R_e$ . Some values had to be extrapolated to a constant slope since the radial profiles could not reach  $1.0 R_e$  due to poor SNR. These gradients for  $A_V$ ,  $\mathbf{X}_Y$ ,  $\mathbf{X}_I$  and  $\mathbf{X}_O$ , together with the gradients in

mean age, are shown in a table in the top right corner of Figs 1 and 2.

#### 4.1 AGN hosts versus control galaxies

For each one of the AGN we show the radial variation of the derived properties compared to the two control galaxies in the Appendix. As an example, we have selected to show two typical sets of results

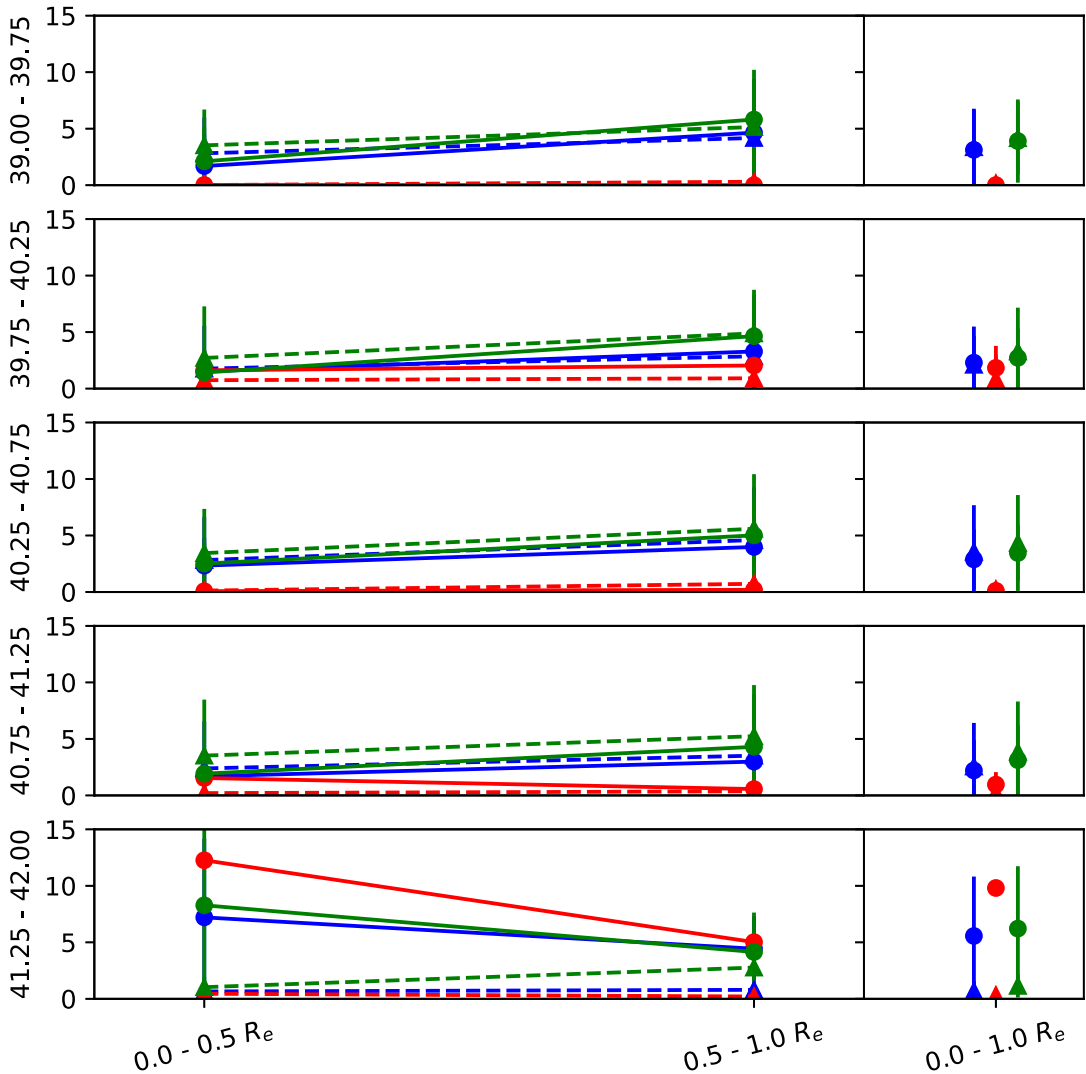


**Figure 10.** Young SP  $x_y$  contribution for five different bins of luminosity (39–39.75, 39.75–40.25, 40.25–40.75, 40.75–41.25, 41.25–42), calculated for three different regions ( $0.0$ – $0.5 R_e$ ,  $0.5$ – $1.0 R_e$ ,  $0.0$ – $1.0 R_e$ ). Each colour represents a different AGN grouping: green for the late-type AGN, red for the early-type AGN and blue for all the AGN sample. Solid lines correspond to the active galaxies and dashed lines to the control galaxies.

in Figs 1 and 2, the results for one ‘late-type’ AGN (MaNGA ID 1-44379) and one ‘early-type’ AGN (MaNGA ID 1-95092) and their control galaxies.

In the case of the late-type AGN of Fig. 1, it shows that the RGB maps are dominated by the contribution of old populations in the centres for both the AGN hosts and the control galaxies. Just outward of the nucleus, younger populations dominate the AGN and the control galaxy CRT2 a bit further out, while the control galaxy CRT1 shows larger contribution of older age components also outside the nucleus. The extinction at the nucleus is stronger for the second control than the AGN while outwards they reach similar values that are higher than those of the first control. Regarding the contribution of the different SP age bins to the light at 5700 Å, there is no difference between the AGN and the controls for the youngest age bins, while for the intermediate-age one, its contribution in the AGN is larger than in its control galaxies at all radii. There is also a difference for the old age bin  $X_O$ , that is lower in the AGN than in the control galaxies everywhere inside  $R_e$ . These results also reflect in the mean age: the mean age of the SP is lower everywhere in the galaxy for the AGN than for the control galaxies. The table listing

the gradients also shows differences between the AGN and control galaxies: for the inner radial bin ( $0$ – $0.5 R_e$ ) and for the full radial range ( $0$ – $1.0 R_e$ ), the AGN host galaxy shows steeper gradients than the controls for all properties.

The early-type AGN case of Fig. 2 shows higher contribution of the old component in the central regions of the galaxies for the AGN and its controls. In this case, however, the AGN’s RGB map shows a more homogeneous population throughout the galaxy, whilst the control galaxies’ RGB maps show an older central region surrounded by a younger population outwards. The extinction for the AGN is larger compared with its control galaxies as can be seen in the  $A_V$  profiles. Although the  $A_V$  maps show higher values for the control galaxies, they are concentrated closer to the limits of  $SNR \leq 10$ , thus less reliable. The population profiles show a more constant distribution of ages for the AGN inside the  $R \leq 1.0 R_e$ , specially between  $0.5$  and  $1.0 R_e$ . This behaviour is reflected in the low gradient values of the  $0.5$ – $1.0 R_e$  bin compared to the control galaxies. The mean age profile of the AGN shows a younger population over almost all of the  $0$ – $1.0 R_e$  range, similar to the late-type case (Fig. 1). The gradients table shows that the outer region

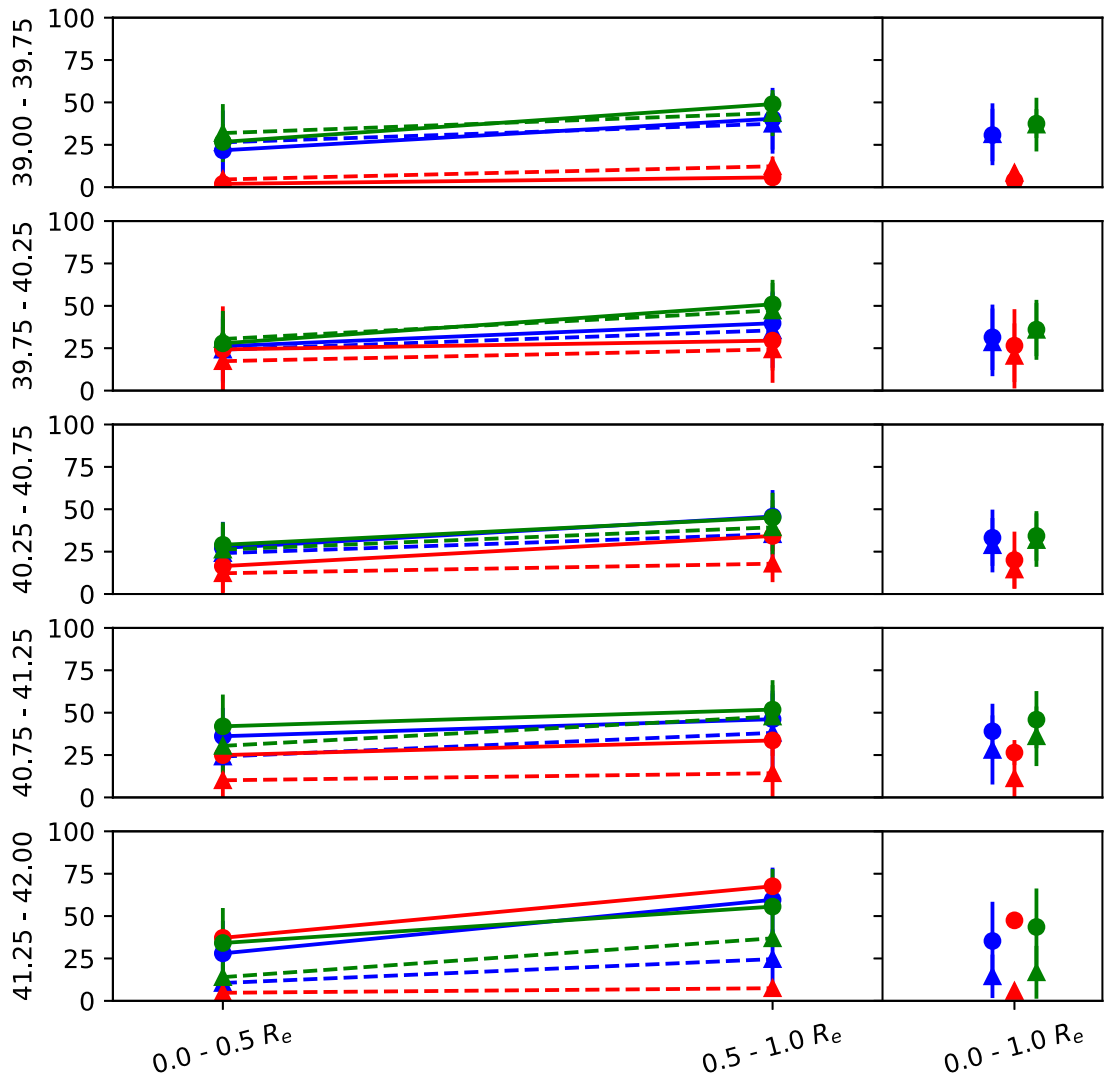


**Figure 11.** Intermediate-age SP  $x_i$  for different bins of luminosity, calculated for three different regions (see Fig. 10).

( $0.5 - 1.0 R_e$ ) has a different behaviour for the AGN compared to the control galaxies (which, in turn, behave similarly).

## 5 DISCUSSION

In order to test for a possible relation between the AGN luminosity and the SFH, we compare the SP profiles derived for the AGN and controls building average profiles for each of five  $L_{[OIII]}$  bins. We grouped them in bins of  $\log_{10} L_{[OIII]}$  as follows: 39 to 39.75, 39.75 to 40.25, 40.25 to 40.75, 40.75 to 41.25 and 41.25 to 42, using the values for  $L_{[OIII]}$  listed in Paper I.

In Figs 4 to 9 we show the mean radial profiles for the different age bins (see Section 4 as well as for the mean ages). In order to see if there are differences in these profiles for early- and late-type galaxies, we show the results for both all the galaxies grouped together and also separated in early- and late-type hosts. In the top panels we show the results for the AGN hosts, in the middle panel for the corresponding controls and in the bottom panels the difference between AGN and controls. In each panel we show the five ranges of  $L_{[OIII]}$  colour coded and the respective number of objects (coloured numbers) included in the average calculation. It

is important to note that some of the AGN are not classified as early- or late-type (because they could not be clearly classified, e.g. could be the result of mergers), so the sum of early- and late-type galaxies may not represent the total number of objects (left column).

As can be seen in Fig. 4, the clearest difference in the profiles occurs for the highest  $[OIII]$  luminosity AGN, which show higher contribution of the young-age component than the controls along the whole galaxy.<sup>1</sup> In addition, the behaviour seems not to depend on the type of host galaxy (early- or late-type), at least up to  $0.6 R_e$ . We note that this bin has only four galaxies, but if we look at the profiles individually, we find the same behaviour in each one of them. Comparing with the non-active galaxies, the corresponding profiles are similar to the other luminosity bins. For the late-type sources, there is a clear shift in the slope at  $\sim 0.7 R_e$ ; for larger values of  $R_e$  it follows the other luminosity ranges. This, and the fact that the differences have a slightly negative slope in all morphology

<sup>1</sup>It is worth mentioning that we have inspected carefully the fits for the highest luminosity AGN, where differences in the young population were detected, and no problems with the synthesis quality were found.

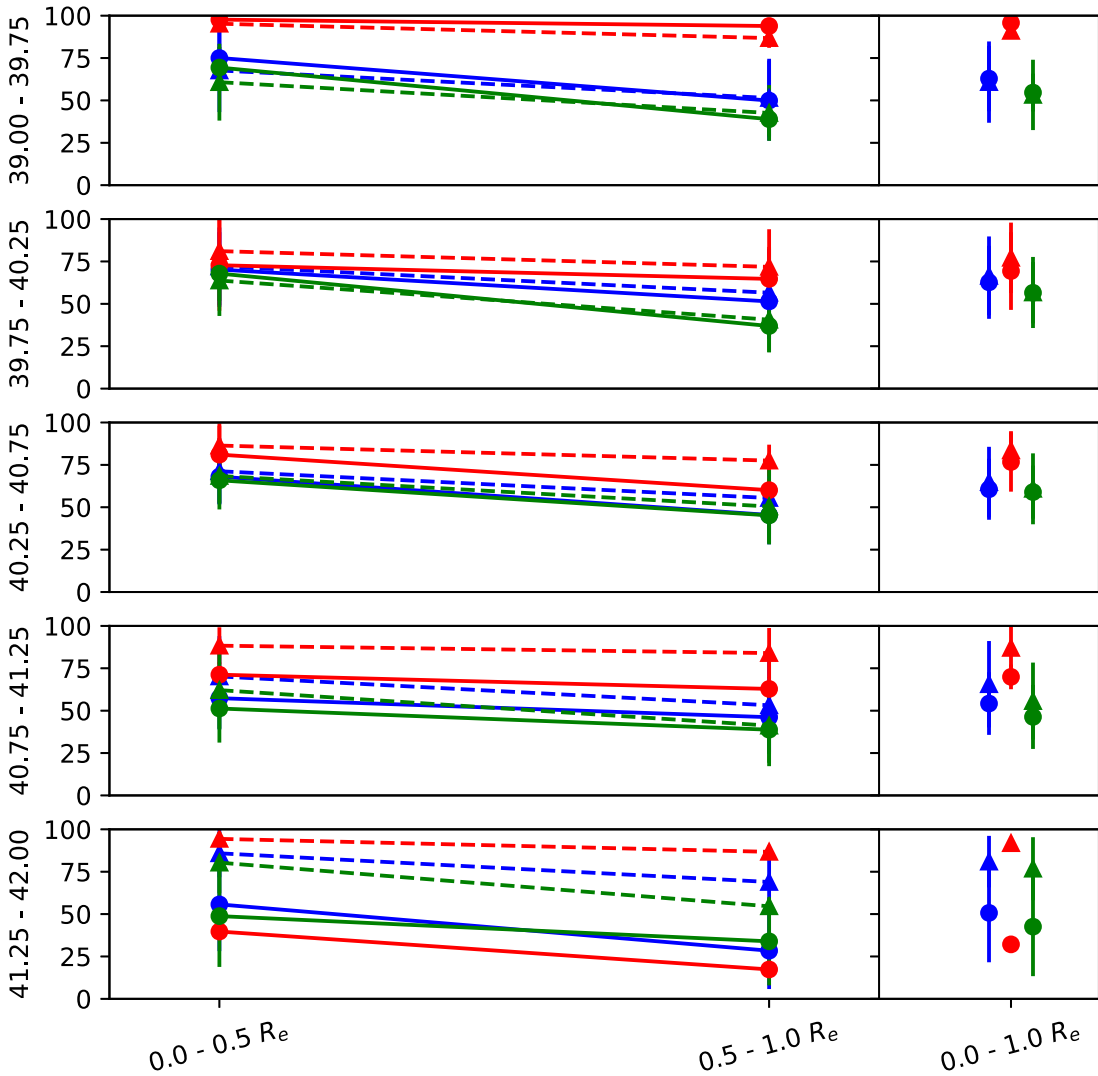


**Figure 12.** Old SP  $x_o$  for different bins of luminosity, calculated for three different regions (see Fig. 10).

groups, suggests that the AGN may enhance the star formation process in the nuclear region ( $R_e \lesssim 0.6$ ).

A similar excess in the AGN as compared to controls is also observed in the intermediate-age bins  $x_y$  and  $x_{ii}$  shown in Figs 5 and 6, although the excess seems to occur farther from the centre. A comparison among Figs 4–6 suggests an age stratification with radius for the highest luminosity sources, showing a larger fraction of younger stars in the central region, with the intermediate-age stars contributing more to the light in the outer regions. Regarding the old component, Fig. 7 shows that, as expected, the high-luminosity AGN has less contribution of this component than the controls, with differences ranging from  $\sim 20$  per cent to 60 per cent. A small trend can be observed also in this figure in the sense that a similar although smaller difference is also observed for the second luminosity bin, with the third and fourth bins showing almost no difference when compared with the controls, while the lowest luminosity bin showing the opposite: the controls having less contribution of the old component than the AGN.

In order to compare the galaxies using a single parameter we plot the radial profiles of their mean ages (see Section 4) in Fig. 9. It is clear from this figure that the higher luminosity AGN hosts are younger than the control galaxies in the entire studied region ( $1R_e$ ).

We interpret these results as due to the fact that AGN hosts do prefer the ‘outside-in’ scenario for the recent star formation, while the galaxy’s global stellar formation history (SFH) is better described by an inside-out scenario. This may reflect the idea that the active nuclei can drive the star formation process in the circumnuclear region.

Although the differences in the SP of the strongest AGN, when compared with the controls, were evident, a problem arises when trying to analyse other luminosity bins: the differences between the radial profiles are too noisy. In order to circumvent this problem, we binned the profiles into three regions ( $0.0-0.5 R_e$ ,  $0.5-1.0 R_e$  and  $0.0-1.0 R_e$ ) and the SPs into  $X_Y$ ,  $X_I$ ,  $X_O$ . We also plotted the contribution of the FC using these radial bins to inspect the light contribution of the AGN continuum. Figs 10–14 show the results of this exercise.<sup>2</sup> What clearly emerges from this test is that the youngest SPs are concentrated in the inner  $0.5 R_e$  of the most luminous AGN hosts (Fig. 10) – where the FC signature is

<sup>2</sup>Some galaxies have limited  $R_e$  coverage, meaning that the statistics gets weaker with radial distance. We addressed this problem by using radial intervals ( $0.5 R_e$ ).

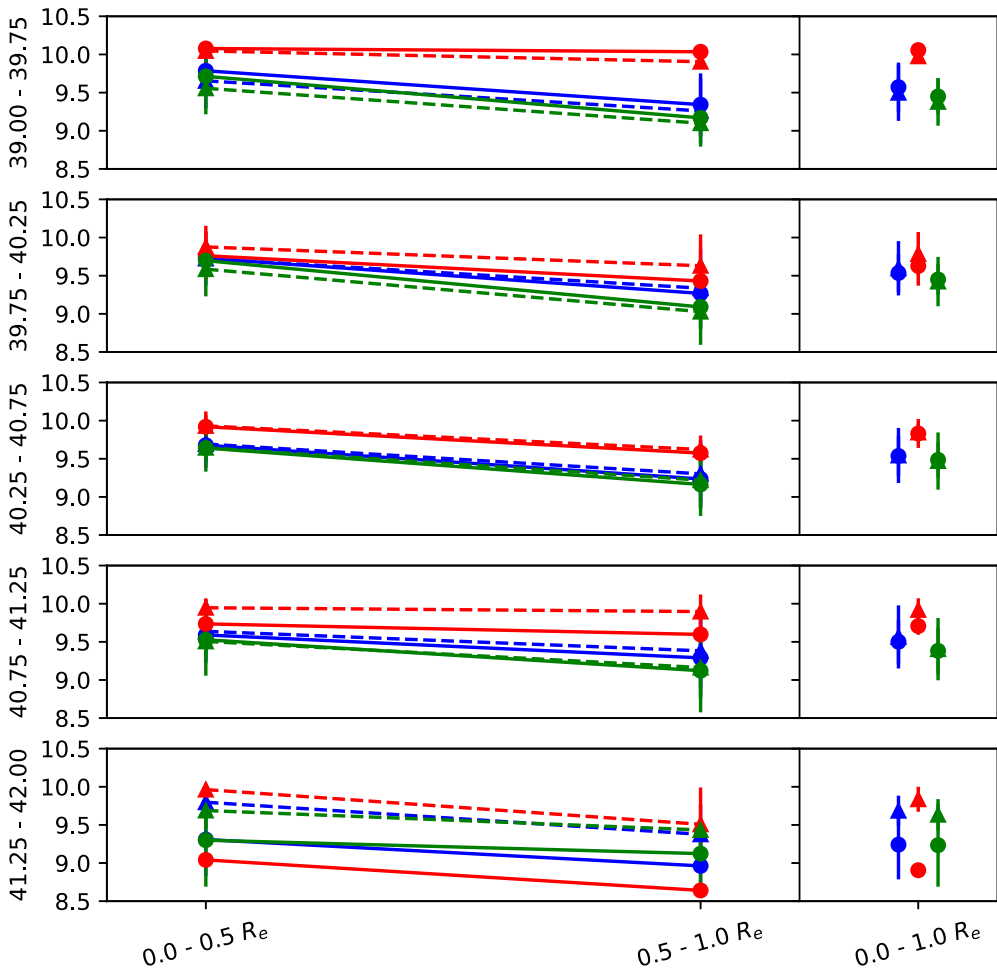


**Figure 13.** Mean age ( $\log t$ ) for different bins of luminosity, calculated for three different regions (see Fig. 10).

the strongest (Fig. 14) – and intermediate-age ones are located in regions with radius  $R \gtrsim 0.5 R_e$  (see Fig. 11) for all AGN luminosities. In addition, the contribution of these SP components is much larger in the AGN hosts (circles) than that in the control galaxies (triangles) in the case of the highest luminosity AGN. Another result shown by these plots is that the youngest age contributions increase outwards for late-type galaxies (both controls and AGN – except the most luminous AGN).

Figs 12 and 13 show that the strongest (highest luminosity) AGN present, in general, younger SPs than their control objects. In addition these plots do allow us to better analyse the other luminosity bins. For  $\log(L[\text{OIII}])$  between 40.75 and 41.25 (the second most luminous bin) no significant differences can be seen for the younger populations, while the intermediate-age contributions are higher for the AGN, being slightly more concentrated at the outer region ( $R \gtrsim 0.5 R_e$ ). For the remaining luminosity bins a similar behaviour is observed, however, when looking at the overall mean values (right side of Fig. 11) it is clear that the difference vanishes with luminosity decrease.

In the case of the old SP bin, the contribution of this population in the AGN hosts is lower than that observed in the control objects, and a decrease is observed from the centre outwards. A significant difference between active and non-active sources is seen for the two highest luminosity bins, especially when using the overall mean values (right side plot). We also separate the objects according

to their Hubble types (colour coded) and no clear difference is observed between early- and late-type galaxies when comparing active and non-active hosts.

The above results reinforce literature results (Kauffmann et al. 2003; Rembold et al. 2017) in the sense that when comparing low- and high-luminosity AGN, the contribution of old SPs decreases, while that of the younger SPs increases in the latter. However, our results do additionally show that this is especially enhanced in the circumnuclear regions ( $R \leq 0.5 R_e$ ) indicating that the inflow of material feeding the AGN is partially being used to form stars. In addition, we suggest that these nuclear starbursts could at least be partially related to a positive AGN feedback, which may be inducing star formation in the host galaxy through enhancing the gas turbulence in the interstellar medium. Such a positive feedback is predicted by simulations (Gabler et al. 2012; Ishibashi & Fabian 2012; Wagner, Bicknell & Umemura 2012; Zubovas et al. 2013; Bieri et al. 2015; Zubovas & Bourne 2017) and was already detected in a few objects (Cresci et al. 2015; Maiolino et al. 2017).

As can be seen from Figs 10 to 13 in general we observe that the fraction of young and intermediate-age SPs increases with the radius, while in the case of the old population, it decreases. These results support the previous findings reported by Sánchez et al. (2013), Ibarra-Medel et al. (2016) and Goddard et al. (2017) favouring an inside-out scenario for the formation of galaxies. However, when considering the most luminous AGN, it no longer applies, and it

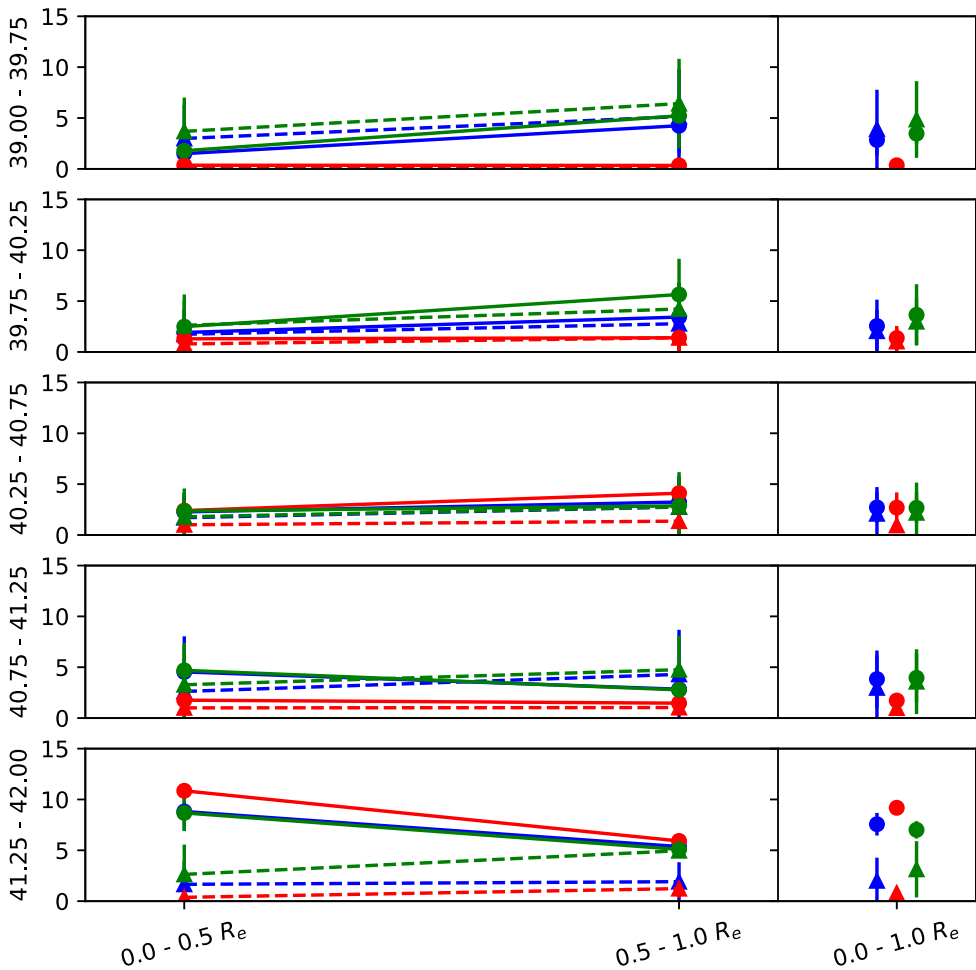


**Figure 14.** Featureless continuum for different bins of luminosity, calculated for three different regions (see Fig. 10).

seems that these AGN have been triggered by a recent supply of gas that has also triggered a recent star formation in their central regions. Our findings are opposite to the results of Goddard et al. (2017) in the case of early-type sources; we derive a slightly negative gradient while they derived a slightly positive one for this Hubble class.<sup>3</sup> On the other hand, our findings seem to agree with those of Ibarra-Medel et al. (2016), who showed that the radial stellar mass growth histories of early-type galaxies are on average nearly inside-out, though with a trend much less pronounced than that of the late-type galaxies.

## 6 CONCLUSIONS

We studied the stellar content of the first 62 AGN observed with SDSS-IV MaNGA and compared them with a matched sample of inactive galaxies presented in Paper I. We constructed spatially resolved SP age maps, corresponding average radial profiles and gra-

dients for these sources using the STARLIGHT code, aimed at studying the effects of the AGN on the SFH of the host galaxies.

We found that the fraction of the young SP ( $t \lesssim 40$  Myr) is related with the AGN luminosity. For high-luminosity AGN ( $L_{\text{[O III]}} \gtrsim 10^{41.25}$  erg s<sup>-1</sup>) it increases in the inner ( $R \leq 0.5R_e$ ) regions when compared with the objects in the control sample. In the case of the low-luminosity AGN, both AGN and control sample hosts present very similar fractions of young stars. This result indicates that the inflow of material, besides feeding the nuclear engine, is being used to form new stars, thus rejuvenating the stellar content of the nuclear region of the AGN hosts. In addition, this very young starburst could also be enhanced by a positive AGN feedback produced by the high-luminosity AGN.

The fraction of the intermediate-age,  $X_I$  ( $40 \text{ Myr} < t \leq 2.6 \text{ Gyr}$ ), SP of the AGN hosts slightly increase outwards, with a clear enhancement over the entire galaxy when compared with the control sample. In addition, our results show that the inner region of the galaxies is dominated by an old SP, whose fraction decreases outwards. These results support the previous findings of the CALIFA team (Sánchez et al. 2013), supporting an inside-out scenario for the galaxies' SFH.

<sup>3</sup>Note, however, that we are studying the inner  $1 R_e$  (they used  $1.5 R_e$ ) and a smaller sample than that studied by these authors.

We also investigated for differences on the star formation histories between the different Hubble types. No significant differences were found between early- and late-type host galaxies.

From our results we suggest that an outside-in scenario better describes the recent star formation in the AGN hosts, while an inside-out scenario represents better the older generations of stars.

## ACKNOWLEDGEMENTS

We thank the anonymous referee for the useful comments and suggestions. NDM thanks to CNPq for financial support. RR thanks FAPERGS and CNPq for financial support.

Funding for the Sloan Digital Sky Survey IV has been provided by the Alfred P. Sloan Foundation, the U.S. Department of Energy Office of Science, and the Participating Institutions. SDSS acknowledges support and resources from the Center for High-Performance Computing at the University of Utah. The SDSS web site is [www.sdss.org](http://www.sdss.org).

SDSS is managed by the Astrophysical Research Consortium for the Participating Institutions of the SDSS Collaboration including the Brazilian Participation Group, the Carnegie Institution for Science, Carnegie Mellon University, the Chilean Participation Group, the French Participation Group, Harvard–Smithsonian Center for Astrophysics, Instituto de Astrofísica de Canarias, The Johns Hopkins University, Kavli Institute for the Physics and Mathematics of the Universe (IPMU)/University of Tokyo, Lawrence Berkeley National Laboratory, Leibniz Institut für Astrophysik Potsdam (AIP), Max-Planck-Institut für Astronomie (MPIA Heidelberg), Max-Planck-Institut für Astrophysik (MPA Garching), Max-Planck-Institut für Extraterrestrische Physik (MPE), National Astronomical Observatories of China, New Mexico State University, New York University, University of Notre Dame, Observatório Nacional/MCTI, The Ohio State University, Pennsylvania State University, Shanghai Astronomical Observatory, United Kingdom Participation Group, Universidad Nacional Autónoma de México, University of Arizona, University of Colorado Boulder, University of Oxford, University of Portsmouth, University of Utah, University of Virginia, University of Washington, University of Wisconsin, Vanderbilt University and Yale University.

## REFERENCES

- Baldwin J. A., Phillips M. M., Terlevich R., 1981, *PASP*, 93, 5  
 Bieri R., Dubois Y., Silk J., Mamon G. A., 2015, *ApJ*, 812, L36  
 Bruzual G., Charlot S., 2003, *MNRAS*, 344, 1000  
 Bundy K. et al., 2015, *ApJ*, 798, 7  
 Cardelli J. A., Clayton G. C., Mathis J. S., 1989, *ApJ*, 345, 245  
 Cid Fernandes R., Gu Q., Melnick J., Terlevich E., Terlevich R., Kunth D., Rodrigues Lacerda R., Joguet B., 2004, *MNRAS*, 355, 273  
 Cid Fernandes R., Mateus A., Sodré L., Stasińska G., Gomes J. M., 2005, *MNRAS*, 358, 363  
 Cid Fernandes R., Stasińska G., Mateus A., Vale Asari N., 2011, *MNRAS*, 413, 1687  
 Cid Fernandes R., Stasińska G., Schlickmann M. S., Mateus A., Vale Asari N., Schoenell W., Sodré L., 2010, *MNRAS*, 403, 1036

- Cresci G. et al., 2015, *ApJ*, 799, 82  
 Davies R. I., Maciejewski W., Hicks E. K. S., Tacconi L. J., Genzel R., Engel H., 2009, *ApJ*, 702, 114  
 Davies R. I., Müller Sánchez F., Genzel R., Tacconi L. J., Hicks E. K. S., Friedrich S., Sternberg A., 2007, *ApJ*, 671, 1388  
 Dawson K. S. et al., 2016, *Astron. J.*, 151, 44  
 de Amorim A. L. et al., 2017, *MNRAS*, 471, 3727  
 Drory N. et al., 2015, *AJ*, 149, 77  
 Gaibler V., Khochfar S., Krause M., Silk J., 2012, *MNRAS*, 425, 438  
 Goddard D. et al., 2017, *MNRAS*, 465, 688  
 Heckman T. M., Best P. N., 2014, *ARA&A*, 52, 589  
 Hicks E. K. S., Davies R. I., Maciejewski W., Emsellem E., Malkan M. A., Dumas G., Müller-Sánchez F., Rivers A., 2013, *ApJ*, 768, 107  
 Ibarra-Medel H. J. et al., 2016, *MNRAS*, 463, 2799  
 Ishibashi W., Fabian A. C., 2012, *MNRAS*, 427, 2998  
 Kauffmann G. et al., 2003, *MNRAS*, 346, 1055  
 Kawakatu N., Wada K., 2008, *ApJ*, 681, 73  
 Kormendy J., Ho L. C., 2013, *ARA&A*, 51, 511  
 Law D. R. et al., 2015, *AJ*, 150, 19  
 Law D. R. et al., 2016, *AJ*, 152, 83  
 Maiolino R. et al., 2017, *Nature*, 544, 202  
 Majewski S. R. et al., 2017, *AJ*, 154, 94  
 Rembold S. B. et al., 2017, *MNRAS*, 472, 4382  
 Riffel R., Pastoriza M. G., Rodríguez-Ardila A., Bonatto C., 2009, *MNRAS*, 400, 273  
 Riffel R. A. et al., 2016, *MNRAS*, 461, 4192  
 Sanchez S. F. et al., 2017, *RMxAA*, 54, 217  
 Sarzi M., Allard E. L., Knapen J. H., Mazzuca L. M., 2007, *MNRAS*, 380, 949  
 Schlegel D. J., Finkbeiner D. P., Davis M., 1998, *ApJ*, 500, 525  
 Sánchez S. F. et al., 2013, *A&A*, 554, A58  
 Wagner A. Y., Bicknell G. V., Umemura M., 2012, *ApJ*, 757, 136  
 Yan R. et al., 2015, *AJ*, 151, 8  
 Yan R. et al., 2016, *AJ*, 152, 197  
 Zheng Z. et al., 2017, *MNRAS*, 465, 4572  
 Zubovas K., Bourne M. A., 2017, *MNRAS*, 468, 4956  
 Zubovas K., Nayakshin S., Sazonov S., Sunyaev R., 2013, *MNRAS*, 431, 793

## SUPPORTING INFORMATION

Supplementary data are available at *MNRAS* online.

### **comparisons\_62\_agn.pdf**

Please note: Oxford University Press is not responsible for the content or functionality of any supporting materials supplied by the authors. Any queries (other than missing material) should be directed to the corresponding author for the article.

## APPENDIX A: AGN - CONTROL GALAXIES COMPARISON IMAGES

We present all the comparisons between AGN and its control galaxies in Figs A1–A62 online.

This paper has been typeset from a  $\text{\TeX}$ / $\text{\LaTeX}$  file prepared by the author.



# The first 62 AGN observed with SDSS-IV MaNGA – III: stellar and gas kinematics

Gabriele S. Ilha<sup>1,2</sup>★ Rogemar A. Riffel<sup>1,2</sup>★ Jaderson S. Schimoia,<sup>1,2,3</sup>  
Thaisa Storchi-Bergmann,<sup>2,3</sup> Sandro B. Rembold,<sup>1,2</sup> Rogério Riffel<sup>1,2,3</sup>  
Dominika Wylezalek<sup>4</sup> Yong Shi<sup>5</sup> Luiz N. da Costa,<sup>2,6</sup> Alice D. Machado,<sup>1,2</sup>  
David R. Law,<sup>7,8</sup> Dmitry Bizyaev,<sup>9,10</sup> Nicolas D. Mallmann,<sup>2,3</sup> Janaina Nascimento,<sup>2,3</sup>  
Marcio A. G. Maia<sup>2,6</sup> and Rafael Cirolini<sup>1,2</sup>

<sup>1</sup>Departamento de Física, CCNE, Universidade Federal de Santa Maria, 97105-900, Santa Maria, RS, Brazil

<sup>2</sup>Laboratório Interinstitucional de e-Astronomia - LIneA, Rua Gal. José Cristino 77, Rio de Janeiro, RJ - 20921-400, Brazil

<sup>3</sup>Departamento de Física, IF, Universidade Federal do Rio Grande do Sul, CP 15051, 91501-970, Porto Alegre, RS, Brazil

<sup>4</sup>European Southern Observatory, Karl-Schwarzschildstr 2, D-85748 Garching bei München, Germany

<sup>5</sup>Department of Astronomy, Nanjing University, Nanjing 210093, China

<sup>6</sup>Observatório Nacional - MCT, Rua General José Cristino 77, Rio de Janeiro, RJ - 20921-400, Brazil

<sup>7</sup>Space Telescope Science Institute, 3700 San Martin Drive, Baltimore, MD 21218, USA

<sup>8</sup>Dunlap Institute for Astronomy and Astrophysics, University of Toronto, 50 St George Street, Toronto, Ontario M5S 3H4, Canada

<sup>9</sup>Apache Point Observatory, PO Box 59, Sunspot, NM 88349, USA

<sup>10</sup>Sternberg Astronomical Institute, Moscow State University, 119992 Moscow, Russia

Accepted 2018 December 2. Received 2018 November 21; in original form 2018 May 3

## ABSTRACT

We investigate the effects of active galactic nuclei (AGN) on the gas kinematics of their host galaxies, using MaNGA data for a sample of 62 AGN hosts and 109 control galaxies (inactive galaxies). We compare orientation of the line of nodes (kinematic position angle – PA) measured from the gas and stellar velocity fields for the two samples. We found that AGN hosts and control galaxies display similar kinematic PA offsets between gas and stars. However, we note that AGN have larger fractional velocity dispersion  $\sigma$  differences between gas and stars [ $\sigma_{\text{frac}} = (\sigma_{\text{gas}} - \sigma_{\text{stars}})/\sigma_{\text{stars}}$ ] when compared to their controls, as obtained from the velocity dispersion values of the central (nuclear) pixel (2.5'' diameter). The AGN have a median value of  $\sigma_{\text{frac}}$  of  $\langle \sigma_{\text{frac}} \rangle_{\text{AGN}} = 0.04$ , while the median value for the control galaxies is  $\langle \sigma_{\text{frac}} \rangle_{\text{CTR}} = -0.23$ . 75 per cent of the AGN show  $\sigma_{\text{frac}} > -0.13$ , while 75 per cent of the normal galaxies show  $\sigma_{\text{frac}} < -0.04$ , thus we suggest that the parameter  $\sigma_{\text{frac}}$  can be used as an indicator of AGN activity. We find a correlation between the [O III] $\lambda 5007$  luminosity and  $\sigma_{\text{frac}}$  for our sample. Our main conclusion is that the AGN already observed with MaNGA are not powerful enough to produce important outflows at galactic scales, but at 1–2 kpc scales, AGN feedback signatures are always present on their host galaxies.

**Key words:** galaxies: active – galaxies: general – galaxies: kinematics and dynamics.

## 1 INTRODUCTION

Theoretical studies and numerical simulations suggest that active galactic nuclei (AGN) play an important role in the evolution of their host galaxies (e.g. Hopkins et al. 2005). Currently, it is widely accepted that galaxies with spherical component (bulge of spiral galaxies and elliptical galaxies) host a central supermassive black hole (SMBH; Ferrarese & Merritt 2000; Gebhardt et al. 2000;

Tremaine et al. 2002; Scannapieco et al. 2005) and cosmological simulations that do not include feedback effects from the SMBH result in galaxy stellar masses much higher than observed (Di Matteo, Springel & Hernquist 2005; Springel, Di Matteo & Hernquist 2005; Bower et al. 2006). Massive outflows originated in the accretion flow are claimed to regulate and couple the growth of the galactic bulge and SMBH (Hopkins et al. 2005) and to explain the relation between the mass of the SMBH and stellar velocity dispersion of the bulge – the  $M-\sigma$  relation (e.g. Ferrarese & Merritt 2000; Gebhardt et al. 2000).

\* E-mail: gabrieleilha1994@gmail.com (GSI); rogemar@uol.br (RAR)

According to the Unified Model for AGN (e.g. Antonucci 1993; Urry & Padovani 1995), the narrow-line region (NLR) is expected to present a bi-conical shape, within which gas outflows due to winds from the accretion disc are expected to be observed. However, *Hubble Space Telescope (HST)* narrow-band [O III] $\lambda 5007$  images of a sample of 60 nearby Seyfert galaxies show that the bi-conical shape of the NLR is not as common as expected (Schmitt et al. 2003), and gas outflows are seen only in 33 per cent of Seyfert galaxies, as revealed by long-slit spectroscopy of 48 nearby AGN (Fischer et al. 2013). Nevertheless, long-slit observations are restricted to only one position angle (PA). A better mapping of the outflows and their geometries can be obtained via integral field spectroscopy (IFS), as shown in recent studies both in the optical and near-infrared (e.g. Barbosa et al. 2014; Riffel, Storchi-Bergmann & Riffel 2014; Schnorr-Müller et al. 2014; Lena et al. 2015; Zakamska et al. 2016). The comparison between the gas and stellar kinematics on kiloparsec scales allows the study of the possible impact of AGN outflows on its host galaxy. So far, most studies aimed to investigate gas outflows from AGN have been performed for small samples or individual galaxies. In this work, we use the observations from the Mapping Nearby Galaxies at the Apache Point Observatory (MaNGA) survey (Bundy et al. 2015) to compare the gas and stellar kinematics of a sample composed by 62 AGN observed in the MPL-5 (MaNGA Product Launch V) (Data Release 14, Abolfathi et al. 2018) with those of a control sample of inactive galaxies, matched with the AGN sample by properties of the host galaxies. If an AGN sample presents strong outflows, the large-scale gas velocity fields are expected to be disturbed when compared to the stellar velocity fields, while for inactive galaxies, the stellar and gas velocity fields are expected to be similar. Another way that AGN can affect the gas dynamics is by increasing the gas velocity dispersion due to the shocks of the nuclear outflow with the ambient gas.

The AGN and control samples used in this paper are described in Rembold et al. (2017; hereafter Paper I), which presents also the study of the nuclear stellar populations. This is the third paper of a series aimed to compare properties of AGN hosts and their control galaxies. Besides Paper I, the spatially resolved stellar populations are investigated in Mallmann et al. (2018; Paper II). In addition, the gas excitation and distribution will be presented by Nascimento et al. (in preparation – Paper IV).

This paper is organized as follows: Section 2 presents the samples of active and inactive galaxies and the data analysis methods, while Section 3 presents the results, which are discussed in Section 4. Finally, the conclusions of this work are presented in Section 5.

## 2 THE DATA AND ANALYSIS

### 2.1 Sample and MaNGA data

We use the data cubes obtained within the MaNGA survey of the sample of AGN and matched control sample defined in Paper I. The MaNGA survey is part of the fourth-generation Sloan Digital Sky Survey (SDSS-IV) and is aimed to observe  $\sim 10\,000$  nearby galaxies using optical IFS covering the spectral range 3600–10 000 Å and spectral resolving power  $R \sim 2000$  at a spatial resolution of 1–2 kpc. The MaNGA sample of galaxies was designed to cover at least  $1.5 R_e$  ( $R_e$  – effective radius). Here, the effective radius is defined as the radius that contains the half luminosity of galaxy measured at the  $i$  band as described in Bundy et al. (2015). The MaNGA survey science goals are presented in Bundy et al. (2015), the design and performance of the integral field units are discussed in Drory et al. (2015), and the MaNGA sample is presented in Wake

et al. (2017). Yan et al. (2016b) present the survey design, execution, and data quality, the observing strategy is presented in Law et al. (2015), and the data reduction and calibrations are discussed in Law et al. (2016) and Yan et al. (2016a).

Our sample is composed of the first 62 AGN observed with MaNGA – selected from MaNGA MPL-5 (Data Release 14, Abolfathi et al. 2018). For each AGN, two control inactive galaxies, matched to the AGN hosts in absolute magnitude, galaxy mass, redshift, morphological type and inclination, were selected. The AGN selection realized by Rembold et al. (2017) is based on single-fibre SDSS-III observations. A detailed description and characterization of the AGN and control samples are presented in Paper I. Wylezalek et al. (2018) found 173 galaxies that would not have been selected as AGN candidates based on single-fibre spectral measurements, but MaNGA allowed AGN selection based on the fully spatially resolved optical diagnostics and in the future papers similar work will be done for ‘nuclear’ AGN and ‘off-nuclear’ AGN. Thus, in this work we focus on the ‘nuclear’ AGN. As mentioned in Rembold et al. (2017), our AGN sample includes 34 (55 per cent) spiral and 18 (29 per cent) elliptical galaxies. The remaining 10 objects (16 per cent) comprise six E/S galaxies, one merger, and three unclassified objects.

### 2.2 Spatial filtering and noise removal

In order to remove noise from the observed data cubes, without loss of angular resolution, we performed a spatial filtering of the data cubes using a Butterworth bandpass filter (Gonzalez & Woods 2002). This filter is performed in the frequency domain. We used a low-bandpass filter to remove high spatial frequency components from the cubes, which are usually due to spurious features (e.g. bad pixels or cosmic rays). This procedure allows us to improve the fit, emission and absorption line spectra, compared with the original data cubes.

To perform the spatial filtering, we used the Interactive Data Language (IDL) routine *bandpass\_filter.pro*, which allows the choice of the cut-off frequency ( $\nu$ ) and order of the filter  $n$ . A low value of  $n$  (e.g. 1) is close to a Gaussian filter, while a high value (e.g. 10) corresponds to an ideal filter. We used  $n = 5$  and  $\nu = 0.25$  Ny, chosen by comparing the filtered cubes with the original ones. For lower values of  $\nu$ , besides the removal of spatial noise, the filter excludes also emission from the nucleus of the galaxy.

### 2.3 Spectral fitting

In order to measure the emission-line fluxes and the stellar and gas kinematics from the MaNGA data cubes, we used the Gas AND Absorption Line Fitting (GANDALF) code (Sarzi et al. 2006; Oh et al. 2011). In brief, the GANDALF code fits the emission and absorption lines simultaneously, allowing the separation of the relative contribution of the stellar continuum and of nebular emission in the spectra of the galaxies. To subtract the underlying stellar contribution on the spectra of the galaxy and measure the stellar kinematics, GANDALF uses the Penalized Pixel-Fitting (PPXF) routine (Cappellari & Emsellem 2004; Cappellari 2017). The continuum spectra of the galaxy are fitted using a library of template spectra under the assumption that the line-of-sight velocity distribution (LOSVD) of the stars is well reproduced by a Gauss-Hermite series.

As template spectra, we used 30 selected evolutionary population synthesis models from Bruzual & Charlot (2003), covering ages ranging from 5 Myr to 12 Gyr and three metallicities

( $0.004 Z_{\odot}$ ,  $0.02 Z_{\odot}$ , and  $0.05 Z_{\odot}$ ). During the fit of the spectra, we allowed the use of an order 3 multiplicative Legendre polynomial to correct the shape of the continuum and only the first two Gauss–Hermite moments (velocity and velocity dispersion) were included to represent the LOSVD. We have tested the inclusion of higher order moments, but achieved the best results in the fitting process by considering only the first and second moments.

The emission-line profiles were fitted by Gaussian curves, by keeping tied the centroid velocity and width of the  $[\text{N II}]\lambda\lambda 6548, 6583$  and  $[\text{S II}]\lambda\lambda 6716, 6731$  emission lines, fitting each doublet separately. In addition, the following line flux-ratio was kept fixed to their theoretical value:  $[\text{N II}]\lambda 6583/[\text{N II}]\lambda 6548 = 2.94$  (Osterbrock & Ferland 2006). GANDALF gives output measurements for the centroid velocity and velocity dispersion ( $\sigma$ ) of the stars, and the flux, centroid velocity, and  $\sigma$  of the emission lines for each spaxel, used to construct 2D maps.

#### 2.4 Measurements of the kinematic position angles

In order to measure the global kinematic PA (i.e. the orientation of line of nodes –  $\Psi_0$ ) from the stellar and gas velocity fields, we used the kinemetry method (Krajnović et al. 2005). This method extracts general kinematic properties of the galaxies by the symmetrization of the observed velocity fields, without the need of any assumption on the geometry of the stellar distribution. To obtain the global kinematic PA, the kinemetry method performs the symmetrization of the observed velocity fields. For each possible PA a symmetric velocity field  $V'(x, y)$  is created, with the PA oriented along the  $x$ -axis. The symmetric velocity field is obtained by changing the mean velocity of each bin for the weighted average of the corresponding velocity in the four quadrants of the velocity field. The global kinematic PA is the one that minimizes  $\chi^2 = \sum_{n=1}^N (V'(x, y) - V(x, y)/\Delta V)^2$ , where  $V(x, y)$  is the value of observed velocity field at the position  $(x, y)$ .

We used the IDL routine *fit\_kinemetic\_pa.pro*,<sup>1</sup> which is an implementation of the kinemetry method and allows the measurement of the global kinematic PA and systemic velocity of the galaxy from the observed velocity fields. The routine is an implementation of the method presented in appendix C of Krajnović et al. (2006) and has been used to study the stellar kinematics of large samples of galaxies, for example the SAURON (Cappellari et al. 2007) and ATLAS<sup>3D</sup> (Krajnović et al. 2011) surveys.

### 3 RESULTS

We have performed measurements for the stellar and gas kinematics and emission-line fluxes for  $\text{H}\beta$ ,  $[\text{O III}]\lambda 5007$ ,  $\text{H}\alpha$ ,  $[\text{N II}]\lambda\lambda 6549, 83$ , and  $[\text{S II}]\lambda\lambda 6716, 31$ . With the aim of testing our measurements, we have compared the emission-line fluxes, centroid velocities, and velocity dispersions with measurements provided by the MaNGA Data Analysis Pipeline (DAP – Westfall et al., in preparation), as part of the MPL-7.

Fig. 1 shows an example of our measurements (top row) compared with those from the DAP (bottom row) for the AGN *mangaid* 1-339163. The first column shows a map of the continuum emission, the following columns exhibit maps of emission line fluxes for  $[\text{O III}]\lambda 5007$  Å,  $\text{H}\alpha$ , and  $[\text{N II}]\lambda 6583$  Å, respectively. The comparison

between the top and bottom rows shows that our flux measurements are similar to those provided by the DAP.

In Fig. 2, we show the velocity fields for the same galaxy *mangaid* 1-339163. We present the stellar velocity field together with the gas velocity fields derived for the same emission lines presented in Fig. 1. For comparison, we show our results in the top row, while the results from DAP are shown in the bottom row. The comparison shows that the two velocity fields are similar, although the DAP maps are noisier.

The comparison of the velocity dispersion maps obtained by us and from the DAP is shown in Fig. 3, following the same pattern of organization as the previous figures. As for the centroid velocity and emission-line flux maps, the  $\sigma$  maps from DAP are noisier than ours. The gas and stellar  $\sigma$  values will be used to search for outflows in the central region of the galaxies of our sample.

As noticed in Figs 1–3, our measurements are in general consistent with those provided by DAP, but the spatial filtering of the data allows the exclusion of spurious data, as clearly seen in the maps for the  $[\text{N II}]\lambda 6583$  Å and  $\text{H}\alpha$  velocity dispersion, for which the maps constructed using the DAP show a spurious feature at 4 arcsec east of the nucleus, which is not present in our measurements. On the other hand, the DAP has the advantage of providing measurements for all emission lines present in the galaxy spectra, while we fit only the strongest lines. However, a detailed comparison of our measurements and those provided by DAP is beyond the scope of this paper.

In order to verify if outflows of gas from the central AGN affect significantly the kinematics of AGN hosts, we can compare the kinematic PA ( $\Psi_0$ ) of the gas and stellar velocity fields. The motion of the stars is dictated by the gravitational potential of the galaxy, while for the gas, an additional component due to outflows is expected for the AGN. By comparing the difference between the  $\Psi_0$  values derived from the gas and stellar velocity fields for AGN and control samples, one should expect larger differences for the AGN if strong outflows are present. We derived  $\Psi_0$  for the stellar and gas velocity fields using  $[\text{O III}]\lambda 5007$  Å,  $\text{H}\alpha$ , and  $[\text{N II}]\lambda 6583$  Å emission lines. In Fig. 4, we show two examples of the observed and symmetrized velocity fields for two AGN (*mangaid* 1-95092 and *mangaid* 1-351790). This figure illustrates two distinct results: (i) the  $\Psi_0$  from distinct emission-line velocity fields is very similar to each other for both galaxies, (ii) for the galaxy *mangaid* 1-95092 the  $\Psi_0$  derived from the stellar velocity field is very similar to that derived for the gas velocity field, and (iii) in the case of the AGN host *mangaid* 1-351790 the orientation of the kinematic major axis of the stellar and gas velocity fields shows a significant offset. In Fig. 5, we show a similar figure for two control galaxies: *mangaid* 12-129446 and *mangaid* 1-178838, showing similar results as those observed for the AGN: similar  $\Psi_0$  for all emission lines and in one case a distinct  $\Psi_0$  for the gas and stars. From Figs 4 and 5, we can conclude that for these galaxies both AGN and controls present a rotation pattern in the stellar as well as in the gas velocity fields. In Table A1, we present the kinematic PA derived for all galaxies of our sample and the properties of AGN and control galaxies are shown in Table A2 and Table A3 (Rembold et al. 2017), respectively.

### 4 DISCUSSION

In order to investigate if the AGN feedback in our sample is powerful enough to disturb the gas kinematics on galactic scales and change the orientation of the kinematic major axis of the galaxy, we calculated the frequency of occurrence of a given PA offset in the AGN and control samples. We computed the difference in the

<sup>1</sup>This routine was developed by M. Cappellari and is available at <http://www-astro.physics.ox.ac.uk/~mxc/software>.

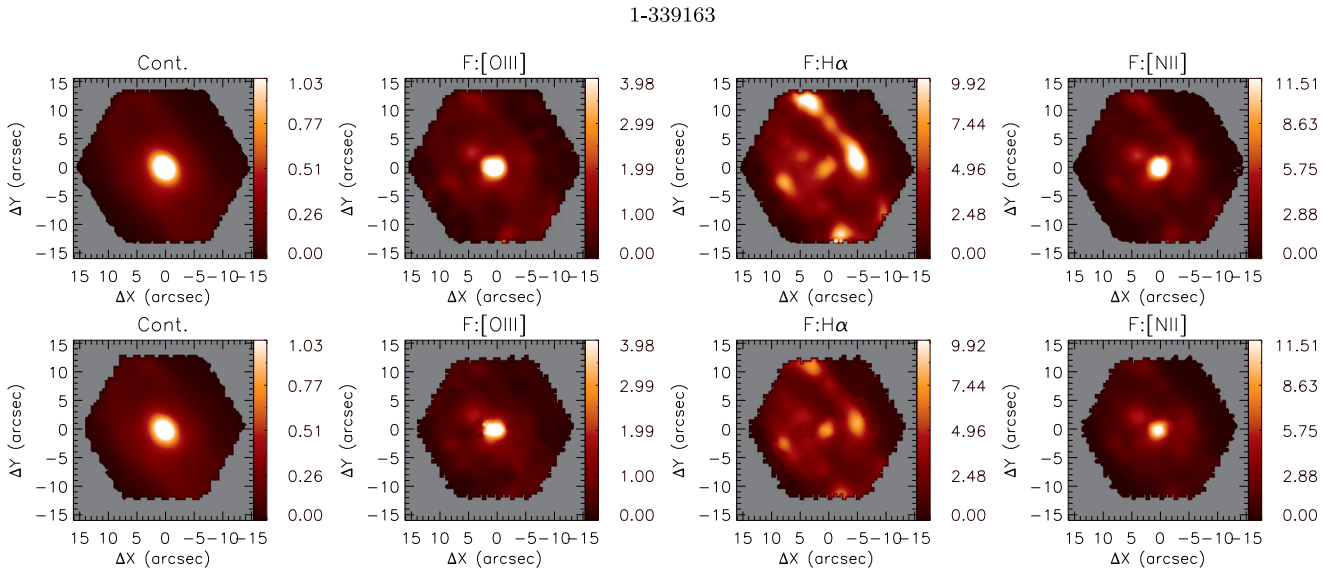


**Figure 1.** Emission lines fluxes for the galaxy with *mangaid* 1-339163. Our measurements are shown at the top row and the MaNGA-DAP measurements at the bottom row. In all panels, the North points up and East to the left and the  $x$  and  $y$  labels show the distance relative to the peak of the continuum emission. The first column shows a map of the continuum emission obtained by collapsing the whole spectral range, the following columns exhibit the spatial distribution of the emission line fluxes for [O III]5007 Å, H $\alpha$ , and [N II]6583 Å, respectively. The colour bars show the fluxes in unit of  $10^{-17}$  erg  $s^{-1}$  cm $^{-2}$  spx $^{-1}$ .

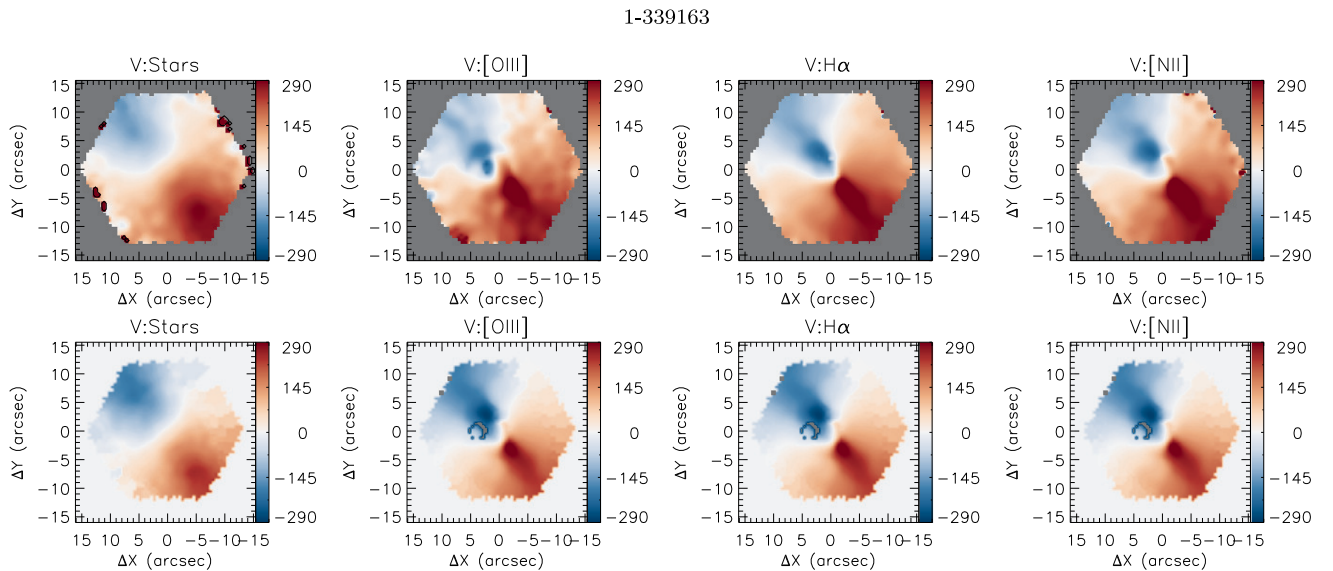


**Figure 2.** Velocity fields for the galaxy *mangaid* 1-339163. Our measurements are shown at the top row and the DAP measurements at the bottom row. In all panels, the North points up and East to the left and the  $x$  and  $y$  labels show the distance relative to the peak of the continuum emission. The systemic velocity has been subtracted from each panel. The first column shows the stellar velocity field and the following columns exhibit the velocity fields for [O III], H $\alpha$ , and [N II], respectively. The velocity maps are in unit of km  $s^{-1}$  relative to the systemic velocity of the galaxy.

$\Psi_{0*}$  of the stellar velocity field with respect to the  $\Psi_{0\text{gas}}$  derived for [O III]5007 Å, H $\alpha$ , and [N II]6583 Å emission-line velocity fields. The resulting histograms of the PA offsets ( $\Delta\text{PA} = |\Psi_{0\text{gas}} - \Psi_{0*}|$ ) are presented in Fig. 6. The top panels show the results using the [O III] velocity fields, while the middle panel shows these results for H $\alpha$  and the bottom panel for [N II]. AGN are represented by the blue colours and control galaxies are shown in red.

We find no clear difference in the distribution of  $\Delta\text{PA}$  for the AGN and control samples. Similar values of  $\Delta\text{PA}$  are observed for distinct emission lines. Although a few galaxies display large  $\Delta\text{PA}$  values, for most of them  $\Delta\text{PA}$  is smaller than 30°. For 79 per cent

of AGN and 81 per cent of control galaxies, the PA offsets are smaller than 30° as measured using the [O III]5007 Å velocity field as representative of the gas velocity field. This result indicates that the AGN feedback is not strong enough to disturb – more than in a control sample – the gas kinematics on the galactic scales probed by MaNGA. Indeed, the sample of active galaxies used here is composed mainly by low-luminosity AGN (Rembold et al. 2017), for which outflows from the accretion disc are expected to be weak, and thus the gas velocity fields of these AGN hosts on galactic scales are expected to be driven by the gravitational potential of the galaxy. Besides that, Wylezalek et al. (2017) only find evidence for

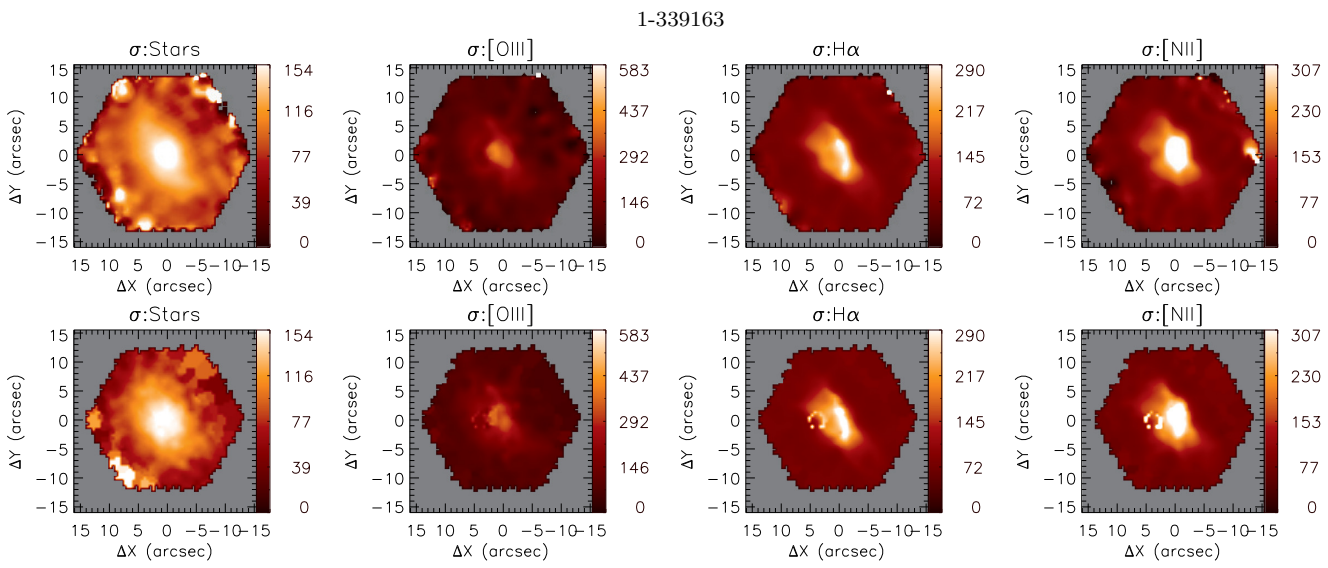


**Figure 3.** Velocity dispersion maps for the galaxy with *mangaid* 1-339163. Our measurements are shown at the top row and the DAP measurements at the bottom row. In all panels, the North points up and East to the left and the  $x$  and  $y$  labels show the distance relative to the peak of the continuum emission. The first column shows the stellar velocity dispersion distribution and the following columns exhibit the gas velocity dispersion distributions for [O III], H $\alpha$ , and [N II], respectively. The colour bars show the velocity dispersion corrected by instrumental broadening in units of  $\text{km s}^{-1}$ .

an AGN-driven outflow in a MaNGA-selected AGN candidate when zoom into the centre with higher spatial resolution. The resolution of MaNGA is only  $1\farcs5$ – $2\farcs5$ , so a lot of small-scale outflows may be hidden. We do not find any clear difference in the  $\Delta\text{PA}$  of high- and low-luminosity AGN.

Penny et al. (2018) analysed low-mass galaxies ( $M_\star \lesssim 5 \times 10^9 M_\odot$ ) of the SDSS-IV MaNGA and found that five galaxies of their sample of 13 possible dwarf AGN host, exhibit ionized gas components in H $\alpha$  that are kinematically offset from their stellar velocity field and these objects have AGN-like emission line ratios at their centres. This fact has been interpreted as a recent accretion episode or outflow. Furthermore, Penny et al. (2018) suggest that AGN feedback may play an important role in these low-mass galaxies. Their sample can be considered an analogous of the ‘Red Geysers’ galaxies reported by Cheung et al. (2016) using MaNGA data. These galaxies do not show recent star formation activity, most of them harbour very low-luminosity AGN, showing large-scale bi-polar outflows in ionized gas and interpreted as being originated by centrally driven winds due to a radiatively inefficient accretion flow on to the SMBH. These galaxies show stellar and gas kinematic major axes misaligned and account for 10 per cent of the population of galaxies with masses of the order of  $2 \times 10^{10} M_\odot$  that do not show recent star formation episodes. Although some galaxies of our sample show  $\Delta\text{PA} > 30^\circ$ , as seen in Fig. 6, the fraction of AGN and control galaxies with significant PA offset is similar (21 per cent and 19 per cent for AGN and control sample, respectively), suggesting that these offsets are not associated with the presence AGN, and probably they are just statistical fluctuations. Thus, we show that standard AGN do not follow the same behaviour of ‘Red Geyser’ galaxies analysed by Cheung et al. (2016) and the low-mass galaxies presented in Penny et al. (2018), as we do not detect significant PA offsets.

The fact that there are no significant PA offsets in our sample does not necessarily mean that the AGN do not show outflows, although it implies they do not play an important role in the galaxy scale

gas kinematics. However, AGN-driven outflows could be seen on smaller scales.

In order to search for signatures of outflows closer to the nuclei of the galaxies, we have compared the stellar and gas velocity dispersion values within the inner  $2\farcs5$  diameter of the galaxies of our sample, as this aperture corresponds to the angular resolution of the MaNGA data cubes. In Table A1, we show these velocity dispersion values. On average, the  $2\farcs5$  aperture corresponds to a physical scale of  $\sim 2$  kpc at the typical redshift of the sample galaxies. In order to quantify the differences between the stellar and gas velocity dispersions measured in the central regions, we calculated the parameter  $\sigma_{\text{frac}}$ , defined as

$$\sigma_{\text{frac}} = \frac{\sigma_{\text{gas}} - \sigma_\star}{\sigma_\star}, \quad (1)$$

which measures the fractional difference between the gas and stellar velocity dispersion, and thus higher values of  $\sigma_{\text{frac}}$  are indicative of a disturbed kinematics (not only due to the gravitational potential of the galaxy) and most probably due to outflows.

We see a trend of AGN having generally higher  $\sigma_{\text{frac}}$  values than inactive galaxies as can be seen in the distributions shown in Fig. 7. The median values of  $\sigma_{\text{frac}}$  for AGN and control sample are  $<\sigma_{\text{frac}}>_{\text{AGN}} = 0.04$  and  $<\sigma_{\text{frac}}>_{\text{CTR}} = -0.23$ , respectively. Besides that, we note that 90 per cent of AGN have  $\sigma_{\text{frac}}$  larger than  $-0.22$  and 75 per cent of them have values larger than  $-0.13$ . For the control sample, 90 per cent of the galaxies show  $\sigma_{\text{frac}} < 0.12$  and for 75 per cent of the sample  $\sigma_{\text{frac}} < -0.04$ . The result of the Anderson–Darling statistical test returns a  $p$ -value of  $10^{-5}$ , which confirms that the AGN and inactive galaxies follow distinct distributions in  $\sigma_{\text{frac}}$ . We thus conclude that the parameter  $\sigma_{\text{frac}}$  can be used as an indicator of AGN activity.

We derived the luminosity of the [O III] $\lambda 5007\text{\AA}$  emission line ( $L_{[\text{O III}]}$ ) of each galaxy (Table A1) using the flux measurements obtained with the GANDALF code within the same aperture used to measure the  $\sigma_{\text{frac}}$ , and then investigated a possible correlation

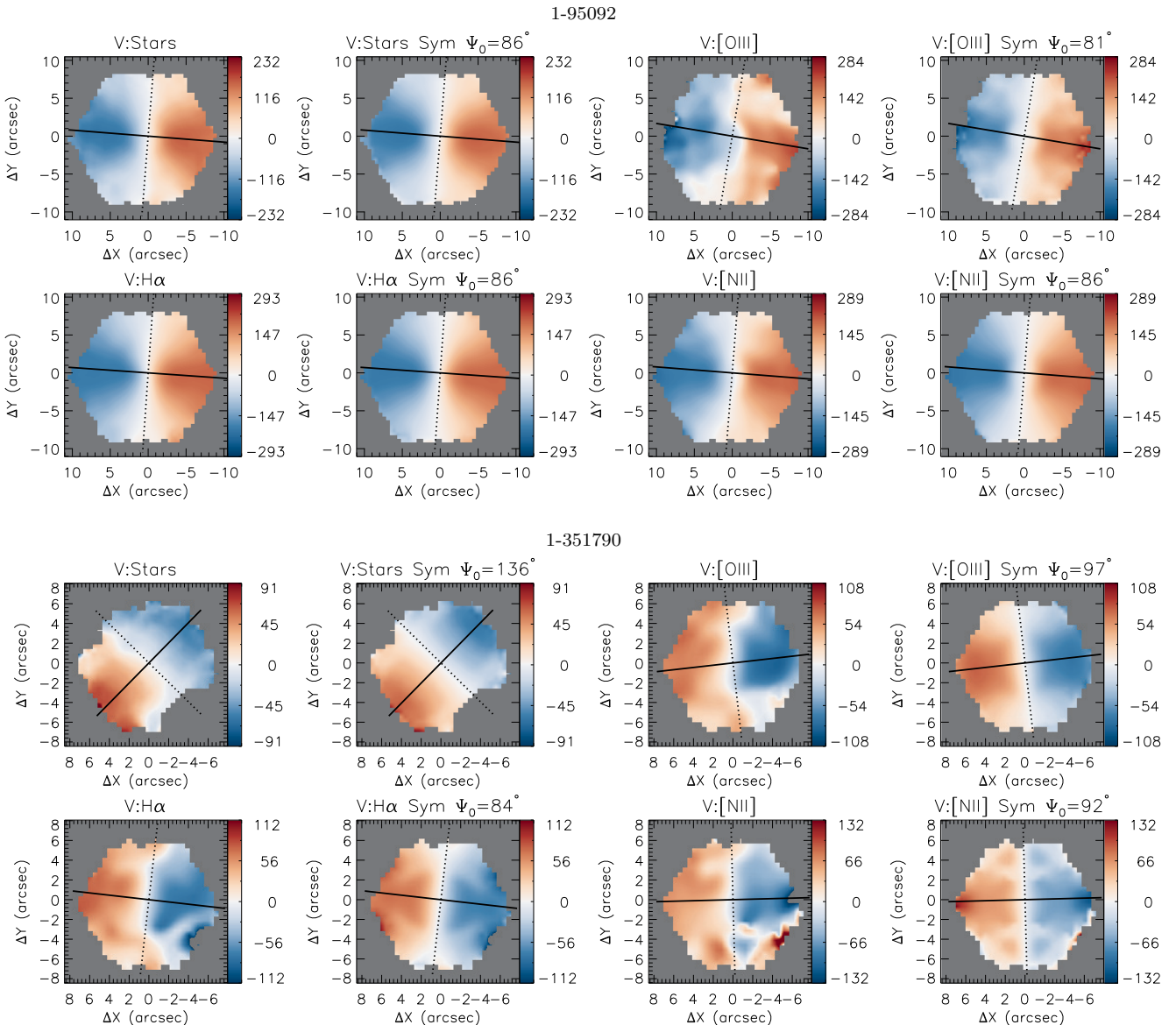


**Figure 4.** In the first two rows, we show the derived velocity fields for the AGN *mangaid* 1-95092. The first row shows, from left to right, the stellar velocity field (V:Stars), the symmetrized stellar velocity field (V:Stars Sym), the gas velocity field for [O III] (V:[O III]), and the corresponding symmetrized velocity field (V:[O III] Sym). The second row shows, from left to right, the H $\alpha$  velocity field (V:H $\alpha$ ), its symmetrized velocity field (V:H $\alpha$  Sym), the velocity and symmetrized velocity fields for [N II] (V:[N II]) and (V:[N II] Sym), respectively. In the bottom two rows, we show the same velocity maps but for the AGN *mangaid* 1-351790. In all velocity maps, the solid black line shows the PA of kinematic major axis, the value of the  $\Psi_0$  is shown in the top right-hand corner of the symmetrized velocity maps. The continuous (dotted) line shows the orientation of the kinematic major (minor) axis of the galaxy. The colour bars show the velocities in units of km s $^{-1}$ .

between  $\sigma_{\text{frac}}$  and  $L_{[\text{O III}]}$ . Fig. 8 shows the plot of  $L_{[\text{O III}]}$  versus  $\sigma_{\text{frac}}$  for the AGN and control samples. There is a clear positive correlation between  $\sigma_{\text{frac}}$  and  $L_{[\text{O III}]}$ , with a Spearman correlation coefficient of 0.53 and a p-value of  $10^{-14}$ . However, it should be noticed that the observed correlation could be artificially produced, as the AGN and inactive galaxies clearly show distinct distributions in  $\sigma_{\text{frac}}$  (Fig. 7). The Spermann test returns a p-value of 0.06 for the AGN sample and  $10^{-5}$  for the control sample, meaning that no strong correlation is found between the  $L_{[\text{O III}]}$  and  $\sigma_{\text{frac}}$  for the AGN sample alone, while these parameters are correlated for the control sample. The absence of correlation for the AGN sample may be due to the fact that our sample covers only a small range of luminosities, as most objects are low-luminosity AGN (Rembold et al. 2017). Fig.

7 shows a trend of AGN having higher  $\sigma_{\text{frac}}$  values than inactive galaxies. The same trend can also be observed in Fig. 8. This result can be interpreted as the higher values seen for AGN compared to control galaxies being due to winds originated in the AGN. Thus, although the AGN of the sample do not show powerful outflows that can affect the gas kinematics on galactic scales, they do show small-scale outflows (within the inner 1–2 kpc).

Our results can be compared with those obtained from single aperture spectra. For example, Woo et al. (2017) find that there is a trend of the [O III]5007 Å velocity dispersion to increase with the increase in the AGN luminosity in a sample of  $\sim 110\,000$  AGN and star-forming (SF) galaxies at  $z < 0.3$ . This trend is also present in composite objects and is not clear for SF galaxies. They interpreted

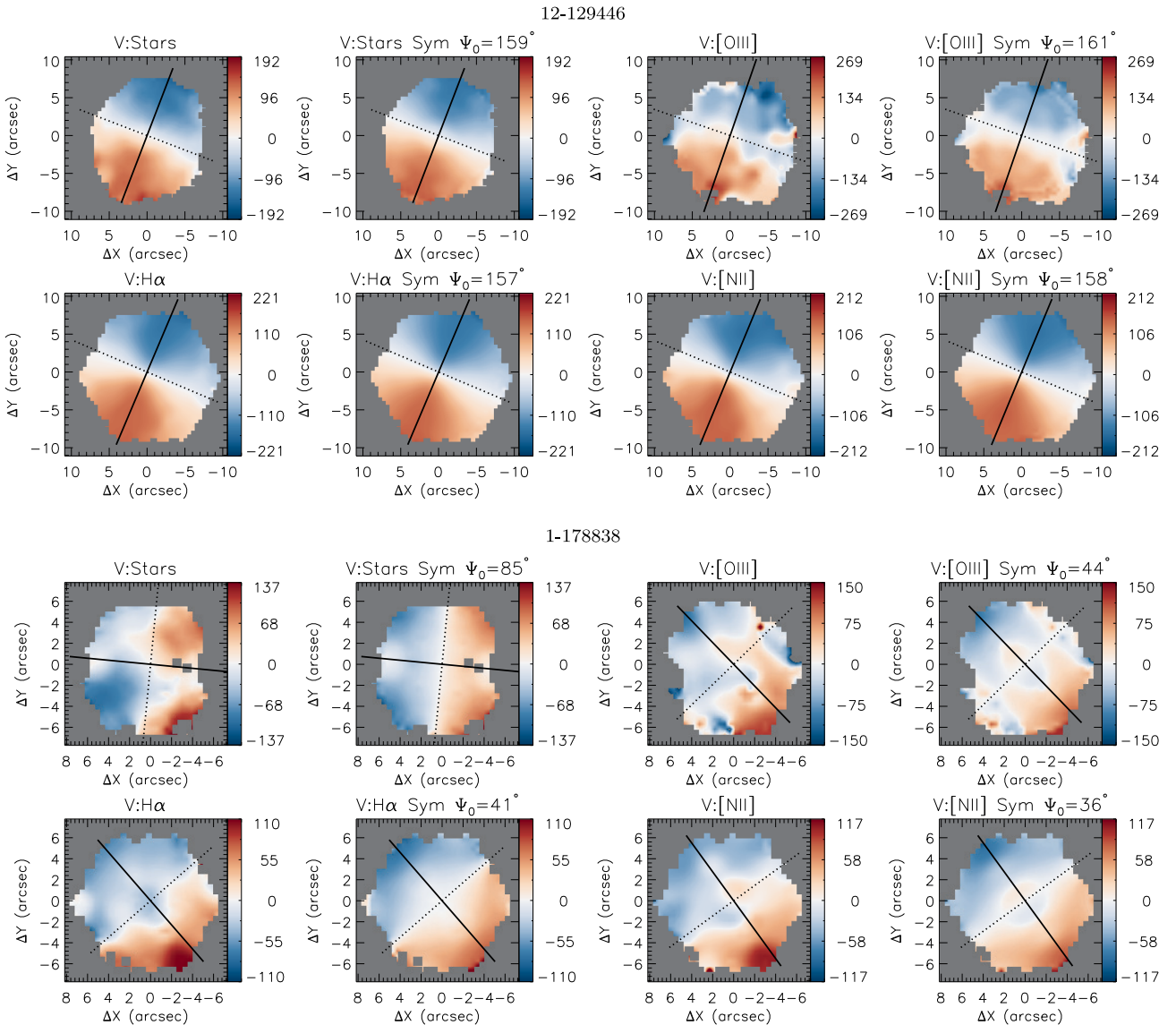


**Figure 5.** Same as Fig. 4 for the control galaxies *mangaid* 12-129446 (first and second row) and *mangaid* 1-178838 (third and fourth row). The velocity fields are in the unit of  $\text{km s}^{-1}$ .

this result due to strong gas outflows in high-luminosity AGN, indicating that AGN energetics are driving these outflows. They find also lower average  $[\text{O III}]$  velocity dispersion values for SF galaxies. Our result is in good agreement with theirs. In addition, optical observations (Wylezalek et al. 2016), radio observations (Zakamska & Greene 2014), and molecular gas (Veilleux et al. 2013) as well as theoretical models (Zubovas & King 2012) have suggested that the AGN need to have enough luminosity for the gas to be pushed out of the galactic potential. This is in agreement with our results, where we see a positive correlation between  $\sigma_{\text{frac}}$  and luminosity.

## 5 CONCLUSIONS

We have mapped the gas and stellar kinematics of a sample of 62 AGN and 109 control galaxies (inactive galaxies) in order to

investigate the effect of the AGN in the large- and small-scale gas kinematics of the AGN host galaxies. We detect evidence of nuclear gas outflows in the 62 AGN, but conclude they are not powerful enough to play an important role in the gas kinematics on galactic scales. The main conclusions of our work are as follows:

(i) There is no significant difference in the  $\Delta\text{PA}$  between active and inactive galaxies, indicating that the galaxy scale gas kinematics are dominated by orbital motion in the gravitational potential of the galaxies, instead of outflows driven by the central AGN.

(ii) We found that the difference between the orientation of the kinematic major axes of the gas and stars ( $\Delta\text{PA}$ ) is larger than  $30^\circ$  for 13 (21 per cent) AGN and 21 control galaxies (19 per cent) using the  $[\text{O III}]5007 \text{\AA}$  kinematics.

(iii) The AGN show larger fractional differences in the velocity dispersions of the gas and stars  $\sigma_{\text{frac}} = \frac{\sigma_{\text{gas}} - \sigma_*}{\sigma_*}$  than inactive galaxies within the inner  $2''.5$  diameter, which corresponds to 1–2 kpc at

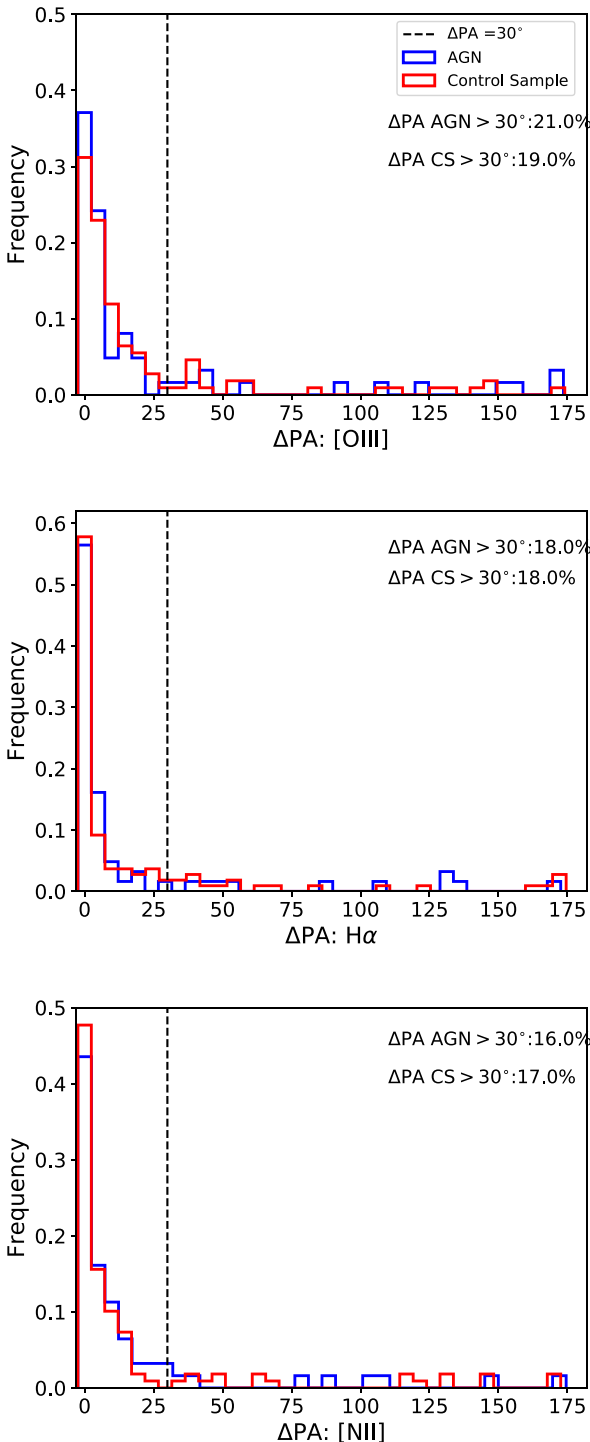


**Figure 6.** Histograms comparing  $\Delta PA$  distributions of AGN and control galaxies for  $[O\text{III}]\lambda 5007$  (top panel),  $H\alpha$  (middle panel), and  $[N\text{II}]\lambda 6583$  (bottom line). AGN are shown in blue and controls in red. The vertical dashed lines show  $\Delta PA = 30^\circ$ .

the galaxies. The mean values are  $\sigma_{\text{frac}} = 0.04$  for the AGN and  $\sigma_{\text{frac}} = -0.23$  for the control sample. This difference is interpreted as being due to outflows from the active nuclei. This indicates that although the AGN of our sample do not affect the gas kinematics on large scale, it does affect it at least within the inner kpc.

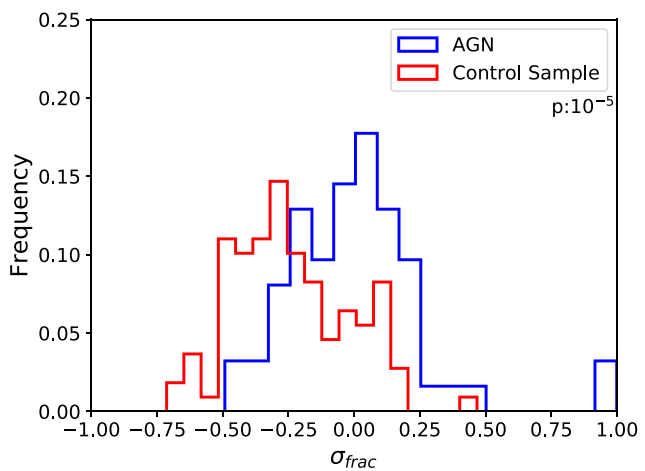


**Figure 7.** Histograms comparing  $\sigma_{\text{frac}}$  distributions of AGN and control galaxies for  $[O\text{III}]\lambda 5007$ . AGN are shown in blue and controls in red. The result of Anderson–Darling statistical test returns a  $p$ -value of  $10^{-5}$ , confirming that AGN and inactive galaxies follow distinct distributions in  $\sigma_{\text{frac}}$ .

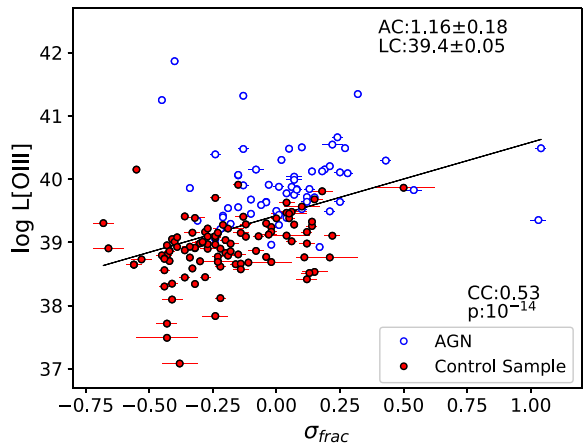


**Figure 8.** Plot of logarithm of  $[O\text{III}]\lambda 5007 \text{ \AA}$  luminosity versus  $\sigma_{\text{frac}}$  for AGN (blue open circles) and inactive galaxies (red closed circles). The Spearman test confirms that these properties are correlated resulting in a correlation coefficient of 0.53 and  $p$ -value of  $10^{-14}$ . The black line is the result of linear fit of data, with linear coefficient of  $LC = 39.4 \pm 0.05$  and angular coefficient of  $AC = 1.16 \pm 0.18$ .

(iv) A correlation between the  $[O\text{III}]\lambda 5007 \text{ \AA}$  luminosity and  $\sigma_{\text{frac}}$  is observed when putting together the AGN and control samples.

## ACKNOWLEDGEMENTS

Funding for the Sloan Digital Sky Survey IV has been provided by the Alfred P. Sloan Foundation and the Participating Institutions. SDSS-IV acknowledges support and resources from the Center for High-Performance Computing at the University of Utah. The SDSS web site is [www.sdss.org](http://www.sdss.org). SDSS-IV is managed by the Astrophysical Research Consortium for the Participating Institutions of the SDSS Collaboration including the Brazilian Participation Group, the Carnegie Institution for Science, Carnegie Mellon University, the Chilean Participation Group, Harvard-Smithsonian Center for Astrophysics, Instituto de Astrofísica de Canarias, The Johns

Hopkins University, Kavli Institute for the Physics and Mathematics of the Universe (IPMU) / University of Tokyo, Lawrence Berkeley National Laboratory, Leibniz Institut für Astro physik Potsdam (AIP), Max-Planck-Institut für Astrophysik (MPA Garching), Max-Planck-Institut für Extraterrestrische Physik (MPE), Max-Planck-Institut für Astronomie (MPIA Heidelberg), National Astronomical Observatory of China, New Mexico State University, New York University, The Ohio State University, Pennsylvania State University, Shanghai Astronomical Observatory, United Kingdom Participation Group, Universidad Nacional Autónoma de México, University of Arizona, University of Colorado Boulder, University of Portsmouth, University of Utah, University of Washington, University of Wisconsin, Vanderbilt University, and Yale University. We thank the support of the Instituto Nacional de Ciéncia e Tecnologia (INCT) e-Universo (CNPq grant 465376/2014-2).

This study was financed in part by the Coordenação de Aperfeiçoamento de Pessoal de Nível Superior – Brasil (CAPES) – Finance Code 001, Conselho Nacional de Desenvolvimento Científico e Tecnológico (CNPq), and Fundação de Amparo à pesquisa do Estado do RS (FAPERGS).

## REFERENCES

- Abolfathi B. et al., 2018, *ApJS*, 235, 42  
 Antonucci R., 1993, *ARA&A*, 31, 473  
 Barbosa F. K. B., Storchi-Bergmann T., McGregor P., Vale T. B., Riffel R. A., 2014, *MNRAS*, 445, 2353  
 Bower R. G., Benson A. J., Malbon R., Helly J. C., Frenk C. S., Baugh C. M., Cole S., Lacey C. G., 2006, *MNRAS*, 370, 645  
 Bruzual G., Charlot S., 2003, *MNRAS*, 344, 1000  
 Bundy K. et al., 2015, *ApJ*, 798, 7  
 Cappellari M., 2017, *MNRAS*, 466, 798  
 Cappellari M., Emsellem E., 2004, *PASP*, 116, 138  
 Cappellari M. et al., 2007, *MNRAS*, 379, 418  
 Cheung E. et al., 2016, *Nature*, 533, 504  
 Conroy C., Gunn J. E., White M., 2009, *ApJ*, 699, 486  
 Di Matteo T., Springel V., Hernquist L., 2005, *Nature*, 433, 604  
 Drory N. et al., 2015, *AJ*, 149, 77  
 Ferrarese L., Merritt D., 2000, *ApJ*, 539, L9  
 Fischer T. C., Crenshaw D. M., Kraemer S. B., Schmitt H. R., 2013, *ApJS*, 209, 1  
 Gebhardt K. et al., 2000, *ApJ*, 539, L13  
 Gonzalez R. C., Woods R. E., 2002, Digital Image Processing, 2nd edn. Prentice-Hall, Upper Saddle River, NJ  
 Hopkins P. F., Hernquist L., Cox T. J., Di Matteo T., Martini P., Robertson B., Springel V., 2005, *ApJ*, 630, 705  
 Krajnović D., Cappellari M., Emsellem E., McDermid R. M., de Zeeuw P. T., 2005, *MNRAS*, 357, 1113  
 Krajnović D., Cappellari M., de Zeeuw P. T., Copin Y., 2006, *MNRAS*, 366, 787  
 Krajnović D., Cappellari M., de Zeeuw P. T., Copin Y., 2011, *MNRAS*, 414, 2993  
 Law D. R. et al., 2015, *AJ*, 150, 19  
 Law D. R. et al., 2015, *AJ*, 152, 83  
 Lena D. et al., 2015, *ApJ*, 806, 84  
 Mallmann N. D., et al., 2018, *MNRAS*, 478, 5491 (Paper II)  
 Oh K., Sarzi M., Schawinski K., Yi S. K., 2011, *ApJS*, 195, 13  
 Osterbrock D. E., Ferland G. J., 2006, Astrophysics of Gaseous Nebulae and Active Galactic Nuclei, 2nd edn. University Science Books, Sausalito, California  
 Penny S. J. et al., 2018, *MNRAS*, 476, 979  
 Rembold S. B. et al., 2017, *MNRAS*, 472, 4382 (Paper I)  
 Riffel R. A., Storchi-Bergmann T., Riffel R., 2014, *ApJ*, 780, L24  
 Sarzi M. et al., 2006, *MNRAS*, 366, 1151  
 Scannapieco E., Silk J., Bouwens R., 2005, *ApJ*, 635, L13  
 Schmitt H. R., Donley J. L., Antonucci R. R. J., Hutchings J. B., Kinney A. L., 2003, *ApJS*, 148, 327  
 Schnorr-Müller A., Storchi-Bergmann T., Nagar N. M., Robinson A., Lena D., Riffel R. A., Couto G. S., 2014, *MNRAS*, 437, 1708  
 Springel V., Di Matteo T., Hernquist L., 2005, *ApJ*, 620, L79  
 Tremaine S. et al., 2002, *ApJ*, 574, 740  
 Urry C. M., Padovani P., 1995, *PASP*, 107, 803  
 Veilleux S. et al., 2013, *ApJ*, 776, 27  
 Wake D. A. et al., 2017, *AJ*, 154, 86  
 Woo J.-H., Son D., Bae H.-J., 2017, *ApJ*, 839, 120  
 Wylezalek D., Zakamska N. L., 2016, *MNRAS*, 461, 3724  
 Wylezalek D. et al., 2017, *MNRAS*, 467, 2612  
 Wylezalek D., Zakamska N. L., Greene J. E., Riffel R. A., Drory N., Andrews B. H., Merloni A., Thomas D., 2018, *MNRAS*, 474, 1499  
 Yan R. et al., 2016a, *AJ*, 151, 8  
 Yan R. et al., 2016b, *AJ*, 152, 197  
 Zakamska N. L., Greene J. E., 2014, *MNRAS*, 442, 784  
 Zakamska N. L. et al., 2016, *MNRAS*, 459, 3144  
 Zubovas K., King A., 2012, *ApJ*, 745, L34

## APPENDIX A: KINEMATIC MEASUREMENTS AND PARAMETERS OF THE AGN AND CONTROL SAMPLE

**Table A1.** Kinematic measurements of the AGN and control samples. Col. 1: *mangaid*; Col. 2: Logarithm of luminosity of [O III]5007 Å in erg s<sup>-1</sup> within the inner 2''.5 diameter; velocity dispersion in km s<sup>-1</sup> obtained for stars, [O III]5007 Å, H $\alpha$ , [N II]6583 Å (cols. 3-6), measured within the inner 2''.5 diameter, and kinematic position angles ( $\Psi_0$ ) for the stars, [O III]5007 Å, H $\alpha$ , [N II]6583 Å (cols. 7-10). In each block we have the parameters obtained for AGN (first line) and their controls (second and third lines).

<i>mangaid</i>	$\log_{10} L_{\text{[O III]}}$	$\sigma_*$	$\sigma_{\text{[O III]}}$	$\sigma_{H\alpha}$	$\sigma_{\text{[N II]}}$	$\Psi_{0*}$	$\Psi_0 \text{ [O III]}$	$\Psi_0 \text{ H}\alpha$	$\Psi_0 \text{ [N II]}$
1-558912	41.32	$269.0 \pm 3.0$	$231.0 \pm 1.0$	$204.0 \pm 2.0$	$209.0 \pm 2.0$	$148.0 \pm 0.5$	$165.0 \pm 0.5$	$117.5 \pm 0.5$	$158.5 \pm 0.5$
1-71481	39.38	$284.0 \pm 2.0$	$194.0 \pm 12.0$	$275.0 \pm 12.0$	$219.0 \pm 11.0$	$174.0 \pm 0.5$	$146.5 \pm 0.5$	$9.5 \pm 0.5$	$163.5 \pm 0.5$
1-72928	39.45	$253.0 \pm 1.0$	$268.0 \pm 19.0$	$161.0 \pm 20.0$	$295.0 \pm 126.0$	$138.0 \pm 0.5$	$134.0 \pm 0.5$	$121.0 \pm 0.5$	$137.5 \pm 0.5$
1-269632	41.35	$153.0 \pm 1.0$	$202.0 \pm 2.0$	$137.0 \pm 2.0$	$155.0 \pm 1.0$	$16.0 \pm 2.2$	$173.5 \pm 0.5$	$11.5 \pm 2.0$	$14.0 \pm 0.8$
1-210700	39.7	$199.0 \pm 2.0$	$150.0 \pm 4.0$	$112.0 \pm 1.0$	$131.0 \pm 1.0$	$130.0 \pm 0.5$	$137.5 \pm 0.5$	$134.5 \pm 0.5$	$119.5 \pm 0.5$
1-378795	39.4	$172.0 \pm 2.0$	$148.0 \pm 5.0$	$109.0 \pm 1.0$	$128.0 \pm 3.0$	$19.5 \pm 0.5$	$25.5 \pm 0.5$	$20.5 \pm 0.5$	$19.0 \pm 0.5$
1-258599	41.87	$349.0 \pm 3.0$	$208.0 \pm 1.0$	$170.0 \pm 1.0$	$166.0 \pm 1.0$	$81.5 \pm 0.5$	$98.5 \pm 0.5$	$122.5 \pm 0.5$	$108.5 \pm 0.5$
1-93876	39.11	$223.0 \pm 1.0$	$230.0 \pm 20.0$	$275.0 \pm 18.0$	$98.0 \pm 18.0$	$146.0 \pm 0.5$	$148.5 \pm 0.5$	$149.5 \pm 0.5$	$136.0 \pm 0.5$
1-166691	38.76	$231.0 \pm 1.0$	$281.0 \pm 25.0$	$175.0 \pm 15.0$	$221.0 \pm 39.0$	$92.0 \pm 0.5$	$146.5 \pm 0.5$	$34.5 \pm 0.5$	$95.0 \pm 0.5$
1-72322	41.25	$287.0 \pm 3.0$	$156.0 \pm 2.0$	$170.0 \pm 2.0$	$182.0 \pm 3.0$	$107.0 \pm 0.8$	$114.5 \pm 0.5$	$116.0 \pm 0.5$	$118.5 \pm 0.5$
1-121717	39.86	$223.0 \pm 2.0$	$334.0 \pm 26.0$	$167.0 \pm 3.0$	$173.0 \pm 4.0$	$134.0 \pm 0.5$	$111.0 \pm 0.5$	$134.0 \pm 0.5$	$134.0 \pm 0.5$
1-43721	39.48	$250.0 \pm 1.0$	$265.0 \pm 14.0$	$132.0 \pm 2.0$	$140.0 \pm 2.0$	$55.0 \pm 2.2$	$52.0 \pm 0.5$	$51.5 \pm 0.5$	$43.0 \pm 0.5$
1-121532	40.55	$260.0 \pm 1.0$	$318.0 \pm 10.0$	$280.0 \pm 8.0$	$300.0 \pm 8.0$	$101.0 \pm 0.5$	$148.5 \pm 0.5$	$10.0 \pm 0.5$	$77.0 \pm 0.5$
1-218427	38.9	$386.0 \pm 13.0$	$130.0 \pm 21.0$	$616.0 \pm 191.0$	$466.0 \pm 133.0$	$136.5 \pm 0.5$	$178.0 \pm 0.5$	$136.5 \pm 0.5$	$136.0 \pm 0.5$
1-177493	39.91	$172.0 \pm 2.0$	$145.0 \pm 2.0$	$156.0 \pm 3.0$	$111.0 \pm 2.0$	$142.0 \pm 3.8$	$145.0 \pm 2.0$	$158.0 \pm 0.5$	$149.0 \pm 0.5$
1-209980	40.66	$179.0 \pm 3.0$	$218.0 \pm 1.0$	$233.0 \pm 1.0$	$245.0 \pm 1.0$	$50.0 \pm 0.8$	$52.0 \pm 0.5$	$55.0 \pm 0.5$	$51.5 \pm 0.5$
1-295095	38.76	$101.0 \pm 1.0$	$112.0 \pm 3.0$	$80.0 \pm 1.0$	$88.0 \pm 2.0$	$1.0 \pm 2.2$	$3.0 \pm 0.8$	$178.0 \pm 1.5$	$1.0 \pm 1.2$
1-92626	39.41	$181.0 \pm 2.0$	$116.0 \pm 2.0$	$138.0 \pm 2.0$	$183.0 \pm 10.0$	$10.5 \pm 0.8$	$13.5 \pm 0.5$	$13.0 \pm 0.5$	$13.0 \pm 0.5$
1-44379	40.49	$133.0 \pm 2.0$	$168.0 \pm 2.0$	$126.0 \pm 3.0$	$159.0 \pm 3.0$	$15.0 \pm 0.5$	$14.0 \pm 0.5$	$16.5 \pm 0.5$	$16.5 \pm 0.8$
1-211082	38.86	$153.0 \pm 1.0$	$89.0 \pm 3.0$	$118.0 \pm 2.0$	$158.0 \pm 1.0$	$157.5 \pm 0.5$	$163.5 \pm 0.5$	$159.0 \pm 0.5$	$159.5 \pm 0.5$
1-135371	38.9	$144.0 \pm 2.0$	$105.0 \pm 4.0$	$116.0 \pm 2.0$	$147.0 \pm 4.0$	$67.5 \pm 0.8$	$72.5 \pm 0.5$	$66.5 \pm 0.8$	$66.5 \pm 0.5$
1-149211	40.5	$107.0 \pm 1.0$	$116.0 \pm 0.0$	$121.0 \pm 1.0$	$134.0 \pm 2.0$	$41.0 \pm 0.5$	$166.0 \pm 0.5$	$174.5 \pm 0.5$	$25.5 \pm 0.5$
1-377321	40.15	$182.0 \pm 6.0$	$77.0 \pm 0.0$	$77.0 \pm 0.0$	$80.0 \pm 0.0$	$17.5 \pm 0.5$	$26.5 \pm 0.5$	$44.0 \pm 0.5$	$85.5 \pm 0.5$
1-491233	39.09	$106.0 \pm 1.0$	$94.0 \pm 1.0$	$83.0 \pm 1.0$	$87.0 \pm 1.0$	$120.5 \pm 1.5$	$105.0 \pm 1.8$	$118.5 \pm 1.2$	$118.5 \pm 1.5$
1-173958	40.49	$101.0 \pm 1.0$	$207.0 \pm 2.0$	$114.0 \pm 1.0$	$142.0 \pm 2.0$	$10.0 \pm 4.2$	$32.0 \pm 0.5$	$18.5 \pm 3.2$	$21.0 \pm 0.5$
1-247456	39.3	$879.0 \pm 34.0$	$172.0 \pm 13.0$	$1090.0 \pm 327.0$	$749.0 \pm 91.0$	$149.0 \pm 1.2$	$169.0 \pm 0.5$	$167.5 \pm 0.8$	$167.5 \pm 0.5$
1-24246	39.1	$110.0 \pm 1.0$	$134.0 \pm 4.0$	$94.0 \pm 2.0$	$105.0 \pm 2.0$	$139.0 \pm 1.5$	$134.0 \pm 0.8$	$134.0 \pm 1.0$	$121.5 \pm 0.5$
1-338922	40.39	$284.0 \pm 2.0$	$215.0 \pm 5.0$	$215.0 \pm 3.0$	$212.0 \pm 1.0$	$47.5 \pm 3.8$	$110.5 \pm 0.5$	$103.0 \pm 0.5$	$129.5 \pm 0.5$
1-286804	39.81	$179.0 \pm 3.0$	$204.0 \pm 5.0$	$171.0 \pm 4.0$	$173.0 \pm 3.0$	$168.5 \pm 0.5$	$164.0 \pm 1.2$	$169.5 \pm 0.5$	$153.0 \pm 0.5$
1-109493	39.56	$257.0 \pm 2.0$	$278.0 \pm 17.0$	$521.0 \pm 140.0$	$215.0 \pm 8.0$	$102.5 \pm 0.5$	$42.0 \pm 0.5$	$58.5 \pm 0.5$	$137.5 \pm 0.5$
1-279147	40.29	$116.0 \pm 1.0$	$163.0 \pm 1.0$	$101.0 \pm 1.0$	$122.0 \pm 1.0$	$31.5 \pm 4.2$	$51.5 \pm 0.5$	$54.0 \pm 0.5$	$1.0 \pm 0.5$
1-283246	38.68	$142.0 \pm 0.0$	$126.0 \pm 3.0$	$157.0 \pm 8.0$	$140.0 \pm 3.0$	$37.0 \pm 2.8$	$59.0 \pm 1.0$	$29.5 \pm 0.5$	$31.0 \pm 0.5$
1-351538	39.26	$109.0 \pm 1.0$	$125.0 \pm 3.0$	$69.0 \pm 0.0$	$76.0 \pm 1.0$	$160.5 \pm 16.2$	$141.0 \pm 0.5$	$169.0 \pm 1.2$	$176.5 \pm 1.2$
1-460812	40.48	$210.0 \pm 3.0$	$179.0 \pm 2.0$	$212.0 \pm 1.0$	$218.0 \pm 3.0$	$78.0 \pm 0.8$	$78.5 \pm 0.5$	$69.5 \pm 0.5$	$68.5 \pm 0.5$
1-270160	39.63	$319.0 \pm 3.0$	$331.0 \pm 9.0$	$362.0 \pm 17.0$	$311.0 \pm 10.0$	$111.0 \pm 0.5$	$112.5 \pm 0.5$	$104.0 \pm 0.5$	$116.5 \pm 1.0$
1-258455	39.15	$214.0 \pm 1.0$	$184.0 \pm 7.0$	$184.0 \pm 3.0$	$194.0 \pm 7.0$	$131.0 \pm 1.5$	$130.0 \pm 0.5$	$128.5 \pm 0.5$	$127.5 \pm 0.5$
1-92866	40.3	$241.0 \pm 1.0$	$244.0 \pm 2.0$	$217.0 \pm 1.0$	$258.0 \pm 2.0$	$18.5 \pm 1.5$	$126.5 \pm 0.5$	$151.0 \pm 0.5$	$123.5 \pm 0.5$
1-94514	38.69	$237.0 \pm 1.0$	$229.0 \pm 18.0$	$373.0 \pm 71.0$	$386.0 \pm 23.0$	$147.5 \pm 1.0$	$147.0 \pm 0.5$	$143.0 \pm 0.5$	$135.0 \pm 0.5$
1-210614	38.91	$223.0 \pm 1.0$	$152.0 \pm 3.0$	$178.0 \pm 2.0$	$157.0 \pm 3.0$	$131.0 \pm 2.2$	$90.0 \pm 0.5$	$95.0 \pm 0.5$	$82.0 \pm 0.5$
1-94784	40.48	$135.0 \pm 1.0$	$142.0 \pm 2.0$	$156.0 \pm 1.0$	$153.0 \pm 2.0$	$65.5 \pm 1.0$	$71.0 \pm 0.5$	$62.5 \pm 0.8$	$67.5 \pm 1.5$
1-211063	38.75	$136.0 \pm 1.0$	$76.0 \pm 2.0$	$141.0 \pm 2.0$	$111.0 \pm 2.0$	$170.0 \pm 1.8$	$164.0 \pm 0.5$	$166.5 \pm 1.8$	$165.0 \pm 1.2$
1-135502	39.16	$164.0 \pm 1.0$	$117.0 \pm 1.0$	$177.0 \pm 2.0$	$163.0 \pm 1.0$	$98.5 \pm 0.5$	$98.5 \pm 0.5$	$101.5 \pm 0.5$	$102.0 \pm 0.5$
1-44303	40.15	$114.0 \pm 1.0$	$135.0 \pm 1.0$	$120.0 \pm 2.0$	$134.0 \pm 2.0$	$56.0 \pm 7.2$	$39.0 \pm 7.8$	$67.5 \pm 2.0$	$62.0 \pm 3.0$
1-339028	39.22	$183.0 \pm 1.0$	$133.0 \pm 2.0$	$170.0 \pm 3.0$	$145.0 \pm 1.0$	$179.5 \pm 2.7$	$173.5 \pm 1.0$	$5.5 \pm 0.8$	$9.0 \pm 1.8$
1-379087	39.27	$131.0 \pm 1.0$	$104.0 \pm 2.0$	$123.0 \pm 1.0$	$125.0 \pm 1.0$	$39.5 \pm 2.2$	$31.5 \pm 0.5$	$42.5 \pm 0.5$	$44.0 \pm 1.0$

**Table A1** – *continued*

<i>mangaid</i>	$\log_{10} L_{\text{[O III]}}$	$\sigma_*$	$\sigma_{\text{[O III]}}$	$\sigma_{H\alpha}$	$\sigma_{\text{[N II]}}$	$\Psi_{0*}$	$\Psi_0 \text{ [O III]}$	$\Psi_0 \text{ H}\alpha$	$\Psi_0 \text{ [N II]}$
1-339094	40.2	$133.0 \pm 1.0$	$160.0 \pm 1.0$	$152.0 \pm 2.0$	$157.0 \pm 2.0$	$0.0 \pm 1.5$	$176.0 \pm 1.8$	$175.0 \pm 0.8$	$8.0 \pm 0.5$
1-274646	38.91	$121.0 \pm 1.0$	$82.0 \pm 1.0$	$108.0 \pm 1.0$	$108.0 \pm 1.0$	$61.5 \pm 17.2$	$175.0 \pm 0.5$	$41.0 \pm 0.5$	$22.5 \pm 0.5$
1-24099	38.34	$125.0 \pm 2.0$	$84.0 \pm 2.0$	$131.0 \pm 17.0$	$153.0 \pm 6.0$	$125.5 \pm 1.2$	$135.5 \pm 0.8$	$134.5 \pm 0.5$	$121.5 \pm 0.5$
1-137883	40.15	$185.0 \pm 5.0$	$164.0 \pm 3.0$	$133.0 \pm 3.0$	$130.0 \pm 2.0$	$55.5 \pm 2.0$	$56.5 \pm 0.8$	$48.0 \pm 1.2$	$41.5 \pm 0.5$
1-178838	38.69	$114.0 \pm 2.0$	$90.0 \pm 5.0$	$107.0 \pm 3.0$	$103.0 \pm 2.0$	$84.5 \pm 1.5$	$44.0 \pm 0.5$	$41.0 \pm 4.8$	$36.0 \pm 2.2$
1-36878	39.07	$138.0 \pm 3.0$	$101.0 \pm 1.0$	$90.0 \pm 1.0$	$98.0 \pm 1.0$	$46.0 \pm 1.0$	$26.0 \pm 0.5$	$43.0 \pm 0.5$	$45.5 \pm 1.2$
1-48116	40.12	$151.0 \pm 1.0$	$178.0 \pm 1.0$	$127.0 \pm 1.0$	$134.0 \pm 1.0$	$56.0 \pm 1.0$	$65.0 \pm 0.5$	$57.0 \pm 1.0$	$56.0 \pm 0.5$
1-386452	39.09	$123.0 \pm 1.0$	$90.0 \pm 1.0$	$89.0 \pm 1.0$	$91.0 \pm 1.0$	$135.0 \pm 2.0$	$131.0 \pm 0.5$	$131.5 \pm 1.0$	$131.0 \pm 1.2$
1-24416	38.76	$157.0 \pm 1.0$	$104.0 \pm 1.0$	$162.0 \pm 3.0$	$148.0 \pm 2.0$	$85.0 \pm 0.8$	$79.5 \pm 0.8$	$83.5 \pm 0.5$	$82.5 \pm 0.5$
1-256446	40.12	$214.0 \pm 2.0$	$244.0 \pm 1.0$	$231.0 \pm 1.0$	$232.0 \pm 1.0$	$158.0 \pm 11.0$	$62.0 \pm 0.5$	$48.0 \pm 4.2$	$49.5 \pm 0.5$
1-322671	38.7	$173.0 \pm 1.0$	$134.0 \pm 12.0$	$360.0 \pm 121.0$	$167.0 \pm 12.0$	$130.0 \pm 3.2$	$109.0 \pm 0.5$	$101.5 \pm 0.5$	$143.0 \pm 0.5$
1-256465	39.38	$217.0 \pm 1.0$	$227.0 \pm 4.0$	$187.0 \pm 3.0$	$216.0 \pm 6.0$	$134.0 \pm 16.0$	$75.0 \pm 0.5$	$62.5 \pm 0.5$	$64.0 \pm 0.5$
1-95585	40.11	$171.0 \pm 1.0$	$214.0 \pm 3.0$	$211.0 \pm 3.0$	$206.0 \pm 2.0$	$69.5 \pm 1.0$	$62.5 \pm 0.5$	$68.0 \pm 0.5$	$69.5 \pm 0.5$
1-166947	38.79	$149.0 \pm 1.0$	$83.0 \pm 3.0$	$143.0 \pm 3.0$	$116.0 \pm 2.0$	$36.0 \pm 3.2$	$123.0 \pm 0.5$	$34.0 \pm 0.8$	$35.5 \pm 0.8$
1-210593	39.04	$160.0 \pm 1.0$	$128.0 \pm 3.0$	$146.0 \pm 4.0$	$147.0 \pm 4.0$	$101.5 \pm 1.0$	$107.5 \pm 0.5$	$104.0 \pm 0.8$	$103.0 \pm 0.5$
1-135641	40.04	$165.0 \pm 4.0$	$168.0 \pm 2.0$	$155.0 \pm 3.0$	$148.0 \pm 1.0$	$164.5 \pm 0.5$	$168.5 \pm 0.5$	$163.5 \pm 0.5$	$166.5 \pm 0.5$
1-635503	39.05	$121.0 \pm 1.0$	$72.0 \pm 1.0$	$82.0 \pm 1.0$	$83.0 \pm 1.0$	$140.0 \pm 1.2$	$145.0 \pm 0.5$	$141.5 \pm 0.5$	$138.5 \pm 0.5$
1-235398	38.74	$154.0 \pm 1.0$	$86.0 \pm 2.0$	$123.0 \pm 1.0$	$120.0 \pm 1.0$	$98.0 \pm 0.5$	$102.0 \pm 0.5$	$99.5 \pm 0.5$	$100.0 \pm 0.5$
1-259142	40.09	$211.0 \pm 1.0$	$272.0 \pm 5.0$	$248.0 \pm 4.0$	$274.0 \pm 4.0$	$102.5 \pm 0.5$	$100.0 \pm 0.5$	$106.5 \pm 0.5$	$101.5 \pm 0.5$
1-55572	38.93	$194.0 \pm 2.0$	$117.0 \pm 1.0$	$208.0 \pm 4.0$	$198.0 \pm 5.0$	$51.0 \pm 0.5$	$52.0 \pm 0.5$	$50.5 \pm 0.5$	$52.0 \pm 0.8$
1-489649	39.05	$170.0 \pm 1.0$	$100.0 \pm 2.0$	$170.0 \pm 6.0$	$155.0 \pm 2.0$	$170.5 \pm 1.5$	$169.0 \pm 0.5$	$1.0 \pm 0.5$	$171.5 \pm 0.8$
1-109056	40.07	$124.0 \pm 1.0$	$104.0 \pm 1.0$	$104.0 \pm 1.0$	$115.0 \pm 1.0$	$157.0 \pm 1.5$	$159.0 \pm 0.5$	$156.0 \pm 1.0$	$154.0 \pm 1.0$
1-73005	38.81	$107.0 \pm 1.0$	$91.0 \pm 4.0$	$91.0 \pm 1.0$	$91.0 \pm 1.0$	$43.5 \pm 2.2$	$59.5 \pm 0.5$	$44.0 \pm 1.0$	$44.0 \pm 1.2$
1-43009	38.65	$94.0 \pm 1.0$	$79.0 \pm 2.0$	$83.0 \pm 1.0$	$85.0 \pm 1.0$	$168.0 \pm 1.2$	$172.5 \pm 1.0$	$171.0 \pm 1.0$	$171.5 \pm 1.0$
1-24148	40.06	$149.0 \pm 1.0$	$126.0 \pm 1.0$	$172.0 \pm 1.0$	$159.0 \pm 1.0$	$155.5 \pm 0.8$	$150.5 \pm 0.5$	$163.5 \pm 0.5$	$134.5 \pm 0.5$
1-285031	38.95	$117.0 \pm 1.0$	$67.0 \pm 1.0$	$83.0 \pm 0.0$	$82.0 \pm 0.0$	$38.0 \pm 0.8$	$38.0 \pm 0.5$	$37.0 \pm 0.8$	$36.5 \pm 0.8$
1-236099	38.51	$85.0 \pm 1.0$	$96.0 \pm 3.0$	$102.0 \pm 4.0$	$83.0 \pm 4.0$	$1.0 \pm 1.7$	$138.0 \pm 2.2$	$37.5 \pm 0.5$	$118.5 \pm 0.5$
1-166919	39.63	$164.0 \pm 2.0$	$158.0 \pm 3.0$	$153.0 \pm 4.0$	$223.0 \pm 4.0$	$105.0 \pm 1.0$	$106.0 \pm 0.5$	$103.0 \pm 0.5$	$102.5 \pm 0.8$
12-129446	39.24	$115.0 \pm 1.0$	$113.0 \pm 3.0$	$84.0 \pm 1.0$	$97.0 \pm 2.0$	$159.0 \pm 1.5$	$161.0 \pm 0.5$	$157.0 \pm 1.0$	$157.5 \pm 0.8$
1-90849	39.1	$115.0 \pm 1.0$	$88.0 \pm 2.0$	$81.0 \pm 1.0$	$95.0 \pm 1.0$	$58.5 \pm 1.0$	$51.5 \pm 0.5$	$55.5 \pm 0.5$	$57.5 \pm 0.5$
1-248389	39.91	$148.0 \pm 0.0$	$144.0 \pm 1.0$	$175.0 \pm 1.0$	$160.0 \pm 1.0$	$177.0 \pm 1.5$	$145.0 \pm 0.5$	$128.5 \pm 0.5$	$145.5 \pm 0.5$
1-94554	38.98	$136.0 \pm 1.0$	$111.0 \pm 3.0$	$135.0 \pm 2.0$	$146.0 \pm 5.0$	$29.5 \pm 2.0$	$37.5 \pm 0.5$	$8.0 \pm 0.8$	$44.0 \pm 0.5$
1-245774	38.97	$130.0 \pm 1.0$	$99.0 \pm 2.0$	$98.0 \pm 1.0$	$107.0 \pm 1.0$	$85.5 \pm 1.2$	$91.5 \pm 0.5$	$85.5 \pm 0.8$	$87.0 \pm 0.5$
1-321739	39.9	$172.0 \pm 4.0$	$145.0 \pm 2.0$	$109.0 \pm 1.0$	$123.0 \pm 1.0$	$172.0 \pm 0.5$	$163.5 \pm 0.5$	$174.0 \pm 0.5$	$179.0 \pm 0.5$
1-247417	38.77	$107.0 \pm 1.0$	$82.0 \pm 2.0$	$85.0 \pm 1.0$	$90.0 \pm 1.0$	$142.0 \pm 0.5$	$141.0 \pm 0.5$	$141.0 \pm 0.5$	$141.5 \pm 0.5$
1-633994	38.79	$238.0 \pm 26.0$	$99.0 \pm 2.0$	$131.0 \pm 4.0$	$201.0 \pm 21.0$	$124.5 \pm 0.8$	$135.5 \pm 0.5$	$123.0 \pm 1.0$	$129.5 \pm 0.5$
1-234618	39.99	$182.0 \pm 17.0$	$167.0 \pm 3.0$	$123.0 \pm 9.0$	$137.0 \pm 1.0$	$23.0 \pm 0.5$	$16.0 \pm 1.2$	$19.0 \pm 0.5$	$23.0 \pm 0.8$
1-282144	39.16	$83.0 \pm 1.0$	$93.0 \pm 2.0$	$70.0 \pm 1.0$	$75.0 \pm 1.0$	$179.0 \pm 2.5$	$163.0 \pm 0.5$	$179.0 \pm 1.5$	$165.5 \pm 0.5$
1-339125	38.97	$181.0 \pm 2.0$	$132.0 \pm 3.0$	$284.0 \pm 44.0$	$653.0 \pm 231.0$	$170.5 \pm 1.5$	$179.5 \pm 0.5$	$141.0 \pm 0.5$	$165.0 \pm 0.5$
1-229010	39.88	$224.0 \pm 1.0$	$237.0 \pm 2.0$	$268.0 \pm 4.0$	$228.0 \pm 1.0$	$177.5 \pm 0.5$	$1.5 \pm 0.5$	$178.0 \pm 0.5$	$0.5 \pm 0.5$
1-210962	39.01	$194.0 \pm 1.0$	$117.0 \pm 2.0$	$147.0 \pm 2.0$	$157.0 \pm 2.0$	$91.5 \pm 1.2$	$96.5 \pm 0.5$	$89.0 \pm 0.5$	$89.5 \pm 0.5$
1-613211	38.65	$242.0 \pm 1.0$	$108.0 \pm 3.0$	$192.0 \pm 3.0$	$188.0 \pm 4.0$	$22.0 \pm 0.5$	$16.5 \pm 0.5$	$18.0 \pm 0.5$	$22.5 \pm 0.5$
1-211311	39.83	$114.0 \pm 1.0$	$173.0 \pm 2.0$	$191.0 \pm 2.0$	$219.0 \pm 3.0$	$160.0 \pm 3.0$	$156.0 \pm 0.5$	$167.5 \pm 2.5$	$166.0 \pm 2.0$
1-25688	38.35	$110.0 \pm 1.0$	$64.0 \pm 2.0$	$110.0 \pm 2.0$	$115.0 \pm 1.0$	$20.5 \pm 1.5$	$13.5 \pm 0.5$	$17.0 \pm 0.8$	$19.5 \pm 1.5$
1-94422	38.87	$129.0 \pm 1.0$	$82.0 \pm 1.0$	$131.0 \pm 2.0$	$123.0 \pm 1.0$	$47.0 \pm 1.0$	$28.0 \pm 0.5$	$49.0 \pm 1.0$	$52.0 \pm 0.8$
1-373161	39.86	$211.0 \pm 0.0$	$139.0 \pm 1.0$	$140.0 \pm 1.0$	$135.0 \pm 1.0$	$124.0 \pm 0.5$	$164.5 \pm 0.5$	$126.0 \pm 0.5$	$33.5 \pm 0.5$
1-259650	39.47	$224.0 \pm 1.0$	$234.0 \pm 5.0$	$161.0 \pm 5.0$	$209.0 \pm 50.0$	$166.5 \pm 0.8$	$170.5 \pm 0.5$	$158.5 \pm 0.5$	$166.0 \pm 0.5$
1-289865	38.73	$271.0 \pm 2.0$	$128.0 \pm 10.0$	$313.0 \pm 13.0$	$213.0 \pm 10.0$	$40.0 \pm 1.8$	$97.5 \pm 0.5$	$58.5 \pm 0.5$	$22.5 \pm 0.5$

**Table A1** – continued

mangaid	$\log_{10} L_{\text{[O III]}}$	$\sigma_*$	$\sigma_{\text{[O III]}}$	$\sigma_{H\alpha}$	$\sigma_{\text{[N II]}}$	$\Psi_{0*}$	$\Psi_0 \text{ [O III]}$	$\Psi_0 \text{ H}\alpha$	$\Psi_0 \text{ [N II]}$
1-210646	39.84	$96.0 \pm 1.0$	$108.0 \pm 1.0$	$91.0 \pm 1.0$	$104.0 \pm 1.0$	$106.5 \pm 0.8$	$107.0 \pm 1.0$	$106.5 \pm 0.5$	$106.5 \pm 0.8$
1-114306	38.65	$101.0 \pm 1.0$	$44.0 \pm 3.0$	$95.0 \pm 1.0$	$113.0 \pm 3.0$	$128.5 \pm 2.0$	$135.0 \pm 0.8$	$134.0 \pm 0.8$	$133.5 \pm 0.8$
1-487130	38.93	$75.0 \pm 1.0$	$50.0 \pm 2.0$	$69.0 \pm 1.0$	$84.0 \pm 2.0$	$97.0 \pm 1.5$	$98.0 \pm 0.5$	$90.5 \pm 0.5$	$95.5 \pm 0.5$
1-351790	39.83	$82.0 \pm 1.0$	$88.0 \pm 1.0$	$83.0 \pm 1.0$	$82.0 \pm 2.0$	$135.5 \pm 2.2$	$96.5 \pm 1.8$	$83.5 \pm 2.2$	$91.5 \pm 0.8$
1-23731	37.83	$140.0 \pm 1.0$	$106.0 \pm 7.0$	$264.0 \pm 16.0$	$406.0 \pm 54.0$	$134.0 \pm 2.0$	$145.5 \pm 0.8$	$108.0 \pm 0.5$	$126.5 \pm 0.5$
1-167334	38.83	$111.0 \pm 1.0$	$89.0 \pm 1.0$	$136.0 \pm 1.0$	$138.0 \pm 1.0$	$120.5 \pm 2.0$	$166.5 \pm 0.5$	$11.0 \pm 34.5$	$56.0 \pm 4.5$
1-163831	39.64	$138.0 \pm 1.0$	$173.0 \pm 3.0$	$157.0 \pm 4.0$	$209.0 \pm 3.0$	$95.5 \pm 1.2$	$93.0 \pm 0.5$	$95.5 \pm 1.2$	$97.0 \pm 0.5$
1-247456	39.3	$879.0 \pm 34.0$	$172.0 \pm 13.0$	$1090.0 \pm 327.0$	$749.0 \pm 91.0$	$149.0 \pm 1.2$	$169.0 \pm 0.5$	$167.5 \pm 0.8$	$167.5 \pm 0.5$
1-210593	39.04	$160.0 \pm 1.0$	$128.0 \pm 3.0$	$146.0 \pm 4.0$	$147.0 \pm 4.0$	$101.5 \pm 1.0$	$107.5 \pm 0.5$	$104.0 \pm 0.8$	$103.0 \pm 0.5$
1-22301	39.84	$163.0 \pm 2.0$	$177.0 \pm 4.0$	$137.0 \pm 5.0$	$177.0 \pm 5.0$	$9.5 \pm 1.5$	$8.5 \pm 1.8$	$4.5 \pm 0.5$	$4.0 \pm 0.5$
1-251871	39.15	$160.0 \pm 2.0$	$108.0 \pm 5.0$	$128.0 \pm 2.0$	$127.0 \pm 3.0$	$63.0 \pm 0.5$	$66.0 \pm 0.5$	$63.0 \pm 0.5$	$61.5 \pm 1.0$
1-72914	39.01	$143.0 \pm 1.0$	$101.0 \pm 4.0$	$110.0 \pm 2.0$	$136.0 \pm 4.0$	$72.5 \pm 0.8$	$82.5 \pm 0.8$	$76.0 \pm 0.5$	$74.0 \pm 0.5$
1-248420	39.71	$138.0 \pm 1.0$	$159.0 \pm 1.0$	$152.0 \pm 2.0$	$151.0 \pm 2.0$	$49.5 \pm 1.0$	$49.5 \pm 1.0$	$49.0 \pm 1.0$	$49.0 \pm 1.0$
1-211063	38.75	$136.0 \pm 1.0$	$76.0 \pm 2.0$	$141.0 \pm 2.0$	$111.0 \pm 2.0$	$170.0 \pm 1.8$	$164.0 \pm 0.5$	$166.5 \pm 1.8$	$165.0 \pm 1.2$
1-211074	38.86	$154.0 \pm 0.0$	$126.0 \pm 2.0$	$150.0 \pm 2.0$	$138.0 \pm 2.0$	$142.5 \pm 1.0$	$133.5 \pm 0.5$	$142.5 \pm 0.8$	$143.0 \pm 0.8$
1-23979	39.72	$118.0 \pm 1.0$	$132.0 \pm 1.0$	$115.0 \pm 1.0$	$120.0 \pm 1.0$	$56.5 \pm 1.8$	$67.5 \pm 0.5$	$75.5 \pm 0.5$	$59.0 \pm 0.5$
1-320681	37.49	$189.0 \pm 2.0$	$104.0 \pm 22.0$	$288.0 \pm 14.0$	$306.0 \pm 31.0$	$53.0 \pm 0.8$	$67.0 \pm 1.0$	$53.0 \pm 9.8$	$33.0 \pm 0.5$
1-519738	38.44	$158.0 \pm 1.0$	$101.0 \pm 3.0$	$135.0 \pm 7.0$	$237.0 \pm 19.0$	$56.5 \pm 1.0$	$52.5 \pm 0.5$	$60.0 \pm 0.5$	$52.5 \pm 0.5$
1-542318	39.88	$143.0 \pm 1.0$	$144.0 \pm 2.0$	$172.0 \pm 2.0$	$164.0 \pm 2.0$	$71.0 \pm 2.8$	$119.0 \pm 0.5$	$82.0 \pm 0.5$	$96.0 \pm 0.5$
1-285052	38.79	$143.0 \pm 1.0$	$114.0 \pm 4.0$	$137.0 \pm 2.0$	$110.0 \pm 1.0$	$98.0 \pm 2.2$	$75.0 \pm 0.5$	$93.5 \pm 1.2$	$97.0 \pm 1.5$
1-377125	38.98	$143.0 \pm 1.0$	$99.0 \pm 2.0$	$144.0 \pm 4.0$	$107.0 \pm 3.0$	$136.5 \pm 9.0$	$100.5 \pm 0.5$	$129.0 \pm 0.8$	$129.0 \pm 0.5$
1-95092	39.75	$143.0 \pm 1.0$	$154.0 \pm 3.0$	$130.0 \pm 2.0$	$154.0 \pm 2.0$	$85.5 \pm 1.0$	$80.5 \pm 0.5$	$86.0 \pm 0.5$	$85.5 \pm 0.5$
1-210962	39.01	$194.0 \pm 1.0$	$117.0 \pm 2.0$	$147.0 \pm 2.0$	$157.0 \pm 2.0$	$91.5 \pm 1.2$	$96.5 \pm 0.5$	$89.0 \pm 0.5$	$89.5 \pm 0.5$
1-251279	39.15	$156.0 \pm 1.0$	$120.0 \pm 2.0$	$117.0 \pm 2.0$	$130.0 \pm 2.0$	$150.0 \pm 1.0$	$142.5 \pm 0.5$	$146.0 \pm 0.5$	$146.0 \pm 0.5$
1-279676	39.54	$155.0 \pm 1.0$	$125.0 \pm 2.0$	$120.0 \pm 2.0$	$145.0 \pm 2.0$	$20.0 \pm 1.5$	$27.5 \pm 0.5$	$19.5 \pm 0.5$	$19.5 \pm 0.5$
1-44789	39.1	$154.0 \pm 2.0$	$142.0 \pm 3.0$	$173.0 \pm 4.0$	$148.0 \pm 1.0$	$85.0 \pm 0.8$	$95.0 \pm 0.5$	$88.0 \pm 1.5$	$90.0 \pm 0.5$
1-378401	39.38	$224.0 \pm 2.0$	$223.0 \pm 4.0$	$188.0 \pm 7.0$	$232.0 \pm 11.0$	$162.5 \pm 1.0$	$33.5 \pm 0.5$	$38.0 \pm 0.5$	$26.5 \pm 0.5$
1-201561	39.59	$168.0 \pm 2.0$	$157.0 \pm 2.0$	$168.0 \pm 2.0$	$166.0 \pm 1.0$	$23.5 \pm 3.0$	$22.5 \pm 0.5$	$29.5 \pm 0.5$	$42.5 \pm 0.5$
1-24246	39.1	$110.0 \pm 1.0$	$134.0 \pm 4.0$	$94.0 \pm 2.0$	$105.0 \pm 2.0$	$139.0 \pm 1.5$	$134.0 \pm 0.8$	$134.0 \pm 1.0$	$121.5 \pm 0.5$
1-285052	38.79	$143.0 \pm 1.0$	$114.0 \pm 4.0$	$137.0 \pm 2.0$	$110.0 \pm 1.0$	$98.0 \pm 2.2$	$75.0 \pm 0.5$	$93.5 \pm 1.2$	$97.0 \pm 1.5$
1-198182	39.68	$217.0 \pm 1.0$	$195.0 \pm 1.0$	$219.0 \pm 1.0$	$227.0 \pm 2.0$	$44.5 \pm 0.8$	$35.5 \pm 0.8$	$42.5 \pm 0.8$	$55.0 \pm 0.5$
1-256185	39.22	$214.0 \pm 1.0$	$171.0 \pm 10.0$	$151.0 \pm 5.0$	$202.0 \pm 12.0$	$178.5 \pm 0.8$	$162.5 \pm 0.8$	$167.5 \pm 0.8$	$168.0 \pm 1.2$
1-48053	–	$286.0 \pm 1.0$	$116.0 \pm 36.0$	$184.0 \pm 10.0$	$294.0 \pm 13.0$	$12.0 \pm 0.8$	$161.5 \pm 0.5$	$39.0 \pm 0.5$	$160.0 \pm 0.5$
1-96075	39.53	$122.0 \pm 1.0$	$133.0 \pm 2.0$	$115.0 \pm 2.0$	$137.0 \pm 2.0$	$42.0 \pm 0.8$	$47.5 \pm 0.5$	$43.5 \pm 0.5$	$44.0 \pm 0.5$
1-166947	38.79	$149.0 \pm 1.0$	$83.0 \pm 3.0$	$143.0 \pm 3.0$	$116.0 \pm 2.0$	$36.0 \pm 3.2$	$123.0 \pm 0.5$	$34.0 \pm 0.8$	$35.5 \pm 0.8$
1-52259	38.98	$89.0 \pm 1.0$	$100.0 \pm 3.0$	$63.0 \pm 0.0$	$63.0 \pm 0.0$	$90.5 \pm 4.2$	$103.0 \pm 0.5$	$87.5 \pm 12.0$	$99.5 \pm 6.2$
1-519742	39.78	$96.0 \pm 1.0$	$99.0 \pm 0.0$	$86.0 \pm 1.0$	$80.0 \pm 1.0$	$133.0 \pm 4.0$	$124.5 \pm 0.5$	$129.5 \pm 1.8$	$120.5 \pm 1.0$
1-37079	37.71	$72.0 \pm 1.0$	$39.0 \pm 3.0$	$78.0 \pm 1.0$	$96.0 \pm 2.0$	$157.5 \pm 6.0$	$15.0 \pm 0.5$	$177.5 \pm 3.0$	$25.5 \pm 0.5$
1-276679	38.42	$88.0 \pm 1.0$	$99.0 \pm 4.0$	$61.0 \pm 0.0$	$71.0 \pm 0.0$	$152.0 \pm 2.2$	$137.5 \pm 0.5$	$151.5 \pm 0.8$	$152.5 \pm 0.5$
1-491229	39.64	$189.0 \pm 1.0$	$213.0 \pm 5.0$	$249.0 \pm 3.0$	$226.0 \pm 2.0$	$101.5 \pm 1.2$	$82.5 \pm 0.5$	$99.5 \pm 0.5$	$105.0 \pm 0.5$
1-94554	38.98	$136.0 \pm 1.0$	$111.0 \pm 3.0$	$135.0 \pm 2.0$	$146.0 \pm 5.0$	$29.5 \pm 2.0$	$37.5 \pm 0.5$	$8.0 \pm 0.8$	$44.0 \pm 0.5$
1-604048	39.14	$163.0 \pm 1.0$	$126.0 \pm 1.0$	$124.0 \pm 2.0$	$129.0 \pm 3.0$	$58.5 \pm 2.5$	$71.0 \pm 0.5$	$59.0 \pm 1.8$	$67.0 \pm 1.8$
1-604761	39.64	$193.0 \pm 2.0$	$186.0 \pm 3.0$	$178.0 \pm 2.0$	$189.0 \pm 3.0$	$70.0 \pm 0.5$	$68.0 \pm 0.5$	$66.5 \pm 0.5$	$66.5 \pm 0.5$
1-210173	39.28	$155.0 \pm 2.0$	$137.0 \pm 4.0$	$113.0 \pm 2.0$	$135.0 \pm 3.0$	$122.5 \pm 1.0$	$121.0 \pm 0.5$	$121.0 \pm 0.5$	$124.5 \pm 0.5$
1-71525	39.0	$136.0 \pm 1.0$	$94.0 \pm 5.0$	$242.0 \pm 135.0$	$685.0 \pm 263.0$	$126.5 \pm 1.2$	$138.0 \pm 0.5$	$130.5 \pm 0.8$	$130.5 \pm 0.5$
1-25725	39.39	$190.0 \pm 2.0$	$198.0 \pm 3.0$	$195.0 \pm 4.0$	$225.0 \pm 4.0$	$138.5 \pm 2.2$	$136.5 \pm 0.5$	$133.0 \pm 1.2$	$144.5 \pm 0.5$
1-211079	38.53	$198.0 \pm 1.0$	$228.0 \pm 11.0$	$250.0 \pm 18.0$	$252.0 \pm 15.0$	$178.5 \pm 0.8$	$167.0 \pm 0.5$	$126.5 \pm 0.5$	$125.5 \pm 0.5$
1-322074	38.12	$120.0 \pm 0.0$	$93.0 \pm 3.0$	$227.0 \pm 13.0$	$234.0 \pm 49.0$	$35.5 \pm 2.5$	$68.5 \pm 0.5$	$120.0 \pm 0.5$	$160.5 \pm 0.5$

**Table A1** – *continued*

<i>mangaid</i>	$\log_{10} L_{\text{[O III]}}$	$\sigma_*$	$\sigma_{\text{[O III]}}$	$\sigma_{H\alpha}$	$\sigma_{\text{[N II]}}$	$\Psi_{0*}$	$\Psi_0 \text{ [O III]}$	$\Psi_0 \text{ H}\alpha$	$\Psi_0 \text{ [N II]}$
1-94604	39.5	$110.0 \pm 1.0$	$109.0 \pm 1.0$	$136.0 \pm 4.0$	$343.0 \pm 54.0$	$153.0 \pm 2.0$	$166.0 \pm 0.5$	$157.5 \pm 0.5$	$144.0 \pm 0.5$
1-295095	38.76	$101.0 \pm 1.0$	$112.0 \pm 3.0$	$80.0 \pm 1.0$	$88.0 \pm 2.0$	$1.0 \pm 2.2$	$3.0 \pm 0.8$	$178.0 \pm 1.5$	$1.0 \pm 1.2$
1-134239	39.17	$138.0 \pm 1.0$	$136.0 \pm 3.0$	$119.0 \pm 3.0$	$140.0 \pm 3.0$	$32.5 \pm 1.5$	$31.5 \pm 0.5$	$34.0 \pm 1.5$	$35.5 \pm 1.5$
1-37036	39.42	$220.0 \pm 1.0$	$173.0 \pm 2.0$	$206.0 \pm 2.0$	$197.0 \pm 3.0$	$98.0 \pm 0.8$	$86.0 \pm 0.5$	$84.0 \pm 0.5$	$99.0 \pm 0.5$
1-210785	37.08	$165.0 \pm 1.0$	$102.0 \pm 12.0$	$569.0 \pm 171.0$	$2128.0 \pm 444.0$	$125.5 \pm 0.8$	$130.0 \pm 0.5$	$113.5 \pm 0.5$	$107.0 \pm 0.5$
1-25680	39.08	$230.0 \pm 1.0$	$140.0 \pm 3.0$	$176.0 \pm 3.0$	$189.0 \pm 4.0$	$55.5 \pm 2.0$	$168.0 \pm 0.5$	$1.0 \pm 0.5$	$174.5 \pm 0.5$
1-167688	39.56	$96.0 \pm 1.0$	$81.0 \pm 0.0$	$95.0 \pm 0.0$	$89.0 \pm 1.0$	$35.5 \pm 9.2$	$18.0 \pm 1.0$	$40.0 \pm 0.8$	$70.5 \pm 1.5$
1-235587	38.59	$125.0 \pm 0.0$	$84.0 \pm 1.0$	$105.0 \pm 2.0$	$106.0 \pm 2.0$	$85.5 \pm 2.2$	$92.0 \pm 0.5$	$99.0 \pm 1.8$	$100.0 \pm 1.0$
1-37062	39.02	$79.0 \pm 1.0$	$83.0 \pm 1.0$	$91.0 \pm 1.0$	$96.0 \pm 1.0$	$21.5 \pm 3.5$	$173.0 \pm 0.5$	$19.0 \pm 12.0$	$31.0 \pm 0.5$
1-279666	39.45	$115.0 \pm 1.0$	$103.0 \pm 1.0$	$104.0 \pm 1.0$	$121.0 \pm 1.0$	$57.5 \pm 2.2$	$52.0 \pm 0.5$	$60.0 \pm 1.8$	$46.5 \pm 1.5$
1-392976	38.57	$108.0 \pm 1.0$	$94.0 \pm 3.0$	$133.0 \pm 5.0$	$123.0 \pm 4.0$	$16.0 \pm 0.5$	$56.0 \pm 0.5$	$80.5 \pm 0.5$	$166.0 \pm 0.5$
1-47499	38.86	$110.0 \pm 0.0$	$102.0 \pm 3.0$	$128.0 \pm 4.0$	$121.0 \pm 4.0$	$108.0 \pm 2.2$	$82.5 \pm 1.8$	$108.0 \pm 0.5$	$126.0 \pm 0.5$
1-339163	39.35	$159.0 \pm 1.0$	$323.0 \pm 6.0$	$245.0 \pm 4.0$	$353.0 \pm 8.0$	$38.5 \pm 0.5$	$42.0 \pm 0.5$	$39.0 \pm 0.5$	$39.0 \pm 0.5$
1-136125	38.56	$109.0 \pm 1.0$	$61.0 \pm 2.0$	$118.0 \pm 2.0$	$112.0 \pm 2.0$	$68.0 \pm 0.5$	$69.0 \pm 0.5$	$67.5 \pm 0.5$	$67.5 \pm 0.5$
1-626830	38.62	$137.0 \pm 1.0$	$107.0 \pm 3.0$	$115.0 \pm 2.0$	$136.0 \pm 2.0$	$22.5 \pm 0.5$	$29.5 \pm 0.5$	$22.5 \pm 0.5$	$19.5 \pm 0.5$
1-258774	39.4	$143.0 \pm 0.0$	$114.0 \pm 2.0$	$110.0 \pm 1.0$	$135.0 \pm 0.0$	$154.0 \pm 4.2$	$152.0 \pm 1.2$	$155.0 \pm 3.2$	$172.5 \pm 3.8$
1-379660	39.12	$139.0 \pm 1.0$	$132.0 \pm 3.0$	$118.0 \pm 4.0$	$127.0 \pm 4.0$	$115.5 \pm 1.2$	$106.0 \pm 0.5$	$111.5 \pm 0.8$	$113.5 \pm 0.5$
1-48208	38.7	$162.0 \pm 1.0$	$94.0 \pm 2.0$	$140.0 \pm 4.0$	$91.0 \pm 5.0$	$71.5 \pm 2.2$	$75.0 \pm 0.5$	$76.0 \pm 0.5$	$66.5 \pm 0.5$
1-198153	39.29	$176.0 \pm 1.0$	$145.0 \pm 2.0$	$177.0 \pm 1.0$	$178.0 \pm 1.0$	$93.5 \pm 0.5$	$96.0 \pm 0.5$	$94.5 \pm 0.5$	$94.5 \pm 0.5$
1-211063	38.75	$136.0 \pm 1.0$	$76.0 \pm 2.0$	$141.0 \pm 2.0$	$111.0 \pm 2.0$	$170.0 \pm 1.8$	$164.0 \pm 0.5$	$166.5 \pm 1.8$	$165.0 \pm 1.2$
1-135810	38.45	$112.0 \pm 1.0$	$80.0 \pm 2.0$	$95.0 \pm 2.0$	$101.0 \pm 2.0$	$52.0 \pm 0.8$	$54.5 \pm 0.5$	$50.5 \pm 0.8$	$50.5 \pm 0.5$
1-91016	39.49	$103.0 \pm 1.0$	$125.0 \pm 2.0$	$138.0 \pm 3.0$	$173.0 \pm 4.0$	$50.5 \pm 4.0$	$44.5 \pm 1.2$	$51.5 \pm 1.2$	$57.0 \pm 2.0$
1-338828	39.3	$94.0 \pm 1.0$	$90.0 \pm 1.0$	$80.0 \pm 1.0$	$80.0 \pm 1.0$	$103.0 \pm 0.5$	$101.5 \pm 0.5$	$96.0 \pm 0.5$	$86.0 \pm 1.2$
1-386695	39.68	$105.0 \pm 2.0$	$119.0 \pm 1.0$	$105.0 \pm 1.0$	$107.0 \pm 1.0$	$129.0 \pm 1.2$	$88.0 \pm 0.5$	$141.5 \pm 0.5$	$89.5 \pm 0.5$
1-279073	39.34	$231.0 \pm 1.0$	$161.0 \pm 4.0$	$186.0 \pm 2.0$	$181.0 \pm 3.0$	$15.0 \pm 1.5$	$169.5 \pm 0.8$	$155.5 \pm 0.5$	$164.0 \pm 0.5$
1-211100	38.09	$198.0 \pm 1.0$	$116.0 \pm 7.0$	$275.0 \pm 44.0$	$346.0 \pm 14.0$	$152.0 \pm 4.8$	$127.0 \pm 0.5$	$103.0 \pm 0.5$	$165.0 \pm 0.5$
1-210784	38.3	$171.0 \pm 0.0$	$97.0 \pm 4.0$	$159.0 \pm 2.0$	$218.0 \pm 3.0$	$90.0 \pm 2.2$	$101.0 \pm 0.5$	$59.0 \pm 1.2$	$62.5 \pm 0.5$
1-135044	39.44	$115.0 \pm 1.0$	$116.0 \pm 2.0$	$156.0 \pm 2.0$	$167.0 \pm 3.0$	$95.5 \pm 1.2$	$96.5 \pm 0.5$	$96.5 \pm 1.2$	$98.5 \pm 0.5$
1-218280	38.7	$148.0 \pm 0.0$	$104.0 \pm 1.0$	$121.0 \pm 1.0$	$114.0 \pm 3.0$	$99.0 \pm 1.0$	$96.0 \pm 0.5$	$98.0 \pm 0.5$	$98.0 \pm 0.5$
1-211063	38.75	$136.0 \pm 1.0$	$76.0 \pm 2.0$	$141.0 \pm 2.0$	$111.0 \pm 2.0$	$170.0 \pm 1.8$	$164.0 \pm 0.5$	$166.5 \pm 1.8$	$165.0 \pm 1.2$
1-148068	39.21	$156.0 \pm 1.0$	$121.0 \pm 4.0$	$169.0 \pm 2.0$	$156.0 \pm 1.0$	$63.5 \pm 0.8$	$59.0 \pm 0.5$	$65.0 \pm 0.8$	$66.5 \pm 0.5$
1-166947	38.79	$149.0 \pm 1.0$	$83.0 \pm 3.0$	$143.0 \pm 3.0$	$116.0 \pm 2.0$	$36.0 \pm 3.2$	$123.0 \pm 0.5$	$34.0 \pm 0.8$	$35.5 \pm 0.8$
1-55572	38.93	$194.0 \pm 2.0$	$117.0 \pm 1.0$	$208.0 \pm 4.0$	$198.0 \pm 5.0$	$51.0 \pm 0.5$	$52.0 \pm 0.5$	$50.5 \pm 0.5$	$52.0 \pm 0.8$
1-277552	39.27	$118.0 \pm 1.0$	$119.0 \pm 1.0$	$99.0 \pm 1.0$	$112.0 \pm 1.0$	$3.5 \pm 0.5$	$4.0 \pm 0.5$	$2.5 \pm 0.5$	$2.5 \pm 0.8$
1-264513	39.28	$99.0 \pm 1.0$	$106.0 \pm 1.0$	$77.0 \pm 0.0$	$85.0 \pm 1.0$	$0.5 \pm 0.5$	$177.0 \pm 3.8$	$175.5 \pm 1.5$	$175.5 \pm 2.0$
1-136125	38.56	$109.0 \pm 1.0$	$61.0 \pm 2.0$	$118.0 \pm 2.0$	$112.0 \pm 2.0$	$68.0 \pm 0.5$	$69.0 \pm 0.5$	$67.5 \pm 0.5$	$67.5 \pm 0.5$
1-217050	39.05	$203.0 \pm 1.0$	$154.0 \pm 2.0$	$200.0 \pm 2.0$	$208.0 \pm 3.0$	$60.5 \pm 0.5$	$83.0 \pm 0.5$	$82.0 \pm 0.5$	$78.0 \pm 0.5$
1-135372	38.66	$212.0 \pm 1.0$	$183.0 \pm 6.0$	$1011.0 \pm 363.0$	$280.0 \pm 13.0$	$20.0 \pm 0.8$	$23.0 \pm 0.5$	$22.5 \pm 0.5$	$29.5 \pm 0.5$
1-274663	38.87	$216.0 \pm 1.0$	$125.0 \pm 3.0$	$188.0 \pm 3.0$	$188.0 \pm 5.0$	$153.5 \pm 1.8$	$163.5 \pm 0.5$	$111.5 \pm 0.5$	$155.5 \pm 0.5$
1-25554	38.96	$114.0 \pm 0.0$	$111.0 \pm 1.0$	$117.0 \pm 1.0$	$112.0 \pm 2.0$	$74.5 \pm 1.2$	$67.5 \pm 0.5$	$76.5 \pm 0.5$	$82.0 \pm 0.5$
1-135625	39.33	$98.0 \pm 1.0$	$111.0 \pm 2.0$	$98.0 \pm 1.0$	$98.0 \pm 1.0$	$17.5 \pm 1.2$	$16.0 \pm 1.5$	$15.0 \pm 0.5$	$12.5 \pm 1.0$
1-216958	38.9	$99.0 \pm 0.0$	$78.0 \pm 0.0$	$67.0 \pm 0.0$	$72.0 \pm 0.0$	$58.0 \pm 5.8$	$41.0 \pm 0.5$	$60.0 \pm 4.5$	$81.5 \pm 0.5$
1-135285	38.93	$133.0 \pm 1.0$	$155.0 \pm 2.0$	$166.0 \pm 2.0$	$162.0 \pm 1.0$	$116.5 \pm 0.5$	$112.0 \pm 0.5$	$114.0 \pm 0.5$	$113.0 \pm 0.5$
1-633990	38.77	$97.0 \pm 0.0$	$93.0 \pm 1.0$	$99.0 \pm 0.0$	$103.0 \pm 1.0$	$33.5 \pm 1.2$	$30.0 \pm 0.5$	$31.5 \pm 0.5$	$37.5 \pm 0.5$
1-25688	38.35	$110.0 \pm 1.0$	$64.0 \pm 2.0$	$110.0 \pm 2.0$	$115.0 \pm 1.0$	$20.5 \pm 1.5$	$13.5 \pm 0.5$	$17.0 \pm 0.8$	$19.5 \pm 1.5$

**Table A2.** Parameters of AGN in MaNGA–MPL5: (1) galaxy identification in the MaNGA survey, (2–3) RA/Dec. (2000) in degrees, (4) spectroscopic redshift from SDSS-III, (5) integrated absolute  $r$ -band magnitude from SDSS-III, (6) stellar mass in units of  $M_{\odot}$ , errors associated with the stellar masses of galaxies in our sample are typically under 0.03 dex (Conroy, Gunn & White 2009), (7) elliptical/spiral/merging classification from Galaxy Zoo I, (8–9)  $r$ -band concentration and asymmetry, and (10) [O III] luminosity in units of  $10^{40}$  erg s $^{-1}$ . Table extracted from Rembold et al. (2017).

mangaid (1)	RA (2)	Dec. (3)	$z$ (4)	$M_r$ (5)	$\log M^*/M_{\odot}$ (6)	GZ1 $_c$ (7)	$C$ (8)	$A$ (9)	$L(\text{[O III]})$ (10)
1-558912	166.129410	42.624554	0.1261	-20.46	11.25	-	0.37	0.12	$56.82 \pm 1.25$
1-269632	247.560974	26.206474	0.1315	-21.78	11.62	S	0.47	0.05	$30.08 \pm 1.69$
1-258599	186.181000	44.410770	0.1256	-21.24	11.68	E	0.50	0.11	$20.95 \pm 0.67$
1-72322	121.014198	40.802612	0.1262	-21.81	12.05	S	0.34	0.08	$20.66 \pm 0.43$
1-121532	118.091110	34.326569	0.1400	-20.51	11.34	E	0.33	0.05	$11.68 \pm 0.96$
1-209980	240.470871	45.351940	0.0420	-19.70	10.79	S	0.57	0.04	$11.01 \pm 0.17$
1-44379	120.700706	45.034554	0.0389	-19.89	10.97	S	0.24	0.06	$8.94 \pm 0.14$
1-149211	168.947800	50.401634	0.0473	-18.27	10.16	S	0.29	0.03	$7.88 \pm 0.14$
1-173958	167.306015	49.519432	0.0724	-20.53	11.31	S	0.33	0.06	$6.79 \pm 0.30$
1-338922	114.775749	44.402767	0.1345	-20.27	11.13	M	0.44	0.03	$6.77 \pm 0.90$
1-279147	168.957733	46.319565	0.0533	-19.51	10.66	S	0.45	0.03	$6.77 \pm 0.20$
1-460812	127.170799	17.581400	0.0665	-19.81	11.44	-	0.38	0.05	$6.46 \pm 0.31$
1-92866	243.581818	50.465611	0.0603	-20.56	11.69	E	0.49	0.05	$6.12 \pm 0.30$
1-94784	249.318420	44.418228	0.0314	-20.06	10.85	S	0.42	0.03	$5.96 \pm 0.12$
1-44303	119.182152	44.856709	0.0499	-19.72	10.62	S	0.29	0.10	$5.56 \pm 0.12$
1-339094	117.472420	45.248482	0.0313	-19.02	10.52	E	0.36	0.03	$5.29 \pm 0.09$
1-137883	137.874756	45.468319	0.0268	-18.06	10.77	E/S	0.41	0.01	$3.87 \pm 0.12$
1-48116	132.653992	57.359669	0.0261	-19.18	10.60	S	0.31	0.06	$3.79 \pm 0.08$
1-256446	166.509872	43.173473	0.0584	-19.40	11.14	E	0.49	0.05	$3.74 \pm 0.15$
1-95585	255.029877	37.839500	0.0633	-20.88	11.24	S	0.27	0.08	$3.58 \pm 0.16$
1-135641	249.557312	40.146820	0.0304	-19.03	11.19	S	0.28	0.08	$3.52 \pm 0.09$
1-259142	193.703995	44.155567	0.0543	-20.75	11.29	S	0.39	0.06	$3.47 \pm 0.20$
1-109056	39.446587	0.405085	0.0473	-19.27	10.57	-	0.32	0.05	$3.24 \pm 0.08$
1-24148	258.827423	57.658772	0.0282	-18.51	10.56	S	0.31	0.04	$3.17 \pm 0.05$
1-166919	146.709106	43.423843	0.0722	-20.85	11.28	S	0.37	0.06	$2.64 \pm 0.25$
1-248389	240.658051	41.293427	0.0348	-19.36	10.57	S	0.49	0.12	$2.55 \pm 0.09$
1-321739	226.431656	44.404903	0.0283	-18.91	11.12	S	0.40	0.14	$2.24 \pm 0.10$
1-234618	202.128433	47.714039	0.0608	-19.64	11.37	S	0.31	0.09	$2.23 \pm 0.23$
1-229010	57.243038	-1.144831	0.0407	-20.51	11.46	-	0.41	0.03	$2.11 \pm 0.09$
1-211311	248.426392	39.185120	0.0298	-19.04	10.44	E/S	0.43	0.02	$1.99 \pm 0.06$
1-373161	222.810074	30.692245	0.0547	-21.30	11.60	E	0.43	0.00	$1.87 \pm 0.11$
1-210646	245.157181	41.466873	0.0606	-20.38	10.98	S	0.18	0.05	$1.80 \pm 0.10$
1-351790	121.147926	50.708557	0.0227	-18.09	9.92	E	0.39	0.02	$1.72 \pm 0.03$
1-163831	118.627846	25.815987	0.0631	-20.84	11.26	S	0.27	0.05	$1.67 \pm 0.13$
1-22301	253.405563	63.031269	0.1052	-21.19	11.18	S	0.29	0.08	$1.67 \pm 0.23$
1-248420	241.823395	41.403603	0.0346	-19.71	10.90	S	0.21	0.07	$1.66 \pm 0.06$
1-23979	258.158752	57.322422	0.0266	-18.27	10.42	E	0.44	0.06	$1.60 \pm 0.05$
1-542318	245.248306	49.001778	0.0582	-19.75	10.91	E	0.34	0.01	$1.58 \pm 0.07$
1-95092	250.846420	39.806461	0.0302	-19.95	11.20	E	0.47	0.04	$1.54 \pm 0.07$
1-279676	173.981888	48.021458	0.0587	-19.40	10.81	-	0.32	0.02	$1.52 \pm 0.14$
1-201561	118.053215	28.772579	0.0637	-19.73	10.88	S	0.30	0.07	$1.37 \pm 0.15$
1-198182	224.749649	48.409855	0.0359	-20.22	11.09	E	0.49	0.01	$1.34 \pm 0.11$
1-96075	253.946381	39.310535	0.0631	-21.12	11.35	S	0.29	0.07	$1.26 \pm 0.13$
1-519742	206.612457	22.076742	0.0276	-17.62	9.64	S	0.23	0.04	$1.19 \pm 0.03$
1-491229	172.607544	22.216530	0.0393	-20.25	11.12	E	0.51	0.02	$1.14 \pm 0.11$
1-604761	113.472275	37.025906	0.0618	-20.92	11.34	S	0.26	0.12	$1.00 \pm 0.13$
1-25725	262.996735	59.971638	0.0291	-18.30	10.55	E	0.44	0.04	$0.92 \pm 0.05$
1-94604	251.335938	42.757790	0.0493	-19.44	10.52	S	0.37	0.01	$0.86 \pm 0.07$
1-37036	41.699909	0.421577	0.0283	-19.02	10.66	E	0.40	0.09	$0.84 \pm 0.06$
1-167688	155.885559	46.057755	0.0258	-17.86	9.75	E	0.52	0.04	$0.84 \pm 0.02$
1-279666	173.911240	47.515518	0.0455	-18.83	10.42	E	0.31	0.02	$0.84 \pm 0.07$
1-339163	116.280205	46.072422	0.0312	-20.02	10.97	S	0.30	0.10	$0.82 \pm 0.07$
1-258774	186.400864	45.083858	0.0384	-19.60	10.77	-	0.55	0.03	$0.77 \pm 0.10$
1-198153	224.289078	48.633968	0.0354	-19.83	11.00	S	0.27	0.07	$0.76 \pm 0.08$
1-91016	234.810974	56.670856	0.0463	-18.60	10.56	S	0.27	0.06	$0.76 \pm 0.09$
1-279073	170.588150	46.430504	0.0323	-19.53	10.79	E	0.51	0.01	$0.63 \pm 0.06$
1-135044	247.907990	41.493645	0.0303	-19.76	10.65	S	0.31	0.05	$0.61 \pm 0.04$

**Table A2** – *continued*

<i>mangaid</i> (1)	RA (2)	Dec. (3)	$z$ (4)	$M_r$ (5)	$\log M^*/M_\odot$ (6)	$GZ1_c$ (7)	$C$ (8)	$A$ (9)	$L(\text{[O III]})$ (10)
1-148068	156.805679	48.244793	0.0610	-20.72	11.41	S	0.22	0.04	$0.45 \pm 0.15$
1-277552	167.034561	45.984623	0.0362	-19.72	10.83	S	0.21	0.15	$0.44 \pm 0.05$
1-217050	136.719986	41.408253	0.0274	-19.66	10.93	E	0.47	0.02	$0.43 \pm 0.03$
1-25554	262.486053	58.397408	0.0268	-19.27	10.52	S	0.36	0.04	$0.24 \pm 0.03$
1-135285	247.216949	42.812012	0.0316	-19.66	10.78	–	0.32	0.05	$0.20 \pm 0.04$

**Table A3.** Control sample parameters: (1) identification of the AGN host associated with the control galaxy and (2–11) same as (1–10) of Table A2. A total of 12 control sample objects have been paired to two different AGN hosts and appear more than once in the table. Table extracted from Rembold et al. (2017).

AGN <i>mangaid</i> (1)	<i>mangaid</i> (2)	RA (3)	Dec. (4)	$z$ (5)	$M_r$ (6)	$\log M^*/M_\odot$ (7)	$GZ1_c$ (8)	$C$ (9)	$A$ (10)	$L(\text{[O III]})$ (11)
1-558912	1-71481	117.456001	34.883911	0.1312	-20.95	11.70	E	0.47	0.02	$0.10 \pm 0.20$
	1-72928	127.256485	45.016773	0.1270	-20.62	11.52	E	0.40	0.21	$0.09 \pm 0.23$
1-269632	1-210700	248.140564	39.131020	0.1303	-20.96	11.67	S	0.36	0.03	$1.55 \pm 0.44$
	1-378795	118.925613	50.172771	0.0967	-20.77	11.35	S	0.32	0.03	$0.72 \pm 0.31$
1-258599	1-93876	246.942947	44.177521	0.1394	-20.75	11.50	E	0.44	0.01	$0.46 \pm 0.36$
	1-166691	146.047348	42.900040	0.1052	-20.50	11.36	E	0.51	0.04	$0.09 \pm 0.49$
1-72322	1-121717	118.803429	35.596798	0.1098	-21.11	11.61	S	0.39	0.12	$1.40 \pm 0.57$
	1-43721	116.967567	43.383499	0.1114	-21.41	11.86	S	0.32	0.01	$1.91 \pm 0.52$
1-121532	1-218427	124.342316	27.796206	0.1496	-21.30	11.47	E	0.47	0.04	$0.72 \pm 0.62$
	1-177493	257.085754	31.746916	0.1081	-20.90	11.30	E	0.38	0.06	$2.29 \pm 0.28$
1-209980	1-295095	248.348663	24.776577	0.0410	-18.40	10.14	E	0.35	0.05	$0.15 \pm 0.03$
	1-92626	241.799545	48.572563	0.0434	-20.04	11.04	S	0.36	0.03	$0.76 \pm 0.07$
1-44379	1-211082	247.620041	39.626045	0.0304	-19.72	11.07	E	0.31	0.06	$0.19 \pm 0.04$
	1-135371	250.156235	39.221634	0.0352	-19.20	10.76	S	0.28	0.11	$0.25 \pm 0.07$
1-149211	1-377321	110.556152	42.183643	0.0444	-19.02	9.89	S	0.31	0.03	$4.53 \pm 0.13$
	1-491233	172.563995	22.992010	0.0332	-18.39	10.59	S	0.29	0.06	$0.25 \pm 0.03$
1-173958	1-247456	232.823196	45.416538	0.0705	-20.05	10.83	–	0.40	0.02	$0.57 \pm 0.16$
	1-24246	264.840790	56.567070	0.0818	-19.91	10.57	S	0.75	0.36	$0.11 \pm 0.06$
1-338922	1-286804	211.904861	44.482269	0.1429	-20.03	10.50	M	0.44	0.32	$2.23 \pm 0.43$
	1-109493	56.425140	-0.378460	0.1093	-20.46	11.26	–	0.49	-0.01	$0.15 \pm 0.18$
1-279147	1-283246	191.078873	46.407131	0.0496	-19.17	10.55	S	0.47	0.04	$0.23 \pm 0.06$
	1-351538	119.145126	47.563850	0.0692	-19.67	11.00	S	0.35	0.08	$0.46 \pm 0.13$
1-460812	1-270160	248.274612	26.211815	0.0660	-20.37	11.46	S	0.50	0.02	$0.70 \pm 0.39$
	1-258455	183.612198	45.195454	0.0653	-20.02	11.03	E	0.40	0.03	$0.49 \pm 0.14$
1-92866	1-94514	248.241180	42.524670	0.0614	-20.60	11.17	E	0.51	0.00	–
	1-210614	244.501755	41.392189	0.0612	-20.64	11.48	E	0.49	0.01	$0.40 \pm 0.14$
1-94784	1-211063	247.058411	40.313835	0.0331	-19.87	10.79	S	0.33	0.09	$0.20 \pm 0.04$
	1-135502	247.764175	39.838505	0.0305	-19.51	11.13	S	0.40	0.09	$0.50 \pm 0.05$
1-44303	1-339028	116.097923	44.527740	0.0497	-20.01	11.24	S	0.36	0.06	$0.44 \pm 0.08$
	1-379087	119.910118	51.792362	0.0534	-19.60	11.02	S	0.38	0.10	$0.72 \pm 0.13$
1-339094	1-274646	158.017029	43.859268	0.0284	-18.70	10.36	E	0.53	0.02	$0.35 \pm 0.04$
	1-24099	258.027618	57.504009	0.0282	-18.67	10.34	E	0.44	0.01	$0.06 \pm 0.03$
1-137883	1-178838	312.023621	0.068841	0.0247	-17.54	10.46	–	0.51	0.19	$0.10 \pm 0.02$
	1-36878	42.542126	-0.867116	0.0232	-18.88	10.77	E	0.45	0.07	$0.28 \pm 0.04$
1-48116	1-386452	136.228333	28.384314	0.0269	-19.54	10.57	S	0.49	0.09	$0.32 \pm 0.04$
	1-24416	263.033173	56.878746	0.0281	-19.16	10.66	S	0.37	0.03	$0.22 \pm 0.03$
1-256446	1-322671	235.797028	39.238773	0.0637	-19.77	10.82	E	0.49	0.04	–
	1-256465	166.752243	43.089901	0.0575	-19.70	10.79	E	0.50	0.01	$0.59 \pm 0.11$
1-95585	1-166947	147.335007	43.442989	0.0720	-20.79	10.81	S	0.29	0.02	$0.13 \pm 0.08$
	1-210593	244.419754	41.899155	0.0605	-19.76	10.90	S	0.36	0.06	$0.43 \pm 0.14$
1-135641	1-635503	318.990448	9.543076	0.0293	-19.37	10.91	S	0.22	0.10	$0.15 \pm 0.06$
	1-235398	213.149185	47.253059	0.0281	-18.91	10.99	S	0.28	0.10	$0.16 \pm 0.05$
1-259142	1-55572	133.121307	56.112690	0.0454	-20.11	11.03	S	0.40	0.06	$0.12 \pm 0.04$
	1-489649	171.954834	21.386103	0.0406	-19.94	10.95	S	0.40	0.03	$0.30 \pm 0.08$
1-109056	1-73005	125.402306	45.585476	0.0514	-19.47	10.65	S	0.31	0.05	$0.20 \pm 0.06$
	1-43009	113.553879	39.076836	0.0510	-19.41	10.43	S	0.26	0.03	$0.12 \pm 0.04$

**Table A3** – continued

AGN mangaid (1)	mangaid (2)	RA (3)	Dec. (4)	$z$ (5)	$M_r$ (6)	$\log M^*/M_\odot$ (7)	GZ1 <sub>c</sub> (8)	$C$ (9)	$A$ (10)	$L(\text{[O III]})$ (11)
1-24148	1-285031	198.701370	47.351547	0.0303	-18.47	10.72	S	0.34	0.05	0.26 ± 0.04
	1-236099	225.236221	41.566265	0.0205	-17.36	9.91	S	0.33	0.04	0.07 ± 0.01
1-166919	12-129446	203.943542	26.101791	0.0670	-20.57	11.32	S	0.34	0.03	0.28 ± 0.09
	1-90849	237.582748	56.131981	0.0661	-20.39	11.16	E	0.30	0.04	0.28 ± 0.05
1-248389	1-94554	248.914688	42.461296	0.0318	-18.96	10.57	S	0.55	0.07	0.22 ± 0.04
	1-245774	214.863297	54.100300	0.0426	-20.22	10.83	S	0.40	0.08	0.29 ± 0.07
1-321739	1-247417	233.319382	45.698528	0.0294	-19.25	10.76	S	0.28	0.09	0.16 ± 0.04
	1-633994	247.419952	40.686954	0.0305	-18.27	11.04	S	0.39	0.11	0.36 ± 0.09
1-234618	1-282144	184.592514	46.155350	0.0492	-18.92	10.31	S	0.21	0.08	0.10 ± 0.02
	1-339125	117.739944	45.989529	0.0534	-18.97	11.17	S	0.35	0.05	0.45 ± 0.23
1-229010	1-210962	246.358719	39.870697	0.0290	-20.49	11.09	S	0.47	0.07	0.35 ± 0.06
	1-613211	167.861847	22.970764	0.0323	-19.87	11.32	E	0.48	0.04	0.16 ± 0.06
1-211311	1-25688	261.284851	58.764687	0.0292	-18.79	10.32	S	0.29	0.06	0.10 ± 0.02
	1-94422	250.453201	41.818737	0.0316	-19.15	10.55	S	0.37	0.05	0.24 ± 0.03
1-373161	1-259650	196.611053	45.289001	0.0509	-21.07	11.68	E	0.44	0.06	0.67 ± 0.20
	1-289865	322.048584	0.299885	0.0525	-20.90	11.35	–	0.49	0.02	0.11 ± 0.09
1-210646	1-114306	323.742737	11.296529	0.0637	-20.58	10.83	S	0.26	0.05	0.33 ± 0.16
	1-487130	164.447296	21.233431	0.0587	-20.47	10.86	S	0.26	0.11	0.27 ± 0.10
1-351790	1-23731	260.746704	60.559292	0.0205	-18.20	10.19	E	0.40	0.02	0.02 ± 0.01
	1-167334	151.894836	46.093983	0.0243	-18.89	10.60	E	0.43	0.04	0.47 ± 0.05
1-163831	1-247456	232.823196	45.416538	0.0705	-20.05	10.83	–	0.40	0.02	0.57 ± 0.16
	1-210593	244.419754	41.899155	0.0605	-19.76	10.90	S	0.36	0.06	0.43 ± 0.14
1-22301	1-251871	214.506760	41.827644	0.1027	-21.17	11.68	S	0.26	0.05	0.24 ± 0.18
	1-72914	127.580818	45.075867	0.0970	-20.88	11.31	S	0.23	0.08	0.13 ± 0.07
1-248420	1-211063	247.058411	40.313835	0.0331	-19.87	10.79	S	0.33	0.09	0.20 ± 0.04
	1-211074	247.462692	39.766510	0.0318	-19.71	10.79	S	0.30	0.18	0.20 ± 0.04
1-23979	1-320681	213.813095	47.873344	0.0279	-18.76	10.77	E	0.48	0.01	0.09 ± 0.07
	1-519738	206.514709	22.118843	0.0277	-19.49	10.73	E	0.45	0.03	0.11 ± 0.04
1-542318	1-285052	199.061493	47.599365	0.0573	-19.77	10.85	S	0.32	0.04	0.11 ± 0.03
	1-377125	112.221359	41.307812	0.0585	-19.67	10.84	S	0.41	0.02	0.57 ± 0.14
1-95092	1-210962	246.358719	39.870697	0.0290	-20.49	11.09	S	0.47	0.07	0.35 ± 0.06
	1-251279	209.251984	43.362034	0.0329	-20.11	10.97	E	0.47	0.04	0.37 ± 0.06
1-279676	1-44789	120.890366	47.892406	0.0586	-19.33	10.92	–	0.31	0.13	0.32 ± 0.09
	1-378401	117.904335	48.000526	0.0612	-19.65	11.02	E	0.41	0.02	0.57 ± 0.14
1-201561	1-24246	264.840790	56.567070	0.0818	-19.91	10.57	S	0.75	0.36	0.11 ± 0.06
	1-285052	199.061493	47.599365	0.0573	-19.77	10.85	S	0.32	0.04	0.11 ± 0.03
1-198182	1-256185	165.568695	44.271709	0.0370	-20.00	11.03	E	0.50	0.06	0.25 ± 0.04
	1-48053	132.595016	55.378742	0.0308	-20.24	11.49	E	0.50	0.01	–
1-96075	1-166947	147.335007	43.442989	0.0720	-20.79	10.81	S	0.29	0.02	0.13 ± 0.08
	1-52259	59.411037	-6.274680	0.0678	-20.69	11.12	S	0.23	0.07	0.30 ± 0.09
1-519742	1-37079	42.092335	0.986465	0.0274	-17.25	9.55	E	0.27	0.02	0.02 ± 0.01
	1-276679	161.272629	44.054291	0.0253	-18.27	10.10	S	0.24	0.03	0.05 ± 0.01
1-491229	1-94554	248.914688	42.461296	0.0318	-18.96	10.57	S	0.55	0.07	0.22 ± 0.04
	1-604048	50.536137	-0.836265	0.0365	-20.37	10.91	S	0.42	0.09	0.39 ± 0.08
1-604761	1-210173	241.341766	42.488312	0.0778	-20.71	11.10	S	0.33	0.07	0.52 ± 0.13
	1-71525	118.344856	36.274380	0.0457	-20.17	10.97	S	0.27	0.10	0.19 ± 0.06
1-25725	1-211079	247.438034	39.810539	0.0304	-18.97	10.54	E	0.54	0.01	0.03 ± 0.04
	1-322074	228.700729	43.665970	0.0274	-18.15	10.10	E	0.45	0.02	–
1-94604	1-295095	248.348663	24.776577	0.0410	-18.40	10.14	E	0.35	0.05	0.15 ± 0.03
	1-134239	241.416443	46.846561	0.0571	-19.83	10.70	S	0.36	0.04	0.23 ± 0.06
1-37036	1-210785	246.765076	39.527386	0.0338	-20.22	10.97	E	0.47	0.01	–
	1-25680	261.968872	60.097275	0.0278	-19.41	10.84	E	0.52	0.02	0.34 ± 0.04
1-167688	1-235587	214.854660	45.864250	0.0267	-18.88	10.48	E	0.44	0.01	0.08 ± 0.02
	1-37062	41.846367	0.058757	0.0248	-18.30	10.40	E	0.49	0.03	0.27 ± 0.03
1-279666	1-392976	156.428894	37.497524	0.0432	-17.91	10.09	E	0.37	0.02	0.10 ± 0.03
	1-47499	132.037582	54.309921	0.0461	-18.53	10.51	E	0.27	0.04	0.15 ± 0.06
1-339163	1-136125	254.044144	34.836521	0.0316	-19.33	10.50	S	0.25	0.09	0.08 ± 0.02
	1-626830	204.683838	26.328539	0.0282	-19.23	10.67	S	0.28	0.07	0.15 ± 0.04
1-258774	1-379660	119.973717	55.374817	0.0357	-19.44	10.74	E	0.47	0.03	0.37 ± 0.07
	1-48208	134.008118	57.390965	0.0406	-19.57	10.85	S	0.50	0.01	0.12 ± 0.04
1-198153	1-211063	247.058411	40.313835	0.0331	-19.87	10.79	S	0.33	0.09	0.20 ± 0.04
	1-135810	250.123138	39.235115	0.0297	-19.38	10.59	S	0.24	0.09	0.08 ± 0.02

**Table A3** – *continued*

AGN <i>mangaid</i> (1)	<i>mangaid</i> (2)	RA (3)	Dec. (4)	$z$ (5)	$M_r$ (6)	$\log M^*/M_\odot$ (7)	$GZ1_c$ (8)	$C$ (9)	A (10)	$L(\text{[O III]})$ (11)
1-91016	1-338828	115.641609	44.215858	0.0418	-18.10	10.42	S	0.28	0.03	0.43 ± 0.05
	1-386695	137.983505	27.899269	0.0474	-19.33	10.48	S	0.27	0.09	0.81 ± 0.09
1-279073	1-211100	247.830322	39.744129	0.0309	-19.15	10.62	E	0.56	0.02	–
	1-210784	247.097122	39.570305	0.0292	-19.61	10.86	E	0.48	0.00	0.15 ± 0.05
1-135044	1-218280	124.003311	27.075895	0.0255	-19.57	10.81	S	0.27	0.08	0.12 ± 0.03
	1-211063	247.058411	40.313835	0.0331	-19.87	10.79	S	0.33	0.09	0.20 ± 0.04
1-148068	1-166947	147.335007	43.442989	0.0720	-20.79	10.81	S	0.29	0.02	0.13 ± 0.08
	1-55572	133.121307	56.112690	0.0454	-20.11	11.03	S	0.40	0.06	0.12 ± 0.04
1-277552	1-264513	236.941513	28.641697	0.0333	-20.92	11.28	S	0.25	0.18	0.33 ± 0.05
	1-136125	254.044144	34.836521	0.0316	-19.33	10.50	S	0.25	0.09	0.08 ± 0.02
1-217050	1-135372	250.116714	39.320118	0.0301	-20.29	11.08	E	0.49	0.02	0.01 ± 0.23
	1-274663	157.660522	44.012722	0.0280	-19.88	11.00	E	0.50	0.01	0.08 ± 0.02
1-25554	1-135625	248.507462	41.347946	0.0284	-19.06	10.56	S	0.43	0.05	0.56 ± 0.04
	1-216958	136.200287	40.591721	0.0270	-18.95	10.41	S	0.51	0.03	0.23 ± 0.02
1-135285	1-633990	247.304123	41.150871	0.0296	-19.06	10.46	S	0.34	0.03	0.25 ± 0.03
	1-25688	261.284851	58.764687	0.0292	-18.79	10.32	S	0.29	0.06	0.10 ± 0.02

This paper has been typeset from a  $\text{\TeX}/\text{\LaTeX}$  file prepared by the author.

# THE FOURTEENTH DATA RELEASE OF THE SLOAN DIGITAL SKY SURVEY: FIRST SPECTROSCOPIC DATA FROM THE EXTENDED BARYON OSCILLATION SPECTROSCOPIC SURVEY AND FROM THE SECOND PHASE OF THE APACHE POINT OBSERVATORY GALACTIC EVOLUTION EXPERIMENT

BELA ABOLFATHI<sup>1</sup>, D. S. AGUADO<sup>2</sup>, GABRIELA AGUILAR<sup>3</sup>, CARLOS ALLENDE PRIETO<sup>2,4</sup>, ANDRES ALMEIDA<sup>5</sup>, TONIMA TASNIM ANANNA<sup>6</sup>, FRIEDRICH ANDERS<sup>7</sup>, SCOTT F. ANDERSON<sup>8</sup>, BRETT H. ANDREWS<sup>9</sup>, BORJA ANGUIANO<sup>10</sup>, ALFONSO ARAGÓN-SALAMANCA<sup>11</sup>, MARIA ARGUDO-FERNÁNDEZ<sup>12</sup>, ERIC ARMENGAUD<sup>13</sup>, METIN ATA<sup>7</sup>, ERIC AUBOURG<sup>14</sup>, VLADIMIR AVILA-REESE<sup>3</sup>, CARLES BADENES<sup>9</sup>, STEPHEN BAILEY<sup>15</sup>, KATHLEEN A. BARGER<sup>16</sup>, JORGE BARRERA-BALLESTEROS<sup>17</sup>, CURTIS BARTOSZ<sup>8</sup>, DOMINIC BATES<sup>18</sup>, FALK BAUMGARTEN<sup>7,19</sup>, JULIAN BAUTISTA<sup>20</sup>, RACHAEL BEATON<sup>21</sup>, TIMOTHY C. BEERS<sup>22</sup>, FRANCESCO BELFOIRE<sup>23,24,25</sup>, CHAD F. BENDER<sup>26</sup>, MARIANGELA BERNARDI<sup>27</sup>, MATTHEW A. BERSHADY<sup>28</sup>, FLORIAN BEUTLER<sup>29</sup>, JONATHAN C. BIRD<sup>30</sup>, DMITRY BIZYAEV<sup>31,32,33</sup>, GUILLERMO A. BLANC<sup>21</sup>, MICHAEL R. BLANTON<sup>34</sup>, MICHAEL BLOMQVIST<sup>35</sup>, ADAM S. BOLTON<sup>36</sup>, MÉDÉRIC BOQUIEN<sup>12</sup>, JURA BORISOVA<sup>37,38</sup>, JO BOVY<sup>39,40,41</sup>, CHRISTIAN ANDRES BRADNA DIAZ<sup>42</sup>, WILLIAM NIELSEN BRANDT<sup>43,44,45</sup>, JONATHAN BRINKMANN<sup>31</sup>, JOEL R. BROWNSTEIN<sup>20</sup>, KEVIN BUNDY<sup>25</sup>, ADAM J. BURGASSER<sup>46</sup>, ETIENNE BURTIN<sup>13</sup>, NICOLÁS G. BUSCA<sup>14</sup>, CALEB I. CAÑAS<sup>43</sup>, MARIANA CANO-DÍAZ<sup>47</sup>, MICHELE CAPPELLARI<sup>48</sup>, RICARDO CARRERA<sup>2,4</sup>, ANDREW R. CASEY<sup>49</sup>, YANPING CHEN<sup>50</sup>, BRIAN CHERINKA<sup>51</sup>, CRISTINA CHIAPPINI<sup>7</sup>, PETER DOOHYUN CHOI<sup>52</sup>, DREW CHOJNOWSKI<sup>32</sup>, CHIA-HSUN CHUANG<sup>7</sup>, HAEUN CHUNG<sup>53</sup>, NICOLAS CLERC<sup>54,55,56</sup>, ROGER E. COHEN<sup>57,58</sup>, JOHAN COMPARAT<sup>54</sup>, JANAINA CORREA DO NASCIMENTO<sup>59,60</sup>, LUIZ DA COSTA<sup>60,61</sup>, MARIE-CLAUDE COUSINOU<sup>62</sup>, KEVIN COVEY<sup>63</sup>, JEFFREY D. CRANE<sup>21</sup>,IRENE CRUZ-GONZALEZ<sup>3</sup>, KATIA CUNHA<sup>61,26</sup>, GUILLERMO J. DAMKE<sup>10,64,65</sup>, JEREMY DARLING<sup>66</sup>, JAMES W. DAVIDSON JR.<sup>10</sup>, KYLE DAWSON<sup>20</sup>, MIGUEL ANGEL C. DE ICaza LIZAOLA<sup>3</sup>, AXEL DE LA MACORRA<sup>67</sup>, SYLVAIN DE LA TORRE<sup>35</sup>, NATHAN DE LEE<sup>68,30</sup>, VICTORIA DE SAINTE AGATHE<sup>69</sup>, ALICE DECONTO MACHADO<sup>70,60</sup>, FLAVIA DELL'AGLI<sup>2,4</sup>, TIMOTHÉE DELUBAC<sup>71</sup>, ALEKSANDAR M. DIAMOND-STANIC<sup>42</sup>, JOHN DONOR<sup>16</sup>, JUAN JOSÉ DOWNES<sup>72</sup>, NIV DRORY<sup>73</sup>, HÉLION DU MAS DES BOURBOUX<sup>13</sup>, CHRISTOPHER J. DUCKWORTH<sup>18</sup>, TOM DWELLY<sup>54</sup>, JAMIE DYER<sup>20</sup>, GARRETT EBELKE<sup>10</sup>, ARTHUR DAVIS EIGENBROT<sup>28</sup>, DANIEL J. EISENSTEIN<sup>74</sup>, YVONNE P. ELSWORTH<sup>75</sup>, ERIC EMSLELEM<sup>76</sup>, MIKE ERACLEOUS<sup>44</sup>, STEPHANIE ESCOFFIER<sup>62</sup>, XIAOHUI FAN<sup>26</sup>, EMMA FERNÁNDEZ ALVAR<sup>3</sup>, J. G. FERNANDEZ-TRINCADO<sup>57</sup>, RAFAEL FERNANDO CIROLINI<sup>60</sup>, DIANE FEUILLET<sup>77</sup>, ALEXIS FINOQUENOV<sup>54</sup>, SCOTT W. FLEMING<sup>58</sup>, ANDREU FONT-RIBERA<sup>78</sup>, GORDON FREISCHLAD<sup>31</sup>, PETER FRINCHABOY<sup>16</sup>, HAI FU<sup>126</sup>, YILEN GÓMEZ MAQUEO CHEW<sup>3</sup>, LLUÍS GALBANY<sup>9</sup>, ANA E. GARCÍA PÉREZ<sup>2</sup>, R. GARCIA-DIAS<sup>2,4</sup>, D. A. GARCÍA-HERNÁNDEZ<sup>2,4</sup>, PATRICK GAULME<sup>31</sup>, JOSEPH GELFAND<sup>34</sup>, HÉCTOR GIL-MARÍN<sup>79,80</sup>, BRUCE A. GILLESPIE<sup>31</sup>, DANIEL GODDARD<sup>29</sup>, JONAY I. GONZÁLEZ HERNÁNDEZ<sup>2,4</sup>, VIOLETA GONZALEZ-PEREZ<sup>29</sup>, KATHLEEN GRABOWSKI<sup>31</sup>, PAUL J. GREEN<sup>74</sup>, CATHERINE J. GRIER<sup>43,44</sup>, ALAIN GUEGUEN<sup>54</sup>, HONG GUO<sup>81</sup>, JULIEN GUY<sup>69</sup>, ALEX HAGEN<sup>44</sup>, PAUL HARDING<sup>82</sup>, STEN HASSELQUIST<sup>32</sup>, SUZANNE HAWLEY<sup>8</sup>, FRED HEARTY<sup>43</sup>, SASKIA HEKKER<sup>83</sup>, JESUS HERNANDEZ<sup>3</sup>, HECTOR HERNANDEZ TOLEDO<sup>3</sup>, DAVID W. HOGG<sup>34</sup>, KELLY HOLLEY-BOCKELMANN<sup>30</sup>, JON HOLTZMAN<sup>32</sup>, JIAMIN HOU<sup>54</sup>, BAU-CHING HSIEH<sup>84</sup>, JASON A. S. HUNT<sup>40</sup>, TIMOTHY A. HUTCHINSON<sup>20</sup>, HO SEONG HWANG<sup>53</sup>, CAMILO EDUARDO JIMENEZ ANGEL<sup>2,4</sup>, JENNIFER A. JOHNSON<sup>85,86</sup>, AMY JONES<sup>87</sup>, HENRIK JÖNSSON<sup>2,4</sup>, ERIC JULLO<sup>35</sup>, FAHIM SAKIL KHAN<sup>42</sup>, KAREN KINEMUCHI<sup>31</sup>, DAVID KIRKBY<sup>1</sup>, CHARLES C. KIRKPATRICK IV<sup>88</sup>, FRANCISCO-SHU KITAURA<sup>2,4</sup>, GILLIAN R. KNAPP<sup>89</sup>, JEAN-PAUL KNEIB<sup>71</sup>, JUNA A. KOLLMEIER<sup>21</sup>, IVAN LACERNA<sup>38,90,91</sup>, RICHARD R. LANE<sup>90</sup>, DUSTIN LANG<sup>40</sup>, DAVID R. LAW<sup>58</sup>, JEAN-MARC LE GOFF<sup>13</sup>, YOUNG-BAE LEE<sup>52</sup>, HONGYU LI<sup>92</sup>, JIANHUI LIAN<sup>29</sup>, YU LIANG<sup>93</sup>, LIHWAI LIN (林俐暉)<sup>84</sup>, DAN LONG<sup>31</sup>, SARA LUCATELLO<sup>94</sup>, BRITT LUNDGREN<sup>95</sup>, J. TED MACKERETH<sup>96</sup>, CHELSEA L. MACLEOD<sup>74</sup>, SVVRATH MAHADEVAN<sup>43</sup>, MARCIO ANTONIO-GEIMBA MAIA<sup>61,60</sup>, STEVEN MAJEWSKI<sup>10</sup>, ARTURO MANCHADO<sup>2,4</sup>, CLAUDIA MARASTON<sup>29</sup>, VIVEK MARIAPPAN<sup>20</sup>, RUI MARQUES-CHAVES<sup>2,4</sup>, THOMAS MASSERON<sup>2,4</sup>, KAREN L. MASTERS (何凱論)<sup>29,97</sup>, RICHARD M. McDERMID<sup>98</sup>, IAN D. McGREER<sup>26</sup>, MATTHEW MELENDEZ<sup>16</sup>, SOFIA MENESSES-GOYTIA<sup>29</sup>, ANDREA MERLONI<sup>54</sup>, MICHAEL R. MERRIFIELD<sup>11</sup>, SZabolcs MESZAROS<sup>99,100</sup>, ANDRES MEZA<sup>101,127</sup>, IVAN MINCHEV<sup>7</sup>, DANTE MINNITI<sup>101,38,102</sup>, EVA-MARIA MUELLER<sup>29</sup>, FRANCISCO MULLER-SANCHEZ<sup>66</sup>, DEMITRI MUNA<sup>86</sup>, ADAM D. MYERS<sup>103</sup>, PREETHI NAIR<sup>104</sup>, KIRPAL NANDRA<sup>54</sup>, MELISSA NESS<sup>77</sup>, JEFFREY A. NEWMAN<sup>9</sup>, ROBERT C. NICHOL<sup>29</sup>, DAVID L. NIDEVER<sup>36</sup>, CHRISTIAN NITSCHELM<sup>12</sup>, PASQUIER NOTERDAEME<sup>105</sup>, JULIA O'CONNELL<sup>16</sup>, RYAN JAMES OELKERS<sup>30</sup>, AUDREY ORAVETZ<sup>31</sup>, DANIEL ORAVETZ<sup>31</sup>, ERIK AQUINO ORTÍZ<sup>3</sup>, YEISSON OSORIO<sup>2,4</sup>, ZACH PACE<sup>28</sup>, NELSON PADILLA<sup>90</sup>, NATHALIE PALANQUE-DELABROUILLE<sup>13</sup>, PEDRO ALONSO PALICIO<sup>2,4</sup>, HSI-AN PAN<sup>84</sup>, KAIKE PAN<sup>31</sup>, TANIYA PARikh<sup>29</sup>, ISABELLE PÂRIS<sup>35</sup>, CHANGBOM PARK<sup>53</sup>, SEBASTIEN PEIRANI<sup>105</sup>, MARCOS PELLEJERO-IBÁÑEZ<sup>2,4</sup>, SAMANTHA PENNY<sup>29</sup>, WILL J. PERCIVAL<sup>29</sup>, ISMAEL PEREZ-FOURNON<sup>2,4</sup>, PATRICK PETITJEAN<sup>105</sup>, MATTHEW M. PIERI<sup>35</sup>, MARC PINSONNEAULT<sup>85</sup>, ALICE PISANI<sup>62</sup>, FRANCISCO PRADA<sup>106,107</sup>, ABHISHEK PRAKASH<sup>9</sup>, ANNA BÁRBARA DE ANDRADE QUEIROZ<sup>59,60</sup>, M. JORDAN RADDICK<sup>17</sup>, ANAND RAICHOOR<sup>71</sup>, SANDRO BARBOZA REMBOLD<sup>70,60</sup>, HANNAH RICHSTEIN<sup>16</sup>, ROGEMAR A. RIFFEL<sup>70,60</sup>, ROGÉRIO RIFFEL<sup>59,60</sup>, HANS-WALTER RIX<sup>77</sup>, ANNIE C. ROBIN<sup>108</sup>, SERGIO RODRÍGUEZ TORRES<sup>109</sup>, CARLOS ROMÁN-ZUÑIGA<sup>110</sup>, ASHLEY J. ROSS<sup>86</sup>, GRAZIANO ROSSI<sup>52</sup>, JOHN RUAN<sup>8</sup>, ROSSANA RUGGERI<sup>29</sup>, JOSE RUIZ<sup>42</sup>, MARA SALVATO<sup>54</sup>, ARIEL G. SÁNCHEZ<sup>54</sup>, SEBASTIÁN F. SÁNCHEZ<sup>3</sup>, JORGE SÁNCHEZ ALMEIDA<sup>2</sup>, JOSÉ R. SÁNCHEZ-GALLEGO<sup>8</sup>, BASÍLIO XAVIER SANTIAGO<sup>59,60</sup>, RICARDO P. SCHIAVON<sup>96</sup>, JADERSON S. SCHIMOIA<sup>59,60</sup>, EDWARD SCHLAFLY<sup>15</sup>, DAVID SCHLEGEL<sup>15</sup>, DONALD P. SCHNEIDER<sup>43,44</sup>, WILLIAM J. SCHUSTER<sup>3,110</sup>, AXEL SCHWOPE<sup>7</sup>, HEE-JONG SEO<sup>111</sup>, ALDO SERENELLI<sup>112</sup>, SHIYIN SHEN<sup>81</sup>, YUE SHEN<sup>113,114</sup>, MATTHEW SHETRONE<sup>73</sup>, MICHAEL SHULL<sup>66</sup>, VÍCTOR SILVA AGUIRRE<sup>115</sup>, JOSHUA D. SIMON<sup>21</sup>, MIKE SKRUTSKIE<sup>10</sup>, ANŽE SLOSAR<sup>116</sup>, REBECCA SMETHURST<sup>11</sup>, VERNE SMITH<sup>36</sup>, JENNIFER SOBECK<sup>8</sup>, GARRETT SOMERS<sup>30</sup>, BONNIE J. SOUTER<sup>17</sup>, DIOGO SOUTO<sup>61</sup>, ASHLEY SPINDLER<sup>117</sup>, DAVID V. STARK<sup>118</sup>, KEIVAN STASSUN<sup>30</sup>, MATTHIAS STEINMETZ<sup>7</sup>, DENNIS STELLO<sup>119,120,115</sup>, THAISA STORCHI-BERGMANN<sup>59,60</sup>, ALINA STREBLYANSKA<sup>2,4</sup>, GUY STRINGFELLOW<sup>66</sup>, GENARO SUÁREZ<sup>3</sup>, JING SUN<sup>16</sup>, LASZLO SZIGETI<sup>99</sup>, MANUCHEHR TAGHIZADEH-POPP<sup>17</sup>, MICHAEL S. TALBOT<sup>20</sup>, BAITIAN TANG<sup>57</sup>, CHARLING TAO<sup>93,62</sup>, JAMIE TAYAR<sup>85</sup>, MITA TEMBE<sup>10</sup>, DANIEL THOMAS<sup>29</sup>, PATRICIA TISSERA<sup>101</sup>, RITA TOJEIRO<sup>18</sup>, CHRISTY TREMONTI<sup>28</sup>, NICHOLAS W. TROUP<sup>10</sup>, MEG URRY<sup>6</sup>, O. VALENZUELA<sup>47</sup>, REMCO VAN DEN BOSCH<sup>77</sup>, JAIME VARGAS-GONZÁLEZ<sup>65</sup>, MARIANA VARGAS-MAGAÑA<sup>67</sup>, JOSE ALBERTO VAZQUEZ<sup>116</sup>, SANDRO VILLANOVA<sup>57</sup>, NICOLE VOGT<sup>32</sup>, DAVID WAKE<sup>117,95</sup>, YUTING WANG<sup>92</sup>, BENJAMIN ALAN WEAVER<sup>36</sup>, ANNE-MARIE WEIJMANS<sup>18</sup>, KYLE B. WESTFALL<sup>121</sup>, DAVID G. WHELAN<sup>122</sup>, ERIC WILCOTS<sup>28</sup>, VIVIENNE WILD<sup>18</sup>, ROB A.

WILLIAMS<sup>96</sup>, JOHN WILSON<sup>10</sup>, W. M. WOOD-VASEY<sup>9</sup>, DOMINIKA WYLEZALEK<sup>51</sup>, TING XIAO (肖婷)<sup>81</sup>, RENBIN YAN<sup>123</sup>, MENG YANG<sup>18</sup>, JASON E. YBARRA<sup>124</sup>, CHRISTOPHE YÈCHE<sup>13</sup>, NADIA ZAKAMSKA<sup>17</sup>, OLGA ZAMORA<sup>2,4</sup>, PAULINE ZARROUK<sup>13</sup>, GAIL ZASOWSKI<sup>58,20</sup>, KAI ZHANG<sup>123</sup>, CHENG ZHAO<sup>93</sup>, GONG-BO ZHAO<sup>92,29</sup>, ZHENG ZHENG<sup>20</sup>, ZHI-MIN ZHOU<sup>92</sup>, GUANGTUN ZHU<sup>51,125</sup>, JOEL C. ZINN<sup>85</sup>, HU ZOU<sup>92</sup>

*Draft version November 16, 2017*

## Abstract

The fourth generation of the Sloan Digital Sky Survey (SDSS-IV) has been in operation since July 2014. This paper describes the second data release from this phase, and the fourteenth from SDSS overall (making this, Data Release Fourteen or DR14). This release makes public data taken by SDSS-IV in its first two years of operation (July 2014–2016). Like all previous SDSS releases, DR14 is cumulative, including the most recent reductions and calibrations of all data taken by SDSS since the first phase began operations in 2000.

New in DR14 is the first public release of data from the extended Baryon Oscillation Spectroscopic Survey (eBOSS); the first data from the second phase of the Apache Point Observatory (APO) Galactic Evolution Experiment (APOGEE-2), including stellar parameter estimates from an innovative data driven machine learning algorithm known as The Cannon; and almost twice as many data cubes from the Mapping Nearby Galaxies at APO (MaNGA) survey as were in the previous release ( $N = 2812$  in total).

This paper describes the location and format of the publicly available data from SDSS-IV surveys. We provide references to the important technical papers describing how these data have been taken (both targeting and observation details) and processed for scientific use. The SDSS website ([www.sdss.org](http://www.sdss.org)) has been updated for this release, and provides links to data downloads, as well as tutorials and examples of data use.

SDSS-IV is planning to continue to collect astronomical data until 2020.

*Subject headings:* Atlases — Catalogs — Surveys

[spokesperson@sdss.org](mailto:spokesperson@sdss.org)

<sup>1</sup> Department of Physics and Astronomy, University of California, Irvine, Irvine, CA 92697, USA

<sup>2</sup> Instituto de Astrofísica de Canarias, E-38205 La Laguna, Tenerife, Spain

<sup>3</sup> Instituto de Astronomía, Universidad Nacional Autónoma de México, A.P. 70-264, 04510, México, D.F., México

<sup>4</sup> Departamento de Astrofísica, Universidad de La Laguna (ULL), E-38206 La Laguna, Tenerife, Spain

<sup>5</sup> Instituto de Investigación Multidisciplinario en Ciencia y Tecnología, Universidad de La Serena, Benavente 980, La Serena, Chile

<sup>6</sup> Yale Center for Astronomy and Astrophysics, Yale University, New Haven, CT, 06520, USA

<sup>7</sup> Leibniz-Institut für Astrophysik Potsdam (AIP), An der Sternwarte 16, D-14482 Potsdam, Germany

<sup>8</sup> Department of Astronomy, Box 351580, University of Washington, Seattle, WA 98195, USA

<sup>9</sup> Pitt PACC, Department of Physics and Astronomy, University of Pittsburgh, Pittsburgh, PA 15260, USA

<sup>10</sup> Department of Astronomy, University of Virginia, 530 McCormick Road, Charlottesville, VA 22904-4325, USA

<sup>11</sup> School of Physics & Astronomy, University of Nottingham, Nottingham, NG7 2RD, United Kingdom

<sup>12</sup> Unidad de Astronomía, Fac. Cs. Básicas, Universidad de Antofagasta, Avda. U. de Antofagasta 02800, Antofagasta, Chile

<sup>13</sup> CEA, Centre de Saclay, IRFU, F-91191, Gif-sur-Yvette, France

<sup>14</sup> APC, University of Paris Diderot, CNRS/IN2P3, CEA/IRFU, Observatoire de Paris, Sorbonne Paris Cite, France

<sup>15</sup> Lawrence Berkeley National Laboratory, 1 Cyclotron Road, Berkeley, CA 94720, USA

<sup>16</sup> Department of Physics and Astronomy, Texas Christian University, Fort Worth, TX 76129, USA

<sup>17</sup> Department of Physics and Astronomy, Johns Hopkins University, 3400 N. Charles St., Baltimore, MD 21218, USA

<sup>18</sup> School of Physics and Astronomy, University of St Andrews, North Haugh, St Andrews, KY16 9SS

<sup>19</sup> Humboldt-Universität zu Berlin, Institut für Physik, Newtonstrasse 15, D-12589, Berlin, Germany

<sup>20</sup> Department of Physics and Astronomy, University of Utah,

115 S. 1400 E., Salt Lake City, UT 84112, USA

<sup>21</sup> The Observatories of the Carnegie Institution for Science, 813 Santa Barbara St., Pasadena, CA 91101, USA

<sup>22</sup> Department of Physics and JINA Center for the Evolution of the Elements, University of Notre Dame, Notre Dame, IN 46556, USA

<sup>23</sup> Cavendish Laboratory, University of Cambridge, 19 J. J. Thomson Avenue, Cambridge CB3 0HE, United Kingdom

<sup>24</sup> Kavli Institute for Cosmology, University of Cambridge, Madingley Road, Cambridge CB3 0HA, UK

<sup>25</sup> University of California Observatories, University of California, Santa Cruz, CA 95064, USA

<sup>26</sup> Steward Observatory, The University of Arizona, 933 North Cherry Avenue, Tucson, AZ 85721-0065, USA

<sup>27</sup> Department of Physics and Astronomy, University of Pennsylvania, Philadelphia, PA 19104, USA

<sup>28</sup> Department of Astronomy, University of Wisconsin-Madison, 475 N. Charter St., Madison, WI 53726, USA

<sup>29</sup> Institute of Cosmology & Gravitation, University of Portsmouth, Dennis Sciama Building, Portsmouth, PO1 3FX, UK

<sup>30</sup> Vanderbilt University, Department of Physics & Astronomy, 6301 Stevenson Center Ln., Nashville, TN 37235, USA

<sup>31</sup> Apache Point Observatory, P.O. Box 59, Sunspot, NM 88349, USA

<sup>32</sup> Department of Astronomy, New Mexico State University, Box 30001, MSC 4500, Las Cruces NM 88003, USA

<sup>33</sup> Sternberg Astronomical Institute, Moscow State University, Moscow

<sup>34</sup> Center for Cosmology and Particle Physics, Department of Physics, New York University, 726 Broadway, Room 1005, New York, NY 10003, USA

<sup>35</sup> Aix Marseille Univ, CNRS, LAM, Laboratoire d'Astrophysique de Marseille, Marseille, France

<sup>36</sup> National Optical Astronomy Observatory, 950 North Cherry Avenue, Tucson, AZ 85719, USA

<sup>37</sup> Departamento de Física y Astronomía, Universidad de Valparaíso, Av. Gran

<sup>38</sup> Instituto Milenio de Astrofísica, Av. Vicuña Mackenna 4860, Macul, Santiago, Chile

<sup>39</sup> Department of Astronomy and Astrophysics, University of Toronto, 50 St. George Street, Toronto, ON, M5S 3H4, Canada

<sup>40</sup> Dunlap Institute for Astronomy and Astrophysics, Univer-

## 1. INTRODUCTION

It is now sixteen years since the first data release from the Sloan Digital Sky Survey (SDSS; York et al. 2000). This Early Data Release, or EDR, occurred in June 2001 (Stoughton et al. 2002). Since this time, annual data releases from SDSS have become part of the landscape of astronomy, making the SDSS's 2.5 meter Sloan Foundation Telescope (Gunn et al. 2006) one of the most pro-

ductive observatories in the world (Madrid & Macchietto 2009), and populating databases used by thousands of astronomers worldwide (Raddick et al. 2014a,b). This paper describes the fourteenth public data release from SDSS, or DR14, released on 31st July 2017.

The SDSS has completed three phases and is currently in its fourth phase. SDSS-I and -II conducted a Legacy survey of galaxies and quasars (York et al. 2000), the

sity of Toronto, 50 St. George Street, Toronto, Ontario M5S 3H4, Canada

<sup>41</sup> Alfred P. Sloan Fellow

<sup>42</sup> Department of Physics and Astronomy, Bates College, 44 Campus Avenue, Lewiston, ME 04240, USA

<sup>43</sup> Department of Astronomy and Astrophysics, Eberly College of Science, The Pennsylvania State University, 525 Davey Laboratory, University Park, PA 16802, USA

<sup>44</sup> Institute for Gravitation and the Cosmos, The Pennsylvania State University, University Park, PA 16802, USA

<sup>45</sup> Department of Physics, The Pennsylvania State University, University Park, PA 16802, USA

<sup>46</sup> Center for Astrophysics and Space Science, University of California San Diego, La Jolla, CA 92093, USA

<sup>47</sup> CONACYT Research Fellow, Instituto de Astronomía, Universidad Nacional Autónoma de México, A.P. 70-264, 04510, México, D.F., México

<sup>48</sup> Sub-department of Astrophysics, Department of Physics, University of Oxford, Denys Wilkinson Building, Keble Road, Oxford OX1 3RH, UK

<sup>49</sup> School of Physics & Astronomy, Monash University, Wellington Road, Clayton, Victoria 3800, Australia

<sup>50</sup> NYU Abu Dhabi, PO Box 129188, Abu Dhabi, UAE

<sup>51</sup> Center for Astrophysical Sciences, Department of Physics and Astronomy, Johns Hopkins University, 3400 North Charles Street, Baltimore, MD 21218, USA

<sup>52</sup> Department of Astronomy and Space Science, Sejong University, Seoul 143-747, Korea

<sup>53</sup> Korea Institute for Advanced Study, 85 Hoegiro, Dongdaemun-gu, Seoul 02455, Republic of Korea

<sup>54</sup> Max-Planck-Institut für Extraterrestrische Physik, Gießenbachstr. 1, D-85748 Garching, Germany

<sup>55</sup> CNRS, IRAP, 9 Av. Colonel Roche, BP 44346, F-31028 Toulouse cedex 4, France

<sup>56</sup> Université de Toulouse, UPS-OMP, IRAP, Toulouse, France

<sup>57</sup> Departamento de Astronomía, Casilla 160-C, Universidad de Concepción, Concepción, Chile

<sup>58</sup> Space Telescope Science Institute, 3700 San Martin Drive, Baltimore, MD 21218, USA

<sup>59</sup> Instituto de Física, Universidade Federal do Rio Grande do Sul, Campus do Vale, Porto Alegre, RS, Brasil, 91501-970

<sup>60</sup> Laboratório Interinstitucional de e-Astronomia, 77 Rua General José Cristino, Rio de Janeiro, 20921-400, Brasil

<sup>61</sup> Observatório Nacional, Rio de Janeiro, Brasil

<sup>62</sup> Aix Marseille Univ, CNRS/IN2P3, CPPM, Marseille, France

<sup>63</sup> Department of Physics and Astronomy, Western Washington University, 516 High Street, Bellingham, WA 98225, USA

<sup>64</sup> Centro Multidisciplinario de Ciencia y Tecnología, Universidad de La Serena, Cisternas 1200, La Serena, Chile

<sup>65</sup> Departamento de Física, Facultad de Ciencias, Universidad de La Serena, Cisternas 1200, La Serena, Chile

<sup>66</sup> Center for Astrophysics and Space Astronomy, Department of Astrophysical and Planetary Sciences, University of Colorado, 389 UCB, Boulder, CO 80309-0389, USA

<sup>67</sup> Instituto de Física, Universidad Nacional Autónoma de México, Apdo. Postal 20-364, México.

<sup>68</sup> Department of Physics, Geology, and Engineering Tech, Northern Kentucky University, Highland Heights, KY 41099, USA

<sup>69</sup> LPNHE, CNRS/IN2P3, Université Pierre et Marie Curie Paris 6, Université Denis Diderot Paris, 4 place Jussieu, 75252 Paris CEDEX, France

<sup>70</sup> Departamento de Física, CCNE, Universidade Federal de Santa Maria, 97105-900, Santa Maria, RS, Brazil

<sup>71</sup> Institute of Physics, Laboratory of Astrophysics, Ecole Polytechnique Fédérale de Lausanne (EPFL), Observatoire de

Sauverny, 1290 Versoix, Switzerland

<sup>72</sup> Centro de Investigaciones de Astronomía, AP 264, Mérida 5101-A, Venezuela

<sup>73</sup> McDonald Observatory, The University of Texas at Austin, 1 University Station, Austin, TX 78712, USA

<sup>74</sup> Harvard-Smithsonian Center for Astrophysics, 60 Garden St, Cambridge, MA 02138, USA

<sup>75</sup> School of Physics and Astronomy, University of Birmingham, Edgbaston, Birmingham B15 2TT, UK

<sup>76</sup> European Southern Observatory, Karl-Schwarzschild-Str. 2, 85748 Garching, Germany

<sup>77</sup> Max-Planck-Institut für Astronomie, Königstuhl 17, D-69117 Heidelberg, Germany

<sup>78</sup> Department of Physics & Astronomy, University College London, Gower Street, London, WC1E 6BT, UK

<sup>79</sup> Sorbonne Universités, Institut Lagrange de Paris (ILP), 98 bis Boulevard Arago, 75014 Paris, France

<sup>80</sup> Laboratoire de Physique Nucléaire et de Hautes Energies, Université Pierre et Marie Curie, 4 Place Jussieu, 75005 Paris, France

<sup>81</sup> Shanghai Astronomical Observatory, Chinese Academy of Science, 80 Nandan Road, Shanghai 200030, China

<sup>82</sup> Department of Astronomy, Case Western Reserve University, Cleveland, OH 44106, USA

<sup>83</sup> Max Planck Institute for Solar System Research, Justus-von-Liebig-Weg 3, 37077 Goettingen, Germany

<sup>84</sup> Academia Sinica Institute of Astronomy and Astrophysics, P.O. Box 23-141, Taipei 10617, Taiwan

<sup>85</sup> Department of Astronomy, Ohio State University, 140 W. 18th Ave., Columbus, OH 43210, USA

<sup>86</sup> Center for Cosmology and AstroParticle Physics, The Ohio State University, 191 W. Woodruff Ave., Columbus, OH 43210, USA

<sup>87</sup> Max-Planck-Institut für Astrophysik, Karl-Schwarzschild-Str. 1, D-85748 Garching, Germany

<sup>88</sup> Department of Physics, University of Helsinki, Gustaf Hällströmin katu 2a, FI-00014 Helsinki, Finland

<sup>89</sup> Department of Astrophysical Sciences, Princeton University, Princeton, NJ 08544, USA

<sup>90</sup> Instituto de Astrofísica, Pontificia Universidad Católica de Chile, Av. Vicuña Mackenna 4860, 782-0436 Macul, Santiago, Chile

<sup>91</sup> Astrophysical Research Consortium, Physics/Astronomy Building, Rm C319, 3910 15th Avenue NE, Seattle, WA 98195, USA

<sup>92</sup> National Astronomical Observatories, Chinese Academy of Sciences, 20A Datun Road, Chaoyang District, Beijing 100012, China

<sup>93</sup> Tsinghua Center for Astrophysics & Department of Physics, Tsinghua University, Beijing 100084, China

<sup>94</sup> Astronomical Observatory of Padova, National Institute of Astrophysics, Vicolo Osservatorio 5 - 35122 - Padova, Italy

<sup>95</sup> Department of Physics, University of North Carolina Asheville, One University Heights, Asheville, NC 28804, USA

<sup>96</sup> Astrophysics Research Institute, Liverpool John Moores University, IC2, Liverpool Science Park, 146 Brownlow Hill, Liverpool L3 5RF, UK

<sup>97</sup> SDSS-IV Spokesperson (Corresponding Author)

<sup>98</sup> Department of Physics and Astronomy, Macquarie University, Sydney NSW 2109, Australia

<sup>99</sup> ELTE Eötvös Loránd University, Gothard Astrophysical Observatory, Szombathely, Hungary

<sup>100</sup> Premium Postdoctoral Fellow of the Hungarian Academy of Sciences

<sup>101</sup> Departamento de Física, Facultad de Ciencias Exactas, Universidad Andres Bello, Av. Fernandez Concha 700, Las Condes, Santiago, Chile.

<sup>102</sup> Vatican Observatory, V00120 Vatican City State, Italy

SDSS-II Supernova Survey (Frieman et al. 2008; Sako et al. 2014), and conducted observations of stars for the Sloan Extension for Galactic Understanding and Exploration 1 (SEGUE-1; Yanny et al. 2009). These surveys made use of the SDSS imaging camera (Gunn et al. 1998) and 640-fiber optical spectrograph (Smee et al. 2013). SDSS-III continued observations of stars with SEGUE-2, and conducted two new surveys with new instrumentation (Eisenstein et al. 2011).

The Baryon Oscillation Spectroscopic Survey (BOSS; Dawson et al. 2013) upgraded the optical spectrograph to 1000 fibers (named the BOSS spectrograph; Smee et al. 2013) to conduct a large volume cosmological redshift survey which built on the work of both SDSS-II (York et al. 2000) and 2dFGRS (Colless et al. 2003). At the same time, the Apache Point Observatory Galactic Evolution Experiment 1 (APOGEE-1; Majewski et al. 2017) employed a high resolution near-infrared spectrograph to observe stars in the Milky Way. All of these

observations were conducted at Apache Point Observatory, and data were publicly released in DR12 (Alam, et al. 2015).

This paper contains new data and data reductions produced by SDSS-IV (Blanton, et al. 2017). SDSS-IV began observations in July 2014, and consists of three programs.

1. The extended Baryon Oscillation Spectroscopic Survey (eBOSS; Dawson et al. 2016) is surveying galaxies and quasars at redshifts  $z \sim 0.6\text{--}3.5$  for large scale structure. eBOSS covers a wider class of galaxies than BOSS at higher effective redshifts. In particular the size and depth of the quasar sample is a huge leap forwards over previous surveys. eBOSS will also observe Emission Line Galaxies, extending the WiggleZ survey (Blake et al. 2011) in the Southern Sky to a larger sample of galaxies at higher redshifts. Following on from eBOSS, the TAIPAN survey (da Cunha et al. 2017) will soon provide a low-redshift complement in the Southern hemisphere. All of these surveys will be eclipsed by forthcoming experiments including DESI (Aghamousa et al. 2016a,b) and Euclid (Laureijs et al. 2011), which will use new instrumentation to obtain galaxies surveys an order of magnitude larger than ongoing surveys. Two major subprograms are being conducted concurrently with eBOSS:

- SPectroscopic IDentification of ERosita Sources (SPIDERS) investigates the nature of  $X$ -ray emitting sources, including active galactic nuclei and galaxy clusters. This contains the largest systematic spectroscopic followup sample of  $X$ -ray selected clusters (for details see Section 4), reaching into a regime where meaningful dynamical estimates of clusters properties are possible for hundreds of massive systems. It contains a highly complete sample of the most luminous  $X$ -ray selected AGN, that will only be superseded by the spectroscopic followup programs of the eROSITA survey (mainly in SDSS-V and 4MOST)

- Time Domain Spectroscopic Survey (TDSS; Morganson et al. 2015) is exploring the physical nature of time-variable sources through spectroscopy. The main TDSS program of optical followup of variables from Pan-STARRS1 imaging is the first large – by order(s) of magnitude – program of optical spectroscopy of photometrically variable objects, selected without *a priori* restriction based on specific photometric colors or light-curve character. About 20% of TDSS targets involve repeat spectroscopy of select classes of known objects with earlier epochs of spectroscopy, e.g., searching for variability among known BAL quasars, and build and expand on earlier such programs (e.g., Filiz Ak et al. 2014); a comprehensive description of the latter such TDSS repeat spectroscopy programs may be found in MacLeod et al. (2017).

<sup>103</sup> Department of Physics and Astronomy, University of Wyoming, Laramie, WY 82071, USA

<sup>104</sup> University of Alabama, Tuscaloosa, AL 35487, USA

<sup>105</sup> Institut d’Astrophysique de Paris, UMR 7095, CNRS - UPMC, 98bis bd Arago, 75014 Paris, France

<sup>106</sup> Instituto de Física Teórica (IFT) UAM/CSIC, Universidad Autónoma de Madrid, Cantoblanco, E-28049 Madrid, Spain

<sup>107</sup> Instituto de Astrofísica de Andalucía (IAA-CSIC), Glorieta de la Astronomía s/n, E-18008, Granada, Spain

<sup>108</sup> Institut UTINAM, CNRS UMR6213, Univ. Bourgogne Franche-Comté, OSU THETA Franche-Comté-Bourgogne, Observatoire de Besançon, BP 1615, 25010 Besançon Cedex, France

<sup>109</sup> Departamento de Física Teórica M8, Universidad Autónoma de Madrid (UAM), Cantoblanco, E-28049, Madrid, Spain

<sup>110</sup> Instituto de Astronomía, Universidad Nacional Autónoma de México, Unidad Académica en Ensenada, Ensenada BC 22860, México

<sup>111</sup> Department of Physics and Astronomy, Ohio University, Clippinger Labs, Athens, OH 45701, USA

<sup>112</sup> Institute of Space Sciences (CSIC-IEEC), Carrer de Can Magrans S/N, Campus UAB, Barcelona, E-08193, Spain

<sup>113</sup> Department of Astronomy, University of Illinois, 1002 W. Green Street, Urbana, IL 61801, USA

<sup>114</sup> National Center for Supercomputing Applications, 1205 West Clark St., Urbana, IL 61801, USA

<sup>115</sup> Stellar Astrophysics Centre, Department of Physics and Astronomy, Aarhus University, Ny Munkegade 120, DK-8000 Aarhus C, Denmark

<sup>116</sup> Brookhaven National Laboratory, Upton, NY 11973, USA

<sup>117</sup> Department of Physical Sciences, The Open University, Milton Keynes, MK7 6AA, UK

<sup>118</sup> Kavli Institute for the Physics and Mathematics of the Universe, Todai Institutes for Advanced Study, the University of Tokyo, Kashiwa, Japan 277- 8583

<sup>119</sup> Sydney Institute for Astronomy, School of Physics, University of Sydney, NSW 2006, Australia

<sup>120</sup> School of Physics, University of New South Wales, NSW 2052, Australia

<sup>121</sup> Department of Astronomy and Astrophysics, University of California Santa Cruz, 1156 High St., Santa Cruz, CA, 95064, USA

<sup>122</sup> Department of Physics, Austin College, Sherman, TX 75090, USA

<sup>123</sup> Department of Physics and Astronomy, University of Kentucky, 505 Rose St., Lexington, KY, 40506-0055, USA

<sup>124</sup> Department of Physics, Bridgewater College, 402 E. College St., Bridgewater, VA 22812 USA

<sup>125</sup> Hubble Fellow

<sup>126</sup> Department of Physics & Astronomy, University of Iowa, Iowa City, IA 52245

<sup>127</sup> Facultad de Ingeniería, Universidad Autónoma de Chile, Pedro de Valdivia 425, Santiago, Chile

2. Mapping Nearby Galaxies at APO (MaNGA; Bundy et al. 2015) is using integral field spectroscopy (IFS) to study 10,000 nearby galaxies. MaNGA builds on a number of successful IFS surveys (e.g., ATLAS-3D, Capellari et al. 2011; DiskMass, Bersady et al. 2010; and CALIFA, Sánchez et al. 2012) surveying a significantly larger and more diverse samples of galaxies over a broader spectral range at higher spectral resolution. It has finer spatial sampling and a final sample size three times that of the similar SAMI survey (Bryant et al. 2014), and in this release becomes the largest set of public IFS observations available.
3. APOGEE/APOGEE-2 perform a large-scale and systematic investigation of the entire Milky Way Galaxy with near-infrared, high-resolution, and multiplexed instrumentation. For APOGEE-2, observations are being carried out at both Northern and Southern Hemisphere locations: the 2.5m Sloan Foundation Telescope of the Apache Point Observatory (APOGEE-2N; Q3 2014 operations start) and the 2.5m du Pont Telescope of the Las Campanas Observatory (APOGEE-2S; Q2 2017 operations start). APOGEE/APOGEE-2 is the only large scale ( $>1,000,000$  spectra) NIR spectroscopic survey of stars, ensuring it has a unique view of all parts of our Galaxy, unhampered by interstellar obscuration in the Galactic plane. Most equivalent scale surveys (e.g. those which have happened such as RAVE (Steinmetz et al. 2006), SEGUE-1 (Yanny et al. 2009), SEGUE-2 (Rockosi et al. 2009), and ARGOS (Freeman et al. 2013) or are currently underway such as LAMOST (Cui et al. 2012), Gaia/ESO (Gilmore et al. 2012), GALAH (Zucker et al. 2012), and Gaia (Perryman et al. 2001) – or are envisaged – e.g., those associated with the WEAVE (Dalton et al. 2014), 4MOST (de Jong et al. 2014), and MOONS (Cirasuolo et al. 2014)) have been done in the optical, and also (apart from GALAH and the Gaia/ESO survey) also are limited to only medium resolution spectroscopy.

SDSS-IV has had one previous data release (DR13; Albareti et al. 2017; for a “behind the scenes” view of how this is done see Weijmans et al. 2016), which contained the first year of MaNGA data, new calibrations of the SDSS imaging data set, and new processing of APOGEE-1 and BOSS data (along with a small amount of BOSS-related data taken during SDSS-IV).

DR14 contains new reductions and new data for all programs, roughly covering the first two years of SDSS-IV operations. This release contains the first public release of data from eBOSS and APOGEE-2, and almost doubles the number of data cubes publicly available from MaNGA.

The full scope of the data release is described in Section 2, and information on data distribution is given in Section 3. Each of the sub-surveys is described in its own section, with eBOSS (including SPIDERS and TDSS) in Section 4, APOGEE-2 in Section 5, and MaNGA in Section 6. We discuss future plans for SDSS-IV and beyond in Section 7.

## 2. SCOPE OF DATA RELEASE 14

As has been the case for all public SDSS data releases, DR14 is cumulative, and includes re-releases of all previously released data processed through the most current data reduction pipelines. In some cases this pipeline has not changed for many DR (see summary below). New data released in DR14 were taken by the Sloan Foundation 2.5m telescope between Aug 23 2014 (MJD=56893)<sup>1</sup> and July 10, 2016 (MJD=57580). The full scope of the release is summarized in Table 1.

We discuss the data released by each of the main surveys in detail below, but briefly, DR14 includes:

- Data from 496 new eBOSS plates covering  $\sim 2480$  square degrees observed from September 2014 to May 2016. We also include data from a transitional project between BOSS and eBOSS called the Sloan Extended Quasar, ELG, and LRG Survey (SEQUELS), designed to test target selection algorithms for eBOSS. The complete SEQUELS dataset was previously released in DR13, however DR14 is the first release for eBOSS. The eBOSS data contain mainly Luminous Red Galaxy (LRG) and Quasar spectra, as well as targets from TDSS and SPIDERS. Twenty-three new eBOSS Emission Line Galaxy (ELG) plates are included in DR14 to test final target selection algorithms. The full ELG survey started collecting spectra in September 2016 and will be part of a future data release. We include in DR14 the first part of the ELG target catalogue (see Table 2) described in Raichoor et al. (2017). Other eBOSS value added catalogs (VACs) are also released, namely (1) the redshift measurement and spectral classification catalogue using Redmonster (Hutchinson et al. 2016), (2) the quasar catalogue Paris et al. (in prep.), and (3) a set of composite spectra of quasars binned on spectroscopic parameters (Jensen et al. 2016)).
- APOGEE visit-combined spectra as well as pipeline-derived stellar atmospheric parameters and individual elemental abundances for more than 263,000 stars, sampling all major components of the Milky Way. This release includes all APOGEE-1 data from SDSS-III (Aug 2011-Jul 2014) as well as two years of APOGEE-2 data from SDSS-IV (Jul 2014-Jul 2016). APOGEE VACs include (1) an updated version of the APOGEE red-clump catalog (APOGEE-RC; Pinsonneault et al. in prep.), (2) a cross match between APOGEE and the Tycho-Gaia Astrometric Solution (APOGEE-TGAS; Anders et al. in prep), and (3) a compilation of four different methods to estimate distances to APOGEE stars (Schultheis et al. 2014; Santiago et al. 2016; Wang et al. 2016; Queiroz et al. 2017; Holtzman et al., 2017).
- Data from 166 MaNGA plates, which results in 2812 reconstructed 3D data cubes (for 2744 unique galaxies, primarily from the main MaNGA target sample, but these data also include ancillary targets and  $\sim 50$  repeat observations). Internally this

<sup>1</sup> this is the date for eBOSS, for APOGEE and MaNGA it was July 2015

TABLE 1  
REDUCED SPECTROSCOPIC DATA IN DR14

Target Category	# DR13	# DR13+14
eBOSS		
LRG samples	32968	138777
ELG Pilot Survey	14459	35094
Main QSO Sample	33928	188277
Variability Selected QSOs	22756	87270
Other QSO samples	24840	43502
TDSS Targets	17927	57675
SPIDERS Targets	3133	16394
Standard Stars/White Dwarfs	53584	63880
APOGEE-2		
All Stars	164562	263444
NMSU 1-meter stars	894	1018
Telluric stars	17293	27127
APOGEE-N Commissioning stars	11917	12194
MaNGA Cubes	1390	2812
MaNGA main galaxy sample:		
PRIMARY_v1_2	600	1278
SECONDARY_v1_2	473	947
COLOR-ENHANCED_v1_2	216	447
MaNGA ancillary targets <sup>1</sup>	31	121

<sup>1</sup> Many MaNGA ancillary targets were also observed as part of the main galaxy sample, and are counted twice in this table; some ancillary targets are not galaxies.

set of galaxies have been referred to as MaNGA Product Launch-5 (MPL-5); however the reduction pipeline is a different version from that internal release. The new data relative to what was released in DR13 was taken between 13 Aug 2015 (MJD= 57248) and July 10 2016. The MaNGA release also includes two VACs, which provide spatially resolved stellar population and ionized gas properties from PIPE3D (Sánchez et al. 2016a,b; see Section 6.4.1) and FIREFLY (Goddard et al. 2017; see Section 6.4.2).

- The largest ever number of SDSS Value Added Catalogues (VACs) produced by scientists in the collaboration – twelve in total. See Table 2.
- A re-release of the most current reduction of all data from previous versions of SDSS. In some cases the data reduction pipeline hasn't changed for many DRs, and so has not been re-run. The most recent imaging was released in DR13 (Albareti et al. 2017); however only the photometric calibrations changed in that release; the astrometry is the same as in DR9 (Ahn et al. 2012) and the area released and the other aspects of the photometric reduction remain the same as that in DR8 (Aihara et al. 2011). Legacy Spectra (those observed with the SDSS spectrograph) have also not changed since DR8. There have also been no changes to SEGUE-1 or SEGUE-2 since DR9, or MARVELS since DR12 (Alam, et al. 2015). For DR14 we have re-reduced BOSS spectra using the eBOSS pipeline, where flux calibration has been improved by adding new atmospheric distortion corrections at the per-exposure level (Margala et al. 2016) and by employing an unbiased coaddition algorithm.

### 3. DATA DISTRIBUTION

The DR14 data are distributed through the same mechanisms as DR13, with the addition of a web application to interactively interface with optical and infrared spectra. We describe our three distribution mechanisms below. These methods are also documented on the SDSS website ([http://www.sdss.org/dr14/data\\_access](http://www.sdss.org/dr14/data_access)), and tutorial examples for accessing and working with SDSS data can be found at <http://www.sdss.org/dr14/tutorials>.

The raw and processed imaging and spectroscopic data, as well as the value added catalogs, are available through the Science Archive Server (SAS, [data.sdss.org/sas/dr14](http://data.sdss.org/sas/dr14)). Data can be downloaded from the SAS directly by browsing the directory structure, and also in bulk using rsync, wget and Globus Online (see [http://www.sdss.org/dr14/data\\_access/bulk](http://www.sdss.org/dr14/data_access/bulk) for more details). The data files available on the SAS all have their own datamodel, which describes the content of each file in detail. These datamodels are available at <https://data.sdss.org/datamodel>.

The processed imaging and optical and infrared spectra on the SAS are also available through an interactive web application (<https://dr14.sdss.org>). This web application allows the user to search for spectra based on specific parameters, e.g. plate, redshift, coordinates, or observing program. Searches can be saved through permalinks and options are provided to download the spectra directly from the SAS, either individually or in bulk. Previous data releases back to DR8 are available through the same interface. A link is also provided to the SkyServer explore page for each object.

Finally, the DR14 data can be found on the Catalog Archive Server (CAS, Thakar et al. 2008; Thakar 2008). The CAS stores catalogs of photometric, spectroscopic and derived quantities; these are available through the SkyServer web application (<http://skyserver.sdss.org>) for browser-based queries in synchronous mode, and through CasJobs (<http://skyserver.sdss.org/>)

TABLE 2  
VALUE ADDED CATALOGUES NEW TO DR14

Description	Reference(s)
APOGEE: DR14 APOGEE red-clump catalog DR14 APOGEE-TGAS Catalogue APOGEE DR14 Distance Estimations from Four Groups BPG (Bayesian Method) NAOC (Bayesian Method) NICE (Isochrone Matching Technique) NMSU (Bayesian Method)	Bovy et al. (2014) Anders et al. in prep. Santiago et al. (2016); Queiroz et al. (2017) Wang et al. (2016) Schultheis et al. (2014) Holtzman et al., (2017)
eBOSS/TDSS/SPIDERS: Redshift Measurement and Spectral Classification Catalog with Redmonster eBOSS: Emission Line Galaxy (ELG) Target Catalog The SDSS DR14 Quasar Catalog Composite Spectra of BOSS Quasars Binned on Spectroscopic Parameters from DR12Q SPIDERS x-ray galaxy cluster catalogue for DR14 Multiwavelength properties of RASS AGN Multiwavelength properties of XMMSL AGN	Hutchinson et al. (2016) Raichoor et al. (2017) Paris et al. in prep. Jensen et al. (2016) Clerc et al. (2016) Merloni et al., in prep Del Moro et al., in prep.
MaNGA: MaNGA Pipe3D: Spatially resolved and integrated properties of galaxies MaNGA FIREFLY Stellar Populations	Sánchez et al. (2016a,b, 2017b) Goddard et al. (2017)

**casjobs**), which offers more advanced and extensive query options in asynchronous or batch mode, with more time-consuming queries able to run in the background (Li & Thakar 2008). The CAS is part of the SciServer (<http://www.sciserver.org>) collaborative science framework, which provides users access to a collection of data-driven collaborative science services, including SkyServer and CasJobs. Other services include SciDrive, a “drag-and-drop” file hosting system that allows users to share files; SkyQuery, a database system for cross-matching astronomical multi-wavelength catalogs; and SciServer Compute, a system that allows users to upload analysis scripts as Jupyter notebooks (supporting Python, MatLab and R) and run these databases in Docker containers.

In addition to the data, the data processing software used by the APOGEE-2, eBOSS, and MaNGA teams to derive their data products from the raw frames, is available at <http://www.sdss.org/dr14/software/products>.

#### 4. EBOSS, TDSS AND SPIDERS

The extended Baryon Oscillation Spectroscopic Survey (eBOSS; Dawson et al. 2016) is surveying galaxies and quasars at redshifts  $z \sim 0.6 - 3.5$  to map the large scale structure of the Universe with the main goal to provide Baryonic Acoustic Oscillation (BAO) measurements in the uncharted redshift range spanning  $0.6 < z < 2.2$ . eBOSS achieves this by observing a new set of targets: high redshift LRGs, ELGs, and quasars. The three new tracers will provide BAO distance measurements with a precision of 1% at  $z = 0.7$  (LRGs), 2% at  $z = 0.85$  (ELGs), and 2% at  $z = 1.5$  (quasars). The Lyman- $\alpha$  forest imprinted on approximately 120,000 new quasar spectra will give eBOSS an improved BAO measurement of  $1.4\times$  over that achieved by BOSS (Delubac et al. 2015; Bautista et al. 2017). Furthermore, the clustering from eBOSS tracers will allow new measurements of redshift-space distortions (RSD), non-Gaussianity in the primordial density field, and the summed mass of neutrino species. eBOSS will provide the first percent-level distance measurements with BAO in the redshift range  $0.6 < z < 3$ , when cosmic expansion transitioned from deceleration to acceleration. The new redshift coverage

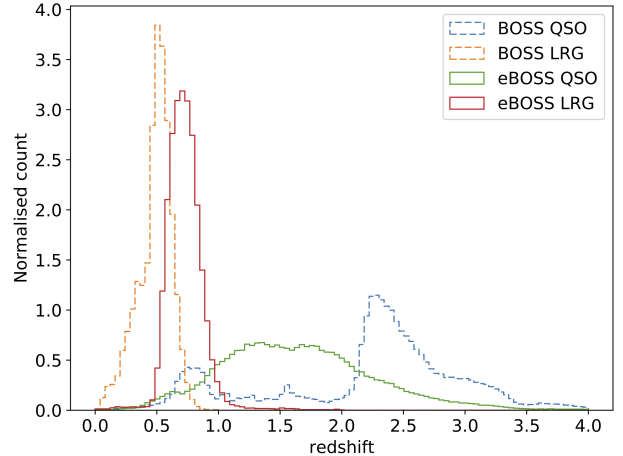


FIG. 1.—  $N(z)$  of eBOSS DR14 QSO and LRG compared to DR12 BOSS, demonstrating how eBOSS is filling in the redshift desert between  $z \sim 0.8 - 2.0$ . Note that this shows only QSO and LRG targets because no significant number of ELGs have been released in DR14. To convert from Normalized Count to number as a function of redshift, multiply by the total numbers (given in Table 1 for the full survey) times the bin size of  $dz = 0.04$ .

of eBOSS obtained by targeting three classes of targets (LRG, ELG and Quasars) will have the statistical power to improve constraints relative to BOSS by up to a factor of 1.5 in  $\Omega_M$ , a factor of three in the Dark Energy Task Force Figure of Merit (Albrecht et al. 2006), and a factor of 1.8 in the sum of the neutrino masses (Zhao et al. 2016).

We show in Figure 1 the  $N(z)$  in eBOSS DR14 QSO and LRG targets compared to the final BOSS release in DR12 (Alam, et al. 2015), demonstrating how eBOSS is filling in the redshift desert between  $z \sim 0.8 - 2.0$ . DR14 does not contain any significant number of ELG targets, which will be released in future DRs.

A significant number of fibers on the eBOSS plates are devoted to two additional dark-time programs. TDSS (Time Domain Spectroscopic Survey; Morganson et al.

2015) seeks to understand the nature of celestial variables by targeting objects that vary in combined SDSS DR9 and Pan-STARRS1 data (PS1; Kaiser et al. 2002). A large number of the likely TDSS quasar targets are also targeted by the main eBOSS algorithms and therefore meet the goals of both surveys. TDSS-only targets fill  $\sim 10$  spectra per square degree. SPIDERS (Spectroscopic Identification of eROSITA Sources) aims to characterize a subset of X-ray sources identified by eROSITA (extended Roentgen Survey with an Imaging Telescope Array; Predehl et al. 2014). However, until the first catalog of eROSITA sources is available, SPIDERS will target sources from the RASS (Roentgen All Sky Survey; Voges et al. 1999) and XMM-Newton (X-ray Multi-mirror Mission; Jansen et al. 2001). SPIDERS will also obtain on average  $\sim 10$  spectra per square degree over the course of SDSS-IV, but the number of fibers per square degree on a plate is weighted toward the later years to take advantage of the new data from eROSITA.

A small fraction of eBOSS time is dedicated to an ancillary program to perform multi-object reverberation mapping for a single  $7 \text{ deg}^2$  field. This program (SDSS-RM) aims to detect the lags between the broad-line flux and continuum flux in quasars over a broad range of redshift and luminosity with spectroscopic monitoring, which allows the measurement of the masses of these quasar black holes. Started as an ancillary program in SDSS-III, SDSS-RM continues in SDSS-IV with  $\sim 12$  epochs (each at nominal eBOSS depth) per year to extend the time baseline of the monitoring and to detect lags on multi-year timescales. The details of the SDSS-RM program can be found in Shen et al. (2015), and initial results on lag detections are reported in Shen et al. (2016) and Grier et al. (2017).

eBOSS started in September 2014 by taking spectra of LRG and Quasars, while further development on the definition of the ELG targets sample was conducted in parallel. In May 2016, eBOSS completed its first major cosmological sample containing LRG and Quasars from the first 2 years eBOSS data and from SEQUELS (already part of the DR13 release). These data have already been used to improve the classification of galaxy spectra (Hutchinson et al. 2016), introduce new techniques to the modeling of incompleteness in galaxy clustering, and to provide measurements of clustering on BAO scales at  $1 < z < 2$  for the first time (Ata et al. 2017).

#### 4.1. Data description

DR14 includes the data from 496 plates observed under the eBOSS program; it also includes the 126 SEQUELS plates (already released in DR13), from an ancillary program to take advantage of some of the dark time released when BOSS was completed early. The SEQUELS targets are similar to the eBOSS targets as it was a program to test the selection algorithms of eBOSS, in particular the LRG (Prakash et al. 2016) and quasars (Myers et al. 2015). The final ELG target recipe is not following the one tested during SEQUELS. The new ELG recipe is documented in the DR14 release following the description given by Raichoor et al. (2017).

For the TDSS program, combined SDSS DR9 and Pan-STARRS1 data (PS1; Kaiser et al. 2002) are used to select variable object targets (Morganson et al. 2015; Ruan et al. 2016); while for SPIDERS, the objects are

selected from a combination of X-ray and optical imaging for the SPIDERS cluster (Clerc et al. 2016) and AGN (Dwelly et al. 2017) programs.

The sky distribution of the DR14 data from eBOSS is shown in Figure 2. Table 3 summarizes the content and gives brief explanations of the targeting categories.

#### 4.2. Retrieving eBOSS data

All SDSS data releases are cumulative and therefore the eBOSS data also includes the SEQUELS data taken in SDSS-III or SDSS-IV, reduced with the latest pipelines. eBOSS targets can be identified using the EBOSS.TARGET1 bitmask. The summary `spAll-v5-10.0.fits` datafile, which includes classification information from the pipeline, is located on the SAS<sup>2</sup>; the data can also be queried via the `specObjAll` table on the CAS.

#### 4.3. eBOSS/TDSS/SPIDERS VACs

We include seven VACs based on BOSS, eBOSS, TDSS or SPIDERS data or target selection in this DR. Brief details of each are given below, and for more details we refer you to the relevant papers in Table 2.

##### 4.3.1. Redshift Measurement and Spectral Classification Catalog with Redmonster

The redmonster software<sup>3</sup> is a sophisticated and flexible set of Python utilities for redshift measurement, physical parameter measurement, and classification of one-dimensional astronomical spectra. A full description of the software is given in Hutchinson et al. (2016). The software approaches redshift measurement and classification as a  $\chi^2$  minimization problem by cross-correlating the observed spectrum with a theoretically-motivated template within a spectral template class over a discretely sampled redshift interval. In this VAC the software has been run on all DR14 LRG spectra. Redmonster was able to successfully measure redshifts for  $\sim 90\%$  of LRG spectra in DR14. This is an increase of  $\sim 15\%$ , in absolute terms, over `spectro1d`, and nearly matches the most optimistic estimate for the fraction of measurable redshifts as determined by visual inspections.

##### 4.3.2. The SDSS-IV Extended Baryon Oscillation Spectroscopic Survey: Emission Line Galaxy Target Catalog

We publish the south galactic cap Emission Line Galaxy (ELG) catalog used for eBOSS (Raichoor et al. 2017). Targets were selected using photometric data from the Dark Energy Camera Legacy Survey (DECaLS; <http://legacysurvey.org/>). We selected roughly 240 ELG targets per square degree. The great majority of these ELG lie in the redshift range  $0.67 < z < 1.1$  (median redshift 0.85).

##### 4.3.3. The SDSS DR14 Quasar Catalog

Following the tradition established by SDSS-I/II/III the SDSS-IV/eBOSS collaboration is producing a visually inspected quasar catalog. The SDSS-DR14 quasar catalog (DR14Q; Paris et al. in prep.) is the first to be

<sup>2</sup> <https://data.sdss.org/sas/dr14/eboss/spectro/redux/v5.10.0/>

<sup>3</sup> <https://github.com/timahutchinson/redmonster>

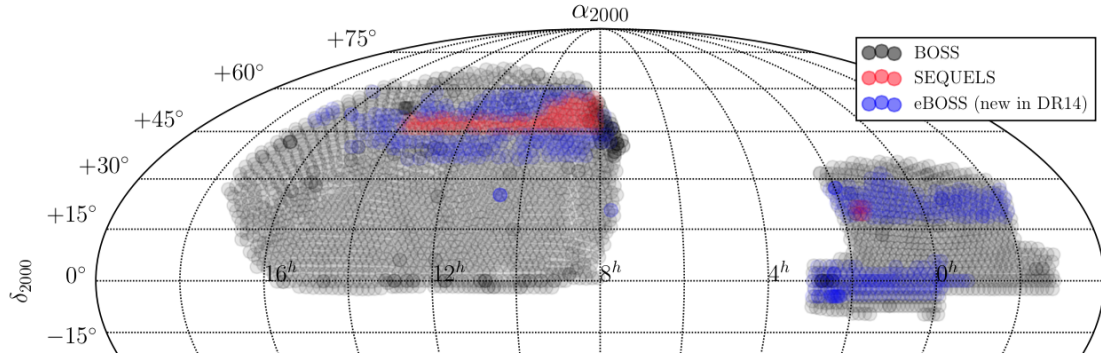


FIG. 2.— DR14 eBOSS spectroscopic coverage in Equatorial coordinates (map centered at RA = 8h.) BOSS coverage is shown in grey, SEQUELS in red, and the eBOSS data newly released for DR14 is shown in blue.

TABLE 3  
eBOSS SPECTROSCOPIC TARGET CATEGORIES IN DR14

Target Category	Target Flag	# DR14	Reference(s)
Main LRG sample	LRG1_WISE	105764	Prakash et al. (2016)
Ancillary LRG sample	LRG1_IDROP	45	Prakash et al. (2016)
Main QSO selection	QSO1_EBOSS_CORE	154349	Myers et al. (2015)
Variability-selected QSOs	QSO1_VAR_S82	10477	Palanque-Delabrouille et al. (2016)
	QSO1_PTF	54037	Myers et al. (2015)
Reobserved BOSS QSOs	QSO1_REOBS	16333	Myers et al. (2015)
	QSO1_BAD_BOSS	584	
QSOs from FIRST survey	QSO1_EBOSS_FIRST	1792	Myers et al. (2015)
All eBOSS QSOs also in BOSS	QSO_BOSS_TARGET	583	Myers et al. (2015)
All eBOSS QSOs also in SDSS	QSO_SDSS_TARGET	20	Myers et al. (2015)
All “known” QSOs	QSO_KNOWN	11	Myers et al. (2015)
Time-domain spectroscopic survey (TDSS)	TDSS_TARGET	39748	Morganson et al. (2015); MacLeod et al. (2017)
X-ray sources from RASS	SPIDERS_TARGET	13261	Clerc et al. (2016); Dwelly et al. (2017)
X-ray sources in Stripe 82	S82X_TILE1	2775	LaMassa et al in prep. (also see LaMassa et al. 2016)
	S82X_TILE2	2621	
	S82X_TILE3	4	
ELG Pilot Survey	ELG_TEST1	15235	Delubac et al. (2017); Raichoor et al. (2016)
	ELG1_EBOSS	4741	
	ELG1_EXTENDED	659	
Standard stars	STD_FSTAR	8420	Dawson et al. (2016)
Standard white dwarfs	STD_WD	546	Dawson et al. (2016)

released that contains new identifications that are mostly from eBOSS. The contents of this are similar to the DR12 version (which contained final data from BOSS as well as data from the preliminary eBOSS survey ”SEQUELS”) as described in Paris et al. (2017).

#### 4.3.4. Composite Spectra of BOSS Quasars Binned on Spectroscopic Parameters from DR12Q

We present high signal-to-noise composite spectra of quasars over the redshift range  $2.1 \leq z \leq 3.5$ . These spectra, based on the DR12 BOSS quasar catalog (Alam, et al. 2015) are binned by luminosity, spectral index, and redshift. As discussed in Jensen et al. (2016), these composite spectra can be used to reveal spectral evolution while holding luminosity and spectral index constant. These composite spectra allow investigations into quasar diversity, and can be used to improve the templates used in redshift classification. See Jensen et al. (2017) for more details.

#### 4.3.5. SPIDERS X-ray galaxy cluster catalogue for DR14

A substantial fraction of SPIDERS fibers target red-sequence galaxies in candidate X-ray galaxy clusters. The systems were found by filtering X-ray photon over-

densities in the ROSAT All-Sky Survey (RASS) with an optical cluster finder (see Clerc et al. 2016, for details on the samples and targeting strategy). Adding together the DR14 eBOSS sky area with the SEQUELS area (Fig. 1), 573 of these systems show a richness  $\lambda_{\text{OPT}} > 30$ , have been completely observed as part of DR14. A complete observation means that all tiled galaxies in a cluster red sequence have got a spectrum in DR14; these clusters must also contain at least one redshift from SDSS-I to -IV in their red-sequence. Systems located at a border of the DR14 footprint, but in the interior of the full eBOSS footprint, will be fully covered through later observations by overlapping plates.

A total of 9,029 valid redshifts were associated with these candidate rich galaxy clusters, leading to a median number of 15 redshifts per red sequence. An automated algorithm performed a preliminary membership assignment and interloper removal based on standard iterative  $\sigma$ -clipping method. The results of the algorithm were visually inspected by 8 experienced galaxy cluster observers, ensuring at least two independent evaluators per system. A web-based interface was specifically developed to this purpose: using as a starting point the result of the automated algorithm, the tool allows each inspector

to interactively assess membership based on high-level diagnostics and figures (see Fig. 16 in Clerc et al. 2016). A final decision is made by each evaluator whether to validate the system as a bona-fide galaxy cluster, or “un-validate” the system by lack of data or identification of a false candidate. Validation is in most cases a consequence of finding three or more red-sequence galaxies in a narrow redshift window, compatible with them all being galaxy cluster members. A robust weighted average of the cluster members redshifts provides the cluster systemic redshift. A majority vote was required for each system to be finally “validated” or “unvalidated”; in the former case, an additional condition for agreement is the overlap of the cluster redshifts 95% confidence intervals. A second round of evaluations involving four inspectors per system was necessary to resolve cases with no clear majority.

In total, 520 of these systems are validated as true galaxy clusters based on spectroscopic data and they form the SPIDERS X-ray galaxy cluster Value-Added catalogue for DR14. Among them 478 are unique components along a line-of-sight. A total of 7,352 spectroscopic galaxies are members of a galaxy cluster. This catalogue in particular lists each galaxy cluster redshift and its uncertainty, its number of spectroscopic members and its X-ray luminosity, assuming each component along a line-of-sight contributes the flux measured in RASS data.

#### 4.3.6. Multiwavelength properties of RASS and XMMSL AGN

In these two VACs, we present the multi-wavelength characterization over the area covered by the SEQUELS and eBOSS DR14 surveys ( $2500 \text{ deg}^2$ ) of two highly complete samples of X-ray sources:

1. The ROSAT All-Sky Survey (RASS) X-ray source catalogue (2XRS; Boller et al. 2016)
2. The XMM-Newton Slew Survey point source catalog (XMMSL; Saxton et al. 2008; version 1.6).

We provide information about X-ray properties of the sources, as well as of their counterparts at longer wavelength (Optical, IR, Radio) identified first in the All-WISE IR catalog<sup>4</sup> via a Bayesian cross-matching algorithm (Dwelly et al. 2017; Salvato et al. 2017, submitted). We complement this with dedicated visual inspection of the SDSS spectra, providing accurate redshift estimates (with objective confidence levels) and source classification, beyond the standard eBOSS pipeline results.

## 5. APOGEE-2

DR14 is the fourth release from the Apache Point Observatory Galactic Evolution Experiment (APOGEE). DR14 presents, for the first time, the first two years of SDSS-IV APOGEE-2 data (Jul 2014-Jul 2016) as well as re-processed data from SDSS-III APOGEE-1 (Aug 2011-Jul 2014). Note that the general term APOGEE data, employed throughout this paper, refers to both APOGEE-1 and APOGEE-2 data. APOGEE-2 data are substantively the same as APOGEE-1 data, however, one

of the three detectors in the instrument was replaced at the end of APOGEE-1 because it exhibited a substantial amount of persistence (i.e. light from previous exposures lead to excess recorded charge in subsequent exposures). The new detector is substantially better in this regard.

APOGEE data in DR14 includes visit-combined spectra as well as pipeline-derived stellar atmospheric parameters and individual elemental abundances for 263,444 stars<sup>5</sup>, sampling all major components of the Milky Way. In addition to the Milky Way bulge, disk, and halo, DR14 includes, for the first-time, data from stars in satellite galaxies, which are typically fainter targets than those from the main portion of the survey. DR14 incorporates a few modifications in the Data Reduction Pipeline (DRP) as well as in the APOGEE Stellar Parameter and Chemical Abundance Pipeline (ASPCAP). It also includes a separate set of stellar parameters and abundances from The Cannon (Ness et al. 2015)<sup>6</sup>.

Two separate papers will provide more in-depth discussion and analysis of APOGEE data released in DR13/DR14: Holtzman et al. (in prep.) describes in detail the DR13/DR14 pipeline processing as well as the associated data products; and Jönsson et al. (in prep.) compares stellar parameter and element abundances from DR13/DR14 with those from the literature.

### 5.1. Targeting

The targeting strategy of APOGEE-2 departs slightly from that of APOGEE-1 and is set based on three-tier priority scheme: core, goal, and ancillary (Zasowski et al. 2017). The core science targets, which are the highest priority, are those that directly address the primary science objectives of APOGEE and include the Galactic bulge, disk, and halo, globular and open clusters, *Kepler* field spectroscopic follow-up, and satellite galaxies (unique in APOGEE-2). “Goal” science targets fall in line with APOGEE science goals with a second-tier prioritization and include M dwarfs, eclipsing binaries, sub-stellar companions, *Kepler* Objects of Interest, young (star-forming) clusters, and Extended *Kepler* Mission (K2) spectroscopic follow-up. The third-tier priority are ancillary science targets, for which a general solicitation was issued for programs that could harness the unique capability of the APOGEE instrument. Since the ancillary programs of APOGEE-1 were largely successful and broadened its scientific scope, APOGEE-2 continues in this vein and DR14 presents some of the first ancillary program data. As in APOGEE-1, the primary stellar targets of APOGEE-2 are red giant branch (RGB) stars. APOGEE-2 extends the target stellar classes with designated observations of red clump (RC) stars in the bulge as well as faint stars (e.g., dwarf Spheroidal and halo stream members with  $H \geq 14$ ). On top of the APOGEE-led programs, additional data are collected with the MaNGA co-targeting program. For the MaNGA pointings, APOGEE data is collected concurrently, with the targeted fields in the direction of the Galactic caps. To document the APOGEE-2 targeting scheme, a new

<sup>5</sup> The figure of 263,444 results from the removal of duplicate observations for a single star. Note that DR14 has a total of 277,731 entries.

<sup>6</sup> Named in recognition of the stellar classification work of Annie-Jump Cannon (Cannon & Pickering 1918).

<sup>4</sup> <http://wise2.ipac.caltech.edu/docs/release/allwise/>

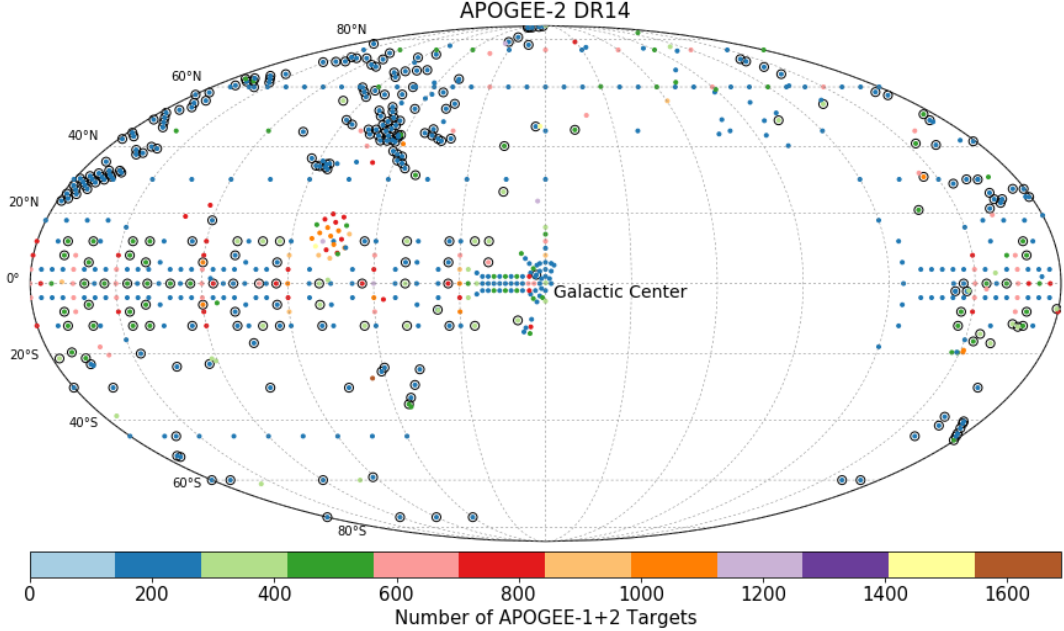


FIG. 3.— DR14 APOGEE spectroscopic coverage in Galactic coordinates (map centered on the Galactic center). The color coding indicates the number of APOGEE-1+2 targets observed per field, as shown in the key. Fields new to DR14 are outlined in black.

set of bit flags is employed in DR14: APOGEE2\_TARGET1, APOGEE2\_TARGET2, and APOGEE2\_TARGET3. Further details with regard to the APOGEE-2 targeting strategy and field design may be found in Zasowski et al. (2017), including information on APOGEE-2S targets which will be planned to be part of the next data release.

### 5.2. Pipeline Reduction and Data Product Extraction

As with the previous data releases, all spectra are processed through the DRP, which includes dark current subtraction, cosmic ray removal, flat-fielding, spectral extraction, telluric correction, wavelength calibration, and dither combination. Radial velocities (RVs) are determined for each individual visit and the individual visit spectra are resampled to rest-wavelength and combined to generate a single spectrum for each object. Associated DRP data products are the visit-combined spectra and radial velocity (RV) values. For DR14, modifications to the RV determination and associated star combination have occurred. The RV values are now determined both relative to the combined spectrum (in an iterative fashion) as well as to the best-matching model. The radial velocities from the method that yields the lower scatter are adopted (VHELIO\_AVG) and estimates of the associated error and scatter are generated. Note that the new methodology has resulted in improved RV determinations for low signal-to-noise observations (and consequently, faint stars), but there can still be potentially significant issues with some of the faintest targets. The distribution of  $S/N$  values for spectra released in DR14 (compared to those released in DR13; Albareti et al. 2017) are shown in Figure 4.

#### 5.2.1. Persistence

As discussed in Nidever et al. (2015) and Holtzman et al. (2015), one of the three APOGEE-1 detectors (the

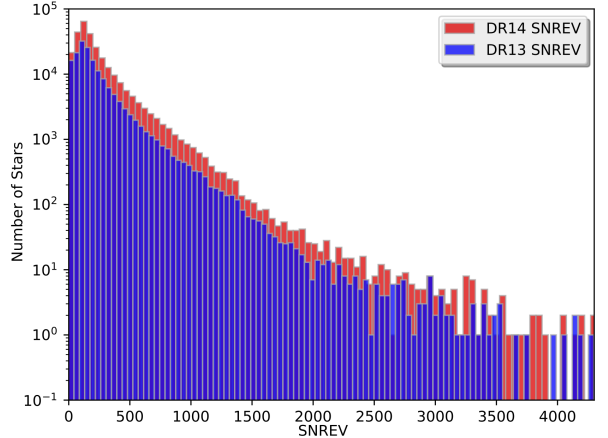


FIG. 4.— A comparison of the  $S/N$  distribution of APOGEE spectra released in DR14 (red) with those released in DR13 (blue). The  $S/N$  quantity displayed in the figure is SNREV, a revised  $S/N$  estimate which considers persistence issues.

“blue” detector) exhibited significant levels of persistence (*i.e.*.. charge which is held between exposures) over one third of the detector area, and another (the “green” detector) exhibited persistence at a somewhat lower level over a smaller area. This persistence affected derived stellar abundances (Holtzman et al. 2015). As mentioned above, the “blue” detector was replaced for APOGEE-2 in part to solve this problem. For the APOGEE-1 data, we attempt to subtract out persistence based on a persistence model and also de-weight pixels affected by persistence during visit combination so that, for stars with a mix of persistence-affected and non-persistence-affected visits, the combined spectra are dominated by the non-

affected visits. This results in a reduction in systematic error but a slight increase in random error. This process significantly reduces the impact of persistence (Holtzman et al. in prep); however, it can still have an effect, especially for fainter targets. Users of the APOGEE spectra should pay careful attention to the pixel-level data flags and the pixel uncertainties.

### 5.2.2. ASPCAP

After the DRP stage, the visit-combined stellar spectra are processed by ASPCAP, which derives the stellar atmospheric parameters (e.g., effective temperature  $T_{\text{eff}}$ , surface gravity  $\log g$ , metallicity  $[M/H]$ ) as well as abundances for more than 20 species. The ASPCAP determination proceeds in three stages: an initial pass through ASPCAP gives coarse values for a few key atmospheric parameters to identify which spectral grids should be used on each object, a second pass yields the full set of parameters, and then a final pass determines abundances for each element with stellar parameters fixed. For DR14, ASPCAP modifications include a new normalization scheme for both observed and synthetic spectra. Rather than using an iteratively asymmetrically-clipped fit, the continuum is determined by a polynomial fit to the spectra after masking of sky lines, because the asymmetric clipping is expected to lead to systematic differences in continuum normalization as a function of S/N. Another change is that the ASPCAP parameter determination was done by  $\chi^2$ -minimization over a 7-dimensional grid for giants which included a microturbulence dimension. This leads to slightly lower abundance scatter in clusters as well as smaller trends of  $[M/H]$  with temperature.

One caveat of the DR14 ASPCAP analysis is that new grids were not constructed for APOGEE-2 line spread functions (LSFs): grids made with the APOGEE-1 LSFs were used. Since the only change was the detector replacement, no large LSF changes were expected, nor were they observed, but the re-installation of the detector package may have led to subtle differences.

### 5.3. Calibration and Data Product Usage

As with previous DRs, DR14 includes a post-ASPCAP calibration of the final stellar atmospheric parameter and element abundances. A variety of different stellar clusters and standards are employed in the calibration of the results. These calibrations include a metallicity-dependent temperature correction, a surface gravity calibration based on asteroseismic gravities, an internal and external calibration of metallicity ( $[M/H]$ ), and a temperature-dependent and zero-point calibration for elemental abundances. Note that surface gravity calibration is not done for dwarfs because we do not have independent estimates of surface gravities from which to derive such calibrations. Calibrations are applied to abundances over temperature ranges that are determined by looking at the ranges over which data in star clusters produce the same abundance. Based on cluster results and inspection of the spectra, we do not provide calibrated abundances for Cu, Ge, Y, Rb, and Nd, since these do not appear to be reliable.

Several different bitmasks (STARFLAG, PARAMFLAG, ASPCAPFLAG) are included that provide information on

factors that affect data quality, and users are strongly encouraged to pay attention to these

### 5.4. New DR14 Data Product: Results from The Cannon

New in DR14 is the inclusion of parameters and abundances derived from The Cannon (Ness et al. 2015), which has been shown to have the potential to deliver parameters and abundances of higher precision. The Cannon is a data-driven model that provides parameters and abundances (collectively called labels) from the spectra, after training the sensitivity of each pixel to parameters and abundances based on a training set with independently derived labels. For DR14, we train The Cannon on ASPCAP results for a subset of high S/N giant stars, and apply the model to all objects within the range of parameters covered by the training set. DR14 Cannon results have been derived using the Cannon-2 code (Casey et al. 2016), but with a few modifications. First, we adopted uncertainties from the ASPCAP pipeline, which do a better job de-weighting areas around imperfectly subtracted sky lines. Second, and more importantly, we use “censoring” in the derivation of individual elemental abundances, which forces the model to only use pixels where there are known lines of a given element (rather than the full spectrum) to derive the abundance of that element. This was done because it was discovered that, when using the full spectrum, pixels without known lines of an element (and sometimes, with known lines of another element) contributed to the model sensitivity for that element. This suggests that the model may be affected by correlations of abundances within the training set stars. Without censoring, such correlations can lead to abundances that appear to be of higher precision, but this precision may not reflect higher accuracy, if the correlations are not present over the entire data set. While results for some elements with censoring show less scatter than ASPCAP results, results for other elements can look significantly worse. The implementation of censoring was done by using the elemental windows used by the ASPCAP analysis; it is possible that this is overly conservative because the ASPCAP windows reject regions in the spectrum that have abundance sensitivity if they are also sensitive to other abundances in the same elemental abundance group.

### 5.5. APOGEE VACs

Three APOGEE related VACs are included in DR14. They are briefly summarized below. For more details we refer the reader to the relevant paper in Table 2.

#### 5.5.1. DR14 APOGEE red-clump catalog

DR14 contains an updated version of the APOGEE red-clump (APOGEE-RC) catalog. This catalog is created using the same procedure as the original APOGEE-RC catalog (Bovy et al. 2014) now applied to the ASPCAP parameters derived in this data release. To account for changes in how the ASPCAP-derived  $\log g$  is calibrated in DR14, we have made the upper  $\log g$  cut more stringent by 0.1 dex (the upper  $\log g$  limit in Equation [2] in Bovy et al. (2014) now has 2.4 instead of 2.5). Like in the original release, we also apply an additional  $\log g$  cut to remove further contaminants (Equation [9]

in Bovy et al. 2014). Otherwise the catalog is created in the same manner as the original catalog.

The DR14 APOGEE-RC catalog contains 29,502 unique stars, about 50% more than in DR13. Note that because of changes in the target selection in APOGEE-2, the relative number of RC stars in APOGEE-2 is smaller than in APOGEE-1. We provide proper motions by matching to the UCAC-4 (Zacharias et al. 2013) and HSOY (Altmann et al. 2017) catalogs. Contamination by non-RC stars in the DR14 RC catalog is estimated to be less than 5% by comparing against true RC stars in the APOKASC catalog (M. Pinsonneault et al. in prep.).

#### 5.5.2. DR14 APOGEE-TGAS Catalogue

The first data release of the Gaia mission contains improved parallaxes and proper motions for more than 2 million stars contained in the Tycho-2 catalogue, among them 46,033 objects (10,250 of them unique stars) contained in APOGEE DR14. This is known as the Tycho-Gaia Astrometric Solution (TGAS). We provide the cross-matched catalog, together with precise combined astrometric/spectro-photometric distances and extinctions determined with *StarHorse* (Queiroz et al. 2017) for 29,661 stars. We also include orbital parameters calculated using the *GravPot16* code<sup>7</sup> (Fernandez-Trincado et al., in prep.). For more details see Anders et al. (in prep.).

#### 5.5.3. APOGEE DR14 Distance Estimations from Four Groups

This VAC provides spectro-photometric distance estimates for APOGEE stars that have been calculated by four groups, using slightly different isochrone techniques. All groups used the DR14 calibrated ASPCAP stellar parameters, if they fall inside the calibration ranges (see Holtzman et al., in prep.). The distances come from (1) the *StarHorse* code (Santiago et al. 2016; Queiroz et al. 2017, in prep.) (2) the code described in Wang et al. (2016), (3) the isochrone-matching technique described in Schultheis et al. (2014), and (4) the distance code described in Holtzman et al., (2017).

### 6. MANGA

In the context of the MaNGA Survey, DR14 roughly doubles the sample size of associated data products that were first made public in DR13. Spanning observations from the first two years of operations, the DR14 products include raw observations, intermediate reduction output, such as reduced fiber spectra, and final data cubes as constructed by the Data Reduction Pipeline (DRP; Law et al. 2016, hereafter L16). A summary *drpa11* catalog provides target identification information, sky positions, and object properties like photometry and redshifts. The MaNGA observing strategy is described in Law et al. (2015), and the flux calibration scheme presented in Yan et al. (2016b). An overview of the survey execution strategy and data quality is provided in Yan et al. (2016a). Weijmans (2016) provides a short summary to the entire survey, which is comprehensively described in Bundy et al. (2015).

DR14 includes observations from 166 MaNGA plates resulting in 2812 datacubes comprising targets in the

main samples as well as ancillary programmes, and around 50 repeat observations. The sky layout of the DR14 released MaNGA data is shown in Figure 5.

#### 6.1. MaNGA Target Classes

The target selection for the MaNGA Survey is described in detail by Wake et al. (2017). MaNGA's main galaxy sample contains galaxies with stellar masses,  $M_* > 10^9 M_\odot$ , and is comprised of three main subsamples that are defined on the basis of SDSS-I/II photometry and spectroscopic redshifts to deliver a final distribution that is roughly flat in  $\log M_*$ . The Primary sample achieves radial coverage out to 1.5 times the effective radii ( $1.5 R_e$ ) for target galaxies, while the Secondary sample reaches  $2.5 R_e$ . The Color-Enhanced supplement expands the selection of the Primary sample to include under-represented regions of  $M_*$ -color space. We refer to the combination of the Primary and Color-Enhanced supplements as "Primary+" which balances the restframe color distribution at fixed  $M_*$ . The MaNGA samples can be weighted so that they are equivalent to a volume limited sample. The required volume weights are described in Wake et al. (2017) and are provided in the DR14 version of the targeting file.

DR14 includes 1278 Primary galaxies, 947 Secondary galaxies and 447 Color-Enhanced supplement galaxies. Which sample a given target galaxy belongs to is given by the MANGA\_TARGET1 bitmask (or mnngtarg1 in the "drpall" file). Bits 10, 11, and 12 signal that galaxies were selected as Primary, Secondary, or Color-Enhanced targets respectively. In addition to  $\sim 121$  ancillary program targets,  $\sim 50$  galaxies were observed as fillers and do not fall into these target categories. They should be ignored in statistical studies of the MaNGA data.

MaNGA has also begun observing Milky Way stars in a bright-time survey program called the MaNGA Stellar Library (MaStar) that makes use of MaNGA IFUs during APOGEE-2 observations. The goal of MaStar is to build a new stellar library comprising  $> 8000$  stars that span the widest accessible ranges in effective temperature, surface gravity, metallicity, and element abundance ratios (Yan et al. in prep; see Yan et al 2017 for a conference proceeding describing the plans). Reduced stellar spectra will be included in DR15.

As described in the DR13 paper, roughly 5% of MaNGA IFUs are allocated to targets defined by approved ancillary programs. These sources can be identified using the MANGA\_TARGET3 bitmask (or mnngtarg3 in the drpall file). Most of the programs represented in DR14 are described in DR13<sup>8</sup>. They include targeted followup of AGN hosts, starburst galaxies, merging systems, dwarf galaxies, Milky Way analogs, and brightest cluster galaxies. New in DR14, we include deep observations reaching  $\sim 20$  hours in the center of the Coma cluster (Gu et al. 2017) and IFU observations allocated as part of an ancillary program to a nearby dwarf galaxy that is part of the ACS Nearby Galaxy Survey (Dalcanton et al. 2009).

#### 6.2. Working with MaNGA Data

<sup>7</sup> <https://fernandez-trincado.github.io/GravPot16/>

<sup>8</sup> also see <http://www.sdss.org/dr14/manga/manga-target-selection/ancillary-targets>

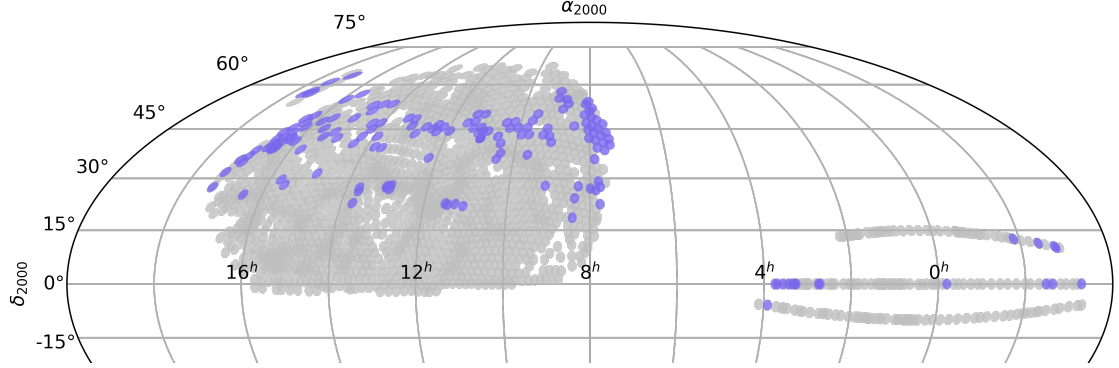


FIG. 5.— The sky distribution (Molleweide equatorial projection for Dec >  $-20^\circ$ ) of possible MaNGA plates (in grey). Because MaNGA targets are selected from a sample with SDSS-I photometry and redshifts, this footprint corresponds to the Data Release 7 imaging data (Abazajian et al. 2009). Each plate contains 17 MaNGA targets, and around 30% of all possible plates will be observed in the full 6-year survey. The purple indicates plates with data released as part of DR14.

All MaNGA data products take the form of multi-extension FITS files. As we describe in DR13, the DRP data products consist of intermediate reduced data (sky-subtracted, flux-calibrated fiber spectra with red and blue data combined for individual exposures of a plate) and final-stage data products (summary row-stacked spectra and data cubes) for each target galaxy. The summary row stacked spectra (RSS files) are two-dimensional arrays provided for each galaxy in which each row corresponds to a single fiber spectrum.

The three-dimensional data cubes are created by combining the individual spectra for a given galaxy together onto a regularized  $0.5''$  grid (see L16 for more detail). The associated wavelength arrays for both the data cubes and RSS files can be accessed in logarithmic and linear scales. Each data cube contains additional extensions with information that includes the inverse variance, a bad-pixel mask, instrumental resolution, reconstructed broadband images, and the effective spatial point-spread function. The full data model for all MaNGA DRP data products can be found online at <http://www.sdss.org/dr14/manga/manga-data/data-model> and in Appendix B of L16.

The DR14 pipeline for MaNGA is nearly identical to that in DR13 with a few small exceptions listed below:

- The spectral resolution reported is worse by about 10%. This change reflects growing understanding of the data quality to account for the effects of both pre- vs post-pixelization gaussian profile fitting and changes in the line spread function (LSF) introduced by the wavelength rectification. There are likely to be further small change in future data releases.
- Local reddening maps (rather than plate averages) have been used in calculations of S/N of the spectra
- Spaxels flagged as containing foreground stars are now ignored by the astrometric routines. This may result in some small changes in astrometry for some objects.
- The bias calculation in the blue camera has been improved. The impact of this will be negligible except to improve the quality of some extremely bright emission lines.

- Adjustments were made to the sky subtraction algorithms to optimize performance for the Coma cluster ancillary program.
- There have been improvements in the data quality flagging for cubes with dead fibres.

Instructions for accessing the MaNGA data products are given on the SDSS website<sup>9</sup>. We summarize available options here and refer the reader to the DR13 paper for additional details. All data products are stored on the Science Archive Server at <http://data.sdss.org/sas/dr14/manga/spectro/redux/>. Here you will find the drpall summary table as well as subdirectories that store reduction output for each plate, both for observations obtained on a specific night and for the results of combining all observations of a given plate into a “stack.” The drpall table may be queried either after downloading this file to disk or through the SDSS CASJobs system. Such queries define selections of galaxies of interest and can return the plate-IFU combination for those galaxies that identifies how they were observed. These in turn can be used to find the SAS directory locations of the corresponding data products. Large downloads can be accomplished via rsync calls as described on the SDSS website. Finally, the SDSS SkyServer Explore tool provides basic information about MaNGA targets.

Several features of the MaNGA data should be kept in mind while using the data. Most important, each MaNGA data cube has a FITS header keyword DRP3QUAL indicating the quality of the reduction. 1-2% of the data cubes are flagged as significantly problematic—galaxies with CRITICAL quality bit (=30) set should be treated with extreme caution (see L16). Please also use the MASK extension of each datacube to identify problematic spaxels. A simple summary DONOTUSE bit is of particular importance indicating elements that should be masked out for scientific analyses.

There is significant covariance between adjacent spaxels in data cubes, given that the spaxel size ( $0.5''$ ) is much smaller than the fiber size ( $2''$  diameter). A simple method that accounts for covariance when one desires to spatially bin spaxels together is discussed in §9.3 of L16. The typical reconstructed point spread function of the MaNGA data cubes has a FWHM of  $2.5''$ . Sparse corre-

<sup>9</sup> <http://www.sdss.org/dr14/manga/manga-data/data-access/>

lation matrices in the *ugriz* central wavelengths are also now provided in the data cubes.

As discussed by L16, the instrumental line spread function (LSF) in the DR13 data was underestimated by about  $10 \pm 2\%$ . This has been corrected in DR14 and the reported LSF is described by a post-pixelized gaussian.

Additional issues and caveats are discussed in <http://www.sdss.org/dr14/manga/manga-caveats/>.

### 6.3. Highlights of MaNGA Science with DR14 Data

The MaNGA survey has produced a number of scientific results based on data acquired so far, indicating the breadth of research possible with the MaNGA data. In the [DR13 paper we provided](#) a summary of science highlights with early data. Here we briefly summarize the results of papers that have been completed within the SDSS-IV collaboration using the MaNGA sample released as part of DR14.

For example, published results based on the MaNGA DR14 data include, Barrera-Ballesteros et al. (2017) who discuss the integrated stellar mass-metallicity relation for more than 1700 galaxies, Zhu et al. (2017) who revisit the relation between the stellar surface density, the gas surface density and the gas-phase metallicity of typical disc galaxies in the local Universe, Belfiore et al. (2017) who study the gas phase metallicity and nitrogen abundance gradients traced by star-forming regions in a representative sample of 550 nearby galaxies, and Lin et al. (2017) who report the discovery of a mysterious giant H $\alpha$  blob that is  $\sim 8$  kpc away from a component of a dry galaxy merger. In Bizyaev et al. (2017) was presented a study of the kinematics of the extraplanar ionized gas around several dozen galaxies, while Jones et al. (2017) conducted a detailed study of extra-planar diffuse ionized gas stacking spectra from 49 edge-on, late-type galaxies as a function of distance from the midplane of the galaxy. Numerous other results based on DR14 data are in preparation.

### 6.4. MaNGA VACs

This data release also contains two VACs based on MaNGA data. They are briefly summarized below, and for more details we refer you to the papers given in Table 2

#### 6.4.1. MaNGA Pipe3D value added catalog: Spatially resolved and integrated properties of galaxies

PIPE3D is an IFU-focused analysis pipeline that calculates intermediate dataproducts and is able to obtain both the stellar population and the ionized gas properties extracted from the datacubes in an automatic way. This pipeline is based on FIT3D, details of which are presented in Sánchez et al. (2016a,b) which show some examples based on CALIFA (Sánchez-Menguiano et al. 2016; Cano-Díaz et al. 2016; Sánchez et al. 2017a) and MaNGA/P-MaNGA (Ibarra-Medel et al. 2016; Barrera-Ballesteros et al. 2016; Lin et al. 2017; Barrera-Ballesteros et al. 2017) datasets. The MaNGA dataproducts provided by Pipe3D are presented in Sánchez et al. (2017b)<sup>10</sup>. The VAC consists of a sin-

gle table containing integrated (cumulative), characteristic (values at the effective radius), and gradient of different quantities, included stellar mass, star-formation (and their densities), oxygen and nitrogen abundances, dust attenuation, estimated gas density, stellar and gas velocity dispersions.

For each galaxy, data is presented as an individual FITS file including four extensions, each one corresponding to a data cube that comprises (1) the spatial resolved properties required to recover the star-formation histories, (2) the average properties of the stellar populations, (3) the emission line properties for 56 strong and weak emission lines (including the former ones together with the EW of the lines), and (4) the most frequently used stellar indices. The details of each individual extension was described in Sánchez et al. (2016b), and the final adopted format in Sánchez et al. (in prep.).

#### 6.4.2. MaNGA FIREFLY Stellar Populations

The MaNGA FIREFLY VAC (Goddard et al. 2017) provides measurements of spatially resolved stellar population properties in MaNGA galaxies. It is built on and complements the products of the MaNGA data analysis pipeline (DAP, Westfall et al, in preparation) by providing higher-order and model-based data products. These are measurements of optical absorption line-strengths, as well as the physical properties age, metallicity and dust attenuation. The latter are derived from full spectral fitting with the code FIREFLY (Wilkinson et al. 2015, 2017) using the supercomputer SCIAMMA2 at Portsmouth University. The VAC is a single fits file (4 GB) containing measurements all DR14 MaNGA galaxies. The catalogue contains basic galaxy information from the literature (i.e., galaxy identifiers, redshift, mass), global derived parameters (i.e., light-weighted and mass-weighted stellar population ages and metallicities for a central 3 arcsec aperture and for an elliptical shell at 1 effective radius), gradient parameters (i.e., gradients in age and metallicity measured within  $1.5 R_e$ ) and spatially resolved quantities (i.e., 2-D maps of age, metallicity, dust attenuation, mass and surface mass density, and 28 absorption line indices).

More detail on the catalogue, and the method of creating the 2-dimensional maps is provided in Goddard et al. (2017) and the data is available from the data release website<sup>11</sup>.

## 7. FUTURE PLANS

SDSS-IV is planning a 6-year survey, with operations at both the 2.5 meter Sloan Foundation Telescope at Apache Point Observatory, New Mexico, USA and the du Pont Telescope at Las Campanas, Chile scheduled through 2020. Future data releases from SDSS-IV will include data observed with both telescopes; the final SDSS-IV data release is planned to be DR18, currently scheduled for December 2020.

For APOGEE, future data releases will include, for the first time, southern hemisphere observations taken with the new APOGEE-S instrument at the Las Campanas Observatory with the duPont 2.5m telescope. These observations will extend APOGEE coverage to

<sup>10</sup> <http://www.sdss.org/dr14/manga/manga-data/manga-pipe3d-value-added-catalog>

<sup>11</sup> <http://www.sdss.org/dr14/manga/manga-data/manga-firefly-value-added-catalog>

the full Galaxy, with significantly increased observations of the Galactic bulge and also include observations in the Magellanic Clouds, globular clusters, and dwarf spheroidal galaxies only accessible from the southern hemisphere. As usual, future data releases will also include re-reductions of all APOGEE-N data. Plans for improved stellar parameter/abundance analysis include using a new homogeneous grid of MARCS stellar atmospheres, and the use of “minigrids” to analyze elements whose absorption features are too blended with those of other elements to be reliably extracted with the abundance techniques used to date.

For MaNGA, it is planned that the DR15 data release will include the  $\sim 4000$  MaNGA galaxies which have been observed up to summer shutdown 2017. In addition, we anticipate a number of new data products to be released in this and future DRs. These include reduced spectra from the MaStar stellar library (Yan et al. in prep.), which is making use of commensal observations during APOGEE-2 time to obtain spectroscopic observations of stars which will be used to build a new stellar library through the MaNGA instrumentation; and output from the MaNGA Data Analysis Pipeline (DAP; Westfall et al. in prep.). The DAP produces maps of emission line fluxes, gas and stellar kinematics, and stellar population properties. Some similar derived data products are already available as Value Added Catalogs (see Table 2 and Section 6.4.1 and 6.4.2). Finally, we intend for DR15 to mark the first release of the “Marvin” ecosystem which includes powerful python tools for seamlessly downloading and querying the MaNGA data as well as web interface that provides advanced search functionality, an user interface to the MaNGA datacubes, and the ability to quickly choose and display maps of key quantities measured by the DAP.

For eBOSS, future data releases will include the ELG survey results as well as the continuation of the LRG-QSO surveys. They will also include further value added catalogues: in particular the continuation of the quasar catalogue, a detailed ELG catalogue, as well as large scale structure clustering catalogues required for independent clustering analysis. Further improvement on the redshift measurement and spectral classification catalogue is also likely.

For TDSS, a future SDSS data release will include very recent spectra from its Repeat Quasar Spectroscopy (RQS) program, which obtains multi-epoch spectra for thousands of known quasars, **all of which have** least one epoch of SDSS spectroscopy available (and often already archived). Quasar spectral variability on multi-year timescales is **currently poorly** characterized for large samples **although** there are many exciting results from smaller select subsets (see Runnoe et al. 2016 and McGraw et al. 2017 for examples of studies based on repeat spectroscopy, ranging from discoveries of new changing look quasars, to **broad absorption line or BAL** emergence and disappearance). The RQS program in TDSS will ultimately observe  $\sim 10^4$  known (SDSS) quasars in the ELG survey region (Raichoor et al. 2017) adding at least one additional spectral epoch. This will allow for an extension of earlier work to a systematic investigation of quasar spectroscopic variability, both by making a larger sample, but also by including large numbers of

quasars as targets for repeat spectra that were selected without *a priori* knowledge of their specific quasar spectroscopic sub-class or variability properties. A recent detailed technical description of target selection for all of the TDSS repeat spectroscopy programs (including RQS), may be found in MacLeod et al. (2017).

For SPIDERS, future data releases will focus on higher-level data products, such as black hole masses and host galaxy properties of the X-ray AGN, as well as rich characterization of the X-ray selected clusters (in particular, dynamical properties and calibrated cluster masses). The first spectra of counterparts of eROSITA sources, however, will only be obtained beginning in Spring 2019, so they will be part of DR18 and subsequent releases only.

Planning has begun for the SDSS-V project, to begin in 2020 (Kollmeier et al. 2017). SDSS-V will build on the SDSS infrastructure and expand the instrumentation (especially for optical IFU spectroscopy) in both hemispheres. This expansion of SDSS’s legacy will enable an enormous sample of millions of spectra of quasars, galaxies, and stars, with scientific goals ranging from the growth of supermassive black holes to the detailed architecture of planetary systems and the astrophysics of stellar interiors.

## 8. ACKNOWLEDGEMENTS

We would like to thank the University of St Andrews, Scotland for their hospitality during DocuCeilidh 2017.

Funding for the Sloan Digital Sky Survey IV has been provided by the Alfred P. Sloan Foundation, the U.S. Department of Energy Office of Science, and the Participating Institutions. SDSS-IV acknowledges support and resources from the Center for High-Performance Computing at the University of Utah. The SDSS web site is [www.sdss.org](http://www.sdss.org).

SDSS-IV is managed by the Astrophysical Research Consortium for the Participating Institutions of the SDSS Collaboration including the Brazilian Participation Group, the Carnegie Institution for Science, Carnegie Mellon University, the Chilean Participation Group, the French Participation Group, Harvard-Smithsonian Center for Astrophysics, Instituto de Astrofísica de Canarias, The Johns Hopkins University, Kavli Institute for the Physics and Mathematics of the Universe (IPMU) / University of Tokyo, Lawrence Berkeley National Laboratory, Leibniz Institut für Astrophysik Potsdam (AIP), Max-Planck-Institut für Astronomie (MPIA Heidelberg), Max-Planck-Institut für Astrophysik (MPA Garching), Max-Planck-Institut für Extraterrestrische Physik (MPE), National Astronomical Observatories of China, New Mexico State University, New York University, University of Notre Dame, Observatório Nacional / MCTI, The Ohio State University, Pennsylvania State University, Shanghai Astronomical Observatory, United Kingdom Participation Group, Universidad Nacional Autónoma de México, University of Arizona, University of Colorado Boulder, University of Oxford, University of Portsmouth, University of Utah, University of Virginia, University of Washington, University of Wisconsin, Vanderbilt University, and Yale University.

## REFERENCES

- Abazajian, K. N., Adelman-McCarthy, J. K., Agüeros, M. A., et al. 2009, ApJS, 182, 543
- Albrecht, A., Bernstein, G., Cahn, R., et al. 2006, ArXiv Astrophysics e-prints
- Aghamousa, A., Aguilar, J., et al. 2016a, arXiv:1611.00036 (DESI Collaboration)
- Aghamousa, A., Aguilar, J., et al. 2016b, arXiv:1611.00037 (DESI Collaboration)
- Ahn, C. P., Alexandroff, R., Allende Prieto, C., et al. 2012, ApJS, 203, 21
- Aihara, H., et al. 2011, ApJS, 193, 29
- Alam, S. et al. 2015, ApJS, 219, 12
- Albareti, F. D., Allende Prieto, C., et al. 2017, ApJS submitted (arXiv:1608.02013; DR13)
- Altmann, M., Roeser, S., Demleitner, M., Bastian, U., & Schilbach, E. 2017, A&A, 600, L4
- Ata, M., Baumgarten, F., Bautista, J., et al. 2017, arXiv:1705.06373
- Barrera-Ballesteros, J. K., Heckman, T. M., Zhu, G. B., et al. 2016, MNRAS, 463, 2513
- Barrera-Ballesteros, J. K., Sánchez, S. F., Heckman, T., & Blanc, G. A. 2017, ApJ in press (arXiv:1706.09893)
- Bautista, J. E., Busca, N. G., Guy, J., et al. 2017, arXiv:1702.00176
- Belfiore, F., Maiolino, R., Tremonti, C., et al. 2017, MNRAS, 469, 151
- Bershady, M. A., Verheijen, M. A. W., Swaters, R. A., et al. 2010, ApJ, 716, 198
- Bizyaev, D., Walterbos, R. A. M., Yoachim, P., et al. 2017, ApJ, 839, 87
- Blake, C., Davis, T., Poole, G. B., et al. 2011, MNRAS, 415, 2892
- Blanton, M. R., Bershady, M. A., Abolfathi, B., et al. 2017, AJ, 154, 28
- Boller, T., Freyberg, M. J., Trümper, J., et al. 2016, A&A, 588, A103
- Bovy, J., Nidever, D. L., Rix, H.-W., et al. 2014, ApJ, 790, 127
- Bryant, J. J., Owers, M. S., Robotham, A. S. G., et al. 2015, MNRAS, 447, 2857
- Bundy, K., et al. 2015, ApJ, 798, 7
- Cannon, A. J., & Pickering, E. C. 1918, Annals of Harvard College Observatory, 91, 1
- Cano-Díaz, M., Sánchez, S. F., Zibetti, S., et al. 2016, ApJ, 821, L26
- Cappellari, M., Emsellem, E., Krajnović, D., et al. 2011, MNRAS, 413, 813
- Casey, A. R., Hogg, D. W., Ness, M., et al. 2016, arXiv:1603.03040
- Chevallier, M., & Polarski, D. 2001, International Journal of Modern Physics D, 10, 213
- Chojnowski, S. D., et al. 2017, arXiv:1708.00155
- Colless, M., Peterson, B. A., Jackson, C., et al. 2003, arXiv:astro-ph/0306581
- Comparat, J., Delubac, T., Jouvel, S., et al. 2016, A&A, 592, A121
- Clerc, N., Merloni, A., Zhang, Y.-Y., et al. 2016, MNRAS, 463, 4490
- da Cunha, E., Hopkins, A. M., Colless, M., et al. 2017, PASA, 34, e047
- Dalcanton, J. J., Williams, B. F., Seth, A. C., et al. 2009, ApJS, 183, 67
- Dawson, K. S., Schlegel, D. J., Ahn, C. P., et al. 2013, AJ, 145, 10
- Dawson, K., et al. 2016, AJ, 151, 44
- Delubac, T., Bautista, J. E., Busca, N. G., et al. 2015, A&A, 574, A59
- Delubac, T., Raichoor, A., Comparat, J., et al. 2017, MNRAS, 465, 1831
- Dwelly, T., Salvato, M., Merloni, A., et al. 2017, MNRAS, 469, 1065
- Eisenstein, D. J., Weinberg, D. H., Agol, E., et al. 2011, AJ, 142, 72
- Frieman, J. A., Bassett, B., Becker, A., et al. 2008, AJ, 135, 338
- Goddard, D., Thomas, D., Maraston, C., et al. 2017, MNRAS, 466, 4731
- Grier, C. J., Trump, J. R., Shen, Y., et al. 2017, ApJ, submitted
- Gu, M., Conroy, C., Law, D., et al. 2017, ApJ submitted, arXiv:1709.07003
- Gunn, J. E., Carr, M., Rockosi, C., et al. 1998, AJ, 116, 3040
- Gunn et al 2006, AJ 131, 2332
- Holtzman, J. A., Shetrone, M., Johnson, J. A., et al. 2015, AJ, 150, 148
- Holtzman et al., in prep
- Hutchinson, T. A., Bolton, A. S., Dawson, K. S., et al. 2016, AJ, 152, 205
- Ibarra-Medel, H. J., Sánchez, S. F., Avila-Reese, V., et al. 2016, MNRAS, 463, 2799
- Jansen, F., Lumb, D., Altieri, B., et al. 2001, A&A, 365, L1
- Jensen, T. W., Vivek, M., Dawson, K. S., et al. 2016, ApJ, 833, 199
- Jones, A., Kauffmann, G., D'Souza, R., et al. 2017, A&A, 599, A141
- Kaiser, N., Aussel, H., Burke, B. E., et al. 2002, Proc. SPIE, 4836, 154
- Kollmeier, J. A., Zasowski, G., Rix, H.-W., et al. 2017, arXiv:1711.03234
- LaMassa, S. M., Urry, C. M., Cappelluti, N., et al. 2016, ApJ, 817, 172
- Laureijs, R., Amiaux, J., Arduini, S., et al. 2011, arXiv:1110.3193
- Law, D. R., Yan, R., Bershady, M. A., et al. 2015, AJ, 150, 19
- Law, D. R., Cherinka, B., Yan, R., et al. 2016, AJ, 152, 83
- Li, N., & Thakar, A. R. 2008, Computing in Science and Engineering, 10, 18
- Lin, L., Lin, J.-H., Hsu, C.-H., et al. 2017, ApJ, 837, 32
- Linder, E., & SNAP Collaboration 2002, Bulletin of the American Astronomical Society, 34, 97.02
- MacLeod, C. L., Green, P. J., Anderson, S. F., et al. 2017, arXiv:1706.04240
- Madrid, J. P., & Macchietto, D. 2009, BAAS, 41, 913
- Majewski, S. R., Schiavon, R. P., Frinchaboy, P. M., et al. 2017, AJ, submitted, arXiv:1509.05420
- Margala, D., Kirby, D., Dawson, K., et al. 2016, ApJ, 831, 157
- McGraw, S. M., Brandt, W. N., Grier, C. J., et al. 2017, MNRAS, 469, 3163
- Morganson, E., Green, P. J., Anderson, S. F., et al. 2015, ApJ, 806, 244
- Myers, A. D., Palanque-Delabrouille, N., Prakash, A., et al. 2015, ApJS, 221, 27
- Nidever, D. L., Holtzman, J. A., Allende Prieto, C., et al. 2015, AJ, 150, 173
- Palanque-Delabrouille, N., Magneville, C., Yèche, C., et al. 2016, A&A, 587, A41
- Páris, I., Petitjean, P., Ross, N. P., et al. 2017, A&A, 597, A79
- Prakash, A., Licquia, T. C., Newman, J. A., et al. 2016, ApJS, 224, 34
- Predehl, P., Andritschke, R., Becker, W., et al. 2014, Proc. SPIE, 9144, 91441T
- Queiroz et al. 2017 in prep.
- Raddick, M. Jordan, Ani R. Thakar, Alexander S. Szalay, & Rafael DC Santos. 2014, Computing in Science and Engineering 16, 22.
- Raddick, M. Jordan, Ani R. Thakar, Alexander S. Szalay, & Rafael DC Santos. 2014, Computing in Science and Engineering 16, 32.
- Raichoor, A., Comparat, J., Delubac, T., et al. 2016, A&A, 585, A50
- Raichoor, A., Comparat, J., Delubac, T., et al. 2017, MNRAS submitted (arXiv:1704.00338)
- Ruan, J. J., Anderson, S. F., Cales, S. L., et al. 2016, ApJ, 826, 188
- Runnoe, J. C., Cales, S., Ruan, J. J., et al. 2016, MNRAS, 455, 1691
- Sako, M., Bassett, B., Becker, A. C., et al. 2014, arXiv:1401.3317
- Sánchez, S. F., Kennicutt, R. C., Gil de Paz, A., et al. 2012, A&A, 538, A8
- Sánchez, S. F., Pérez, E., Sánchez-Blázquez, P., et al. 2016a, RMxAA, 52, 21
- Sánchez, S. F., Pérez, E., Sánchez-Blázquez, P., et al. 2016b, RMxAA, 52, 171
- Sánchez, S. F., Barrera-Ballesteros, J. K., Sánchez-Menguiano, L., et al. 2017a, MNRAS, 469, 2121

- Sánchez, S. F., Avila-Reese, V., Hernandez-Toledo, H., et al. 2017b, RMxAA submitted, arXiv:1709.05438
- Sánchez-Menguiano, L., Sánchez, S. F., Pérez, I., et al. 2016, A&A, 587, A70
- Santiago, B. X., Brauer, D. E., Anders, F., et al. 2016, A&A, 585, A42
- Saxton, R. D., Read, A. M., Esquej, P., et al. 2008, A&A, 480, 611
- Schultheis, M., Zasowski, G., Allende Prieto, C., et al. 2014, AJ, 148, 24
- Shen, Y., Brandt, W. N., Dawson, K. S., et al. 2015, ApJS, 216, 4
- Shen, Y., Horne, K., Grier, C. J., et al. 2016, ApJ, 818, 30
- Smeeth, S.A., et al. 2013, AJ, 146, 32
- Stoughton, C., Lupton, R. H., Bernardi, M., et al. 2002, AJ, 123, 485
- Thakar, A. R., Szalay, A., Fekete, G., & Gray, J. 2008, Computing in Science and Engineering, 10, 30
- Thakar, A. R. 2008, Computing in Science and Engineering, 10, 9
- Voges, W., Aschenbach, B., Boller, T., et al. 1999, A&A, 349, 389
- Wake, D. A., Bundy, K., Diamond-Stanic, A. M., et al. 2017, arXiv:1707.02989
- Wang, J., Shi, J., Pan, K., et al. 2016, MNRAS, 460, 3179
- Weijmans, A.-M., & MaNGA Team 2016, Multi-Object Spectroscopy in the Next Decade: Big Questions, Large Surveys, and Wide Fields, 507, 257 (arXiv:1508.04314)
- Weijmans, A.-M., Blanton, M., Bolton, A. S., et al. 2016, arXiv:1612.05668
- Wilkinson, D. M., Maraston, C., Thomas, D., et al. 2015, MNRAS, 449, 328
- Wilkinson, D. M., et al. 2017, MNRAS, in press.
- Wylezalek, D., Schnorr Müller, A., Zakamska, N. L., et al. 2017, MNRAS, 467, 2612
- Yan, R., Bundy, K., Law, D. R., et al. 2016a, AJ, 152, 197
- Yan, R., Tremonti, C., Bershady, M. A., et al. 2016b, AJ, 151, 8
- Yan, R., & the MaStar Team 2017, Conference proceeding for the International Workshop on Spectral Stellar Libraries held in Campos de Jordao, SP, Brazil in February 2017 arXiv:1708.04688
- Yanny, B., Rockosi, C., Newberg, H. J., et al. 2009, AJ, 137, 4377-4399
- York, D.G., et al. 2000, AJ, 120, 1579
- Zacharias, N., Finch, C. T., Girard, T. M., et al. 2013, AJ, 145, 44
- Zasowski, G., Cohen, R. E., Chojnowski, S. D., et al. 2017, arXiv:1708.00155
- Zhao, G.-B., Wang, Y., Ross, A. J., et al. 2016, MNRAS, 457, 2377
- Zhu, G. B., Barrera-Ballesteros, J. K., Heckman, T. M., et al. 2017, MNRAS, 468, 4494

# Referências Bibliográficas

- [1] ANTONUCCI, R. Unified models for active galactic nuclei and quasars. **Annual Review of Astronomy and Astrophysics**, v. 31, p. 473–521, 1993.
- [2] BAÑADOS, EDUARDO, CARILLI, CHRIS, WALTER, FABIAN, MOMJIAN, EMMANUEL, DECARLI, ROBERTO, FARINA, EMANUELE P., MAZZUCHELLI, CHIARA, VENEMANS, BRAM P. A Powerful Radio-loud Quasar at the End of Cosmic Reionization. **Astrophysical Journal**, v. 861, n. 2, p. L14, Jul 2018.
- [3] BALDWIN, PHILLIPS & TERLEVICH , . Classification parameters for the emission-line spectra of extragalactic objects. **Publications of the Astronomical Society of the Pacific**, v. 93, p. 5–19, February 1981.
- [4] BARBOSA, F. K. B., STORCHI-BERGMANN, T., MCGREGOR, P., VALE, T. B., ROGEMAR RIFFEL, A. Modelling the [Fe II]  $\lambda 1.644 \mu\text{m}$  outflow and comparison with H<sub>2</sub> and H<sup>+</sup> kinematics in the inner 200 pc of NGC 1068. **Monthly Notices of the Royal Astronomical Society**, v. 445, p. 2353–2370, December 2014.
- [5] BELFIORE, F., MAIOLINO, R., BUNDY, K., THOMAS, D., MARASTON, C., WILKINSON, D., SÁNCHEZ, S. F., BERSHADY, M., BLANC, G. A., BOTHWELL, M., CALES, S. L., COCCATO, L., DRORY, N., EMSELLEM, E., FU, H., GELFAND, J., LAW, D., MASTERS, K., PAREJKO, J., TREMONTI, C., WAKE, D., WEIJMANS, A., YAN, R., XIAO, T., ZHANG, K., ZHENG, T., BIZYAEV, D., KINEMUCHI, K., ORAVETZ, D., SIMMONS, A. P-MaNGA Galaxies: emission-lines properties - gas ionization and chemical abundances from prototype observations. **Monthly Notices of the Royal Astronomical Society**, v. 449, p. 867–900, May 2015.

- [6] BENNERT, N., FALCKE, H., SCHULZ, H., WILSON, A. S., WILLS, B. J. Size and Structure of the Narrow-Line Region of Quasars. **Astrophysical Journal Letters**, v. 574, p. L105–L109, August 2002.
- [7] BENNERT, N., JUNGWIERT, B., KOMOSSA, S., HAAS, M., CHINI, R. Size and properties of the narrow-line region in Seyfert-1 galaxies from spatially-resolved optical spectroscopy. **Astronomy and Astrophysics**, v. 459, p. 55–69, November 2006.
- [8] BERG, D. A., SKILLMAN, E. D., MARBLE, A. R. Re-examining High Abundance Sloan Digital Sky Survey Mass-Metallicity Outliers: High N/O, Evolved Wolf-Rayet Galaxies? **Astrophysical Journal**, v. 738, p. 2, September 2011.
- [9] BISCHETTI, M., PICONCELLI, E., VIETRI, G., BONGIORNO, A., FIORE, F., SANI, E., MARCONI, A., DURAS, F., ZAPPACOSTA, L., BRUSA, M., COMASTRI, A., CRESCI, G., FERUGLIO, C., GIALLONGO, E., LA FRANCA, F., MAINIERI, V., MANNUCCI, F., MARTOCCHIA, S., RICCI, F., SCHNEIDER, R., TESTA, V., VIGNALI, C. The WISSH quasars project. I. Powerful ionised outflows in hyper-luminous quasars. **Astronomy and Astrophysics**, v. 598, p. A122, February 2017.
- [10] BORDALO, V., PLANAS, H., TELLES, E. The Internal Kinematics of the H II Galaxy II Zw 40. **Astrophysical Journal**, v. 696, p. 1668–1682, May 2009.
- [11] BRUSA, M., BONGIORNO, A., CRESCI, G., PERNA, M., MARCONI, A., MAINIERI, V., MAIOLINO, R., SALVATO, M., LUSSO, E., SANTINI, P., COMASTRI, A., FIORE, F., GILLI, R., LA FRANCA, F., LANZUISI, G., LUTZ, D., MERLONI, A., MIGNOLI, M., ONORI, F., PICONCELLI, E., ROSARIO, D., VIGNALI, C., ZAMORANI, G. X-shooter reveals powerful outflows in  $z \gtrsim 1.5$   $X-ray selected obscured quasi-stellar objects$ . **Monthly Notices of the Royal Astronomical Society**, v. 446, p. 2394 – 2417, January 2015.
- [12] BRUSA, M., CRESCI, G., DADDI, E., PALADINO, R., PERNA, M., BONGIORNO, A., LUSSO, E., SARGENT, M. T., CASASOLA, V., FERUGLIO, C., FRATERNALI, F., GEORGIEV, I., MAINIERI, V., CARNIANI, S., COMASTRI, A., DURAS, F., FIORE, F., MANNUCCI, F., MARCONI, A., PICONCELLI, E., ZAMORANI, G., GILLI, R., LA FRANCA, F., LANZUISI, G., LUTZ, D., SANTINI, P., SCOVILLE, N. Z., VIGNALI, C., VITO, F.,

RABIEN, S., BUSONI, L., BONAGLIA, M. Molecular outflow and feedback in the obscured quasar XID2028 revealed by ALMA. **Astronomy and Astrophysics**, v. 612, p. A29, April 2018.

- [13] BUNDY, K., BERSHADY, M. A., LAW, D. R., YAN, R., DRORY, N., MACDONALD, N., WAKE, D. A., CHERINKA, B., SÁNCHEZ-GALLEGO, J. R., WEIJMANS, A.-M., THOMAS, D., TREMONTI, C., MASTERS, K., COCCATO, L., DIAMOND-STANIC, A. M., ARAGÓN-SALAMANCA, A., AVILA-REESE, V., BADENES, C., FALCÓN-BARROSO, J., BELFIORE, F., BIZYAEV, D., BLANC, G. A., BLAND-HAWTHORN, J., BLANTON, M. R., BROWNSTEIN, J. R., BYLER, N., CAPPELLARI, M., CONROY, C., DUTTON, A. A., EMSELLEM, E., ETHERINGTON, J., FRINCHABOY, P. M., FU, H., GUNN, J. E., HARDING, P., JOHNSTON, E. J., KAUFFMANN, G., KINEMUCHI, K., KLAENE, M. A., KNAPEN, J. H., LEAUTAUD, A., LI, C., LIN, L., MAIOLINO, R., MALANUSHENKO, V., MALANUSHENKO, E., MAO, S., MARASTON, C., MCDERMID, R. M., MERRIFIELD, M. R., NICHOL, R. C., ORAVETZ, D., PAN, K., PARJEJKO, J. K., SANCHEZ, S. F., SCHLEGEL, D., SIMMONS, A., STEELE, O., STEINMETZ, M., THANJAVUR, K., THOMPSON, B. A., TINKER, J. L., VAN DEN BOSCH, R. C. E., WESTFALL, K. B., WILKINSON, D., WRIGHT, S., XIAO, T., ZHANG, K. Overview of the SDSS-IV MaNGA Survey: Mapping nearby Galaxies at Apache Point Observatory. **Astrophysical Journal**, v. 798, p. 7, January 2015.
- [14] CANO-DÍAZ, M., MAIOLINO, R., MARCONI, A., NETZER, H., SHEMMER, O., CRESCI, G. Observational evidence of quasar feedback quenching star formation at high redshift. **Astronomy and Astrophysics**, v. 537, p. L8, January 2012.
- [15] CARNIANI, S., MARCONI, A., MAIOLINO, R., BALMAVERDE, B., BRUSA, M., CANO-DÍAZ, M., CICONE, C., COMASTRI, A., CRESCI, G., FIORE, F., FERUGLIO, C., LA FRANCA, F., MAINIERI, V., MANNUCCI, F., NAGAO, T., NETZER, H., PICONCELLI, E., RISALITI, G., SCHNEIDER, R., SHEMMER, O. Ionised outflows in  $z \sim 2.4$  quasar host galaxies. **Astronomy and Astrophysics**, v. 580, p. A102, August 2015.
- [16] CARNIANI, S., MARCONI, A., MAIOLINO, R., BALMAVERDE, B., BRUSA, M., CANO-DÍAZ, M., CICONE, C., COMASTRI, A., CRESCI, G., FIORE,

- F., FERUGLIO, C., LA FRANCA, F., MAINIERI, V., MANNUCCI, F., NAGAO, T., NETZER, H., PICONCELLI, E., RISALITI, G., SCHNEIDER, R., SHEMMER, O. Fast outflows and star formation quenching in quasar host galaxies. **Astronomy and Astrophysics**, v. 591, p. A28, June 2016.
- [17] CID FERNANDES, R., MATEUS, A., SODRÉ, L., STASIŃSKA, G., GOMES, J. M. Semi-empirical analysis of Sloan Digital Sky Survey galaxies - I. Spectral synthesis method. **Monthly Notices of the Royal Astronomical Society**, v. 358, p. 363–378, April 2005.
- [18] CID FERNANDES, R., STASIŃSKA, G., MATEUS, A., VALE ASARI, N. A comprehensive classification of galaxies in the Sloan Digital Sky Survey: how to tell true from fake AGN? **Monthly Notices of the Royal Astronomical Society**, v. 413, p. 1687–1699, May 2011.
- [19] CID FERNANDES, R., STASIŃSKA, G., SCHLICKMANN, M. S., MATEUS, A., VALE ASARI, N., SCHOENELL, W., SODRÉ, L. Alternative diagnostic diagrams and the ‘forgotten’ population of weak line galaxies in the SDSS. **Monthly Notices of the Royal Astronomical Society**, v. 403, p. 1036–1053, April 2010.
- [20] CRESCI, G., MAINIERI, V., BRUSA, M., MARCONI, A., PERNA, M., MANNUCCI, F., PICONCELLI, E., MAIOLINO, R., FERUGLIO, C., FIORE, F., BONGIORNO, A., LANZUISI, G., MERLONI, A., SCHRAMM, M., SILVERMAN, J. D., CIVANO, F. Blowin’ in the Wind: Both “Negative” and “Positive” Feedback in an Obscured High-z Quasar. **Astrophysical Journal**, v. 799, p. 82, January 2015.
- [21] CROTON, D. J., SPRINGEL, V., WHITE, S. D. M., DE LUCIA, G., FRENK, C. S., GAO, L., JENKINS, A., KAUFFMANN, G., NAVARRO, J. F., YOSHIDA, N. The many lives of active galactic nuclei: cooling flows, black holes and the luminosities and colours of galaxies. **Monthly Notices of the Royal Astronomical Society**, v. 365, p. 11–28, January 2006.
- [22] DAVIES, R. I., MACIEJEWSKI, W., HICKS, E. K. S., TACCONI, L. J., GENZEL, R., ENGEL, H. Stellar and Molecular Gas Kinematics Of NGC 1097: Inflow Driven by a Nuclear Spiral. **Astrophysical Journal**, v. 702, p. 114–128, September 2009.

- [23] DAVIES, R. L., KEWLEY, L. J., HO, I.-T., DOPITA, M. A. Starburst-AGN mixing - II. Optically selected active galaxies. **Monthly Notices of the Royal Astronomical Society**, v. 444, p. 3961–3974, November 2014.
- [24] DEHARVENG, L., PEÑA, M., CAPLAN, J., COSTERO, R. Oxygen and helium abundances in Galactic Hii regions - II. Abundance gradients. **Monthly Notices of the Royal Astronomical Society**, v. 311, p. 329–345, January 2000.
- [25] DEMPSEY & ZAKAMSKA, . The size-luminosity relationship of quasar narrow-line regions. **Monthly Notices of the Royal Astronomical Society**, v. 477, p. 4615–4626, July 2018.
- [26] DHANDA BATRA & BALDWIN, J. A. The Metallicities of the Broad Emission Line Regions in the Nitrogen-Loudest Quasars. **arXiv e-prints**, January 2014.
- [27] DI MATTEO, T., COLBERG, J., SPRINGEL, V., HERNQUIST, L., SIJACKI, D. Direct Cosmological Simulations of the Growth of Black Holes and Galaxies. **Astrophysical Journal**, v. 676, p. 33–53, March 2008.
- [28] DI MATTEO, T., SPRINGEL, V., HERNQUIST, L. Energy input from quasars regulates the growth and activity of black holes and their host galaxies. **Nature**, v. 433, p. 604–607, February 2005.
- [29] DIAMOND-STANIC, A. M., RIEKE, G. H. The Relationship between Black Hole Growth and Star Formation in Seyfert Galaxies. **Astrophysical Journal**, v. 746, p. 168, February 2012.
- [30] DÍAZ, A. I., PÉREZ-MONTERO, E. An empirical calibration of nebular abundances based on the sulphur emission lines. **Monthly Notices of the Royal Astronomical Society**, v. 312, p. 130–138, February 2000.
- [31] DO NASCIMENTO, JANAÍNA C., STORCHI-BERGMANN, THAISA, MALLMANN, NÍCOLAS D., RIFFEL, ROGÉRIO, ILHA, GABRIELE S., RIFFEL, ROGEMAR A., REMBOLD, SANDRO B. The gas metallicities in nearby manga agn, August 2020.
- [32] DO NASCIMENTO, JANAÍNA C., STORCHI-BERGMANN, THAISA, MALLMANN, NÍCOLAS D., RIFFEL, ROGÉRIO, ILHA, GABRIELE S., RIFFEL,

ROGEMAR A., REMBOLD, SANDRO B., SCHIMOIA, JÁDERSON, DA COSTA, LUIZ NICOLACI, MAIA, MARCIO A. G., MACHADO, ALICE D. The first 62 AGN observed with SDSS-IV MaNGA - IV. Gas excitation and star formation rate distributions. **Monthly Notices of the Royal Astronomical Society**, v. 486, n. 4, p. 5075–5093, Jul 2019.

- [33] DOPITA, M. A., GROVES, B. A., SUTHERLAND, R. S., BINETTE, L., CECIL, G. Are the Narrow-Line Regions in Active Galaxies Dusty and Radiation Pressure Dominated? **Astrophysical Journal**, v. 572, p. 753–761, June 2002.
- [34] DORS & COPETTI, . Abundance gradients in a sample of barred spiral galaxies. **Astronomy and Astrophysics**, v. 437, p. 837–847, July 2005.
- [35] DORS, O. L., CARDACI, M. V., HÄGELE, G. F., RODRIGUES, I., GREBEL, E. K., PILYUGIN, L. S., FREITAS-LEMES, P., KRABBE, A. C. On the central abundances of active galactic nuclei and star-forming galaxies. **Monthly Notices of the Royal Astronomical Society**, v. 453, p. 4102–4111, November 2015.
- [36] DORS, O. L., JR., ARELLANO-CÓRDOVA, K. Z., CARDACI, M. V., HÄGELE, G. F. New quantitative nitrogen abundance estimations in a sample of Seyfert 2 active galactic nuclei. **Monthly Notices of the Royal Astronomical Society**, v. 468, p. L113–L117, June 2017.
- [37] DRESSLER, A., RICHSTONE, D. O. Stellar dynamics in the nuclei of M31 and M32 - Evidence for massive black holes? **Astrophysical Journal**, v. 324, p. 701–713, January 1988.
- [38] EISENSTEIN, D. J., WEINBERG, D. H., AGOL, E., AIHARA, H., ALLENDE PRIETO, C., ANDERSON, S. F., ARNS, J. A., AUBOURG, É., BAILEY, S., BALBINOT, E., ET . SDSS-III: Massive Spectroscopic Surveys of the Distant Universe, the Milky Way, and Extra-Solar Planetary Systems. **Astronomical Journal**, v. 142, p. 72, September 2011.
- [39] ESQUEJ, P., ALONSO-HERRERO, A., GONZÁLEZ-MARTÍN, O., HÖNIG, S. F., HERNÁN-CABALLERO, A., ROCHE, P., RAMOS ALMEIDA, C., MASON, R. E., DÍAZ-SANTOS, T., LEVENSON, N. A., ARETXAGA, I., RODRÍGUEZ ESPINOSA, J. M., PACKHAM, C. Nuclear Star Formation

Activity and Black Hole Accretion in Nearby Seyfert Galaxies. **The Astrophysical Journal**, v. 780, n. 1, p. 86, Jan 2014.

- [40] FABIAN, A. C. Observational Evidence of Active Galactic Nuclei Feedback. **Annual Review of Astronomy and Astrophysics**, v. 50, p. 455–489, September 2012.
- [41] FAUCHER-GIGUÈRE & QUATAERT, . The physics of galactic winds driven by active galactic nuclei. **Monthly Notices of the Royal Astronomical Society**, v. 425, p. 605–622, September 2012.
- [42] FELTRE, CHARLOT & GUTKIN, J. Nuclear activity versus star formation: emission-line diagnostics at ultraviolet and optical wavelengths. **Monthly Notices of the Royal Astronomical Society**, v. 456, p. 3354–3374, March 2016.
- [43] FERLAND, GARY J., BALDWIN, JACK A., KORISTA, KIRK T., HAMANN, FRED, CARSWELL, R. F., PHILLIPS, MARK, WILKES, BELINDA, WILLIAMS, ROBERT E. High Metal Enrichments in Luminous Quasars. **Astrophysical Journal**, v. 461, p. 683, Apr 1996.
- [44] FERRARESE, L., FORD, H. Supermassive Black Holes in Galactic Nuclei: Past, Present and Future Research. **Space Science Reviews**, v. 116, p. 523–624, February 2005.
- [45] FERRARESE, L., MERRITT, D. A Fundamental Relation between Supermassive Black Holes and Their Host Galaxies. **Astrophysical Journal Letters**, v. 539, p. L9–L12, August 2000.
- [46] FERUGLIO, C., FERRARA, A., BISCHETTI, M., DOWNES, D., NERI, R., CECCARELLI, C., CICONE, C., FIORE, F., GALLERANI, S., MAIOLINO, R., MENCI, N., PICONCELLI, E., VIETRI, G., VIGNALI, C., ZAPPACOSTA, L. On the discovery of fast molecular gas in the UFO/BAL quasar APM 08279+5255 at  $z = 3.912$ . **Astronomy and Astrophysics**, v. 608, p. A30, December 2017.
- [47] FISCHER, T. C., KRAEMER, S. B., SCHMITT, H. R., LONGO MIC-CHI, L. F., CRENSHAW, D. M., REVALSKI, M., VESTERGAARD, M., ELVIS, M., GASKELL, C. M., HAMANN, F., HO, L. C., HUTCHINGS, J., MUSHOTZKY, R., NETZER, H., STORCHI-BERGMANN, T.,

STRAUGHN, A., TURNER, T. J., WARD, M. J. Hubble Space Telescope Observations of Extended [O III] $\lambda$  5007 Emission in Nearby QSO2s: New Constraints on AGN Host Galaxy Interaction. **Astrophysical Journal**, v. 856, p. 102, April 2018.

- [48] FRANK, J., KING, A., RAINES, D. J. **Accretion Power in Astrophysics: Third Edition**: January 2002.
- [49] FU, H. & STOCKTON, A. Extended Emission-Line Regions: Remnants of Quasar Superwinds? **Astrophysical Journal**, v. 690, p. 953–973, January 2009.
- [50] FUKUGITA, M., ICHIKAWA, T., GUNN, J. E., DOI, M., SHIMASAKU, K., SCHNEIDER, D. P. The Sloan Digital Sky Survey Photometric System. **Astronomical Journal**, v. 111, p. 1748, April 1996.
- [51] GEBHARDT, K., BENDER, R., BOWER, G., DRESSLER, A., FABER, S. M., FILIPPENKO, A. V., GREEN, R., GRILLMAIR, C., HO, L. C., KORMENDY, J., LAUER, T. R., MAGORRIAN, J., PINKNEY, J., RICHSTONE, D., TREMAINE, S. A Relationship between Nuclear Black Hole Mass and Galaxy Velocity Dispersion. **Astrophysical Journal Letters**, v. 539, p. L13–L16, August 2000.
- [52] GREENE, J., STORCHI-BERGMANN, T., KOCEVSKI, D., SCHRAMM, M., HECKMAN, T., RIFFEL, R. A. MaNGA auxiliary proposal: Targeting luminous AGN with MaNGA, August 2014.
- [53] GREENE, JENNIFER E., ZAKAMSKA, NADIA L., HO, LUIS C., BARTH, AARON J. FEEDBACK IN LUMINOUS OBSCURED QUASARS. **The Astrophysical Journal**, v. 732, n. 1, p. 9, apr 2011.
- [54] GROVES, B. A., DOPITA, M. A., SUTHERLAND, R. S. Dusty, Radiation Pressure-Dominated Photoionization. I. Model Description, Structure, and Grids. **Astrophysical Journal Supplement Series**, v. 153, p. 9–73, July 2004a.
- [55] GROVES, B. A., DOPITA, M. A., SUTHERLAND, R. S. Dusty, Radiation Pressure-Dominated Photoionization. II. Multiwavelength Emission Line Diagnostics for Narrow-Line Regions. **Astrophysical Journal Supplement Series**, v. 153, p. 75–91, July 2004b.

- [56] GUNN, J. E., SIEGMUND, W. A., MANNERY, E. J., OWEN, R. E., HULL, C. L., LEGER, R. F., CAREY, L. N., KNAPP, G. R., YORK, D. G., BOROSKI, W. N., KENT, S. M., LUPTON, R. H., ROCKOSI, C. M., EVANS, M. L., WADDELL, P., ANDERSON, J. E., ANNIS, J., BARENTINE, J. C., BARTOSZEK, L. M., BASTIAN, S., BRACKER, S. B., BREWINGTON, H. J., BRIEGEL, C. I., BRINKMANN, J., BROWN, Y. J., CARR, M. A., CZARAPATA, P. C., DRENNAN, C. C., DOMBECK, T., FEDERWITZ, G. R., GILLESPIE, B. A., GONZALES, C., HANSEN, S. U., HARVANEK, M., HAYES, J., JORDAN, W., KINNEY, E., KLAENE, M., KLEINMAN, S. J., KRON, R. G., KRESINSKI, J., LEE, G., LIMMONGKOL, S., LINDENMEYER, C. W., LONG, D. C., LOOMIS, C. L., MCGEHEE, P. M., MANTSCH, P. M., NEILSEN, E. H., JR., NESWOLD, R. M., NEWMAN, P. R., NITTA, A., PEOPLES, J., JR., PIER, J. R., PRIETO, P. S., PROSAPIO, A., RIVETTA, C., SCHNEIDER, D. P., SNEDDEN, S., WANG, S.-I. The 2.5 m Telescope of the Sloan Digital Sky Survey. **Astronomical Journal**, v. 131, p. 2332–2359, April 2006.
- [57] HARMS, R. J., FORD, H. C., TSVETANOV, Z. I., HARTIG, G. F., DRESSEL, L. L., KRISS, G. A., BOHLIN, R., DAVIDSEN, A. F., MARGON, B., KOCHHAR, A. K. HST FOS spectroscopy of M87: Evidence for a disk of ionized gas around a massive black hole. **Astrophysical Journal Letters**, v. 435, p. L35–L38, November 1994.
- [58] HARRISON, C. M., ALEXANDER, D. M., MULLANEY, J. R., SWINBANK, A. M. Kiloparsec-scale outflows are prevalent among luminous AGN: outflows and feedback in the context of the overall AGN population. **Monthly Notices of the Royal Astronomical Society**, v. 441, p. 3306–3347, July 2014.
- [59] HECKMAN, T. M. Activity in the nuclei of normal galaxies. **Highlights of Astronomy**, v. 5, p. 185–190, 1980.
- [60] HICKS, E. K. S., DAVIES, R. I., MACIEJEWSKI, W., EMSELLEM, E., MALKAN, M. A., DUMAS, G., MÜLLER-SÁNCHEZ, F., RIVERS, A. Fueling Active Galactic Nuclei. I. How the Global Characteristics of the Central Kiloparsec of Seyferts Differ from Quiescent Galaxies. **Astrophysical Journal**, v. 768, p. 107, May 2013.
- [61] HIRSCHMANN, M., DOLAG, K., SARO, A., BACHMANN, L., BORGANI, S., BURKERT, A. Cosmological simulations of black hole growth: AGN lumi-

nosities and downsizing. **Monthly Notices of the Royal Astronomical Society**, v. 442, p. 2304–2324, August 2014.

- [62] HUSEMANN, B., SCHÄRWÄCHTER, J., BENNERT, V. N., MAINIERI, V., WOO, J.-H., KAKKAD, D. Large-scale outflows in luminous QSOs revisited. The impact of beam smearing on AGN feedback efficiencies. **Astronomy and Astrophysics**, v. 594, p. A44, October 2016.
- [63] ILHA, GABRIELE S., RIFFEL, ROGEMAR A., SCHIMOIA, JADERSON S., STORCHI-BERGMANN, THAISA, REMBOLD, SANDRO B., RIFFEL, ROGÉRIO, WYLEZALEK, DOMINIKA, SHI, YONG, DA COSTA, LUIZ N., MACHADO, ALICE D., LAW, DAVID R., BIZYAEV, DMITRY, MALLMANN, NICOLAS D., NASCIMENTO, JANAINA, MAIA, MARCIO A. G., CIROLINI, RAFAEL. The first 62 AGN observed with SDSS-IV MaNGA - III: stellar and gas kinematics. **Monthly Notices of the Royal Astronomical Society**, v. 484, n. 1, p. 252–268, Mar 2019.
- [64] KAKKAD, D., MAINIERI, V., PADOVANI, P., CRESCI, G., HUSEMANN, B., CARNIANI, S., BRUSA, M., LAMASTRA, A., LANZUISI, G., PICONCELLI, E., SCHRAMM, M. Tracing outflows in the AGN forbidden region with SINFONI. **Astronomy and Astrophysics**, v. 592, p. A148, August 2016.
- [65] KAUFFMANN, G., HECKMAN, T. M., TREMONTI, C., BRINCHMANN, J., CHARLOT, S., WHITE, S. D. M., RIDGWAY, S. E., BRINKMANN, J., FU-KUGITA, M., HALL, P. B., IVEZIĆ, Ž., RICHARDS, G. T., SCHNEIDER, D. P. The host galaxies of active galactic nuclei. **Monthly Notices of the Royal Astronomical Society**, v. 346, p. 1055–1077, December 2003.
- [66] KAWAKATU & WADA, K. Coevolution of Supermassive Black Holes and Circumnuclear Disks. **Astrophysical Journal**, v. 681, p. 73–83, July 2008.
- [67] KEEL, WILLIAM C., CHOJNOWSKI, S. DREW, BENNERT, VARDHA N., SCHAWINSKI, KEVIN, LINTOTT, CHRIS J., LYNN, STUART, PANCOAST, ANNA, HARRIS, CHELSEA, NIERENBERG, A. M., SONNENFELD, ALESSANDRO, PROCTOR, RICHARD. The Galaxy Zoo survey for giant AGN-ionized clouds: past and present black hole accretion events. **Monthly Notices of the Royal Astronomical Society**, v. 420, n. 1, p. 878–900, Feb 2012.

- [68] KENNICUTT, JR., ROBERT C. Star Formation in Galaxies Along the Hubble Sequence. **Annual Review of Astronomy and Astrophysics**, v. 36, p. 189–232, Jan 1998.
- [69] KEWLEY, L. J., DOPITA, M. A. Using Strong Lines to Estimate Abundances in Extragalactic H II Regions and Starburst Galaxies. **Astrophysical Journal Supplement Series**, v. 142, p. 35–52, September 2002.
- [70] KEWLEY, L. J., ELLISON, S. L. Metallicity Calibrations and the Mass-Metallicity Relation for Star-forming Galaxies. **Astrophysical Journal**, v. 681, p. 1183–1204, July 2008.
- [71] KEWLEY, L. J., GROVES, B., KAUFFMANN, G., HECKMAN, T. The host galaxies and classification of active galactic nuclei. **Monthly Notices of the Royal Astronomical Society**, v. 372, p. 961–976, November 2006.
- [72] KHACHIKIAN, E. E., WEEDMAN, D. W. A spectroscopic study of luminous galactic nuclei. **Astrofizika**, v. 7, p. 389–406, 1971.
- [73] KORMENDY, J., HO, L. C. Coevolution (Or Not) of Supermassive Black Holes and Host Galaxies. **Annual Review of Astronomy and Astrophysics**, v. 51, p. 511–653, August 2013.
- [74] LAW, D. R., CHERINKA, B., YAN, R., ANDREWS, B. H., BERSHADY, M. A., BIZYAEV, D., BLANC, G. A., BLANTON, M. R., BOLTON, A. S., BROWNSTEIN, J. R., BUNDY, K., CHEN, Y., DRORY, N., D’SOUZA, R., FU, H., JONES, A., KAUFFMANN, G., MACDONALD, N., MASTERS, K. L., NEWMAN, J. A., PAREJKO, J. K., SÁNCHEZ-GALLEGO, J. R., SÁNCHEZ, S. F., SCHLEGEL, D. J., THOMAS, D., WAKE, D. A., WEIJMANS, A.-M., WESTFALL, K. B., ZHANG, K. The Data Reduction Pipeline for the SDSS-IV MaNGA IFU Galaxy Survey. **Astronomical Journal**, v. 152, p. 83, October 2016.
- [75] LINTOTT, C., SCHAWINSKI, K., BAMFORD, S., SLOSAR, A., LAND, K., THOMAS, D., EDMONDSON, E., MASTERS, K., NICHOL, R. C., RADICK, M. J., SZALAY, A., ANDREESCU, D., MURRAY, P., VANDENBERG, J. Galaxy Zoo 1: data release of morphological classifications for nearly 900 000 galaxies. **Monthly Notices of the Royal Astronomical Society**, v. 410, p. 166–178, January 2011.

- [76] LIU, G., ZAKAMSKA, N. L., GREENE, J. E. Similarity of ionized gas nebulae around unobscured and obscured quasars. **Monthly Notices of the Royal Astronomical Society**, v. 442, p. 1303–1318, August 2014.
- [77] LIU, G., ZAKAMSKA, N. L., GREENE, J. E., NESVADBA, N. P. H., LIU, X. Observations of feedback from radio-quiet quasars - II. Kinematics of ionized gas nebulae. **Monthly Notices of the Royal Astronomical Society**, v. 436, p. 2576–2597, December 2013.
- [78] LÓPEZ-SÁNCHEZ & ESTEBAN, C. Massive star formation in Wolf-Rayet galaxies. IV. Colours, chemical-composition analysis and metallicity-luminosity relations. **Astronomy and Astrophysics**, v. 517, p. A85, July 2010.
- [79] LYNDEN-BELL, D. Galactic Nuclei as Collapsed Old Quasars. **Nature**, v. 223, p. 690–694, August 1969.
- [80] MACHADO, ALICE D.ET, A., ROGEMAR, ROGÉRIO ANDDO NASCIMENTO, JANAÍNA C. Ionized gas kinematics in nearby active galaxies: Velocity and extension of outflows, August 2019.
- [81] MAIOLINO, R., NAGAO, T., GRAZIAN, A., COCCHIA, F., MARCONI, A., MANNUCCI, F., CIMATTI, A., PIPINO, A., BALLERO, S., CALURA, F., CHIAPPINI, C., FONTANA, A., GRANATO, G. L., MATTEUCCI, F., PASTORINI, G., PENTERICCI, L., RISALITI, G., SALVATI, M., SILVA, L. AMAZE. I. The evolution of the mass-metallicity relation at  $z \geq 3$ . **Astronomy and Astrophysics**, v. 488, p. 463–479, September 2008.
- [82] MALLMANN, NÍCOLAS DULLIUS, RIFFEL, ROGÉRIO, STORCHI-BERGMANN, THAISA, REMBOLD, SANDRO BARBOZA, RIFFEL, ROGEMAR A., SCHIMOIA, JADERSON, DA COSTA, LUIZ NICOLACI, ÁVILA-REESE, VLADIMIR, SANCHEZ, SEBASTIAN F., MACHADO, ALICE D., CIROLINI, RAFAEL, ILHA, GABRIELE S., NASCIMENTO, JANAÍNA C. DO. The first 62 AGN observed with SDSS-IV MaNGA - II. Resolved stellar populations. **Monthly Notices of the Royal Astronomical Society**, v. 478, n. 4, p. 5491–5504, Aug 2018.
- [83] MARCONI, A., RISALITI, G., GILLI, R., HUNT, L. K., MAIOLINO, R., SALVATI, M. Local supermassive black holes, relics of active galactic nuclei and the X-ray background. **Monthly Notices of the Royal Astronomical Society**, v. 351, p. 169–185, June 2004.

- [84] MARTINI, PAUL, REGAN, MICHAEL W., MULCHAEY, JOHN S., POGGE, RICHARD W. Circumnuclear Dust in Nearby Active and Inactive Galaxies. II. Bars, Nuclear Spirals, and the Fueling of Active Galactic Nuclei. **The Astrophysical Journal**, v. 589, n. 2, p. 774–782, Jun 2003.
- [85] MCELROY, R., CROOM, S. M., PRACY, M., SHARP, R., HO, I.-T., MEDLING, A. M. IFU observations of luminous type II AGN - I. Evidence for ubiquitous winds. **Monthly Notices of the Royal Astronomical Society**, v. 446, p. 2186–2204, January 2015.
- [86] MENANTEAU, F., FORD, H. C., MOTTA, V., BENÍTEZ, N., MARTEL, A. R., BLAKESLEE, J. P., INFANTE, L. The Morphological Demographics of Galaxies in the Advanced Camera for Surveys Hubble Ultra Deep Parallel Fields. **Astronomical Journal**, v. 131, p. 208–215, January 2006.
- [87] MIYOSHI, M., MORAN, J., HERRNSTEIN, J., GREENHILL, L., NAKAI, N., DIAMOND, P., INOUE, M. Evidence for a black hole from high rotation velocities in a sub-parsec region of NGC4258. **Nature**, v. 373, p. 127–129, January 1995.
- [88] MOOS, H. W., SEMBACH, K. R., VIDAL-MADJAR, A., YORK, D. G., FRIEDMAN, S. D., HÉBRARD, G., KRUK, J. W., LEHNER, N., LEMOINE, M., SONNEBORN, G., WOOD, B. E., AKE, T. B., ANDRÉ, M., BLAIR, W. P., CHAYER, P., GRY, C., DUPREE, A. K., FERLET, R., FELDMAN, P. D., GREEN, J. C., HOWK, J. C., HUTCHINGS, J. B., JENKINS, E. B., LINSKY, J. L., MURPHY, E. M., OEGERLE, W. R., OLIVEIRA, C., ROTH, K., SAHNOW, D. J., SAVAGE, B. D., SHULL, J. M., TRIPP, T. M., WELLER, E. J., WELSH, B. Y., WILKINSON, E., WOODGATE, B. E. Abundances of Deuterium, Nitrogen, and Oxygen in the Local Interstellar Medium: Overview of First Results from the FUSE Mission. **The Astrophysical Journal Supplement Series**, v. 140, n. 1, p. 3–17, May 2002.
- [89] MULLANEY, J. R., DADDI, E., BÉTHERMIN, M., ELBAZ, D., JUNEAU, S., PANNELLA, M., SARGENT, M. T., ALEXANDER, D. M., HICKOX, R. C. The Hidden “AGN Main Sequence”: Evidence for a Universal Black Hole Accretion to Star Formation Rate Ratio since  $z \sim 2$  Producing an  $M_{BH}$ - $M_*$  Relation. **Astrophysical Journal Letters**, v. 753, p. L30, July 2012.

- [90] MUSHOTZKY, R. F., SHIMIZU, T. T., MELÉNDEZ, M., KOSS, M. Do Most Active Galactic Nuclei Live in High Star Formation Nuclear Cusps? **Astrophysical Journal Letters**, v. 781, p. L34, February 2014.
- [91] NENKOVA, M., IVEZIĆ, Ž., ELITZUR, M. Dust Emission from Active Galactic Nuclei. **Astrophysical Journal Letters**, v. 570, p. L9–L12, May 2002.
- [92] NETZER, H., SHEMMER, O., MAIOLINO, R., OLIVA, E., CROOM, S., CORBETT, E., DI FABRIZIO, L. Near-Infrared Spectroscopy of High-Redshift Active Galactic Nuclei. II. Disappearing Narrow-Line Regions and the Role of Accretion. **Astrophysical Journal**, v. 614, p. 558–567, October 2004.
- [93] OBIED, G., ZAKAMSKA, N. L., WYLEZALEK, D., LIU, G. Giant scattering cones in obscured quasars. **Monthly Notices of the Royal Astronomical Society**, v. 456, p. 2861–2876, March 2016.
- [94] OSTERBROCK & FERLAND, . **Astrophysics of gaseous nebulae and active galactic nuclei**: 2006.
- [95] PADOVANI, P., ALEXANDER, D. M., ASSEF, R. J., DE MARCO, B., GIOMMI, P., HICKOX, R. C., RICHARDS, G. T., SMOLČIĆ, V., HATZIMINAOGLOU, E., MAINIERI, V., SALVATO, M. Active galactic nuclei: what's in a name? **The Astronomy and Astrophysics Review**, v. 25, p. 2, August 2017.
- [96] PEREZ-MONTERO & DIAZ, . VizieR Online Data Catalog: Oxygen abundances of HII regions (Perez-Montero+, 2005). **VizieR Online Data Catalog**, v. 736, August 2005.
- [97] PÉREZ-MONTERO & CONTINI, . The impact of the nitrogen-to-oxygen ratio on ionized nebula diagnostics based on [NII] emission lines. **Monthly Notices of the Royal Astronomical Society**, v. 398, p. 949–960, September 2009.
- [98] PETERSON, B. M. **An Introduction to Active Galactic Nuclei**: An introduction to active galactic nuclei, Publisher: Cambridge, New York Cambridge University Press, 1997 Physical description xvi, 238 p. ISBN 0521473489, February 1997.
- [99] PETERSON, B. M., DENNEY, K. D., DE ROSA, G., GRIER, C. J., POGGE, R. W., BENTZ, M. C., KOCHANEK, C. S., VESTERGAARD, M., KILERCI-

ESER, E., DALLA BONTÀ, E., CIROI, S. The Size of the Narrow-line-emitting Region in the Seyfert 1 Galaxy NGC 5548 from Emission-line Variability. **Astrophysical Journal**, v. 779, p. 109, December 2013.

- [100] PETERSON, B. M., FERRARESE, L., GILBERT, K. M., KASPI, S., MALKAN, M. A., MAOZ, D., MERRITT, D., NETZER, H., ONKEN, C. A., POGGE, R. W., VESTERGAARD, M., WANDEL, A. Central Masses and Broad-Line Region Sizes of Active Galactic Nuclei. II. A Homogeneous Analysis of a Large Reverberation-Mapping Database. **Astrophysical Journal**, v. 613, p. 682–699, October 2004.
- [101] PETERSON, B. M., WANDEL, A. Evidence for Supermassive Black Holes in Active Galactic Nuclei from Emission-Line Reverberation. **Astrophysical Journal Letters**, v. 540, p. L13–L16, September 2000.
- [102] PETTINI, MAX, PAGEL, BERNARD E. J. [OIII]/[NII] as an abundance indicator at high redshift. **Monthly Notices of the Royal Astronomical Society**, v. 348, n. 3, p. L59–L63, Mar 2004.
- [103] PILYUGIN, L. S. On the oxygen abundance determination in H<sub>2</sub> regions. The problem of the line intensities - oxygen abundance calibration. **Astronomy and Astrophysics**, v. 362, p. 325–332, October 2000.
- [104] PILYUGIN, L. S. On the oxygen abundance determination in HII regions. High-metallicity regions. **Astronomy and Astrophysics**, v. 369, p. 594–604, April 2001.
- [105] PILYUGIN, L. S., FERRINI, F., SHKVARUN, R. V. On the oxygen abundance in our Galaxy. **Astronomy and Astrophysics**, v. 401, p. 557–563, Apr 2003.
- [106] PILYUGIN, L. S., GREBEL, E. K. New calibrations for abundance determinations in H II regions. **Monthly Notices of the Royal Astronomical Society**, v. 457, n. 4, p. 3678–3692, Apr 2016.
- [107] REES, M. J. Black Hole Models for Active Galactic Nuclei. **Annual Review of Astronomy and Astrophysics**, v. 22, p. 471–506, 1984.
- [108] REMBOLD, S. B., SHIMOIA, J. S., STORCHI-BERGMANN, T., RIFFEL, R., RIFFEL, R. A., MALLMANN, N. D., DO NASCIMENTO, J. C., MOREIRA,

T. N., ILHA, G. S., MACHADO, A. D., CIROLINI, R., DA COSTA, L. N., MAIA, M. A. G., SANTIAGO, B. X., SCHNEIDER, D. P., WYLEZALEK, D., BIZYAEV, D., PAN, K., MÜLLER-SÁNCHEZ, F. The first 62 AGNs observed with SDSS-IV MaNGA - I. Their characterization and definition of a control sample. **Monthly Notices of the Royal Astronomical Society**, v. 472, p. 4382–4403, December 2017.

- [109] RICHARDSON, C. T., ALLEN, J. T., BALDWIN, J. A., HEWETT, P. C., FERLAND, G. J. Interpreting the ionization sequence in AGN emission-line spectra. **Monthly Notices of the Royal Astronomical Society**, v. 437, p. 2376–2403, January 2014.
- [110] RIFFEL, R., RIFFEL, R. A., FERRARI, F., STORCHI-BERGMANN, T. Intermediate-age stars as the origin of low stellar velocity dispersion nuclear rings: the case of Mrk 1157. **Monthly Notices of the Royal Astronomical Society**, v. 416, p. 493–500, September 2011.
- [111] RIFFEL, R. A., STORCHI-BERGMANN, T., RIFFEL, R. Feeding versus feedback in active galactic nuclei from near-infrared integral field spectroscopy - X. NGC 5929. **Monthly Notices of the Royal Astronomical Society**, v. 451, p. 3587–3605, August 2015.
- [112] RIFFEL, R. A., STORCHI-BERGMANN, T., WINGE, C., MCGREGOR, P. J., BECK, T., SCHMITT, H. Mapping of molecular gas inflow towards the Seyfert nucleus of NGC4051 using Gemini NIFS. **Monthly Notices of the Royal Astronomical Society**, v. 385, p. 1129–1142, April 2008.
- [113] ROLLESTON, W. R. J., SMARTT, S. J., DUFTON, P. L., RYANS, R. S. I. The Galactic metallicity gradient. **Astronomy and Astrophysics**, v. 363, p. 537–554, November 2000.
- [114] ROSARIO, D. J., BURTSCHER, L., DAVIES, R. I., KOSS, M., RICCI, C., LUTZ, D., RIFFEL, R., ALEXANDER, D. M., GENZEL, R., HICKS, E. H., LIN, M.-Y., MACIEJEWSKI, W., MÜLLER-SÁNCHEZ, F., ORBAN DE XIVRY, G., RIFFEL, R. A., SCHARTMANN, M., SCHAWINSKI, K., SCHNORR-MÜLLER, A., SAINTONGE, A., SHIMIZU, T., STERNBERG, A., STORCHI-BERGMANN, T., STURM, E., TACCONI, L., TREISTER, E., VEILLEUX, S. LLAMA: normal star formation efficiencies of molecular gas in the centres of luminous Seyfert galaxies. **Monthly Notices of the Royal Astronomical Society**, v. 473, p. 5658–5679, February 2018.

- [115] RUPKE, D. S. N., VEILLEUX, S. The Multiphase Structure and Power Sources of Galactic Winds in Major Mergers. **Astrophysical Journal**, v. 768, p. 75, May 2013.
- [116] RUPKE & VEILLEUX, S. Integral Field Spectroscopy of Massive, Kiloparsec-scale Outflows in the Infrared-luminous QSO Mrk 231. **Astrophysical Journal Letters**, v. 729, p. L27, March 2011.
- [117] SALOMÉ, P., COMBES, F., EDGE, A. C., CRAWFORD, C., ERLUND, M., FABIAN, A. C., HATCH, N. A., JOHNSTONE, R. M., SANDERS, J. S., WILMAN, R. J. Cold molecular gas in the Perseus cluster core. Association with X-ray cavity, H $\alpha$  filaments and cooling flow. **Astronomy and Astrophysics**, v. 454, p. 437–445, August 2006.
- [118] SALOMÉ, P., COMBES, F., REVAZ, Y., EDGE, A. C., HATCH, N. A., FABIAN, A. C., JOHNSTONE, R. M. Cold gas in the Perseus cluster core: excitation of molecular gas in filaments. **Astronomy and Astrophysics**, v. 484, p. 317–325, June 2008.
- [119] SALPETER, E. E. Accretion of Interstellar Matter by Massive Objects. **Astrophysical Journal**, v. 140, p. 796–800, August 1964.
- [120] SANCHEZ, S. F., AVILA-REESE, V., HERNANDEZ-TOLEDO, H., CORTES-SUAREZ, E., RODRIGUEZ-PUEBLA, A., IBARRA-MEDEL, H., CANO-DIAZ, M., BARRERA-BALLESTEROS, J. K., NEGRETE, C. A., CALLETTE, A. R., DE LORENZO-CACERES, A., ORTEGA-MINAKATA, R. A., AQUINO, E., VALENZUELA, O., CLEMENTE, J. C., STORCHI-BERGMANN, T., RIFFEL, R., SCHIMOIA, J., RIFFEL, R. A., REMBOLD, S. B., BROWNSTEIN, J. R., PAN, K., YATES, R., MALLMANN, N., BITSAKIS, T. SSDSS IV MaNGA - Properties of AGN host galaxies. **ArXiv e-prints**, v. 1, September 2017.
- [121] SARGENT, W. L. W., YOUNG, P. J., LYNNDS, C. R., BOKSENBERG, A., SHORTRIDGE, K., HARTWICK, F. D. A. Dynamical evidence for a central mass concentration in the galaxy M87. **Astrophysical Journal**, v. 221, p. 731–744, May 1978.
- [122] SARZI, M., ALLARD, E. L., KNAPEN, J. H., MAZZUCA, L. M. Star formation and stellar populations across nuclear rings in galaxies. **Monthly Notices of the Royal Astronomical Society**, v. 380, p. 949–962, September 2007.

- [123] SCHMITT, H. R., DONLEY, J. L., ANTONUCCI, R. R. J., HUTCHINGS, J. B., KINNEY, A. L. A Hubble Space Telescope Survey of Extended [O III]  $\lambda$ 5007 Emission in a Far-Infrared Selected Sample of Seyfert Galaxies: Observations. **Astrophysical Journal Supplement Series**, v. 148, p. 327–352, October 2003a.
- [124] SCHMITT, H. R., DONLEY, J. L., ANTONUCCI, R. R. J., HUTCHINGS, J. B., KINNEY, A. L., PRINGLE, J. E. A Hubble Space Telescope Survey of Extended [O III]  $\lambda$ 5007 Å Emission in a Far-Infrared-Selected Sample of Seyfert Galaxies: Results. **Astrophysical Journal**, v. 597, p. 768–779, November 2003b.
- [125] SCHNEIDER, P. **Extragalactic Astronomy and Cosmology: An Introduction:** 2015.
- [126] SCHNORR-MÜLLER, A., STORCHI-BERGMANN, T., NAGAR, N. M., ROBINSON, A., LENA, D., RIFFEL, R. A., COUTO, G. S. Feeding and feedback in the inner kiloparsec of the active galaxy NGC 2110. **Monthly Notices of the Royal Astronomical Society**, v. 437, p. 1708–1724, January 2014.
- [127] SCHNORR MÜLLER, A., STORCHI-BERGMANN, T., RIFFEL, R. A., FERRARI, F., STEINER, J. E., AXON, D. J., ROBINSON, A. Gas streaming motions towards the nucleus of M81. **Monthly Notices of the Royal Astronomical Society**, v. 413, p. 149–161, May 2011.
- [128] SILVERMAN, J. D., GREEN, P. J., BARKHOUSE, W. A., KIM, D.-W., KIM, M., WILKES, B. J., CAMERON, R. A., HASINGER, G., JANNUZI, B. T., SMITH, M. G., SMITH, P. S., TANANBAUM, H. The Luminosity Function of X-Ray-selected Active Galactic Nuclei: Evolution of Supermassive Black Holes at High Redshift. **Astrophysical Journal**, v. 679, p. 118–139, May 2008.
- [129] SIMÕES LOPES, R. D., STORCHI-BERGMANN, T., DE FÁTIMA SARAIVA, M., MARTINI, P. A Strong Correlation between Circumnuclear Dust and Black Hole Accretion in Early-Type Galaxies. **Astrophysical Journal**, v. 655, p. 718–734, February 2007.
- [130] SMEE, S. A., GUNN, J. E., UOMOTO, A., ROE, N., SCHLEGEL, D., ROCKOS, C. M., CARR, M. A., LEGER, F., DAWSON, K. S., OLMSTEAD, M. D., BRINKMANN, J., OWEN, R., BARKHouser, R. H., HONScheid,

K., HARDING, P., LONG, D., LUPTON, R. H., LOOMIS, C., ANDERSON, L., ANNIS, J., BERNARDI, M., BHARDWAJ, V., BIZYAEV, D., BOLTON, A. S., BREWINGTON, H., BRIGGS, J. W., BURLES, S., BURNS, J. G., CASTANDER, F. J., CONNOLLY, A., DAVENPORT, J. R. A., EBELKE, G., EPPS, H., FELDMAN, P. D., FRIEDMAN, S. D., FRIEMAN, J., HECKMAN, T., HULL, C. L., KNAPP, G. R., LAWRENCE, D. M., LOVEDAY, J., MANNERY, E. J., MALANUSHENKO, E., MALANUSHENKO, V., MERRELLI, A. J., MUNA, D., NEWMAN, P. R., NICHOL, R. C., ORAVETZ, D., PAN, K., POPE, A. C., RICKETTS, P. G., SHELDEN, A., SANDFORD, D., SIEGMUND, W., SIMMONS, A., SMITH, D. S., SNEDDEN, S., SCHNEIDER, D. P., SUBBARAO, M., TREMONTI, C., WADDELL, P., YORK, D. G. The Multi-object, Fiber-fed Spectrographs for the Sloan Digital Sky Survey and the Baryon Oscillation Spectroscopic Survey. **Astronomical Journal**, v. 146, p. 32, August 2013.

- [131] SOMERVILLE, R. S., HOPKINS, P. F., COX, T. J., ROBERTSON, B. E., HERNQUIST, L. A semi-analytic model for the co-evolution of galaxies, black holes and active galactic nuclei. **Monthly Notices of the Royal Astronomical Society**, v. 391, p. 481–506, December 2008.
- [132] STORCHI-BERGMANN & SCHNORR-MÜLLER, . Observational constraints on the feeding of supermassive black holes. **Nature Astronomy**, v. 3, p. 48–61, Jan 2019.
- [133] STORCHI-BERGMANN, T., DALL'AGNOL DE OLIVEIRA, B., LONGO MICCHI, L. F., SCHMITT, H. R., FISCHER, T. C., KRAEMER, S., CRENSHAW, M., MAKSYM, P., ELVIS, M., FABBIANO, G., COLINA, L. Bipolar Ionization Cones in the Extended Narrow-line Region of Nearby QSO2s. **The Astrophysical Journal**, v. 868, n. 1, p. 14, Nov 2018.
- [134] STORCHI-BERGMANN, T., LOPES, R. D. S., MCGREGOR, P. J., RIFFEL, R. A., BECK, T., MARTINI, P. Feeding versus feedback in NGC4151 probed with Gemini NIFS - II. Kinematics. **Monthly Notices of the Royal Astronomical Society**, v. 402, p. 819–835, February 2010.
- [135] STORCHI-BERGMANN, T., MCGREGOR, P. J., RIFFEL, R. A., SIMÕES LO-PES, R., BECK, T., DOPITA, M. Feeding versus feedback in NGC4151 probed with Gemini NIFS - I. Excitation. **Monthly Notices of the Royal Astronomical Society**, v. 394, p. 1148–1166, April 2009.

- [136] STORCHI-BERGMANN, THAISA, SCHMITT, HENRIQUE R., CALZETTI, DANIELA, KINNEY, ANNE L. Chemical Abundance Calibrations for the Narrow-Line Region of Active Galaxies. **Astronomical Journal**, v. 115, n. 3, p. 909–914, Mar 1998.
- [137] UNGER, S. W., PEDLAR, A., AXON, D. J., WHITTLE, M., MEURS, E. J. A., WARD, M. J. The extended narrow-line region in radio Seyferts - Evidence for a collimated nuclear UV field? **Monthly Notices of the Royal Astronomical Society**, v. 228, p. 671–679, October 1987.
- [138] URRY, C. M., PADOVANI, P. Unified Schemes for Radio-Loud Active Galactic Nuclei. **Publications of the Astronomical Society of the Pacific**, v. 107, p. 803, September 1995.
- [139] VALE ASARI, N., STASÍNSKA, G., MORISSET, C., CID FERNANDES, R. BOND: Bayesian Oxygen and Nitrogen abundance Determinations in giant H II regions using strong and semistrong lines. **Monthly Notices of the Royal Astronomical Society**, v. 460, p. 1739–1757, August 2016.
- [140] VEILLEUX, S., OSTERBROCK, D. E. Spectral classification of emission-line galaxies. **Astrophysical Journal Supplement Series**, v. 63, p. 295–310, February 1987.
- [141] WARNER, C., HAMANN, F., SHIELDS, J. C., CONSTANTIN, A., FOLTZ, C. B., CHAFFEE, F. H. The Metallicity of the Redshift 4.16 Quasar BR 2248-1242. **Astrophysical Journal**, v. 567, p. 68–72, March 2002.
- [142] WEEDMAN, D. W. High-Velocity Gas Motions in Galactic Nuclei. **Astrophysical Journal**, v. 159, p. 405, February 1970.
- [143] WYLEZALEK, D., ZAKAMSKA, N. L. Evidence of suppression of star formation by quasar-driven winds in gas-rich host galaxies at  $z \geq 1$ ? **Monthly Notices of the Royal Astronomical Society**, v. 461, p. 3724–3739, October 2016.
- [144] WYLEZALEK, D., ZAKAMSKA, N. L., GREENE, J. E., RIFFEL, R. A., DRORY, N., ANDREWS, B. H., MERLONI, A., THOMAS, D. SDSS-IV MaNGA: identification of active galactic nuclei in optical integral field unit surveys. **Monthly Notices of the Royal Astronomical Society**, v. 474, p. 1499–1514, February 2018.

- [145] WYLEZALEK, D., ZAKAMSKA, N. L., LIU, G., OBIED, G. Towards a comprehensive picture of powerful quasars, their host galaxies and quasar winds at  $z \sim 0.5$ . **Monthly Notices of the Royal Astronomical Society**, v. 457, p. 745–763, March 2016.
- [146] ZUBOVAS, K., BOURNE, M. A. Do AGN outflows quench or enhance star formation? **Monthly Notices of the Royal Astronomical Society**, v. 468, p. 4956–4967, July 2017.
- [147] ZUBOVAS & KING, . Clearing Out a Galaxy. **Astrophysical Journal Letters**, v. 745, p. L34, February 2012.